ANISOTROPIC RESPONSE OF LASER ADDITIVELY MANUFACTURED NUCLEAR ALLOYS TO RADIATION DAMAGE

A Dissertation

by

JORDAN ANDREW EVANS

Submitted to the Office of Graduate and Professional Studies of
Texas A&M University
in partial fulfillment of the requirements for the degree of

DOCTOR OF PHILOSOPHY

Chair of Committee,	Sean M. McDeavitt
Committee Members,	Lin Shao
	Pavel V. Tsvetkov
	Delia Perez-Nunez
	Patrick J. Shamberger
Head of Department,	Ibrahim Karaman

December 2017

Major Subject: Materials Science and Engineering

ABSTRACT

The impact of radiation-induced effects on the properties of alloys fabricated using additive manufacturing (AM) was evaluated through the implementation of ion beam irradiation testing followed by electron backscatter diffraction (EBSD), scanning electron microscopy (SEM) with energy dispersive spectroscopy (EDS), nanoindentation, scanning probe microscopy (SPM), and transmission electron microscopy (TEM). Inconel 600 (I600) and 316L stainless steel (316L) rods were fabricated by Quad City Manufacturing Laboratory in collaboration with Lockheed Martin for this study. The rods were produced in three distinct orientations (vertical, horizontal, and 45°) using laser additive manufacturing (LAM). Conventionally manufactured I600 and 316L rods were purchased from Metal Samples, Inc. to enable comparative studies. The I600 and 316L LAM specimens were heat treated to 900 °C and 650 °C in argon with no cold working, respectively. Similarly, the conventionally manufactured I600 and 316L control specimens were cold rolled and annealed at 980 °C and 1040 °C in argon with no cold working, respectively.

XRD of unirradiated specimens showed differences in peak ratios between build orientations, indicating anisotropic grain structures for samples fabricated by LAM. All LAM rods contained significantly fewer coincidence site lattice (CSL) boundaries and more residual strain compared to the controls before and after irradiation, regardless of build direction, as determined by EBSD. Material performance parameters such as resistance to radiation-enhanced embrittlement, corrosion, creep, intergranular stress

corrosion cracking, and hydrogen-induced cracking were inferred from CSL theory, which suggests that all LAM rods are more susceptible to grain boundary-related failure mechanisms than their conventionally manufactured counterparts. All alloys built by LAM are strongly textured with <101> parallel to the build direction before and after irradiation. Directionally dependent Taylor Factor distributions suggest that resistance to slip depends on build direction where, from highest to lowest resistance: horizontal > 45° > vertical.

All I600 samples experienced radiation-induced segregation which, according to SEM/EDS and SPM studies, resulted in the formation of chromium carbide precipitates on to the irradiated surfaces. Strong anisotropic mechanical behavior was observed in the LAM rods, as measured by nanoindentation and bulk tensile testing. The hardness of the unirradiated as-annealed specimens, from greatest to least, is: horizontal > 45° > vertical. The radiation-induced hardening of LAM specimens, from greatest to least, is: horizontal > 45° > vertical. The orientation dependence of radiation-induced segregation and hardening mechanisms is discussed.

The ultimate outcome of this work is a first-of-a-kind high-dose radiation damage study of alloys fabricated by LAM, revealing that the radiation-induced changes in material properties for these alloys is dependent upon build orientation.

ACKNOWLEDGEMENTS

I would like to thank my PhD advisor, Dr. Sean McDeavitt, for his guidance and mentorship. Under the tutelage of Dr. McDeavitt, I not only became a better engineer, but I became a better person. Dr. McDeavitt encouraged me to pursue engineering endeavors not directly related to my research obligations, trusting that I would not get distracted from my work at the Texas A&M Fuel Cycle and Materials Laboratory (FCML) to which I was dedicated.

This research was a collaborative effort, and I am thankful to all those involved. I would to thank Dr. Lin Shao for the use of his ion beam accelerators at the Texas A&M Accelerator Laboratory, and Mr. Jonathan Gigax for guidance in performing the ion beam irradiations. I would like to thank Dr. Delia Perez-Nunez for her guidance and work throughout my graduate studies, both directly related to my research and in general at the FCML. I thank Dr. Luis Ortega of the TAMU FCML for his guidance and support through my time at the FCML, and particularly for his guidance in performing SEM/EDS. I thoroughly enjoyed working with and getting to know the members of the FCML.

I would like to thank my friends and family throughout my graduate studies, especially my friends Spencer Mickum, Michael Hackemack, and Ben Sheppard, my parents Wayne and Gesine Evans, and my brothers Justin and Joshua Evans. Most of all, I would like to thank my wife, Maria Evans, for her patience, understanding, and unwavering support throughout my graduate studies.

DEDICATION

I consider myself a perfectionist. There are very few things that I view to be perfect. My wife is the one clear exception. This document likely would not have had the opportunity to exist without her support, and it certainly would not have the same quality or significance without her. This dissertation is dedicated to Maria Evans.

CONTRIBUTORS AND FUNDING SOURCES

This work was supervised by a dissertation committee consisting of (advisor) Professor Sean McDeavitt and Professor Lin Shao of the Departments of Materials Science and Engineering and Nuclear Engineering, Professor Patrick Shamberger of the Department of Materials Science and Engineering, and Professor Pavel Tsvetkov and Dr. Delia Perez-Nunez of the Department of Nuclear Engineering.

Rods were produced using laser additive manufacturing by Dr. Eric J. Faierson at the Quad City Manufacturing Laboratory. Ion beam irradiations were performed by the author with the guidance of Mr. Jonathan Gigax and Dr. Lin Shao of the Texas A&M Accelerator Laboratory, and neutron irradiations were performed by the author with the guidance of Mr. Jan Vermaak of the Texas A&M Nuclear Science Center. Energy dispersive spectroscopy was performed by the author with the guidance of Dr. Luis Ortega of the Texas A&M Fuel Cycle and Materials Laboratory. X-ray diffraction was performed by Dr. Joseph Reibenspies of the Texas A&M X-ray Diffraction Laboratory.

This work was supported by Lockheed Martin and the US Department of Energy under the Nuclear Energy Enabling Technologies – Advanced Manufacturing Methods (NEET-AMM) Initiative through grant number DE-NE0000542. Its contents are solely the responsibility of the author and do not necessarily represent the official views of Lockheed Martin or the US Department of Energy.

NOMENCLATURE

AFM	Atomic force microscopy
ALARA	As low as reasonably achievable
ASTM	American Society for Testing and Materials
ATF	Accident-tolerant nuclear fuel
Bcc	Body centered cubic
BFTEM	Bright field transmission electron microscopy
CAD	Computer aided design
CNT	Classical nucleation theory
Cps	Counts per second
CSDA	Continuously slowing down approximation
CSL	Coincidence site lattice
DBTT	Ductile to brittle transition temperature
DED	Direct energy deposition
DIC	Differential interference contrast microscopy
DMLS	Direct metal laser sintering
DOS	Density of states
DP	Diffraction pattern
Dpa	Displacements per atom
DS	Divergence slit
EAP	Equal area projection

EBM	Electron beam melting
EBR-II	Experimental Breeder Reactor II
EBSD	Electron backscatter diffraction
EBSP	Electron backscatter pattern
EDM	Electron discharge machining
EDS	Energy dispersive spectroscopy
ESTAR	Electron Stopping Powers and Ranges (database)
Fcc	Face centered cubic
FCML	Fuel Cycle and Materials Laboratory
FEM	Finite element method
F/M	Ferritic/martensitic
GAR	Grain aspect ratio
GBE	Grain boundary engineering
GIS	Gas injection system
GND	Geometrically necessary dislocations
HAADF	High angle annular dark field
HAZ	Heat affected zone
HIC	Hydrogen-induced cracking
IGSCC	Intergranular stress corrosion cracking
IPA	Isopropyl alcohol
IPF	Inverse pole figure
ISE	Indentation size effect

KAM	Kernel average misorientation
LAM	Laser additive manufacturing
LENS	Laser engineered net-shaping
LMIS	Liquid metal ion source
LPS	Liquid phase sintering
MA	Mechanical alloying
MAD	Mean angular deviation
MSEN	Department of Materials Science and Engineering
MUD	Multiple of uniform density
NIST	National Institute of Standards and Technology
NM	Nanomanipulator
NSC	Nuclear Science Center
NUEN	Department of Nuclear Engineering
OCC	Overnight construction costs
ODS	Oxide dispersion strengthened
PBF	Powder bed fusion
PCD	Polycrystalline diamond
PF	Pole figure
PIE	Post-irradiation examination
PKA	Primary knock-on atom
PPE	Personal protective equipment
QCML	Quad City Manufacturing Laboratory

RF	Rodrigues-Frank
RMS	Root mean square
SADP	Single area diffraction pattern
SEM	Scanning electron microscopy
SFR	Sodium cooled fast reactor
RGB	Red/green/blue (color mapping)
SLS	Selective laser sintering
SPM	Scanning probe microscopy
SRIM	Stopping and Range of Ions in Matter (computational code)
SSP	Standard stereographic projection
STEM	Scanning transmission electron microscopy
STL	Stereolithography
TAMU	Texas A&M University
TEM	Transmission electron microscopy
TRIGA	Training, Research, Isotopes, General Atomics (nuclear reactor)
USNCDDP	United States National Cladding and Duct Development Program
XRD	X-ray diffraction

TABLE OF CONTENTS

Page

LIST OF FIGURES

Page

LIST OF TABLES

Page

CHAPTER I

INTRODUCTION

I.1 Project Objectives and Significance

The objective of this project was to investigate the impact of additive manufacturing induced microstructure orientation on the radiation response of several alloys produced conventionally and by additive manufacturing (AM). Additive manufacturing offers a potentially cost- and time-efficient alternative to conventional manufacturing methods of nuclear materials [1]. In particular, this project seeks to explore (1) the radiation-induced microstructural evolution, (2) radiation-induced changes in mechanical properties, and (3) grain boundary character which indicates changes in resistance to detrimental phenomena such as hydrogen-induced cracking (HIC), intergranular stress-corrosion cracking (IGSCC), and creep of additively manufacturing alloys. Based on an understanding of the fundamental mechanisms behind these changes, modifications have been recommended to additive manufacturing build procedures to improve as-fabricated properties.

Previous research studies have concluded that AM technology will have profound impacts on manufacturing, businesses, and society as a whole [2]. The Royal Academy of Engineering described AM as a disruptive technology "that has the potential to replace many conventional manufacturing processes, but is also an enabling technology allowing new business models, new products, and new supply chains to flourish" [2]. Studies have shown that the main expense in AM is the investment cost of

the AM machine itself, the cost of which continues to decrease as the technology matures [3, 4]. The reduction in cost achieved by utilizing additive manufacturing varies widely depending on many variables such as component material, size, and additive manufacturing method [5]. The overnight construction costs (OCC) represent the largest component of the total levelized cost of generating electricity with nuclear power at approximately 55% [6]. A significant portion of the OCC of nuclear reactors is associated with the manufacturing, assembly, and qualification of components and structural materials [6].

Materials in nuclear energy systems must perform and survive in extreme conditions under large stresses, high temperatures, and high energy density radiation fields. The intensity of these performance-limiting conditions are being pushed to more extreme levels in advanced system designs seeking to operate for longer times at higher temperatures in increasingly more aggressive chemical and mechanical conditions [7]. Nuclear reactor materials become susceptible to hardening and embrittlement when exposed to high temperatures and radiation fields for extended periods of time [8]. The United States National Cladding and Duct Development Program (USNCDDP) provides a comprehensive review of advanced materials development studies which focus on irradiation effects in three classes of materials: austenitic alloys, ferritic alloys, and precipitation hardened Fe-Ni alloys [9].

Additive manufactured offers a potentially cost- and time-efficient alternative to conventional manufacturing for nuclear materials. Fabricating materials using AM involves large spatial and temporal temperature gradients. As a result, alloys produced

by additive manufacturing can have elongated oriented grain structures characterized by significant texture and residual stress fields [10, 11]. In order to enable additively manufactured materials for service in nuclear energy systems, the impact of fabrication-specific characteristics on component microstructures and potential radiation-exacerbated phenomena must be understood.

I.2 Project Timeline

The work reported here was part of a larger study sponsored by Lockheed Martin where laser additively manufactured (LAM) rods were fabricated at the Quad City Manufacturing Laboratory (Rock Island, Illinois) in three different orientations (vertical, horizontal, and 45°) to study the directionally dependent effects of the laser manufacturing process on radiation response. High dose neutron damage was simulated using ions. The Inconel samples were irradiated using Ni^{+} self-ions to 80 dpa, and the steel samples were irradiated using Fe^{2+} self-ions to 80 dpa. Their microstructural and mechanical properties were characterized using x-ray diffraction (XRD), scanning electron microscopy (SEM) with energy dispersive spectroscopy (EDS), scanning probe microscopy (SPM), nanoindentation, electron backscatter diffraction (EBSD), and transmission electron microscopy (TEM). Conventionally manufactured rods were purchased from a commercial vendor for control. The Inconel 600 and 316L stainless steel samples were also irradiated with neutrons in the 1 MW TRIGA Reactor at the Nuclear Science Center (NSC) at Texas A&M University (TAMU). The damage rate due to the neutron field in this reactor is extremely low, orders of magnitude less than 1

dpa (displacement per atom) per year; the TRIGA Reactor samples were still undergoing neutron irradiation at the time this dissertation was written, and remain outstanding for future study. The overall irradiation campaign proceeded according to the schedule presented in Figure 1.

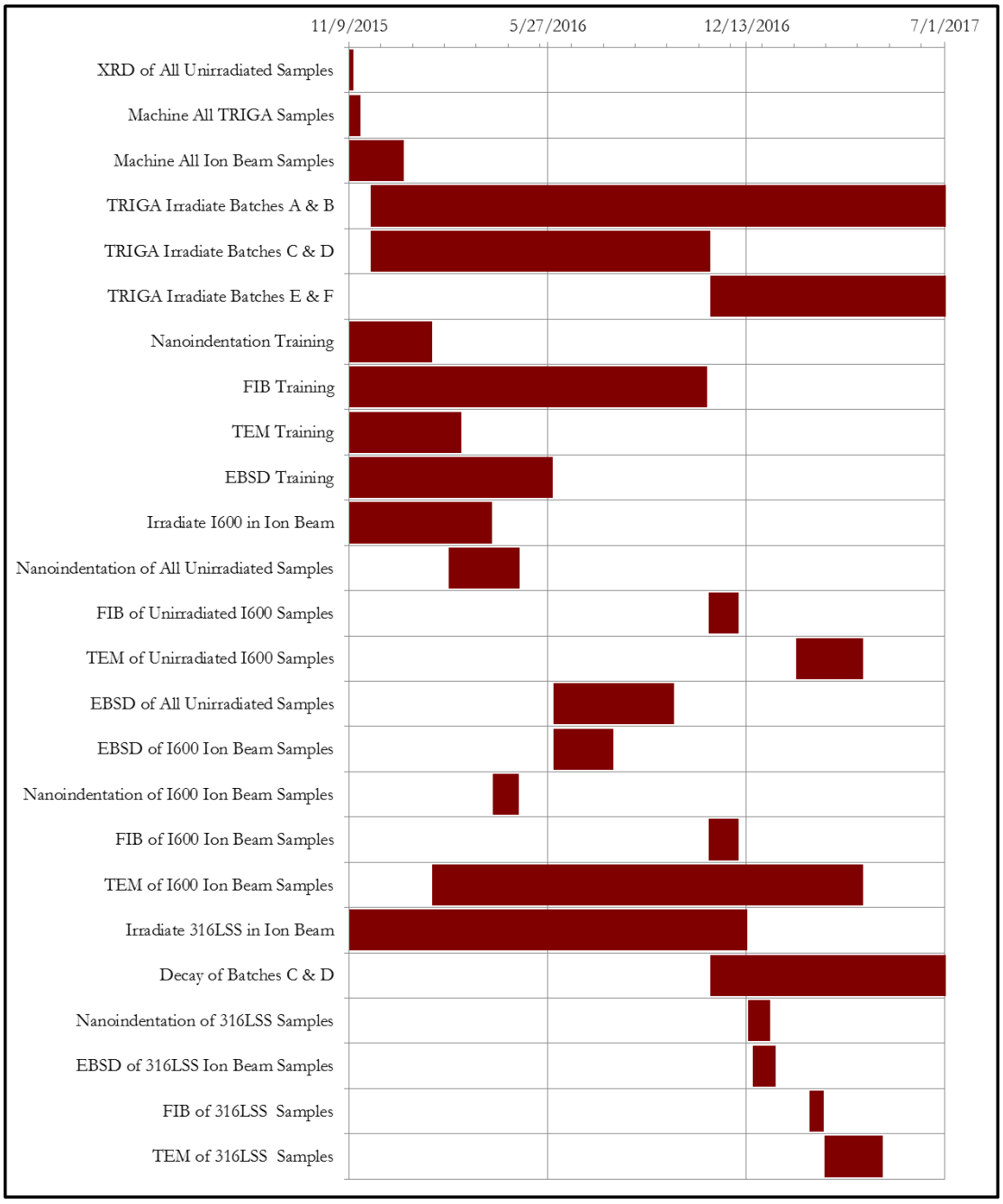

Figure 1: Project Gantt Chart

I.3 Overview of Current Work

The fundamental outcome of this work is the discovery of build orientation dependence associated with typically isotropic radiation-induced effects, such as radiation-induced hardening and radiation-induced segregation, in 316L stainless steel and Inconel 600 built by LAM. This work constitutes a major advancement in the understanding of the behavior of alloys built by LAM in a high dose radiative environment.

This document is organized as follows. Chapter II presents the relevant background context for the laser additive manufacturing process, radiation damage and radiation effects in materials, a description of the alloys under investigation, and a discussion of the characterization techniques utilized in this research: electron backscatter diffraction, scanning electron microscopy with energy dispersive spectroscopy, nanoindentation, scanning probe microscopy, and transmission electron microscopy.

Chapter III presents the experimental and computational methods in this work, including the LAM build process and heat treatment protocols, sample preparation, irradiation, and post-irradiation examinations (PIE). Chapter IV details the experimental results of the various PIE techniques: x-ray diffraction, optical microscopy, scanning electron microscopy, nanoindentation, scanning probe microscopy, electron backscatter diffraction, and transmission electron microscopy. Chapter V presents a discussion of these results by relating measured quantities to relevant material properties (such as hardness to yield strength), relating grain boundary character to common mechanical

failure mechanisms, discussing the mechanisms which cause anisotropic radiation-induced changes in the alloys, and discussing the thermodynamic processes which produce anisotropic properties and microstructures in alloys built by LAM. Chapter VI presents the conclusions of the work, and offers several recommendations for future work. Computational codes used to simulate Taylor factors in fcc crystals and radioactive species produced in the neutron-irradiated alloys in the TAMU TRIGA Reactor are provided in the Appendix, as well as metallurgical test reports of the conventionally manufactured controls. Chapter VI presents conclusions of the project and includes recommendations for future work.

CHAPTER II

BACKGROUND

Chapter II presents the relevant background information for the laser additive manufacturing process, radiation damage and radiation effects in materials, the alloys under investigation, and the characterization methods utilized in this work.

II.1 Laser Additive Manufacturing

Additive manufacturing, also known as 3D printing, has emerged as a viable fabrication tool to create components in complicated geometries for technological applications. A variety of additive manufacturing methods exist for the fabrication of alloys, such as laser additive manufacturing (LAM) and electron beam melting (EBM) [12]. Both LAM and EBM can be powder bed fusion (PBF) processes when alloys are fabricated from a feedstock bed of powder in a stepwise manner. Inconel 600 and 316L stainless steel rods were fabricated by LAM PBF in this work. In PBF, a stationary bed of metal powder is added to a stage and sintered, either by using a laser or an electron beam, layer-by-layer, into a predetermined geometry from a three dimensional computer-aided design (3D CAD) model. The LAM technique has been shown to produce excellent feature resolution and has the capability to create components with complex geometries, such as the waveguide brackets currently on board the Juno spacecraft, or the sheer tie fittings on board the A2100 satellite [13-15].

A brief discussion on additive manufacturing technology will be provided here. There are several key steps involved in the AM process illustrated in Figure 2: (1) design of the AM part using CAD software, (2) conversion of the CAD design to stereolithography (STL) format in which the external closed surfaces of the CAD model are described, (3) transfer of the STL file to the AM machine in which manipulation (sizing, positioning, orientation, etc.) may be necessary, (4) machine setup (material loading, energy source, layer thickness, timings/switches, etc.), (5) building of the AM part, (6) remove of the AM-built part, (7) post-processing of the part (cleaning, polishing, removal of support features, etc.), and (8) assembly and application of the parts for use [16].

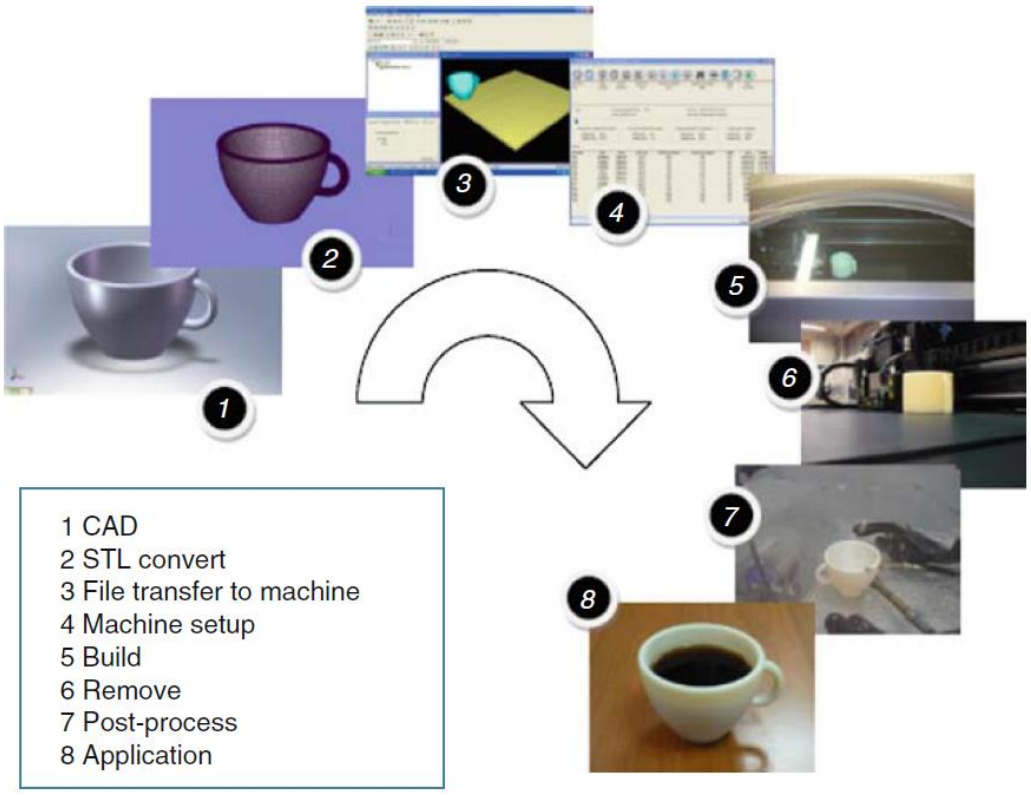

Figure 2: Illustration of Additive Manufacturing Processing Steps (Reprinted from [16])

There are four possible binding mechanisms in powder bed fusion: (1) solid state sintering, (2) chemically induced binding, (3) liquid phase sintering (LPS, aka partial melting), and (4) full melting. Full melting was utilized to fabricate the rods in this project, as is the case for most engineering alloys (titanium, steels, CoCr, etc.); however, multiple mechanisms are present during full melting [16].

Powder bed fusion additive manufacturing requires enough powder to fill the powder bed. Alternatively, laser engineered net-shaping (LENS) manufacturing method is available whereby powder is injected through a nozzle that also houses the laser. Due

to the low abundance of available powders, the ODS samples were fabricated using a LENS system. A schematic illustrating the differences between the PBF and LENS systems is shown in Figure 3 [16].

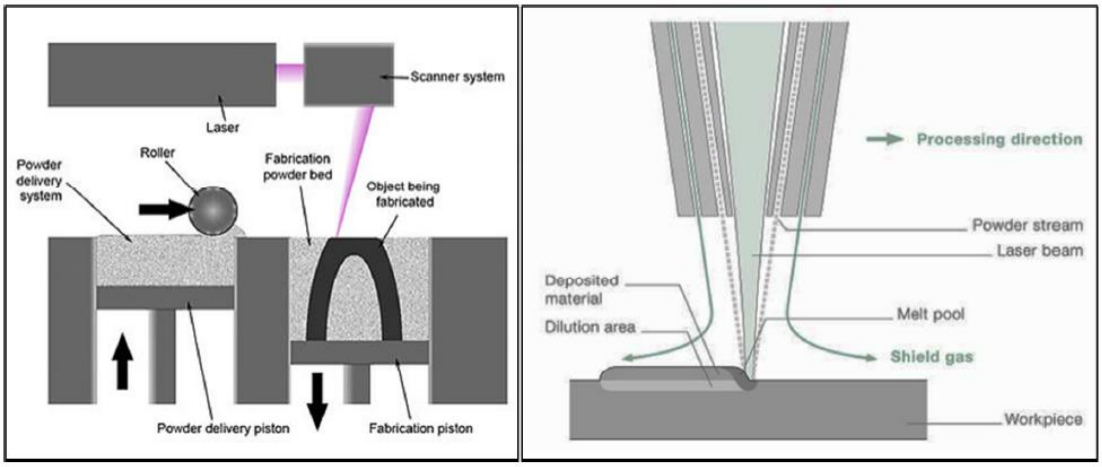

Figure 3: Illustrations of PBF System Used to Make Inconel 600 and 316L Stainless Steel Rods (Left) and LENS System Used to Make ODS Rods (Right)
(Reprinted from [16])

Microstructural properties of materials produced by LAM can vary widely depending on manufacturing conditions. Of particular note is the importance of thermal gradients during LAM. The rate at which energy is added to the powder and the rate at which thermal energy dissipates from the cooling specimen are critical parameters for the residual stress and porosity of the finished piece. In general, higher temperatures of the alloy melt result in better wetting conditions and therefore lower porosity of the finished piece, while higher cooling rates associated with these higher temperatures also tend to result in higher residual strain within the microstructure of the built part [17-19].

II.2 Alloys under Investigation

II.2.1 Inconel 600

The Inconel 600 and 316L stainless steel AM rods fabricated for this research were produced by powder bed fusion via direct metal laser sintering (DMLS) of the mixed powders using an EOS M270 Extended-Titanium system. Inconel 600 is a nickel-based austenitic (fcc) solid solution-hardened superalloy used in the chemical and nuclear applications due to its corrosion resistance and mechanical property retention at high temperatures. Inconel 600 is not precipitation hardenable, but can be hardened by cold work [20]. The precipitated phases that form in Inconel 600 are TiN and chromium/titanium carbides (M_7C_3 and $M_{23}C_6$). At high temperatures, Inconel 600 is susceptible to intergranular attack in corrosive media due to chromium carbide precipitation occurring both in the matrix and at grain boundaries [21]. Similar to other austenitic superalloys, this susceptibility tends to be exacerbated under exposure to radiation damage. In practice, Inconel 600 coiled flux detectors tend to fail after 5-10 years of use in commercial nuclear reactors after suffering from radiation-induced swelling, hardening, and embrittlement [22].

In order to explore potential differences in material properties due to build direction, LAM specimens were built in three different directions: horizontal, vertical, and 45°, shown below in Figure 4 (with permission from Lockheed Martin from an unpublished report). The LAM process parameters, namely laser power and scan speed, were varied and optimized to obtain maximum rod density. Four different laser powers were evaluated: 150 W, 175 W, 185 W, and 195 W, and seven scan speeds were

evaluated: 800 $mm \cdot s^{-1}$, 900 $mm \cdot s^{-1}$, 1000 $mm \cdot s^{-1}$, 1100 $mm \cdot s^{-1}$, 1200 $mm \cdot s^{-1}$, 1300 $mm \cdot s^{-1}$, and 1400 $mm \cdot s^{-1}$. Trends confirmed that lower laser power and higher scan speed produce lower density rods.

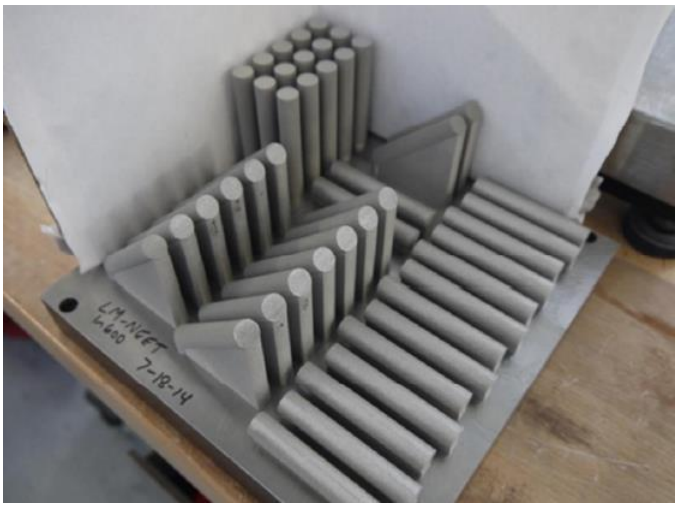

Figure 4: Vertical, Horizontal, and 45° Inconel 600 Rods Produced by LAM

At a laser power of 195 W, the Inconel 600 rods were insensitive to laser scan speed. The Inconel 600 samples were built using a laser power of 195 W and a scan speed of 1100 $mm \cdot s^{-1}$. The average density of LAM Inconel 600 rods was approximately 8.370 $g \cdot cm^{-3}$ (99% theoretical density) with a standard deviation of 0.013 $g \cdot cm^{-3}$. After production, LAM Inconel 600 rods were heat treated at 900 °C for 1 hour with no cold working. Conventionally manufactured Inconel 600 rods were purchased for control from a commercial vendor, Metal Samples Inc., and were solution-annealed by the vendor at 980 °C for 1 hour with no cold working after production as well.

All characterizations of the rods were performed on the face of the rods, perpendicular to the rod axis, as illustrated in Figure 5. As shown in Figure 5, the direction of characterization is parallel to the build direction for vertical LAM, perpendicular to the build direction for horizontal LAM, and at a 45° angle for the 45° LAM.

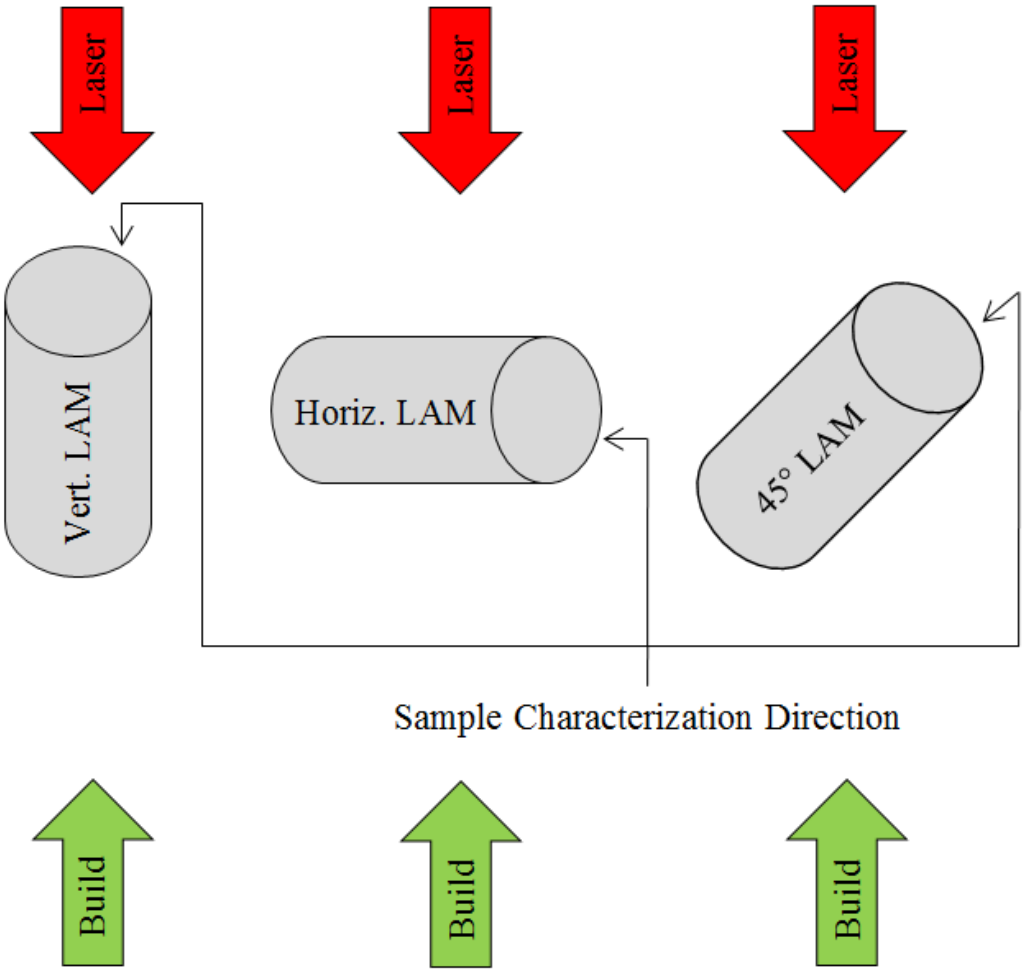

Figure 5: Illustration of Laser and LAM Rod Build Orientations and Sample Characterization Directions

II.2.2 316L Stainless Steel

316L stainless steel is an iron-based austenitic alloy which has high corrosion resistance, resistance to pitting, and superior mechanical property retention at high temperatures in comparison to 304 stainless steel. 316L has lower carbon content than 316 stainless steel, which reduces carbide precipitation during welding. 316L stainless steel rods were built using LAM in three different directions: horizontal, vertical, and 45°, shown in Figure 6 (with permission from Lockheed Martin from an unpublished report). A laser power of 195 W and scan speed of 1200 $mm \cdot s^{-1}$ were used to fabricate the rods. All 316L LAM rods were heat treated at 650 °C for 1 hour with no cold working. As with the Inconel rods, conventionally manufactured 316L stainless steel rods were purchased from Metal Samples Inc. for control. The conventional rods were solution-annealed at 1040 °C for 1 hour with no cold working. The orientations of 316L characterizations are identical to those of the Inconel rods (see Figure 5). Similarly, the direction of characterization is parallel to the build direction for vertical LAM, perpendicular to the build direction for horizontal LAM, and at a 45° angle for the 45° LAM.

Figure 6: Vertical, Horizontal, and 45° 316L Stainless Steel Rods Produced by LAM

II.2.3 Oxide Dispersion Strengthened Steel

316L-based oxide dispersion strengthened (ODS) stainless steel samples were built using laser additive manufacturing for this project, but were received a year after the I600 and 316L rods. Due to time constraints, the ODS rods were not irradiated and therefore will be discussed in the Appendix.

II.3 Radiation Damage and Radiation Effects

II.3.1 Radiation Damage

In order for LAM-derived materials to become qualified for service in a nuclear energy system, the impact of fabrication-specific characteristics of component microstructures and their possible interaction with irradiation-exacerbated phenomena that deviate from conventionally manufactured alloys must be characterized. Microstructure plays a critical role in establishing mechanical properties, and is

dependent on alloy composition, phase morphology, impurity content, and thermal history. Alloys created by LAM often have elongated oriented structures in comparison to the equiaxed coarser grain structures found in their conventionally manufactured counterparts [23]. Computational studies have attempted to simulate the mechanical and microstructural evolution of oriented fine grained materials exposed to high dose radiation damage to better understand the time scales, length scales, and phenomenological driving forces involved [24-26].

The energy in nuclear fuel is released as kinetic energy by nuclear fission; many different particles carry away this energy as kinetic energy. A detailed description of the average energies of particles released from thermal neutron induced fission is provided in Table 1, where γ are gamma rays (photons emitted from the nucleus), β are beta particles (electrons/positrons emitted from the nucleus), and ν are neutrinos/antineutrinos [27].

Table 1: Energy Released from Thermal Fission of ^{233}U, ^{235}U, and ^{239}Pu

	Radiative Particle	^{233}U	^{235}U	^{239}Pu
Instantaneous Released Energy (MeV·fission^{-1})	Fission Fragments	168.2	169.1	175.8
	Prompt Neutrons	4.9	4.8	5.9
	Prompt γ's	7.7	7.0	7.8
Delayed Released Energy (MeV·fission^{-1})	β	5.2	6.5	5.3
	ν	6.9	8.8	7.1
	Delayed γ's	5.0	6.3	5.2
	Delayed Neutrons	9.1	8.8	11.5
Total (MeV·fission^{-1})		207.0	211.3	218.6

For many nuclear energy systems, most of the fission products do not travel far enough to exit the solid fuel pellet/matrix and thus, never contact the cladding. The fission fragment yield spectra for ^{233}U, ^{235}U, and ^{239}Pu are illustrated in Figure 7 [28].

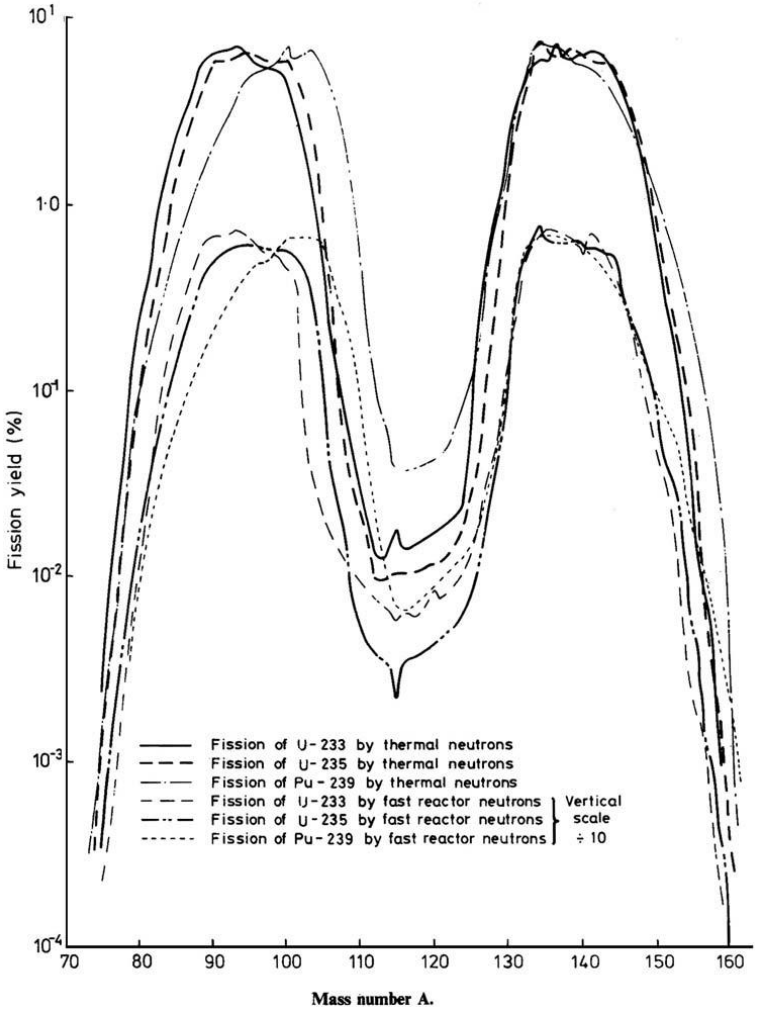

Figure 7: Fission Fragment Yield Spectra for ^{233}U, ^{235}U, and ^{239}Pu (Reprinted from [28])

Energetic particles released from a fission event that escape the solid fuel pellet/matrix can then interact with the cladding. Different types of radiation interact with materials in a variety of ways, and can be classified into two distinct categories: (1) indirectly ionizing radiation, and (2) directly ionizing radiation.

Indirectly ionizing radiation is any radiative emission which does not carry an electric charge. In a nuclear reactor, the three most abundant forms of indirectly ionizing radiation are photons (gamma-rays and x-rays), neutrons, and neutrinos/antineutrinos (ν). Although neutrinos do carry away a noticeable amount of energy from fission (see Table 1), they are ignored in terms of radiation damage or recoverable thermodynamic energy due to their lack of electrical charge and extremely small interaction cross section.

Photons and neutrons are particularly important when considering radiation damage to cladding, because they are capable of traveling long distances through material (i.e. through the fuel/coolant and into the cladding) before stopping. Photons have no electric charge, but can interact with and eject bound electrons (typically via the Compton or photoelectric effects). These ejected electrons are directly ionizing radiation, which will deposit energy as previously discussed [29]. As such, electromagnetic radiation deposits energy over a very long path length (centimeters to several meters), yielding a small amount of non-localized damage [30].

Neutrons are uncharged particles which primarily interact with atomic nuclei via the strong nuclear force. They are capable of scattering off of atomic nuclei, or by being absorbed by atomic nuclei, thereby potentially making the target atom radioactive. If the

neutron transfers sufficient energy to the target atom (either by absorption or scattering), the target atom may be ejected from its lattice site and possibly ionized, creating a vacancy/interstitial pair and a subsequent atomic displacement cascade. In general, the scattered atomic nuclei cause significantly more damage to the material than the neutron itself; this is qualitatively why simulating high dose neutron damage with ion beams is a viable experimental technique. Neutrons themselves deposit energy over a long path length (centimeters to meters), causing significant non-localized damage [30].

An atom or molecule is ionized if a bound electron is ejected. In order for this to occur, the incident particle must transfer sufficient kinetic energy to a bound electron which exceeds the electron's binding energy to the atom/molecule. Since all electrons carry an electric charge of $-e$ (approximately $-1.602 \cdot 10^{-19}$ Coulombs), any incident radiative particle which also carries an electric charge will directly interact with the electron cloud via the Coulomb interaction. Such incident charged radiative particles are called directly ionizing radiation. The most common types of directly ionizing radiation found in a nuclear reactor are beta particles and heavy ions (alpha particles and fission fragments). Directly ionizing radiation with sufficient energy forms a hollow tunnel, or "track", as it slows down through condensed matter, shown in Figure 8 below [31].

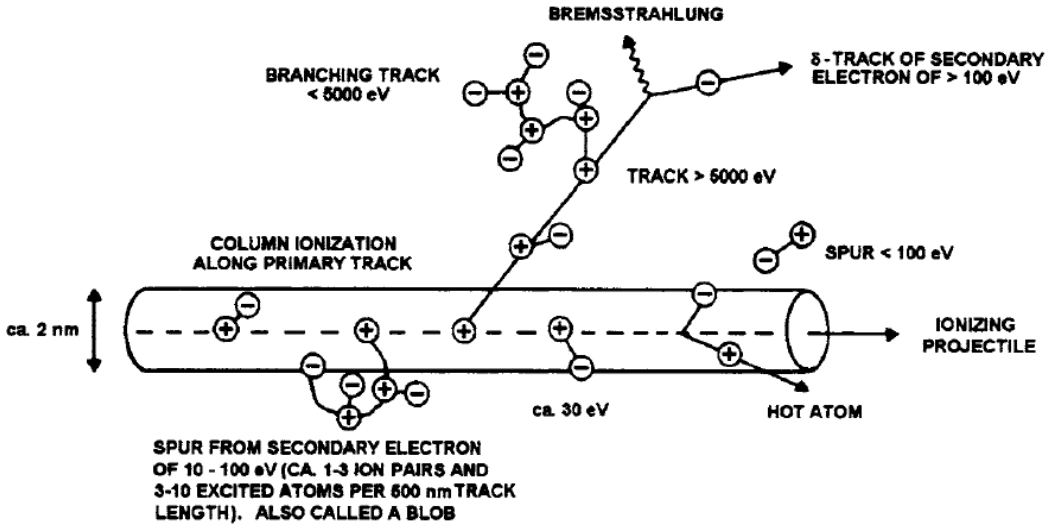

Figure 8: Track Formed by Energetic Directly Ionizing Radiation (Reprinted from [31])

Directly ionizing radiation has the potential to transfer enough energy to a bound electron that the ejected electron can then ionize atoms/molecules as it slows down. These highly energetic ejected electrons are called δ-rays. Since the conservation of momentum applies to these radiation interactions/collisions, and because alpha particles and fission fragments have a charge of +2 or greater (respectively), δ-rays are produced much more frequently/densely from heavy ions than from beta particles [31].

Due to the large mass of ions, alpha particles and fission fragments can transfer enough energy to bound atoms to displace them from their lattice site. In a similar manner to δ-rays, these displaced atoms can then subsequently displace further atoms, causing an "atomic displacement cascade". As a result of the atomic displacement cascade and δ-rays, heavy ions deposit a large amount of energy over a very short path length (around 1-10 μm), producing a large amount of localized damage [30].

Beta particles only have a charge of $\pm e$, and either (a) have the same mass as target electrons in the electron cloud, or (b) have less mass than a target atomic nucleus. As a result, collisions in which large amounts of energy are transferred abruptly do not occur as often for beta particles as with heavy ions. When modeling the transport of beta radiation in matter, beta interactions are typically not considered as discrete events; instead, electrons are modeled to interact via the "continuously slowing down approximation" (CSDA) which approximates that the electron is continuously losing energy as it travels through material [29]. As such, beta particles deposit energy over a path of about 10-100 μm, causing a small amount of localized damage [30].

II.3.2 Radiation Effects

There is a subtle difference between radiation damage and radiation effects. In general, radiation damage is any phenomenon which occurs as a direct and immediate result of ionizing radiation interacting with matter (such as the atomic displacement cascade produced by a heavy ion slowing down through matter). Radiation damage in nuclear materials is typically reported in units of displacements per atom (dpa), which is the average number of times an atom in a material will be displaced from its lattice site. Radiation damage, such as the atomic displacement cascade occurs rapidly at the microscopic scale. Radiation effects, however, are phenomena which develop over time in materials exposed to an energetic radiation field, such as the permanent embrittlement that occurs as a result of radiation exposure. Radiation effects often remain present after the material is removed from the radiation field. Radiation effects can grow and

manifest as macroscopic effects, and must be considered when choosing the appropriate reactor materials.

Nuclear reactor cladding materials are exposed to high energy radiation bombardment. Radiative collisions with the cladding can yield atomic displacement cascades, which generate local groups of randomly distributed defects. These local damage clusters rapidly reorganize, and interstitial/vacancy equilibrium concentrations are reached through various defect elimination processes such as interstitial/vacancy recombination, migration to defect sinks, etc. Some interstitial elements, such as chromium, may migrate more readily than others, yielding atomic segregation within the material. This phenomenon is exacerbated in alloys within the temperature range of $0.3T_M < T < 0.6T_M$, where T_M is the melting temperature of the alloy [32, 33]. Nickel-chromium superalloys are particularly sensitive to this phenomenon whereby depletion of diffusive species becomes noticeable, as shown in Figure 9 and Figure 10 [34, 35].

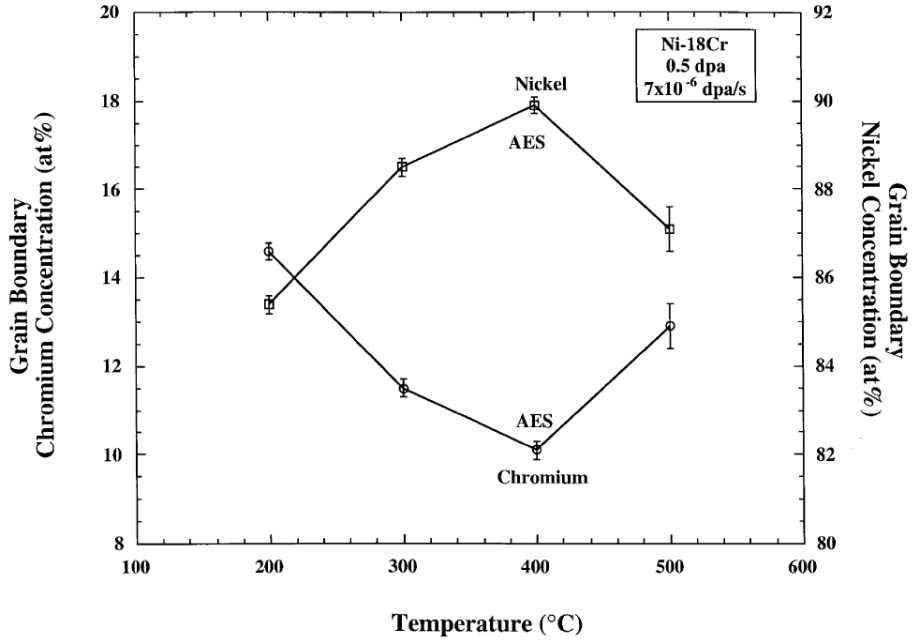

Figure 9: Temperature Dependent Average Grain Boundary Concentration of Cr and Ni for Ni-18Cr Alloy Irradiated to 0.5 dpa (Reprinted with permission from [33])

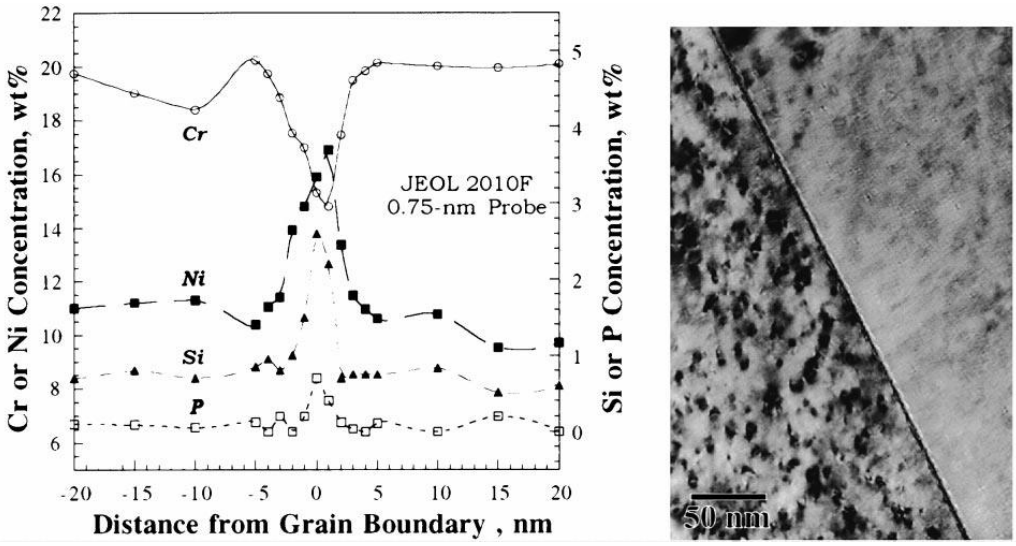

Figure 10: Analytical TEM Measurement of Radiation-induced Segregation of Cr, Ni, Si, and P across the Grain Boundary of 300-Series Stainless Steel under Neutron Irradiation in a LWR Core to Several dpa at 300 °C (Reprinted with permission from [34])

Radiation damage can produce point defects (vacancies and interstitials) within the material lattice. The formation of voids in solid materials can result from local supersaturation and coalescence of radiation-induced vacancies. As void formation continues and cavity volumes increase, insoluble gases can occupy these voids, which produces bubbles that can significantly alter the physical and mechanical properties of the metal [30]. For the case of commercial light water nuclear reactors, the majority of the gases in the cladding are produced by (n, α) reactions since the fission products cannot penetrate further than a few microns. Radiation-induced volumetric swelling in most metals is approximately linearly dependent with radiative dose in metals throughout a wide dose range. This is illustrated in Figure 11 and Figure 12 for a variety of alloys irradiated in the Experimental Breeder Reactor II (EBR-II) [33, 36]. As shown in Figure 11 and Figure 12, the degree of swelling caused by a given radiative dose varies with temperature (*vide infra*).

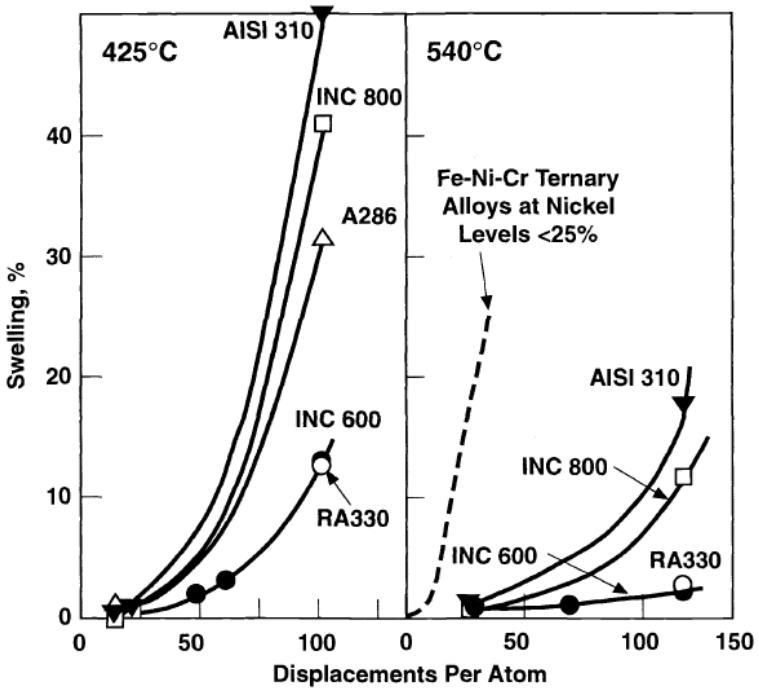

Figure 11: Radiation-induced Swelling of Various Claddings Irradiated in EBR-II
(Reprinted from [36])

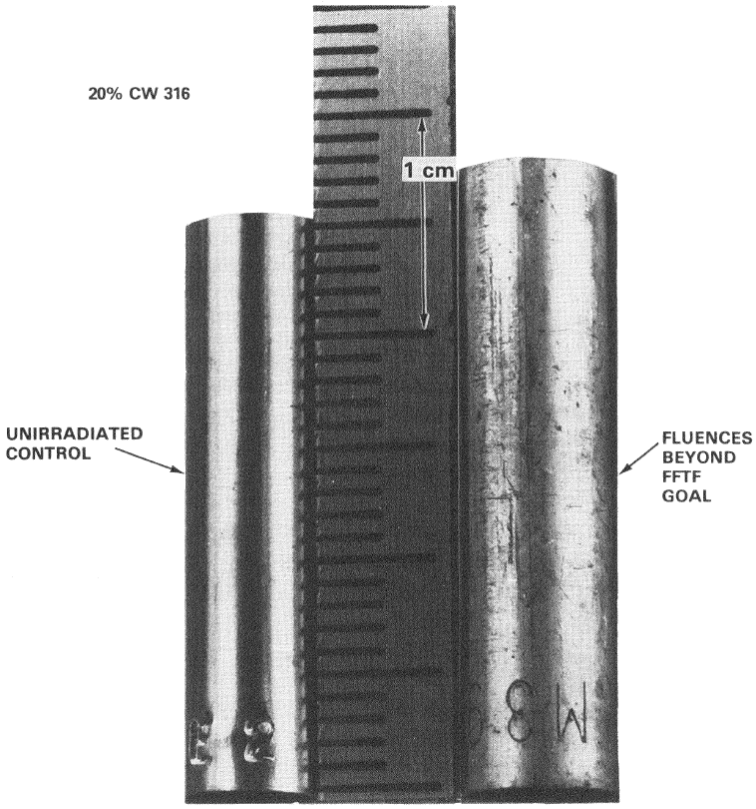

Figure 12: Swelling (~10% Linear, 33% Volumetric) in 20% Cold Worked AISI 316 Cladding, 75 dpa at 510 °C in EBR-II (Reprinted from [36])

Similar to radiation-induced segregation, radiation-induced swelling is also dependent on temperature (see Figure 13) [33, 37]. The chemical composition/stoichiometry of alloys can clearly influence swelling as well, shown in Figure 14 [36]. The temperature associated with the highest radiation-induced swelling is known as the "peak swelling temperature".

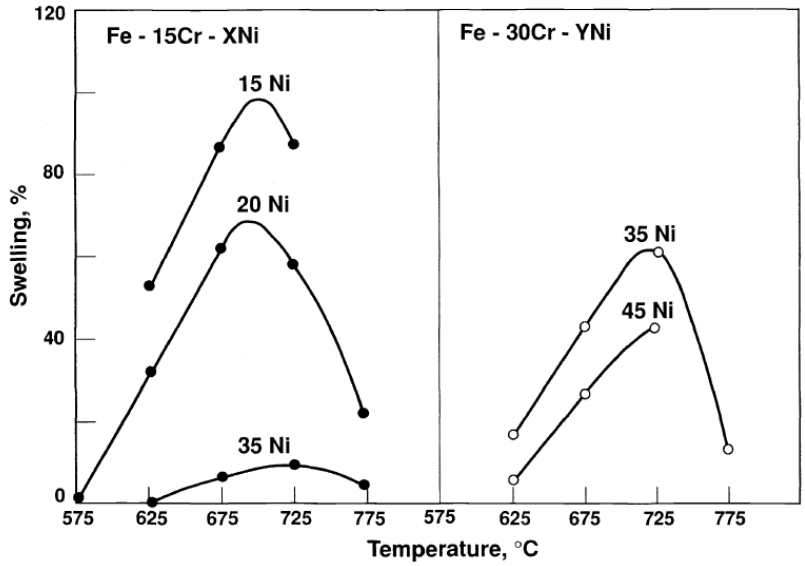

Figure 13: Temperature and Nickel Dependence of Radiation-induced Swelling in Fe-Cr-Ni Alloys to 140 dpa after 5 MeV Ni^+ Ion Irradiation (Reprinted from [36])

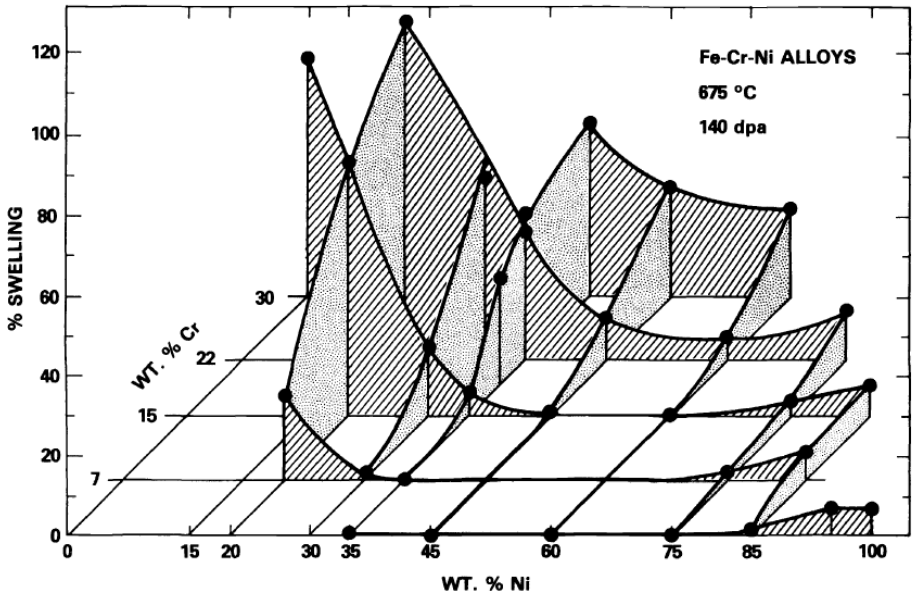

Figure 14: Radiation-induced Swelling vs. Alloy Stoichiometry in Fe-Cr-Ni Alloys after 5 MeV Ni^+ Ion Irradiation to 140 dpa at 675 °C (Reprinted from [36])

Radiation damage can affect cladding in a variety of ways, including production of defect clusters, dislocations, voids/bubbles, and precipitates. This can increase the cladding yield strength over a wide range of temperatures (see Figure 15) due to an increased resistance to dislocation release (called "pinning" or "source hardening") and motion (called "friction hardening") [30]. With the increased yield stress, however, materials often suffer a loss of ductility. These phenomena are more dramatic as radiative dose increases. For example, under sufficiently high doses, some bcc metals will become completely brittle and fracture on the elastic line [30].

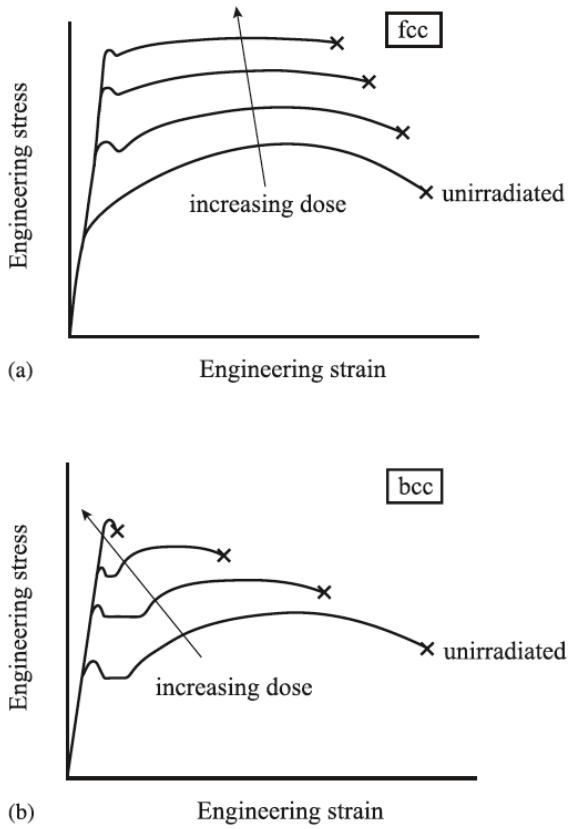

Figure 15: General Effect of Radiation Dose vs. Stress-Strain Behavior in (a) fcc and (b) bcc Alloys (Reprinted from [30])

Creep can be defined as the time-dependent plastic deformation of a material under constant load at high temperature ($T/T_M > 0.3$ for metals) [30]. Creep is generally highly temperature-dependent, whereby the production of vacancies/interstitials requires thermal activation. Higher temperatures offer more thermal energy available to overcome obstacles and barriers, which increases creep rate. Of course, creep rates are also dependent on the nature of the applied stress as well.

Ionizing radiation can generate defects in materials regardless of the material's temperature. Due to this excess defect production, radiation-enhanced creep is somewhat less dependent on temperature; irradiation studies in EBR-II showed that radiation-enhanced creep in 316 stainless steel at high temperatures can exhibit a complicated radiation dose dependence [38]. Radiation-enhanced creep becomes extremely important not only to the nuclear reactor cladding itself, but other reactor internals as well, such as baffle-former bolts and split pins.

II.4 Electron Backscatter Diffraction

Electron backscatter diffraction (EBSD) is a powerful tool for microstructural and textural analysis of materials and was used extensively in this work. Incident electrons generate a variety of detectable signals such as backscatter electrons (BSE), Auger electron, secondary electrons, and x-rays. The regions from which each of these emissions may escape the sample to be detected is illustrated by the "tear drop" electron beam interaction volume in Figure 16 [39]. As shown in Figure 17, electrons can

backscatter in an atomic nucleus, cause the incident electron beam to exit the sample surface.

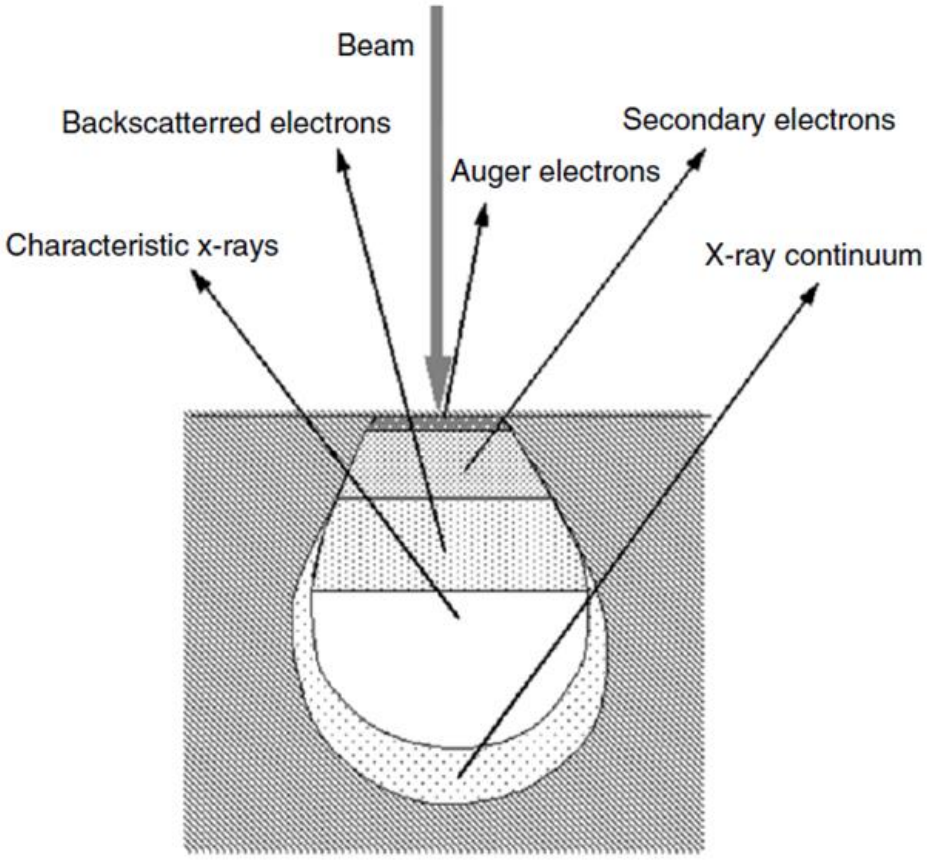

Figure 16: Illustration of Regions from which Detectable Signals are Generated by Incident Electrons in an SEM Sample (Reprinted from [39])

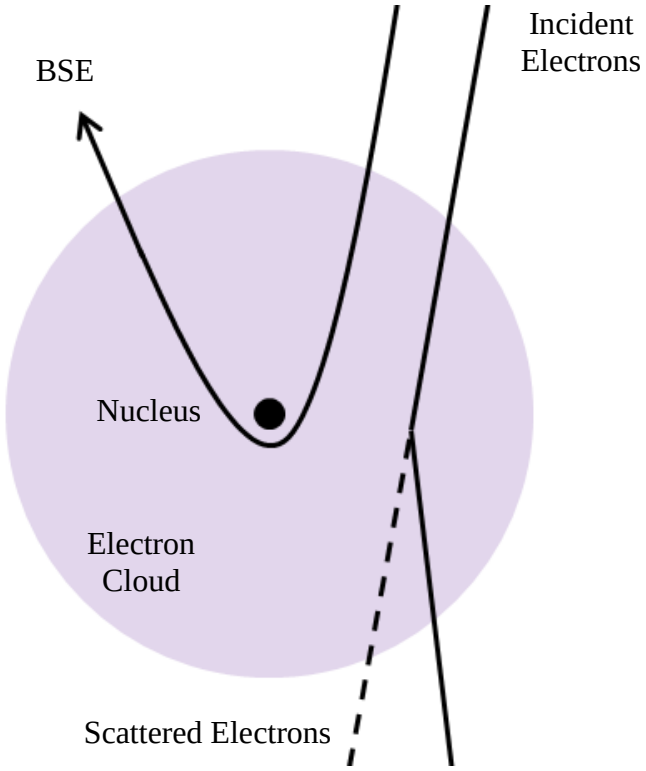

Figure 17: Illustration of an Electron Backscattering inside an Atom

Electrons undergo diffraction in a crystalline solid and obey Bragg's law, shown below in Eq. 1. The angles between the projected plane's normal orientations correspond to interplanar angles, while the angular widths of the reflections equal twice the Bragg angle ϑ_{hkl} and the interplanar spacing d_{hkl}. In Eq. 1, N is an integer representing the order of reflection (or, equivalently, the number of atomic planes the x-rays penetrated before reflection) and λ is the wavelength of the electron beam. The electron wavelength is a function of the beam energy/accelerating voltage via the de Broglie relation. The interplanar spacing for fcc crystals relates to the Miller indices by Eq. 2 where a is the lattice parameter. An illustration of Bragg diffraction is shown in Figure 18 [40].

Eq. 1

$$2d_{hkl}\sin\left(\vartheta_{hkl}\right) = N\lambda$$

Eq. 2

$$d_{hkl} = \frac{a}{\sqrt{h^2 + k^2 + l^2}}$$

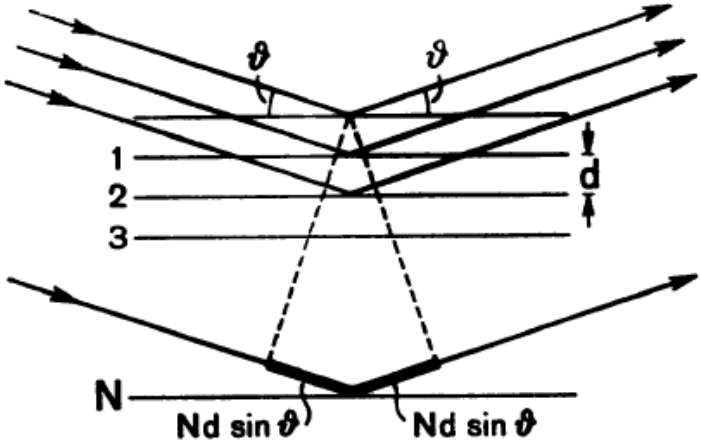

Figure 18: Bragg Reflection off of the Nth Atomic Plane in a Crystalline Solid
(Reprinted from [40])

The intensity of the diffracted electron beam is characterized by bands of constructive and destructive interference, illustrated in Figure 19 [41]. These bands, called "Kikuchi bands" or "Kikuchi lines", are representative of the crystalline lattice from which the electrons were diffracted. The widths and orientations of the Kikuchi bands can be interpreted as a gnomonic projection of the crystal lattice onto a flat phosphor screen to which the EBSD detector is connected.

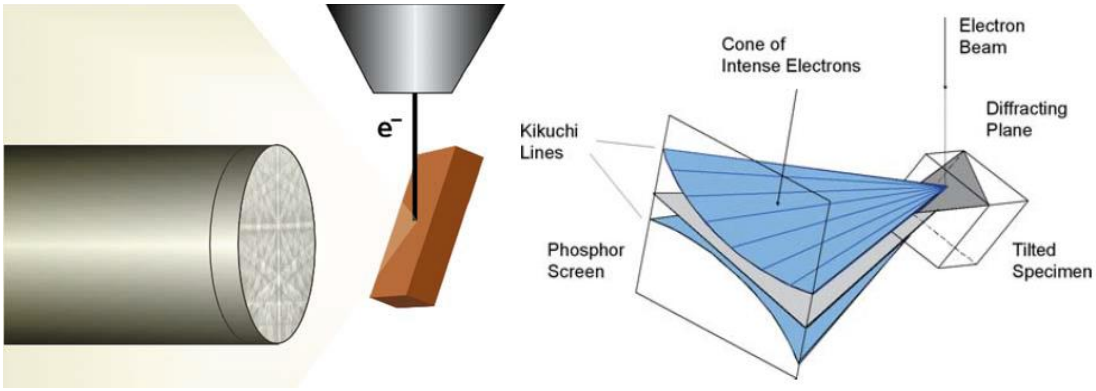

Figure 19: Illustration of Electron Beam Interacting with a Crystalline Sample (Left), Diffracting into Kikuchi Bands (Right) (Reprinted from [41])

The Kikuchi bands are mathematically converted into constant intensity sinusoidal curves of each individual pixel from the band map via a Hough transformation in a process called indexing. This changes the challenging task of detecting a line in the image into simply detecting a single spot in Hough space [42]. When the sample normal (z) and transverse (x-y) directions are indexed, the crystallographic orientation of the surface grains can be described in $(hkl)\langle uvw\rangle$ notation (Bravais), or by the three Euler angles φ_1, Φ, and φ_2, both of which will be discussed in the forthcoming sections.

II.4.1 EBSD Texture Maps – Pole Figures and Inverse Pole Figures

Kikuchi patterns are the result of stereographic projections which show the normal of crystallographic planes onto circles, illustrated in Figure 20 (left) [41]. The source of the projection in Figure 20 (left) is the south pole (i.e. the lines touching the bottom-right part of the sphere). This occurs in EBSD because the electrons penetrate

into the material a given distance before backscattering outward toward the detector. The 2D projection is illustrated as the shaded plane which is perpendicular to the line connecting the center of the sphere and the south pole (see Figure 20, right). Stereographic projections can be viewed by plotting them on other high symmetry orientations, such as the (001) shown in Figure 20 (middle); i.e. the projection illustrated in Figure 20 (middle) is being viewed down the $[001]$ direction which is perpendicular to the (001) plane.

The orientation of a crystallographic plane is specified by the point of intersection of the normal vector to the plane with the (positive) hemisphere of the surrounding unit sphere. This point is called a "pole", and for cubic crystals the pole is identical to the crystallographic axis with the same indices. This is illustrated in Figure 20 (right), where the crystallographic orientation of volume element p is projected onto the 2D circle at point p' [41]. The Kikuchi bands comprising the Inconel 600 electron backscatter pattern (EBSP) from unirradiated horizontal LAM are shown in Figure 21.

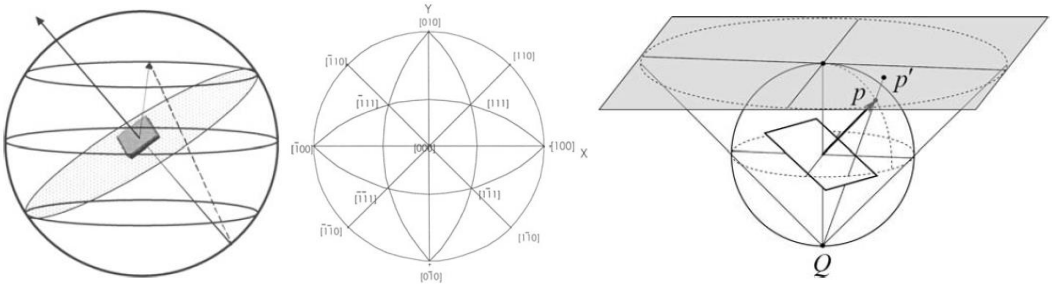

Figure 20: Illustration of Stereographic Projections in EBSD (Reprinted from [41])

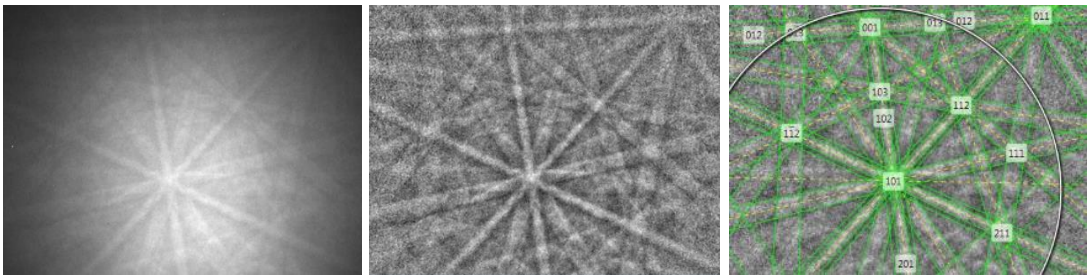

Figure 21: Unirradiated Inconel 600 Horizontal LAM Unprocessed EBSP (Left), Processed EBSP (Middle), and Processed EBSP with Kikuchi bands Labeled (Right)

There are two methods of projection. The most common is the standard stereographic projection (SSP), where the angle between lines drawn on the upper hemisphere is equal to the angle between their projections on the plane. In this method, the angles are preserved at the expense of distorting the apparent density of the poles in the projection. Alternatively, an equal area projection (EAP) preserves the density of the poles but distorts the angles between projected lines.

Point p' represents the orientation of an individual volume element p. A collection of projection points resulting from diffraction off of multiple volume elements yields a circular plot covered in orientation-dependent dots, forming the so-called pole figure (PF). If the volume elements under investigation have completely uniform orientation, then the poles (i.e. dots) in the PF will be uniformly distributed over the projection. There will be equal numbers of poles in equal areas on the surface of the reference sphere centered on the specimen as well. However, there will not be equal numbers of poles on equal areas of the PF since equal areas on the reference sphere are not equal in the stereographic projection. This causes an apparent clustering of poles at

the center of PFs for randomly oriented grains, since distances representing equal angles are smaller in this central region than other parts of the PF.

If the volume elements under investigation do have a preferred orientation, however, the poles will cluster together in certain areas of the projection other than the center, leaving regions of the PF sparsely populated. This is illustrated in Figure 22 for a (100) PF in which each grain is oriented with its (100) planes nearly parallel to the sample surface and the $[001]$ direction in these planes is parallel to the rolling direction [41]. Therefore, PFs will be expressed as standard stereographic projections.

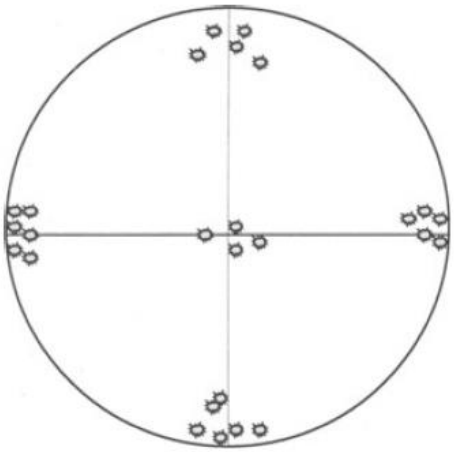

Figure 22: Illustration of (100) Pole Figure with Clustering Around {100} Poles Indicating Preferred Orientation (Reprinted from [41])

A pole figure shows sample directions aligned with a particular crystallographic pole. An inverse pole figure (IPF), however, does the opposite, indicating the crystallographic poles aligned with a specified sample direction. IPFs are of particular

interest for materials in which the processing history may produce directionally dependent structures, such as oriented fibers, growth direction of films, or perhaps the direction of laser rastering from LAM.

The projection procedure for generating IPFs is similar to that of PFs, except it is performed for each individual volume element, while the frame of reference is fixed by the local crystallographic frame. IPFs plot the results of all these projections together. Recall that cubic crystal structures have 24 crystallographically related solutions (i.e. are identical). Consider three different PFs in Figure 23 from the so-called "cube texture" (a), "copper texture" (c), and "brass texture" (e) [41]. The areas of the PFs are divided into 24 identical triangles, with the standard stereographic triangle outlined for conversion into IPFs where $l \geq h \geq k \geq 0$. The Miller indices in Figure 23 indicate the local crystallographic frame.

While IPFs do indicate the orientations of selected crystalline planes or directions, they do not necessarily indicate the orientation of crystals in a polycrystalline material. The development of the stereographic projection is also illustrated below in Figure 24 and Figure 25 in greater detail, and can also be viewed along different directions as shown in Figure 26 [43].

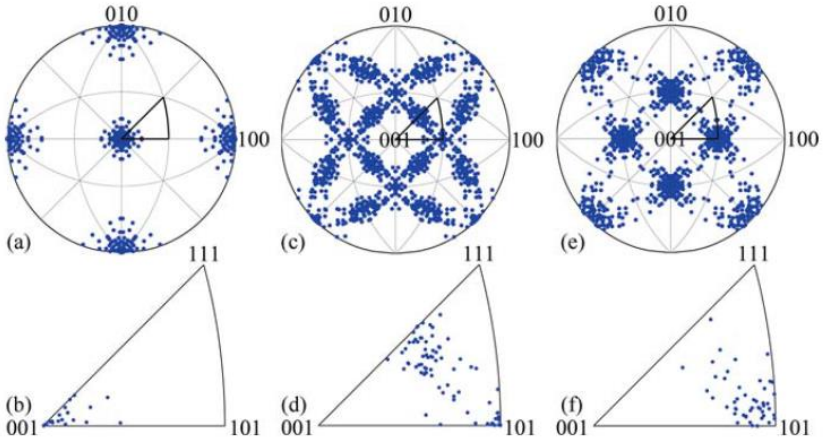

Figure 23: The PFs of (a) Cubic Texture, (c) Copper Texture, and (e) Brass Texture, and the IPFs of (b) Cubic Texture, (d) Copper Texture, and (f) Brass Texture (Reprinted from [41])

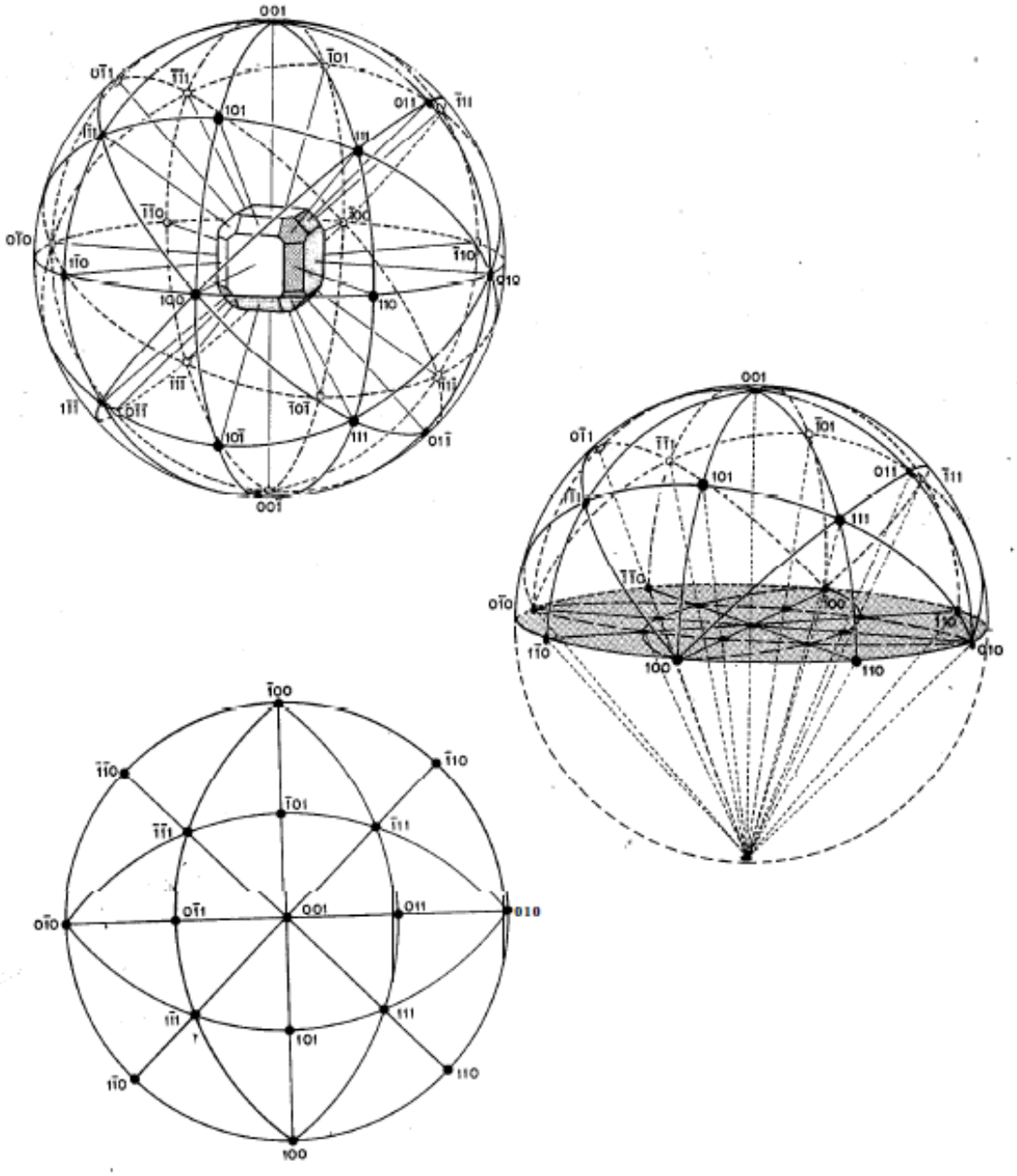

Figure 24: Development of the Stereographic Projection (Reprinted from [43])

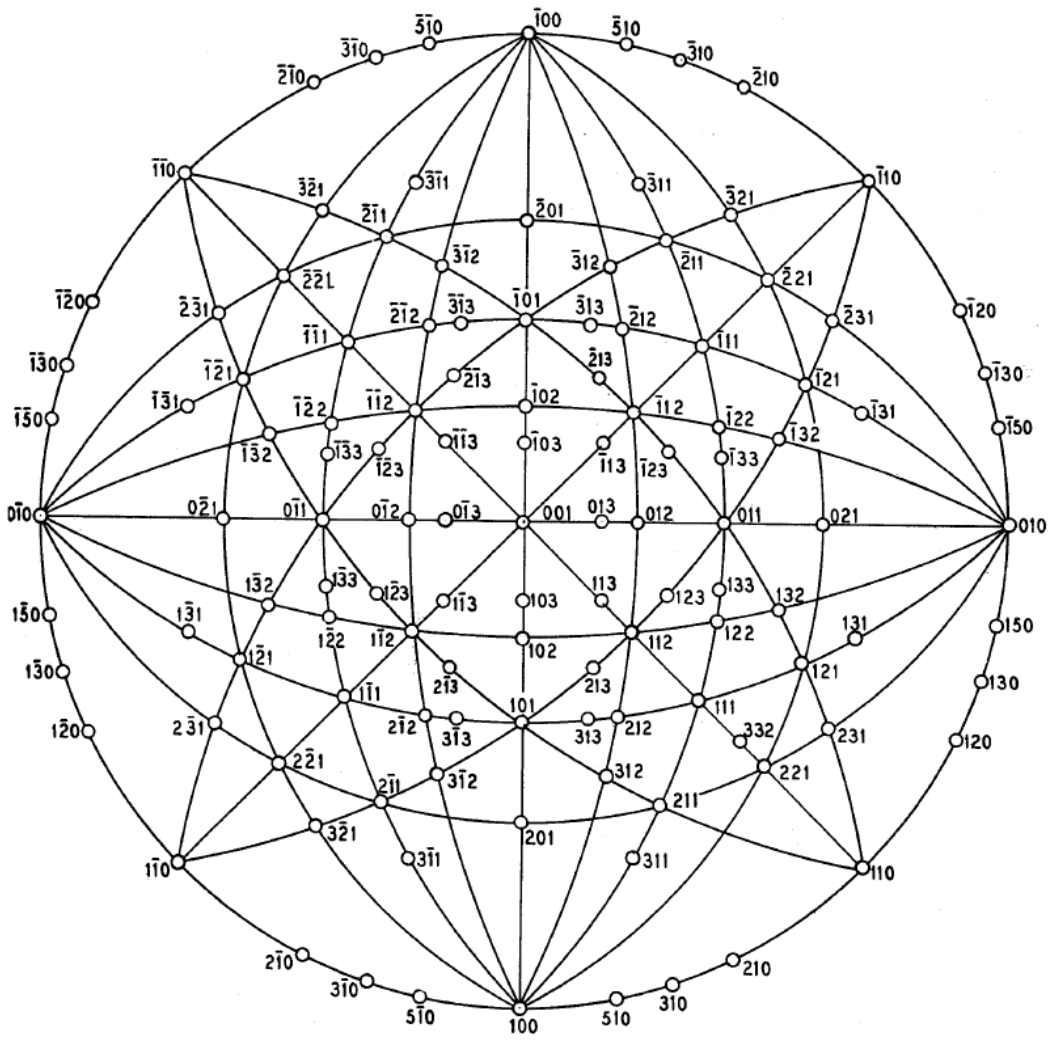

Figure 25: Stereographic Projection of Planes from an FCC Crystal onto (001)
(Reprinted from [43])

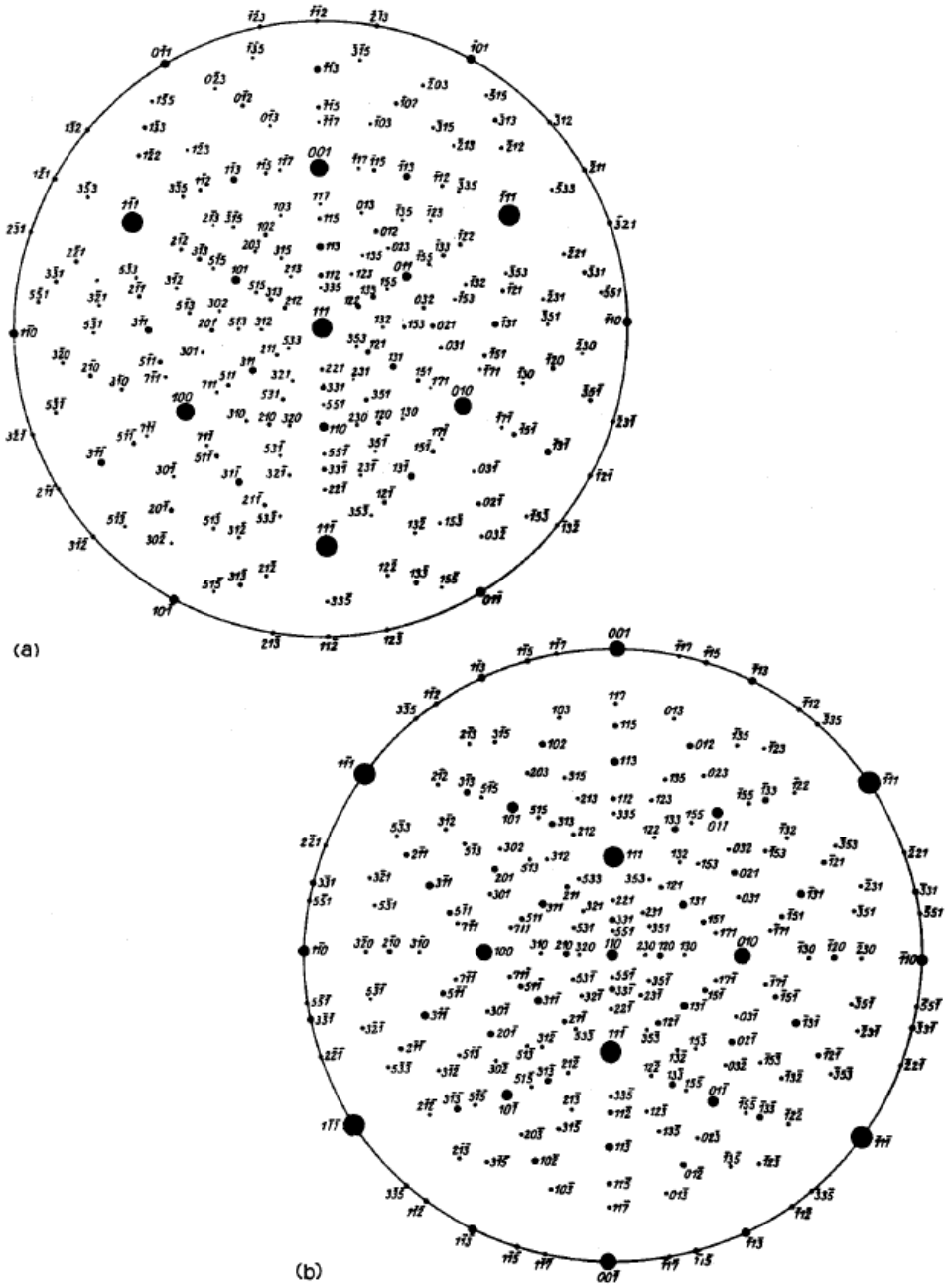

Figure 26: Stereographic Projections of Crystalline Planes of an FCC Crystal Viewed Along Two Different Directions (Reprinted from [43])

II.4.2 Euler Angles and Euler Maps

Crystallographic texture can be quantitatively characterized by using Euler angles. The Euler angles may be used to describe the orientation and coordinate system relative to the macroscopic material under investigation (i.e. the crystal's coordinate system). This is accomplished by rotating one of the coordinate systems about various axes until it comes into coincidence with the other. Different Euler angle conventions exist for cubic crystals, such as Bunge, Canova, Kocks, and Roe [44]. Bunge notation will be used for Euler angles/rotations in this work. Bunge notation describes the relative orientation of two coordinate systems with three rotations: the first rotation is about the *z* axis, followed by a rotation about the *x* axis, followed by a rotation about the *z* axis. These rotations define the Euler angles φ_1, ϕ, and φ_2, respectively, as illustrated in Figure 27 [45].

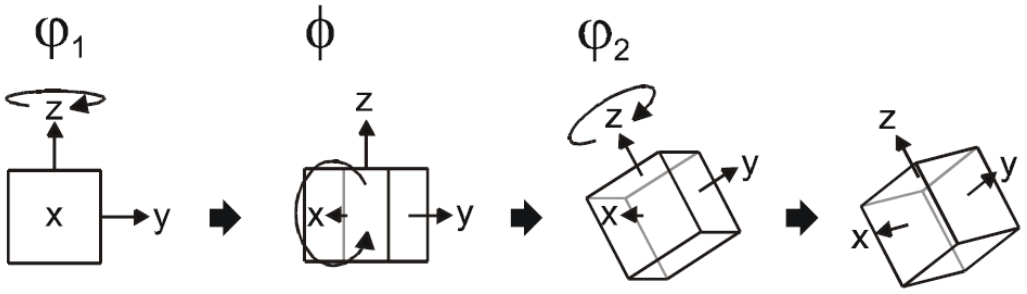

Figure 27: Illustration of Euler Angle Rotations φ_1, ϕ, and φ_2 (Reprinted from [45])

By convention, the values of the angles range from: $0 \leq \varphi_1 \leq 360°$, $0 \leq \phi \leq 90°$, $0 \leq \varphi_2 \leq 90°$. An example of Euler angle rotations is simple to visualize by setting $\varphi_2 = 0$ and varying φ_1 and ϕ, shown in Figure 28 for the face centered cubic unit cell of silicon (black circles represent Si atoms) [45].

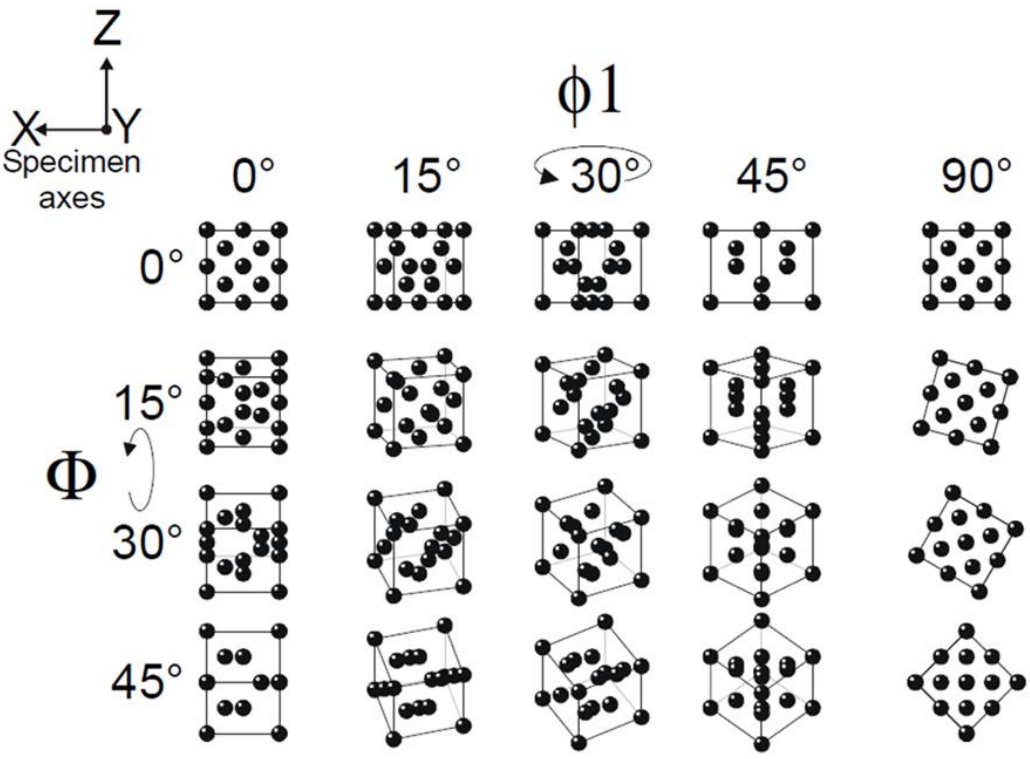

Figure 28: Illustration of φ_1 and ϕ Euler Rotations of the Silicon Unit Cell with φ_2 Fixed at Zero (Reprinted from [45])

Euler angles of the crystals relative to the sample surface are depicted for quick examination using color maps. For cubic crystals, the Euler angles (φ_1, ϕ, φ_2) are represented by red/green/blue (RGB) using the formulae shown in Eq. 3 where Euler angles are degrees.

Eq. 3

$$R = 255 \cdot \frac{\varphi_1}{360},\ G = 255 \cdot \frac{\phi}{90},\ B = 255 \cdot \frac{\varphi_2}{90}$$

II.4.3 Grain Size, Grain Aspect Ratios, and Grain Slope

There are two methods that are regularly used for determining grain size: (1) the average area method, and (2) the line-intercept method. The line-intercept method can yield significant errors for elongated oriented grain structures depending on line-intercept direction. This issue is particularly noticeable with the additively manufactured samples in this study. Therefore, for this work, grain size was measured using the average area method from EBSD analysis in accordance with ASTM E2627 standards [46].

Grain aspect ratios (GAR) are determined using the major/minor axes fitted ellipse technique, whereby the grain is approximated as an ellipsoid and the GAR is calculated as the ratio between the major and minor axes, shown in Eq. 4 [44]. In the fitted ellipse technique, an aspect ratio of unity signifies a perfectly spherical grain, while an aspect ratio of larger than unity signifies an elongated grain. To simplify Eq. 4, the value of the minor axis can be assumed to be $a = 1$ such that the $GAR = b$. If the grains are elongated, then the grain slope can be determined using EBSD as well. The grain slope quantitatively describes the direction and degree in which non-equiaxed grains are aligned.

Eq. 4

$$GAR = \frac{Axis_{Major}}{Axis_{Minor}}$$

$$GAR = \frac{b}{a}, \quad a = 1$$

$$\therefore$$

$$GAR = b$$

II.4.4 Coincidence Site Lattice Boundaries

Grain boundaries are 3D defects with significant misorientation within a crystalline material. A 2D example of such a misorientation is illustrated below in Figure 29 (left), where θ is the misorientation angle. Considering the infinite number of possible orientations between two grains on a grain boundary, some angles exist in which lattice points of one grain coincide with some lattice points of the neighboring grain, illustrated in Figure 29 (right). The collection of these points creates a superstructure called the coincidence site lattice (CSL).

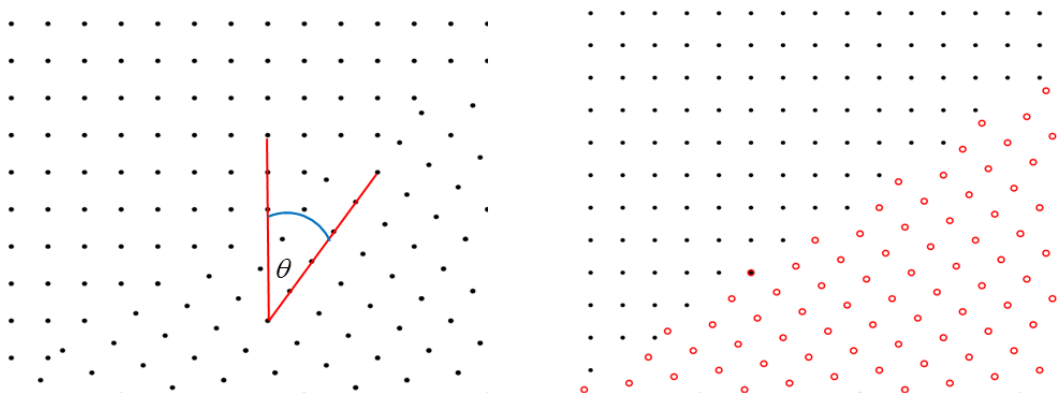

Figure 29: (Left) 2D Illustration of Misorientation between Two Grains, and (Right) 2D Illustration of Lattice Points in Grain 1 (Black) and Grain 2 (Red) with Coincident Lattice Sites

There exists a relationship between the number of lattice points in the unit cell of a CSL and the number of lattice points of the unit cells of the generating lattice. This relationship, represented by Σ, is the "degree of fit" between the two grains, and is defined as the reciprocal of the ratio of coincidence lattice sites to the total number of lattice sites. The permissible deviations from coincidence established by Brandon is applied in this work [47, 48]. As an example, when Σ exactly equals 1 (represented as $\Sigma 1$), the grain boundary angle of misorientation is exactly zero (i.e. all atoms along both sides of the grain boundary coincide, forming a perfect crystal).

Certain CSL boundaries have special properties, such as coherent twin boundaries ($\Sigma 3$) in which one out of every three lattice sites belongs to the CSL. For example, CSL boundaries with $\Sigma \leq 49$ have improved mechanical and chemical properties relative to $\Sigma \geq 49$ CSL boundaries [49]. Low Σ boundaries tend to have greater resistance to sliding, localized corrosion, and fracture [50-52]. Inconel 600 is

known to be susceptible to intergranular stress corrosion cracking (IGSCC). Studies have been conducted with the aim of improving Inconel 600 IGSCC resistance by optimizing the structure of the alloy's grain boundaries [53-59].

II.4.5 Kernel Average Misorientation and Strain Contouring Maps

Deformation within a solid is manifest as internal rotation of the crystal (i.e. within an individual grain). Misorientation maps are often useful for single crystal materials, or for determining deformation within individual grains since the field of view of polycrystals is typically made up of many grains with random orientations. An illustration of crystallographic misorientation is represented using Euler angles in Figure 30 [41]. A local misorientation map displays where the misorientation is present, highlighting regions of higher deformation. The map is produced via a pixel-by-pixel analysis, whereby the average misorientation between every individual pixel and its surrounding pixels is calculated. The mean value of misorientation is then assigned to that pixel.

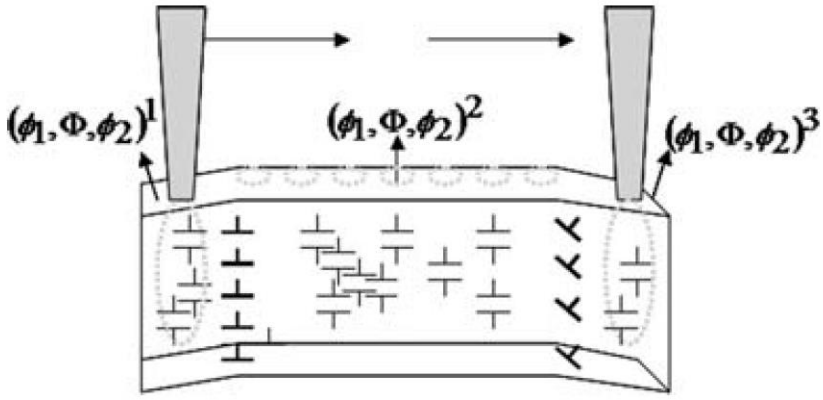

Figure 30: Illustration of Misorientation within a Crystal (Reprinted from [41])

The EBSD methodology is capable of providing an estimate of the extent of deformation (strain) in a crystal and highlighting the degree and location of strain on an EBSD image. This is accomplished by measuring the maximum misorientation between any two points in a grain, and then assigning a maximum misorientation value to be placed in the center of that grain. Surrounding grains are then contoured using a Gaussian filter. Kernel misorientation maps (KAM) are produced when the average of these values within each grain is formed into color contour maps. According to ASTM E2627-13 standards, residual strain is associated with crystallographic misorientation of less than 5° (i.e. $\theta < 5°$ in Figure 29) while misorientation of greater than 5° defines a grain boundary (i.e. $\theta > 5°$ in Figure 29) [46].

II.4.6 EBSD Rodrigues-Frank Space Mappings

Another misorientation space commonly used in EBSD is known as the Rodrigues-Frank (RF) space [60]. Misorientation of a sample's microstructure may be represented using (a) sets of orientation vectors or (b) with one single vector parallel to the rotation axis and a length equal to the rotation angle. The RF vector, *R*, is calculated from the angle-axis pair, $\theta:[uvw]$, which represents the misorientation between a chosen orientation and the reference orientation according to Eq. 5. The RF vector is transformed into an RGB map in a manner similar to Euler angles. Small deviations from the reference orientation appear black while larger angle rotations appear as RGB depending on the axis of rotation (see Table 2 below).

Eq. 5

$$R = \tan\left(\frac{\theta}{2}\right)\cdot[uvw]$$

$$\therefore$$

$$R_x = \tan\left(\frac{\theta_x}{2}\right)\cdot[u,0,0], \quad R_y = \tan\left(\frac{\theta_y}{2}\right)\cdot[0,v,0], \quad R_z = \tan\left(\frac{\theta_z}{2}\right)\cdot[0,0,w]$$

Table 2: Cubic RF Orientation Component Legend Table

Euler Angle	Angle / Axis	Color	Comments
0,0,0	0° <000>	Black	Cubic Orientation is Black
0,45,0	45° <100>	Red	Rot. Of 45° about x-axis
90,45,90	45° <010>	Green	Rot. Of 45° about y-axis
45,0,0	45° <001>	Blue	Rot. Of 45° about z-axis

II.4.7 The Schmid and Taylor Factors

During plastic deformation, the close-packed slip system for austenitic alloys occurs on {111} planes in <101> directions [61]. The Schmid factor of a single crystal can be determined for the orientation at each point and displayed in a color map using EBSD. The resolved shear stress (RSS), τ, is defined by Schmid's Law in Eq. 6, where *m* is the Schmid Factor, φ is the angle between the normal of the slip plane and the

direction of applied stress σ, and λ is the angle between the slip direction and the direction of applied stress [62].

Eq. 6

$$\tau = \sigma \cdot m = \sigma \cos(\varphi)\cos(\lambda)$$

While the Schmid Factor has been shown to be accurate for single crystal fcc metals, the Taylor Factor has shown to be more applicable to polycrystalline fcc metals [63]. The Taylor Factor, *M*, can be approximated by averaging the Schmid Factor values for all the grains constituting the polycrystals (note: the Taylor Factor reflects the greater constraint provided by the least-favorable oriented grains and is therefore not merely a geometric average). In other words, if a polycrystalline material has significant texture, then grains may exist which are preferentially oriented more favorably for slip than others. The Taylor Factor is defined by Eq. 7, where σ_f is the macroscopic flow stress and τ_{CRSS} is the critical resolved shear stress [63].

Eq. 7

$$\sigma_f = M \cdot \tau_{CRSS}$$

The Taylor Factor assumes that grains with low *M* undergo negligible deformation until the grains with high *M* also deform plastically, and the grains with high *M* deform by a combination of stress concentration and work hardening around them. Lower *M* values therefore represent higher resistance to slip.

II.5 Nanoindentation and Scanning Probe Microscopy

II.5.1 Fundamental Principles of Nanoindentation

Nanoindentation is a characterization method by which a hard, small probe with known geometric and mechanical properties is depressed a small depth into a sample, from which mechanical properties of the unknown sample can be determined. Instead of generating a stress-strain curve from a typical tensile test, nanoindentation studies generate "load-displacement curves". An example of a typical nanoindentation load-displacement curve is shown below in Figure 31, and an illustration of the variables described is provided in Figure 32 [64]. In Figure 31, (a) is application of load, (b) is removal of load, (c) is the tangent to curve "b" at F_{max}, (F) is the test load, (F_{max}) is the maximum load, (h_p) is the permanent indentation depth after load removal, (h_r) is the tangent indentation depth, (h_c) is the contact depth of the indenter probe with the sample at F_{max}, (h_{max}) is the maximum indentation depth, (S) is contact stiffness, and (ε) is a geometric constant.

The slopes and values associated with the load-displacement curve are recorded and are dependent upon indenter probe geometry and mechanical properties, as well as the sample's mechanical properties. The elastic modulus, E, describes the elastic (recoverable) behavior of the sample which occurs below the yield stress. The hardness of the sample, H, is a measure of the material's resistance to plastic deformation. Features relating to the shape of the load-displacement curves can reveal material responses like pressure-induced phase changes (Figure 33d) or pop-in events (Figure 33e) [65].

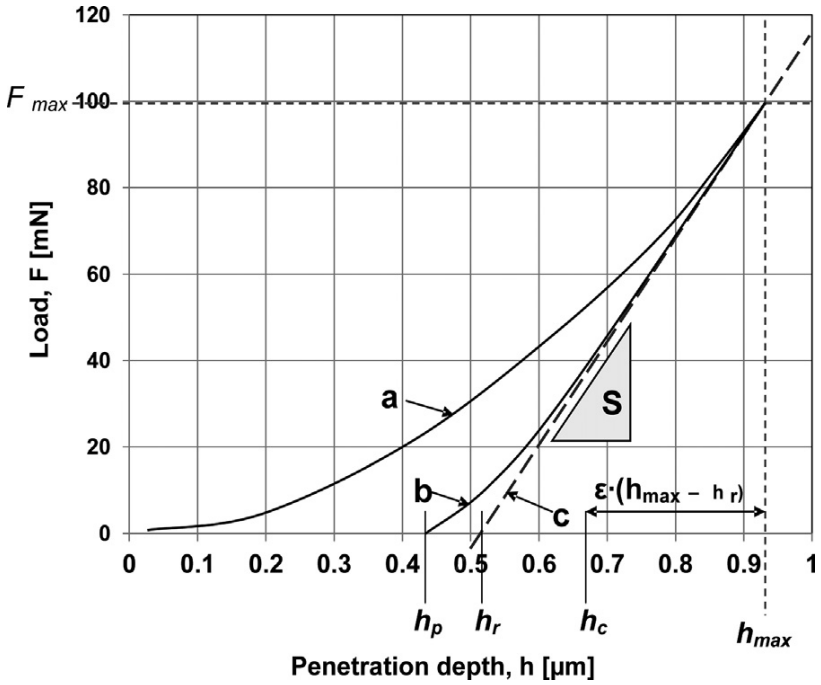

Figure 31: A Typical Nanoindentation Curve (Reprinted from [64])

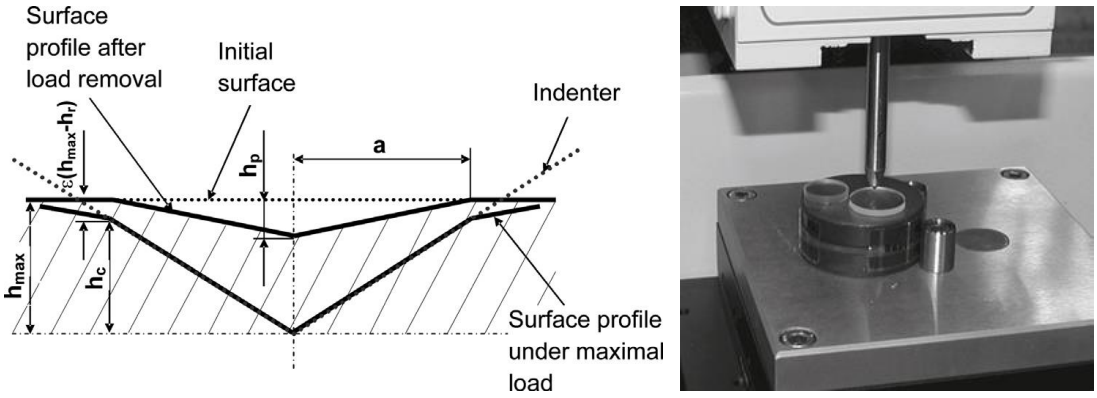

Figure 32: (Left) Schematic of Indenter Probe in Contact with Sample Surface, and (Right) Example of Indenter Probe Examining Fused Silica (Reprinted from [64])

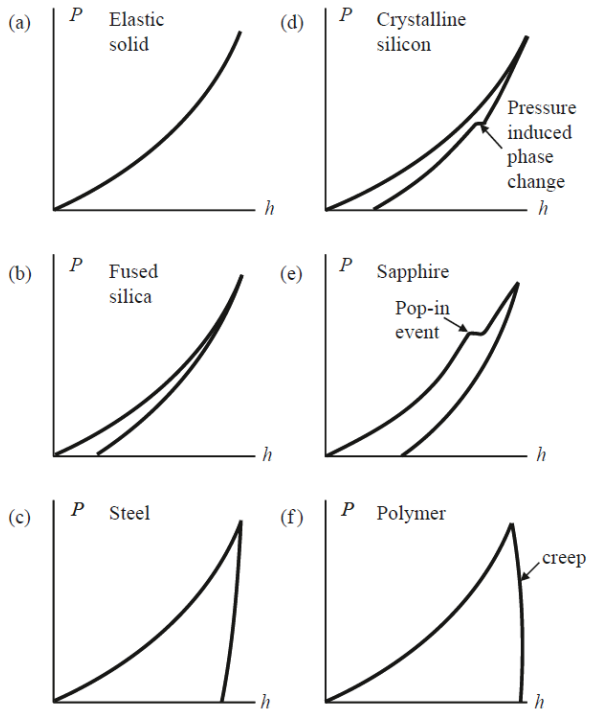

Figure 33: Illustration of Load-Displacement Curves Revealing Different Material Responses (Reprinted from [65])

The mathematical definitions of the variables shown in Figure 31 and Figure 32 are defined by Eq. 8 - Eq. 10 [66]. In the equations below, F_u is the load during the unloading segment of the indentation, and the stiffness, S, is the slope of the unloading segment of the load-displacement curve. The indentation area created by probe-sample surface contact, A, is a function of indentation contact depth h_c. E is the elastic modulus of the sample, E_r is the reduced elastic modulus of the sample-indenter probe system, E_i is the elastic modulus of the indenter probe, v_s is Poisson's ratio for the sample, and v_i is Poisson's ratio for the indenter probe. The probe used in these experiments was standard a diamond Berkovich tip, for which E_i = 1141 GPa and v_i = 0.07 [64]. The constant β is

a geometric factor describing the shape and curvature of the indenter probe tip; for the Berkovich tip, β = 1.034 [64]. The reported room temperature values for the Poisson's ratio of Inconel 600 and 316L stainless steel vary depending on the source, and are typically between 0.29 and 0.32. As a result, the Poisson's ratios for Inconel 600 and 316L stainless steel were assumed to be ν_s = 0.3. The indentation hardness is defined by Eq. 11 where F_{max} is the maximum load and A_{proj} is the projected area of the indenter probe onto the sample surface.

Eq. 8

$$S = \frac{dF_u}{dh}\Big]_{h_{\max}}$$

Eq. 9

$$E_r = \frac{S\sqrt{\pi}}{2\beta\sqrt{A}} = \left[\frac{1-\nu_s^2}{E} + \frac{1-\nu_i^2}{E_i}\right]^{-1}$$

$\therefore$

Eq. 10

$$E = \frac{1-\nu_s^2}{\frac{1}{E_r} - \frac{1-\nu_i^2}{E_i}}$$

Eq. 11

$$H = \frac{F_{\max}}{A_{proj}}$$

II.5.2 The Indentation Size Effect

Many materials respond to nanoindentation by appearing to increase in hardness and elastic modulus as the indenter probes incrementally shallower depths [67-71]. This phenomenon is known as the indentation size effect (ISE). On the basis of classical continuum plasticity theory, however, hardness should be independent of indentation depth [71]. Nanoindentation itself is a nano-scale characterization technique, and therefore the discrete nature of matter must be accounted for.

Different models exist for predicting the plasticity behavior of materials during nanoindentation, one of the most widely used of which was developed by Nix & Gao [72]. This model attributes ISE to geometrically necessary dislocations (GNDs) which must be present near the indent in order to accommodate the volume of material that is displaced by the indenter, shown below in Figure 34 [73]. The depth dependence of the GND model can be summarized mathematically by Eq. 12, where h is indentation depth, $H(h)$ is the measured hardness for a given depth of indentation, H_∞ is the sample hardness in the infinite depth limit, and h^* is a characteristic length that depends on H_∞, the indenter shape, and the shear modulus of the material [72]. The ISE is typically more noticeable for ductile materials.

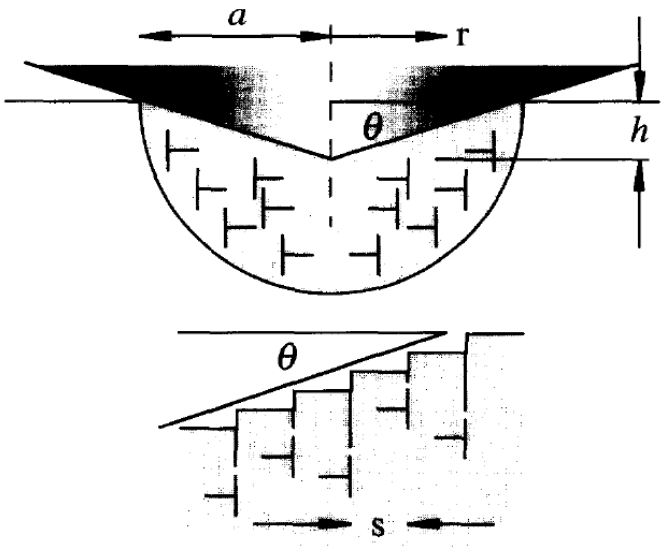

Figure 34: Illustration of Geometrically Necessary Dislocation Loops Created by a Rigid Conical Indentation (Reprinted from [72])

Eq. 12

$$\frac{H(h)}{H_\infty} = \sqrt{1 + \frac{h^*}{h}}$$

II.5.3 Scanning Probe Microscopy and Surface Roughness

Some nanoindenters are capable of performing in-situ scanning probe microscopy (SPM). SPM is a method of microscopy in which images of a sample surface are generated by physically scanning the surface of the sample with a mechanical probe (such as a nanoindenter tip) and recording changes in elevation as the probe scans [74]. In doing so, false-color maps can be generated showing the roughness of the sample surface. An illustration of a rough surface is shown below in Figure 35. Eq. 13

and Eq. 14 below represent the 1D mathematical formulae for the linear average ($\overline{R}$) and root-mean-square (R_{RMS}) surface roughness, respectively.

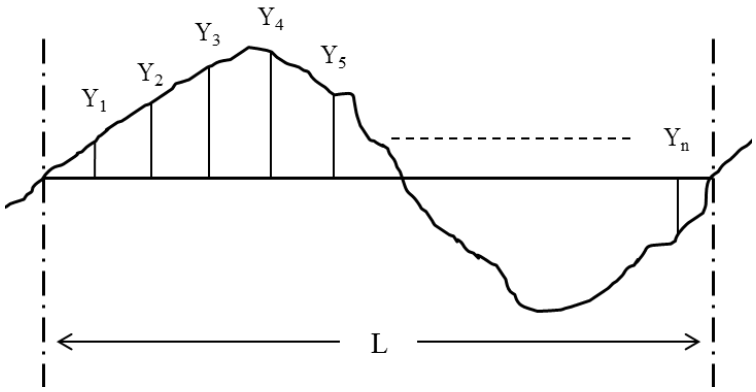

Figure 35: Illustration of a Rough Surface

Eq. 13

$$\overline{R} = \frac{|Y_1| + |Y_2| + \ldots |Y_n|}{n} = \frac{1}{n}\sum_{i=1}^{n}|Y_i|$$

Eq. 14

$$R_{RMS} = \sqrt{\frac{y_1^2 + y_2^2 + \ldots y_n^2}{n}} = \sqrt{\frac{1}{n}\sum_{i=1}^{n} y_i^2}$$

It is important to note that two samples whose average surface roughness is equal do not necessarily have the same surface texture. Figure 36 shows an illustration, generated using CAD software, of three different surface textures which, according to Eq. 13, have the same average surface roughness. Due to the different geometries of the surface, however, they may have different micromechanical properties. As a result, even

though the nanoindenter measured both $\overline{R}$ and R_{RMS}, the RMS surface roughness is more meaningful.

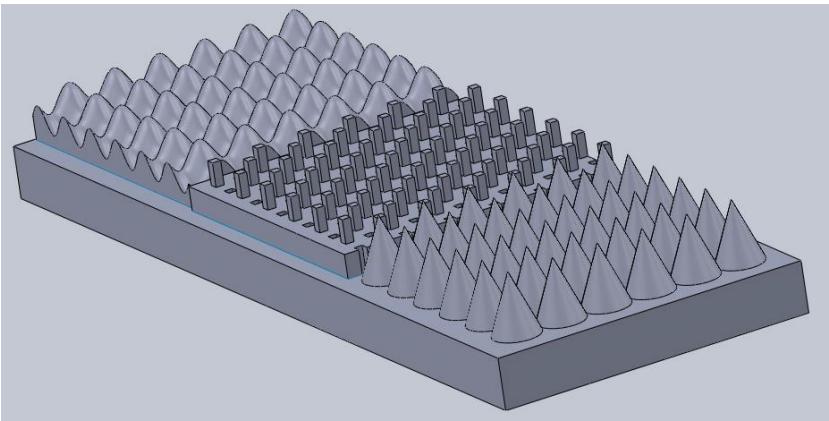

Figure 36: Illustration of Three Different Surface Textures with Equal Average Surface Roughness

II.6 Transmission Electron Microscopy

II.6.1 High Resolution Transmission Electron Microscopy

While SEM systems detect electrons that are ejected from the sample surface facing the electron beam (backscattered electrons, secondary electrons, etc.), transmission electron microscopy (TEM) signals are generated from electrons which have transmitted through a thin specimen, as illustrated in Figure 37 [75]. Although TEM inherently is statistically limited due to the small sample size in high resolution images, high resolution transmission electron microscopy (HRTEM) is capable of imaging materials at the atomic scale. In order to produce TEM images, the sample must be thin enough to be transparent to electrons. This can be accomplished by milling/polishing a lamella using a focused ion beam (FIB).

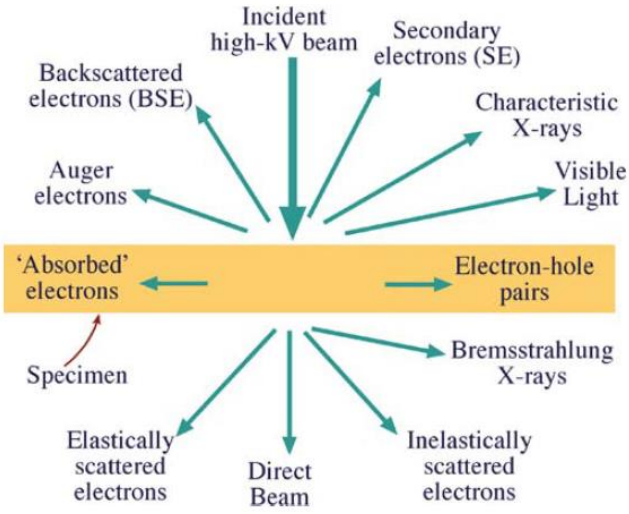

Figure 37: Illustration of Signals Generated from High Energy Electrons Interacting with a Thin Specimen (Reprinted from [75])

Due to the high resolution imaging capabilities of TEM, it is possible to visually confirm the presence of residual strain, either by directly imaging the atoms or by way of aberrations in the resulting diffraction patterns (DPs). While SEM, EDS, and EBSD share many capabilities with TEM (the generation of Kikuchi bands and DPs, elemental identification, etc.), TEM is capable of directly imaging radiation-induced defects, such as voids, dislocations, precipitates, etc. [76]. Previous experiments suggest that radiation-produced voids generated in Fe-Cr-Ni alloys increase in average size as dose increases, as shown in Figure 38 [30, 77]. Likewise, TEM is capable of imaging the dispersoid size distribution in ODS steels, as shown in Figure 39 for 12Cr-ODS samples [78]. TEM is therefore capable of determining how additively manufacturing ODS alloys may influence oxide dispersoid size distribution and coherency in the alloy matrix [79].

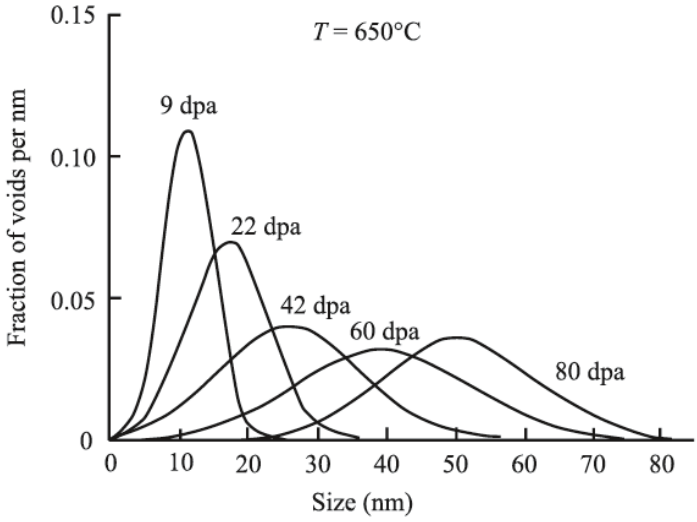

Figure 38: Experimentally Measured Void Size Distribution in Fe-Cr-Ni Alloys Irradiated at 650 °C (Reprinted from [77])

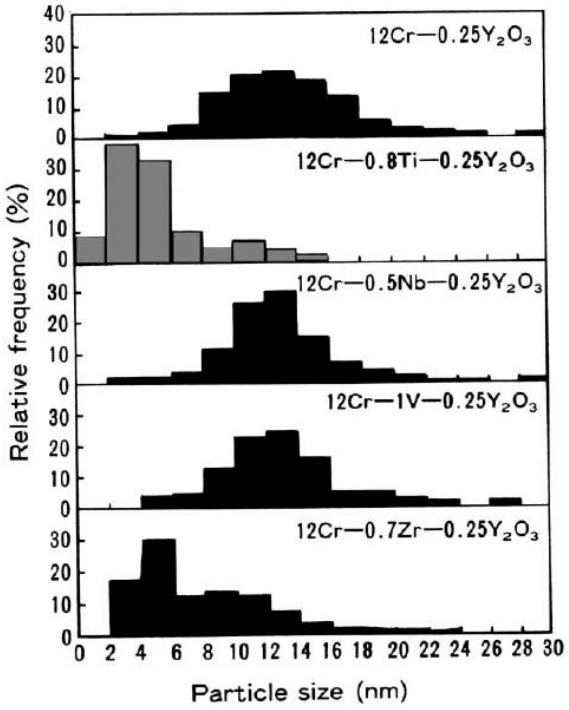

Figure 39: Size Distributions of Dispersoids in 12Cr-ODS Steels (Reprinted with permission from [78])

A dislocation is a defect defined by its direction and Burgers vector. The crystal structure surrounding a dislocation is strained. However, for single dislocations, this strain typically does not generate new spots in the resulting DP [75]. If many dislocations exist and are oriented, then additional spots will be present in the DP, as shown in Figure 40 [75]. Dislocations can be seen in TEM in a variety of ways. Figure 41 shows the Moiré fringes (vide infra) generated by the same dislocation in A, B, and C underlying three different defect-free crystals [75].

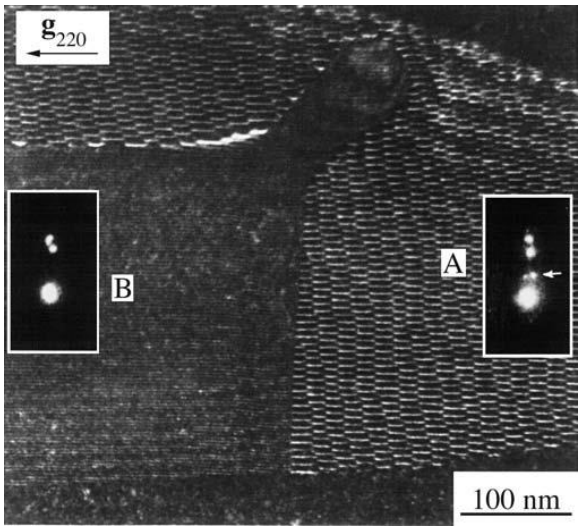

Figure 40: Example of the Diffraction Pattern from a Region with (A) and without (B) Many Oriented Dislocations Producing Moiré Fringes in a TEM Image
(Reprinted from [75])

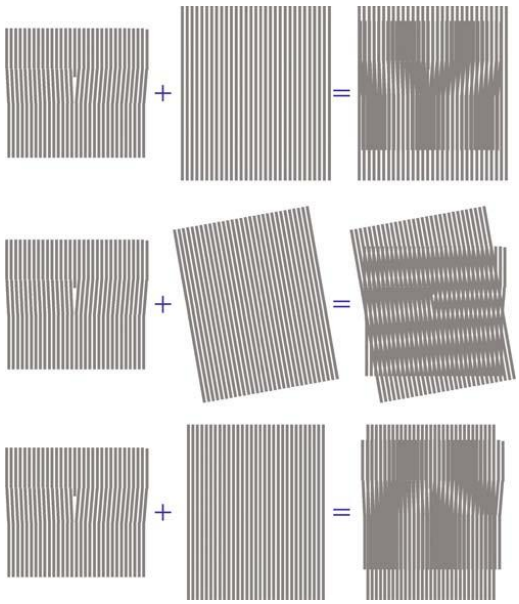

Figure 41: Illustrations of why Moiré Fringes Exist from Dislocations, Which Cannot Be Directly Seen in Any of the Resulting Patterns (Reprinted from [75])

When electrons (or other quanta) are diffracted, they behave according to Bragg's Law (Eq. 1). The Laue conditions represent the reciprocal-space equivalent of Bragg's law [80]. The fcc unit cell has Miller indices a_1, a_2, and a_3. These indices form the fcc Bravais lattice $\vec{g}$ which. Electrons diffracting in a crystalline lattice behave as Bloch waves defined by Eq. 15 in which the atoms in the crystal are arranged in a periodically repeating manner [80]. In the context of the crystal, the reciprocal lattice vectors, b_1, b_2, and b_3, are related to the Miller indices by Eq. 16. Using the reciprocal lattice vectors, one can generate the reciprocal lattice-equivalent of the unit cell, called the "first Brillouin zone", as shown in for the fcc crystal in Figure 42 [81].

Eq. 15

$$\psi(\vec{r}) = e^{i\vec{k}\vec{r}}u\left(\vec{r}\right)$$

Eq. 16

$$b_1 = 2\pi \frac{a_2 \times a_3}{a_1 \left(a_2 \times a_3 \right)}$$

$$b_2 = 2\pi \frac{a_3 \times a_1}{a_1 \left(a_2 \times a_3 \right)}$$

$$b_3 = 2\pi \frac{a_1 \times a_2}{a_1 \left(a_2 \times a_3 \right)}$$

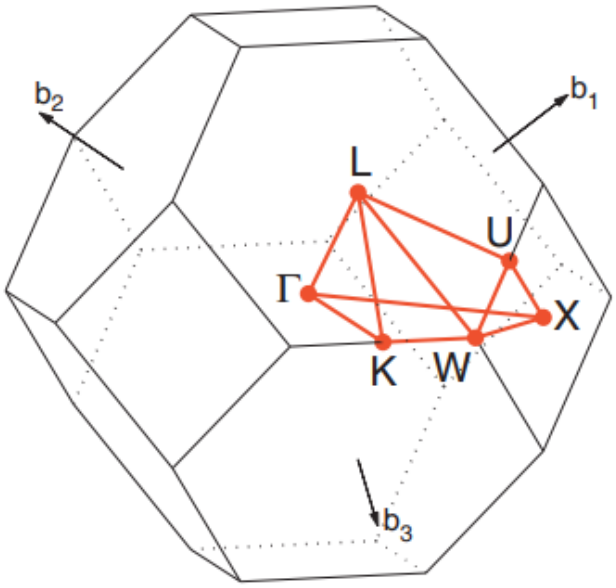

Figure 42: First Brillouin Zone of an fcc Crystal (Reprinted from [81])

An illustration of an edge dislocation and its associated distortion is provided in Figure 43 where white circles represent atoms [82]. Dislocation contrast in bright field transmission electron microscopy (BFTEM) images depends strongly on orientation, as is illustrated in Figure 44 [82]. In Figure 44, the reciprocal lattice vector $\vec{g}$ is essentially

equal to the diffraction vector $\overrightarrow{\Delta k}$, which points into the paper, and the Burger's vector $\vec{b}$ is dependent upon which direction the dislocation is viewed from. When viewing this edge dislocation from the front (Figure 44, middle), $\vec{g}$ and $\vec{b}$ are perpendicular to one another, so $\overrightarrow{\Delta k} \cdot \vec{b} = \|\Delta k\| \|b\| \cos(\theta) = 0$. When viewing this edge dislocation from the side (Figure 44, right), $\vec{g}$ and $\vec{b}$ are parallel to one another, so $\overrightarrow{\Delta k} \cdot \vec{b} = \|\Delta k\| \|b\| \cos(\theta) \neq 0$. In practice, when viewing a dislocation from the side such that $\cos(\theta) \approx 0$, the dislocation is invisible, while the dislocation is most clearly visible when $\cos(\theta) = \pm 1$. This is called the "null contrast rule" or the "$\vec{g} \cdot \vec{b}$ rule" which defines the invisibility criterion of dislocations in TEM images. In practice, if $\left|\vec{g} \cdot \vec{b}\right| \leq 1/3$, the dislocation is invisible [82].

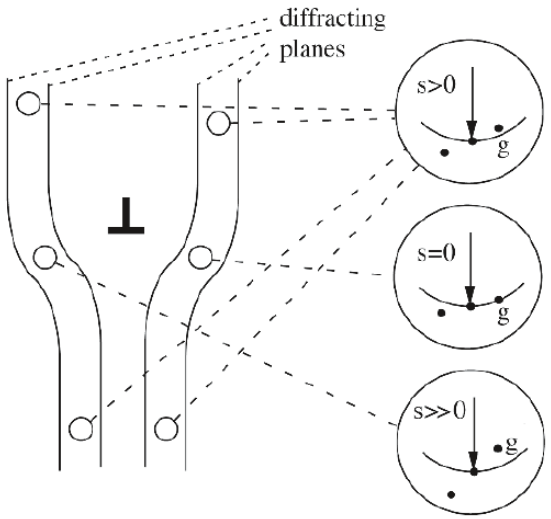

Figure 43: Distortion of Crystal Planes near an Edge Dislocation, with Ewald Sphere Constructions (Right) during TEM (Reprinted from [82])

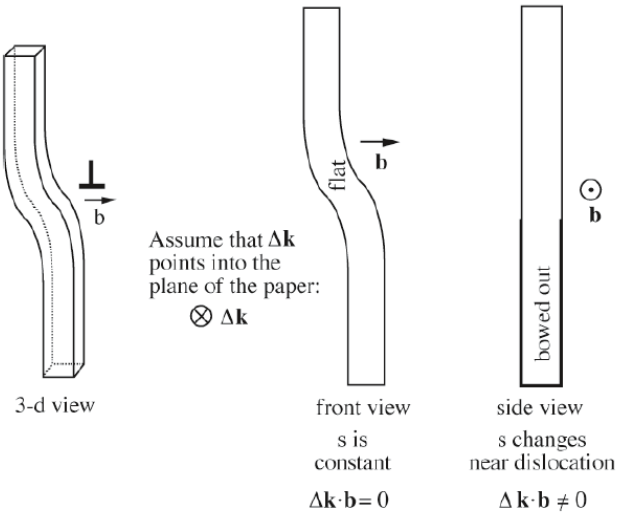

Figure 44: The Left Half of an Edge Dislocation Column showing the TEM Null Contrast Rule (Reprinted from [82])

II.6.2 High Angle Annular Dark Field Scanning Transmission Electron Microscopy

One useful application of TEM is the ability to acquire elemental line scans of a specimen with nano-scale precision. This can be accomplished by using high angle annular dark field (HAADF) scanning transmission electron microscopy (STEM). HAADF STEM images are formed using incoherently scattered electrons, and are therefore unaffected by constructive or destructive interference between phases of wavefunctions of electrons interacting with different atoms. HAADF STEM images are therefore more direct in interpreting atomic positions and types [82].

Electrons which undergo high angle scattering contribute to HAADF STEM images by scattering into the annular detector, shown as the dark ring under the sample in Figure 45 [82]. The interaction cross-section of high angle electron scattering, known

as Rutherford scattering, is proportional to Z^2. Therefore, elemental contrast is low for low-Z elements (like Li, Be… N).

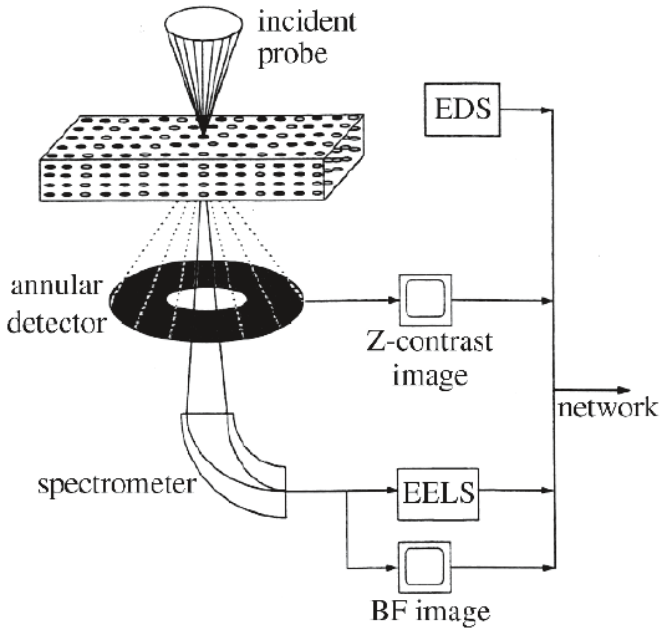

Figure 45: Illustration of High Angle-Scattered Electrons Contributing to the HAADF STEM Signal (Reprinted from [82])

CHAPTER III

METHODS

Chapter III presents the experimental and computational methods in this work, including the LAM build process and heat treatment protocols, sample preparation, irradiation, and post-irradiation examinations (PIE). Additively manufactured ODS alloys and neutron irradiation of I600 and 316L LAM alloys will be discussed in this section for completeness since they were part of the larger scope of the project; however, they were not extensively involved in the analysis of this dissertation and will therefore not be discussed in Chapters IV or V.

III.1 Laser Additive Manufacturing and Sample Labeling

The Inconel 600 and 316L stainless steel LAM test specimens were additively manufactured by Quad City Manufacturing Laboratory (QCML) using an EOS M270 Extended-Titanium PBF system, while the ODS rods were manufactured at the QCML using a LENS system. The optimization of PBF and LENS system parameters for the fabrication of LAM rods is discussed in Chapter II.

One objective of this work was to evaluate potential differences in material properties that may arise as a consequence of different build directions. To this end, cylindrical alloy rods were prepared with axes that were oriented 0°, 45°, and 90° from the LAM beam current (see Figure 4 and Figure 6). The LAM samples were built using a laser power of 195 W and a scan speed of 1100 $mm \cdot s^{-1}$ for I600 and 1200 $mm \cdot s^{-1}$ for

316LSS. The average density of LAM I600 and 316LSS rods were approximately 99% TD. LAM I600 rods were heated treated at 900 °C in argon with no cold working, and LAM 316LSS rods were heat treated at 650°C in argon with no cold working. Similarly, I600 control specimens were cold rolled and annealed at 980 °C in argon with no cold working in the conventional manner, while 316LSS control specimens were cold rolled and annealed at 1040 °C for 1 hour with no cold working.

The metal powders used to fabricate the I600, 316LSS, and ODS LAM specimens were characterized using SEM/EDS at the QCML prior to rod fabrication. These analyses is summarized in Table 3-Table 5 (courtesy Lockheed Martin from an unpublished report). Also included in Table 3-Table 5 is the composition of the control alloy rods purchased from Metal Samples Inc.

Included in Table 3-Table 5 is the relative probability (P_{PKA}) of each element in the rods to be the primary knock on atom (PKA) from a fission spectrum-averaged fast neutron (assuming natural isotopic distributions). The relative probability that an atom of type "*i*" is the PKA is defined by Eq. 17, where A_i is the relative abundance of nuclide species i and σ_i is the average fission spectrum total neutron interaction cross-section of atom i. A robust method of sample identification was required to ensure that samples are not mixed up. The back side of each sample was engraved for sample identification using an electric engraving tool shown in Figure 46.

Eq. 17

$$P_{PKA}(\%) = \frac{A_i \cdot \sigma_i}{\sum_{i=1}^{N} A_i \cdot \sigma_i} \cdot 100$$

Table 3: EDS Composition of Powder Used to Build LAM Inconel 600, Composition of Conventionally Manufactured Control, and Relative Probability of Being the PKA of a Fast Neutron

Component	Ni	Cr	Fe	Mn	S	Si	Cu
LAM Powder (%)	74	16	8.1	1.1	0.0	0.5	0.1
Conventional (%)	73	16	9	0.2	0	0.2	0.2
P_{PKA} (%)	74	16	8	1	~ 0	< 1	~ 0

Table 4: EDS Composition of Powder Used to Build LAM 316L Stainless Steel, Composition of Conventionally Manufactured Control, and Relative Probability of Being the PKA of a Fast Neutron

Component	Fe	Cr	Ni	Mn	S	Si
LAM Powder (%)	71.4	17	9.1	1.7	0.2	0.6
Conventional (%)	71.2	17	10	1.3	0	0.3
P_{PKA} (%)	71	17	10	1	~ 0	< 1

Table 5: EDS Composition of Powder Used to Build LAM ODS Steel, and Relative Probability of Being the PKA of a Fast Neutron

Component	Fe	Cr	Ni	Y	O	Mn	Mo	S	Si
LAM Powder (%)	66.4	17	7.5	5.2	1.4	2.4	0.4	0.0	0.2
Conventional (%)	No Spec for ODS								
P_{PKA} (%)	67	17	8	5	<1	2	<1	0	<1

Figure 46: Sample ID Electrical Engraver

III.2 Electron Discharge Machining and Polishing

The LAM and conventionally manufactured rods were cut into 1 mm thick discs in order to perform multiple tests on each alloy and build orientation. In order to minimize lost material and subsurface cutting damage, electron discharge machining (EDM) was employed for cutting. Although EDM cutting is not as damaging as conventional blade/mechanical cutting, EDM does damage to the sample.

An illustration of the damaged layers that are typically observed from EDM is shown in Figure 47. The physical mechanisms behind the generation of these damaged layers are explained by Choudhary et. al. and are briefly summarized as follows [83]. The EDM method exploits the destructive properties of focused electrical pulses. An electrical pulse is focused on the surface of a workpiece suspended in a dielectric fluid. The process of matter removal (i.e. the cutting action) is due to thermal erosion; heat from the electrical discharge vaporizes a small region of the workpiece, which is then washed from the resulting gap by the continuously flushing dielectric fluid [84]. The cut thickness, also known as the kerf, was approximately 0.33 mm.

If the dielectric material does not flush out all of the molten material quickly enough, some of it may re-solidify on the machined surface due to the rapid cooling in the dielectric fluid. This layer is called the "recast layer", and is generally between 2-50 µm thick [83, 85]. The recast layer is hard, brittle, and porous. Beyond the recast layer is a region which did not vaporize during the electrical pulse, but was superheated and rapidly quenched due to thermal conduction and matter diffusion through the workpiece. This region, called the heat-affected zone (HAZ), is characterized by residual thermal stresses and cracks, and is approximately 25 µm thick for steels [83]. Beyond the HAZ is a "converted layer" in which the grain structure has changed due to stresses which propagated through the HAZ. The converted layer has an average thickness of about 20 µm in steels [86].

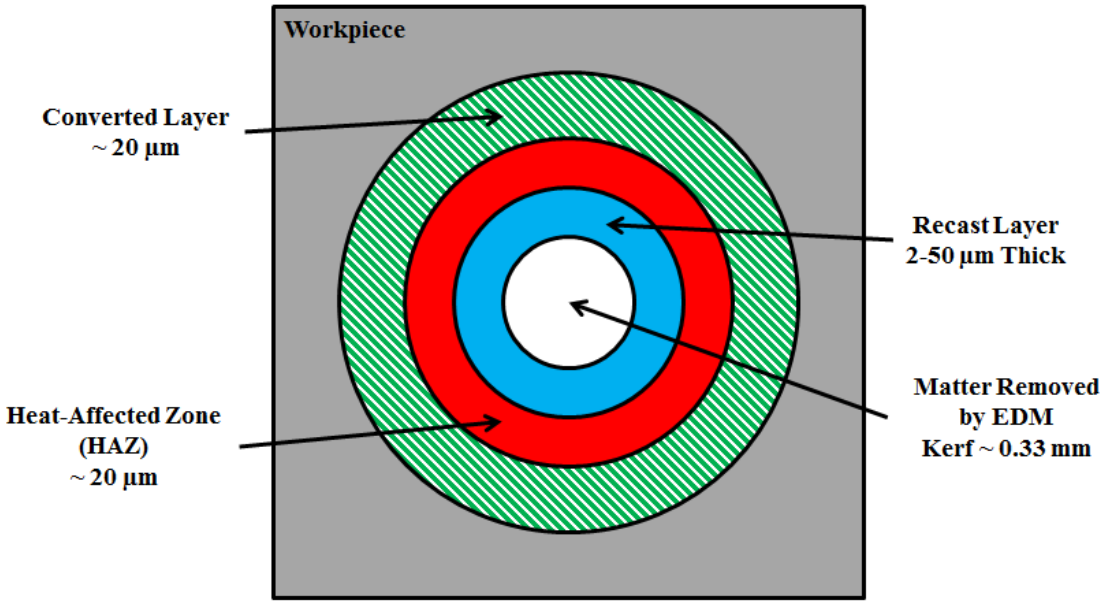

Figure 47: Illustration of Damaged Layers Resulting from EDM Cuts

Excessively thick (i.e. > 1 mm) ion beam samples will yield increasingly large temperature gradients due to ion beam heating. Likewise, large discs would not fit into the sample holder for neutron irradiation. Therefore, each disc was cut to be approximately 1 mm thick. All ion beam discs were then cut into 4-piece slices, illustrated in Figure 48. All discs designated for neutron irradiation were cut in half, illustrated in Figure 49. Figure 50 shows several samples cut by EDM and labeled using the engraver.

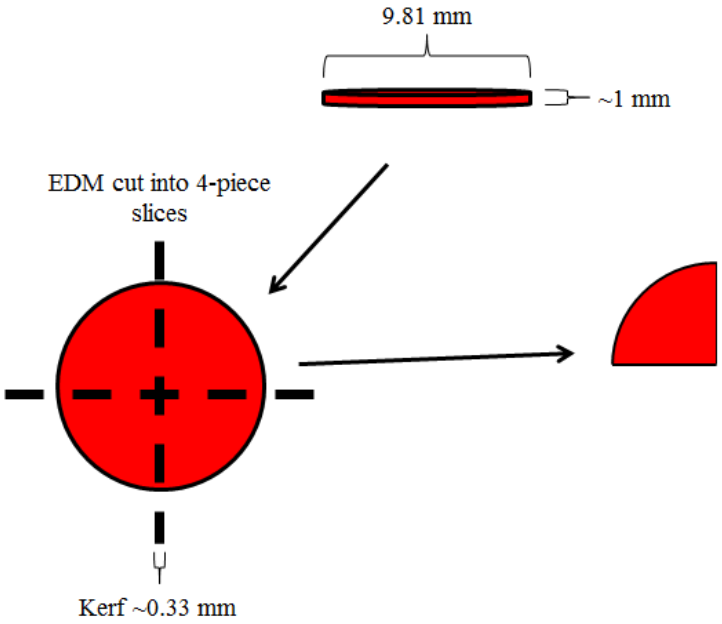

Figure 48: Illustration of EDM Cuts for Ion Beam Samples

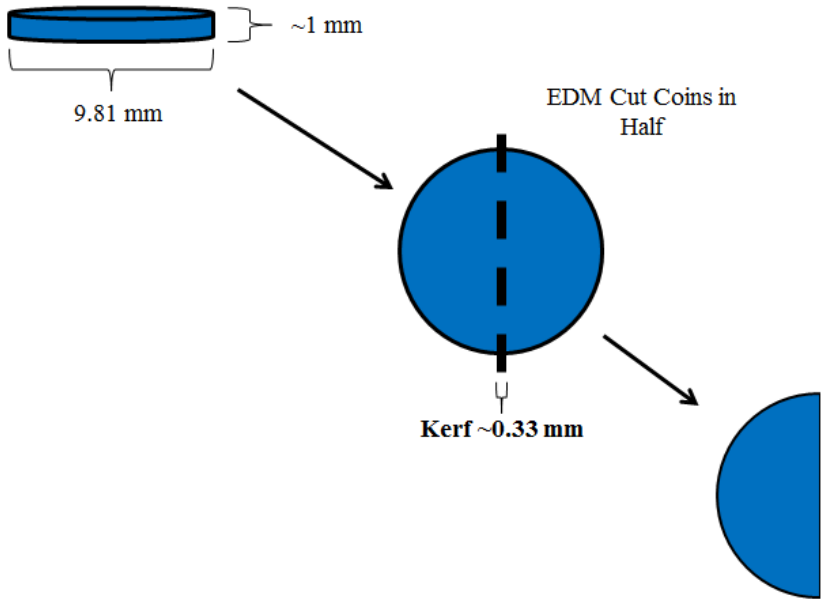

Figure 49: Illustration of EDM Cuts for Neutron Irradiation Samples

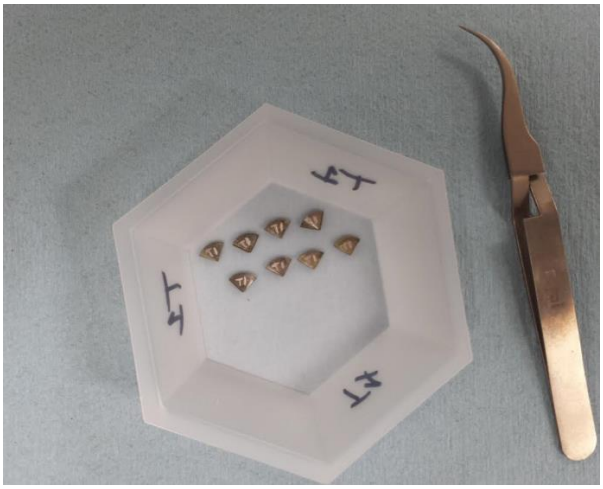

Figure 50: Samples Cut into Quarter-Circles using EDM and Labeled using the Electrical Engraver

Smooth surface polishing is critical for obtaining meaningful EBSD, TEM, and nanoindentation results. Nowell et. al. have compared various polishing methods using Inconel 600 samples for EBSD [87]. Several different polishing protocols were attempted using different materials, both by hand a by using the MiniMet™ 1000 polisher. A vibratory polisher was not available for this work.

The method which achieved the best polish utilized a MiniMet™ 1000 as follows. Samples were initially polished using silicon carbide abrasive papers submerged in distilled water progressively up to 1200 grit for 8 minutes at each step using a speed setting of 35 and a force setting of 0 lbs. Rough polishing was followed by intermediate polishing using 3 µm MetaDi® Supreme Diamond suspension (Buehler, product number 40-6631) on TriDent™ intermediate polishing cloth (Buehler, product number 40-7518), then with 1 µm MetaDi® Supreme Diamond suspension (Buehler, product number 40-6630) on TriDent™ intermediate polishing cloth, both for 20 minutes using a speed setting of 35 and a force setting of 0 lbs. Both intermediate polishing fluids are classified as polycrystalline diamond (PCD) mechanical abrasive suspensions.

Final polishing for all samples utilized a 50 nm chemical/mechanical polishing slurry from Pace Technologies (catalog number CMP-1005-16) on micro-cloth (Buehler, product number 40-7218) for 60 minutes using a speed setting of 35 and a force setting of 0 lbs. (see Figure 51). Prior to applying the slurry, the micro-cloth was first lightly moistened with distilled water. Other final polishing solutions (PCD, alumina, etc.) yielded either significant pullout or abrasive embedment.

After final polishing, the sample was rinsed with distilled water using a squirt bottle. Any remaining slurry abrasives were then mechanically removed by gently rubbing the (wet) sample surface with a cotton swab that was pre-soaked in stilled water. The sample surface was then rinsed thoroughly with isopropyl alcohol (IPA) and rapidly dried with compressed air to prevent staining.

Figure 51: Final Polishing of Ion Beam Samples using the MiniMet™ 1000 and Chemical/Mechanical Polishing Slurry on Micro-Cloth

III.3 Neutron Irradiation

III.3.1 Neutron Irradiation in the 1 MW TAMU TRIGA Reactor

Inconel 600 and 316L stainless steel were placed in the NSC TRIGA irradiation assembly called the "pitchfork". The pitchfork schematics are shown in Figure 52 (courtesy of the TAMU NSC from an unpublished report). The ODS samples were

delivered to TAMU much later than the other samples. As a result, there was not enough time to perform irradiation tests on the ODS samples.

The pitchfork is designed to fit guide tubes in the gaps formed by adjacent fuel bundles. Guide tubes can therefore potentially be placed in every other coolant channel. The horizontal bar on the top is primarily used for placement, but also prevents the guide tubes from moving. In order to achieve the highest dose possible during neutron irradiation, samples were positioned as close to the center of the reactor core as possible (i.e. between fuel bundles near the neutron flux peak). The procedure for handling the support structure is contained in the TAMU NSC Support Structure Safety Assessment, but will be briefly discussed here.

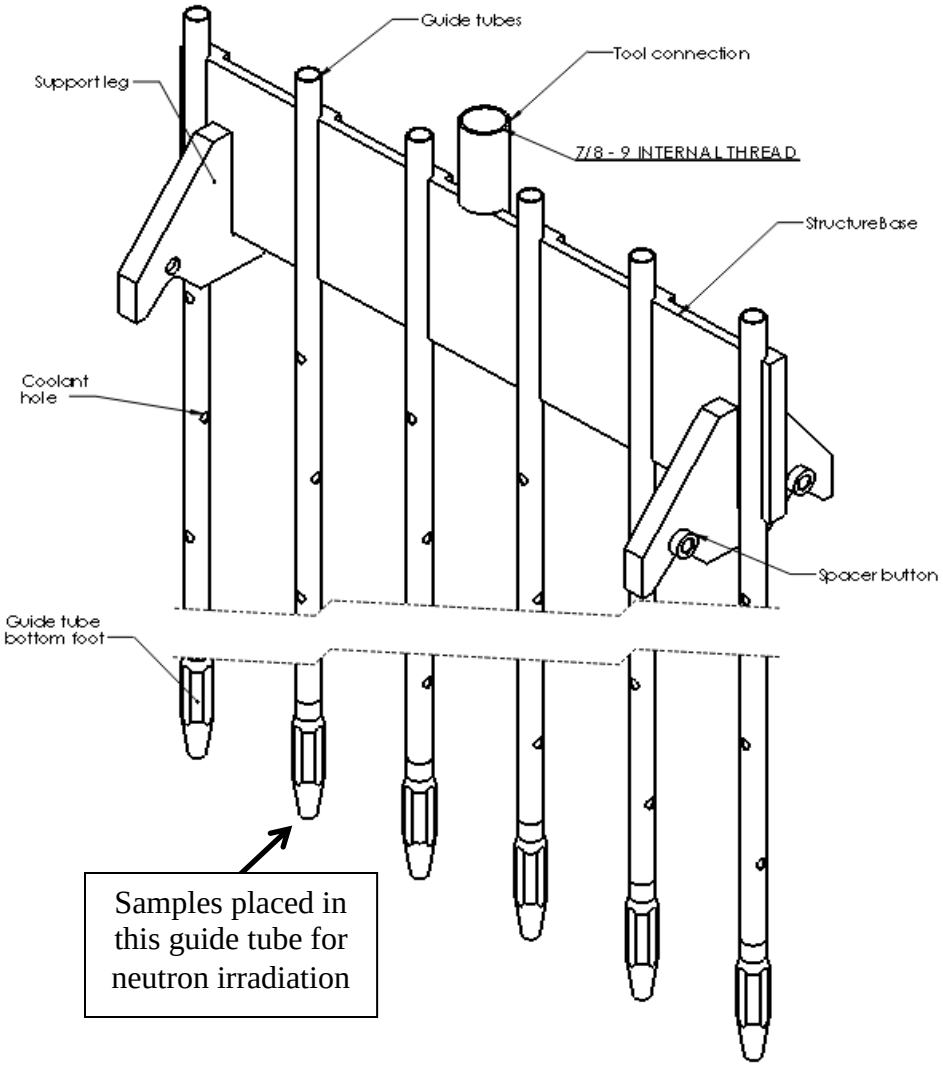

Figure 52: The Pitchfork In-Core Neutron Irradiation Assembly

The Inconel 600 and 316L stainless steel samples were irradiated in three different batches, with each batch exposed to the neutron field for a different duration of time. This corresponds to achieving three different neutron doses from which dose-dependent material responses can be determined. The samples were initially situated in the pitchfork during irradiation as shown in Figure 53. The gray lines indicate the

location of thin aluminum cans which the samples will reside in. These cans were designed to make sample translocation to/from the pitchfork easier, and to prevent Inconel and steel samples from contacting one another during neutron irradiation. Since the samples did not exceed temperatures of 100 °C, no interaction between the aluminum cans and steel/Inconel was expected to occur.

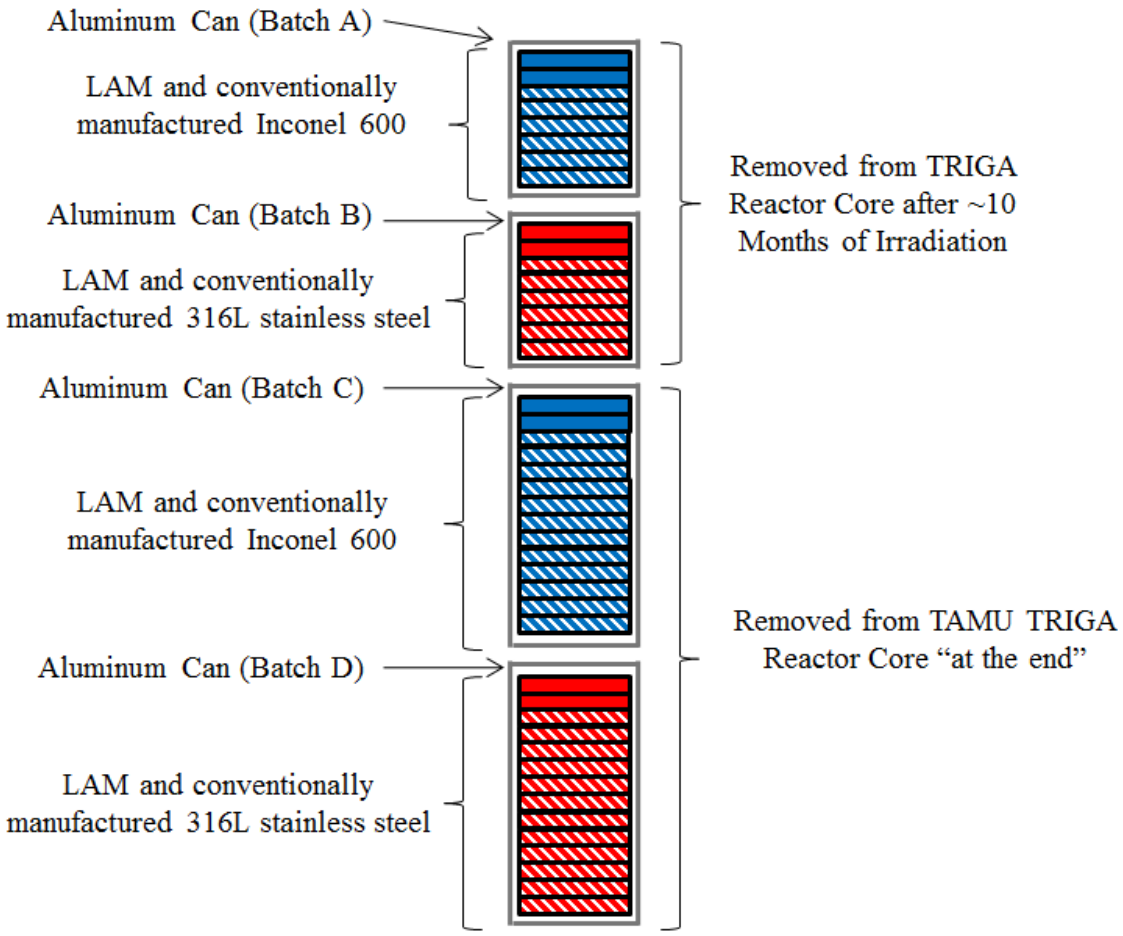

Figure 53: Initial Arrangement for Neutron Irradiation of Batches A, B, C, and D of LAM (dashed) and Conventionally Manufactured (Solid) Inconel 600 (Blue) and 316L Stainless Steel (Red) Samples

After 10 months of residing in the TRIGA Reactor core, batches A and B were extracted from the core and placed on the far side of the reactor pool (far from the neutron field to allow adequate time for radioactive decay before handling), and replaced with Batches E and F, as shown in Figure 54. Batches C, D, E, and F will be extracted at an undetermined later time. This achieves three different neutron doses for batches A/B, C/D, and E/F. The doses each batch has received (at the time this document was written) will be discussed in the next section.

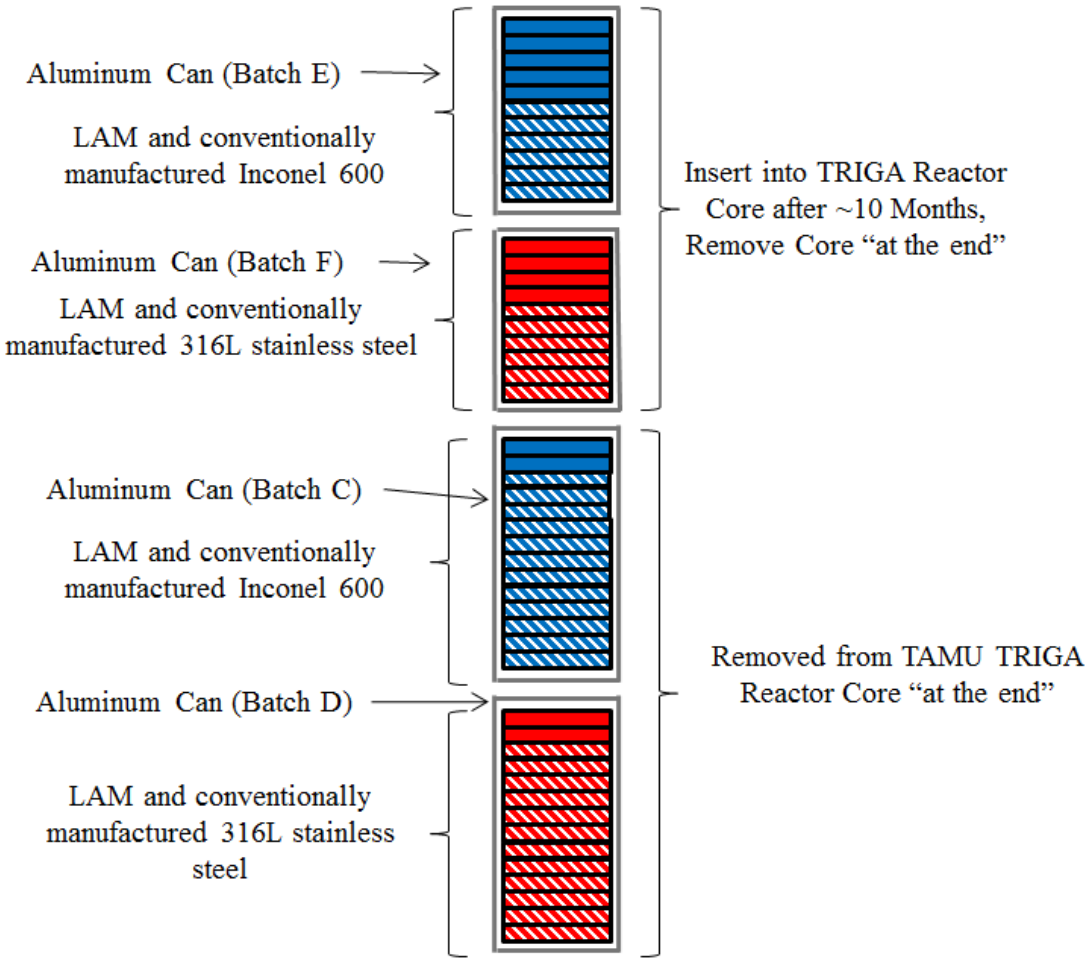

Figure 54: Final Arrangement for Neutron Irradiation of Batches C, D, E, and F of LAM (dashed) and Conventionally Manufactured (Solid) Inconel 600 (Blue) and 316L Stainless Steel (Red) Samples

All handling of the radioactive samples was conducted with the samples still underwater in order to adhere to personnel receiving radiative doses "as low as reasonably achievable" (ALARA). The TRIGA reactor pool is over 30 feet deep; dropping an aluminum can (in which the samples reside) would cause the samples to irretrievably sink to the bottom of the reactor pool. A transfer "funnel" was designed and fabricated in order to ensure that the samples do not sink to the bottom of the reactor

pool if they were dropped during transfer to/from the pitchfork. The funnel was designed and fabricated at the TAMU NSC by NSC Manager of Engineering Jan Vermaak, and is illustrated in Figure 55. During sample transfer, a long rod with a spongy tip which fastens into the aluminum cans, called the "spear", was used to grab onto the aluminum cans, remove samples from the pitchfork tube, and place them inside the funnel decay tubes (labeled 1-6 in Figure 55). Images of the insertion/extraction protocol follow in Figure 56 and Figure 57.

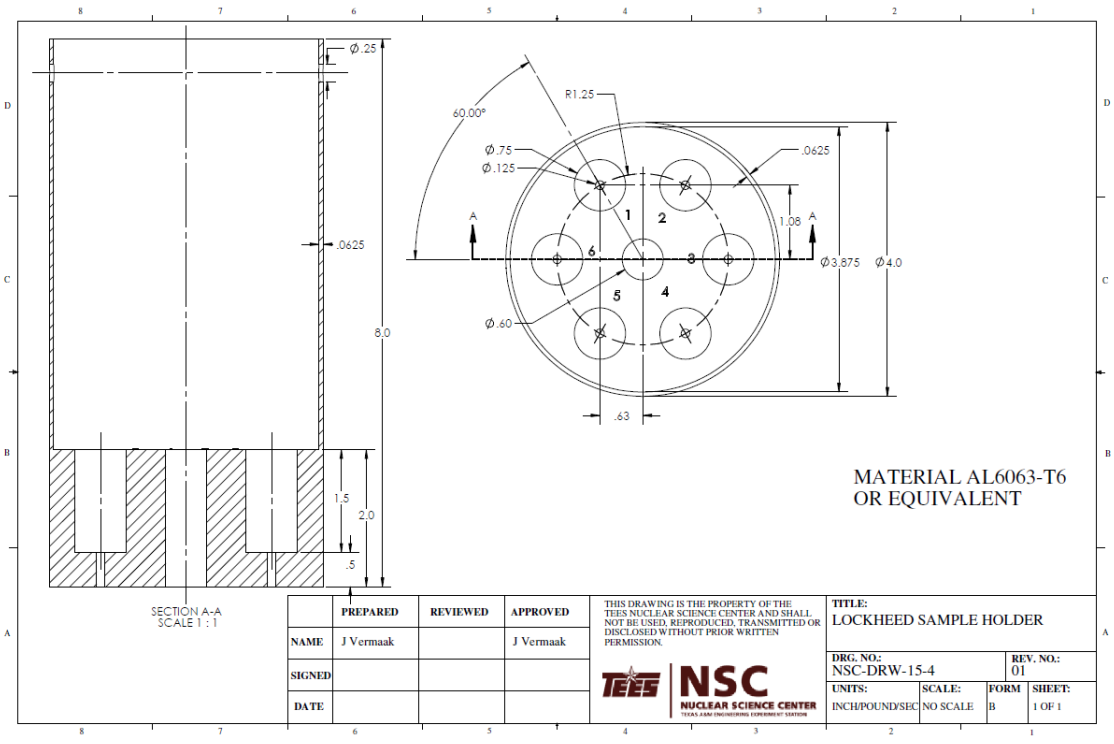

Figure 55: TRIGA Funnel Design with Sample Holder Tubes Numbered 1-6

The protocol for inserting samples into the NSC TRIGA Reactor core is as follows:

1) Place samples inside designated aluminum cans (Note: samples will not be radioactive at this point)
2) Fill a small bucket with water from the TRIGA reactor pool
3) Slowly fill aluminum cans with water from the TRIGA reactor pool to prevent bubbles from causing samples to potentially fall out of the cans during inserting into the pitchfork (Note: do not stand over the reactor pool during this step in case the samples are dropped)
4) Using the forklift, position the pitchfork on the opposite side of the reactor core in the reactor pool so the pitchfork tubes are easily within reach of the "spear" (Note: the pitchfork should remain underwater during this entire time in accordance with ALARA)
5) Fasten the decay funnel in position over the designated pitchfork guide tube
6) Place the samples in pitchfork guide tube in the designated order using the "spear"
7) Once the samples are inside the pitchfork, remove the funnel and place aside
8) Using the forklift, slowly lower the pitchfork back into the reactor pool until fully submerged (Note: slowly lowering the pitchfork into the water reduces the rate at which air bubbles are produced/rise up through the guide tube which may carry the samples/aluminum cans upward and out of the pitchfork with them)
9) Using the forklift, position the pitchfork in the reactor core and irradiate the samples for the designated period of time

The protocol for removing the samples from the TRIGA Reactor core for radioactive decay is as follows:

1) Irradiate samples for the designated period of time in the TRIGA reactor core
2) Using forklift, lift the pitchfork out from the reactor core
3) While remaining completely submerged, slowly move the pitchfork to the far end of the reactor pool opposite from the reactor core
4) Raise the pitchfork so that it is close enough to the surface of the water that the spear can reach the bottom of the pitchfork guide tubes
5) Fasten the funnel over the pitchfork guide tube containing the samples, and tie the free end of the funnel rope down securely
6) Lower the spear into the pitchfork guide tube and depress the spongy tip into the top opening of the topmost aluminum can
7) Lift the aluminum can out of the pitchfork guide tube and place it into an empty decay funnel tubes
8) Tilt the spear to a 30° angle and rotate the spear until the aluminum can detaches from the spongy spear tip. (Note: do not tip the aluminum cans over on their sides or the samples will fall out)
9) Repeat until all designated batches have been extracted
10) Untie the decay funnel rope from the structure it was previously fastened to

11) While keeping the funnel submerged, slowly move the funnel to a designated bucket in the decay cage located inside the periphery of the reactor pool until samples have sufficiently decayed

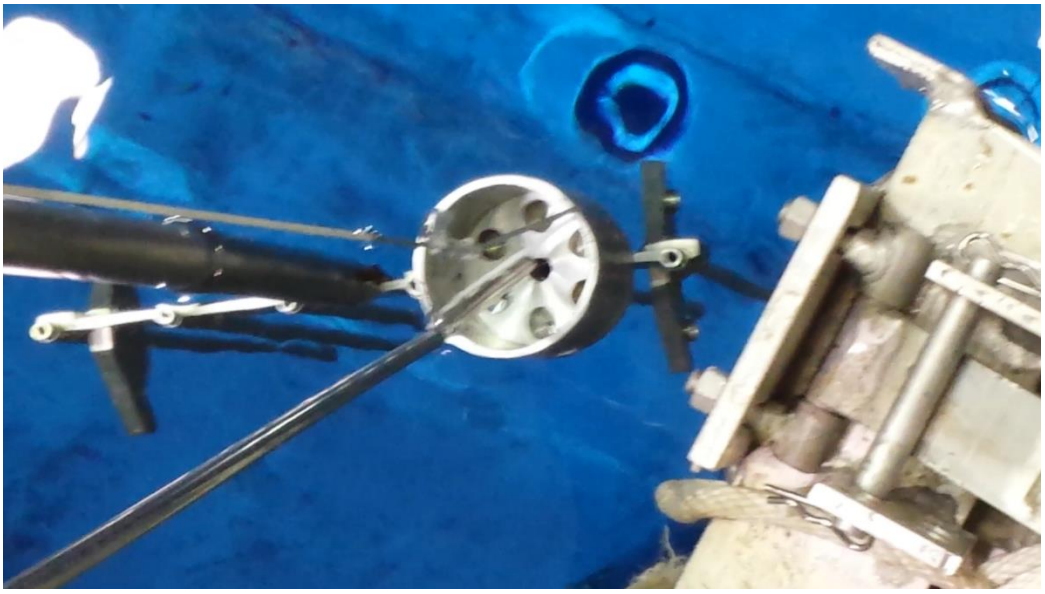

Figure 56: Inserting the Spear through the Submerged Funnel and Into the Pitchfork for Sample Extraction

Figure 57: Tilting the Spear 30° and Rotating to Detach the Aluminum Can from the Spear, Guiding the Can into the Submerged Decay Funnel Tube

III.3.2 Calculation of Neutron Damage

The accumulated doses in Inconel 600 and 316L stainless steel samples from neutron irradiation in the TAMU TRIGA Reactor are summarized in Table 6. Batches A-F are defined in Figure 53 and Figure 54. The calculation of neutron damage is provided in the Appendix.

Table 6: Accumulated Doses in Inconel 600 and 316L Stainless Steel Samples from Neutron Irradiation

Batch	Beginning of Irradiation	End of Irradiation	Irradiation Time (Months)	Dose (dpa)
A	Dec. 1, 2015	Nov. 7, 2016	11	0.02
B	Dec. 1, 2015	Nov. 7, 2016	11	0.02
C	Dec. 1, 2015	Ongoing	23	0.04
D	Dec. 1, 2015	Ongoing	23	0.04
E	Nov. 7, 2016	Ongoing	12	0.02
F	Nov. 7, 2016	Ongoing	12	0.02

III.3.3 Neutron Activation Analysis

Neutron activation analysis (NAA) was conducted by Jan Vermaak, TAMU NSC Manager of Engineering, using the Monte Carlo modeling code FISPACT. A summary of the Inconel 600 and 316L stainless steel NAA is shown below in Table 7 and Table 8, respectively. The activities and doses shown in Table 7 and Table 8 are per gram of material for 6 and 12 month irradiations. Actual samples about 0.5 grams per disc. A full list of nuclides and activities for Inconel and steel neutron irradiations is provided in the Appendix.

Table 7: Inconel 600 NAA Summary

Time in TRIGA Reactor Core (Months)	Decay Time (Days)	Activity ($Bq \cdot g^{-1}$)	Activity ($mCi \cdot g^{-1}$)	Dose Rate ($Sv \cdot g^{-1} \cdot hr^{-1}$)
6	7	9.00E+09	243	2.34E-04
	21	5.67E+09	153	1.84E-04
	28	3.16E+09	85	1.37E-04
12	7	1.27E+10	343	3.75E-04
	21	8.10E+09	219	2.98E-04
	28	4.61E+09	125	2.26E-04

Table 8: 316L Stainless Steel NAA Summary

Time in TRIGA Reactor Core (Months)	Decay Time (Days)	Activity ($Bq \cdot g^{-1}$)	Activity ($mCi \cdot g^{-1}$)	Dose Rate ($Sv \cdot g^{-1} \cdot hr^{-1}$)
6	7	8.17E+09	221	9.11E-05
	21	4.95E+09	134	6.14E-05
	28	2.65E+09	72	3.87E-05
12	7	1.14E+10	308	1.34E-04
	21	6.99E+09	189	9.25E-05
	28	3.83E+09	104	5.96E-05

III.4 Ion Beam Irradiation

III.4.1 Simulation of Ion Damage in Inconel 600

Ion beam irradiation of Inconel 600 was conducted using a particle accelerator at the TAMU Accelerator Laboratory. 3.5 MeV Ni^{+} self-ions were selected to avoid unwanted chemical or gas bubble effects, and also because nickel atoms in Inconel 600 are statistically most likely to be the PKA from fast neutrons in a nuclear reactor (see Table 3). The dose and Ni^{+} implantation concentration as a function of depth were determined by computational simulations using the SRIM code [88]. The atomic displacement threshold energy of 40 eV was used for nickel, chromium, iron, and

manganese in the Kinchin-Pease simulation model in accordance with ASTM E521-83 standards (see Table 9) [89-91]. SRIM 3D simulation output spectra of vacancies, implantation, ionization, and phonons generated from 3.5 Ni^{+} bombardment into Inconel 600 are shown in Figure 58 - Figure 61. 100,000 ions were used in this simulation for statistical purposes. As shown in the SRIM simulation results, the maximum dose (vacancies produced) occurs at a shallower depth than the maximum ion implantation density.

Table 9: Recommended Values of the Atomic Displacement Energy T_d by ASTM E521-83 Standards

Element	T^{min} (eV)[A]	T_d (eV)
Al	16	25
Ti	19	30
V	-	40
Cr	28	40
Mn	-	40
Fe	20	40
Co	22	40
Ni	23	40
Cu	19	30
Zr	21	40
Nb	36	60
Mo	33	60
Ta	34	90
W	40	90
Pb	14	25

[A] Effective threshold measured in polycrystalline specimens

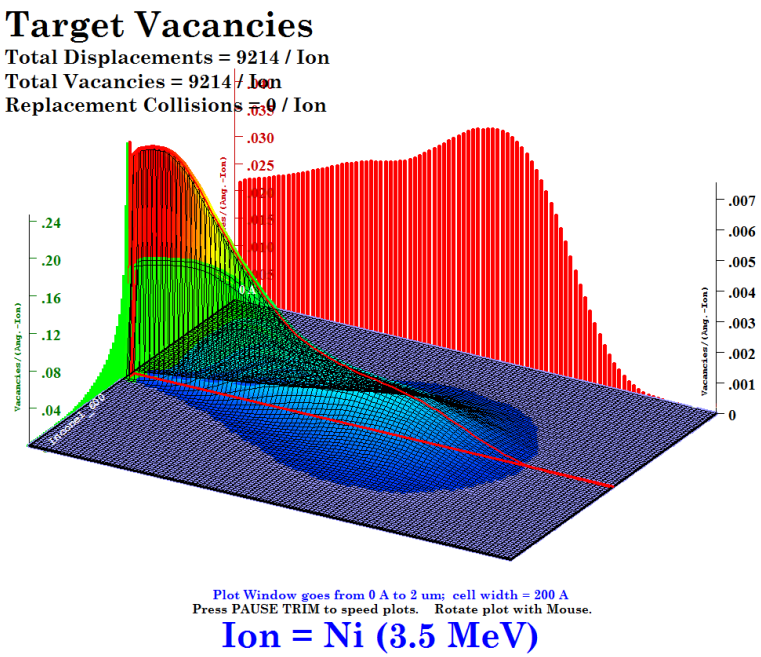

Figure 58: 3D SRIM Vacancy Distribution Spectrum of 3.5 MeV Nickel Ions into Inconel 600

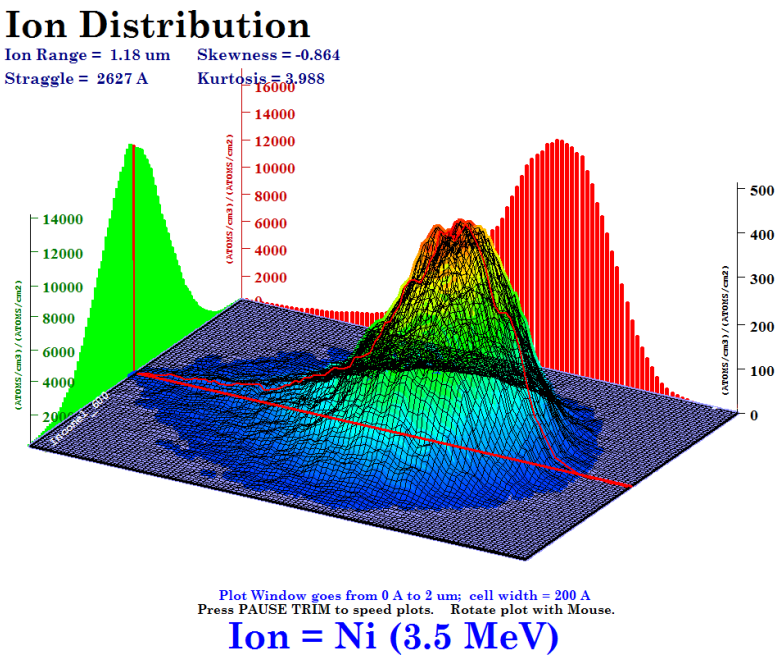

Figure 59: 3D SRIM Implantation Distribution Spectrum of 3.5 MeV Nickel Ions into Inconel 600

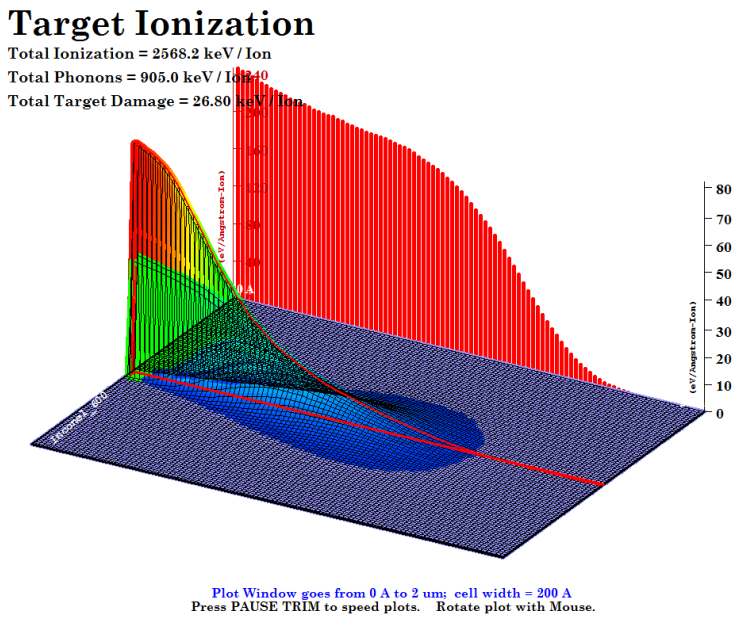

Figure 60: 3D SRIM Ionization Distribution Spectrum of 3.5 MeV Nickel Ions into Inconel 600

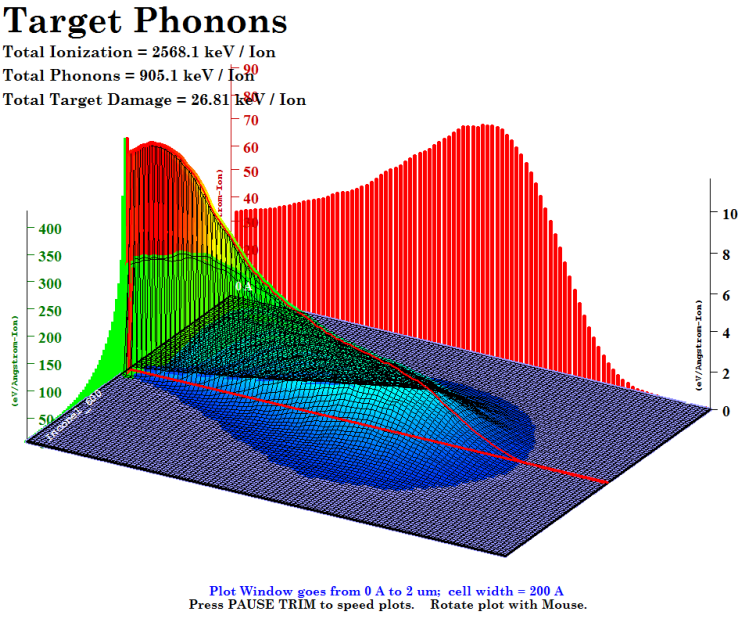

Figure 61: 3D SRIM Phonon Distribution Spectrum of 3.5 MeV Nickel Ions into Inconel 600

SRIM is a Monte Carlo ion transport code that directly calculates many useful quantities as a function of ion penetration depth, such as vacancies per ion, sputtering, etc. SRIM does not, however, calculate dose as a function of depth since this requires knowledge of the ion beam. Eq. 18 can be used to calculate dose D as a function of depth (in dpa), where ξ is the damage rate determined by SRIM (vacancies per ion per unit length, varied by penetration depth), Φ is the flux of the ion beam, ρ is the target material atomic density, and t is ion beam irradiation time at flux Φ. The ion implantation concentration as a function of depth P (ions per unit volume) can be determined using Eq. 19 where χ is the ion implantation per unit length (from SRIM).

Eq. 18

$$D = \xi \Phi t \rho^{-1}$$

Eq. 19

$$P = \chi \Phi t$$

It is worth noting that SRIM calculations have three major limitations: (1) there is no buildup of ions or damage within the target (i.e. each calculation determines the effects of one ion traveling through a target which has suffered no previous dose), (2) SRIM does not consider crystallographic effects such as ion channeling or phase changes, and (3) the calculation does not consider thermal effects such as diffusion.

The dose and implantation concentration as a function of depth are illustrated in Figure 62 which shows that there is significant ion-induced damage in the irradiated Inconel 600 samples up to maximum depth of about 1600 nm with the damage peak at about 1100 nm, while the Ni^+ implantation is negligible until a depth of at least 800 nm. Also shown in Figure 62 is the CSDA range limit from which information can be obtained using a 20 kV electron beam in EBSD as determined via the Electron Stopping Powers and Ranges (ESTAR) database from the National Institute of Standards and Technology (NIST). That is, the average electron which penetrates a depth greater than 830 nm perpendicular to the sample surface will not have sufficient energy to escape the sample, and thus will not contribute to the EBSD data. Therefore, all EBSD data of Inconel 600 only represents features which exist in the top 830 nm of the samples. In practice, however, EBSD samples were mounted to a 70° pre-tilted holder for analysis, which reduces the expected depth-range of electrons capable of reaching the EBSD detector.

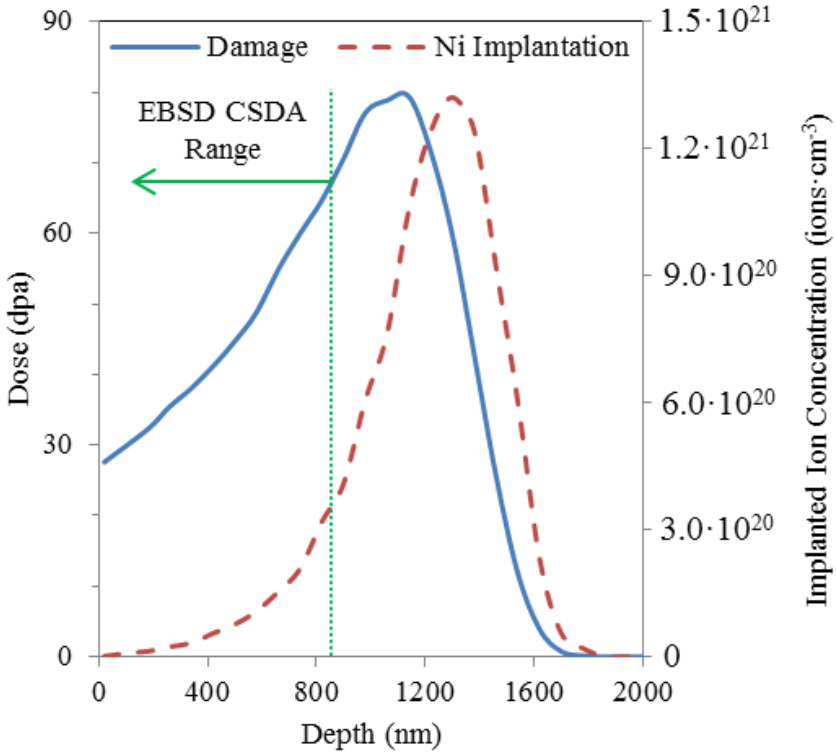

Figure 62: SRIM Calculation of Dose and Ion Implantation Concentration vs. Depth in Inconel 600 Specimens Resulting from Ion Bombardment with 3.5 MeV Nickel Ions using the Kinchin-Pease Model

III.4.2 Protocol for Ion Beam Irradiation of Inconel 600

Irradiation with 3.5 MeV Ni^{+} ions was performed in the arrangement shown below in Figure 63 at the Inconel 600 peak swelling temperature of 650 °C [92]. Temperature fluctuations did not exceed ± 5 °C throughout ion beam irradiation. A 6x6 mm^2 defocused ion beam was chosen over a rastered beam since it more closely resembles neutron damage found in nuclear reactors [89, 93]. The beam current of 250 ± 10 nA produced a maximum dpa rate of $3.4 \cdot 10^{-3}$ dpa·sec^{-1} at the damage peak. The sample chamber pressure was maintained at less than $2 \cdot 10^{-7}$ torr during irradiation.

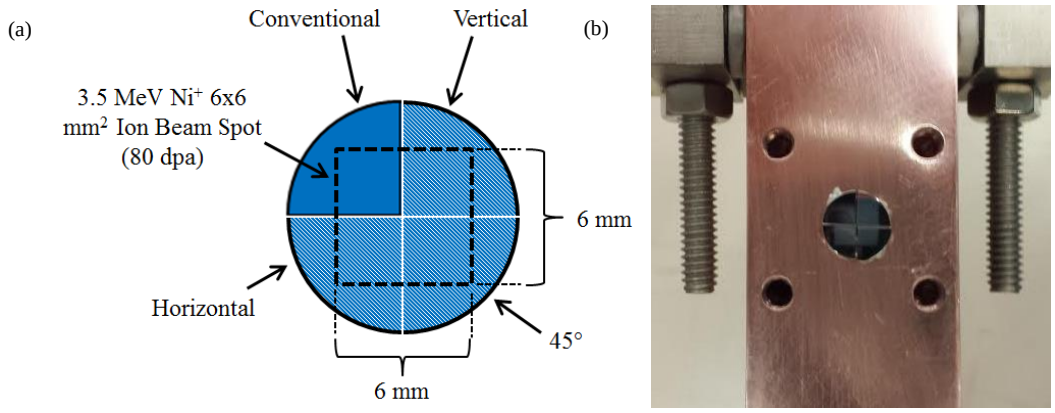

Figure 63: Inconel 600 Sample Arrangement Illustration (a) and Picture (b) for 3.5 MeV Nickel Ion Beam Irradiation to 80 dpa

After ion bombardment, the vacuum was maintained overnight while the samples slowly cooled via radiative heat transfer in order to minimize any unwanted oxidation layers from forming/propagating on the irradiated sample surfaces while they were still warm. The experimental setup (calibrating the beam spot, attaching the samples to the stage, inserting the samples into the chamber, evacuating the chamber, heating the

samples, and allowing the stage/samples to reach thermal equilibrium) took about 3 hours, while the ion beam irradiation took about 6 hours.

A picture of the ion beam accelerator is shown below in Figure 64 with some key components identified. The ion beam spot was tested prior to irradiating the samples by first irradiating a small piece of paper, shown in Figure 65 (top). The burned portion of the paper was then removed with a razor blade, using enough force to scratch the surface of the stage to mark the beam spot (Figure 65, bottom). This allowed the samples to be placed onto the stage such that they were concentric with the ion beam spot. The samples were attached to the stage with Pelco® High Performance Silver Paste as an adhesive (Ted Pella, Inc. prod. # 16047). The silver paste is stable up to about 925 °C in ultra-high vacuum conditions (i.e. no hydrocarbons or volatile organic compounds).

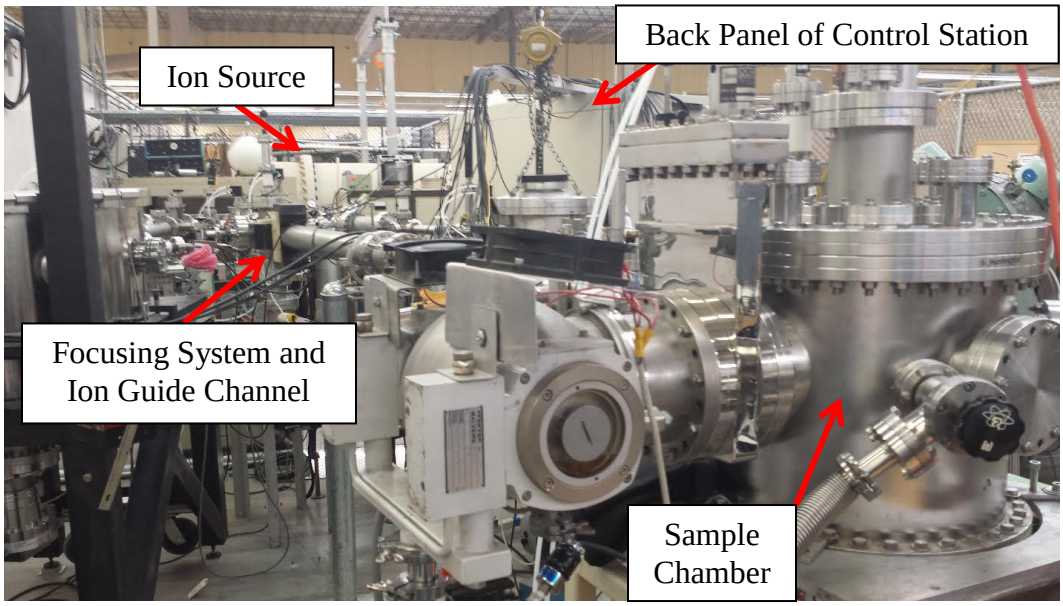

Figure 64: Ion Beam Accelerator System at the Texas A&M Ion Beam Laboratory

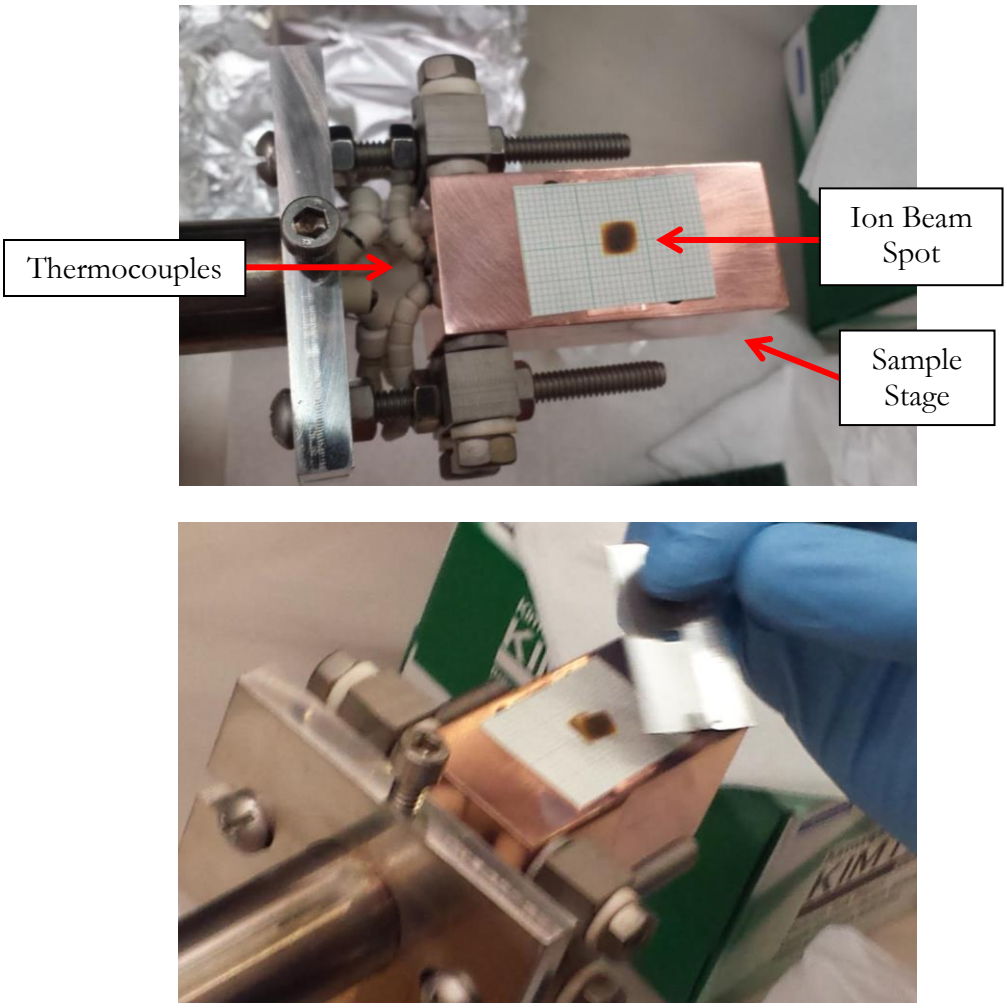

Figure 65: The Ion Beam Spot Calibration Paper (Top), and Engraving of the Ion Beam Spot (Bottom)

III.4.3 Simulation of Ion Damage in 316L Stainless Steel

Ion beam irradiation of 316L stainless steel was conducted using a particle accelerator at the TAMU Accelerator Laboratory. 3.5 MeV iron self-ions were selected to avoid unwanted chemical or gas bubble effects, and also because iron atoms in 316L stainless steel are statistically most likely to be the PKA from fast neutrons in a nuclear reactor. The dose and Fe^{+} implantation concentration as a function of depth was determined by computational simulations using the SRIM code [91]. The atomic displacement threshold energy of 40 eV was used for nickel, chromium, iron, and manganese in the Kinchin-Pease simulation model in accordance with standards [89-91].

SRIM 3D simulation output spectra of vacancies, implantation, ionization, and phonons generated from 3.5 Fe^{2+} bombardment into 316L stainless steel using 100,000 ions are shown in Figure 66 - Figure 69. As shown in Figure 66 - Figure 69, the maximum dose (vacancies produced) occurs at a shallower depth than the maximum ion implantation density. The dose and implantation concentration as a function of depth were calculated using Eq. 18 and Eq. 19 in the same manner as for Inconel 600 before, illustrated in Figure 62 which shows that there is significant ion-induced damage in the irradiated 316L samples up to maximum depth of about 1400 nm with the damage peak at about 900 nm, while the Fe^{+} implantation is negligible until a depth of at least 800 nm. Also shown in Figure 70 is the CSDA range limit from which information can be obtained using a 20 kV electron beam in EBSD.

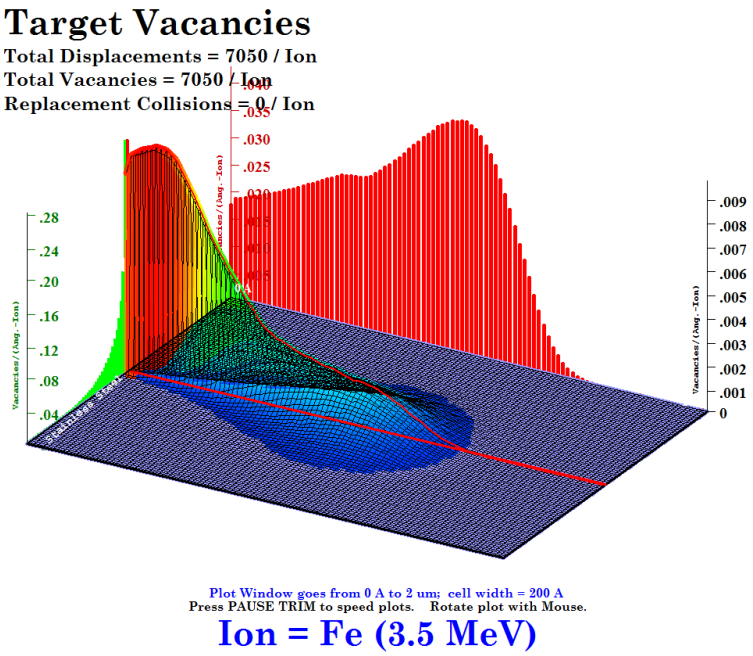

Figure 66: 3D SRIM Vacancy Distribution Spectrum of 3.5 MeV Iron Ions into 316L Stainless Steel

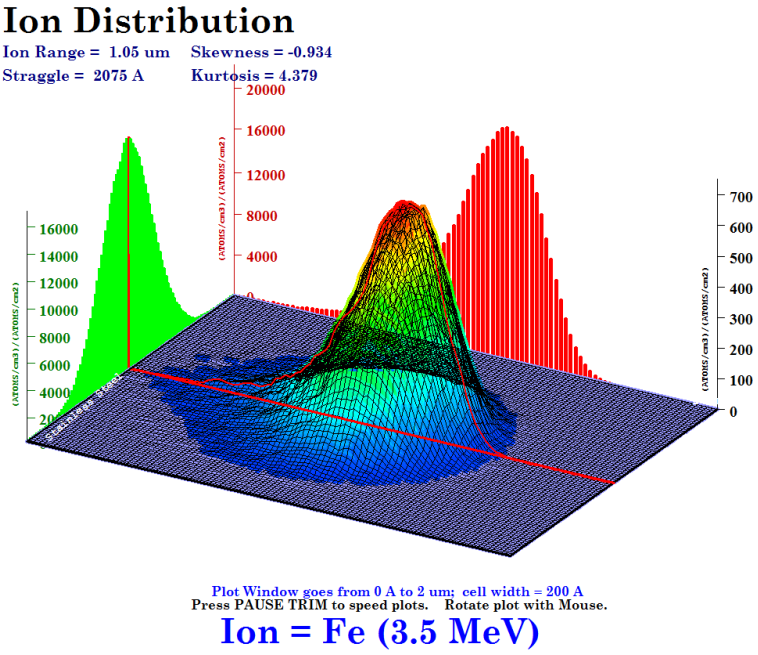

Figure 67: 3D SRIM Implantation Distribution Spectrum of 3.5 MeV Iron Ions into 316L Stainless Steel

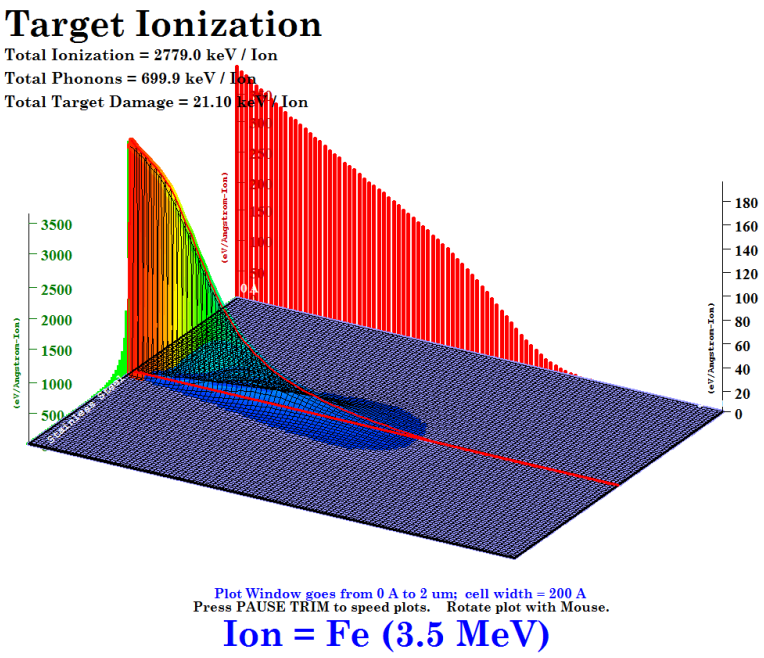

Figure 68: 3D SRIM Ionization Distribution Spectrum of 3.5 MeV Iron Ions into 316L Stainless Steel

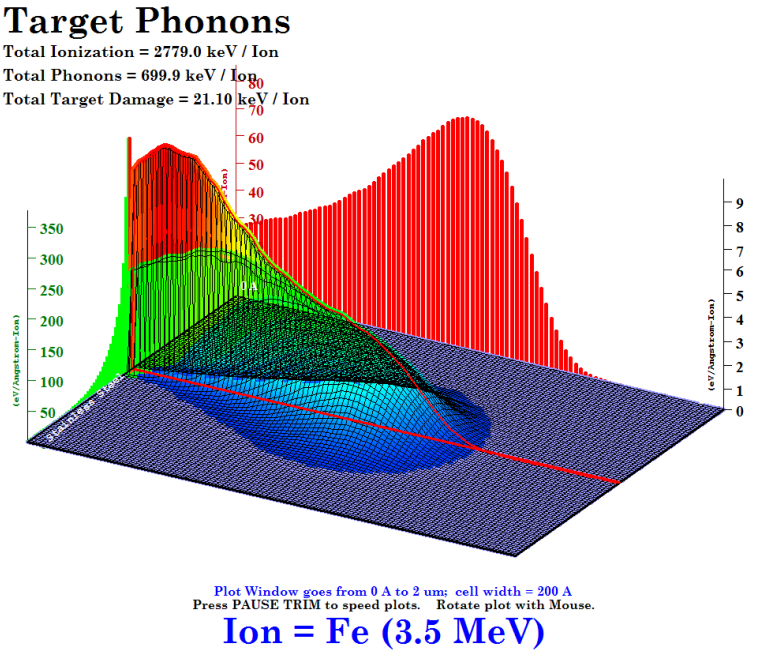

Figure 69: 3D SRIM Phonon Distribution Spectrum of 3.5 MeV Iron Ions into 316L Stainless Steel

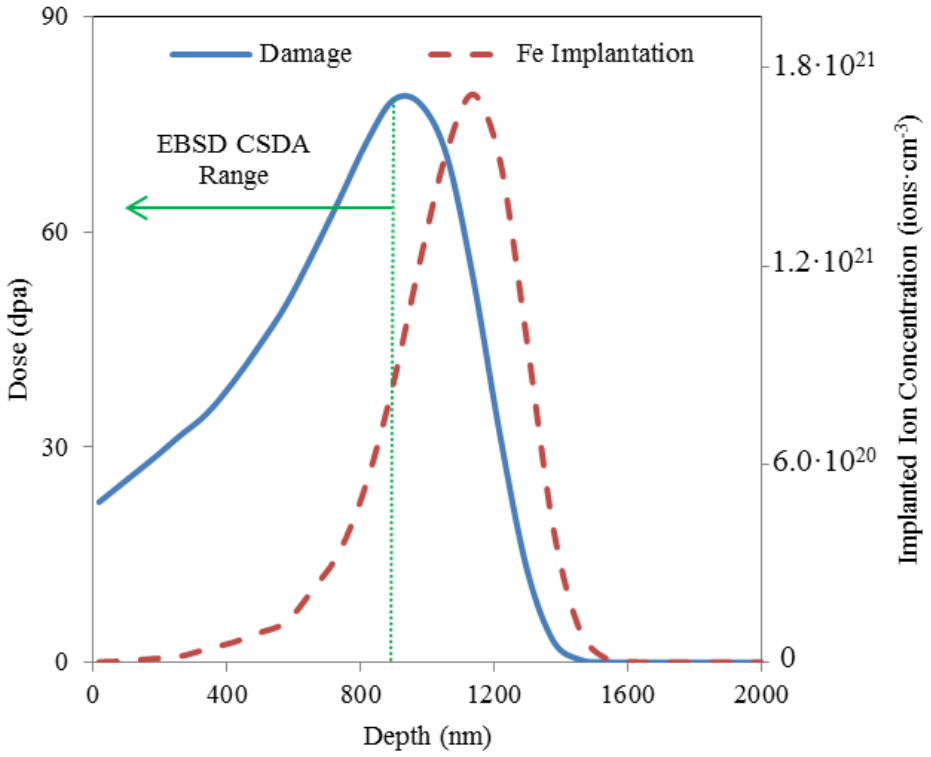

Figure 70: SRIM Calculation of Dose and Ion Implantation Concentration vs. Depth in 316L Stainless Steel Specimens Resulting from Ion Bombardment with 3.5 MeV Iron Ions using the Kinchin-Pease Model

III.4.4 Protocol for Ion Beam Irradiation of 316L Stainless Steel

Irradiation with 3.5 MeV Fe^{2+} ions was performed in the arrangement shown below in Figure 71 at the 316L stainless steel peak swelling temperature of 475 °C [94]. Temperature fluctuations did not exceed ± 5 °C throughout ion beam irradiation. A 6x6 mm^2 defocused ion beam was chosen over a rastered beam since it more closely resembles neutron damage found in nuclear reactors [93]. The beam current of 165 ± 5 nA produced a maximum dpa rate of $1.7 \cdot 10^{-3}$ dpa·sec^{-1} at the damage peak. The sample chamber pressure was maintained at less than $2 \cdot 10^{-7}$ torr during irradiation.

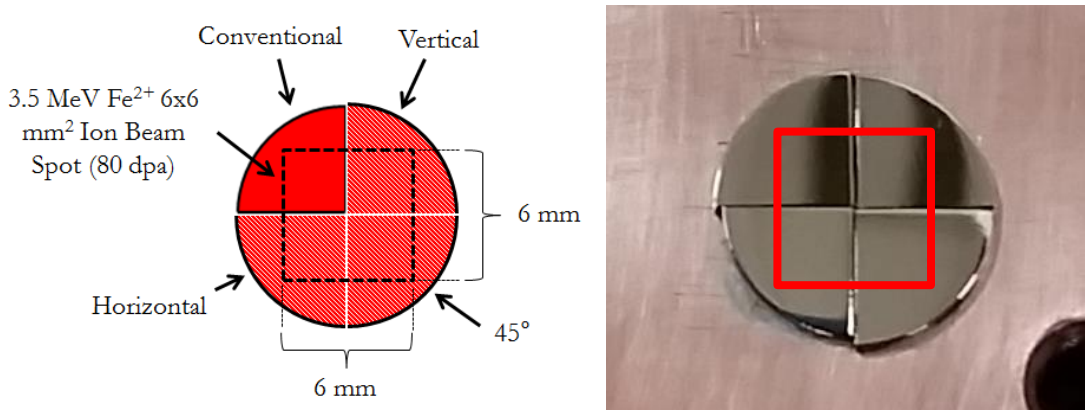

Figure 71: 316L Stainless Steel Sample Arrangement Illustration for 3.5 MeV Iron Ion Beam Irradiation to 80 dpa

III.5 X-ray Diffraction

Preliminary XRD of the unirradiated Inconel 600 and 316L stainless steel samples was performed using the Bruker D8 Advanced X-ray Diffractometer. The samples were placed in the sample holder of a two-circle goniometer and enclosed in the radiation safety housing. The x-ray source was a 2.2 kW Cu x-ray tube, maintained at an operating current of 40 kV and 40 mA. The x-ray optical system used was the standard Bragg-Brentano para-focusing mode with the x-ray diverging from a 1 mm divergence slit (DS) at the tube to strike the sample and converge at a position-sensitive x-ray detector (Lynx-Eye, Bruker-AXS). The two-circle 218 mm diameter goniometer was computer controlled with independent stepper motors and optical encoders for the θ and 2θ circles with the smallest angular step size of 0.0001^{o} 2θ. The XRD parameters used were:

Wavelength	1.54060 Å
Detector	PSD (Lynx-Eye Bruker AXS)

Anti-scatter Slit	12.530 mm
Divergence Slit	1.00 mm
Anti-air-scatter	Knife edge
Scan type	Coupled θ/2θ
Goniometer radius	217.5 mm
Start Angle	5.0 2θ
End Angle	90.0 2θ
Angular Step Size	0.0001 2θ
Total Scan Time	30 minutes

III.6 Scanning Electron Microscopy and Energy Dispersive Spectroscopy

SEM/EDS images were collected using the JOEL JSM-6400 SEM. SEM/EDS data were analyzed using the Iridium Ultra software. Unless otherwise stated, an accelerating voltage of 10 kV was used for JOEL JSM-6400 imaging and elemental maps. Since the alloys are all electrically conductive, no carbon coatings were used. The samples were mounted to the SEM sample holder using double-sided conductive carbon tape (Ted Pella, Inc., Product # 16084-6). Multiple samples were attached to a single mount for SEM characterization, shown in Figure 72.

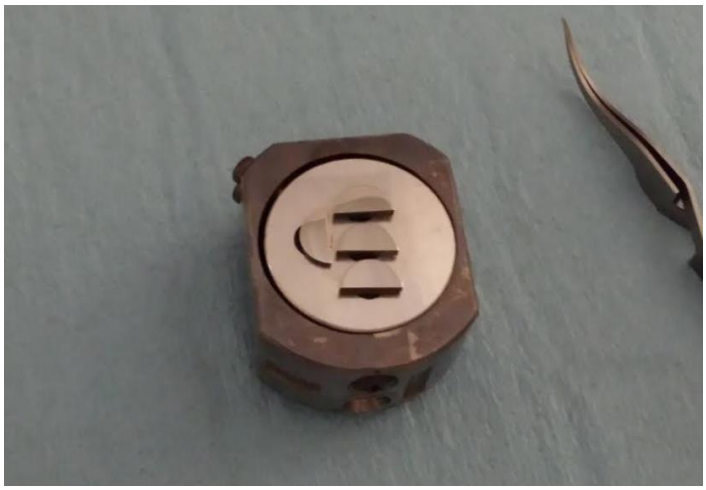

Figure 72: Example of Arrangement of Samples Attached to Mount for SEM Characterization

III.7 Nanoindentation and Scanning Probe Microscopy

Nanoindentation was performed before and after irradiation using the Hysitron TI 950 Triboindenter at the TAMU Materials Characterization Facility (MCF). The Hysitron is equipped with an automated x/y/z staging system as well as SPM imaging using a standard low load transducer and Berkovich tip. Since the low load transducer cannot perform indents beyond a few hundred nm, the 3D Omniprobe High Load Transducer and Berkovich tip were used for nanoindentation (see Figure 73).

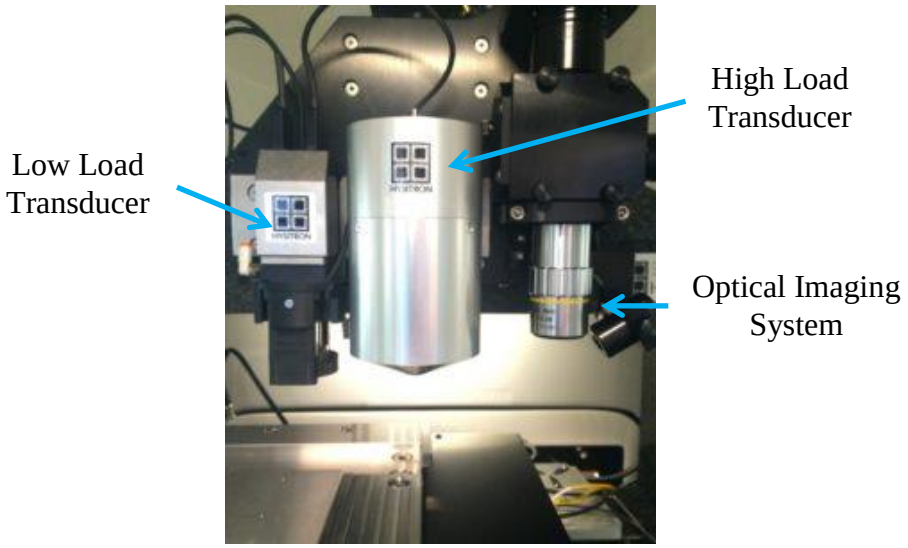

Figure 73: Image of Hysitron TI 950 Triboindenter

The load function used for all nanoindents, in (loading time – holding time – unloading time) was 5s-2s-5s with a 40 µm indentation pitch such that the strain rate remained constant at all depths, shown in Figure 74. The first trial of nanoindents was performed using an 11x2 array at depths of 200 nm, 400 nm, 600 nm, 800 nm, 1000 nm, 1200 nm, 1400 nm, and 1600 nm (176 indents per sample). Nanoindents were repeated using a 6x3 array at depths of 200 nm, 400 nm, 600 nm, 800 nm, 1000 nm, 1200 nm, 1400 nm, and 1600 nm (144 additional indents per sample), shown in Figure 75. The instrument was calibrated before each experiment using a fused quartz standard. SPM images were collected using the standard low load transducer and Berkovich tip using a contact force of 2 µN and varying scan rates (typically 5-10 $\mu m \cdot s^{-1}$) depending on image and feature size.

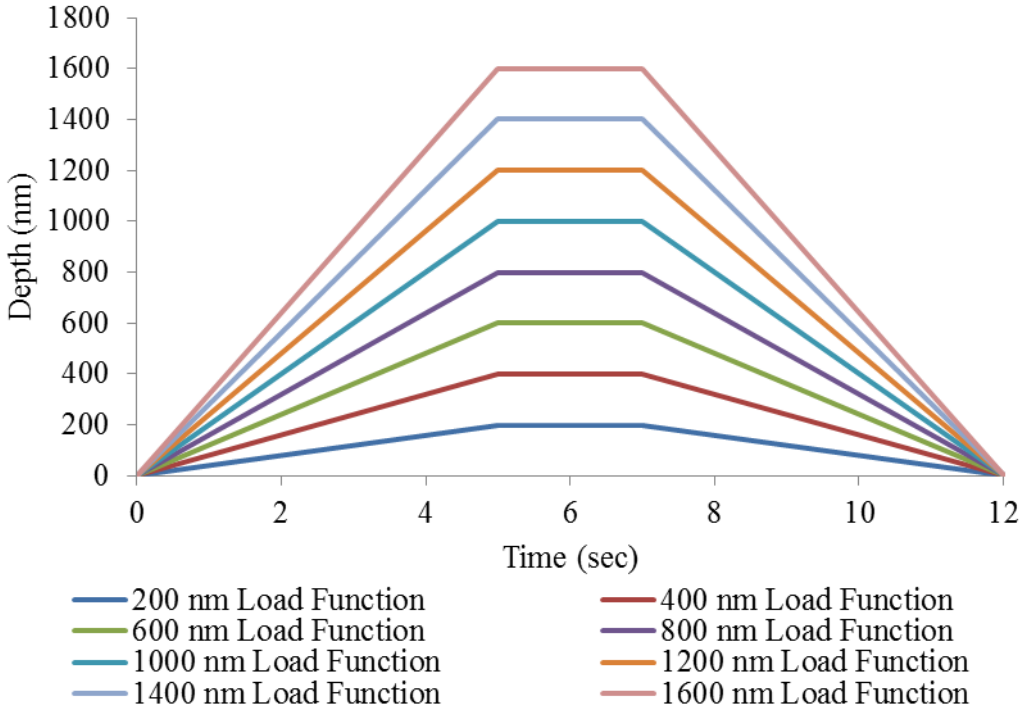

Figure 74: Load Functions used for Nanoindentation Studies

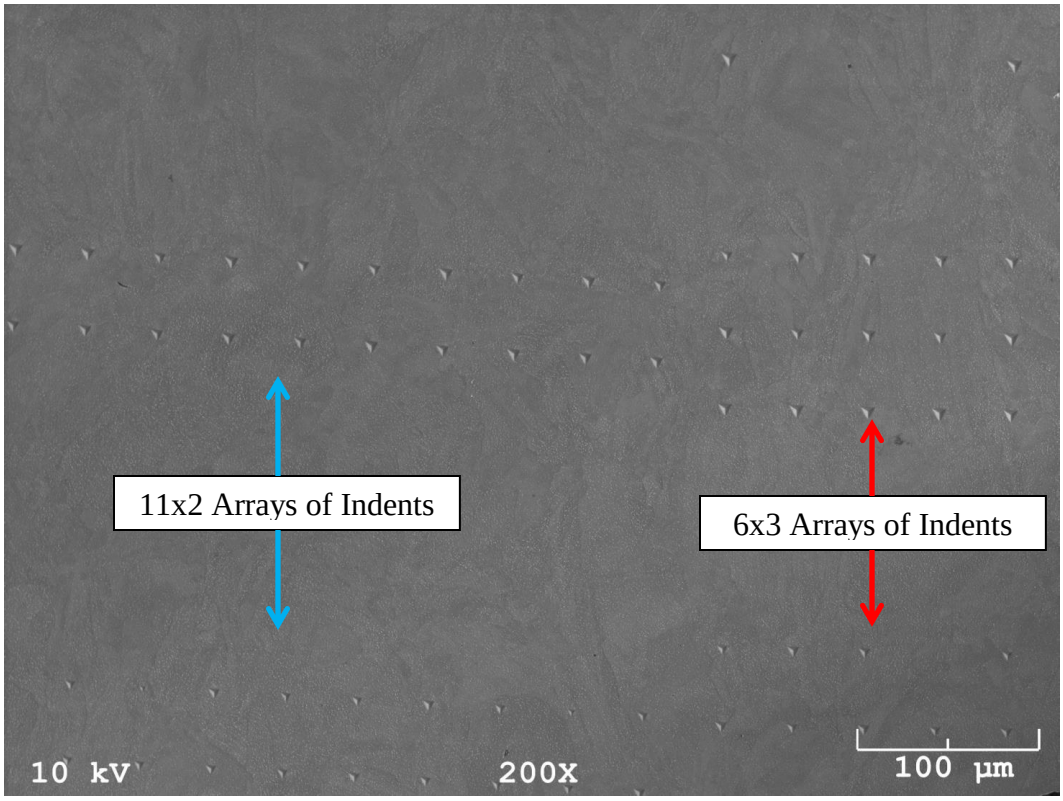

Figure 75: SEM Image of Nanoindentation Arrays in 45° LAM Inconel 600 Irradiated to 80 dpa

Nanoindentation was initially performed using the instrument settings suggested by the instrument's instruction manual. When using the suggested instrument settings, an instrumentation error known as "false engages" was encountered frequently (roughly 1/3 of all nanoindents) in which the instrument mistakenly began performing an indent before achieving contact with the sample surface. As a result, some (or all) of the measurement was erroneously performed above the sample surface rather than in the sample surface. This was resolved by increasing the high load transducer contact threshold to 750 µN. While this did dramatically reduce experiment time due to

reducing false engages, using the larger contact threshold resulted in slightly higher measurement uncertainty at depths shallower than 250 nm.

III.8 Electron Backscatter Diffraction

Computational research efforts have attempted to simulate the mechanical and microstructural response of oriented fine grained materials exposed to high dose radiation damage in order to better understand time scales, length scales, and phenomenological driving forces involved [24-26]. As with all computational simulations, experimental validation is required. Electron backscatter diffraction (EBSD) of irradiated nuclear materials may be used to provide statistically relevant data relating to the size, shape, and orientation of grain structures to improve computational models models [95]. This is particularly useful for alloys which are difficult to etch, as is the case for Inconel 600 [96].

EBSD was performed in this experiment using the Tescan FERA3 Model GMH Focused Ion Beam Microscope. The FERA was equipped with a Schottky field emission electron source and a NordlysNano high sensitivity EBSD camera from Oxford Instruments. The AZtecHKL software package was used for EBSD data processing, and the Channel 5 software package was used for data post-processing. An electron acceleration voltage of 10 kV was observed to produce regions that could not be indexed in the irradiated samples, possibly due to surface roughening caused by ion beam irradiation. Therefore, an acceleration voltage of 20 kV was used.

For all EBSD scans, the sample was mounted to a pre-tiled 70° holder using Pelco® colloidal silver paste (Ted Pella, product number 16034). The EBSD detector was inserted a distance of 218 mm into the sample chamber, and the 4x4 binning mode was implemented for indexing purposes, shown in Figure 76. The EBSD scan statistics for Inconel 600 and 316L stainless steel are provided in Table 10 and Table 11, respectively. The EBSD scan statistics for the unirradiated additively manufactured ODS steel are provided in Table 12. The scan parameters of unirradiated and irradiated samples vary depending on the grain size of the sample in accordance with ASTM standards, but generally varied between step sizes of 0.5 to 1.5 µm and exposure times of 100 to 200 ms with fields of view between 300x300 μm^2 and 500x500 μm^2. All scans achieved a mean angular deviation (MAD) of 0.6 or less (MAD values of less than unity are typically recommended) and an index rate of greater than 95%, indicating an acceptably low level of noise, mis-indexing, and zero-solutions [97, 98].

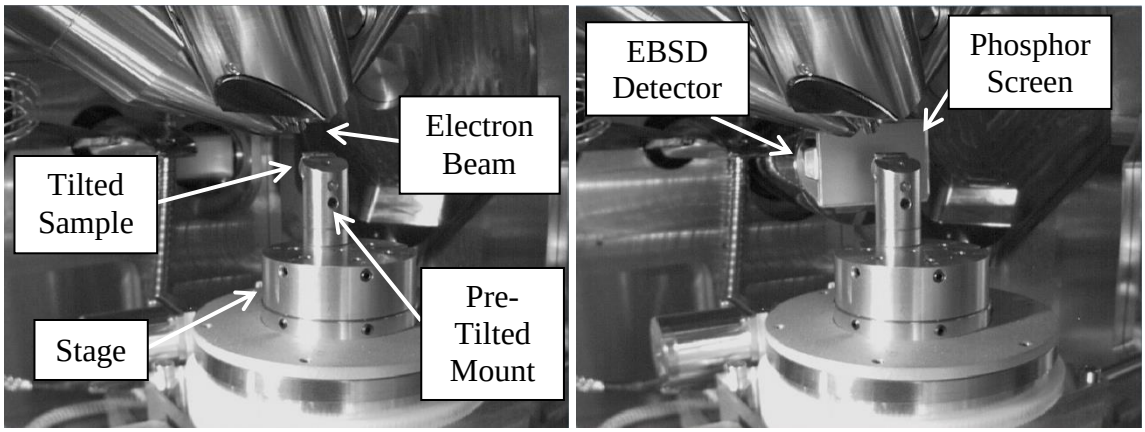

Figure 76: Chamber View of 70° Pre-Tilted Sample Facing the Retracted EBSD Detector (Left), and Facing the Inserted EBSD Detector (Right)

Table 10: Summary of EBSD Scan Settings for Inconel 600 Vertical LAM, Horizontal LAM, 45° LAM, and Conventionally Manufactured Control

	Parameter	Conventional	Vertical LAM	Horizontal LAM	45° LAM
Unirradiated	Resolution (Pixel x Pixel)	245x245	249x249	488x488	529x529
	Step Size (μm)	1.5	0.80	0.72	0.68
	MAD	0.23	0.28	0.36	0.54
	Indexed (%)	99.74	98.16	99.65	98.84
	Zero Solutions (%)	0.26	1.84	0.35	1.16
80 dpa	Resolution (Pixel x Pixel)	500x500	500x500	509x509	508x508
	Step Size (μm)	0.60	0.59	0.58	0.59
	MAD	0.25	0.19	0.26	0.25
	Indexed (%)	99.32	99.53	98.16	97.58
	Zero Solutions (%)	0.68	0.47	1.84	2.42

Table 11: Summary of EBSD Scan Settings for 316L Stainless Steel Vertical LAM, Horizontal LAM, 45° LAM, and Conventionally Manufactured Control

	Parameter	Conventional	Vertical LAM	Horizontal LAM	45° LAM
Unirradiated	Resolution (Pixel x Pixel)	305x305	488x488	503x503	488x488
	Step Size (μm)	0.99	0.90	0.85	0.90
	MAD	0.37	0.42	0.39	0.46
	Indexed (%)	96.00	98.11	97.54	95.55
	Zero Solutions (%)	4.00	1.89	2.47	4.46
80 dpa	Resolution (Pixel x Pixel)	618x618	603x603	602x602	600x600
	Step Size (μm)	0.67	0.70	0.68	0.69
	MAD	0.40	0.46	0.48	0.40
	Indexed (%)	96.84	99.35	99.42	99.43
	Zero Solutions (%)	3.16	0.65	0.58	0.57

Table 12: Summary of EBSD Scan Settings for ODS Steel Vertical LAM, Horizontal LAM, and 45° LAM

	Parameter	Unirradiated Vertical LAM	Unirradiated Horizontal LAM	Unirradiated 45° LAM
Unirradiated	Resolution (Pixel x Pixel)	488x488	484x484	522x522
	Step Size (μm)	0.90	0.89	0.95
	MAD	0.19	0.25	0.23
	Indexed (%)	99.84	99.70	99.31
	Zero Solutions (%)	0.16	0.30	0.69

III.9 Focused Ion Beam Lift-Out of Lamellae

Cross-sectional TEM lamellae were prepared from the irradiated specimens via a FIB lift-out technique using the Tescan LYRA-3 Model GMH Focused Ion Beam Microscope. The LYRA is equipped with a Schottky field emission electron source with a fully integrated Canion Ga liquid metal ion source (LMIS) focused ion beam column and a five-reservoir gas injection system (GIS). The LYRA is also equipped with the SmartAct 3-axis Piezo Nanomanipulator and Controller system for lift-out of TEM lamellae. The irradiated regions of the samples were protected from potential FIB damage by first depositing a 5 μm thick film of platinum on the surface of the sample. All lamellae were final-polished at a tilt angle of ± 5° using an ion accelerating voltage of 5 keV to minimize FIB-induced cross-sectional damage [75].

One complexity associated with the FIB lift-out procedure is that the electron beam imaging system must be focused properly, the ion beam imaging system must be focused properly, and the depth of focus must coincide for both imaging systems. This is illustrated in Figure 77 where the beams intersect at the depth of focus. The lift out procedure requires frequent changes in tilt, height, etc. requiring refocusing of both imaging systems.

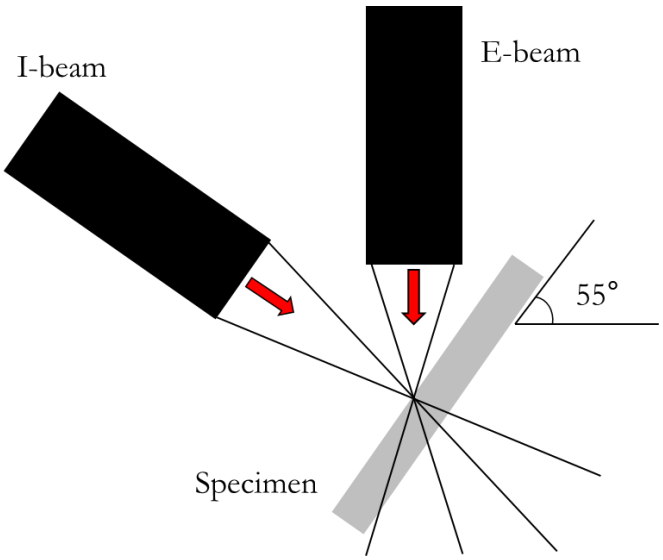

Figure 77: Illustration of FIB-SEM Coincident Depth of Focus

III.9.1 Initial Focused Ion Beam Lift-Out Protocol

The focused ion beam can be used to prepare TEM lamellae whereby an ion beam is used to etch out portions of the sample surface for the removal of a thin sample. This thin sample can then be "lifted out" of the sample surface and characterized. At the onset of this project, a specimen "lift-out" procedure was recommended for Inconel 600 and 316L stainless steel by Tescan. This procedure is explained in this section. With practice, a more successful method was developed and is reported in the next section.

First, a platinum mask is deposited onto the sample surface using the GIS in order to protect the lamella during ion million (the rectangular object in the center of a conventionally manufactured Inconel 600 rod in Figure 78). The volume directly below the rectangular Pt mask is the soon-to-be TEM specimen. The grain boundaries are clearly visible on the FIB images, allowing the placement of the Pt mask to be centrally located directly above a grain boundary, if desired. Next, trenches are etched above and

below the Pt mask with respect to the image orientation using the Ga^+ source, as shown in Figure 79. The left edge, bottom edge, and most of the ridge edge (relative to the image orientation) are etched off using Ga^+, leaving only a small portion of the right edge connected to the lamella; this is called the "U-cut". The nanomanipulator (NM) is then positioned directly beside and welded to the top surface of the lamella via implantation of the Pt^+ ion beam, shown in Figure 80. The right edge is then completely detached via Ga^+ etching, and the lamella is lifted out of the sample, shown in Figure 81a. This step is difficult to perform due to ion re-deposition (Figure 81b) or insufficient welding which causes the weld to break (Figure 81c).

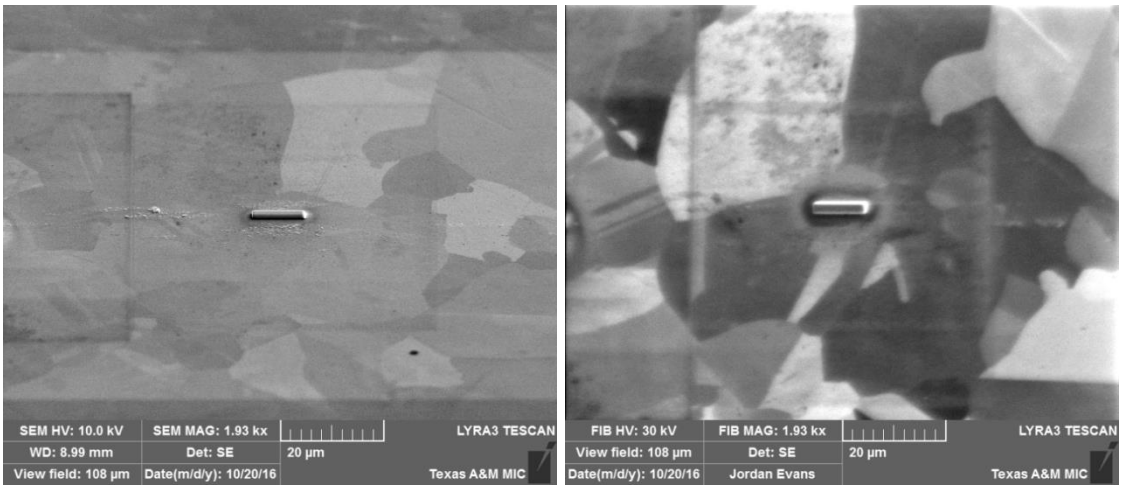

Figure 78: SEM (Left), and FIB (Right) Images of Protective Pt Mask Placed Centrally on a Grain Boundary in Conventionally Manufactured Inconel 600

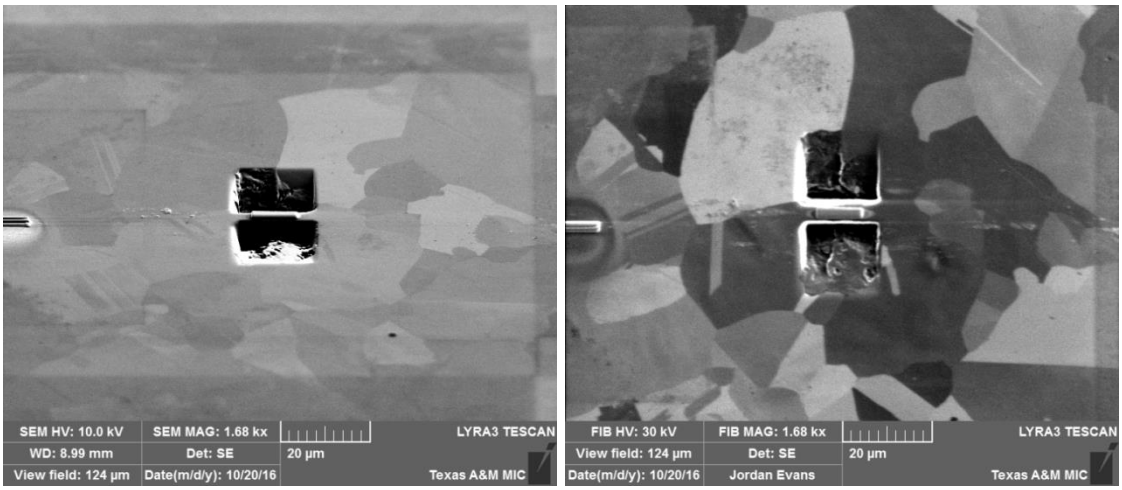

Figure 79: SEM (Left), and FIB (Right) Images of Trenches Above and Below the Pt Mask in Conventionally Manufactured Inconel 600

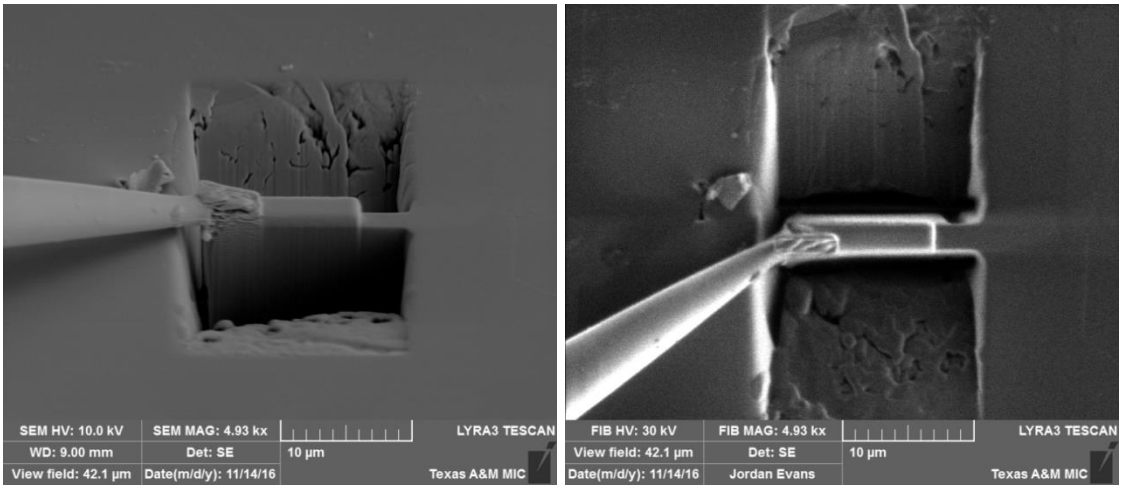

Figure 80: SEM (Left), and FIB (Right) Images of Nanomanipulator Welded to the Edge of a TEM Lamella after Performing the U-cut in Conventionally Manufactured Inconel 600

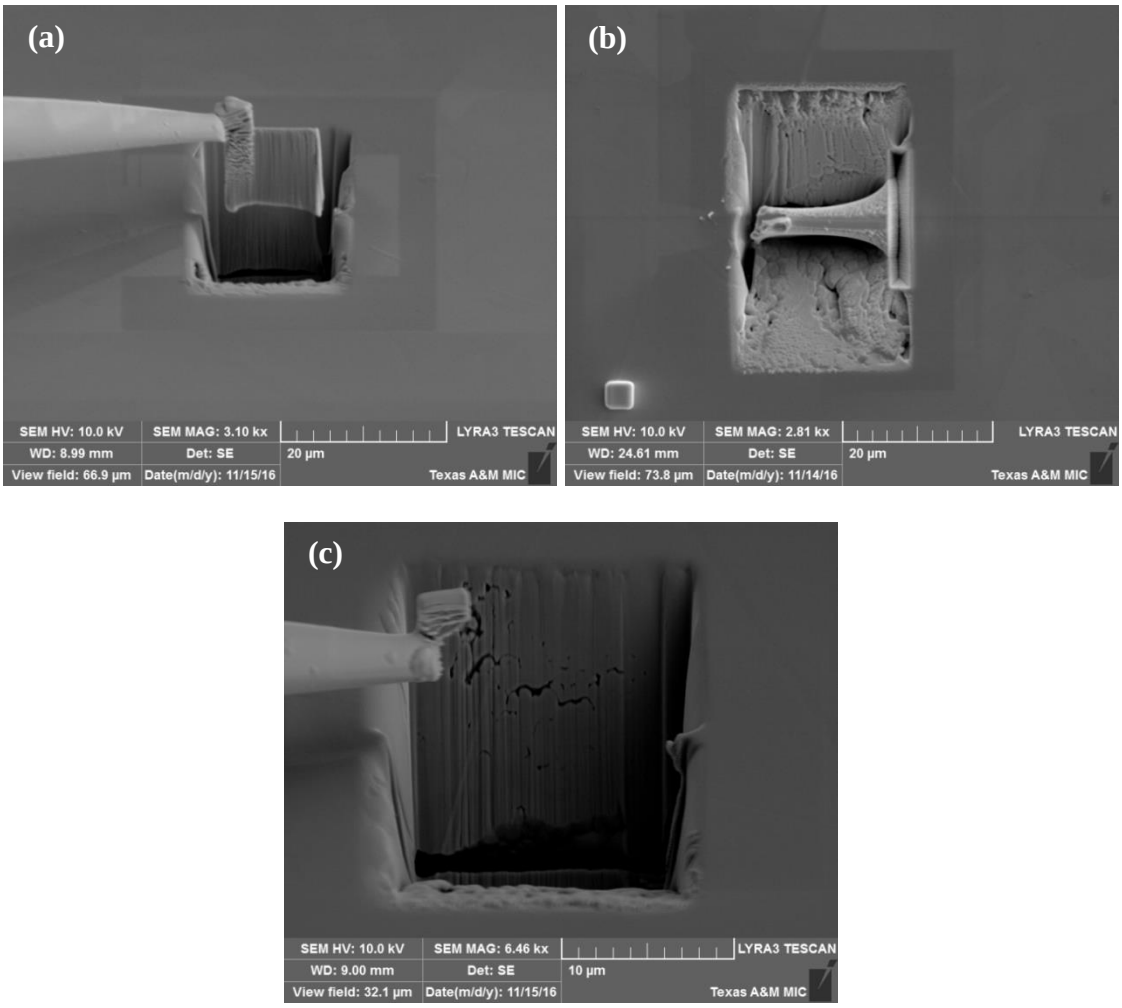

Figure 81: (a) SEM Image of TEM Lamella Lifted Out After Final Right Edge Etching, (b) SEM Image of Re-deposition along Right Edge of Lamella, and (c) SEM Image of Broken Weld in Conventionally Manufactured Inconel 600

III.9.2 Successful Focused Ion Beam Lift-Out Protocol

While it is difficult to weld the bottom of the nanomanipulator to the top of the lamella (see Figure 80), it is much easier to weld the top of the NM to the top of the lamella. However, the NM cannot reach a depth below that of the specimen surface. Therefore, the original lift-out procedures were altered by etching three trenches instead of two, as shown in Figure 82. The left trench is etched first, followed by the bottom, then top trenches in order to minimize re-deposition on the sides of the lamella. This allowed the top of the NM to be co-linear with the top of the lamella, making welding significantly easier and more structurally stable, as shown in Figure 83 (left). The lamella is then transferred to a pillar on the FIB grid (Figure 84), welded to the pillar (Figure 85), detached from the NM via Ga^+ etching (Figure 86), and thinned/polished (Figure 87). The FIB image in Figure 87 is distorted and "fuzzy" because the final thinning/polishing is conducted using a 5 kV ion beam in order to minimize damage to the lamella. The lamella in Figure 87 appears bright on the SEM image, indicating that it is transparent to 10 kV electrons. Figure 88 shows the final lamella ready for TEM characterization.

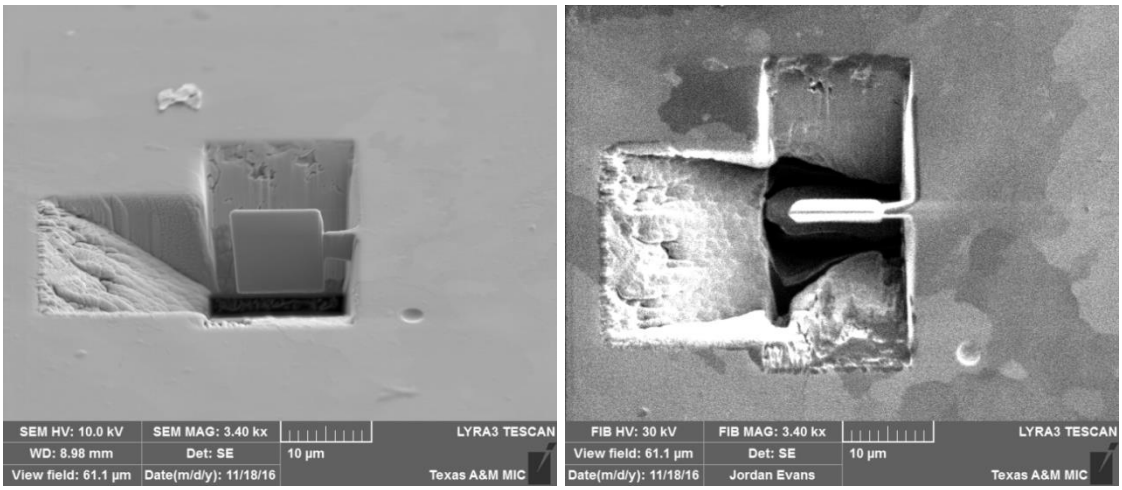

Figure 82: SEM (Left), and FIB (Right) Images of Three-Trench Strategy after U-cut in Conventionally Manufactured Inconel 600

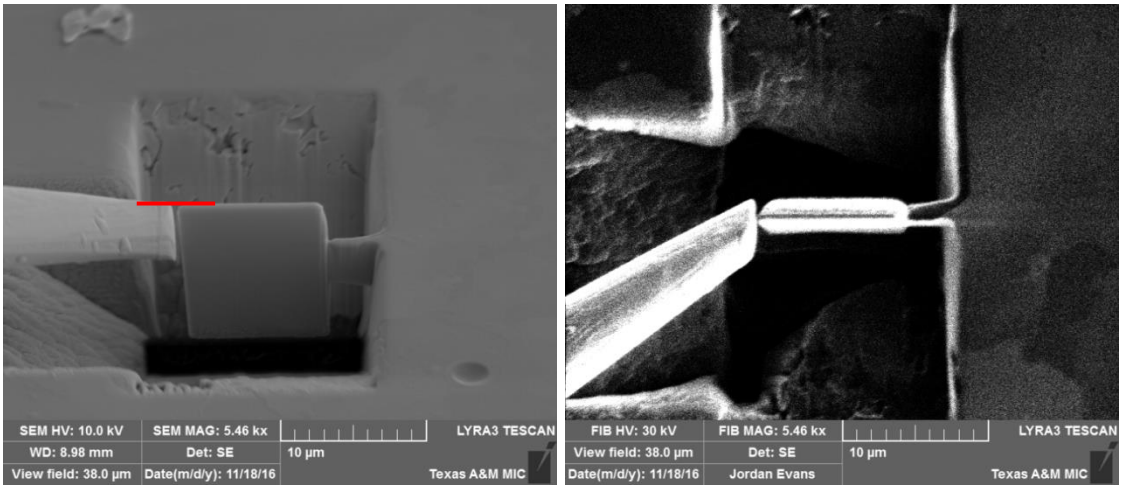

Figure 83: SEM (Left), and FIB (Right) Images of Top of NM Co-Linear with TEM Lamella (Red Line) in Conventionally Manufactured Inconel 600

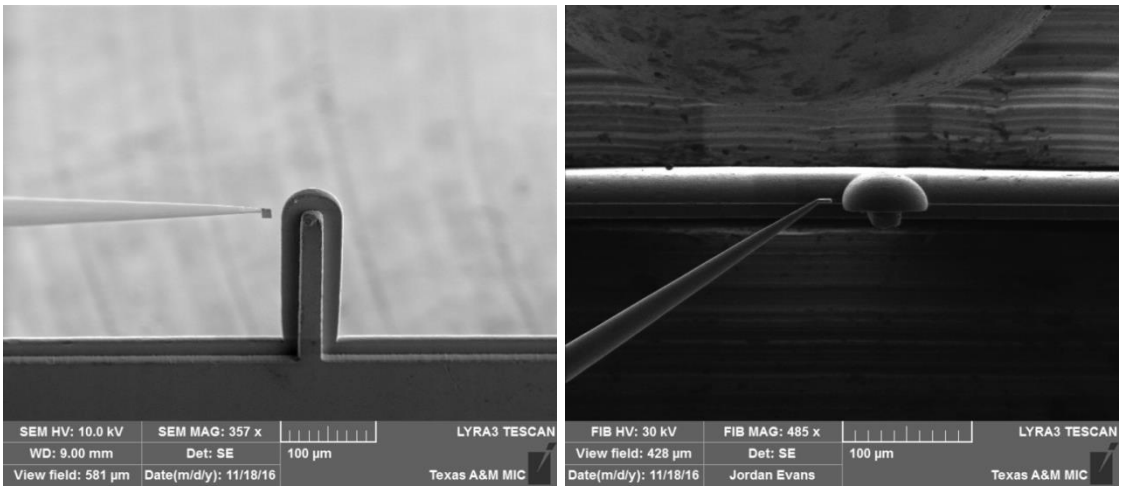

Figure 84: SEM (Left) and FIB (Right) Images of Conventionally Manufactured Inconel 600 TEM Lamella Transferred to a Pillar on the FIB Grid

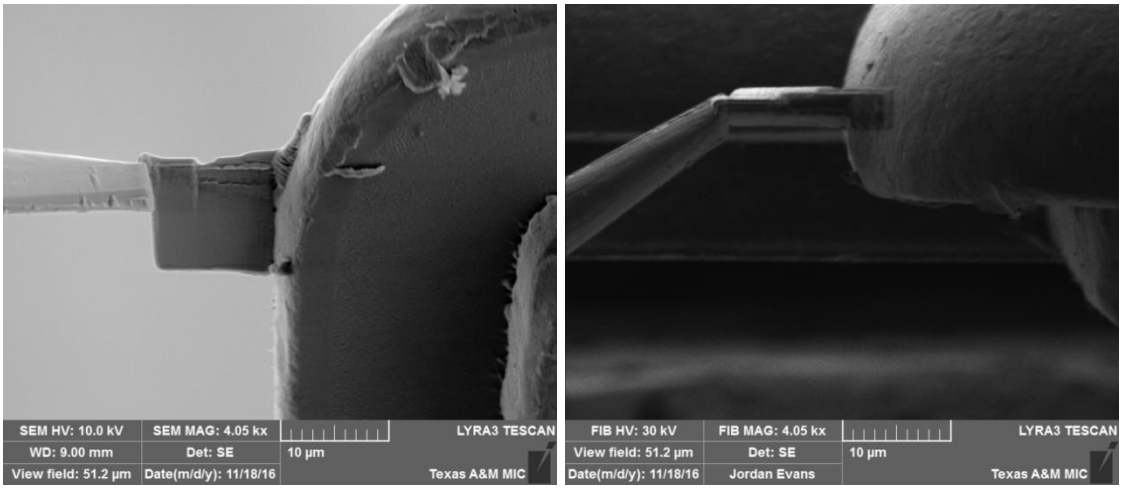

Figure 85: SEM (Left) and FIB (Right) Images of Conventionally Manufactured Inconel 600 TEM Lamella Welded to a Pillar on the FIB Grid

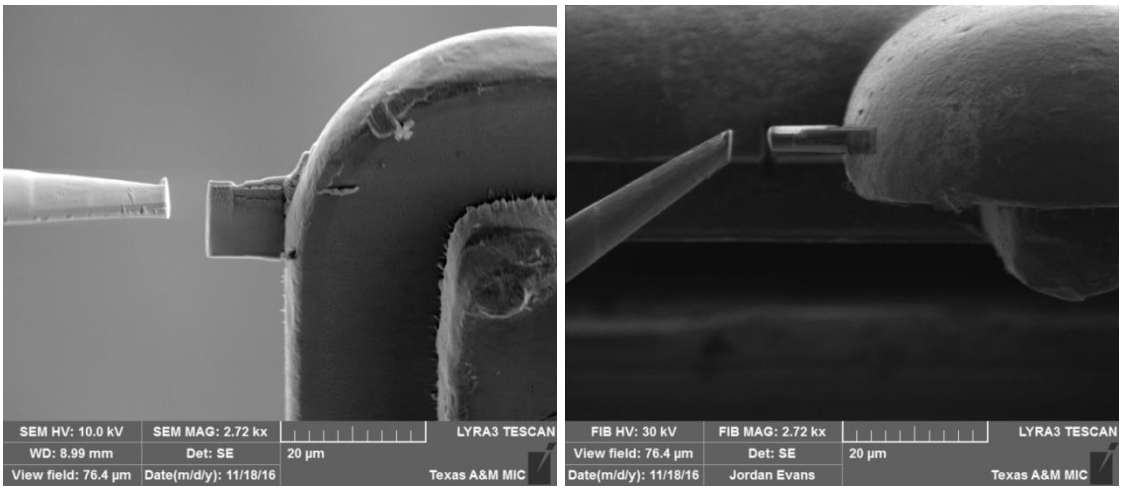

Figure 86: SEM (Left) and FIB (Right) Images of NM Removed from Conventionally Manufactured Inconel 600 TEM Lamella via Gallium Ion Etching

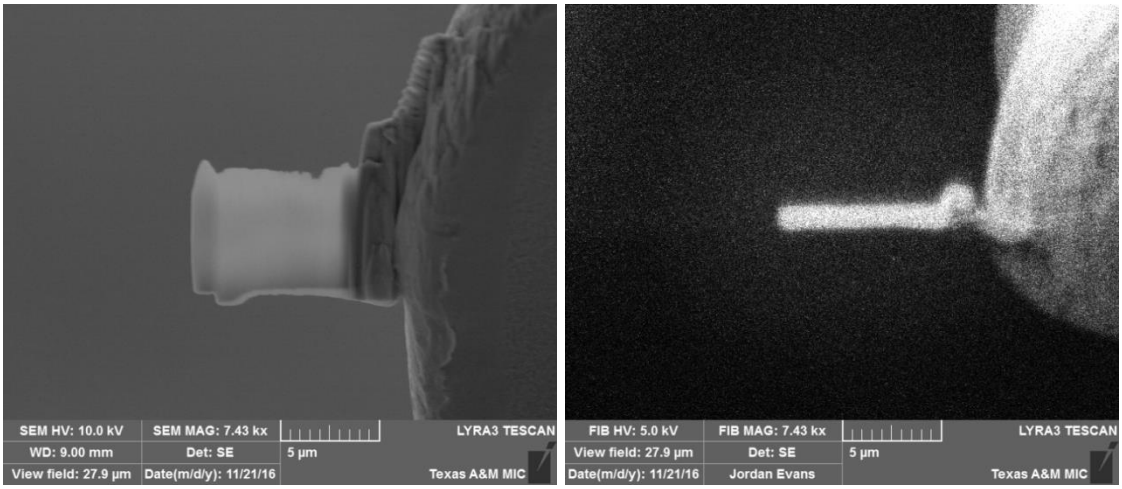

Figure 87: SEM (Left) and FIB (Right) Images of Conventionally Manufactured Inconel 600 TEM Lamella after Final Thinning and Polishing

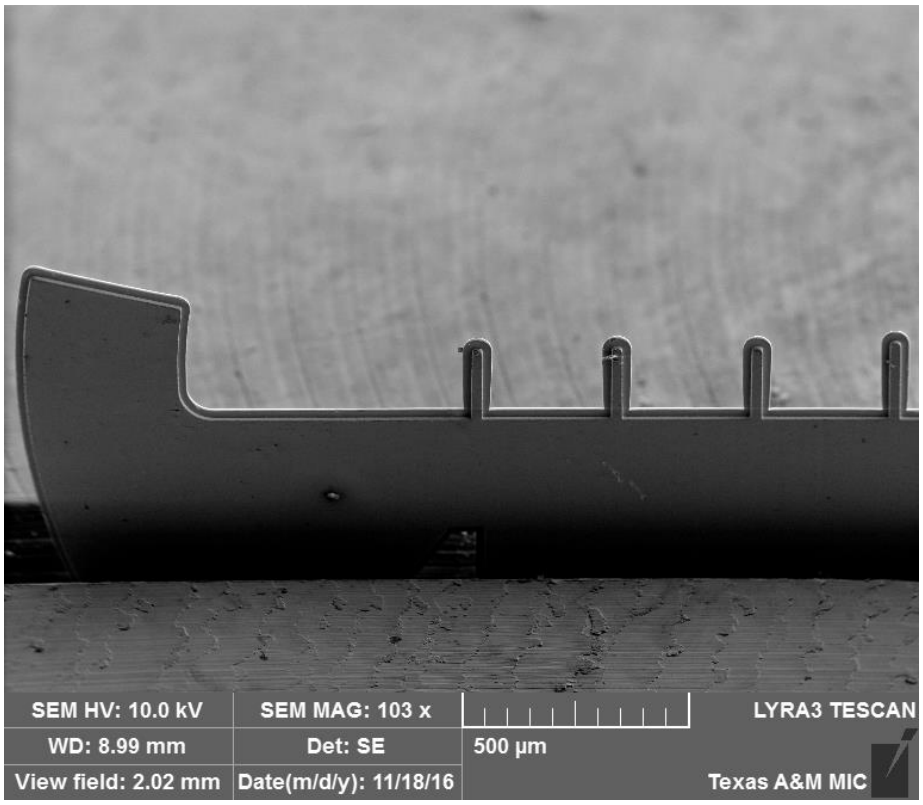

Figure 88: SEM Image of Conventionally Manufactured Inconel 600 Lamella Ready for TEM, Prepared via the Three-Trench FIB Lift-Out Procedure

III.10 Transmission Electron Microscopy

The microstructural changes in the alloys caused by radiation damage were characterized with an FEI Tecnai G^2 F20 Super-Twin Field Emission TEM at the TAMU Materials Imaging Center (MIC) using an accelerating voltage of 200 kV. Crystallographic information files (CIF) for crystalline phases of materials were generated using CrystalMaker™ Student Version software from CrystalMater Software Ltd. Selected area diffraction patterns (SADPs) were indexed using the SingleCrystal™ Student Version software, also from CrystalMaker Software Ltd. The SADPs were indexed assuming all samples were fcc in structure ($Fm\bar{3}m$ space group) with a lattice

parameter of 3.55 Å (reciprocal lattice parameter of 0.2817 $Å^{-1}$) for Inconel 600 and 3.59 Å (0.2786 $Å^{-1}$) for 316L stainless steel.. HAADF STEM was conducted using a Fischione Ultra-High Resolution HAADF STEM detector, and EDS was performed using an EDAX Instruments EDS Detector. EDS area and line scans were analyzed using the AZtecHKL software.

CHAPTER IV

RESULTS

Chapter IV presents the results of the various post-irradiation examination techniques: x-ray diffraction, optical microscopy, scanning electron microscopy, nanoindentation, scanning probe microscopy, electron backscatter diffraction, and transmission electron microscopy. The completion of these methods of the various samples is summarized in Table 13 where "conv." represents conventionally manufactured, "0°" represents vertical LAM, "45°" represents 45°LAM, "90°" represents horizontal LAM, "C" represents measurements that were completed, "I" represents measurements that were not completed due to time constraints. Optical microscopy and XRD were not performed on irradiated samples (vide infra).

Table 13: Characterization Techniques Performed on Unirradiated and Irradiated Samples

		Inconel 600				316L Stainless Steel				ODS		
	Procedure	Conv.	0°	45°	90°	Conv.	0°	45°	90°	0°	45°	90°
Unirradiated	Optical	C	C	C	C	C	C	C	C	C	C	C
	XRD	C	C	C	C	C	C	C	C	I	I	I
	SEM	C	C	C	C	C	C	C	C	C	C	C
	EBSD	C	C	C	C	C	C	C	C	C	C	C
	Nanoind.	I	I	I	I	C	C	C	C	I	I	I
	TEM	C	C	C	C	C	C	C	C	I	I	I
Irradiated	SEM	C	C	C	C	C	C	C	C	I	I	I
	EBSD	C	C	C	C	C	C	C	C	I	I	I
	Nanoind/SPM	I	I	I	I	C	C	C	C	I	I	I
	TEM	C	C	C	C	C	C	C	C	I	I	I

C – Measurements complete
I – Measurements incomplete

IV.1 Pre-Irradiation Examination of Alloy Samples

IV.1.1 X-ray Diffraction

X-ray diffraction data were collected from unirradiated Inconel 600 and 316L stainless steel samples to develop a preliminary understanding of the observable differences in grain structure and texture between LAM build directions and conventional casting. For a review of XRD theory, see Ch. II.4. The texture of the solidification microstructure resulting from the additive manufacturing process is evident from XRD analysis which reveals differences in peak ratios depending on build direction, shown in Figure 89. Of note is the similarity between spectra of the two different alloys built in the identical orientations. Knowing that the wavelength of the x-rays was $\lambda = 1.5406$ Å, the lattice parameter of Inconel 600 is 3.55 Å [99], the lattice parameter of 316L stainless steel is 3.59 Å [100], and the XRD selection rules allow for reflections in fcc crystals about Miller indices where *h*, *k*, and *l* are either all odd or all even [101], the XRD peaks can be summarized in Table 14.

In Table 14, the distance between crystalline planes (d) was determined using Eq. 1, and the measured lattice parameter (a_{msd}) was determined by substituting d into Eq. 2. The relative peak ratios for both I600 and 316L from the XRD data show that the close-packed atomic planes arrange themselves perpendicular to the LAM build direction.

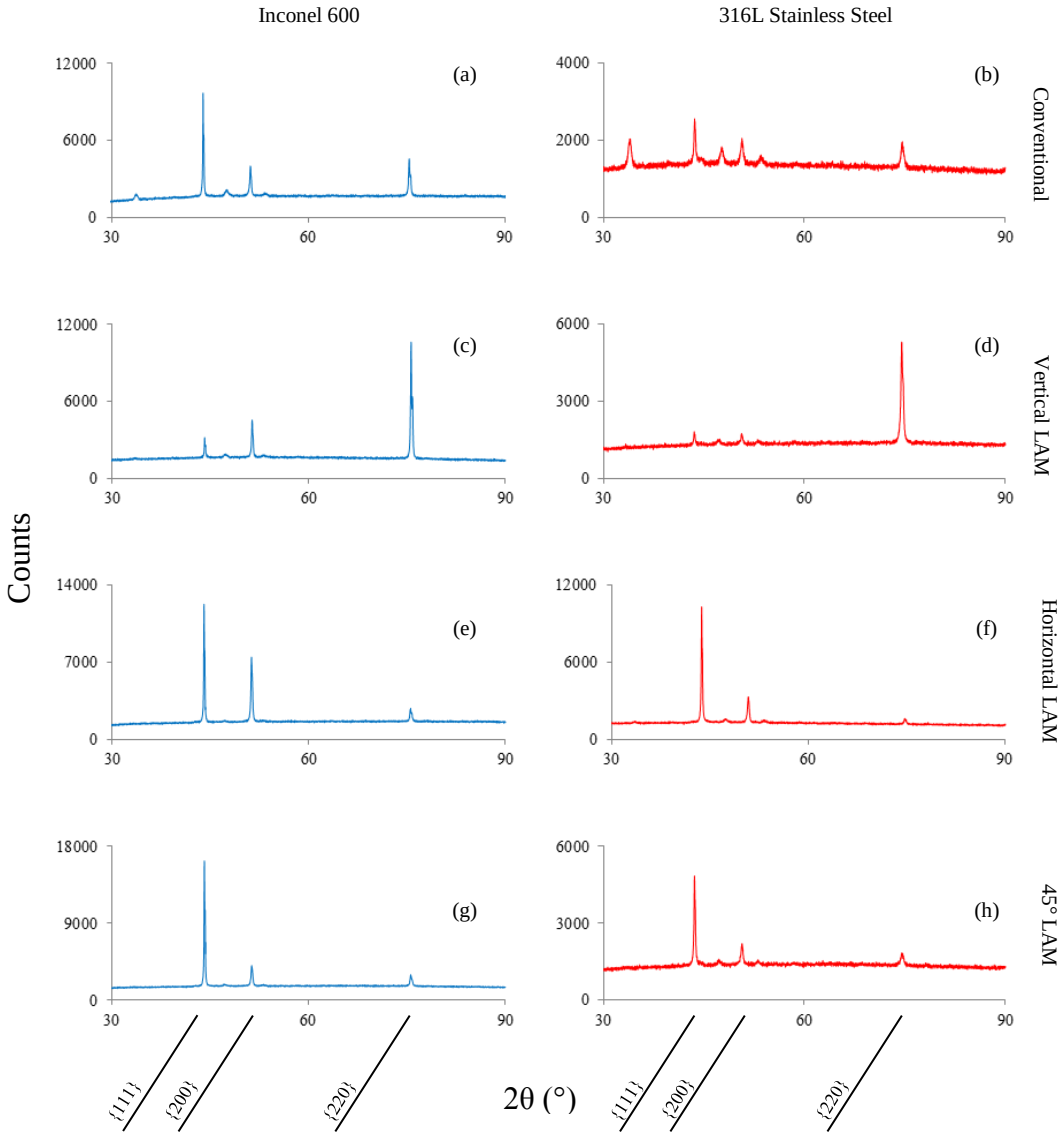

Figure 89: XRD Spectra of Unirradiated (a) Conventionally Manufactured I600, (b) Conventionally Manufactured 316L, (c) Vertical LAM I600, (d) Vertical LAM 316L, (e) Horizontal LAM I600, (f) Horizontal LAM 316L, (g) 45° LAM I600, and (h) 45° LAM 316L

Table 14: XRD Peak Analysis of Inconel 600 and 316L Stainless Steel Samples

	Sample	Peak (°)	Counts	d (Å) [A]	a_{msd} (Å) [B]
Inconel 600	Conv.	43.903	9384	2.061	3.569
		51.119	3910	1.785	3.571
		75.339	4454	1.260	3.565
	0°	44.155	3181	2.049	3.550
		51.385	4531	1.777	3.554
		75.827	6333	1.254	3.546
	45°	44.110	16710	2.051	3.553
		51.326	4152	1.779	3.557
		75.561	3053	1.257	3.556
	90°	44.066	12637	2.053	3.557
		51.297	7712	1.780	3.559
		75.561	2947	1.257	3.556
316L Stainless Stseel	Conv.	43.637	2529	2.073	3.590
		50.676	2075	1.800	3.600
		74.570	1969	1.272	3.597
	0°	43.548	1859	2.077	3.597
		50.631	1789	1.801	3.603
		74.541	5384	1.272	3.598
	45°	43.593	4874	2.075	3.593
		50.690	2221	1.799	3.599
		74.526	1845	1.272	3.598
	90°	43.696	9653	2.070	3.585
		50.838	3113	1.795	3.589
		74.733	1525	1.269	3.590

(A) Calculated using Eq. 1

(B) Calculated using Eq. 2

Based on the associated texture of the LAM rods from Figure 89 and Table 14, the interatomic distance *d* in an arbitrary volume of additively manufactured Inconel or steel is smallest (i.e. close-packed) parallel to the laser/build direction, and largest perpendicular to the laser/build direction, as illustrated in Figure 90.

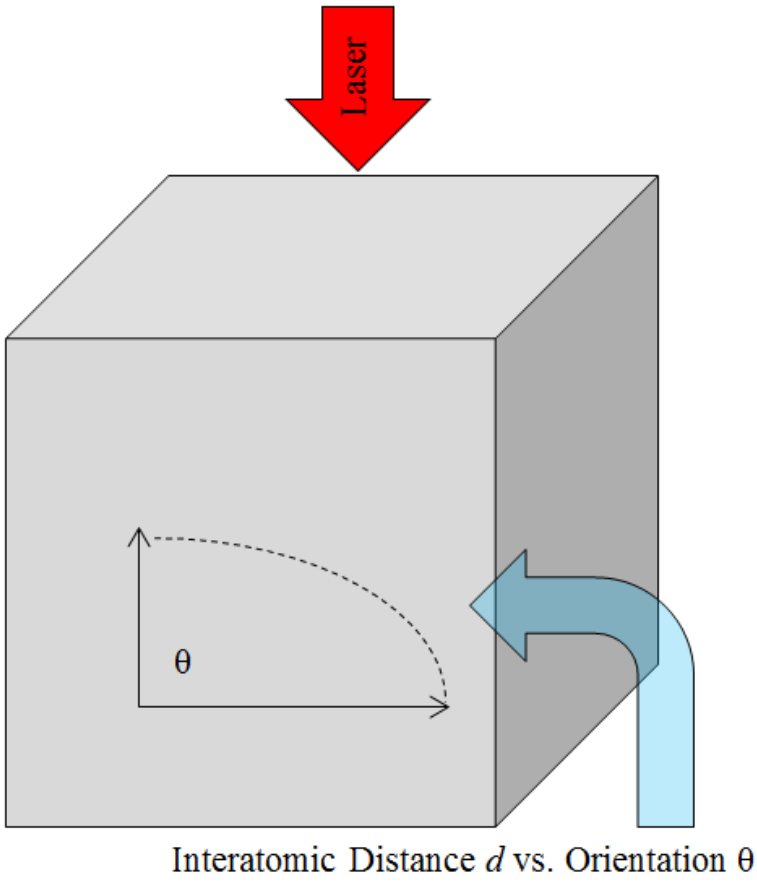

Figure 90: Approximate Interatomic Distance in LAM vs. Laser/Build Orientation

XRD was only performed on unirradiated samples for the following reason. The ion beam only travels up to a maximum depth of about 1.6 μm (see Figure 62 and Figure 70). High energy photons are attenuated as they travel through matter according to Eq. 20 where $I(x)$ is the intensity of mono-energetic photons traveling through a material at depth x, I_0 is the initial intensity of mono-energetic photons incident upon the material surface, and μ is the linear attenuation coefficient for photons of a particular energy interacting with the material. The mass attenuation coefficients (μ/ρ) for the x-rays used in this experiment interacting with nickel and iron are 50 $cm^2 \cdot g^{-1}$ and 300 $cm^2 \cdot g^{-1}$, respectively, where ρ is the density of the material. Knowing that the densities of Inconel 600 and 316L stainless steel are approximately 8.47 $g \cdot cm^{-3}$ and 8.00 $g \cdot cm^{-3}$, respectively, it can be shown via Eq. 20 that the XRD signals for both Inconel 600 and 316L stainless steel are dominated by the unirradiated subsurface (93% and 68%, respectively).

Eq. 20

$$I(x) = I_0 e^{-\mu x}$$

IV.1.2 Optical Microscopy of As-Annealed Samples

Images of as-annealed samples were collected using the Hirox HK-1300 Optical Microscope at the TAMU FCML, shown in Figure 91 - Figure 93. Samples were polished up to 800 grit in order to obtain flat surfaces. Specks and streaks with bright contrast are visible in some areas of these images, indicating polishing abrasive embedment, pullout, and scratching. This issue was resolved with practice.

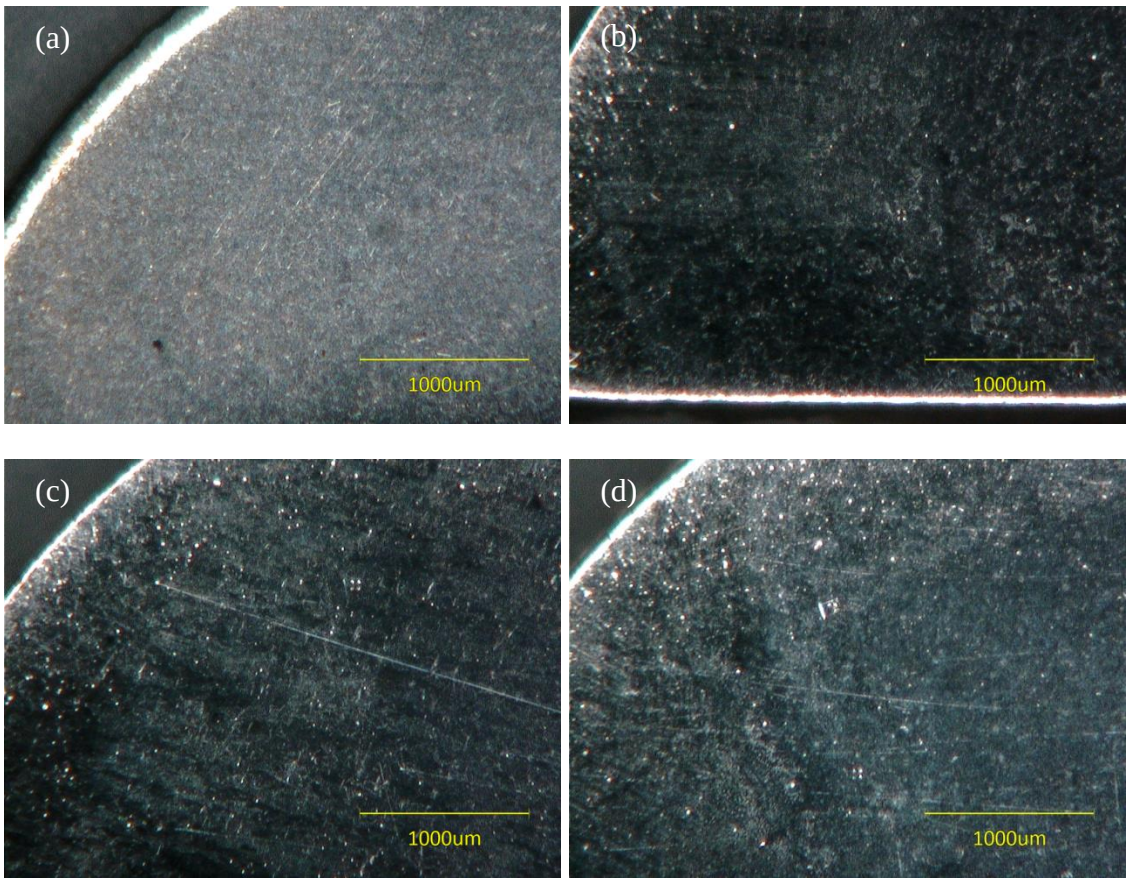

Figure 91: Optical Microscopy Images of As-Annealed Inconel 600 (a) Conventionally Manufactured, (b) Vertical LAM, (c) Horizontal LAM, and (d) 45° LAM

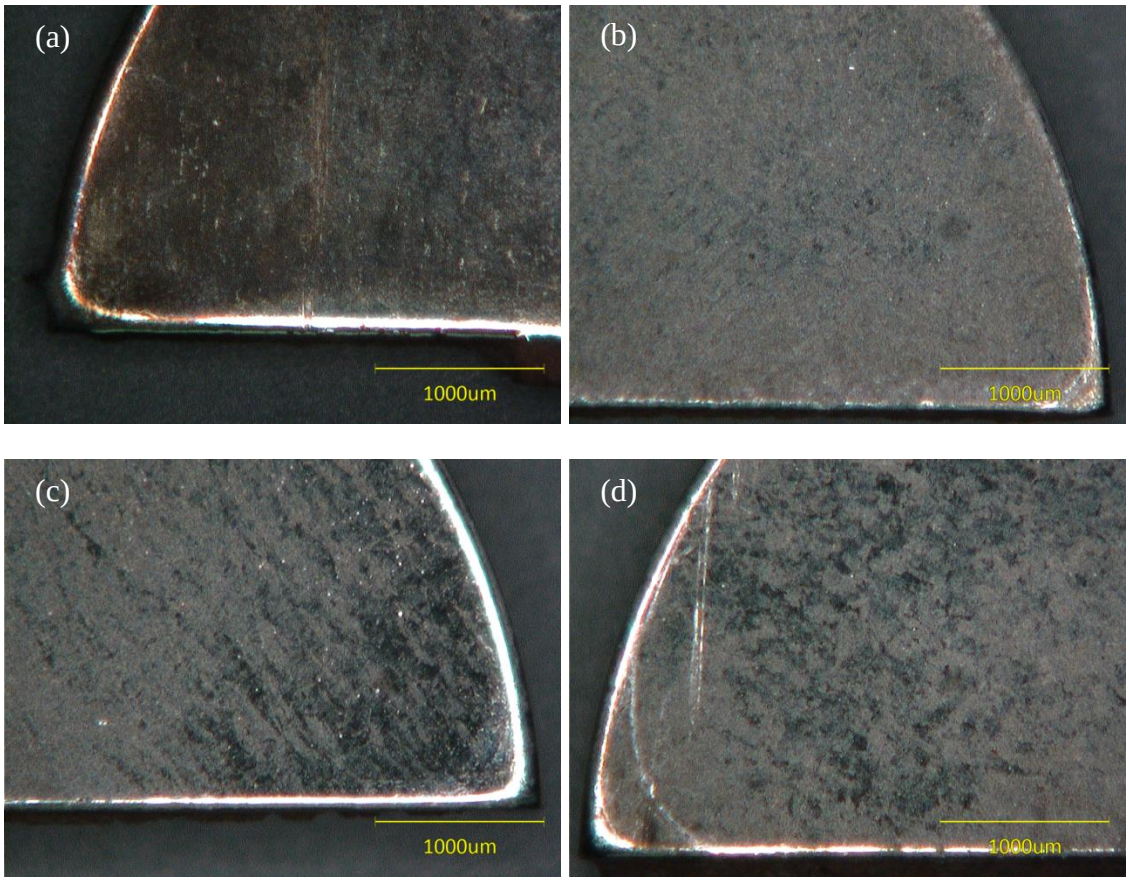

Figure 92: Optical Microscopy Images of As-Annealed 316L Stainless Steel (a) Conventionally Manufactured, (b) Vertical LAM, (c) Horizontal LAM, and (d) 45° LAM

Figure 93 shows large pores aligned with distinctive streaks on the polished surfaces of the ODS steel samples. These streaks trace the laser beam path during manufacturing. The presence of the pores and streaks indicates that the LAM build parameters (laser power, scan rate, etc.) were not thoroughly optimized for the ODS build protocol.

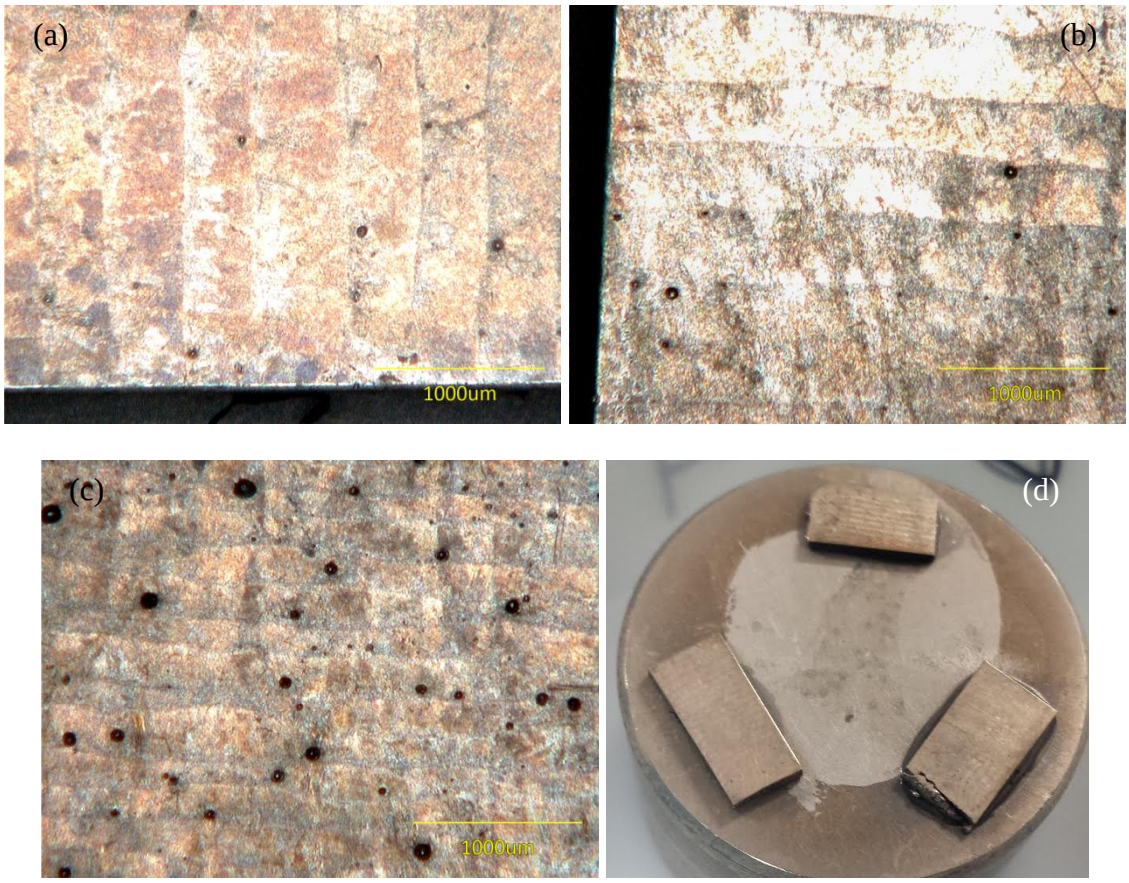

Figure 93: Optical Microscopy Images of As-Annealed ODS Steel (a) Vertical LAM, (b) Horizontal LAM, and (c) 45° LAM, and (d) Image of All Three Samples Attached to Polishing Mount Revealing Visible Streaks

IV.1.3 Optical Microscopy of Etched Samples

Before EBSD, nanoindentation, or FIB/TEM were conducted, an attempt was made to image the grain structure of the alloys using optical microscopy. The Inconel 600 samples were etched first. It should be noted that Inconel 600 is inherently resistant to corrosive media [102, 103]. The etchant selected for the Inconel 600 samples was the Modified Kalling's Superalloy Etchant from ES Laboratory, LLC (Cat. No. 156, Lot No. 21016). The etching was conducted inside a fume hood. This etchant is composed of 5-

10% cupric chloride ($CuCl_2$), 30-35% hydrochloric acid (HCl), and methanol (CH_3OH). Personal protective equipment (PPE) and appropriate safety practices were strictly observed. The sample was exposed to the etchant at room temperature for approximately 60 seconds, then thoroughly rinsed with deionized water and sonicated in distilled water for 10 minutes at room temperature. The sample was then sprayed IPA and dried with compressed air to prevent staining.

Figure 94 and Figure 95 show low magnification and high magnification optical microscopy images, respectively, of unirradiated horizontal LAM Inconel 600 after etching. A rough outline of the elongated grain structure of the specimen is visible in the etched image. However, high magnification optical images reveal damage to the sample surface caused by the etchant.

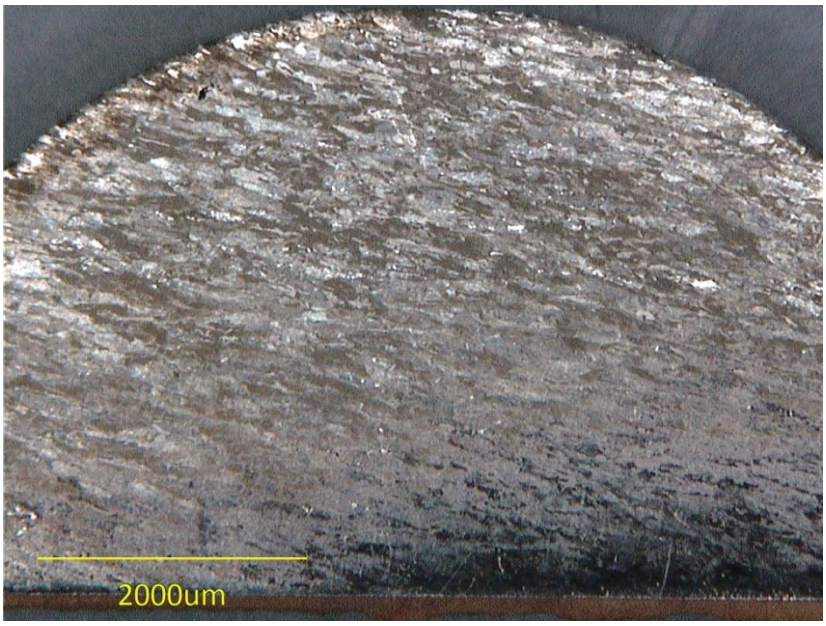

Figure 94: Low Magnification Optical Microscopy Image of Unirradiated Horizontal LAM Inconel 600 after Etching with Modified Kalling's Superalloy Etchant

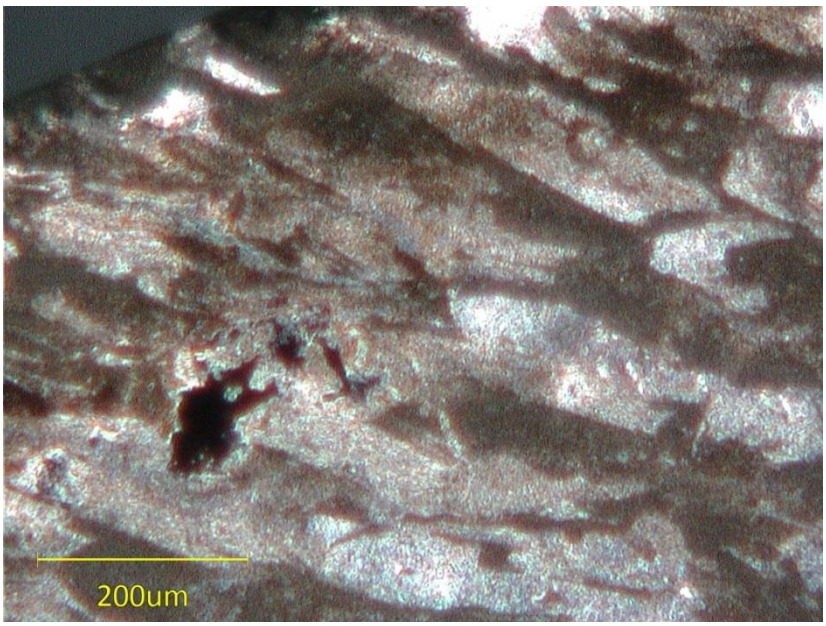

Figure 95: High Magnification Optical Microscopy Image of Unirradiated Horizontal LAM Inconel 600 after Etching with Modified Kalling's Superalloy Etchant Revealing Etchant Damage

The grain structure may be much more clearly visible in optical images collected using differential interference contrast (DIC) microscopy, which utilizes differences in the index of refraction between the etched grains by transforming the phase shift of light into amplitude differences. This method is similar to that of interferometry since it utilizes the phase interference of two difference images, resulting in significantly improved contrast as compared to the conventional reflective optical imaging technique. It is important to note that the fundamental principle of DIC is the utilization of optical path differences, i.e. refractive index and geometric path length, to generate 3D contrast. Therefore, 3D contrast in the resulting images is (a) angle/position-dependent, and (b) may be a result of optical rather than geometric relief. The Zeiss Axiophot Microscope was used for DIC characterization. DIC images of unirradiated horizontal LAM Inconel 600 after etching were collected first to determine if DIC was a viable method of measuring grain characteristics, shown in Figure 96 and Figure 97. Based on the artifacts produced from etching, it was revealed that DIC produced ambiguous results. Further DIC work was terminated in favor of EBSD. It should be noted that the DIC instrument/software does not offer scale bars on images due to the nature in which the image was constructed; instead, the magnification settings are the preferred method of defining image size.

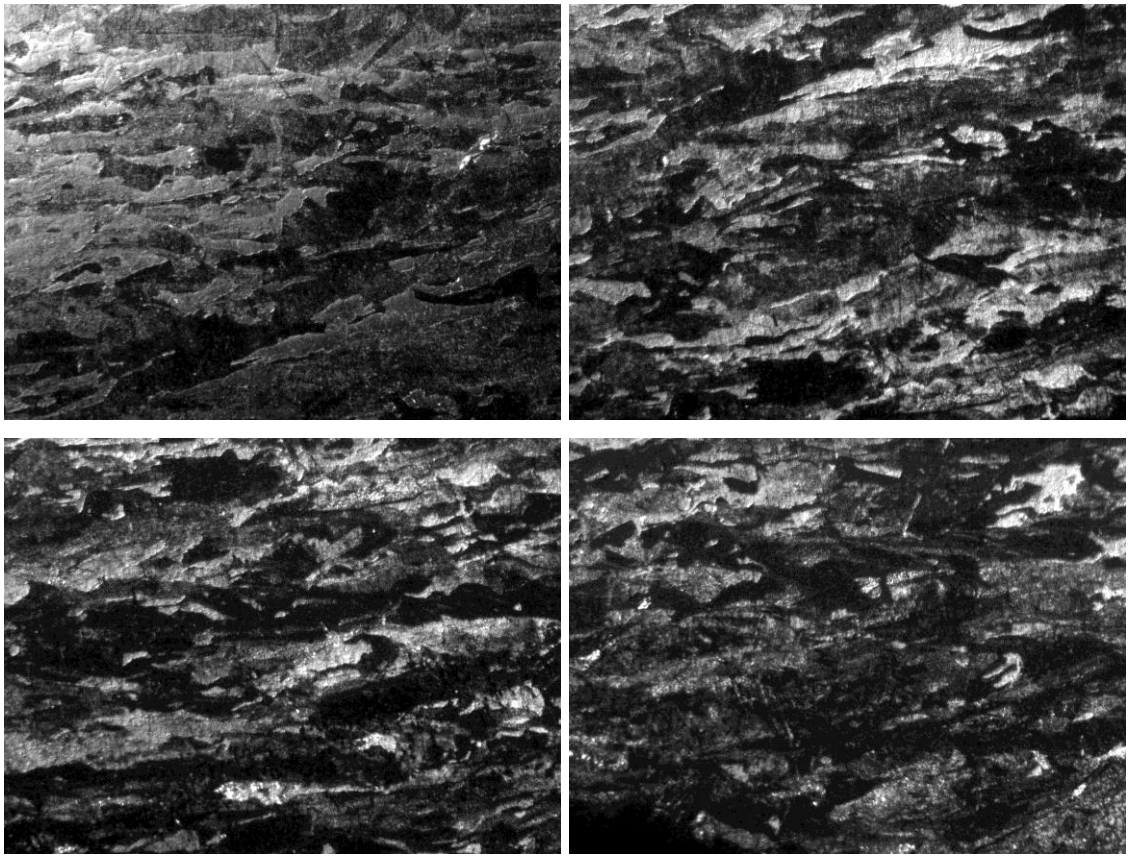

Figure 96: Monochrome DIC Micrographs of Unirradiated Horizontal LAM Inconel 600 after Etching with Kalling's Modified Superalloy Etchant for 60 Seconds (5x1x25x Magnification)

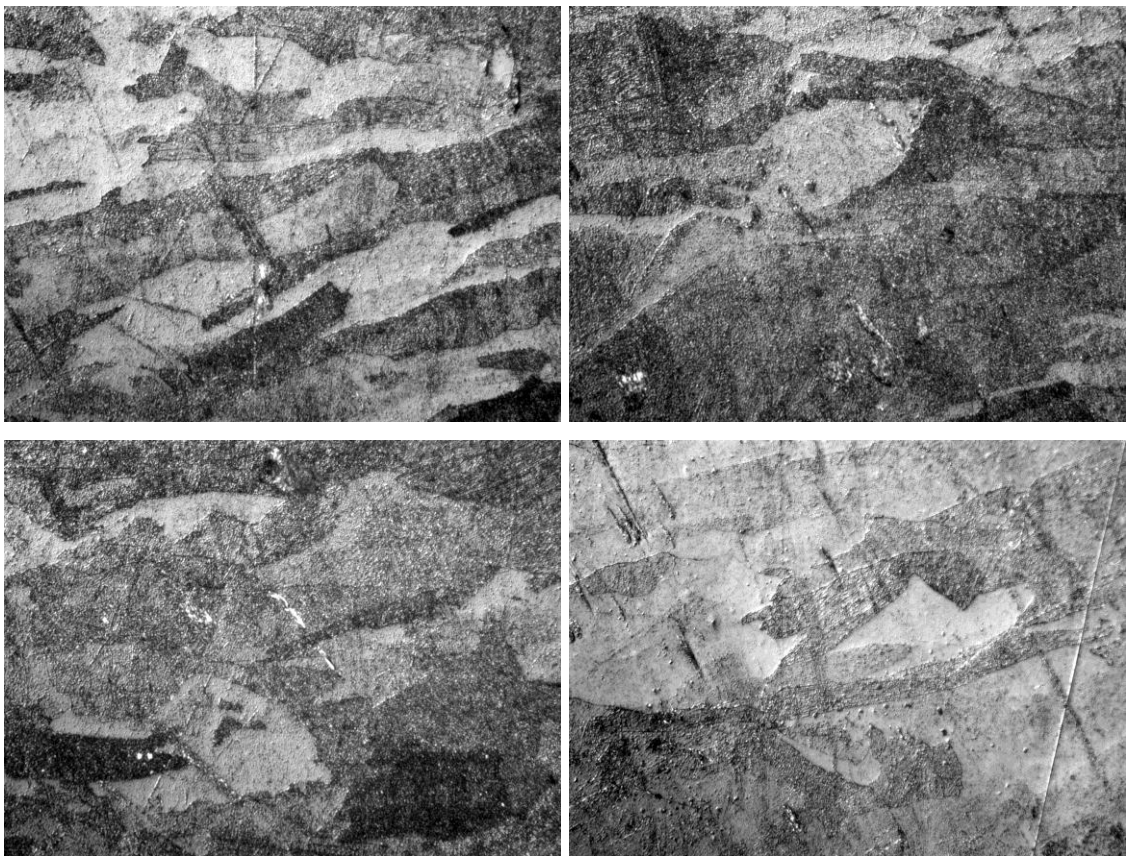

Figure 97: Monochrome DIC Micrographs of Unirradiated Horizontal LAM Inconel 600 after Etching with Kalling's Modified Superalloy Etchant for 60 Seconds (20x1x25x Magnification)

IV.2 Scanning Electron Microscopy and Energy Dispersive Spectroscopy

IV.2.1 Scanning Electron Microscopy of Unirradiated Alloys

Scanning electron micrographs with energy dispersive spectroscopy maps were collected using the JOEL JSM-6400 SEM. Several features are present on the LAM samples of all three alloys in their unirradiated as-annealed conditions which are apparent artifacts associated with the additive manufacturing process. The unirradiated as-annealed Inconel 600 LAM samples contained regions of black agglomerates, shown in Figure 98 - Figure 104. These features exist in a variety of shapes and sizes on the LAM Inconel 600 rods, but were not found on the conventionally manufactured Inconel 600 control. The SEM/EDS maps in Figure 105 - Figure 108 reveal that these black features are chromium-carbon precipitates which formed during the additive manufacturing process. The band of contrast in the middle of some of the SEM/EDS maps (ex. Figure 105) was caused by user error while initially learning to use the Iridium Ultra software.

Figure 98: SEM Image of Black Agglomerates near Nanoindents on the Surface of Unirradiated Vertical LAM Inconel 600

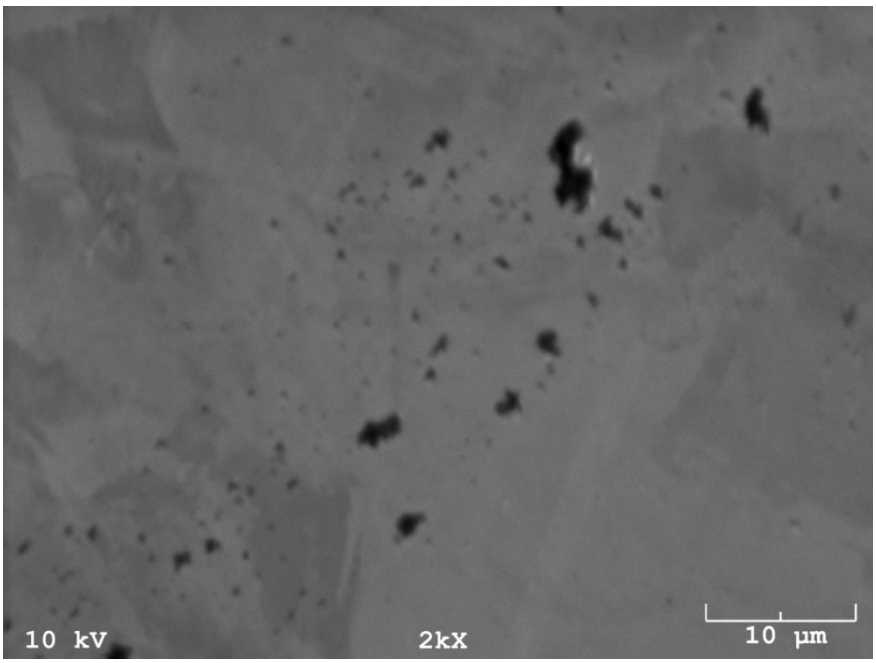

Figure 99: SEM Image of Black Agglomerates on Unirradiated Horizontal LAM Inconel 600

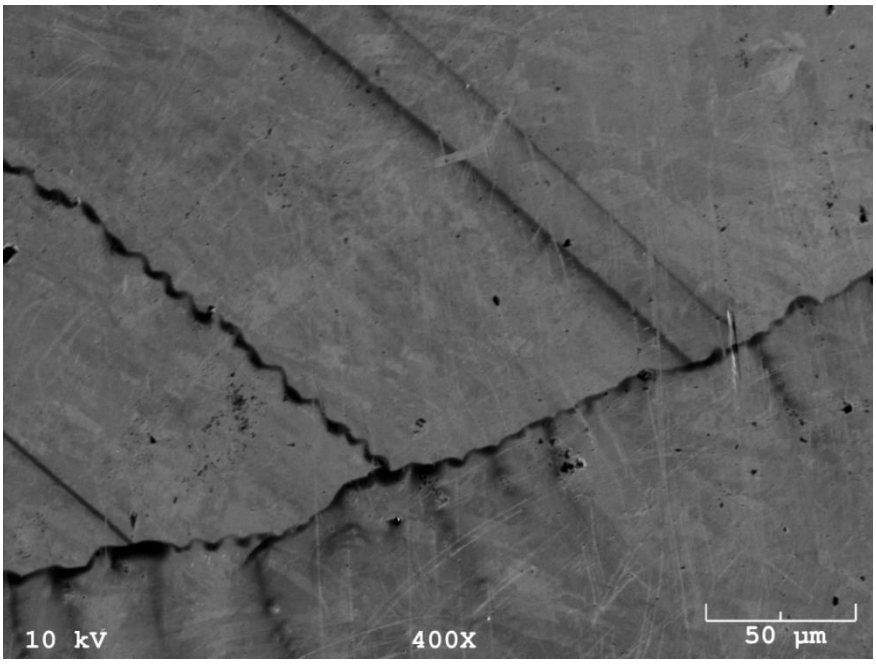

Figure 100: SEM Image of Black Streaks on the Surface of Unirradiated Horizontal LAM Inconel 600

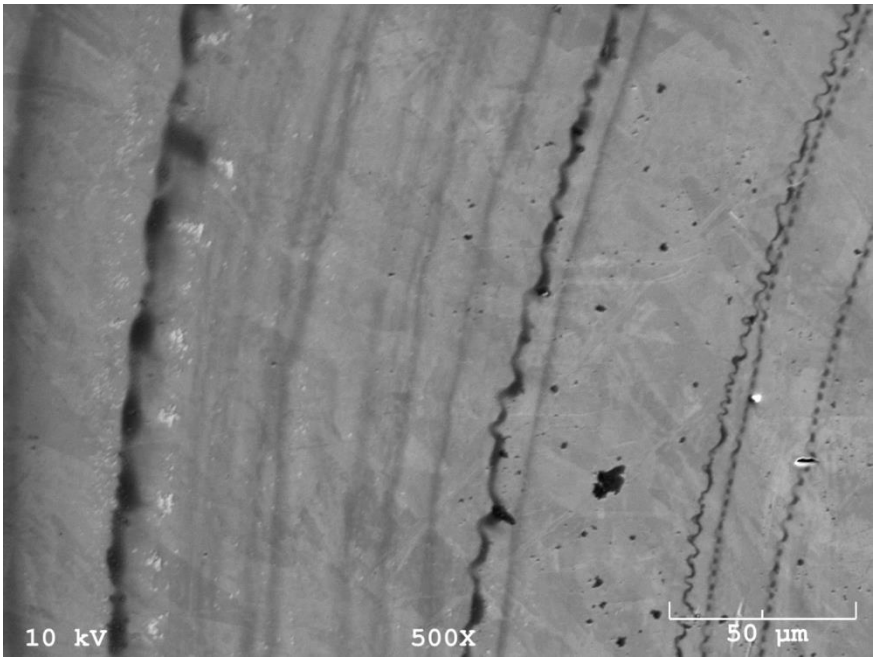

Figure 101: SEM Image of Wavy Black Streaks on the Surface of Unirradiated Horizontal LAM Inconel 600

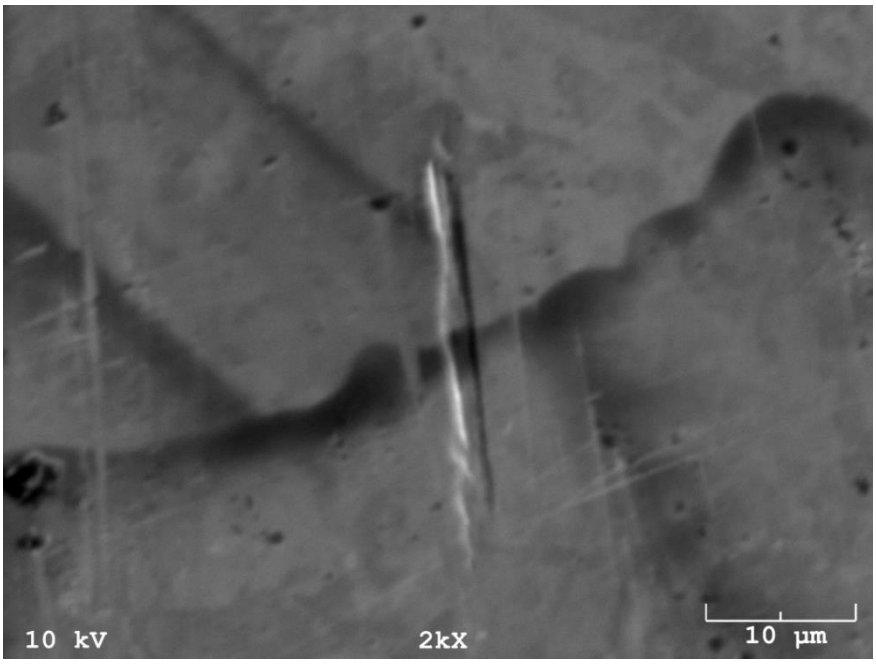

Figure 102: SEM Image of a Scratch within Black Streaks on the Surface of Unirradiated Horizontal LAM Inconel 600

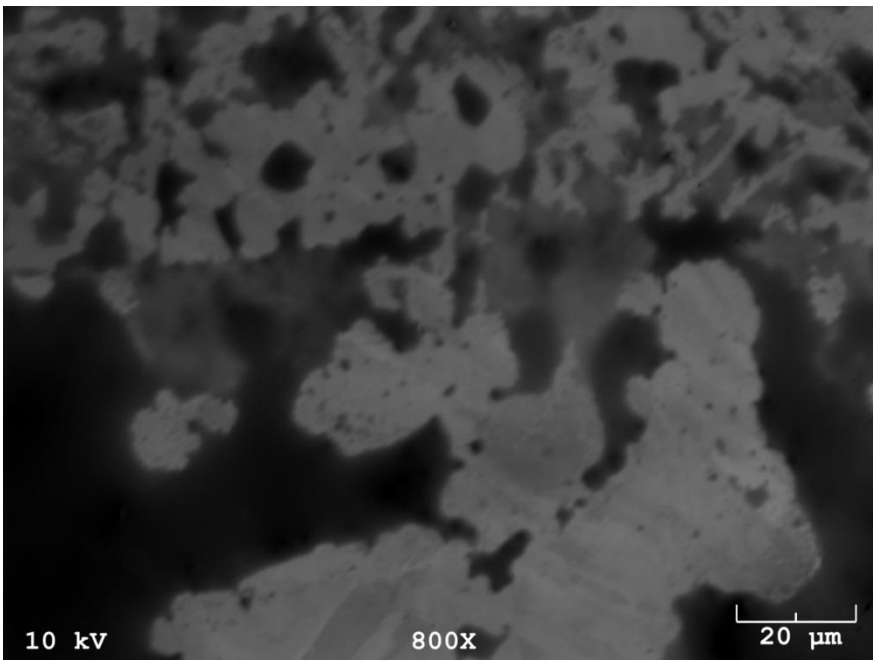

Figure 103: SEM Image of Agglomerates of Black Features on the Surface of Unirradiated Horizontal LAM Inconel 600

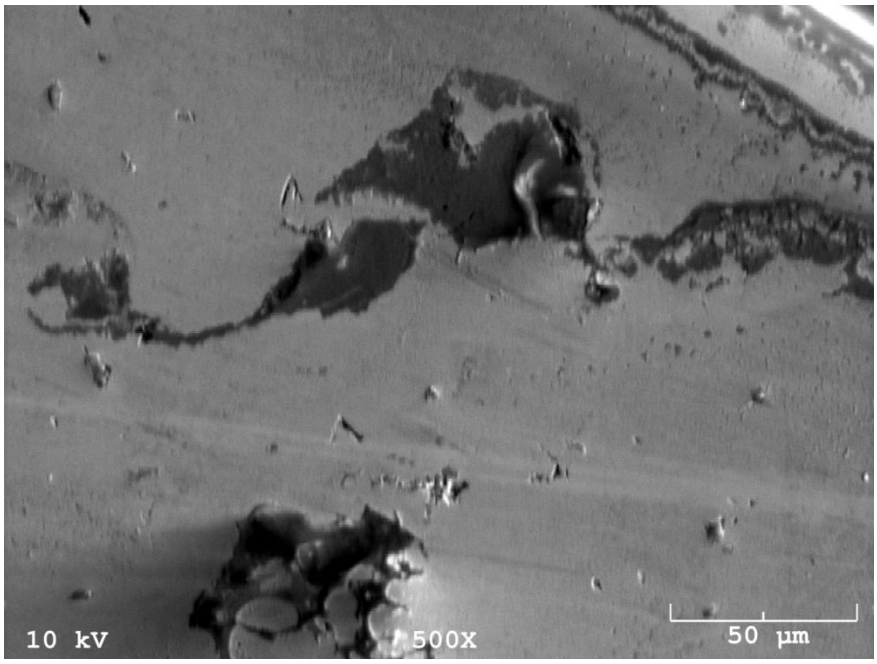

Figure 104: SEM Image of Dark Features on the Surface of Unirradiated 45° LAM Inconel 600

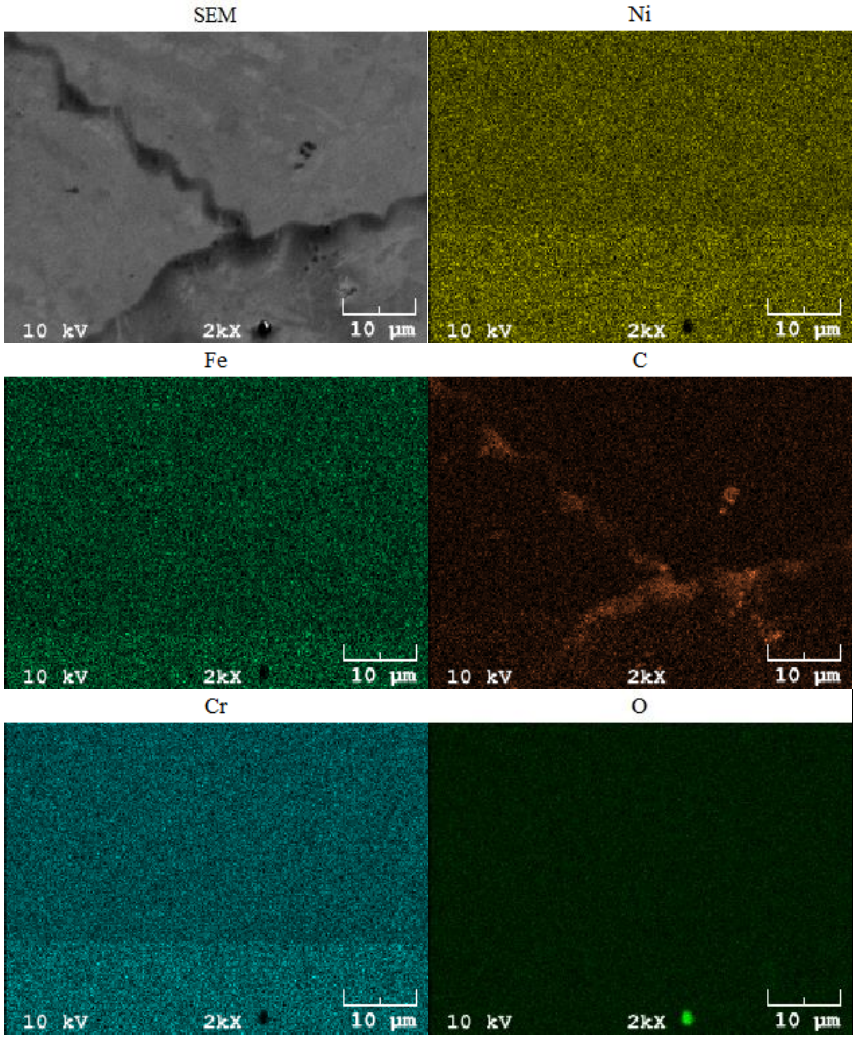

Figure 105: SEM/EDS Maps of Wavy Carbon Streaks on the Surface of Unirradiated Horizontal LAM Inconel 600

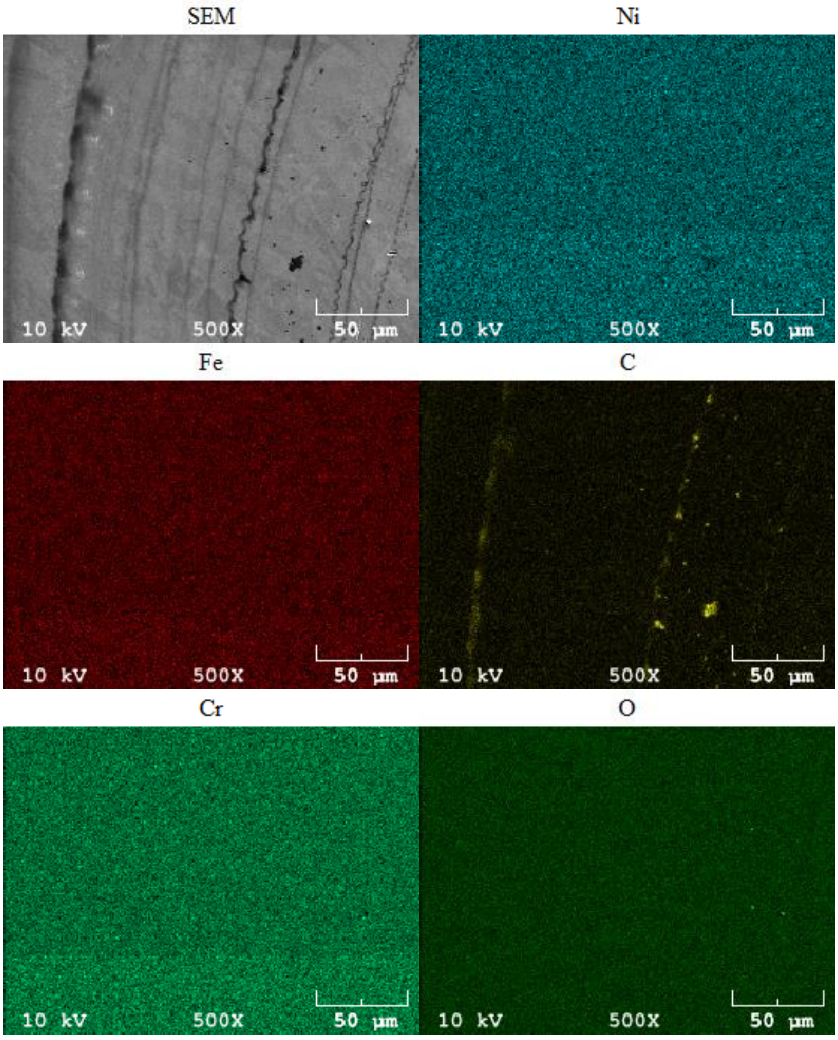

Figure 106: SEM/EDS Maps of Aligned Carbon Streaks on the Surface of Unirradiated Horizontal LAM Inconel 600

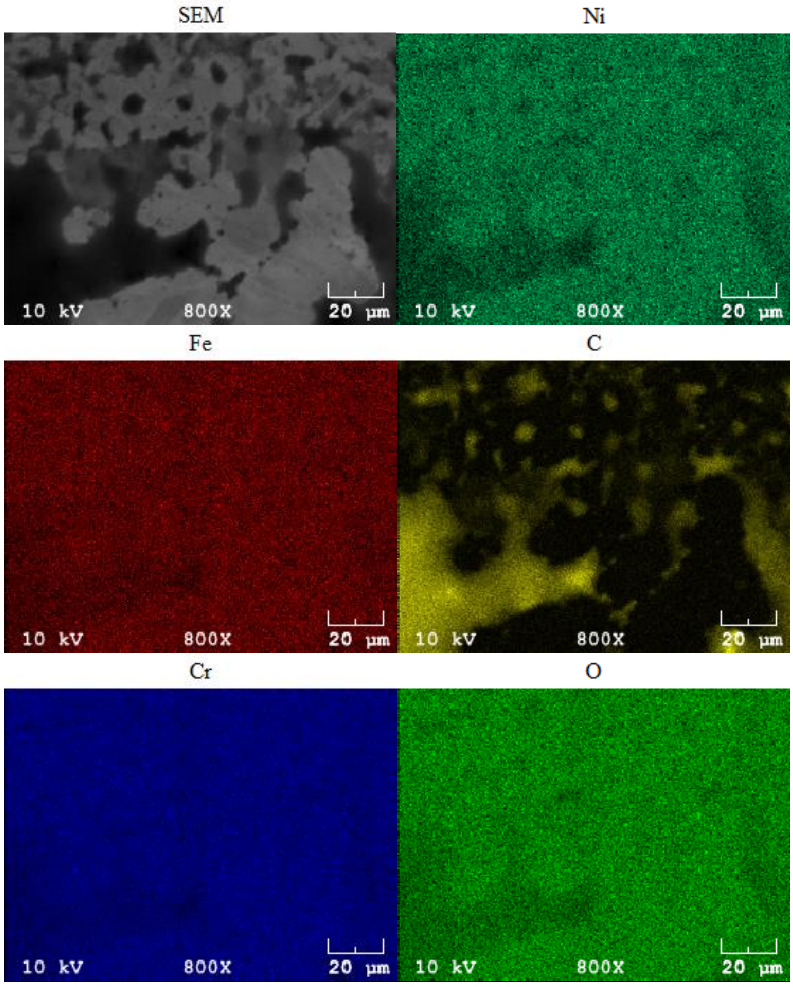

Figure 107: SEM/EDS Maps of Large Carbon Agglomerates on the Surface of Unirradiated Horizontal LAM Inconel 600

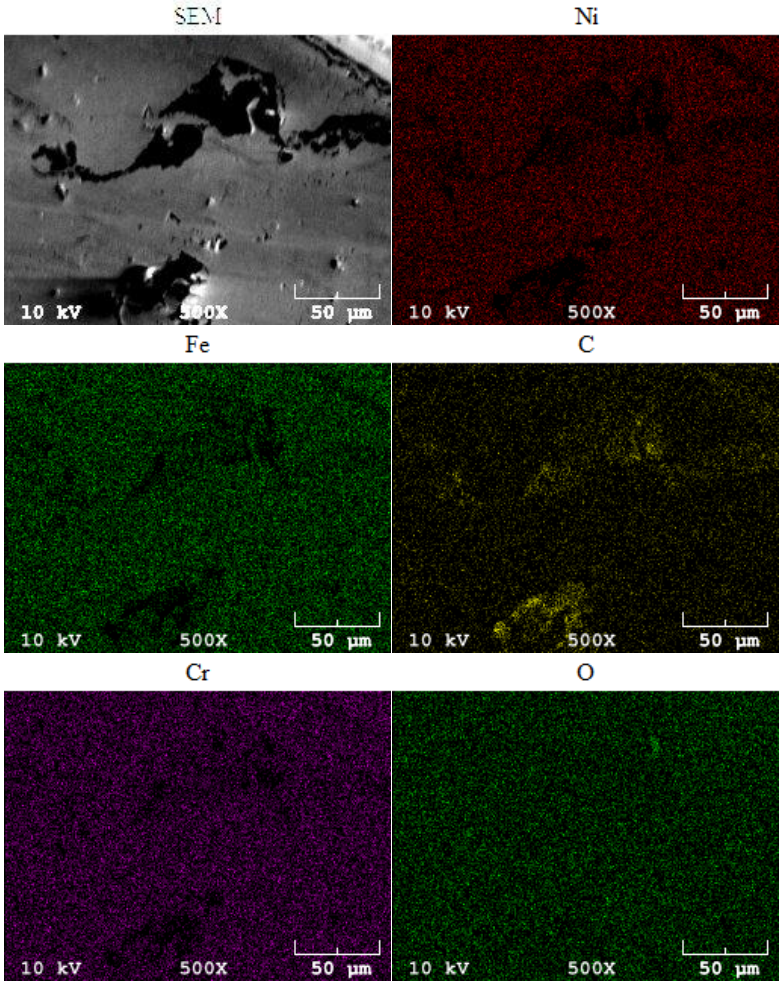

Figure 108: SEM/EDS Maps of Carbon Agglomerates on the Surface of Unirradiated 45° Inconel 600

The carbon agglomerates exist on LAM 316L stainless steel as well (Figure 109 - Figure 112); however, they were not found on the surfaces of any of the ODS samples (Figure 113 - Figure 115). The LAM ODS steel appears to have significantly greater porosity than the other LAM alloys, which is to be expected since the LAM process for the ODS samples was not fully optimized to maximize part density using the LENS system.

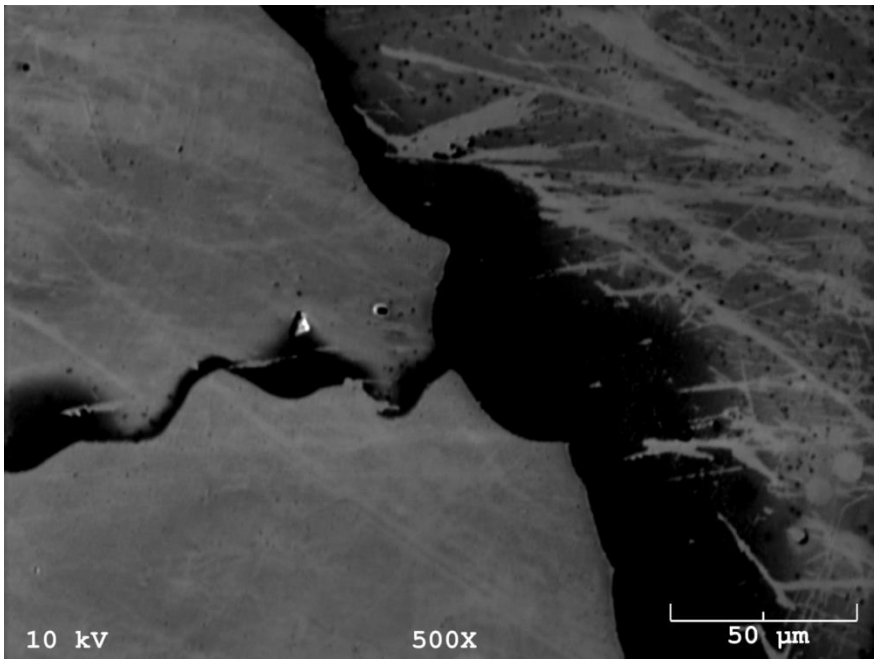

Figure 109: SEM Image of Black Features on the Surface of Unirradiated Vertical LAM 316L Stainless Steel

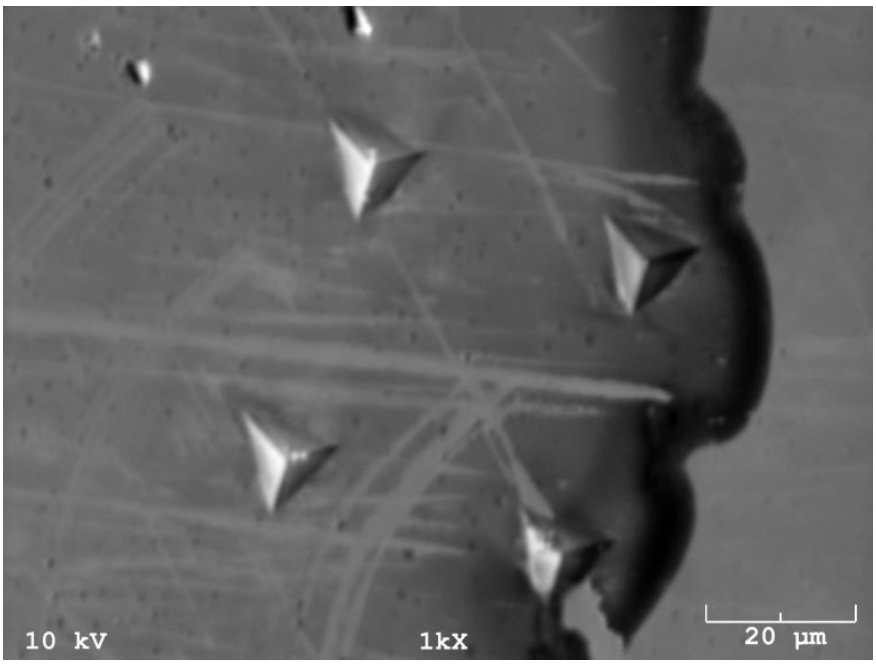

Figure 110: SEM Image of Black Features near Nanoindents on the Surface of Unirradiated 45° LAM 316L Stainless Steel

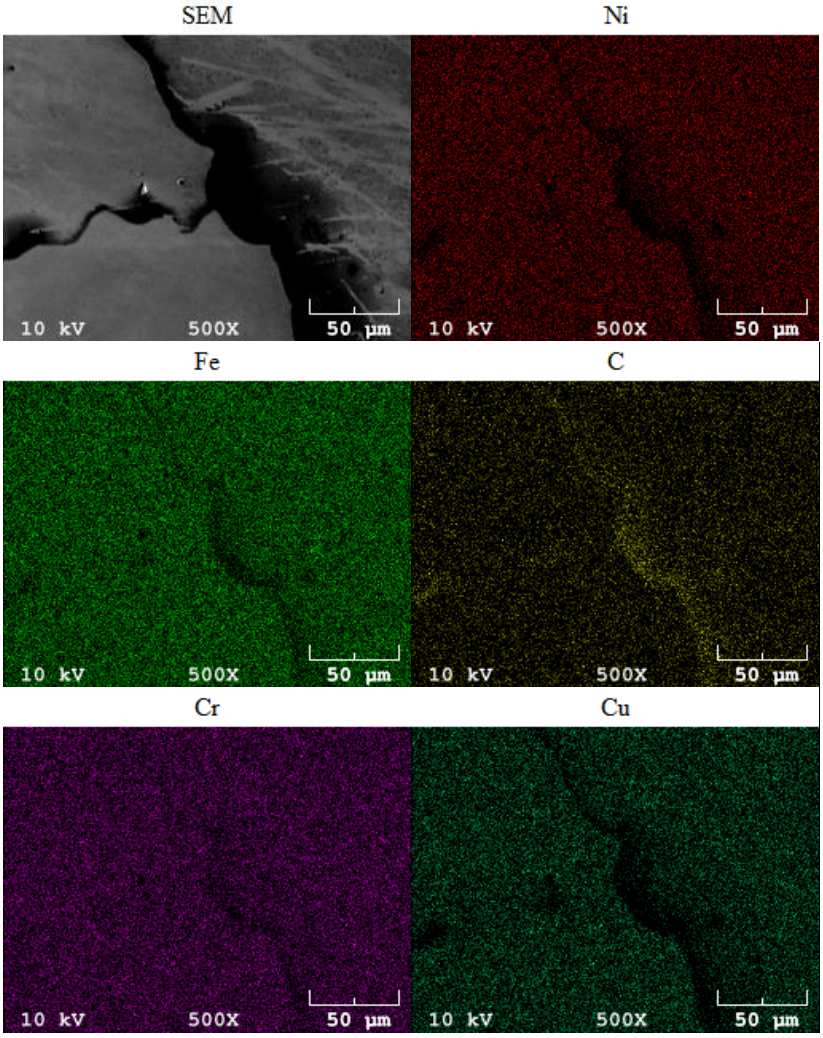

Figure 111: SEM/EDS Maps of Carbon Streaks on the Surface of Unirradiated Vertical LAM 316L Stainless Steel

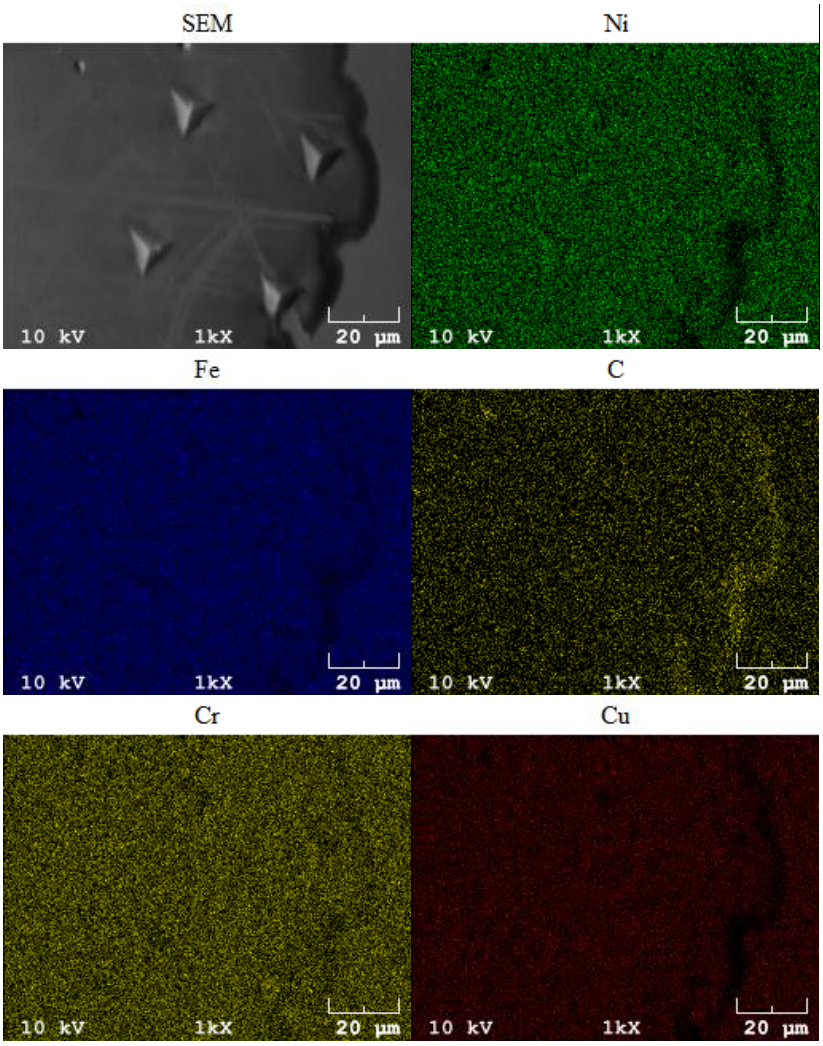

Figure 112: SEM/EDS Maps of Carbon Streaks near Nanoindents on the Surface of Unirradiated 45° LAM 316L Stainless Steel

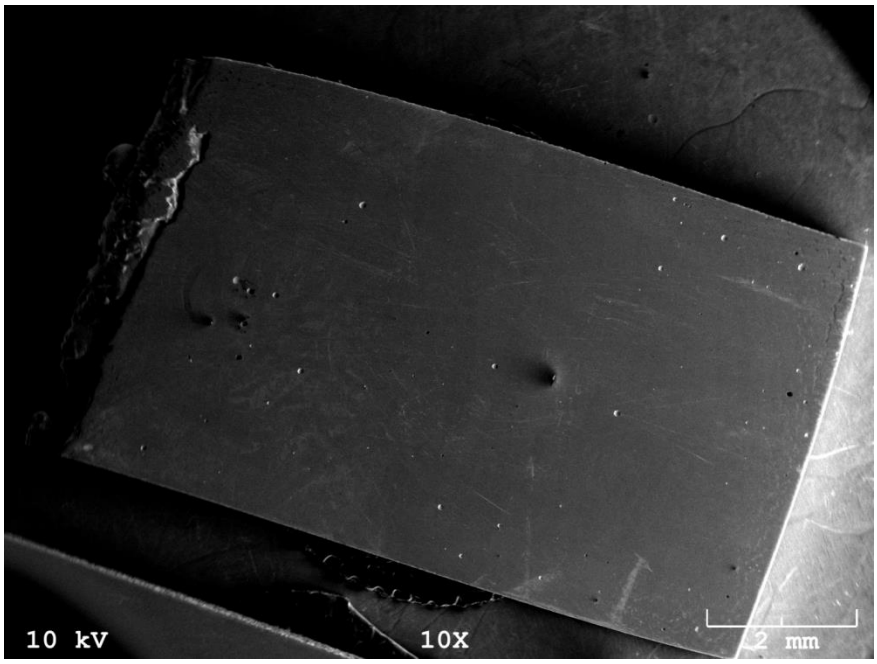

Figure 113: Low Magnification SEM Image of Unirradiated Vertical LAM ODS Steel

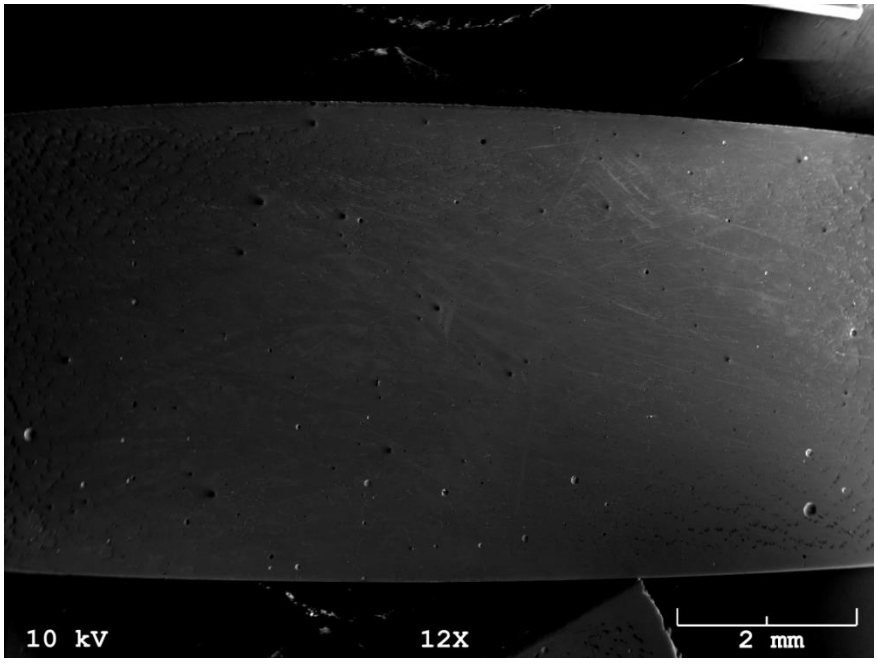

Figure 114: SEM Image of Unirradiated Horizontal LAM ODS Steel

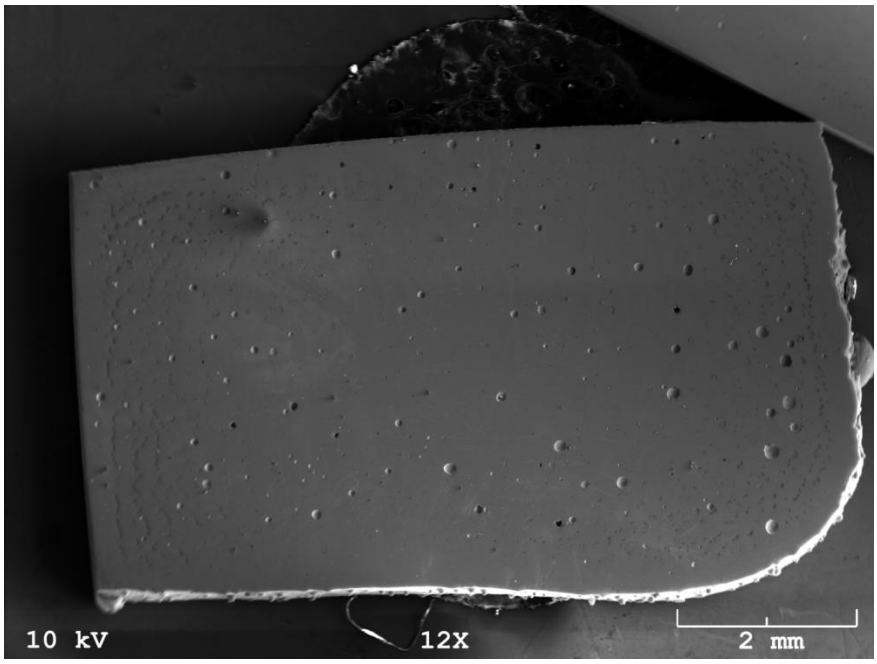

Figure 115: SEM Image of Unirradiated Surface of 45° LAM ODS Steel

IV.2.2 Scanning Electron Microscopy of Inconel 600 Irradiated to 80 dpa

The boundary between the irradiated and unirradiated regions on all Inconel 600 samples, including the conventional control, was easily visible on SEM images shown below in Figure 116 - Figure 119. The irradiation boundary on the steel samples was not clearly visible on SEM images. The difference in contrast between the Inconel 600 and 316L stainless steel samples is due to radiation-induced changes in surface geometry and composition (vide infra).

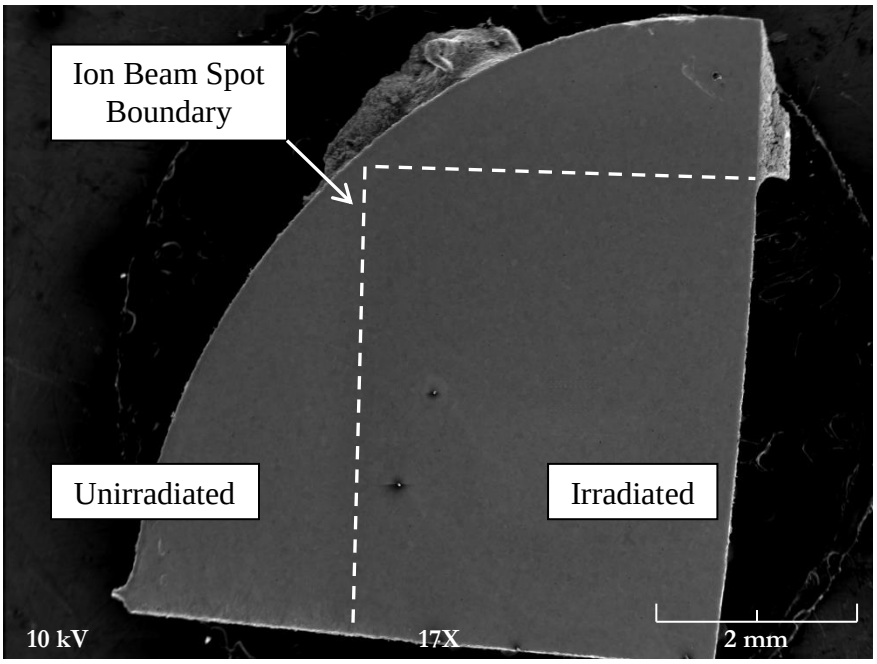

Figure 116: SEM Image of Conventionally Manufactured Inconel 600 Irradiated to 80 dpa

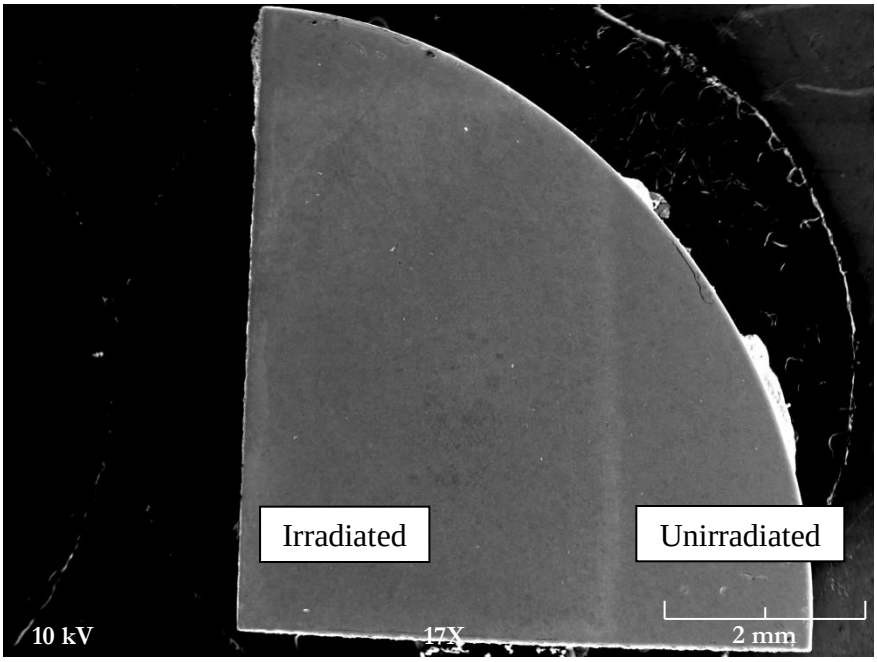

Figure 117: SEM Image of Vertical LAM Inconel 600 Irradiated to 80 dpa

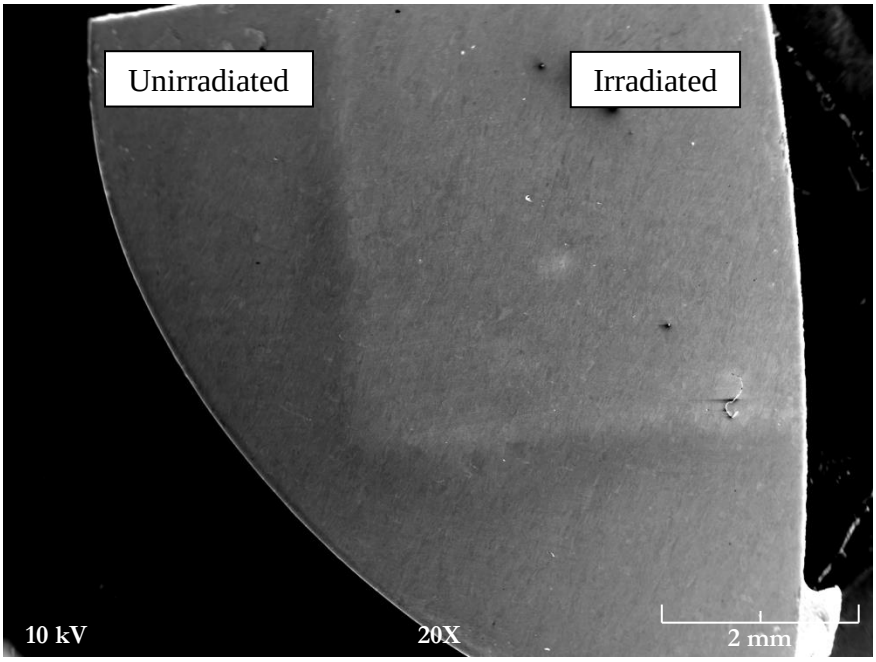

Figure 118: SEM Image of Horizontal LAM Inconel 600 Irradiated to 80 dpa

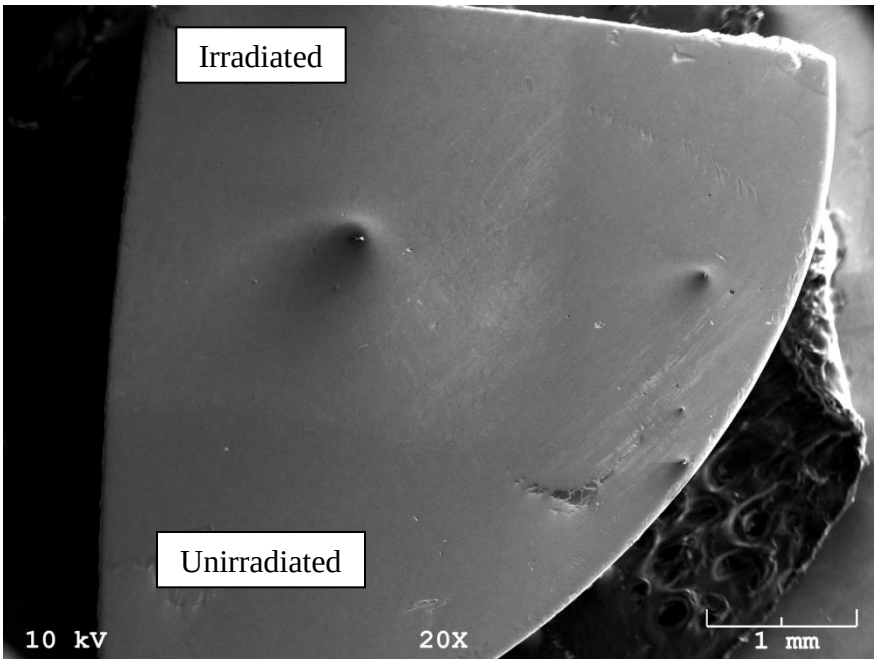

Figure 119: SEM Image of 45° LAM Inconel 600 Irradiated to 80 dpa

All additively manufactured Inconel 600 samples appear to have formed features on their surfaces with bright contrast. These features appear to be circular on the vertical LAM (Figure 122), while they take the form of streaks on the horizontal LAM (Figure 123). Features with bright contrast appeared as "dots" on irradiated 45° LAM (Figure 124), and were not found on the conventionally manufactured control (Figure 121). This suggests that these migratory species are driven to form precipitates which align in cylindrical geometries parallel to the LAM build direction. Figure 120 shows that the radiation-induced precipitates on the surface of the Inconel 600 samples are significantly smaller than the nanoindents. This suggests that nanoindentation measurements would be dominated by the Inconel rather than the precipitates. Radiation-induced precipitates were not found in SEM imaging of the irradiated 316L stainless steel samples.

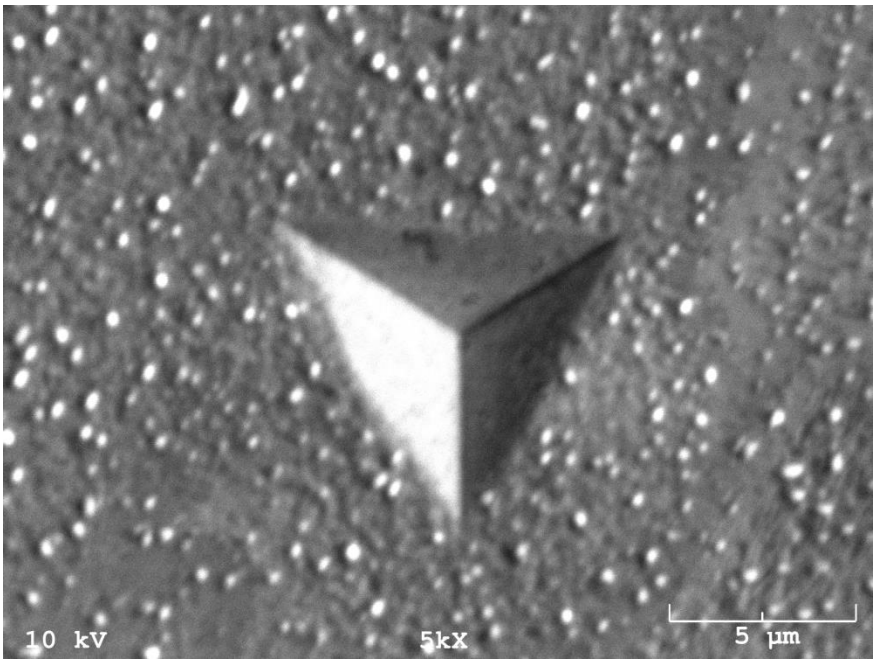

Figure 120: SEM Image Comparing the Size of a 1600 nm Deep Nanoindent to the Radiation-induced Precipitates Rich in Cr, C, and O on the Surface of 45° LAM Inconel 600 Irradiated to 80 dpa

SEM/EDS maps (Figure 125 and Figure 126) reveal that these features are chromium carbide and chromium oxide precipitates. The oxygen may have come from the passivation film which is always present on the surface of these alloys, or it could have come from oxygen-contaminated powders before manufacturing. The increase in chromium compounds at the surface of the additively manufactured samples indicates increased chromium mobility under irradiation in comparison to the conventionally manufactured Inconel 600. The overall effective diffusion coefficient of chromium has recently been observed to increase in Inconel 600 as grain size decreases [104]. This suggests an increased sensitivity to irradiation-assisted stress corrosion cracking

(IASCC) in the LAM specimens toward which chromium depletion to the grain boundaries is known to increase the susceptibility of Inconel 600 [21].

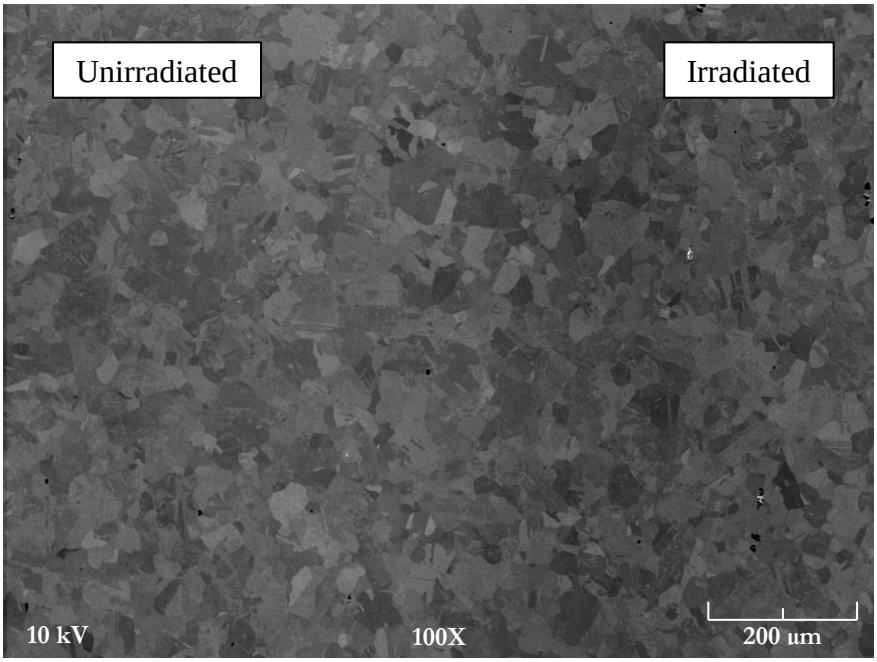

Figure 121: SEM Image of Conventionally Manufactured Inconel 600 Irradiated to 80 dpa without Bright Contrast Features

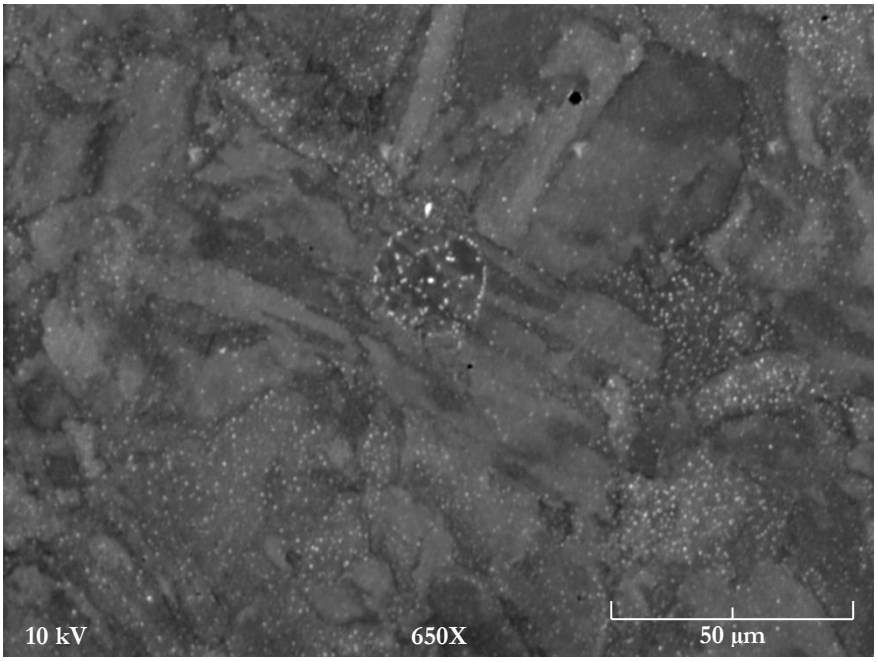

Figure 122: SEM Image of Bright Contrast Circular Feature on Vertical LAM Inconel 600 Irradiated to 80 dpa

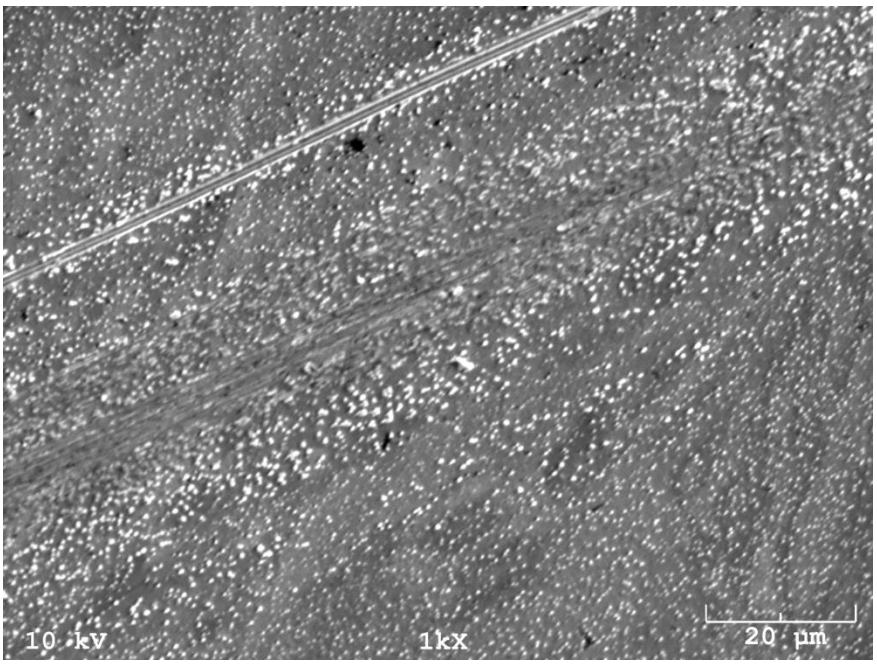

Figure 123: SEM Image of Bright Contrast Parallel Streaks on Horizontal LAM Inconel 600 Irradiated to 80 dpa

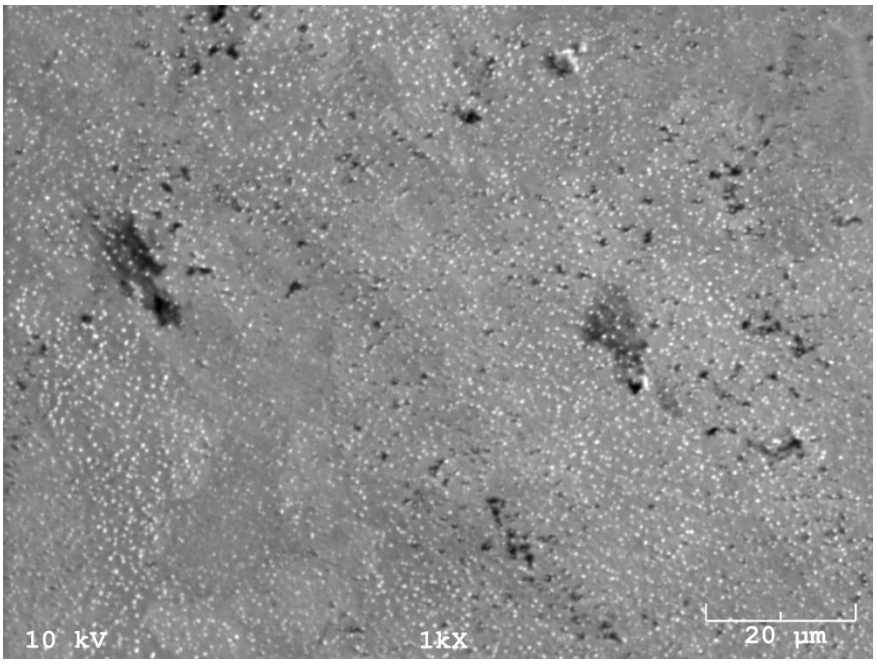

Figure 124: SEM Image of Bright Contrast Spots on 45° LAM Inconel 600 Irradiated to 80 dpa

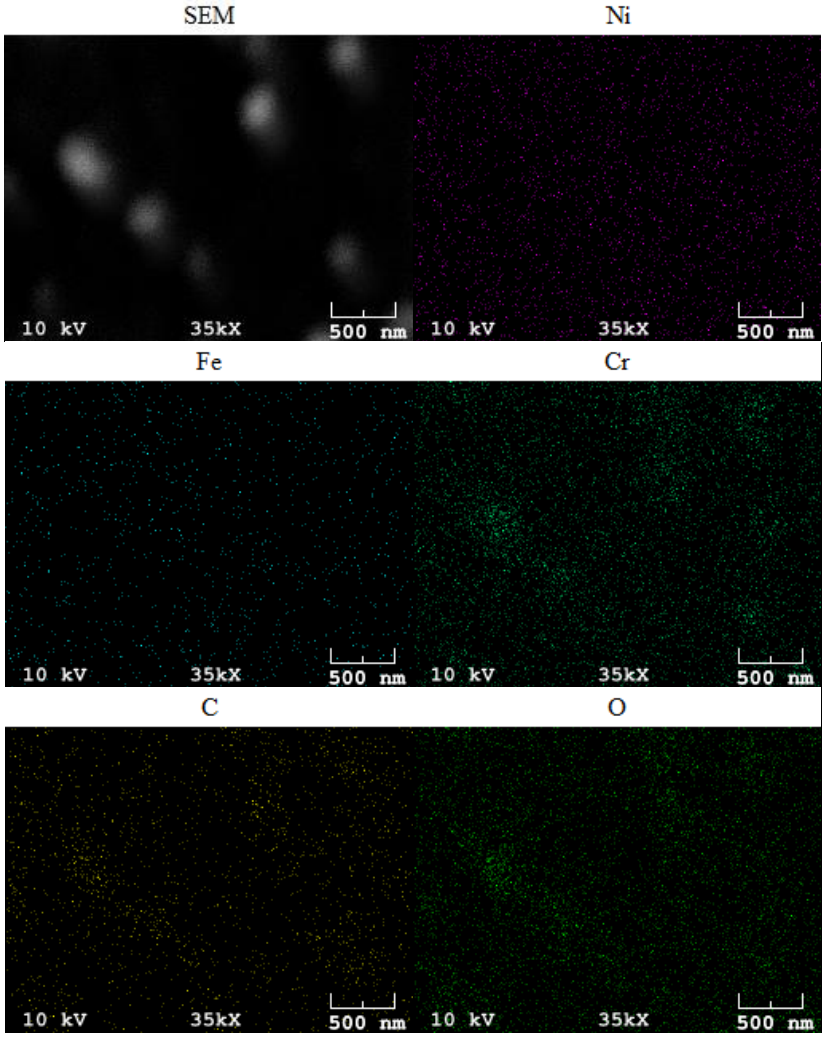

Figure 125: SEM/EDS Maps of Vertical LAM Inconel 600 Irradiated to 80 dpa showing Precipitates Rich in Cr, C, and O

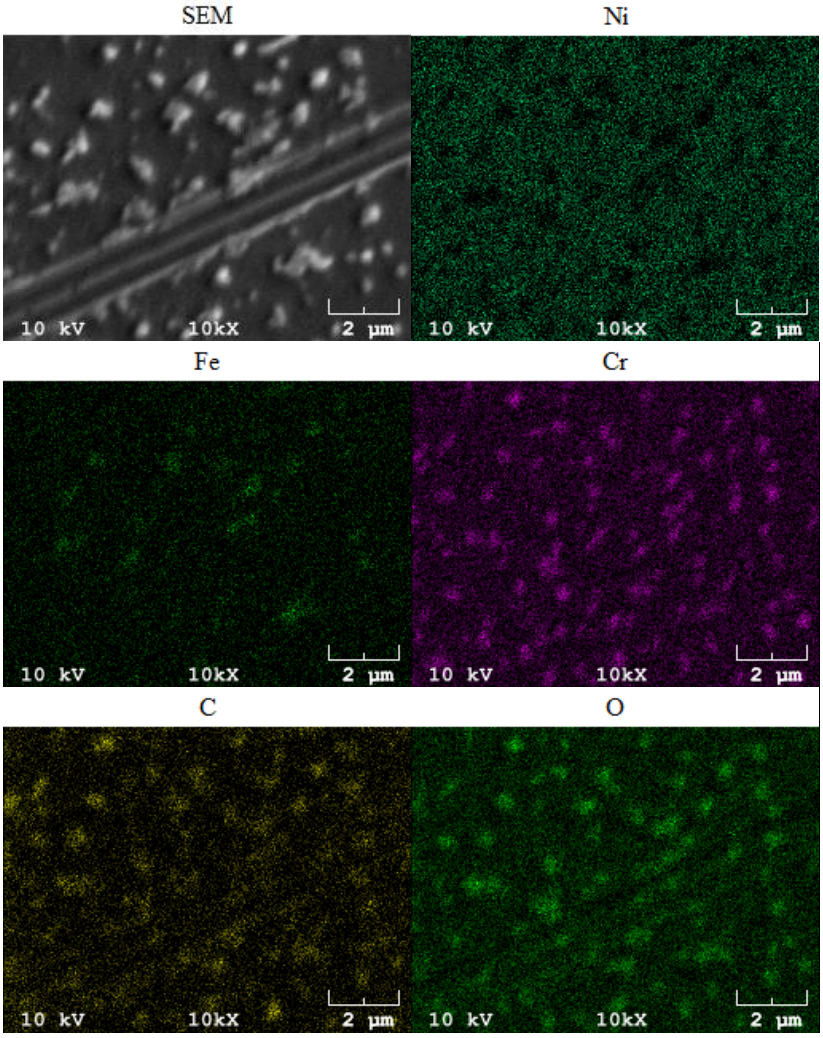

Figure 126: SEM/EDS Maps of Horizontal LAM Inconel 600 Irradiated to 80 dpa showing Precipitates Rich in Cr, C, and O

IV.3 Electron Backscatter Diffraction

This section discusses the characterization results of the unirradiated and irradiated Inconel 600 and 316L steel. Cubic Rodrigues-Frank maps and pole figures of these samples are summarized by Euler maps and inverse pole figures, and are discussed in the Appendix. In all cases, EBSD measurements were collected from regions within the bulk of the rods (i.e. far from the tips), approximately halfway between the radial center and the curved edge of the rods. The unirradiated LAM ODS steel was also characterized and is discussed in the Appendix for completeness. For a review of EBSD theory, see Ch. II.4.

IV.3.1. Grain Size, Shape, and Slope

The grain sizes, grain aspect ratios, and number of neighboring grains for the Inconel 600 and 316L before and after high dose irradiation are summarized below in Table 15 and Table 16, respectively. For a review of grain size, shape, and slope determination in EBSD, see Ch. II.4.3. Grain size maps and histograms of the Inconel 600 and 316L stainless steel samples before and after irradiation are provided in Figure 127 - Figure 134. Note that the x- and y-axes in the histograms are not on identical scales. As shown in the grain size tables and maps, the grain aspect ratios and number of neighbors do not change noticeably due to radiation damage. The grain sizes for the Inconel decrease due to radiation damage, but increase due to radiation damage for the 316L. The cause of these radiation-induced changes is unknown.

Table 15: Summary of Grain Sizes, Aspect Ratios and Neighbors of Inconel 600 Vertical LAM, Horizontal LAM, 45° LAM, and Conventionally Manufactured Control Before and After Irradiation

Parameter	Conventional	Vertical LAM	Horizontal LAM	45° LAM
Unirradiated Grain Size (μm)	8.41	5.23	4.89	5.70
80 dpa Grain Size (μm)	6.55	5.19	4.44	4.71
Δ Grain Size (%)	-22.1	-0.8	-9.2	-17.4
Unirradiated GAR	2.2	2.2	3.1	2.5
80 dpa GAR	2.7	2.2	3.1	2.4
Δ GAR (%)	23	0	0	-4
Unirr. Neighboring Grains	5.4	5.6	4.6	5.7
80 dpa Neighboring Grains	5.2	5.7	4.7	5.4
Δ Neighboring Grains (%)	-3.7	1.8	2.2	-5.3

Table 16: Summary of Grain Sizes, Aspect Ratios and Neighbors of 316L Stainless Steel Vertical LAM, Horizontal LAM, 45° LAM, and Conventionally Manufactured Control Before and After Irradiation

Parameter	Conventional	Vertical LAM	Horizontal LAM	45° LAM
Unirradiated Grain Size (μm)	4.03	5.97	4.74	6.32
80 dpa Grain Size (μm)	3.77	6.26	5.70	6.16
Δ Grain Size (%)	-6.4	4.9	20.2	-2.6
Unirradiated GAR	2.0	2.3	2.5	2.3
80 dpa GAR	2.0	2.3	3.1	2.4
Δ GAR (%)	2	2	23	5
Unirr. Neighboring Grains	5.9	5.4	4.7	5.1
80 dpa Neighboring Grains	6.1	5.5	4.9	5.4
Δ Neighboring Grains (%)	3	3	4	6

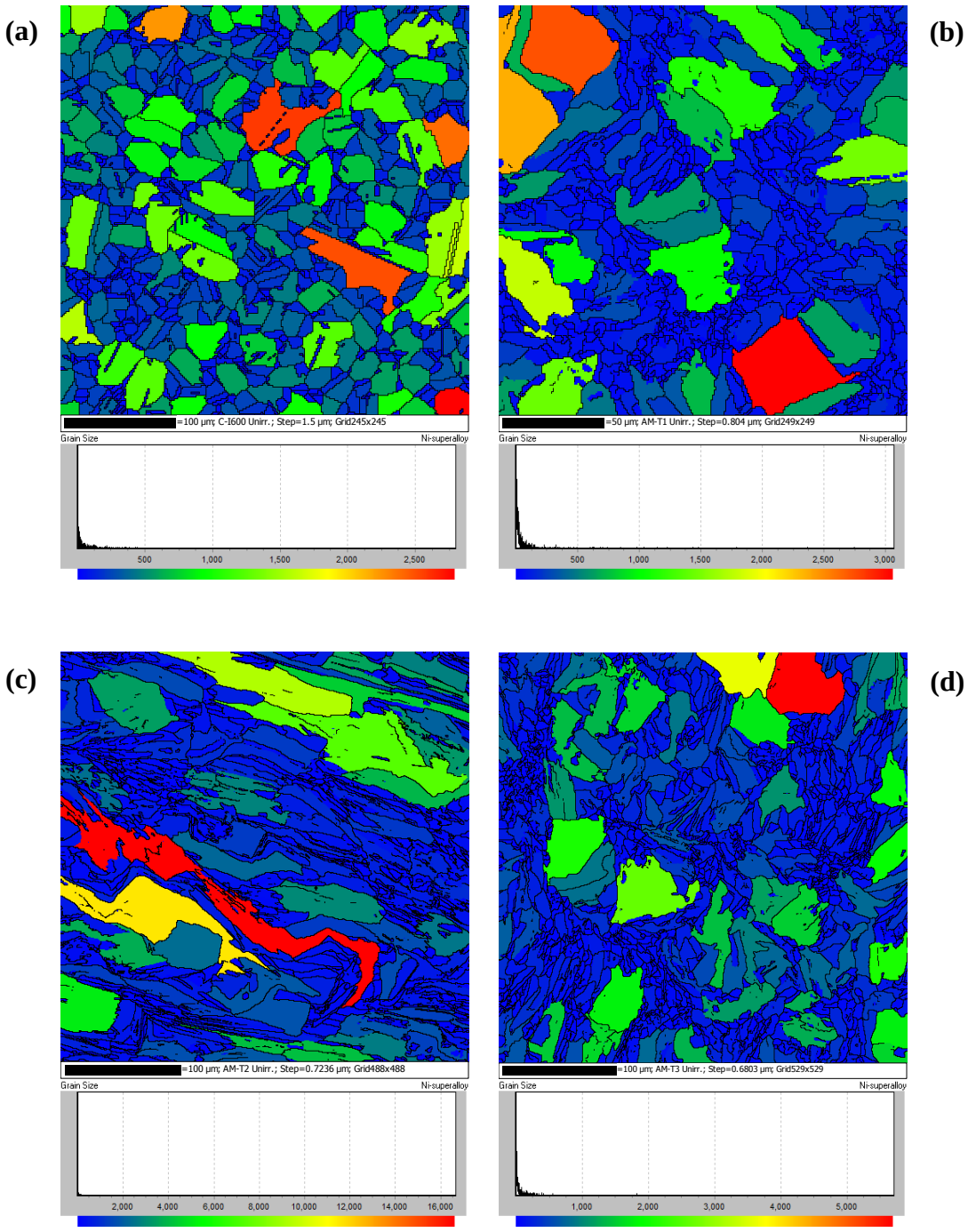

Figure 127: EBSD Grain Size Maps of Unirradiated Inconel 600 (a) Conventionally Manufactured, (b) Vertical LAM, (c) Horizontal LAM, and (d) 45° LAM

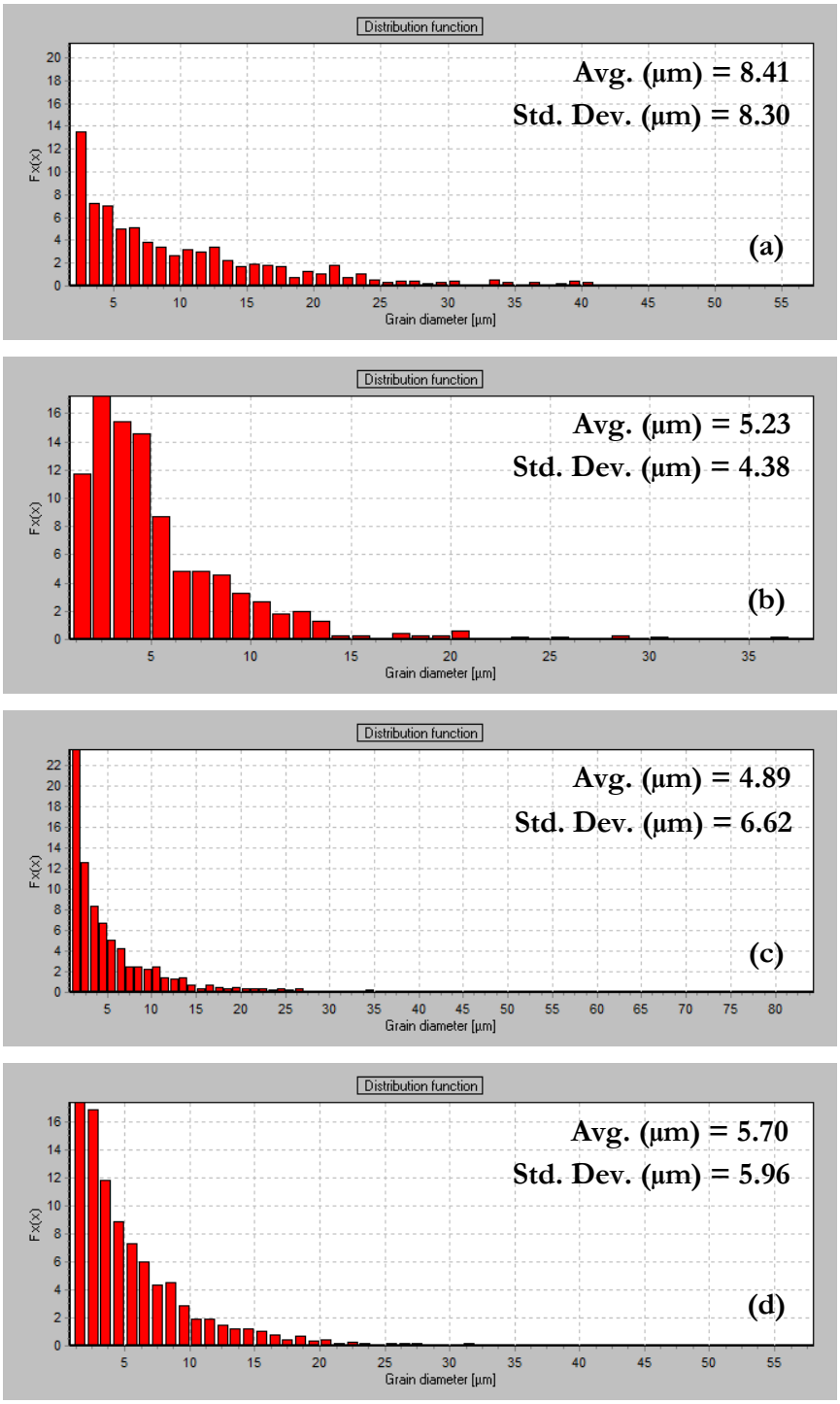

Figure 128: Grain Size Distribution Histograms of Unirradiated Inconel 600 (a) Conventionally Manufactured, (b) Vertical LAM, (c) Horizontal LAM, and (d) 45° LAM

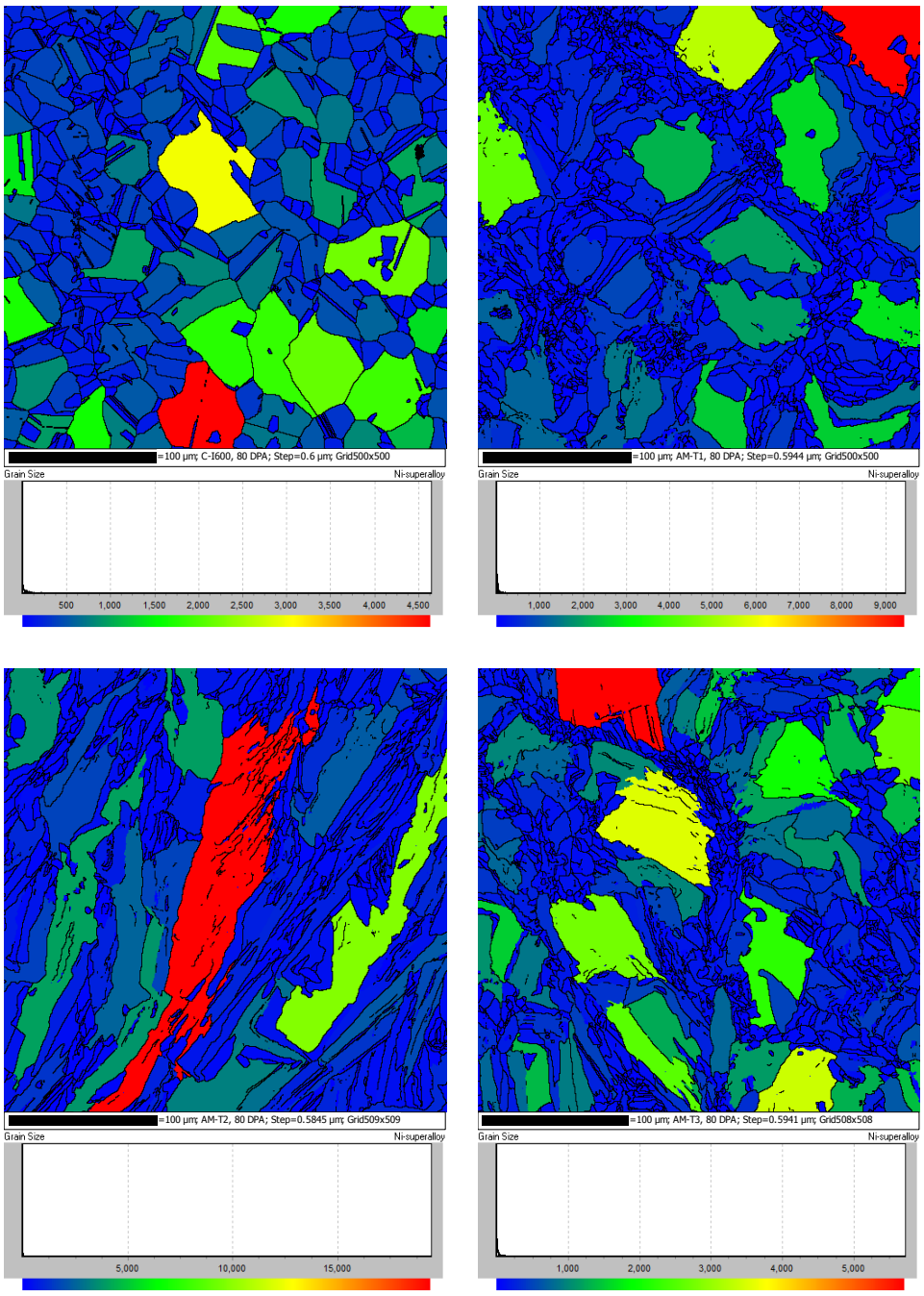

Figure 129: EBSD Grain Size Maps of Inconel 600 (a) Conventionally Manufactured, (b) Vertical LAM, (c) Horizontal LAM, and (d) 45° LAM Irradiated to 80 dpa

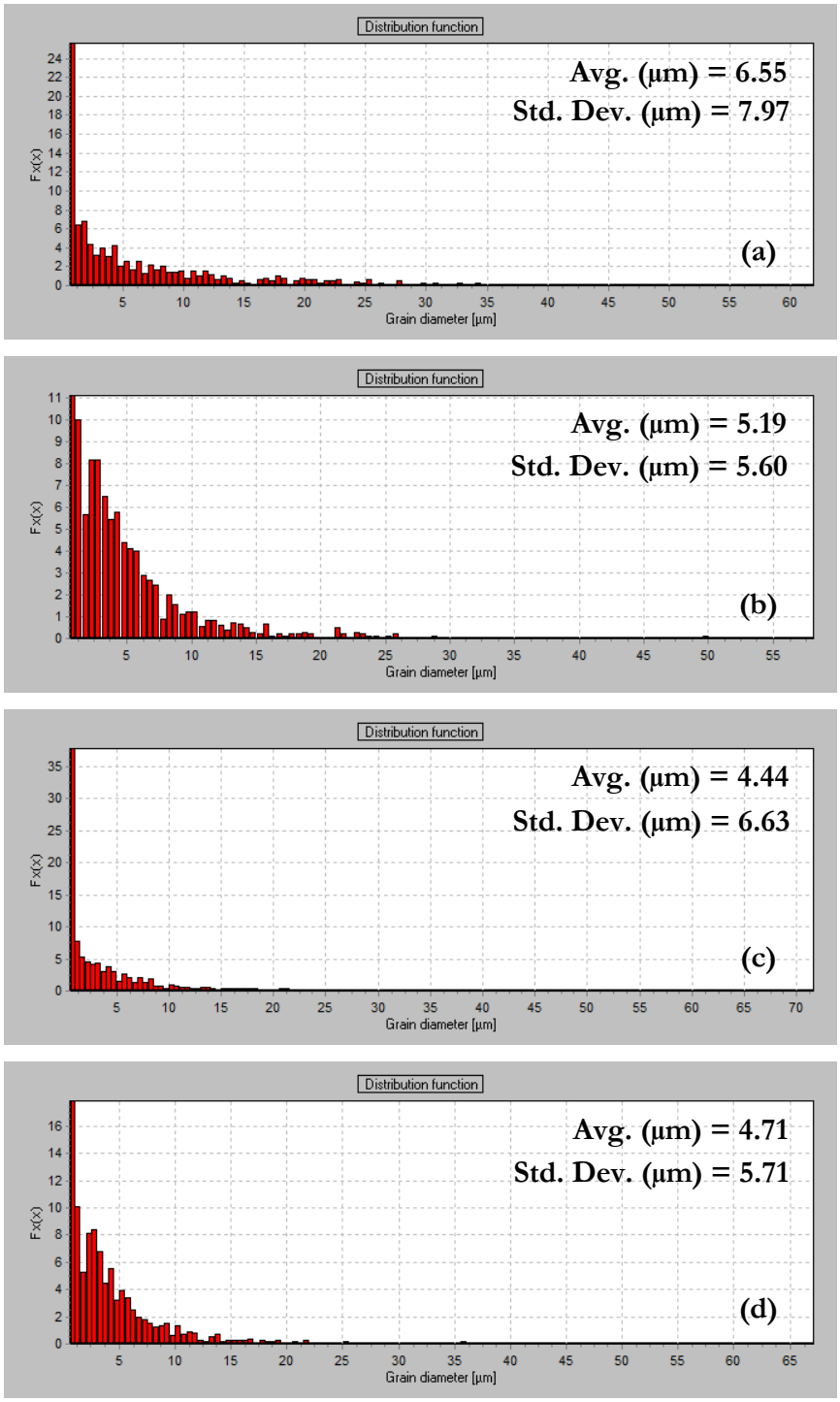

Figure 130: Grain Size Distribution Histograms of Inconel 600 (a) Conventionally Manufactured, (b) Vertical LAM, (c) Horizontal LAM, and (d) 45° LAM Irradiated to 80 dpa

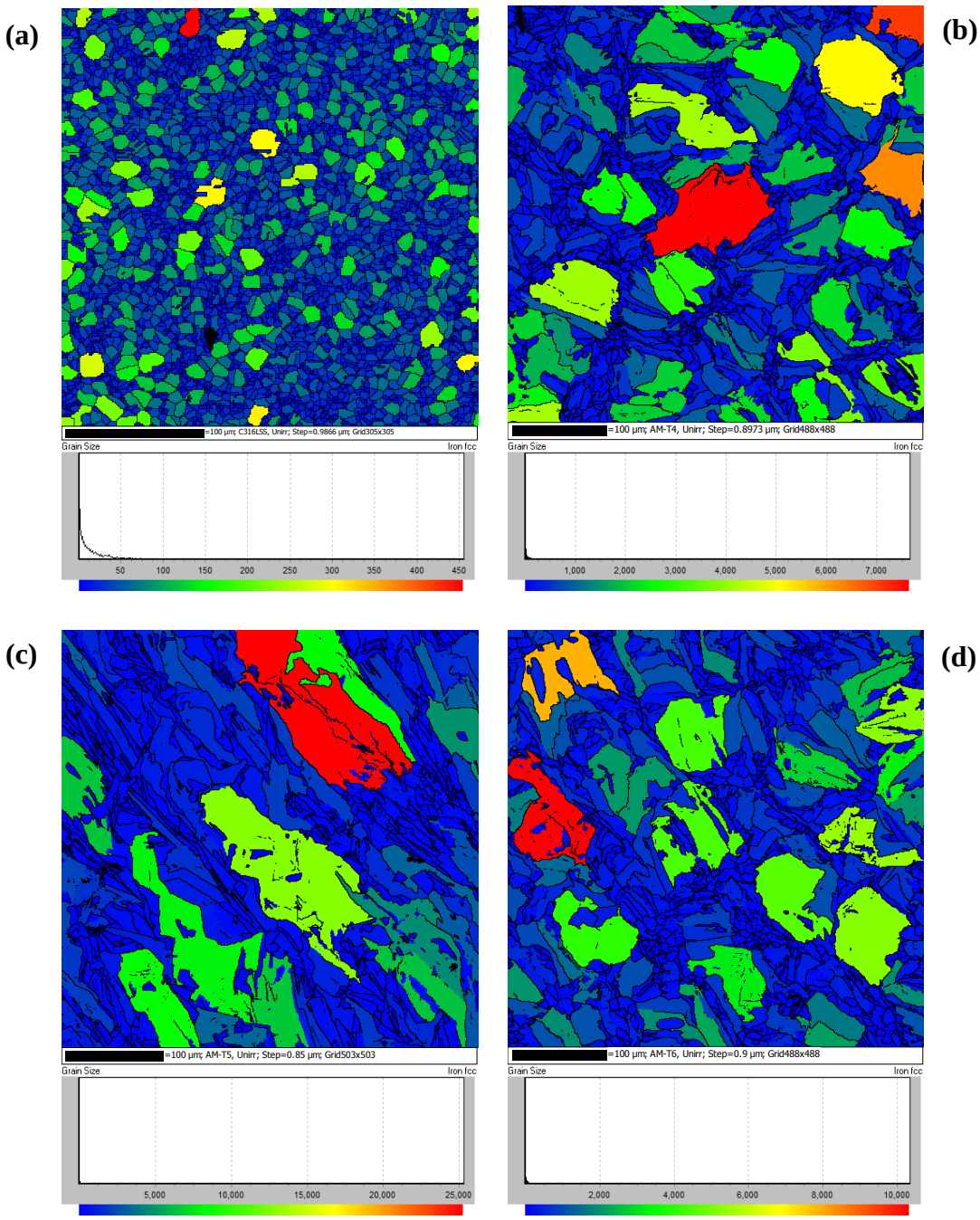

Figure 131: EBSD Grain Size Maps of Unirradiated 316L Stainless Steel (a) Conventionally Manufactured, (b) Vertical LAM, (c) Horizontal LAM, and (d) 45° LAM

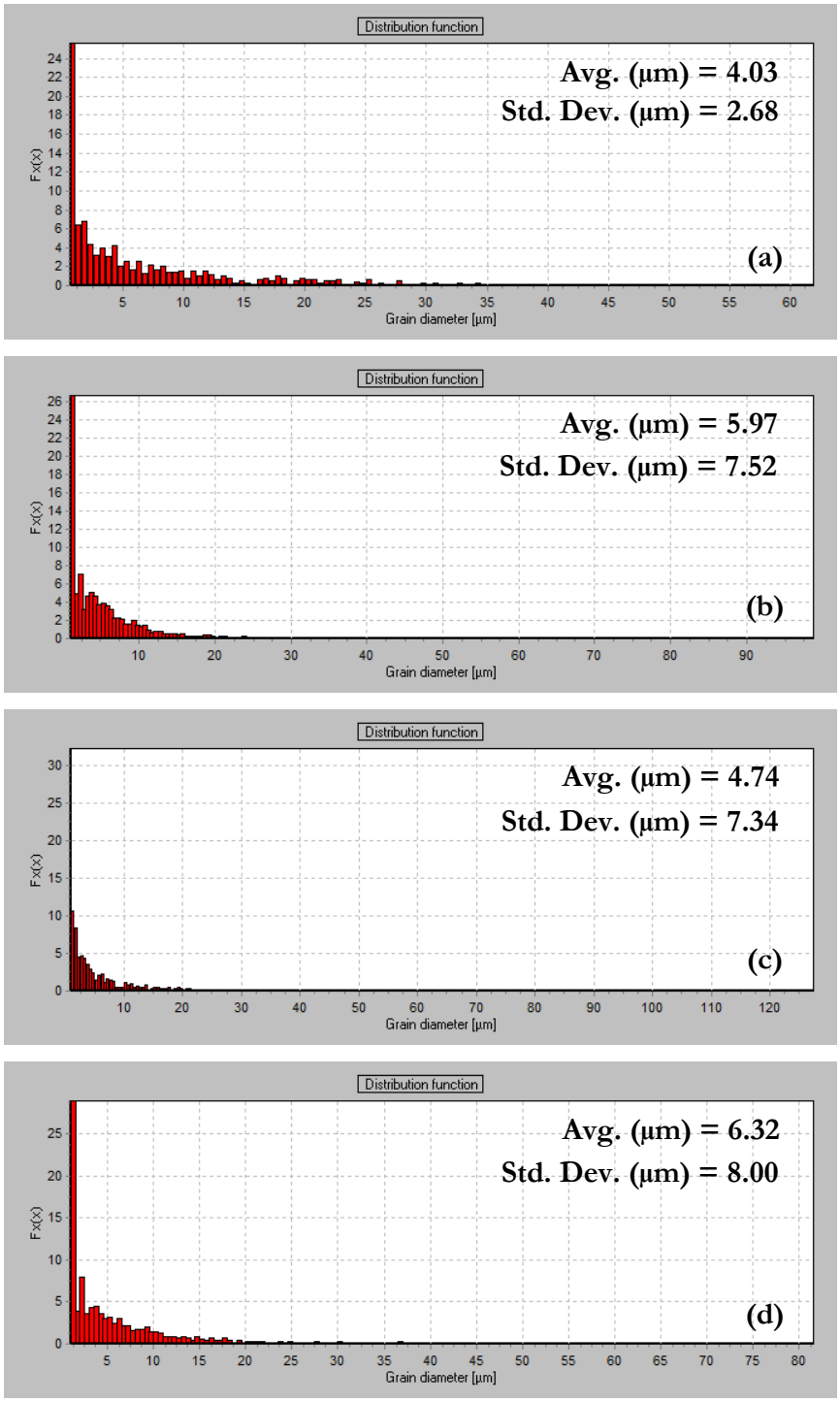

Figure 132: Grain Size Distribution Histograms of Unirradiated 316L Stainless Steel (a) Conventionally Manufactured, (b) Vertical LAM, (c) Horizontal LAM, and (d) 45° LAM

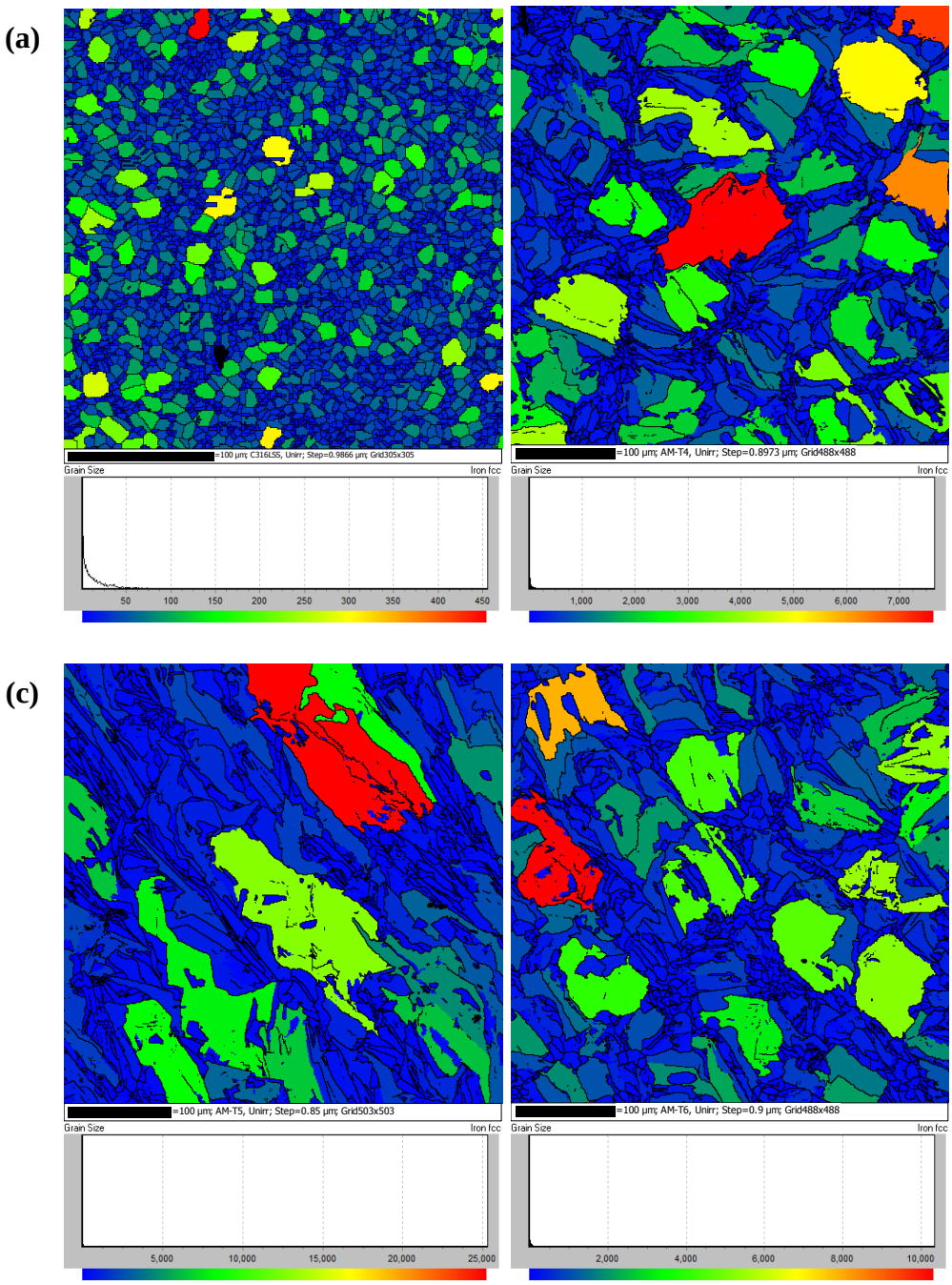

Figure 133: EBSD Grain Size Maps of 316L Stainless Steel (a) Conventionally Manufactured, (b) Vertical LAM, (c) Horizontal LAM, and (d) 45° LAM Irradiated to 80 dpa

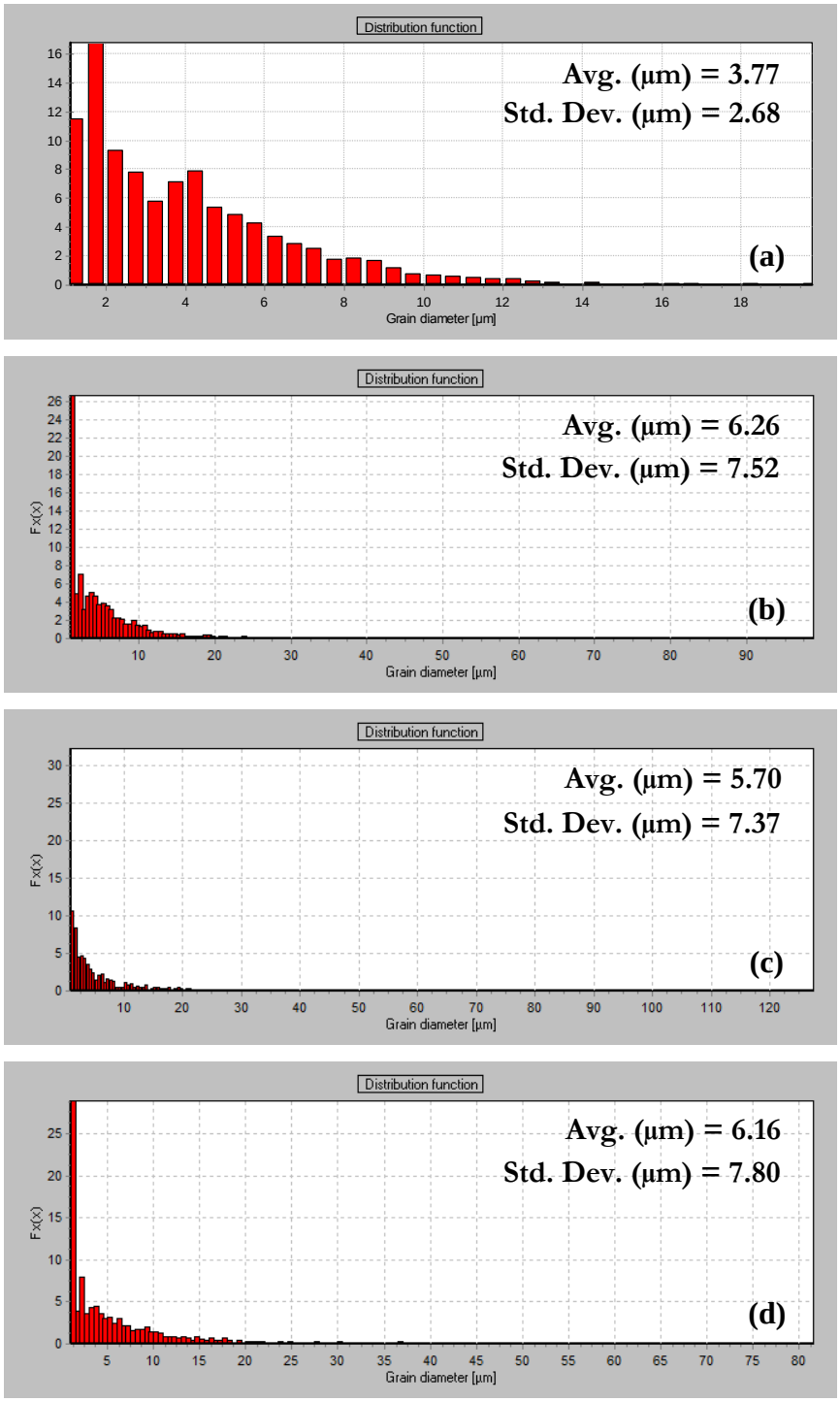

Figure 134: Grain Size Distribution Histograms of 316L Stainless Steel (a) Conventionally Manufactured, (b) Vertical LAM, (c) Horizontal LAM, and (d) 45° LAM Irradiated to 80 dpa

Not shown in Table 15 - Table 16 are the grain slope orientations which describe the degree of grain alignment. The grain slope orientation maps are shown in Figure 135 - Figure 138, where the abscissae are in radians and the colors of the grains correspond to the defined orientation angle in the abscissae. Recall that grain slope orientation maps quantitatively describe the direction in which non-equiaxed grains are oriented. Grain slope orientation maps are therefore less meaningful for nearly equiaxed grain structures (i.e. the conventionally manufactured controls). The grains in the as-annealed conventionally manufactured controls appear to have no preferential orientation; however, the as-annealed conventional 316L grain size is about half that of the conventional Inconel 600 grain size. The vertical LAM grains of both alloys appear to have two distinct regions oriented 90° to one another, while the as-annealed 45° and especially the horizontal LAM grains are highly aligned. Radiation-induced changes in granular orientation for all specimens are negligible.

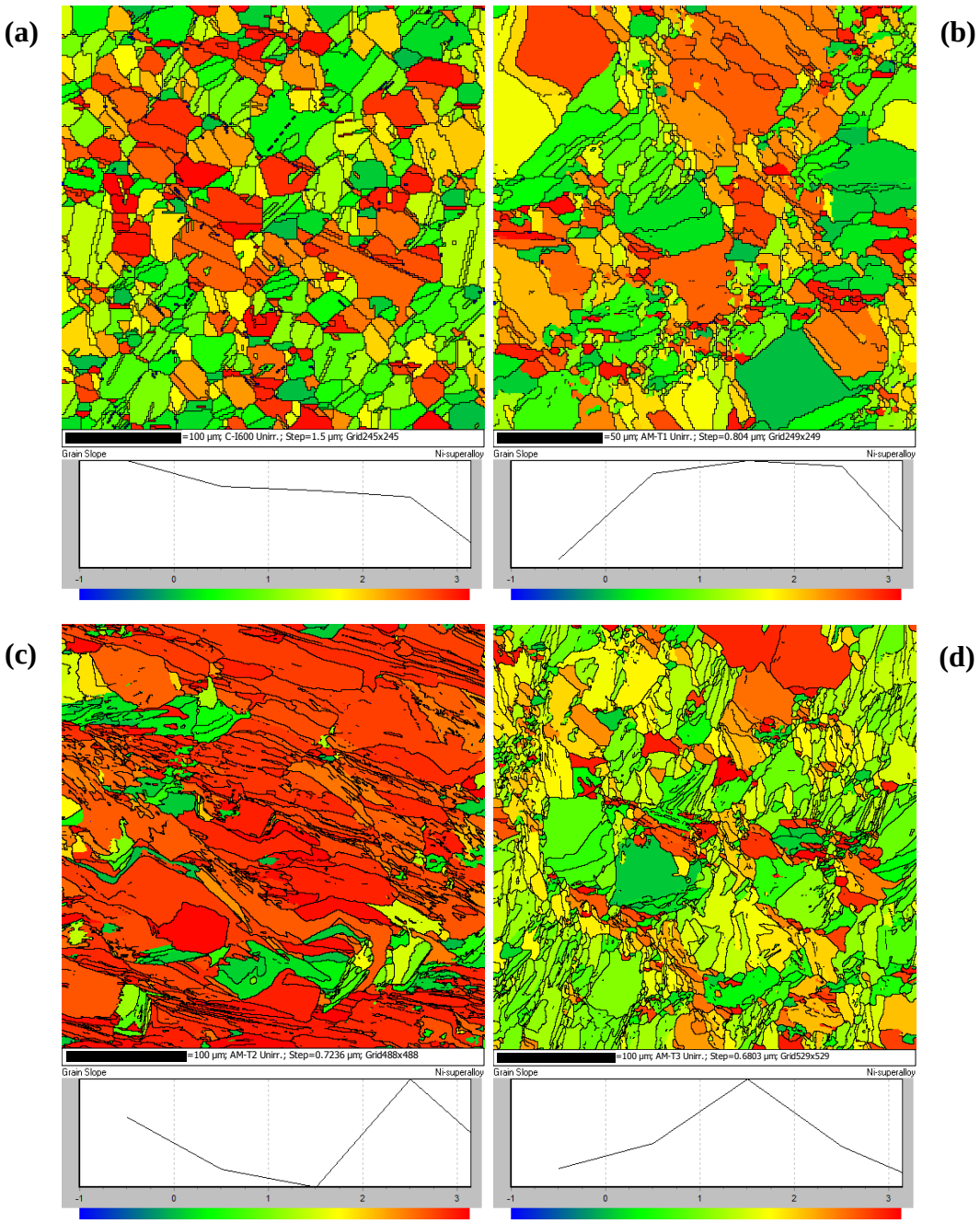

Figure 135: EBSD Grain Slope Orientation of Unirradiated Inconel 600 (a) Conventionally Manufactured, (b) Vertical LAM, (c) Horizontal LAM, and (d) 45° LAM

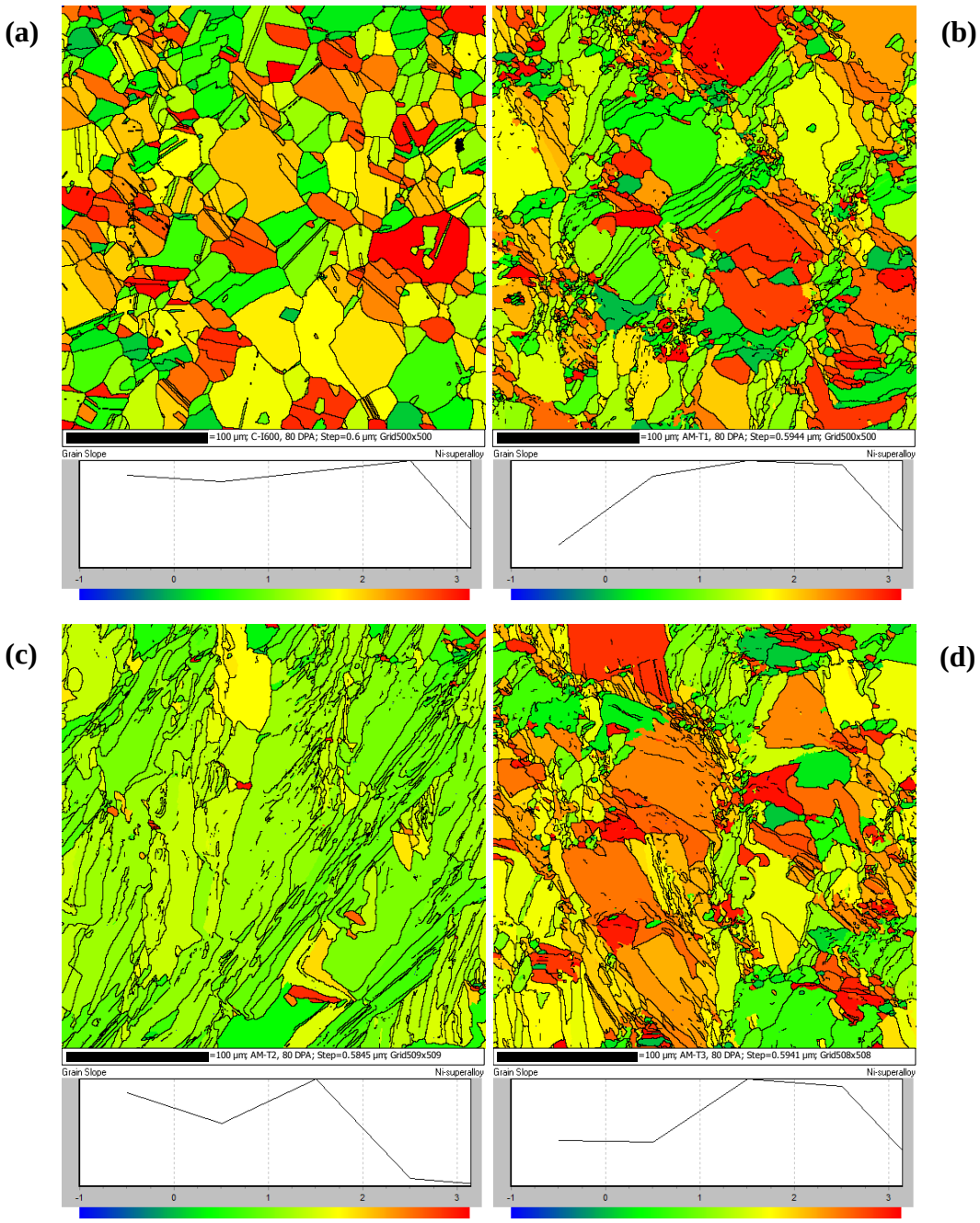

Figure 136: EBSD Grain Slope Orientation of Inconel 600 (a) Conventionally Manufactured, (b) Vertical LAM, (c) Horizontal LAM, and (d) 45° LAM Irradiated to 80 dpa

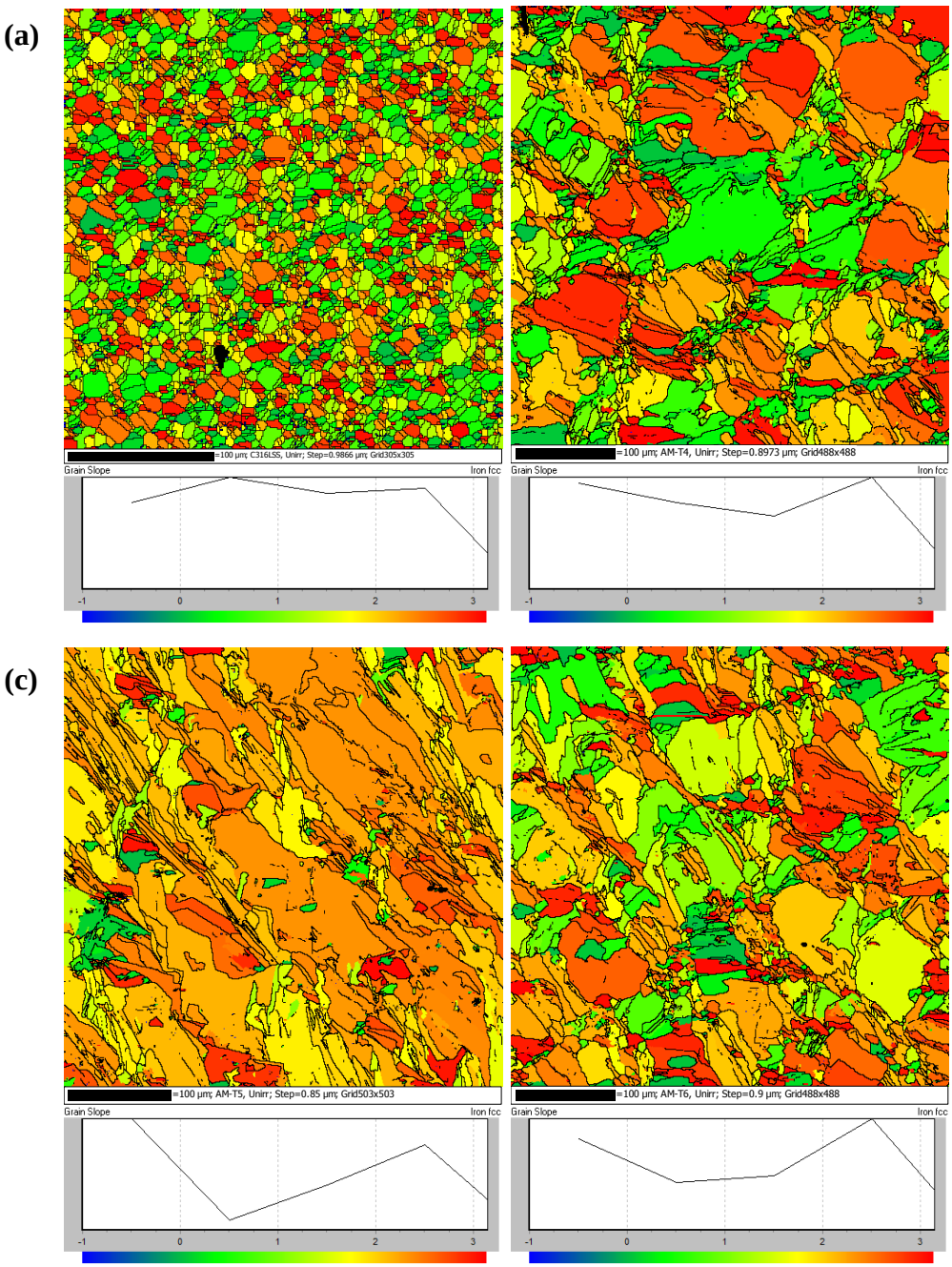

Figure 137: EBSD Grain Slope Orientation of Unirradiated 316L Stainless Steel (a) Conventionally Manufactured, (b) Vertical LAM, (c) Horizontal LAM, and (d) 45° LAM

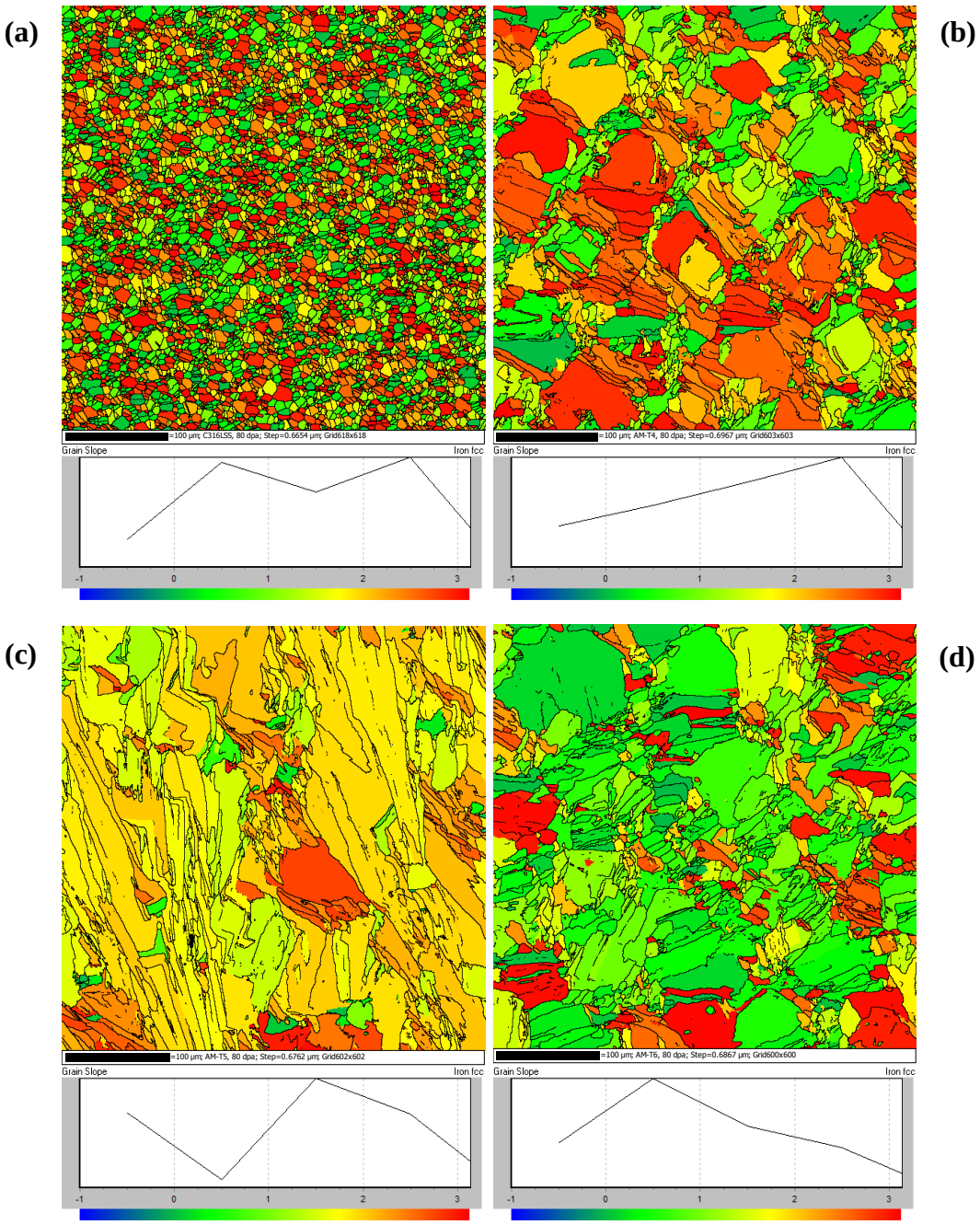

Figure 138: EBSD Grain Slope Orientation of 316L Stainless Steel (a) Conventionally Manufactured, (b) Vertical LAM, (c) Horizontal LAM, and (d) 45° LAM Irradiated to 80 dpa

IV.3.2. Euler Maps

Euler maps of unirradiated and irradiated Inconel 600 and 316L stainless steel are shown in Figure 139 - Figure 150, where the abscissae are in degrees. For a review of Euler angles, see Ch. II.4.2. Neither the conventionally manufactured Inconel 600 nor 316L stainless steel contains significant texture before or after irradiation. For both alloy types, the LAM crystals tend to align themselves parallel to the build direction. After irradiation, slight rotations about the build direction axis are observed, evidenced by changes in Euler angle distributions. Gradual rotations (i.e. changes in color) within grains indicate regions of residual strain. Note that these regions exist in all LAM specimens, but none of the conventional controls.

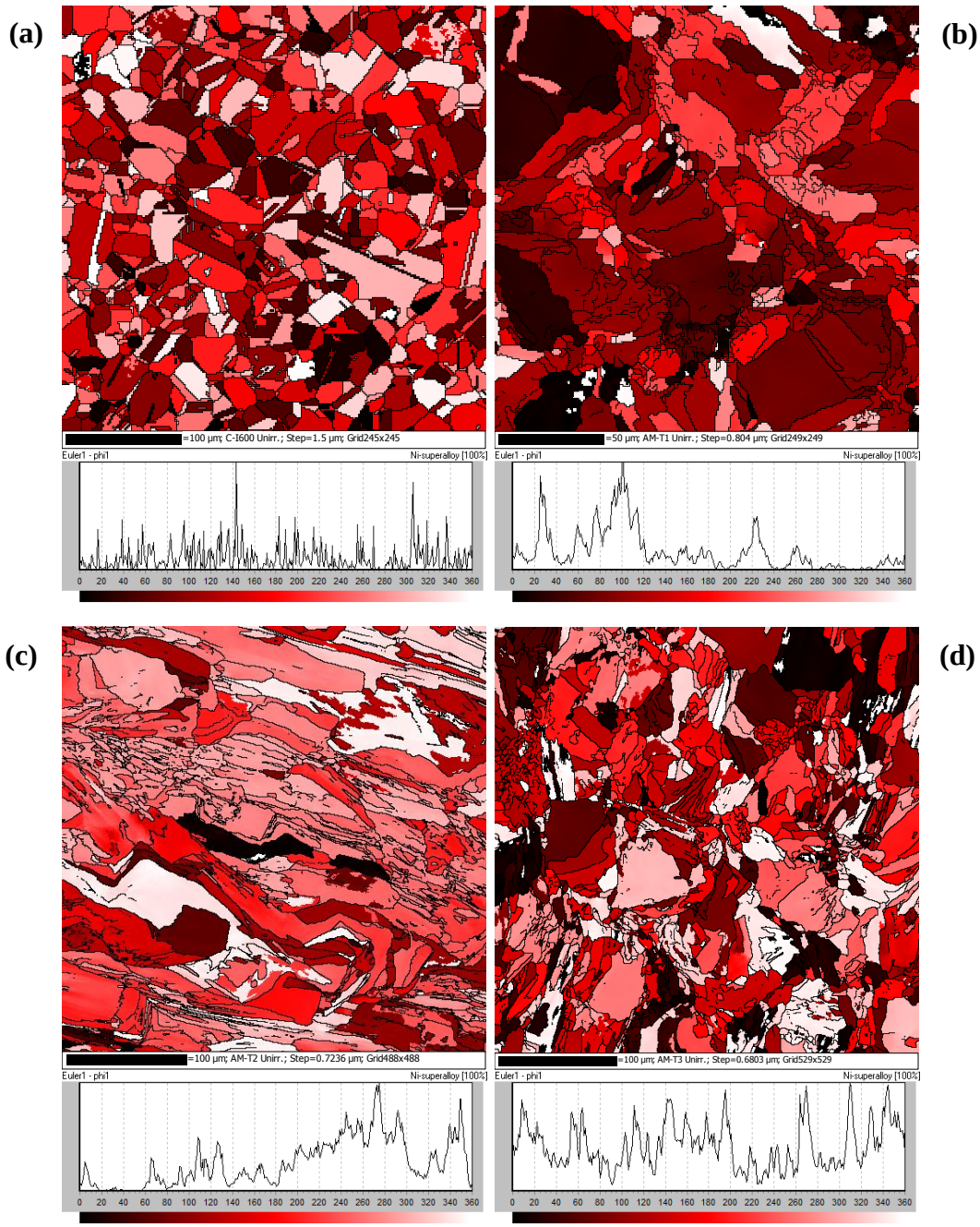

Figure 139: EBSD Euler Maps of φ_1 for Unirradiated Inconel 600 (a) Conventionally Manufactured, (b) Vertical LAM, (c) Horizontal LAM, and (d) 45° LAM

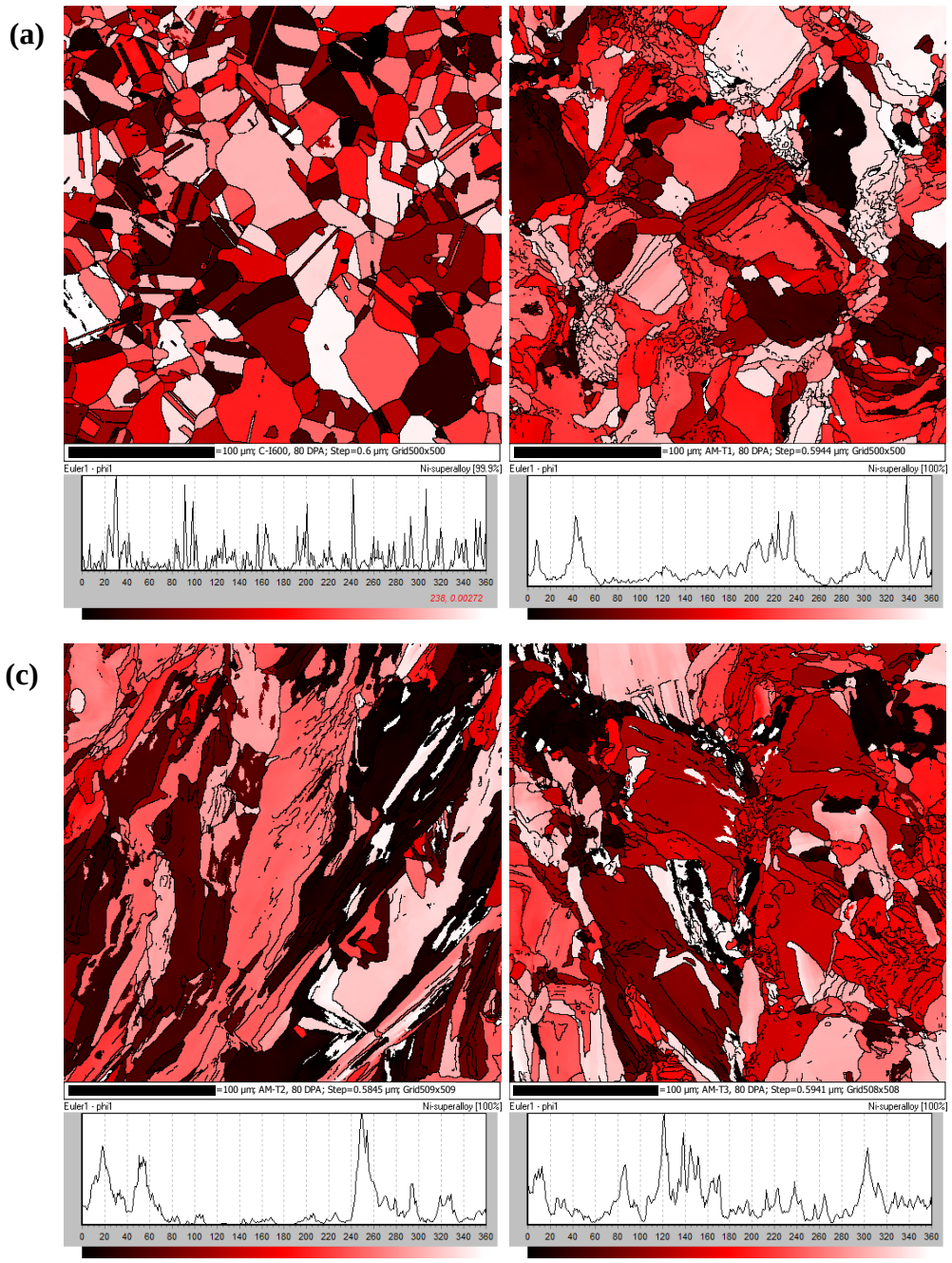

Figure 140: EBSD Euler Maps of φ_1 for Inconel 600 (a) Conventionally Manufactured, (b) Vertical LAM, (c) Horizontal LAM, and (d) 45° LAM Irradiated to 80 dpa

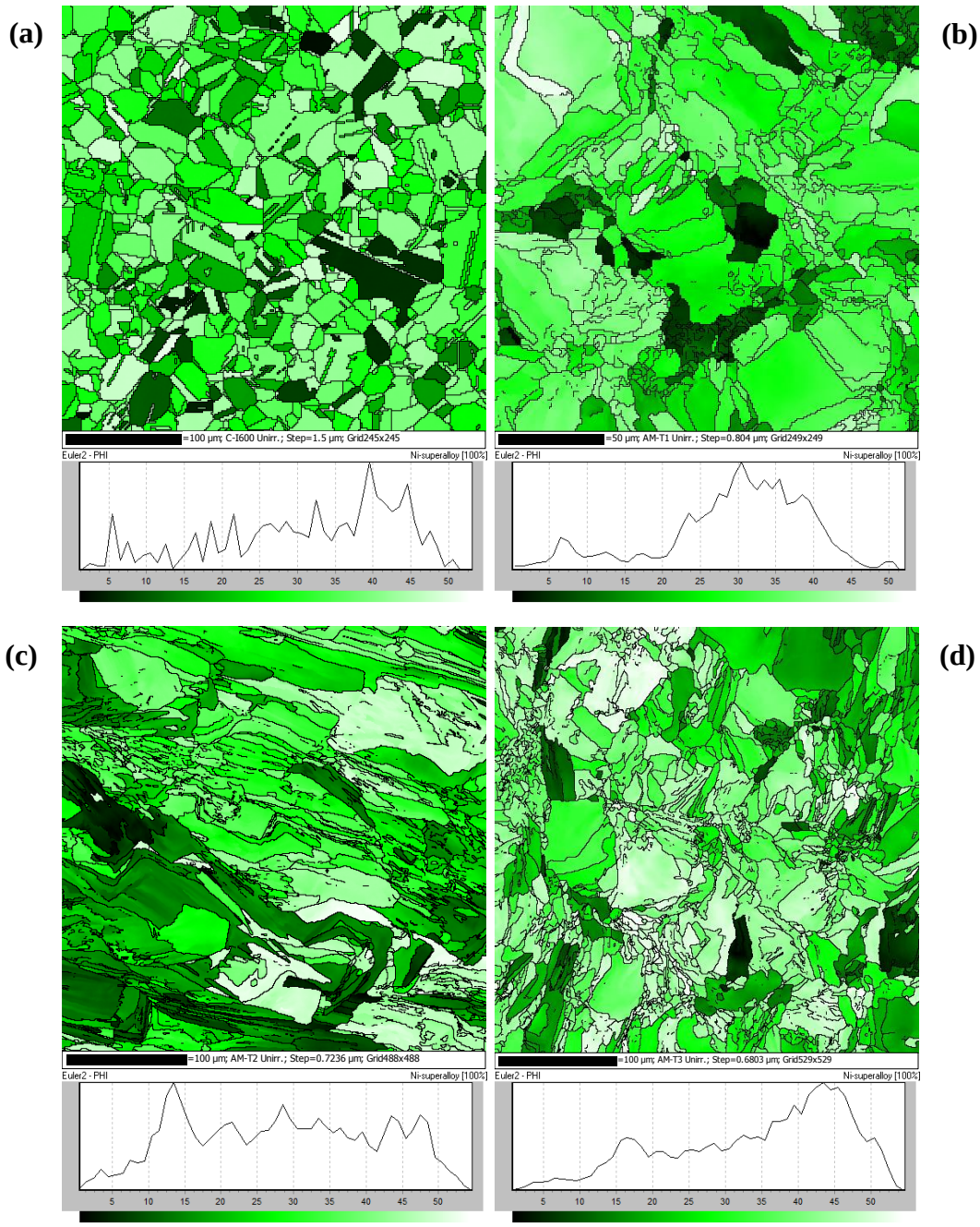

Figure 141: EBSD Euler Maps of Φ for Unirradiated Inconel 600 (a) Conventionally Manufactured, (b) Vertical LAM, (c) Horizontal LAM, and (d) 45° LAM

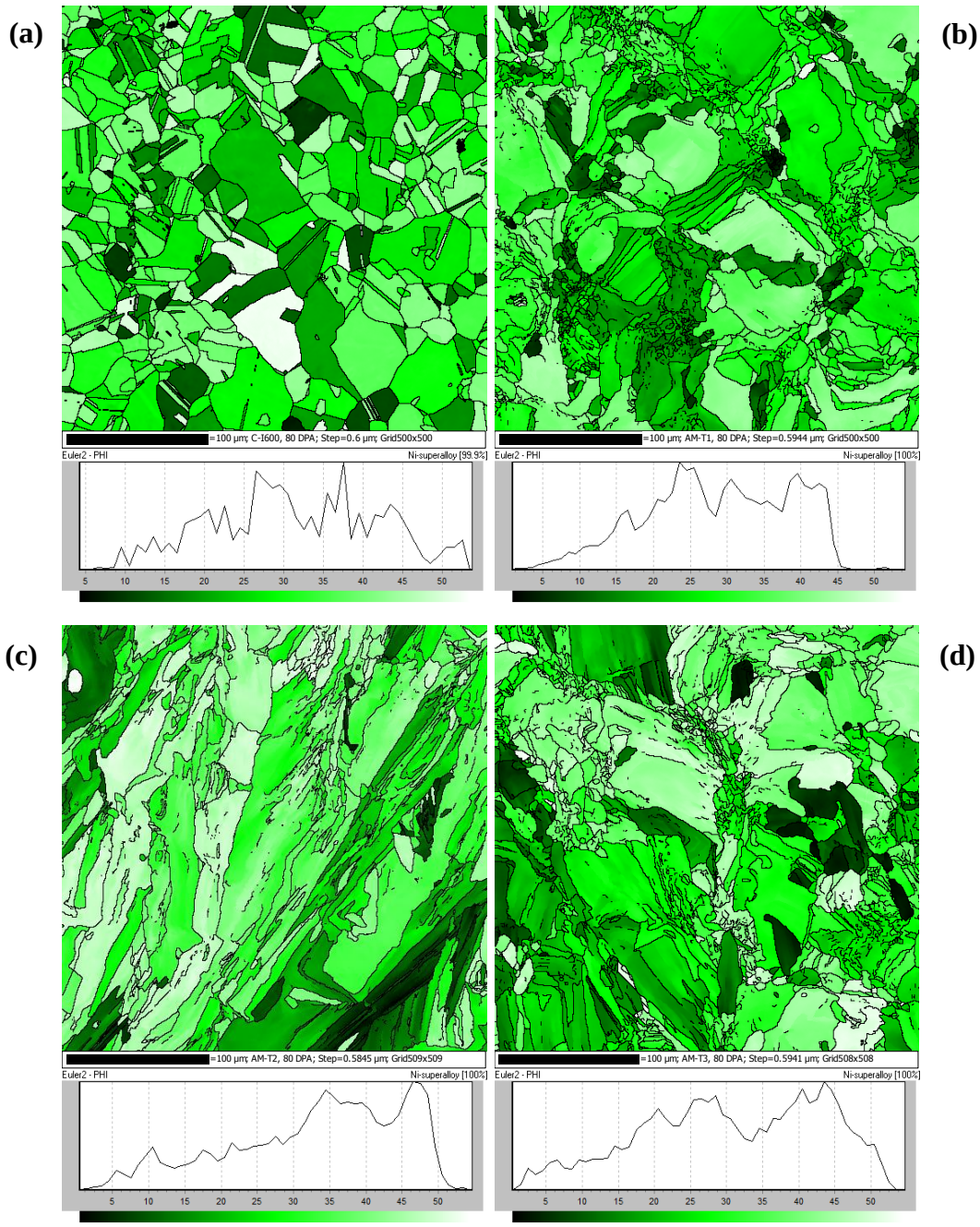

Figure 142: EBSD Euler Maps of Φ for Inconel 600 (a) Conventionally Manufactured, (b) Vertical LAM, (c) Horizontal LAM, and (d) 45° LAM Irradiated to 80 dpa

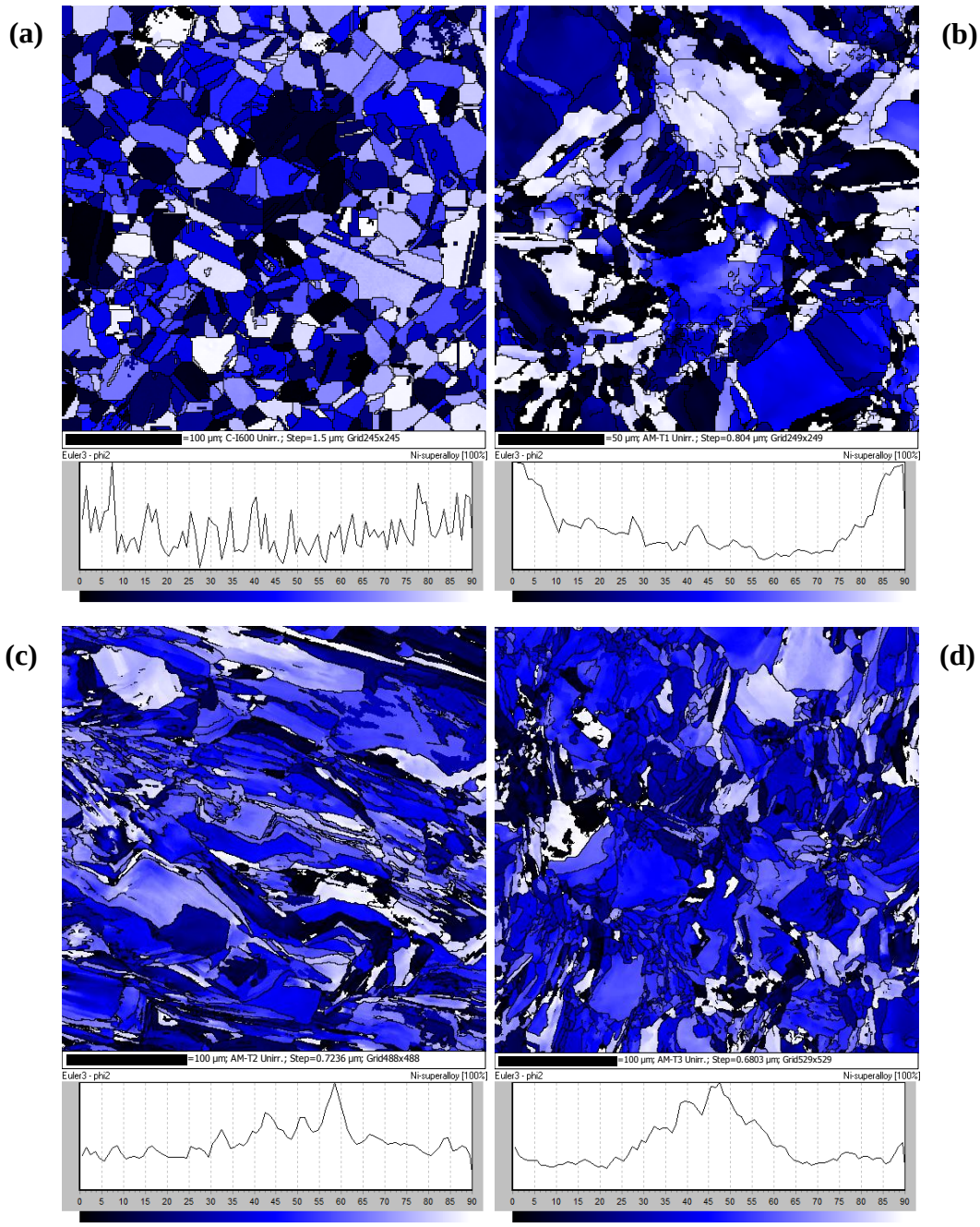

Figure 143: EBSD Euler Maps of φ_2 for Unirradiated Inconel 600 (a) Conventionally Manufactured, (b) Vertical LAM, (c) Horizontal LAM, and (d) 45° LAM

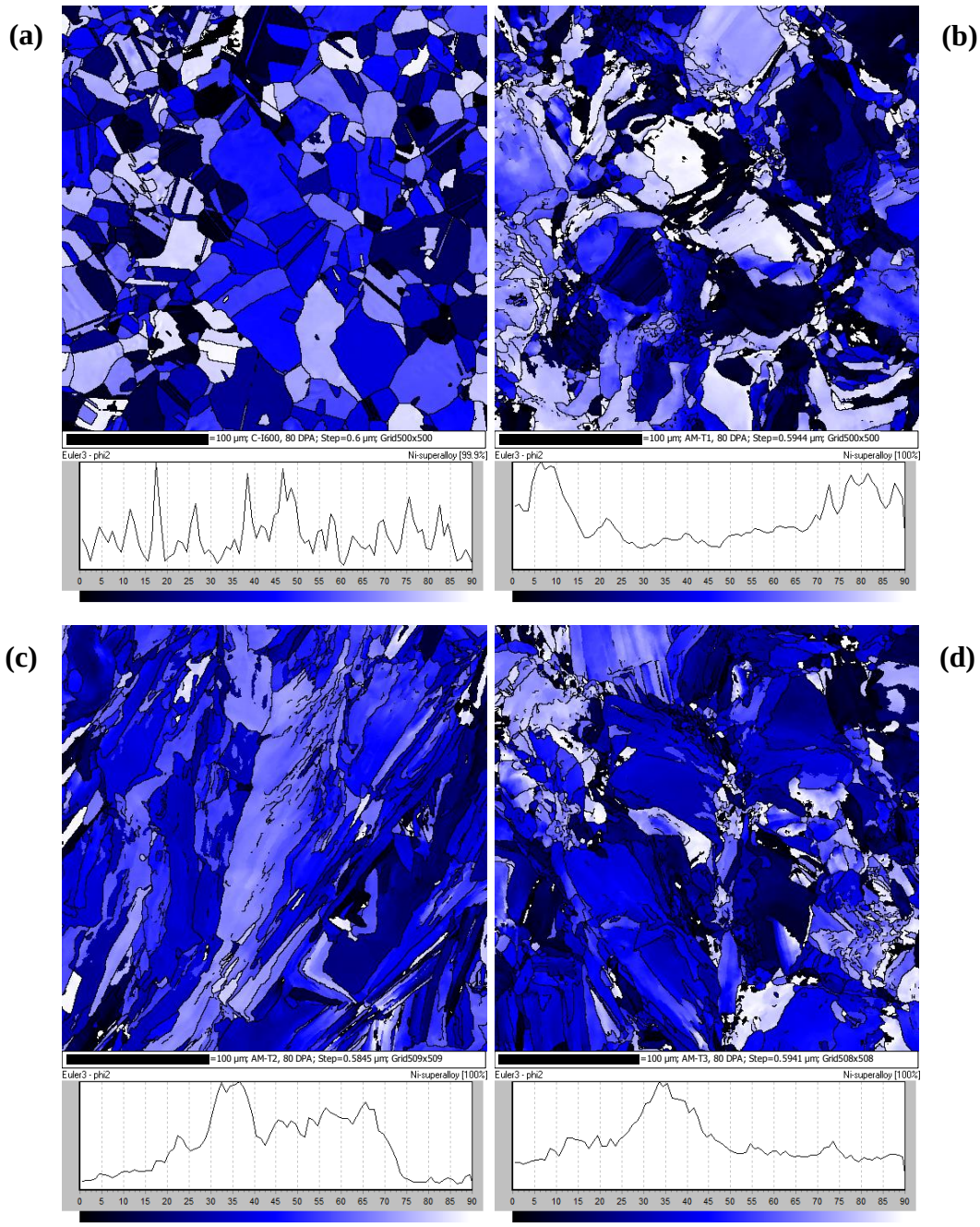

Figure 144: EBSD Euler Maps of φ_2 for Inconel 600 (a) Conventionally Manufactured, (b) Vertical LAM, (c) Horizontal LAM, and (d) 45° LAM Irradiated to 80 dpa

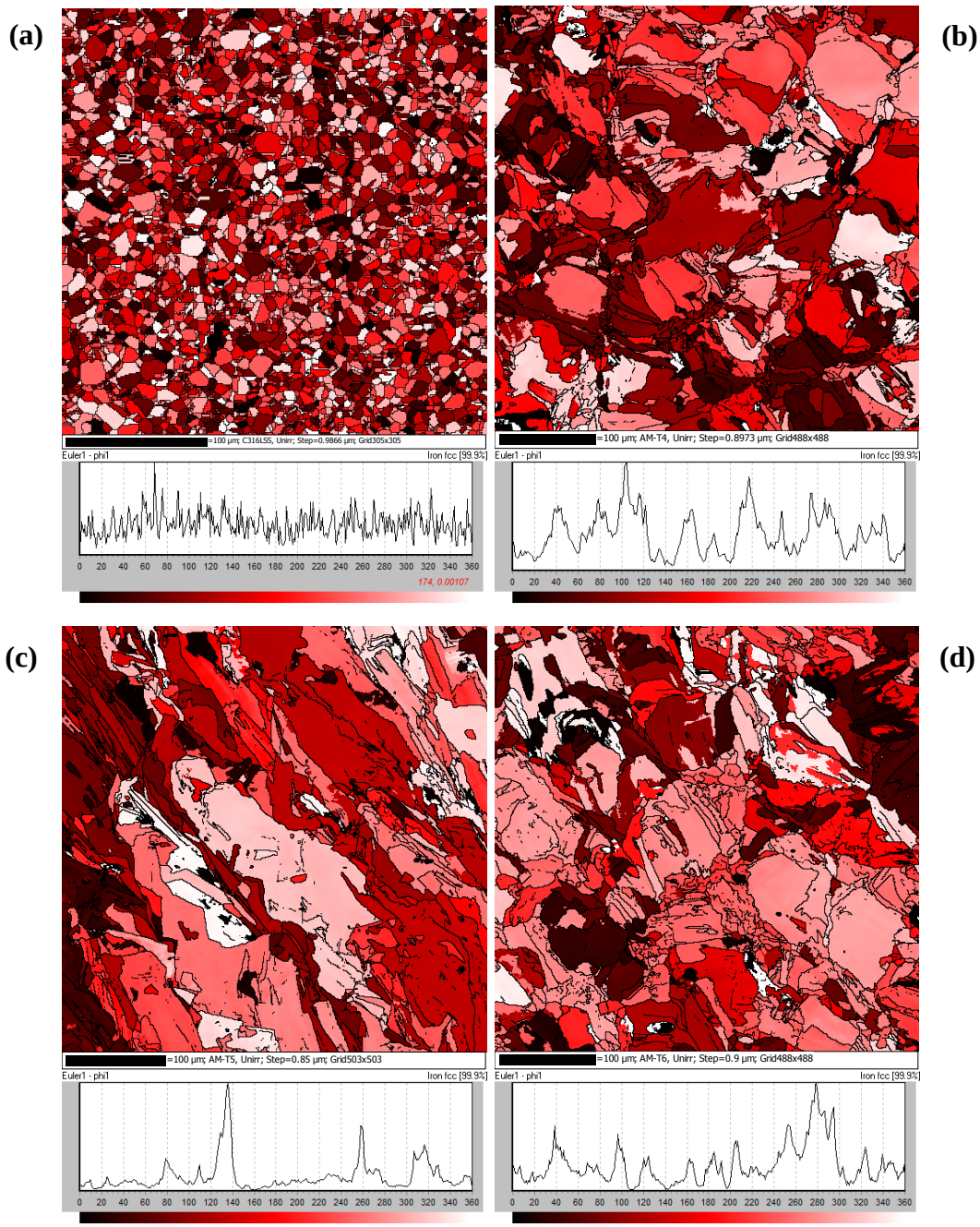

Figure 145: EBSD Euler Maps of φ_1 for Unirradiated 316L Stainless Steel (a) Conventionally Manufactured, (b) Vertical LAM, (c) Horizontal LAM, and (d) 45° LAM

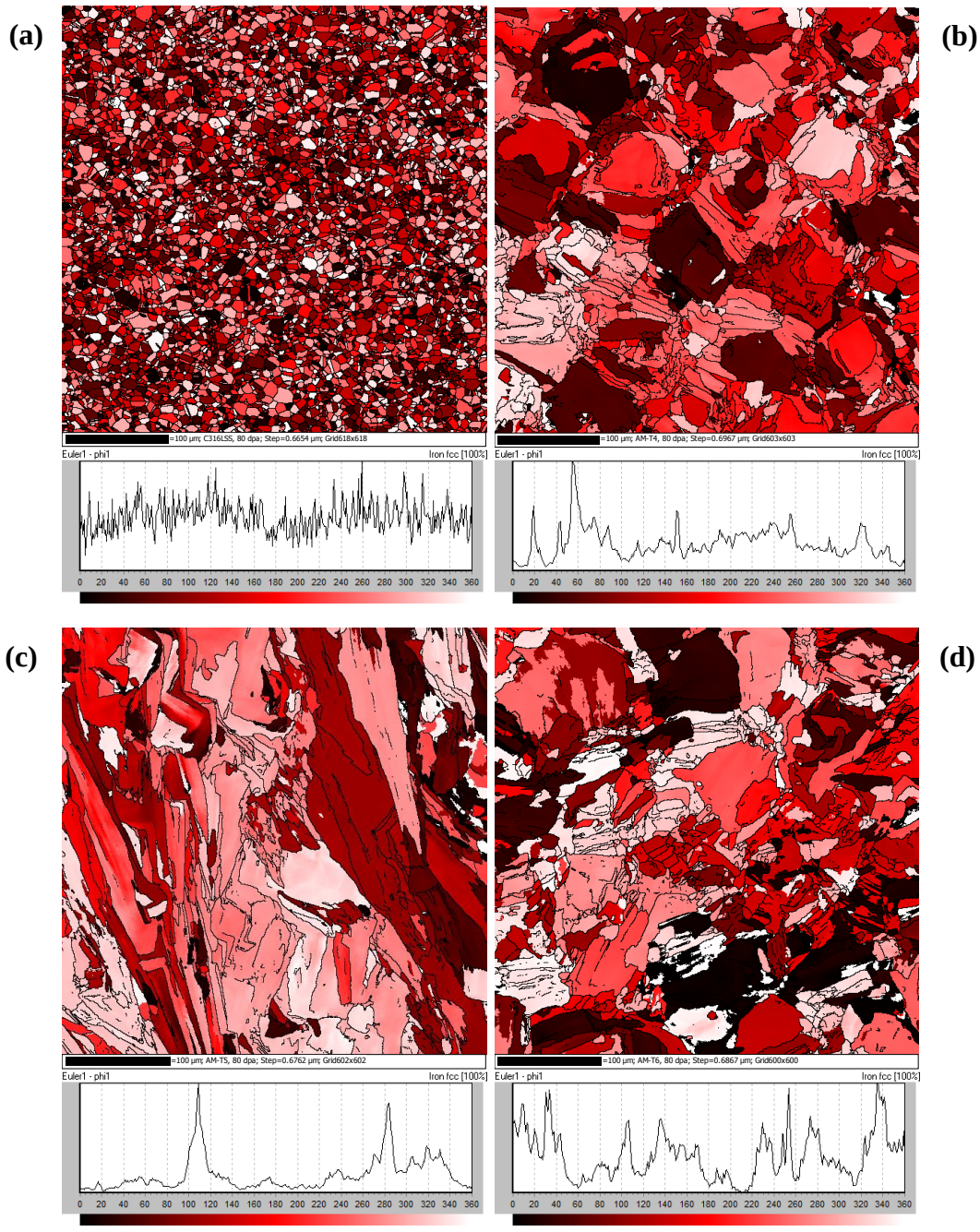

Figure 146: EBSD Euler Maps of φ_1 for 316L Stainless Steel (a) Conventionally Manufactured, (b) Vertical LAM, (c) Horizontal LAM, and (d) 45° LAM Irradiated to 80 dpa

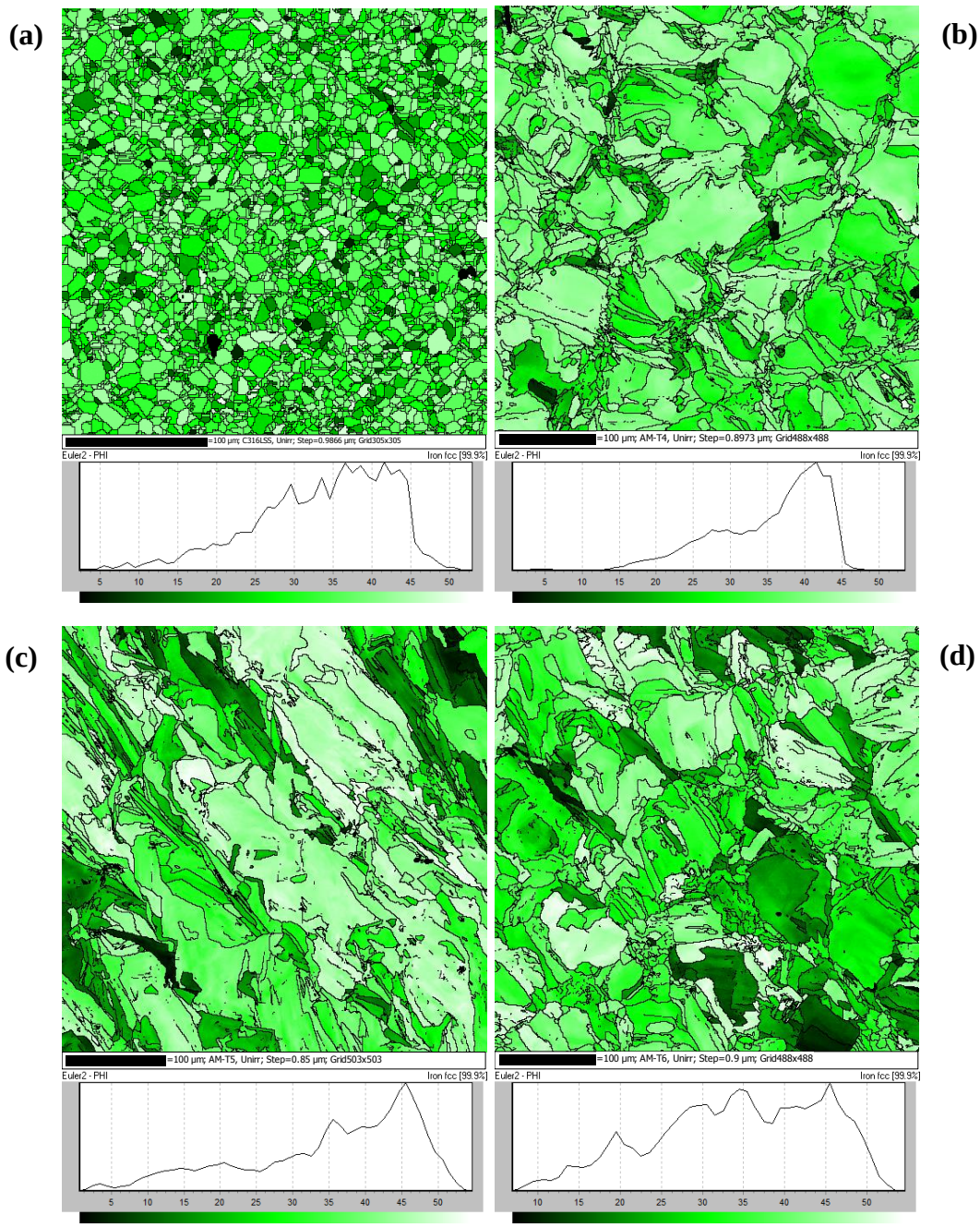

Figure 147: EBSD Euler Maps of Φ for Unirradiated 316L Stainless Steel (a) Conventionally Manufactured, (b) Vertical LAM, (c) Horizontal LAM, and (d) 45° LAM

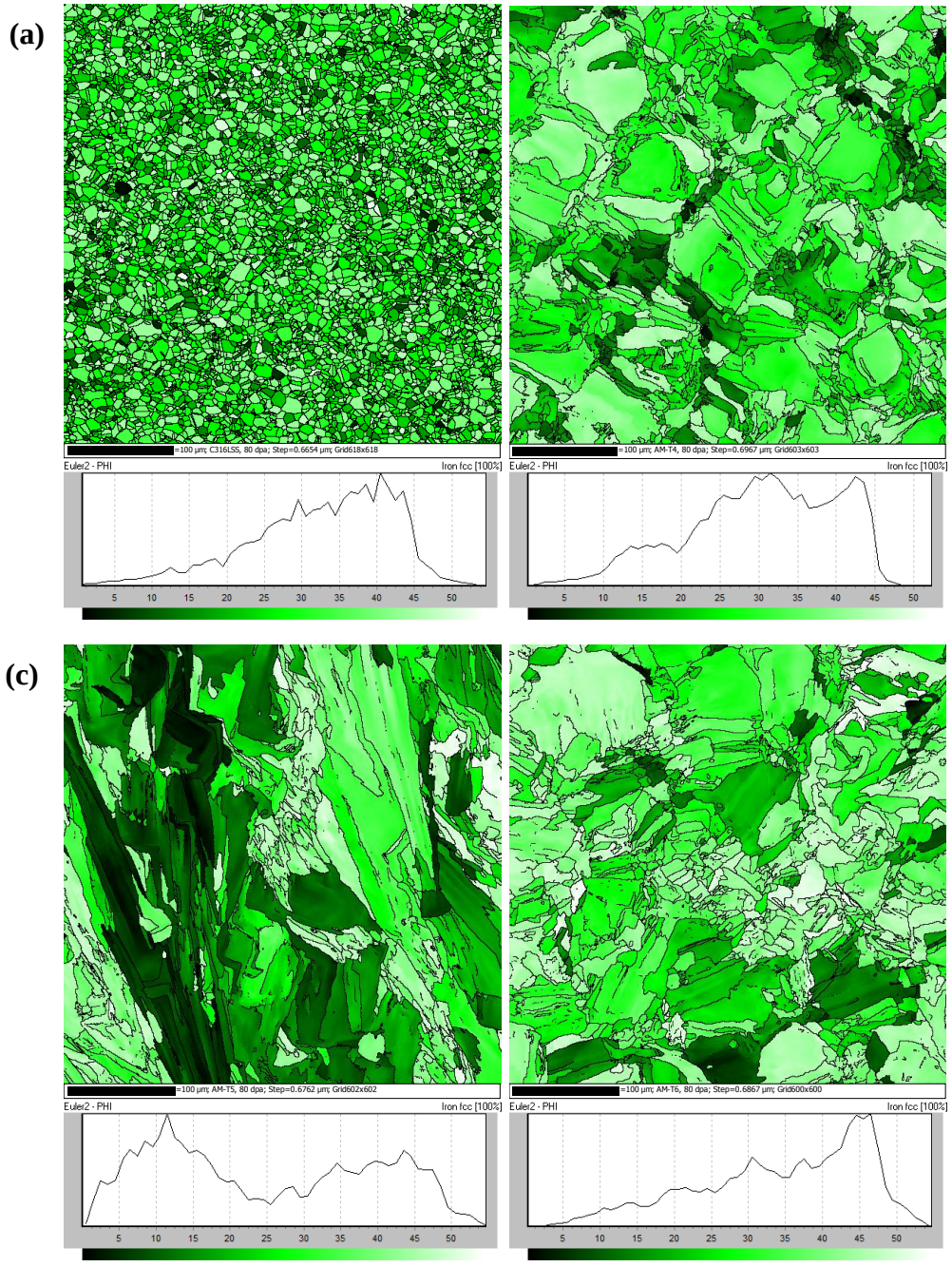

Figure 148: EBSD Euler Maps of Φ for 316L Stainless Steel (a) Conventionally Manufactured, (b) Vertical LAM, (c) Horizontal LAM, and (d) 45° LAM Irradiated to 80 dpa

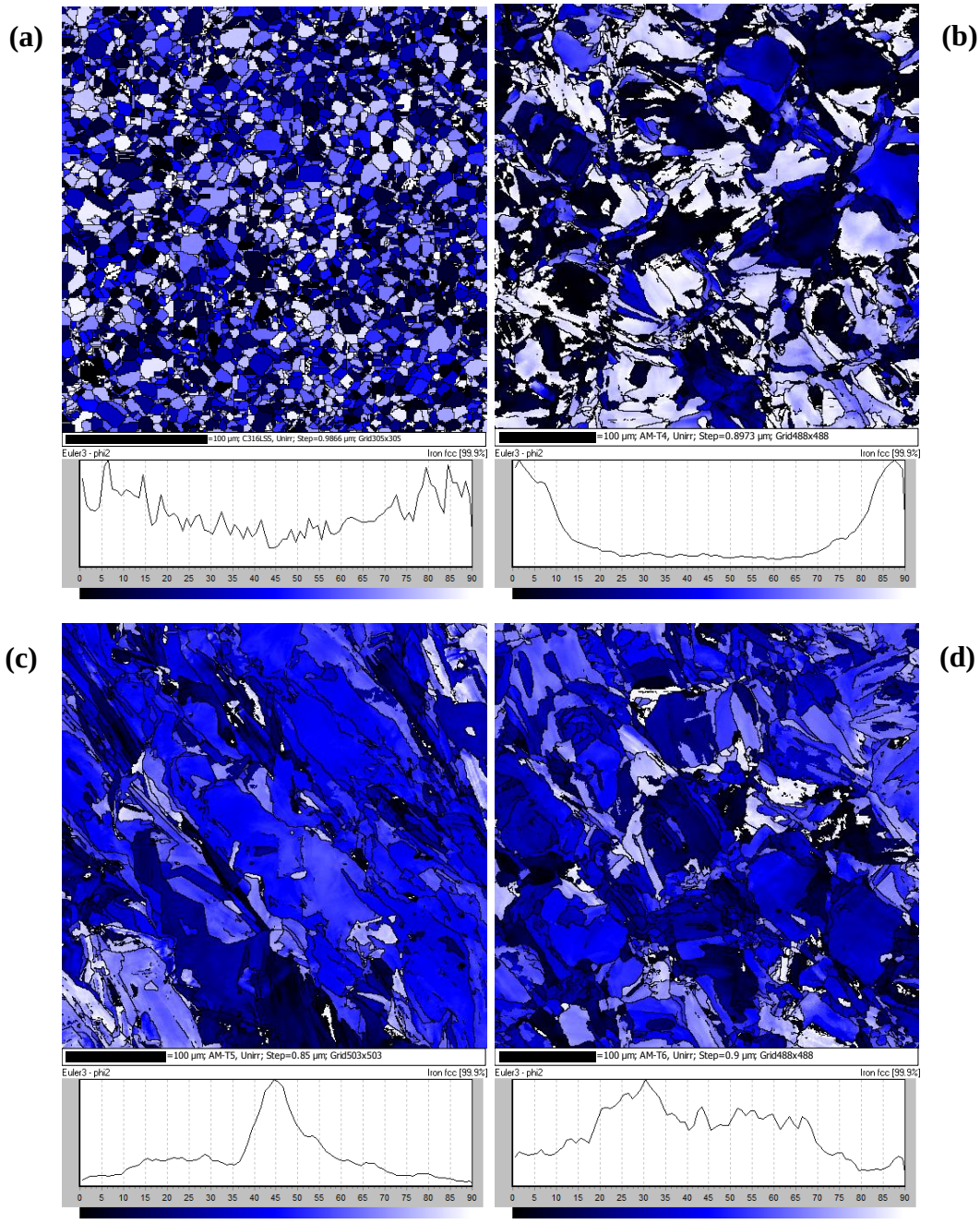

Figure 149: EBSD Euler Maps of φ_2 for Unirradiated 316L Stainless Steel (a) Conventionally Manufactured, (b) Vertical LAM, (c) Horizontal LAM, and (d) 45° LAM

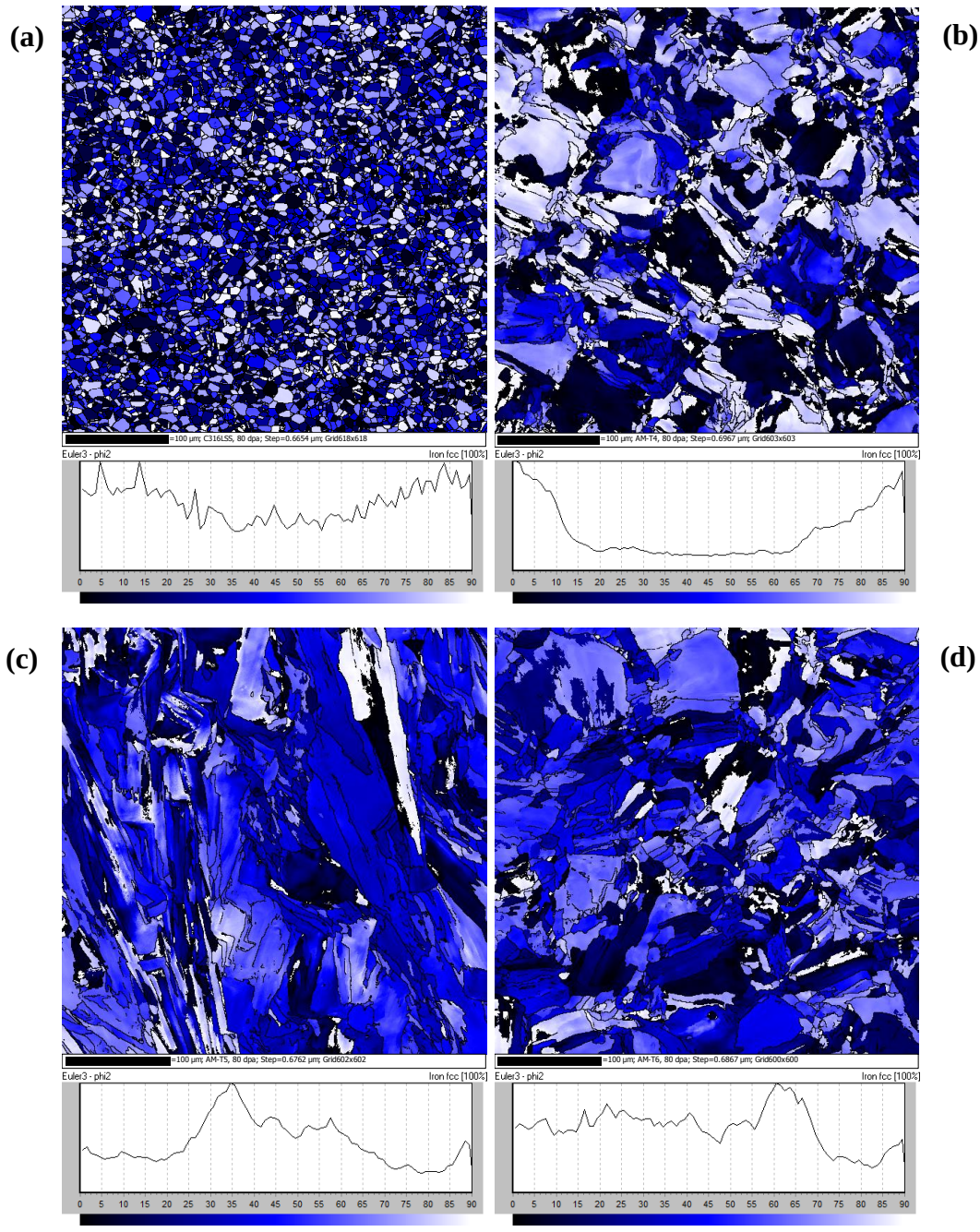

Figure 150: EBSD Euler Maps of φ_2 for 316L Stainless Steel (a) Conventionally Manufactured, (b) Vertical LAM, (c) Horizontal LAM, and (d) 45° LAM Irradiated to 80 dpa

IV.3.3. Microstructural Texture –Inverse Pole Figures

Figure 151 - Figure 154 below show the inverse pole figures of unirradiated and irradiated Inconel 600, and unirradiated and irradiated 316L stainless steel. For a review of inverse pole figures, see Ch. II.4.1. In the IPFs, the IPF map legends, such as Figure 151e, relate to the orientation of grains shown on the pictures (i.e. the portions with scale bars). The contouring on the IPF maps themselves refer to the statistical intensity of crystalline orientations given by the multiple of uniform density (MUD) value. A MUD value of unity corresponds to a material with no preferred crystalline orientation, while a MUD value of greater than unity corresponds to a material with crystalline texture (as is the case for the LAM samples in this study).

The conventional controls for both alloys appear to have little texture before or after irradiation. In contrast, the LAM specimens clearly show texture before and after irradiation. Specifically, both vertical LAM I600 and 316L show an accumulation of grains with <101>||ND orientation before and after irradiation, while both horizontal LAM I600 and 316L are almost entirely lacking grains with <101>||ND orientation where ND is the direction normal to the data acquisition surface of the sample. Since both alloys contained similar textures, this suggests that crystallographic texture is inherent to the laser additive manufacturing process of fcc alloys such that <101>||**B**, where **B** is the build direction.

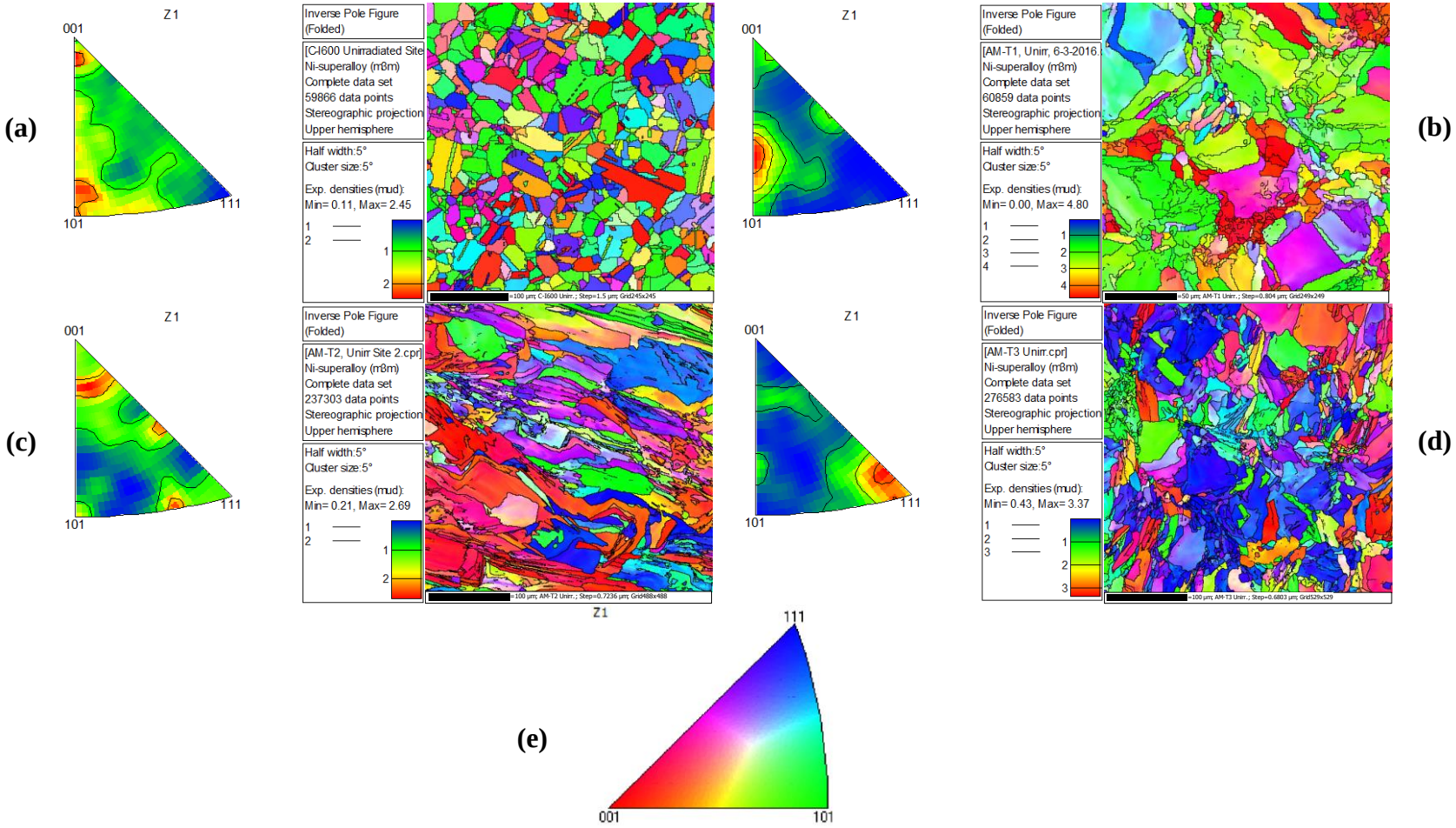

Figure 151: EBSD Stereographic Projection IPFs and IPF Maps for Unirradiated Inconel 600 (a) Conventionally Manufactured, (b) Vertical LAM, (c) Horizontal LAM, (d) 45° LAM, and (e) IPF Map Legend

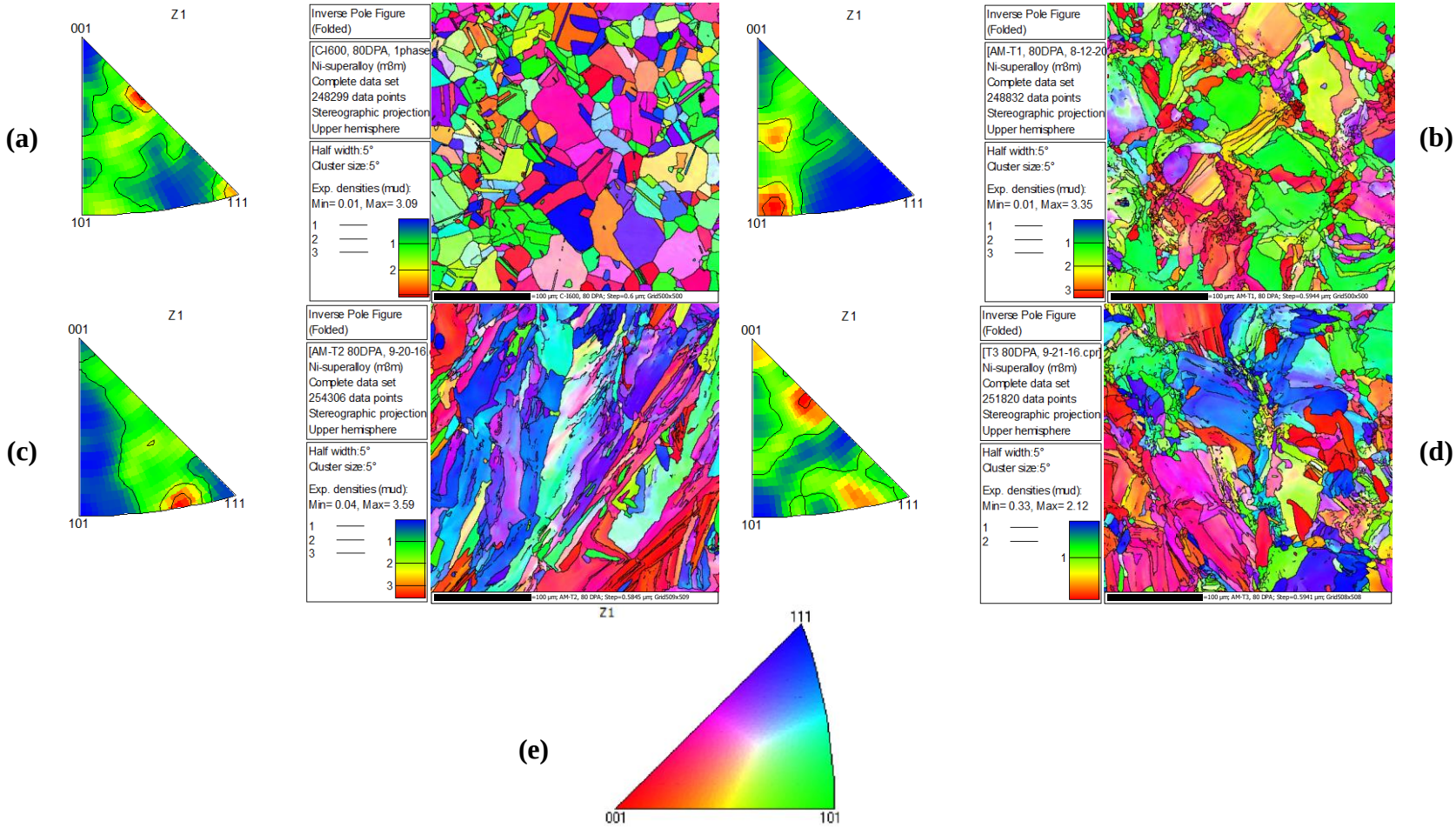

Figure 152: EBSD Stereographic Projection IPFs and IPF Maps for Irradiated Inconel 600 (a) Conventionally Manufactured, (b) Vertical LAM, (c) Horizontal LAM, (d) 45° LAM, and (e) IPF Map Legend

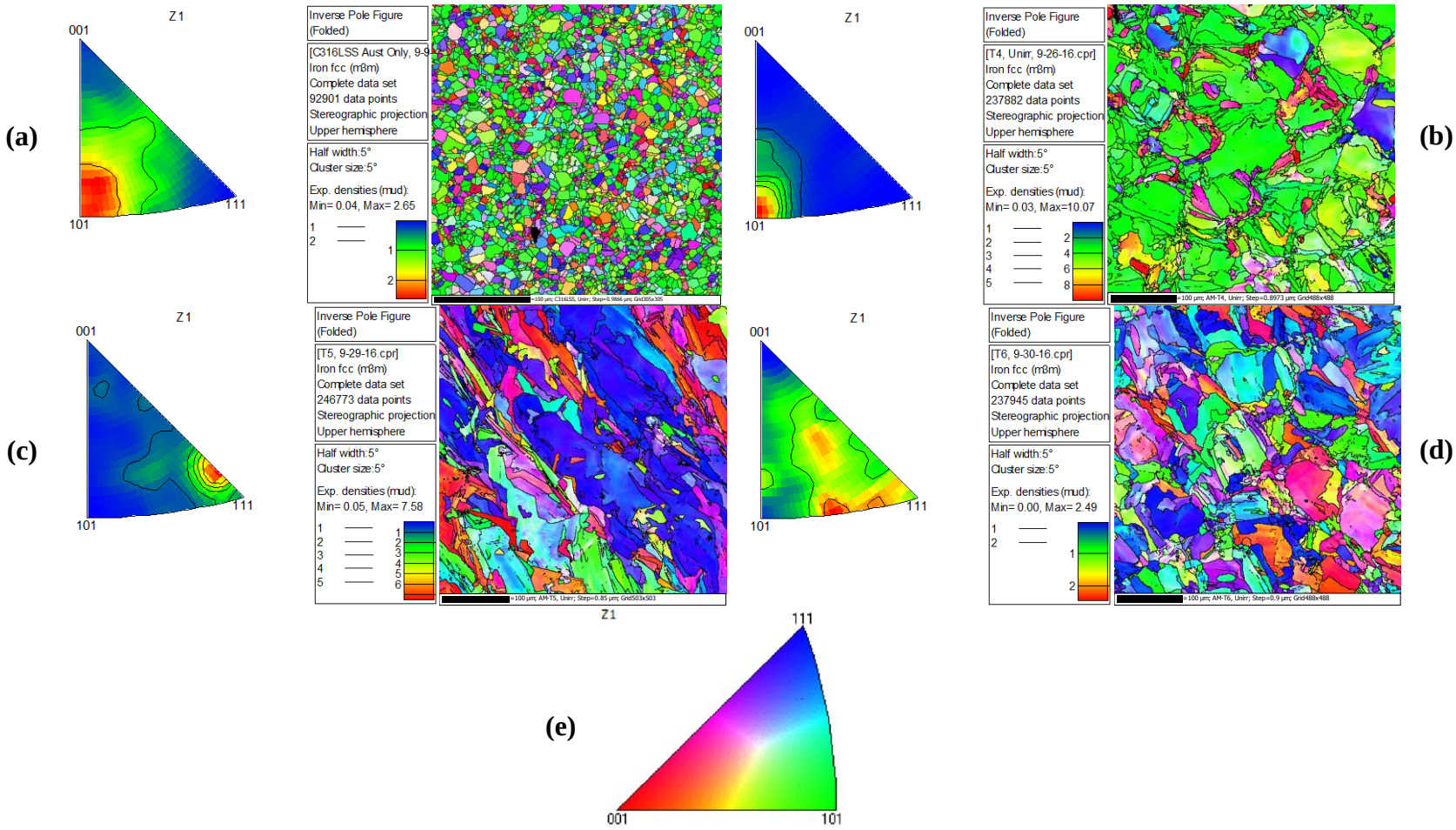

Figure 153: EBSD Stereographic Projection IPFs and IPF Maps for Unirradiated 316L Stainless Steel (a) Conventionally Manufactured, (b) Vertical LAM, (c) Horizontal LAM, (d) 45° LAM, and (e) IPF Map Legend

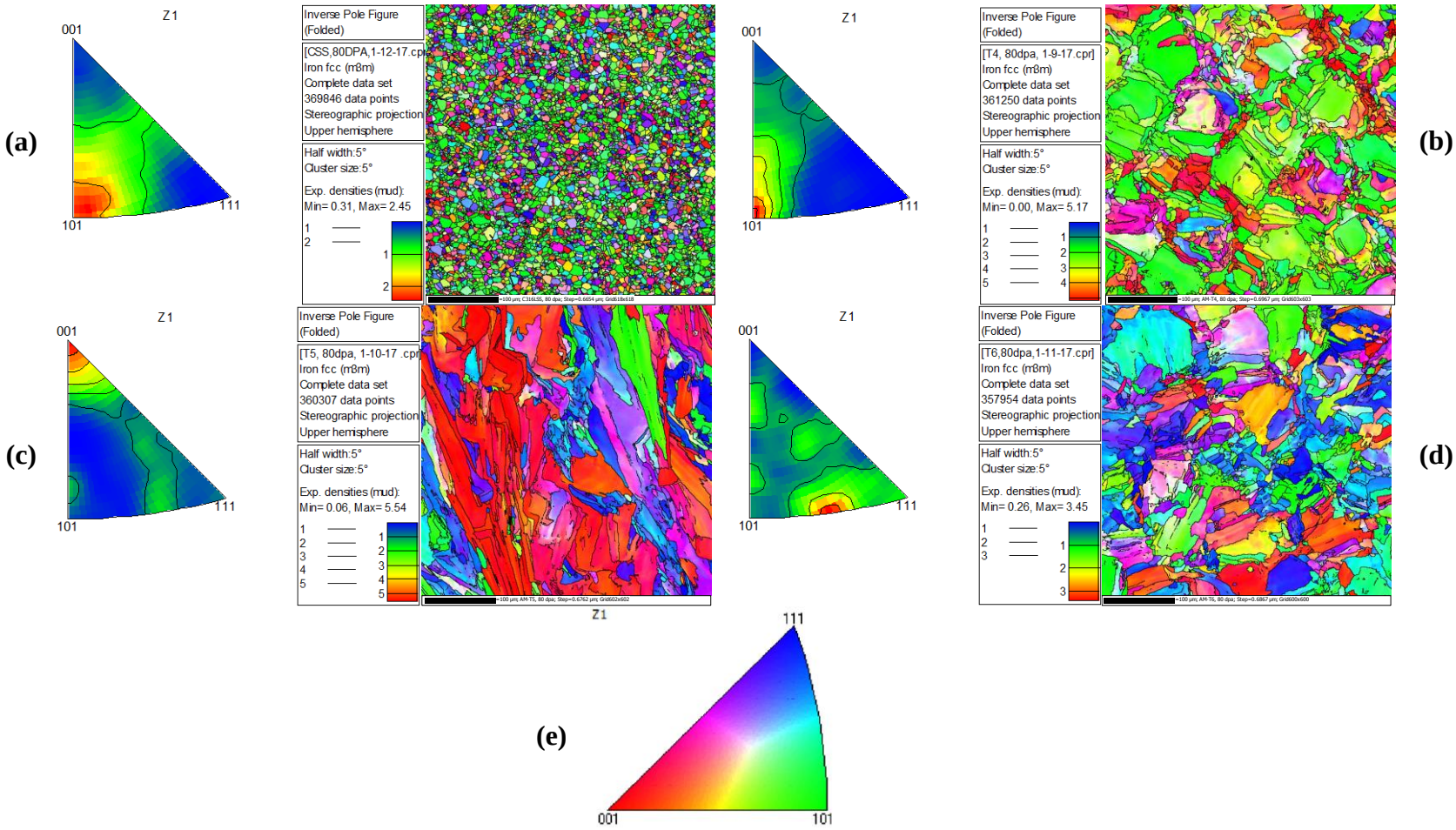

Figure 154: EBSD Stereographic Projection IPFs and IPF Maps for Irradiated 316L Stainless Steel (a) Conventionally Manufactured, (b) Vertical LAM, (c) Horizontal LAM, (d) 45° LAM, and (e) IPF Map Legend

IV.3.4. Coincident Lattice Site Boundaries

The CSL boundary distributions for I600 and 316L rods are summarized in Figure 155 - Figure 158. The associated CSL maps are provided in Figure 159 - Figure 162. The grain boundaries in Figure 159 - Figure 162 correspond to the Σ value as defined by the abscissae. CSL boundaries for the LAM ODS steel samples could not be quantified due to uncertainty in identifying grain boundaries with the yttria phase. For details related to CSL theory, see Ch. II.4.4.

The as-annealed conventionally manufactured Inconel 600 contained approximately 58% CSL boundaries, while the as-annealed LAM specimens all contained around 2-3%. Similarly for 316L stainless steel, the as-annealed conventional control contained approximately 33% CSL boundaries, while the as-annealed LAM specimens all contained around 1-3%. Studies suggest that increasing low-Σ CSL boundaries can improve alloy resistance toward creep, IGSCC, HIC, radiation-induced segregation, and radiation-induced growth [105-114]. The abundance of random grain boundaries suggests that the specimens fabricated by LAM in this study are more sensitive to grain boundary-related detrimental phenomena than their conventionally manufactured counterparts before and after irradiation.

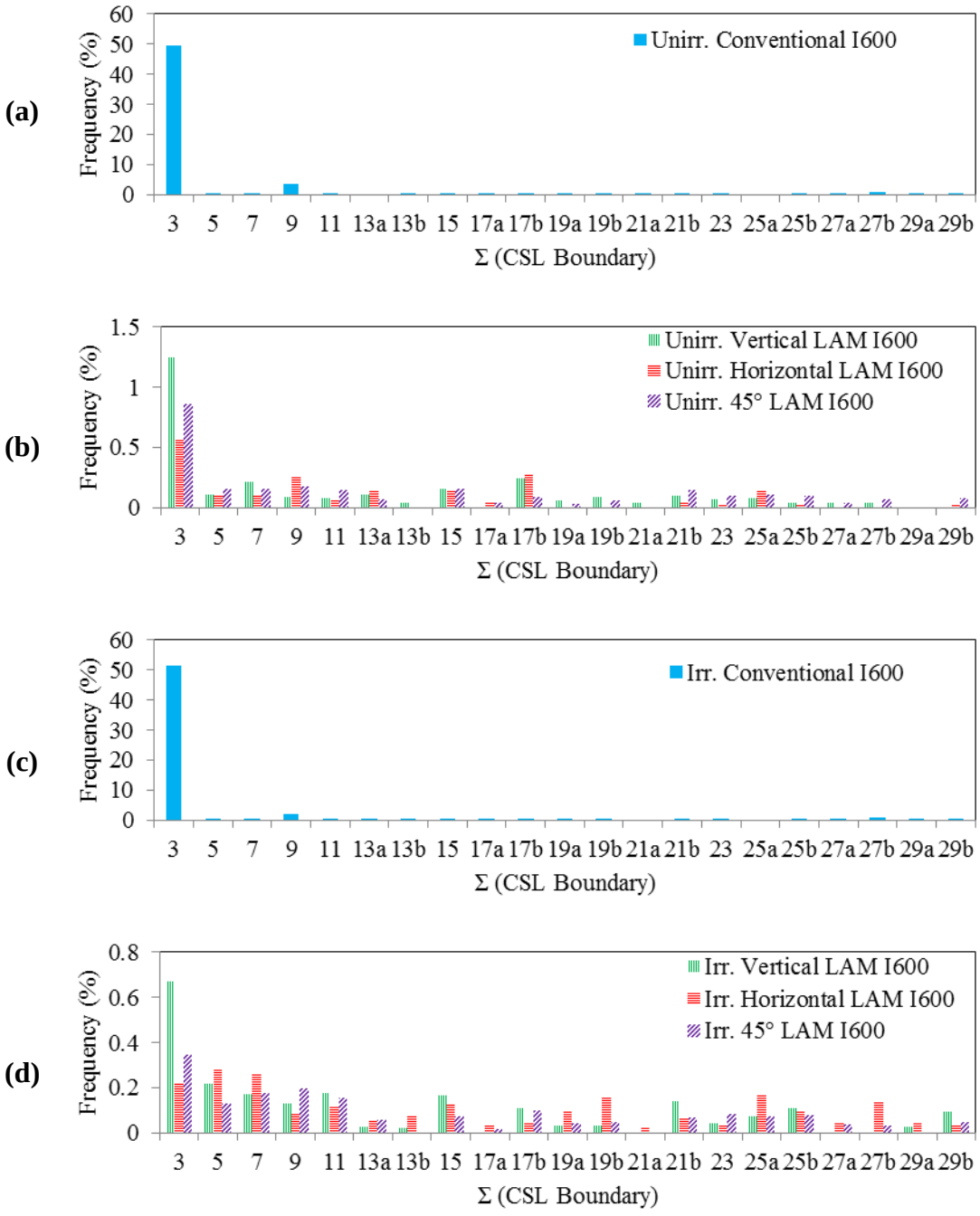

Figure 155: EBSD CSL Boundary Histograms of Inconel 600 (a) Unirradiated Conventionally Manufactured, (b) Unirradiated LAM, (c) Irradiated Conventionally Manufactured, and (d) Irradiated LAM

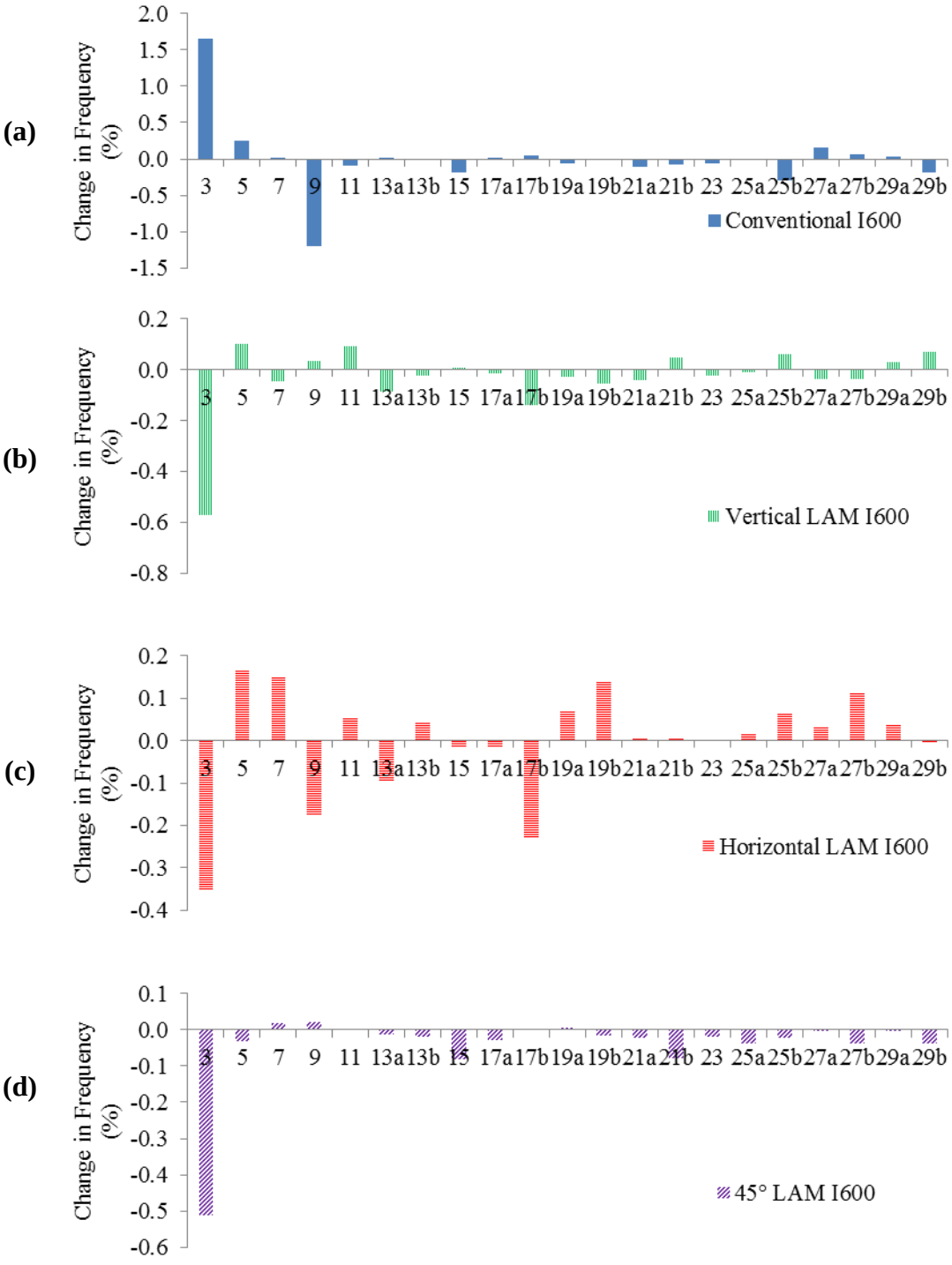

Figure 156: EBSD Histograms of Radiation-induced Change in CSL Boundaries in Inconel 600 (a) Conventionally Manufactured, (b) Vertical LAM, (c) Horizontal LAM, and (d) 45° LAM

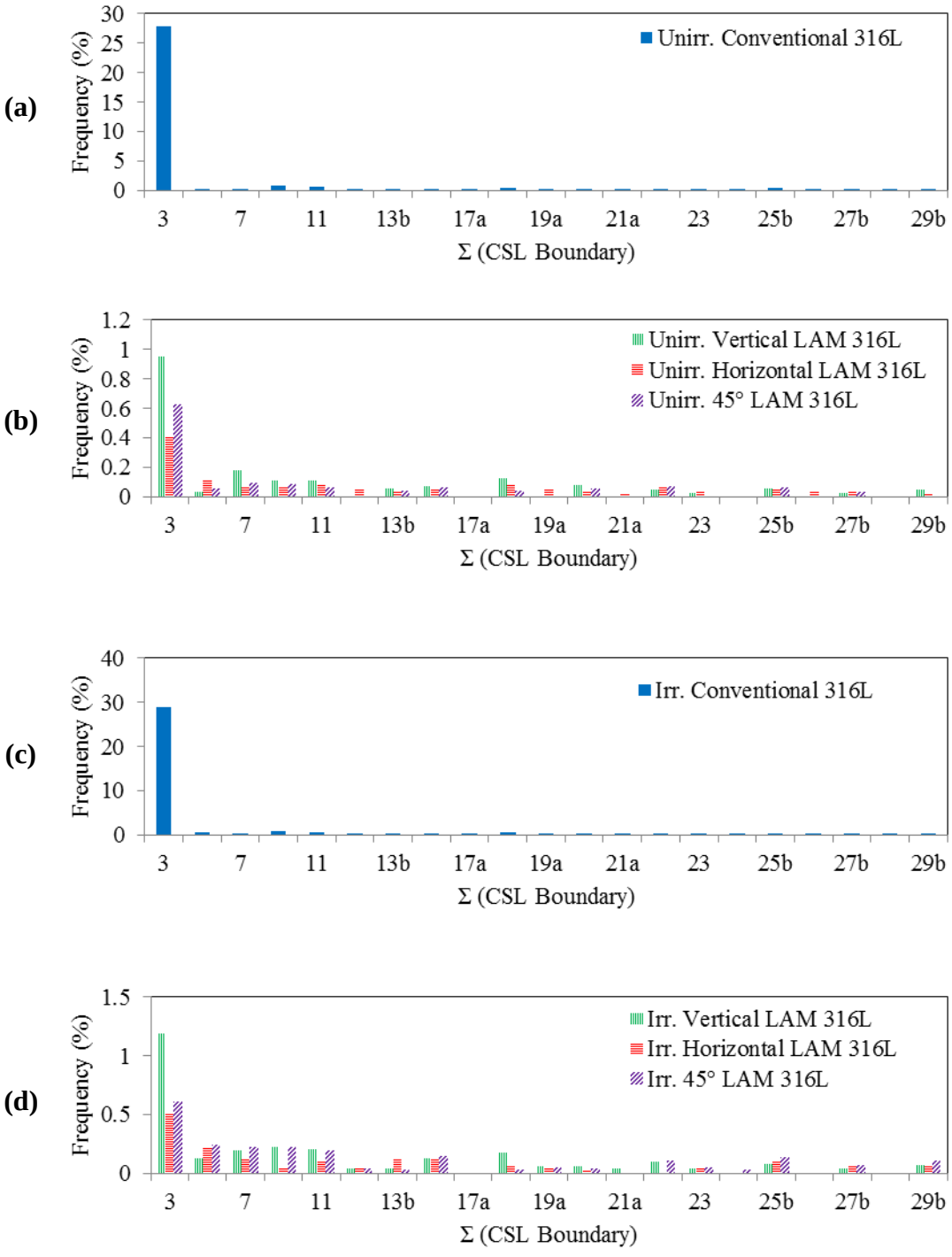

Figure 157: EBSD CSL Boundary Histograms of 316L Stainless Steel (a) Unirradiated Conventionally Manufactured, (b) Unirradiated LAM, (c) Irradiated Conventionally Manufactured, and (d) Irradiated LAM

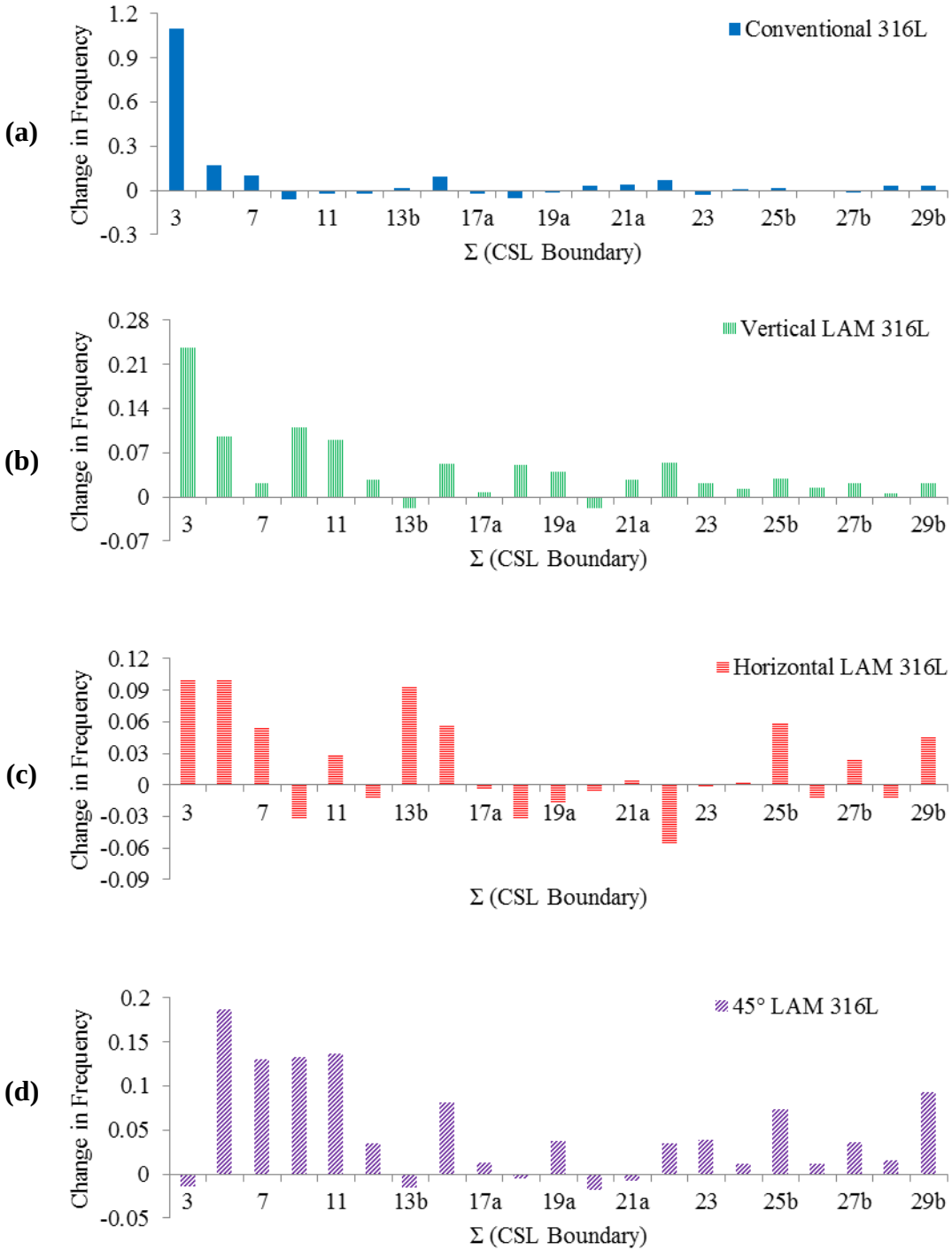

Figure 158: EBSD Histograms of Radiation-induced Change in CSL Boundaries in 316L Stainless Steel (a) Conventionally Manufactured, (b) Vertical LAM, (c) Horizontal LAM, and (d) 45° LAM

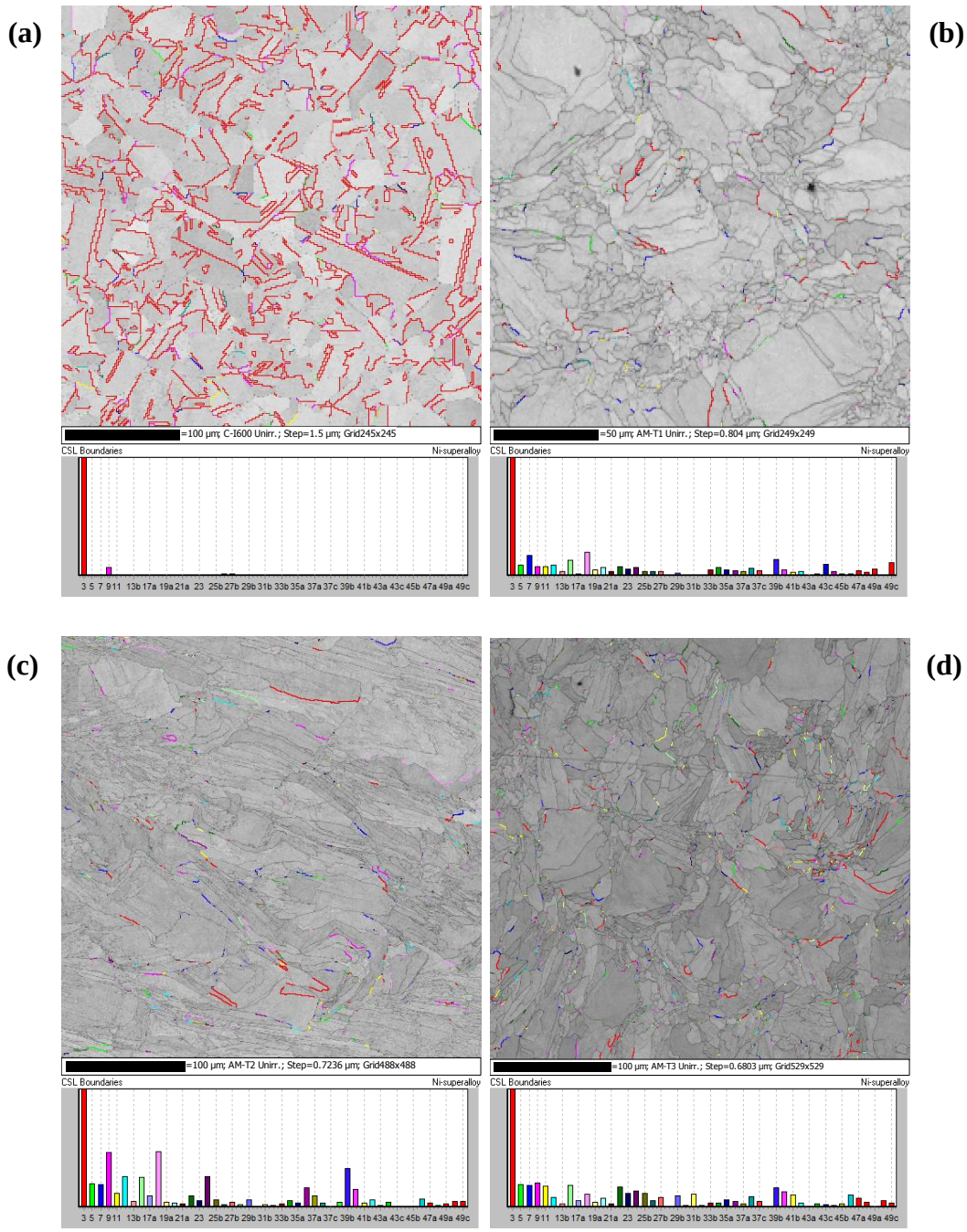

Figure 159: EBSD CSL Boundary Maps of Unirradiated Inconel 600 (a) Conventionally Manufactured, (b) Vertical LAM, (c) Horizontal LAM, and (d) 45° LAM

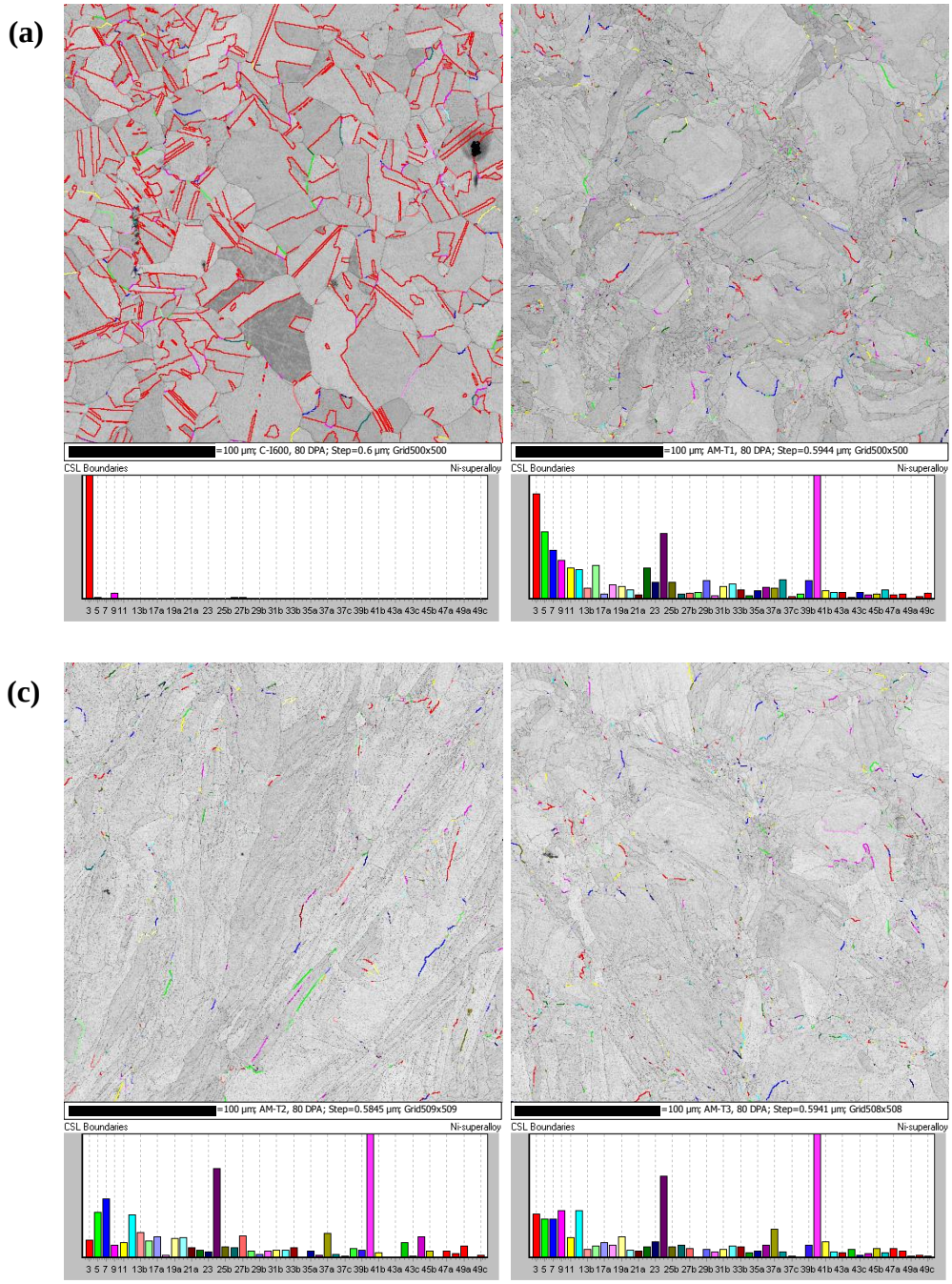

Figure 160: EBSD CSL Boundary Maps of Inconel 600 (a) Conventionally Manufactured, (b) Vertical LAM, (c) Horizontal LAM, and (d) 45° LAM Irradiated to 80 dpa

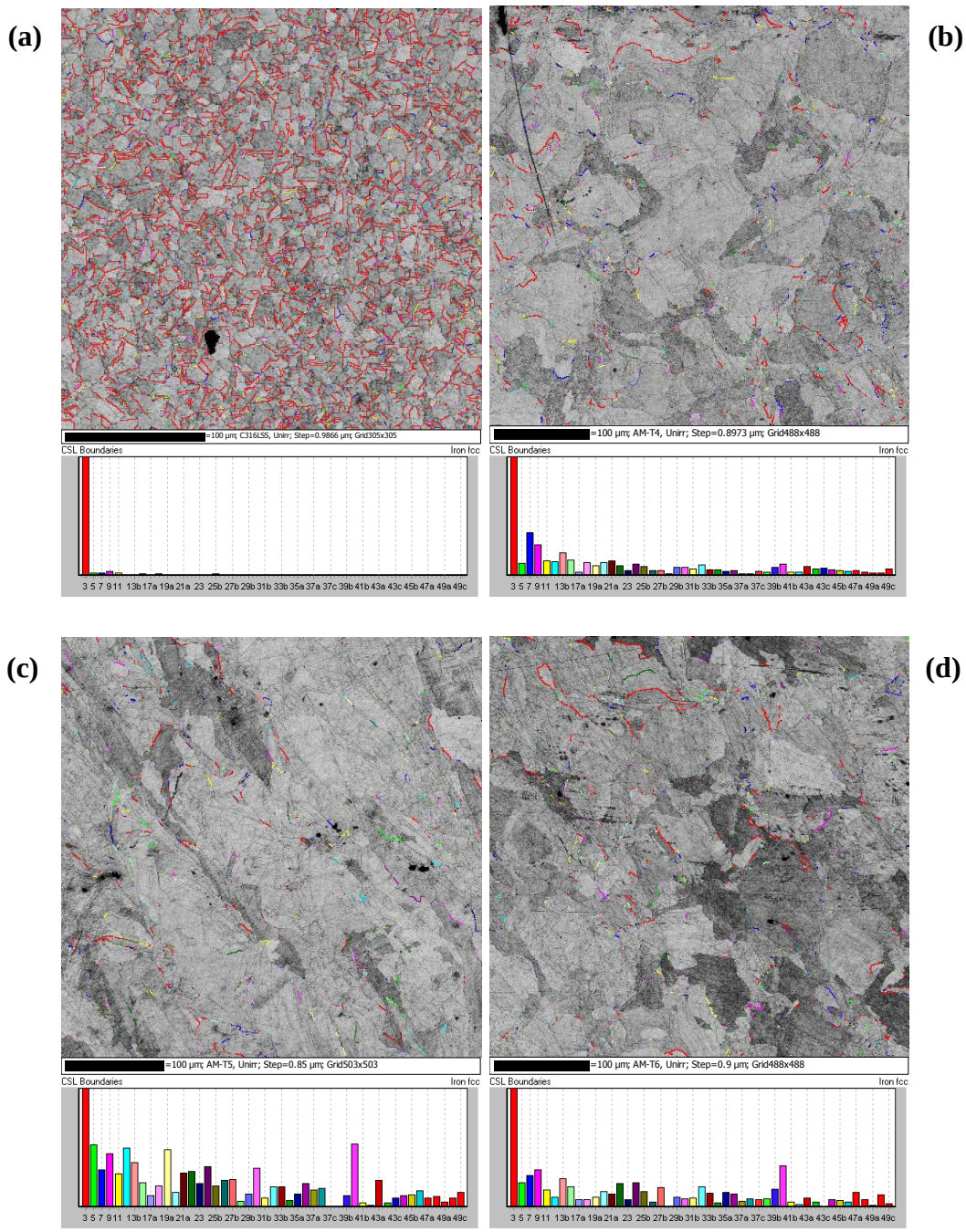

Figure 161: EBSD CSL Boundary Maps of Unirradiated 316L Stainless Steel (a) Conventionally Manufactured, (b) Vertical LAM, (c) Horizontal LAM, and (d) 45° LAM

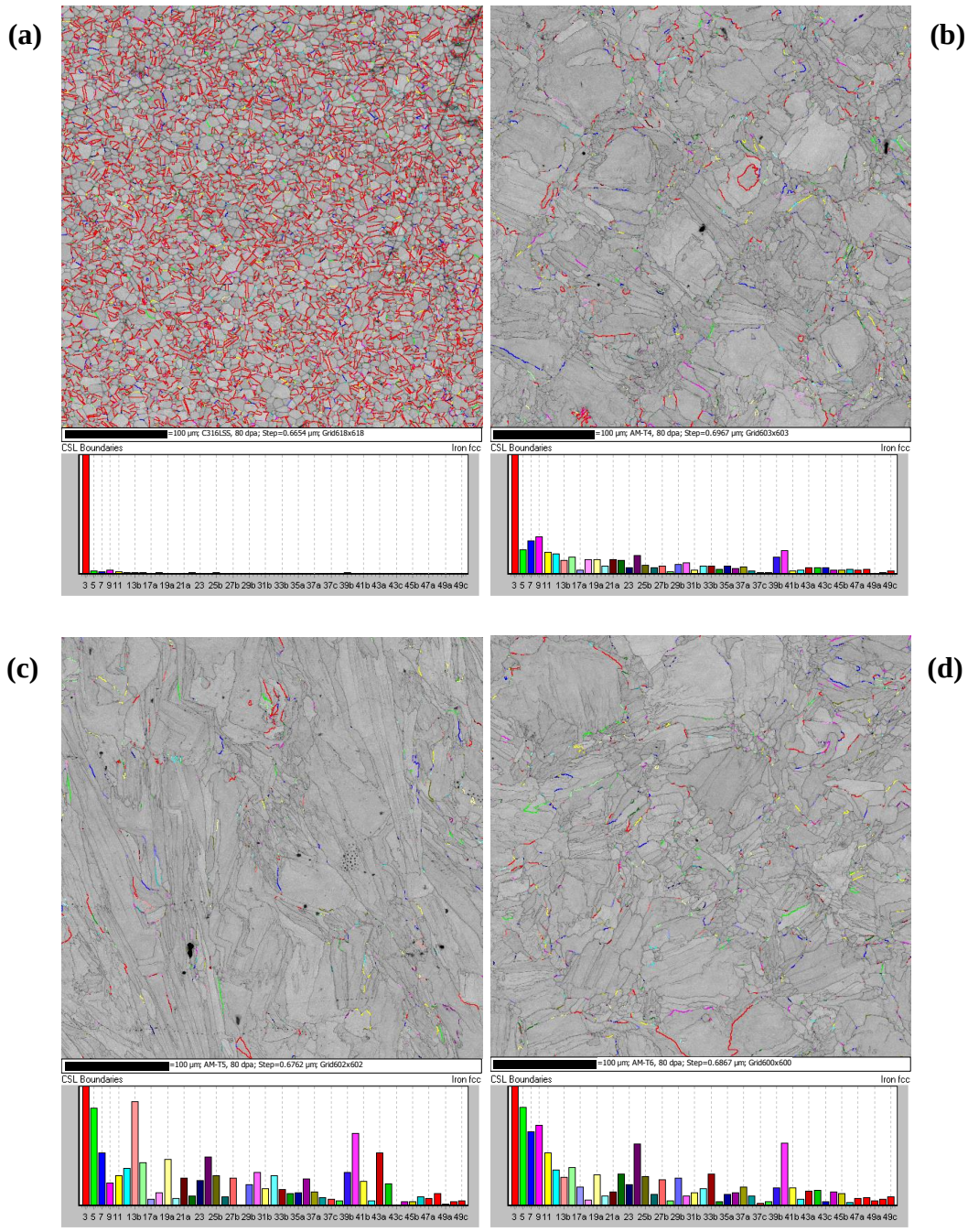

Figure 162: EBSD CSL Boundary Maps of 316L Stainless Steel (a) Conventionally Manufactured, (b) Vertical LAM, (c) Horizontal LAM, and (d) 45° LAM Irradiated to 80 dpa

IV.3.5. Kernel Average Misorientation Maps and Residual Strain

Kernel average misorientation maps of Inconel 600 and 316L stainless steel are provided in Figure 163 and Figure 164, respectively, where the abscissae are in degrees. Misorientation correlates to strains within the crystal structure where, to a close approximation, grains that are shown in colors other than blue or dark green in Figure 163 and Figure 164 contain plastic deformation [115-117]. This residual strain could be associated with significant residual stress fields. In the case of nuclear grade structural and component alloys, residual stress fields are undesirable since they may generate dislocations which can degrade the material's resistance to cracking and failure during use (this will be discussed further in Ch. V). For a review of KAM maps and residual strain in EBSD, see Ch. II.4.5.

The misorientation in the as-annealed LAM rods is significantly larger than in the conventionally manufactured rods for both alloys. The radiation-induced change in misorientation in the conventional control, vertical LAM, horizontal LAM, and 45° LAM are 0.32%, 0.30%, -0.20%, and 0.00% for the I600, respectively, and are -0.05%, -0.07%, -0.19%, and 0.03% for the 316L, respectively. The austenite phase in the unirradiated LAM ODS steel samples appears to have significantly less residual strain than the LAM Inconel or LAM 316L.

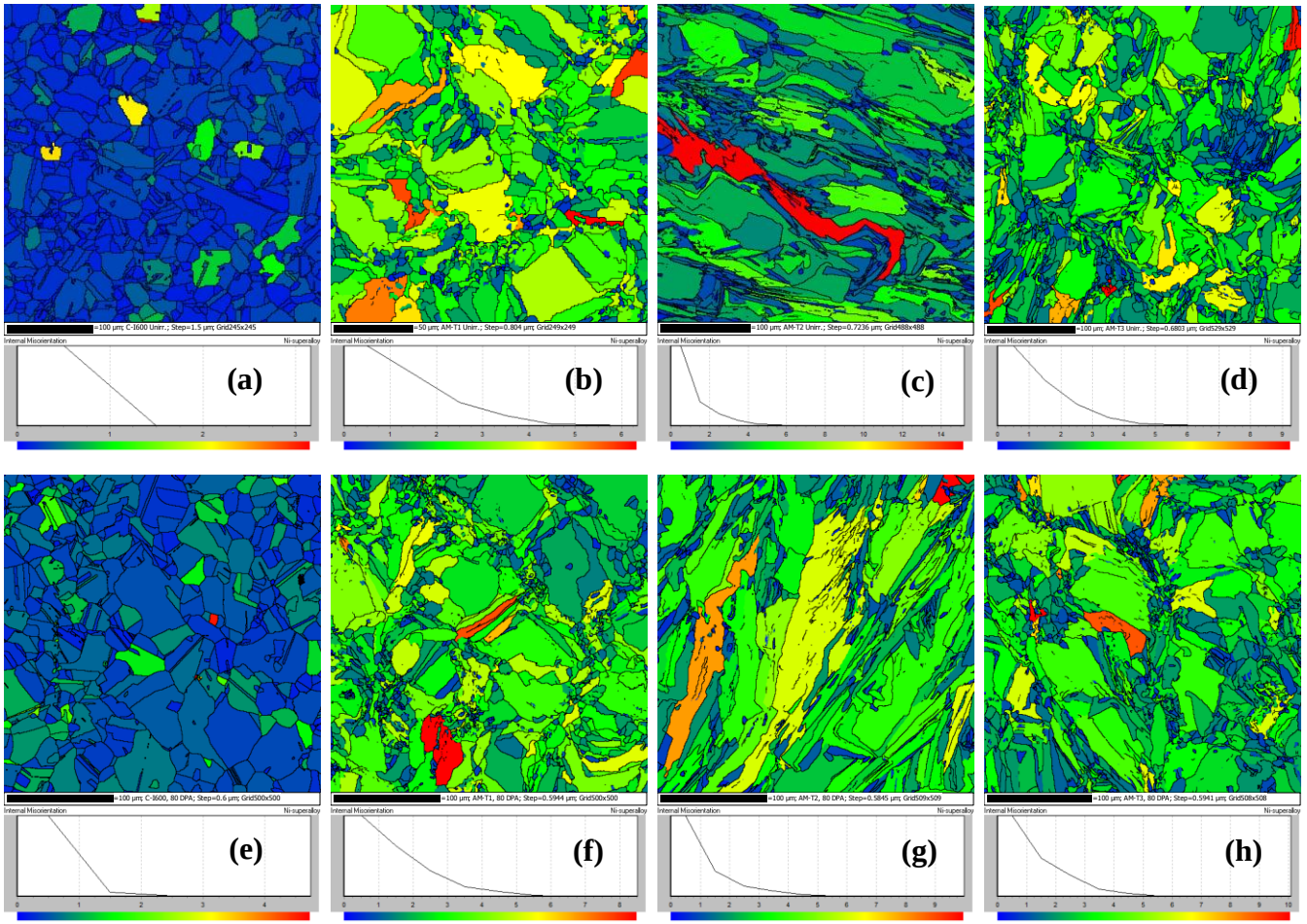

Figure 163: EBSD Misorientation Maps of Inconel 600; Unirradiated (a) Conventional, (b) Vertical LAM, (c) Horizontal LAM, (d) 45° LAM; and Irradiated (e) Conventional, (f) Vertical LAM, (g) Horizontal LAM, (h)and 45° LAM

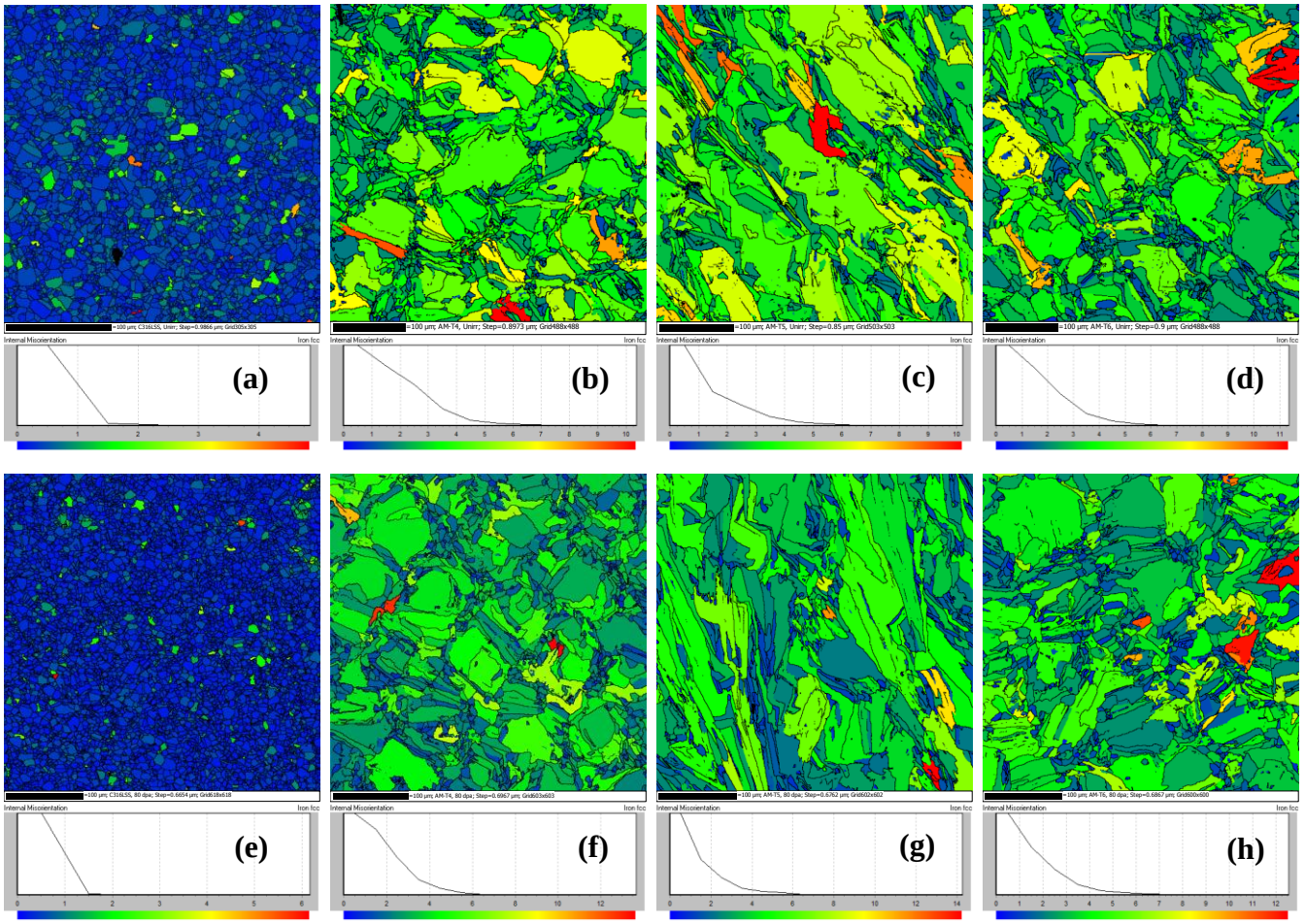

Figure 164: EBSD Misorientation Maps of 316L Stainless Steel; Unirradiated (a) Conventional, (b) Vertical LAM, (c) Horizontal LAM, (d) 45° LAM; and Irradiated (e) Conventional, (f) Vertical LAM, (g) Horizontal LAM, (h) and 45° LAM

IV.3.6. Taylor Factor Maps

For a review of Taylor factor maps or distributions, see Ch. II.4.7. Adjacent grains whose Taylor factor varies by a given amount are related to the CSL boundary character. The Taylor Factor contour plot on the standard stereographic IPF in Figure 165 was derived using the Matlab computational software, where the average Taylor Factor value is determined to be $M = 3.067$. In other words, any fcc polycrystalline material with no texture (preferential crystalline orientation) will have a Taylor Factor of $M = 3.067$.

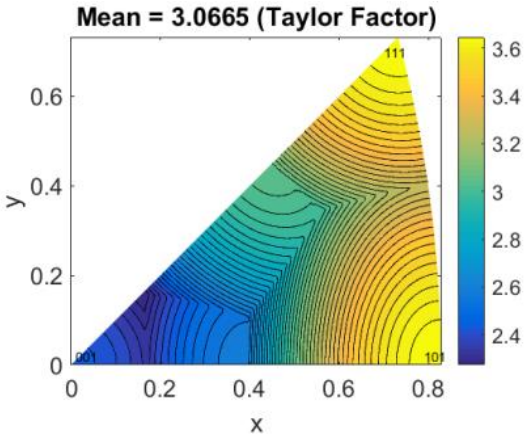

Figure 165: Contour Plot of the Taylor Factor vs. Crystallographic Orientation in an fcc Polycrystalline Material

Taylor factor histograms are shown in Figure 166 and Figure 167, while Taylor factor maps are shown in Figure 168 and Figure 169, respectively. The Taylor factor is related to stress by Eq. 7. Recall that the Taylor factor assumes that grains with low Taylor factors undergo negligible deformation until the grains with high Taylor factors also deform plastically, and the grains with high Taylor factors deform by a combination

of stress concentration and work hardening around them. Lower Taylor factor values represent higher resistance to slip. The average Taylor factor for an fcc polycrystalline material with no texture is approximately 3.067 (see Figure 165).

The average Taylor factors for both I600 and 316L conventionally manufactured controls were 3.059 and 3.081, close to the theoretical value of 3.066 for fcc polycrystals without texture. The unirradiated as-annealed LAM Taylor factors are strongly dependent upon build orientation, where *M* is significantly larger for vertical Inconel 600 and 316L stainless steel LAM (3.324 and 3.100, respectively) as compared to horizontal Inconel 600 and 316L stainless steel LAM (2.935 and 3.067, respectively). The Taylor factor for the 45° LAM is 3.20 and 3.09 for I600 and 316L, respectively (i.e. a combination of both horizontal and vertical LAM). The Taylor factors for all samples changed slightly, either due to radiation damage or to characterizing different regions of the sample surfaces; however, the trends remain unchanged due to radiation damage. *M* for the vertical LAM is consistently much larger than for the horizontal LAM, with 45° LAM being a combination of the two.

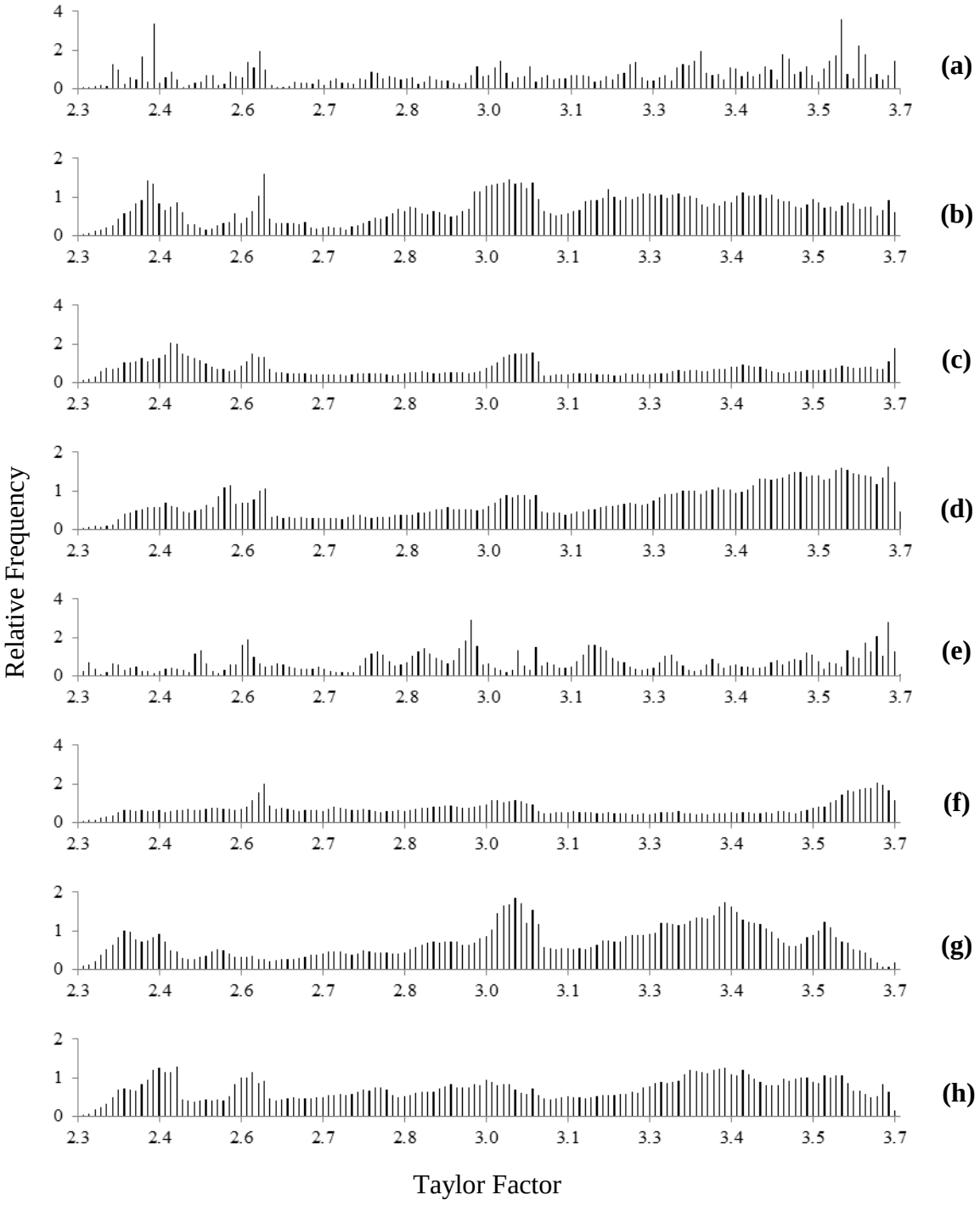

Figure 166: Taylor Factor Histograms of Inconel 600; Unirradiated (a) Conventional, (b) Vertical LAM, (c) Horizontal LAM, (d) 45° LAM; and Irradiated (e) Conventional, (f) Vertical LAM, (g) Horizontal LAM, and (h) 45° LAM

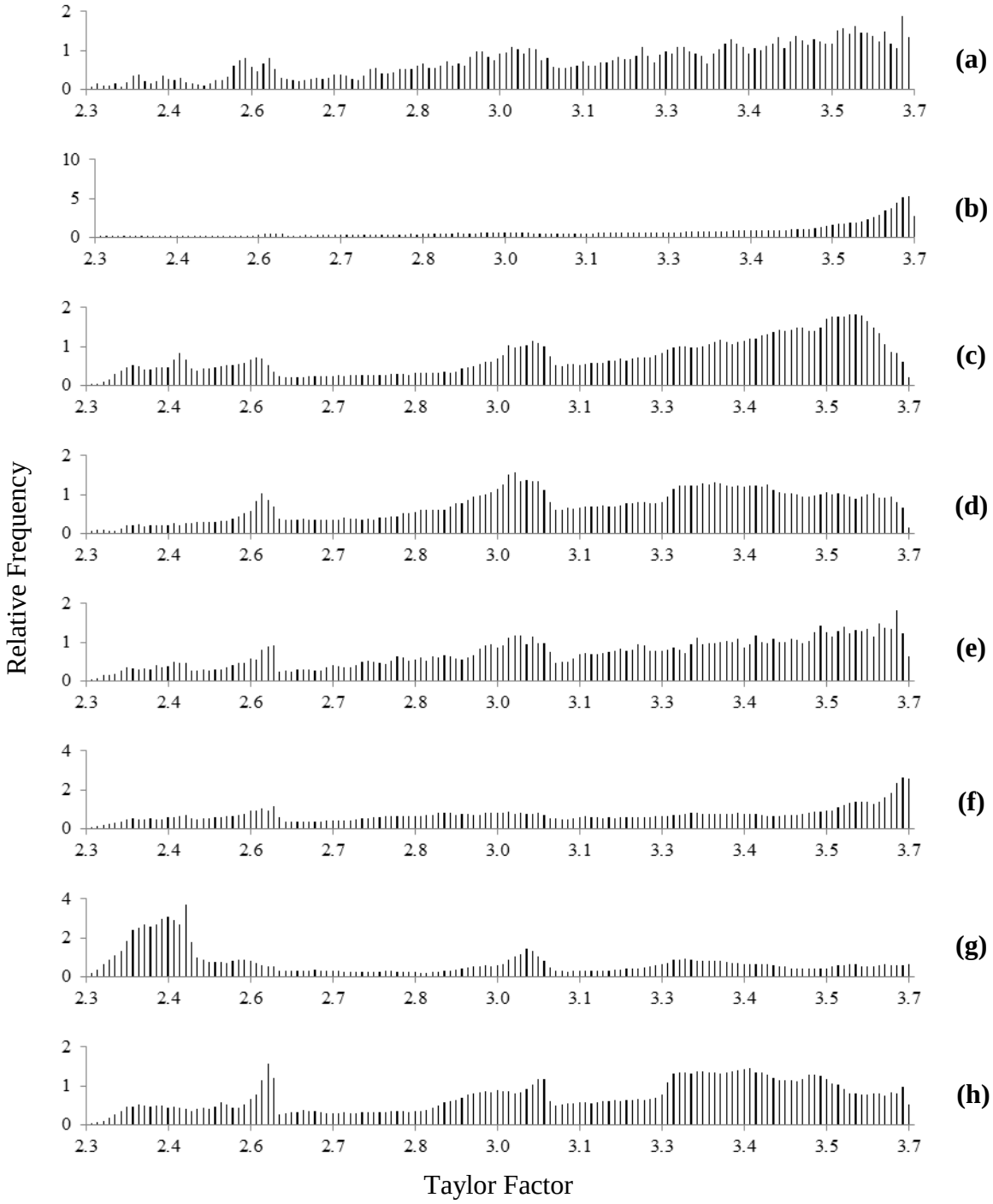

Figure 167: Taylor Factor Histograms of 316L Stainless Steel; Unirradiated (a) Conventional, (b) Vertical LAM, (c) Horizontal LAM, (d) 45° LAM; and Irradiated (e) Conventional, (f) Vertical LAM, (g) Horizontal LAM, and (h) 45° LAM

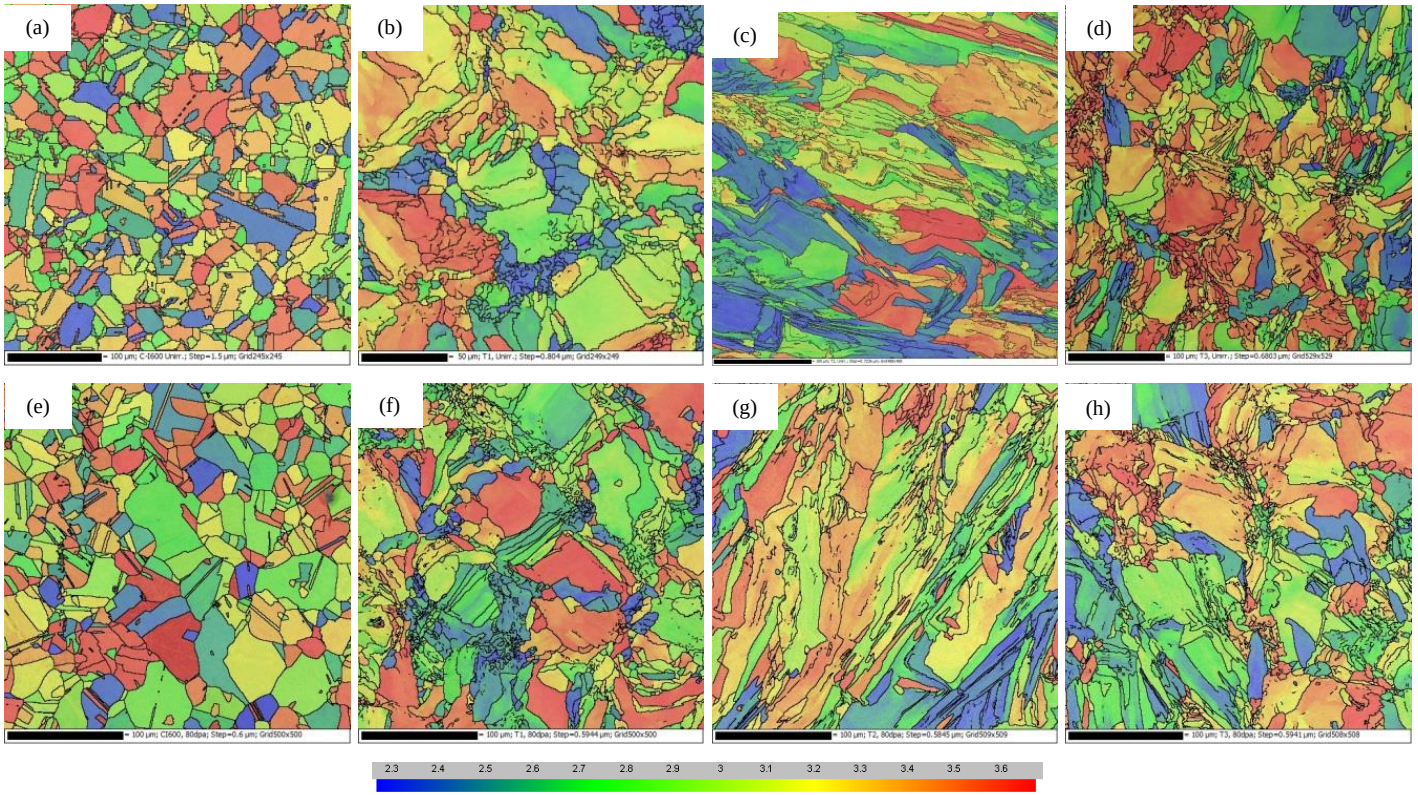

Figure 168: Taylor Factor Maps of Inconel 600; Unirradiated (a) Conventional, (b) Vertical LAM, (c) Horizontal LAM, (d) 45° LAM; and Irradiated (e) Conventional, (f) Vertical LAM, (g) Horizontal LAM, and (h) 45° LAM

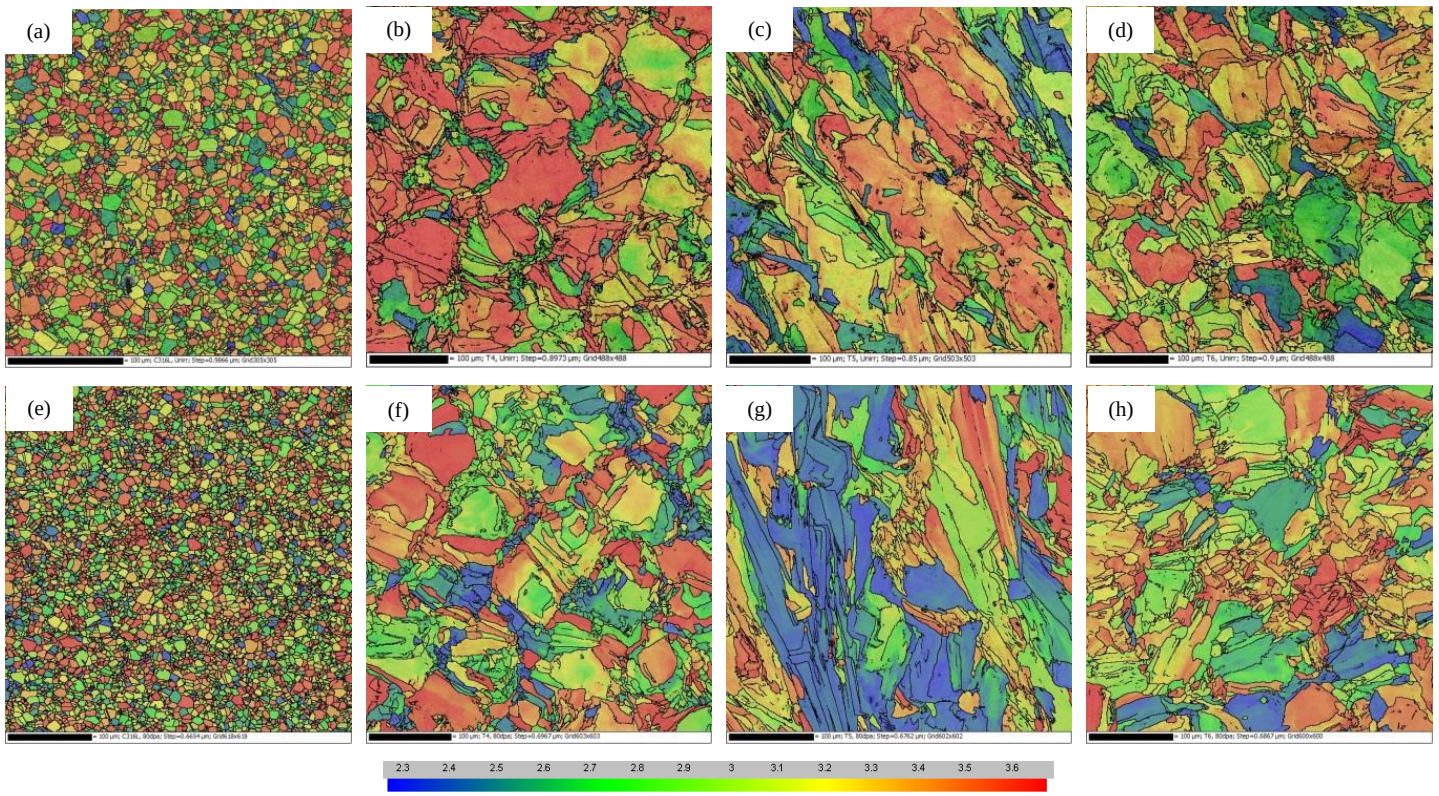

Figure 169: Taylor Factor Maps of 316L Stainless Steel; Unirradiated (a) Conventional, (b) Vertical LAM, (c) Horizontal LAM, (d) 45° LAM; and Irradiated (e) Conventional, (f) Vertical LAM, (g) Horizontal LAM, and (h) 45° LAM

IV.4 Scanning Probe Microscopy, Nanoindentation, and Bulk Tensile Testing

IV.4.1 Scanning Probe Microscopy of Inconel 600

Scanning probe microscopy analysis conducted prior to irradiation indicated root-mean-square (RMS) surface roughness below 5 nm on all polished Inconel and 316L samples. However, SEM/EDS analysis of the irradiated Inconel 600 reveals chromium carbide precipitates on the surface of the specimens (see, for example, Figure 122 - Figure 120). After irradiation, the RMS surface roughness of the conventionally manufactured control specimen had increased to approximately 27 nm, while LAM samples built vertically, horizontally, and at 45° had increased to 40 nm, 52 nm, and 46 nm, respectively. The average increase in surface roughness due to radiation-induced precipitate formation is also anisotropic, with horizontally-built being roughest and vertically-built being smoothest of the LAM samples. The chromium/carbon rich features in Figure 122 - Figure 120 can be seen more clearly in SPM to be protruding out of the alloy surface, as shown in Figure 170 where bright contrast represents an increase in feature height above the surface. For a review of SPM technology, see Ch. II.5.3. For details regarding SPM protocol, see Ch. III.7.

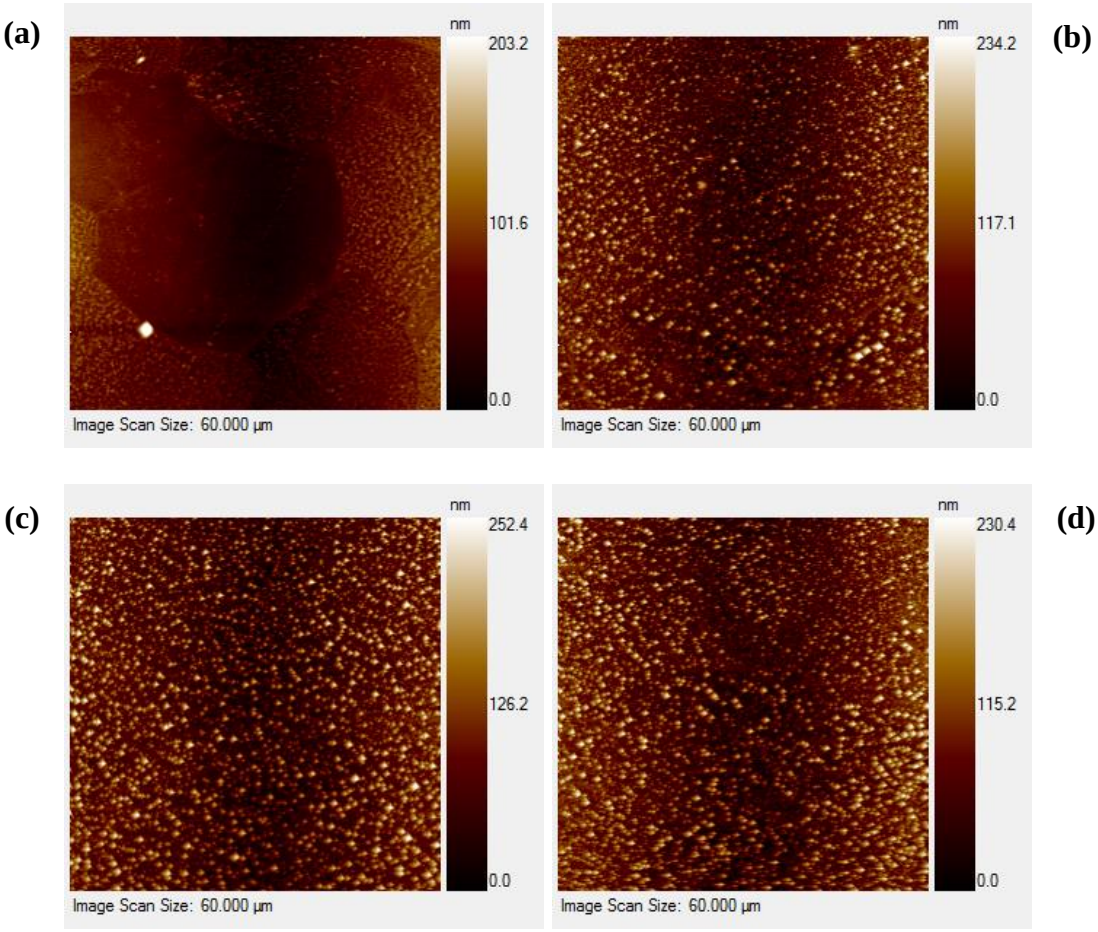

Figure 170: SPM Images of Radiation-induced Chromium and Carbon Rich Precipitates on the Surface of Irradiated Inconel 600 (a) Conventionally Manufactured, (b) Vertical LAM, (c) Horizontal LAM, and (d) 45° LAM

IV.4.2 Bulk Tensile Testing of LAM Inconel 600 and 316L Stainless Steel

Prior to shipping the LAM samples to TAMU, Lockheed Martin performed tensile tests on several unirradiated samples to compare mechanical properties vs. build orientation of the parts which was summarized in an unpublished report. Among the tested samples were the vertical, horizontal, and 45° LAM Inconel 600 and 316L stainless steel. Unirradiated LAM rods were tested using an Instron 4505 with a 1 inch extensometer at a crosshead rate of 0.05 $in \cdot min^{-1}$. The rods were machined and tested in accordance with ASTM E8/E8M standards. Rods were not threaded because the Instron has clamps that grip the rods. The ODS samples were not tested due to time constraints, as they were built much later than the Inconel or 316L. These experiments are important to understanding the build orientation dependence of these alloys, and can be used to validate nanoindentation results.

The load-extension curves for the Inconel 600 and 316L stainless steel rods produced by LAM are shown in Figure 171 (courtesy Lockheed Martin from an unpublished report). The yield strength and work hardening of the alloys is clearly strongly dependent upon orientation. For both Inconel 600 and 316L steel samples built by LAM, the horizontal LAM yield strength is about 3% higher than the vertical LAM and 0.5% higher than 45° LAM. Similarly, the vertical LAM rods are more ductile and experience significantly less work hardening as compared to the horizontal LAM rods, with 45° LAM rods' in between.

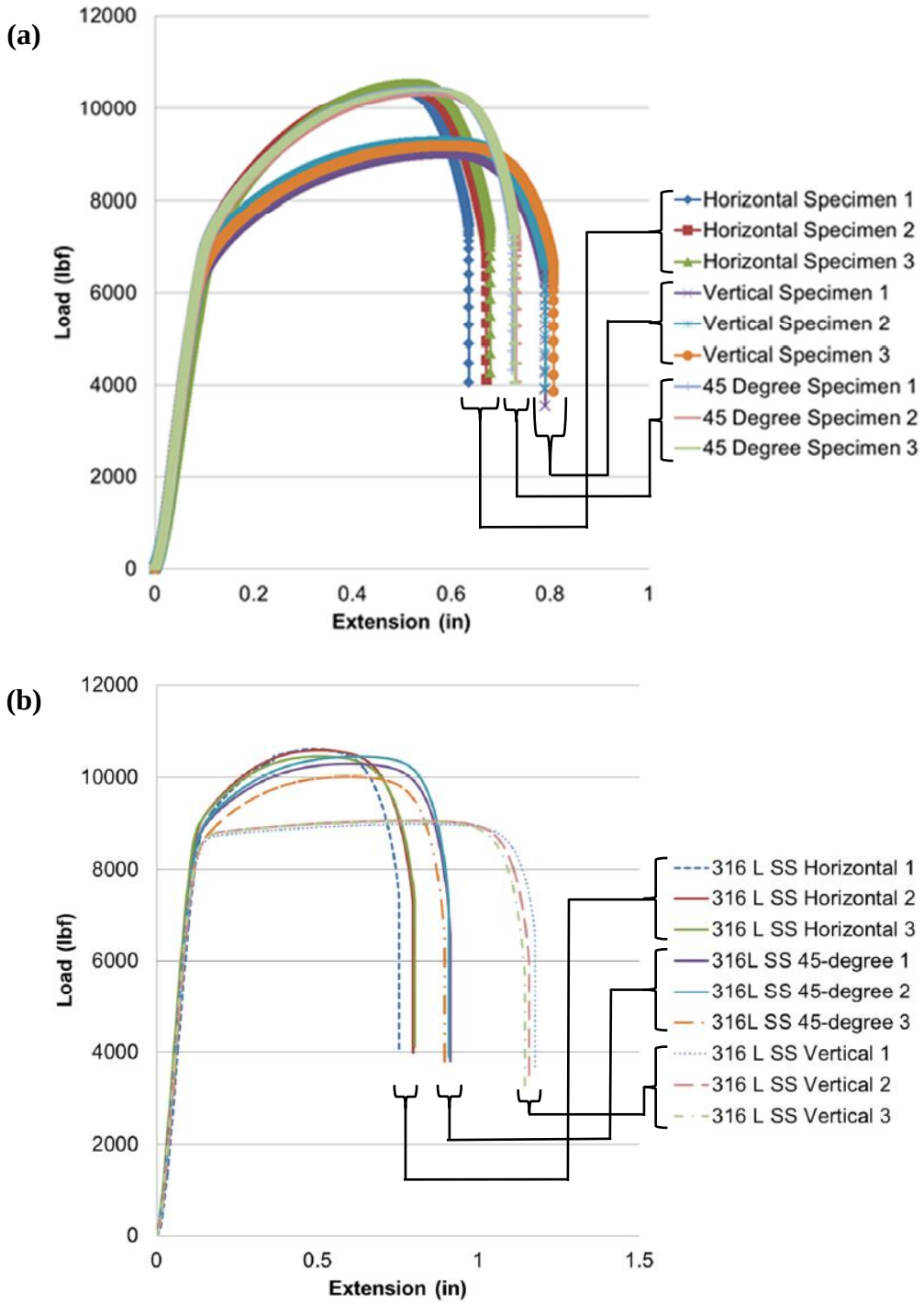

Figure 171: Load-Extension Curves for Unirradiated (a) LAM Inconel 600 and (b) LAM 316L Stainless Steel Rods

IV.4.3 Nanoindentation

SPM imaging confirms that the indents are much larger than the chromium carbide precipitates on the surface of the irradiated Inconel 600 samples (see Figure 172). The load-displacement curves for all 316L stainless steel indents, as well as the drift rates, are provided in Figure 173-Figure 188. Note that attempts in which false-engages or other mechanical errors occurred are included in these plots. Load-displacement data from nanoindentation did not indicate pressure induced phase changes, creep, pop-in events, or other microstructural rearrangement phenomena for any of the samples tested [112, 113, 118-122]. Nanoindentation of LAM and conventionally manufactured samples did not produce cracks in the sample surfaces before or after irradiation, indicating ductile plastic deformation [123, 124]. The load-displacement data collected appear as expected for all examples (see Figure 33c). For a review of nanoindentation, see Ch. II.5. For details regarding nanoindentation protocol, see Ch. III.7.

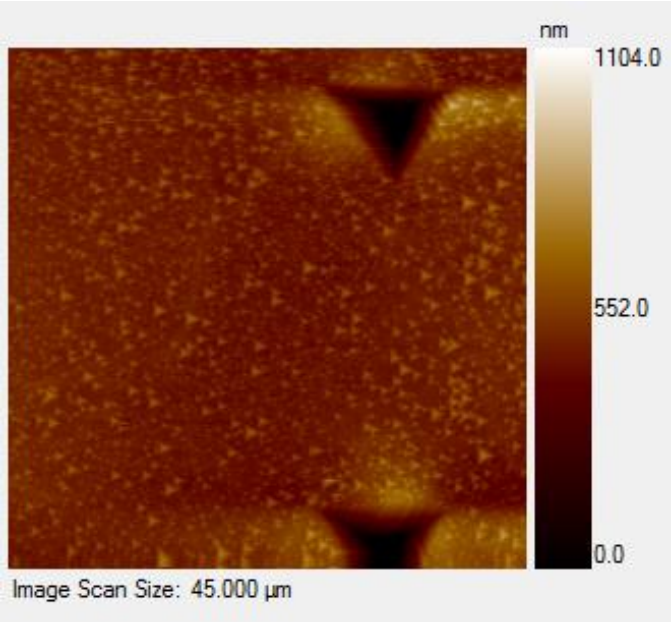

Figure 172: SPM Image Showing Size of Indent Compared to Chromium Carbide Precipitates on the Surface of Irradiated Inconel 600

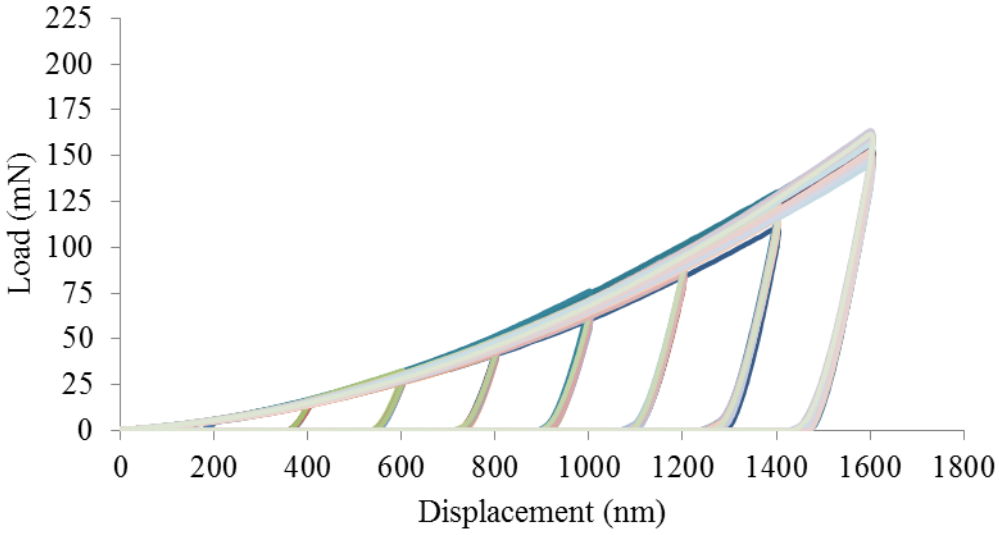

Figure 173: Load-Displacement Curves for Nanoindentation of Unirradiated Conventionally Manufactured 316L Stainless Steel

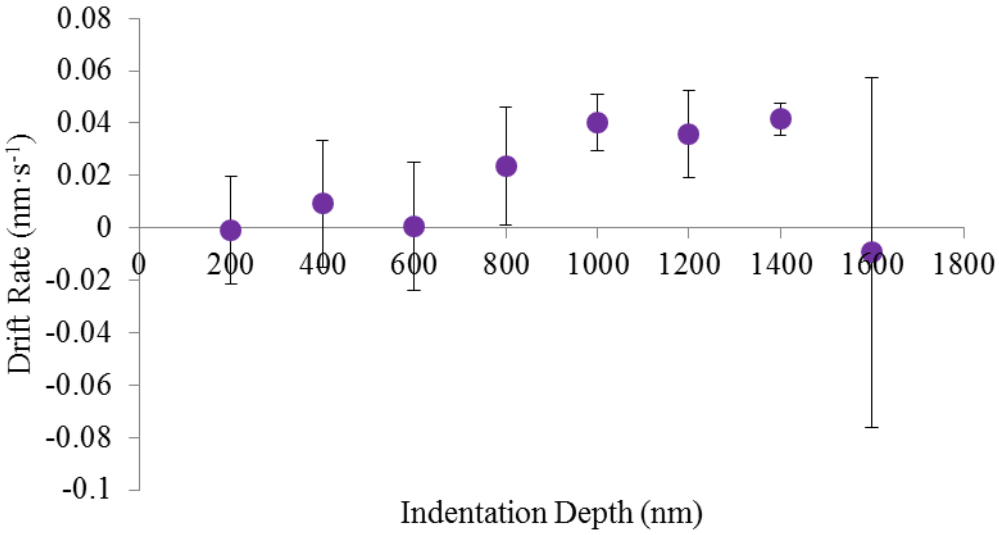

Figure 174: Drift Rate vs. Depth for Nanoindentation of Unirradiated Conventionally Manufactured 316L Stainless Steel

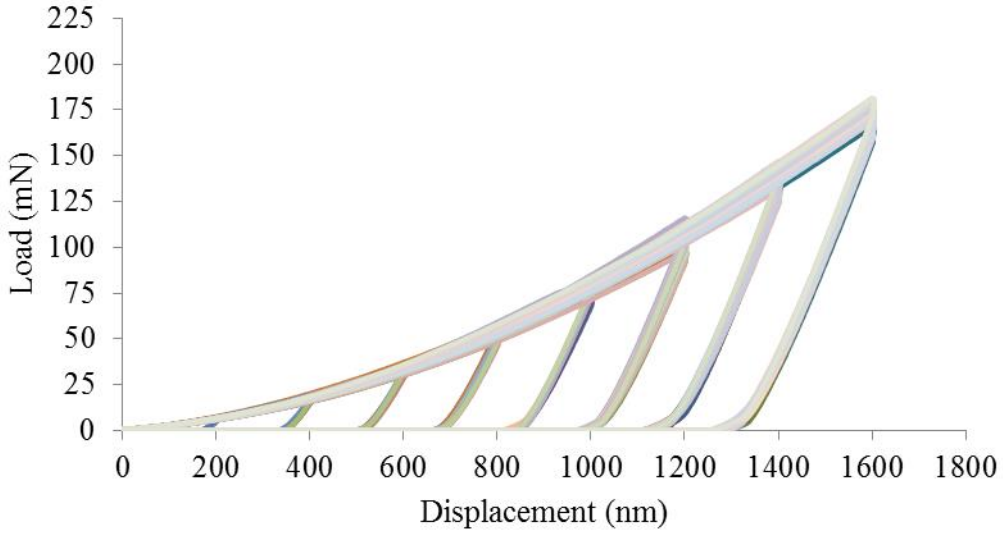

Figure 175: Load-Displacement Curves for Nanoindentation of Unirradiated Vertical LAM 316L Stainless Steel

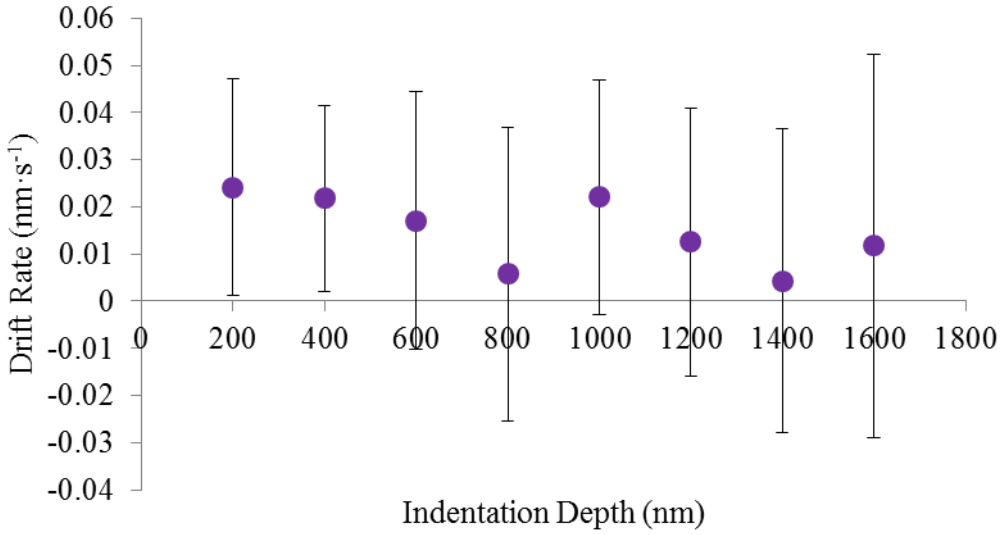

Figure 176: Drift Rate vs. Depth for Nanoindentation of Unirradiated Vertical LAM 316L Stainless Steel

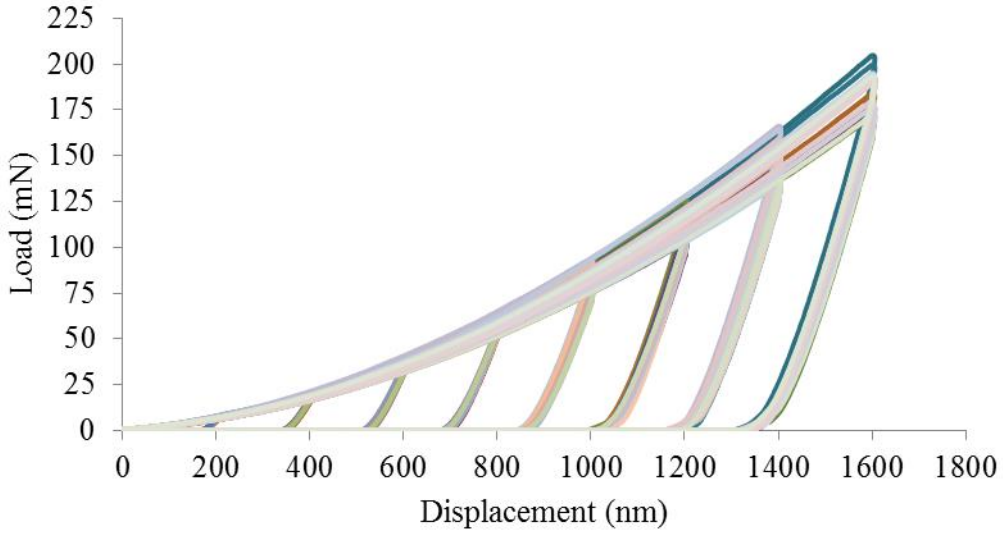

Figure 177: Load-Displacement Curves for Nanoindentation of Unirradiated Horizontal LAM 316L Stainless Steel

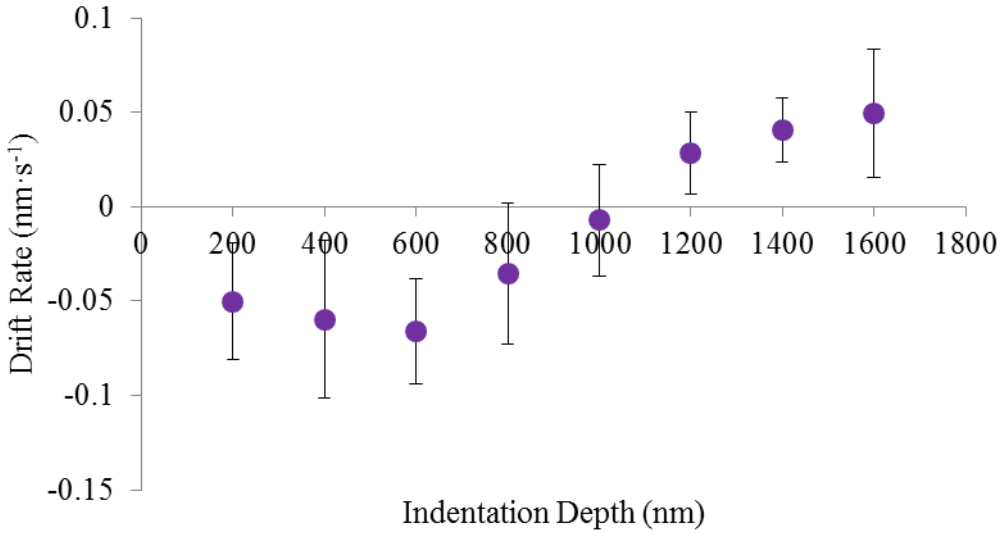

Figure 178: Drift Rate vs. Depth for Nanoindentation of Unirradiated Horizontal LAM 316L Stainless Steel

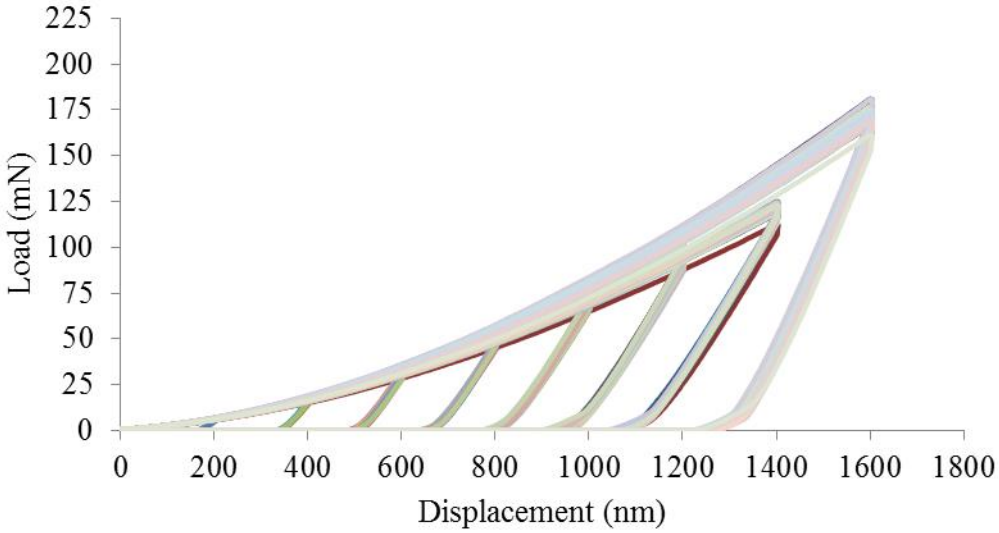

Figure 179: Load-Displacement Curves for Nanoindentation of Unirradiated 45° LAM 316L Stainless Steel

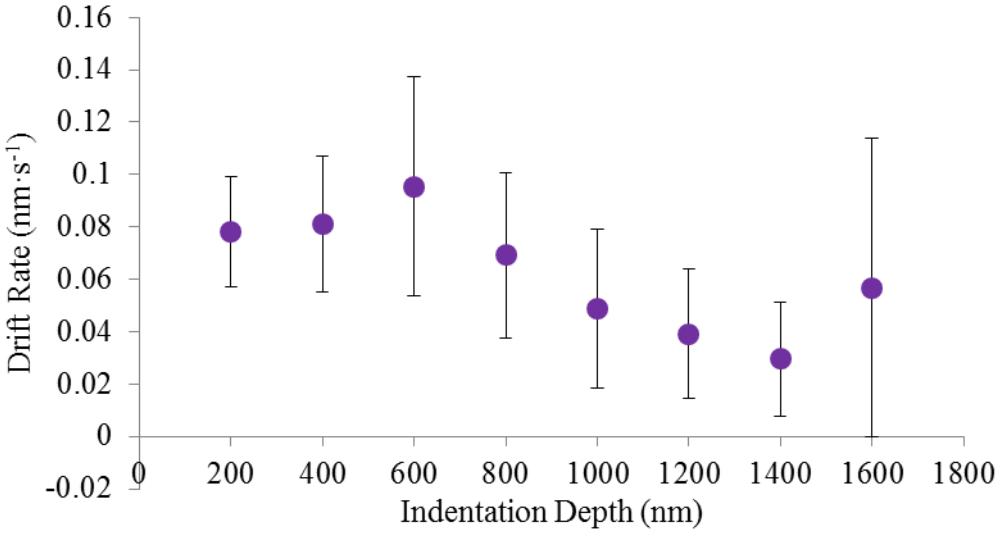

Figure 180: Drift Rate vs. Depth for Nanoindentation of Unirradiated 45° LAM 316L Stainless Steel

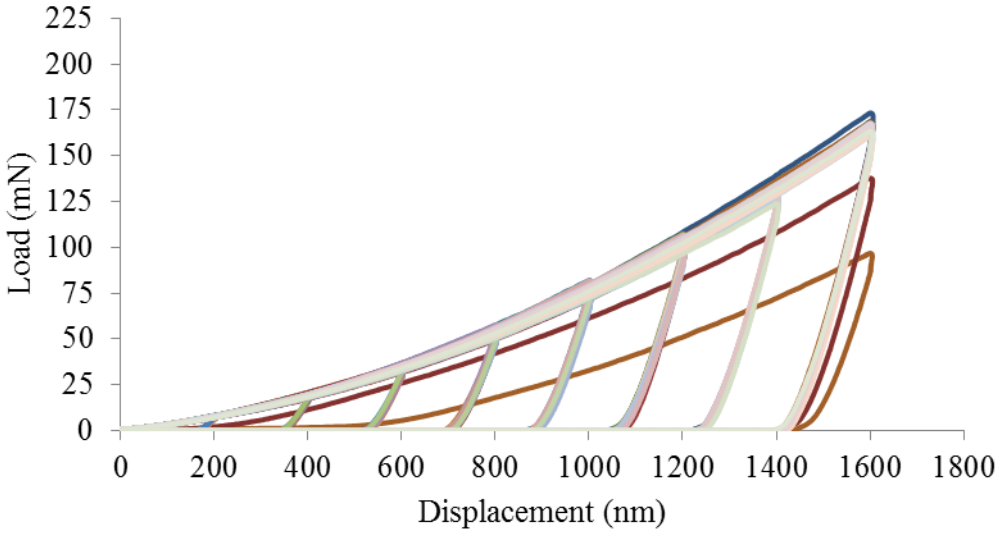

Figure 181: Load-Displacement Curves for Nanoindentation of Irradiated Conventionally Manufactured 316L Stainless Steel

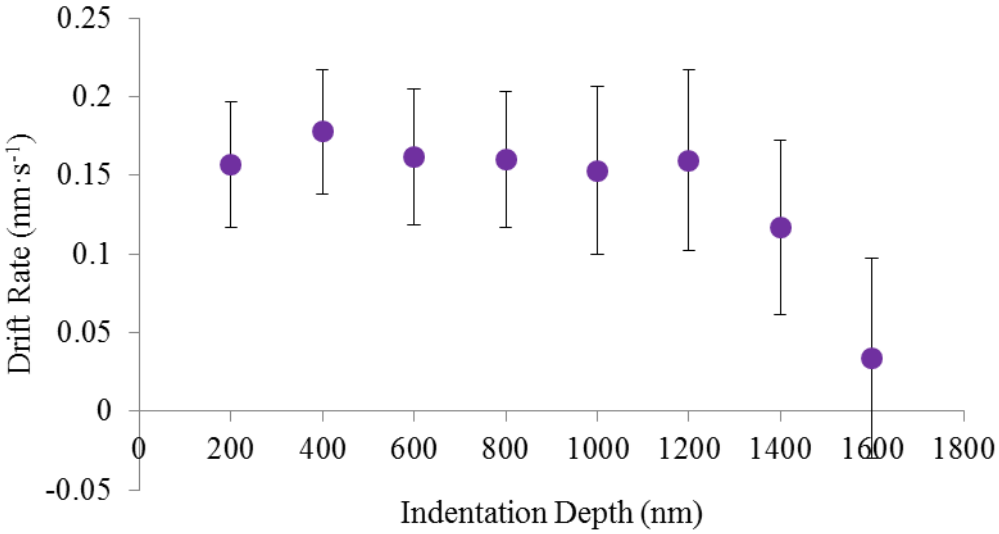

Figure 182: Drift Rate vs. Depth for Nanoindentation of Irradiated Conventionally Manufactured 316L Stainless Steel

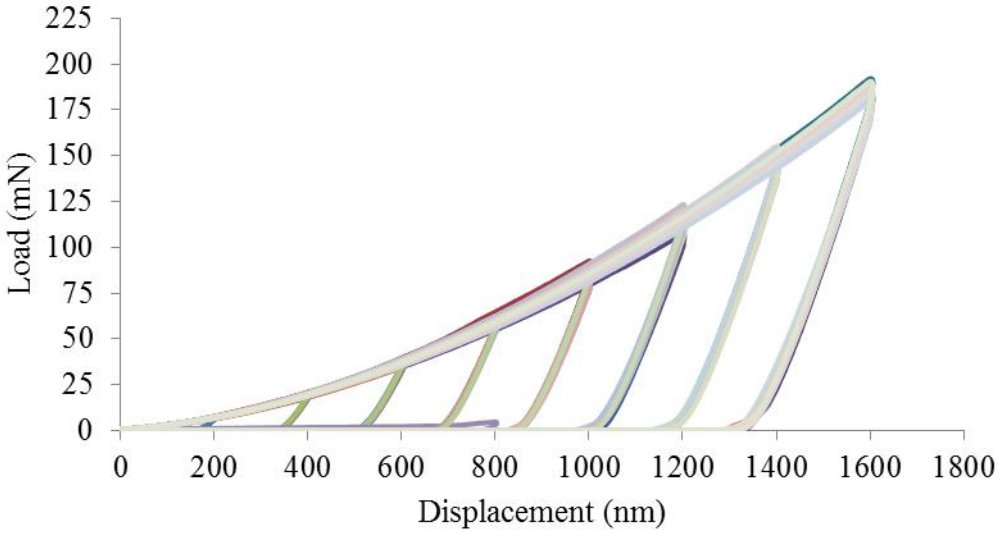

Figure 183: Load-Displacement Curves for Nanoindentation of Irradiated Vertical LAM 316L Stainless Steel

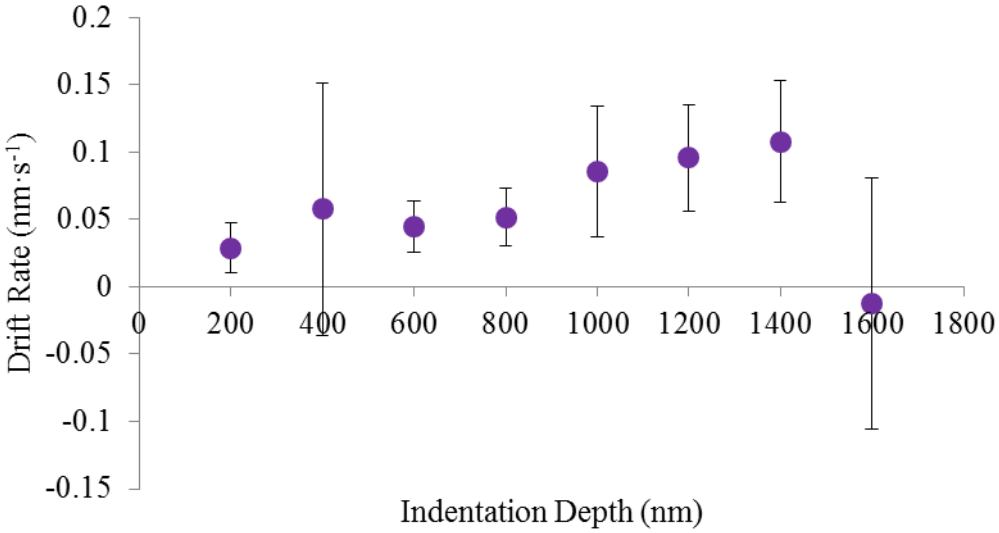

Figure 184: Drift Rate vs. Depth for Nanoindentation of Irradiated Vertical LAM 316L Stainless Steel

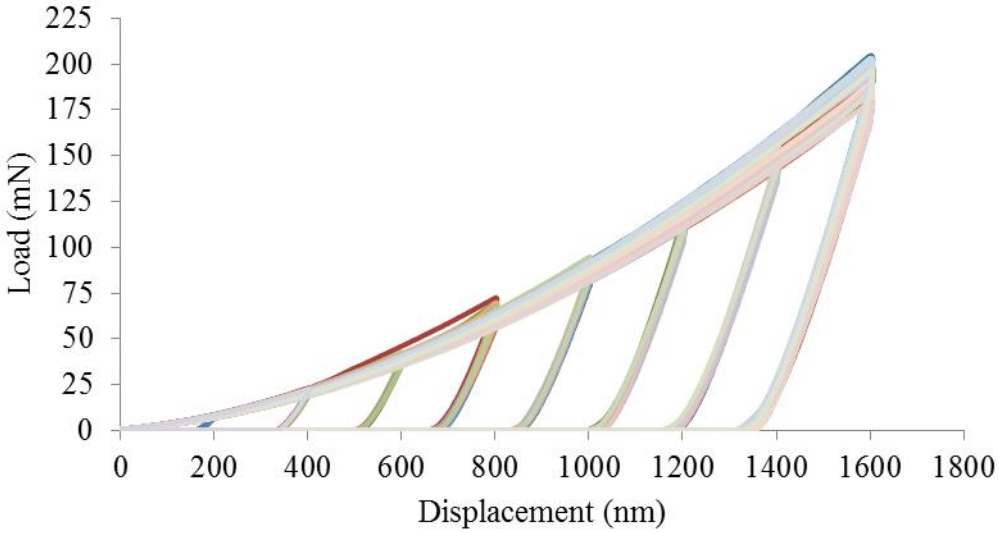

Figure 185: Load-Displacement Curves for Nanoindentation of Irradiated Horizontal LAM 316L Stainless Steel

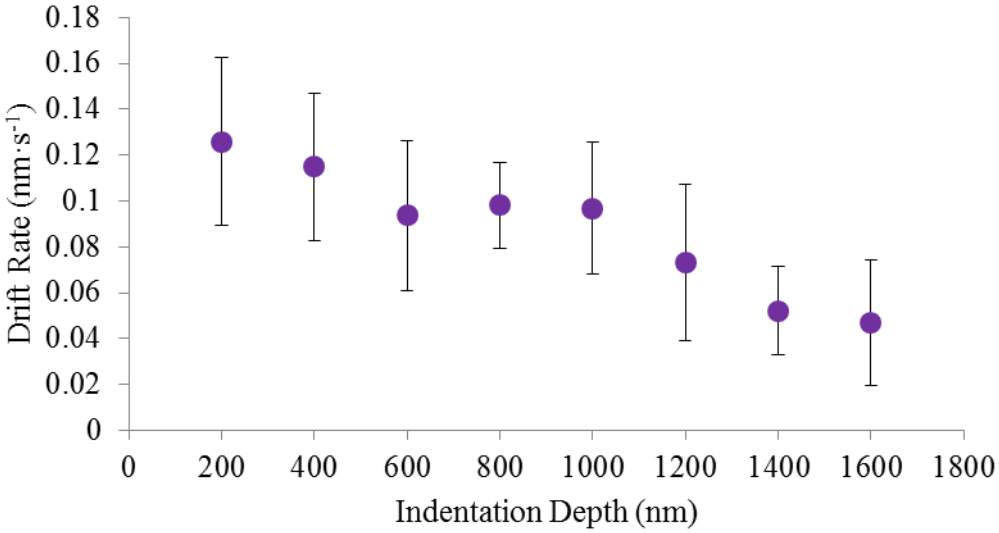

Figure 186: Drift Rate vs. Depth for Nanoindentation of Irradiated Horizontal LAM 316L Stainless Steel

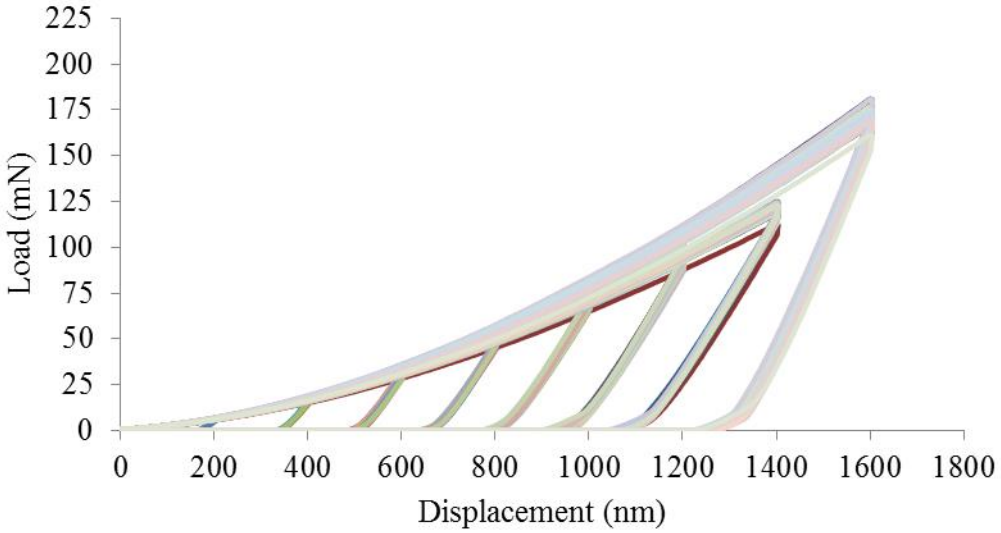

Figure 187: Load-Displacement Curves for Nanoindentation of Irradiated 45° LAM 316L Stainless Steel

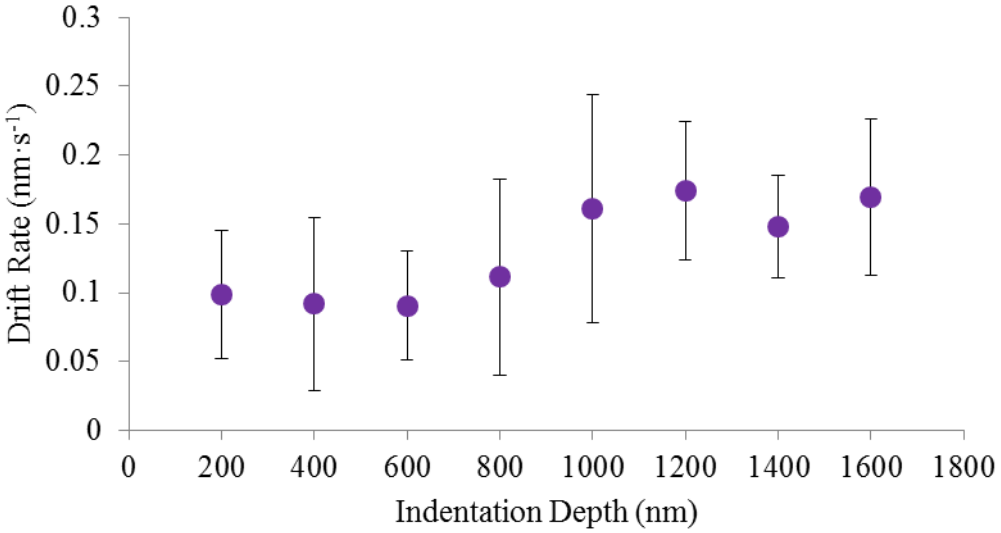

Figure 188: Drift Rate vs. Depth for Nanoindentation of Irradiated 45° LAM 316L Stainless Steel

The nanoindentation hardness data, with false-engages and other mechanical errors excluded, of unirradiated and irradiated 316L samples are summarized in Figure 189. Hardness increases noticeably with decreasing indentation depth for all unirradiated and irradiated samples, indicative of the ISE. The ISE is common in ductile crystalline materials and arises as a result of geometrically necessary dislocations which must be present in the plastic deformation zone near the indent tip in order to accommodate the volume of material being displaced by the indenter probe [67-73]. Not shown in Figure 189 is nanoindentation data for the Inconel 600; this data was not be collected due to instrument damage.

Nanoindentation data shows that the unirradiated hardness for 316L stainless steel depends on build orientation where, from highest to lowest hardness: horizontal LAM > 45° LAM > vertical LAM > conventionally manufactured. This agrees closely with the tensile testing data shown in Figure 171. As to be expected, radiation-induced hardening is observed in all samples [8, 21, 125-128]. However, the radiation-induced hardening is also orientation dependent where, from highest to lowest: horizontal LAM > 45° LAM > vertical LAM > conventionally manufactured (approximately 56%, 53%, 46%, and 34%, respectively).

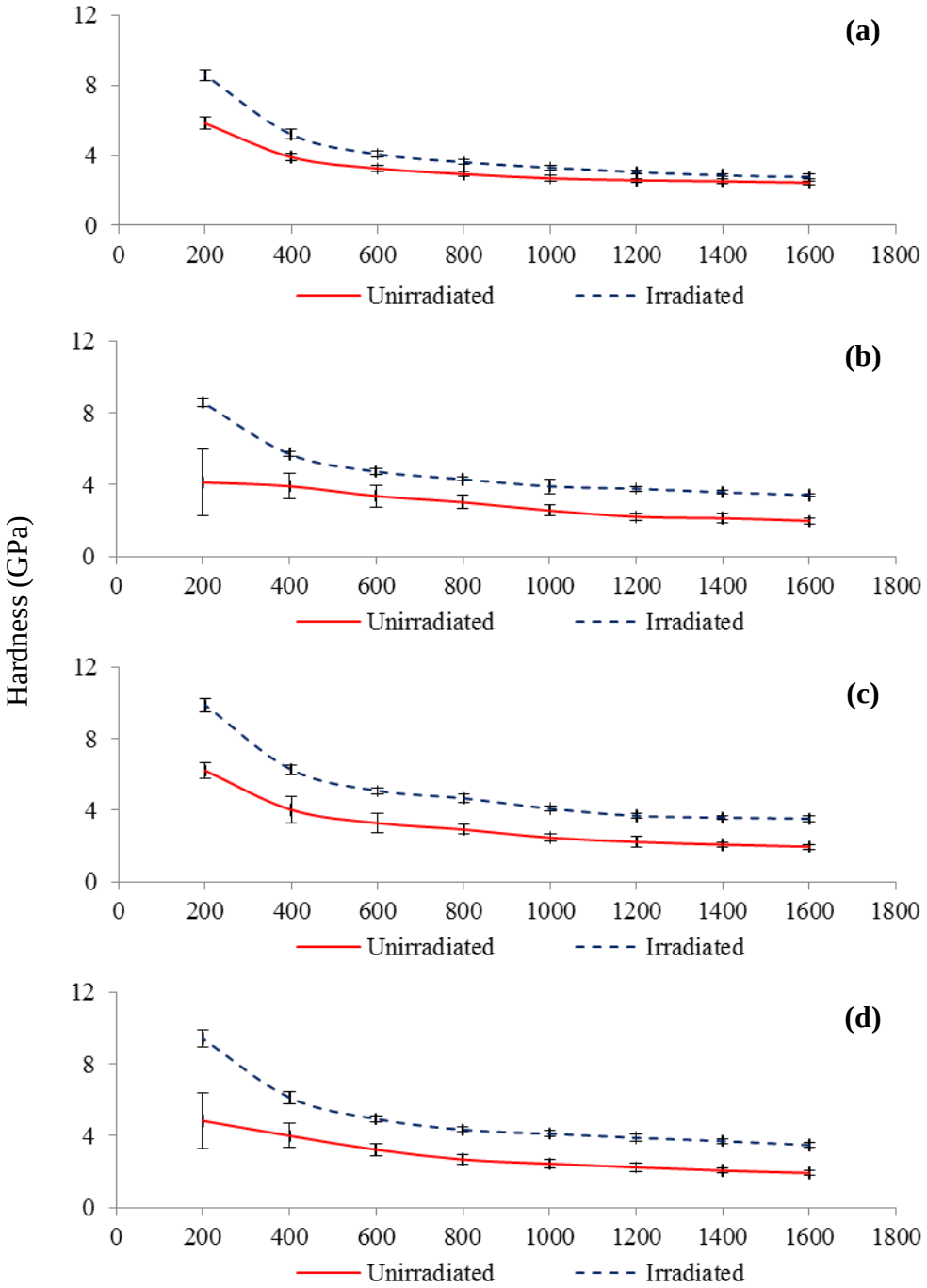

Figure 189: Nanoindentation Hardness of 316L Stainless Steel (a) Conventionally Manufactured, (b) Vertical LAM, (c) Horizontal LAM, and (d) 45 LAM

IV.5 Transmission Electron Microscopy

TEM was performed on Inconel 600 and 316L stainless steel lamellae prepared via the FIB lift out technique. A high magnification TEM image (400kx magnification) of the platinum mask on a LAM Inconel lamella is shown in Figure 190. The bright concentric rings in the diffraction pattern of the Pt mask in Figure 190 indicate that the mask deposited by the FIB is amorphous in structure. If the material was crystalline in structure without microstructural misorientation, then the DP would show constructive electronic interference points in a grid-like pattern. If the material is crystalline with moderate misorientation, then the DP will reveal diffraction points that appear blurry. For a review of TEM, see Ch. II.6.

If the material is crystalline with significant misorientation, the DP will reveal diffraction points with central rings around the center of the image, indicating a mixture of crystalline and partially amorphous material. An example of this is shown in Figure 191 (400kx magnification) where the image is clearly in focus (atomic planes are visible) in crystalline areas, but are associated with significant misorientation and therefore cannot be properly indexed. As a result, if a diffraction pattern is collected too close to the Pt mask, then the DP may be distorted with amorphous rings from due to the interference from the Pt.

(a)

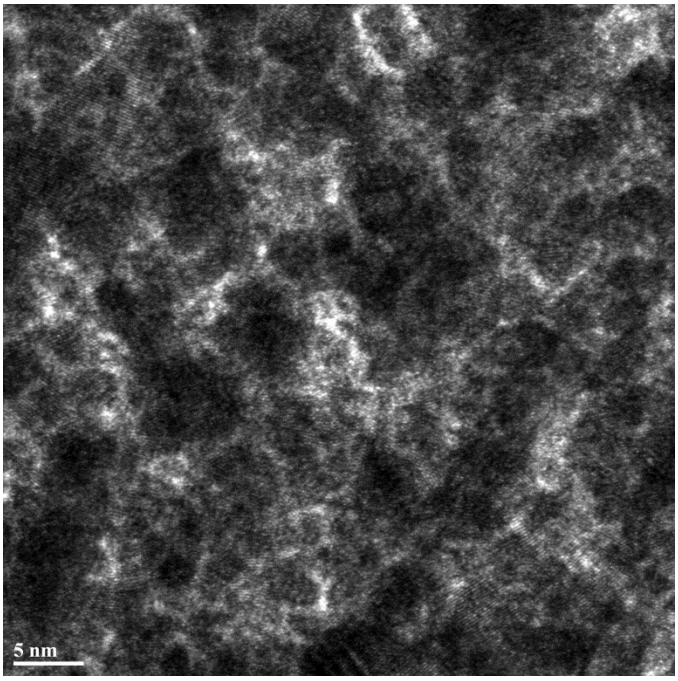

(b)

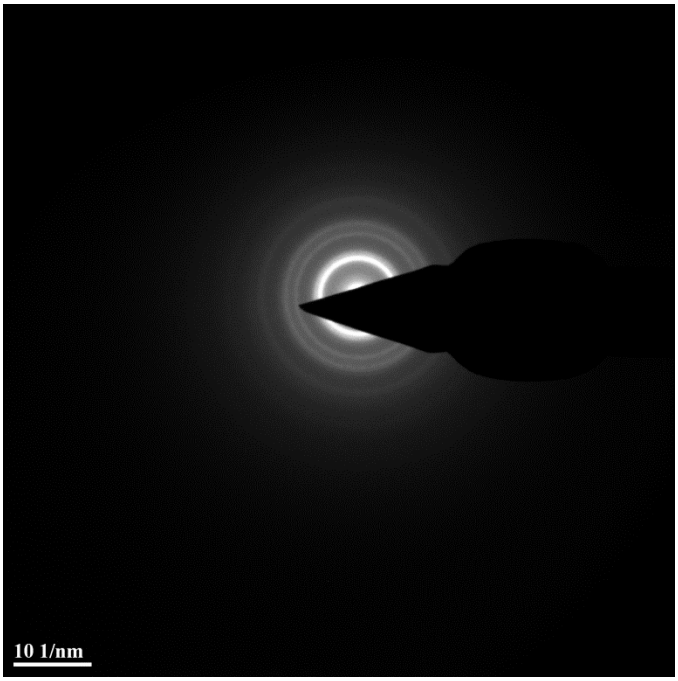

Figure 190: (a) TEM Image of Platinum Mask on the Surface of a TEM Lamella, and (b) the Platinum Mask Diffraction Pattern

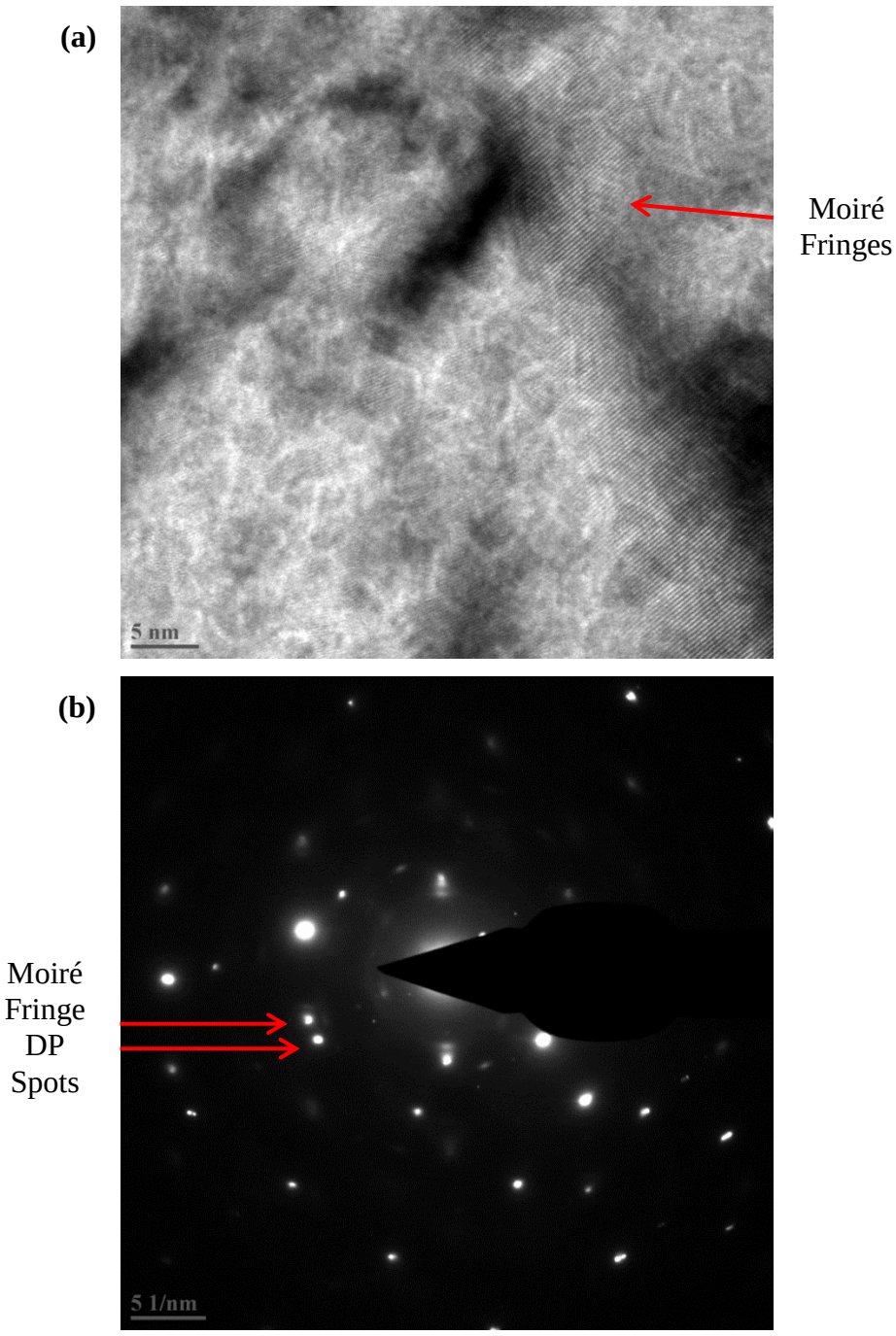

Figure 191: TEM Image of (a) Moiré Fringes in Unirradiated Inconel 600 Vertical LAM with (b) Associated SADP showing Misorientation

The irradiated surface of the vertical LAM I600 specimen is shown at the bottom of Figure 192 where **B** is build direction. The contrast between the irradiated surface and the unirradiated subsurface is clearly visible in the bright field transmission electron micrograph (BFTEM) images. The dark features in the BFTEM images indicate regions of less electron transmission, while the bright areas are regions with greater electron transmission. These features are typically caused by (a) heterogeneous stress fields in the vicinity of defects such as dislocations, (b) precipitates, or (c) areas of reduced atomic density (i.e. voids, which always appear bright in BFTEM images).

Based on Figure 192 the Ni^{+} ion penetration depth varies with location. This could be due to (a) material heterogeneities, such as stress fields or precipitates, or (b) ion channeling. Further, as shown on the left side of the TEM image in Figure 192, the boundary between the radiation-damaged surface and the undamaged subsurface reaches a maximum depth of about 1.86 μm. This is several hundred nm further than the predicted maximum depth from SRIM simulations (see Figure 62). This phenomenon has been previously observed in literature and is attributable to radiation-produced defect migration into the unirradiated subsurface [129].

EBSD results showed that the LAM Inconel and 316L rods were produced with significant residual strain (see Figure 163 and Figure 164). These residual strain fields could be associated with significant stress fields. Certain atomic orientations yield "channels" through which ions can travel, i.e. ion channeling. During ion channeling, the ion interacts primarily with the material's electron cloud rather than crystalline nuclei. These electronic interactions result in small ion scattering angles, which in turn

influence the ion's range through the material as it slows down by a factor of up to 50 [130] [131]. The scattering conditions change during channeling, so the collision cascades change as well, moving the number of ejected secondary electrons and sputtered ions further from the surface of the material. This is ultimately responsible for the image contrast in FIB images where grains (which have differing orientations relative to the ion beam) are clearly visible.

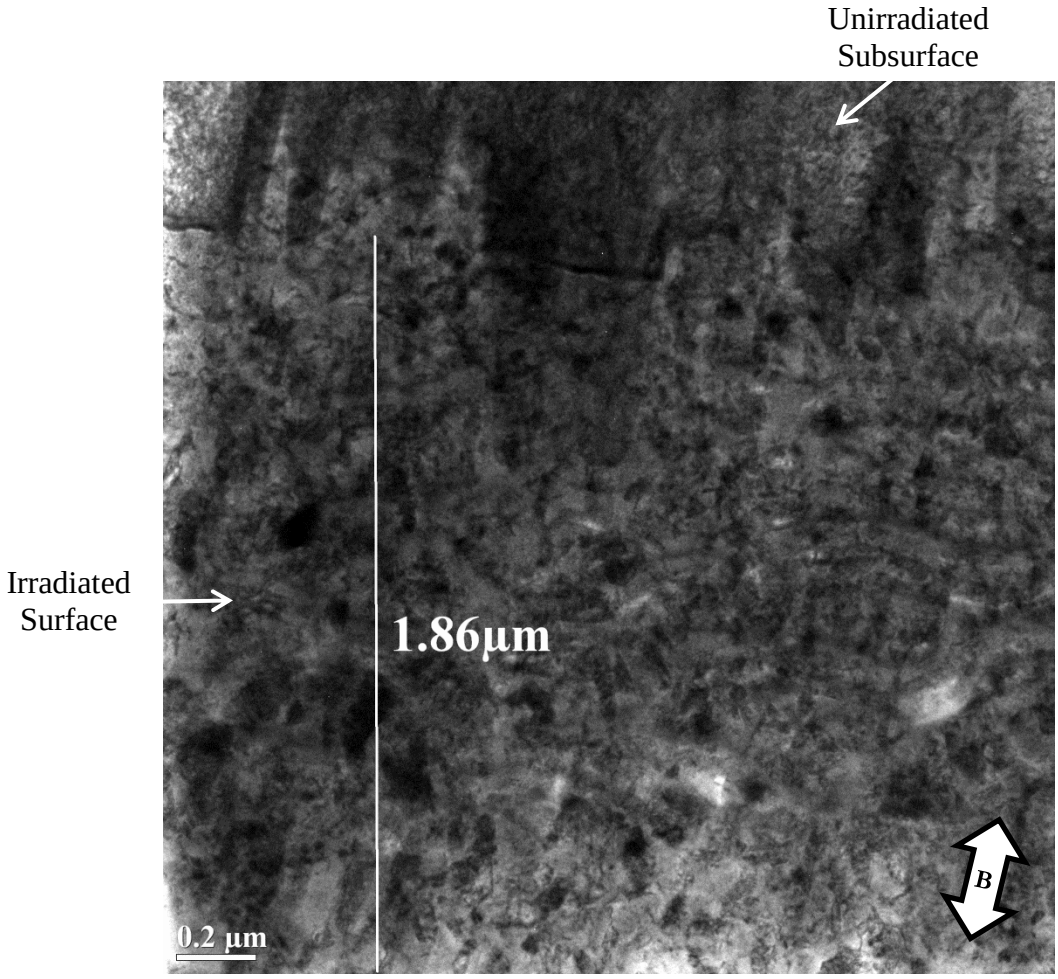

Figure 192: TEM Image of Irradiated Surface of Vertical LAM Inconel 600, 8700x Magnification

The TEM image in Figure 193 reveals features in the peak dose region of irradiated Inconel 600 vertical LAM. The associated indexed SADP, as viewed along $[-1.22, -1.22, 0]$, shows that this region of the crystal is fcc in structure as expected, with misorientation and possibly a collection of other phases or precipitates. HRTEM of this area (Figure 194) reveals significant misorientation between bright and dark areas. Some of the larger features in Figure 193 are also visible in HAADF STEM imaging; see Figure 196 where intensity is shown in counts per second (cps). The EDS spectra from the line scan of irradiated Inconel 600 vertical LAM in Figure 196 clearly shows that the dark features are nickel and iron-depleted chromium precipitates.

These dark features are especially large near and at grain boundaries, as shown at the peak dose depth of Inconel 600 horizontal LAM in Figure 197. The EDS line scan of the HAADF STEM image shows that radiation-induced migration of chromium yields large chromium precipitates at the grain boundaries of the Inconel 600 (Figure 198 and Figure 199). Densely packed oriented defects are observed in HRTEM images of regions far from grain boundaries, such as those shown in Figure 200 for irradiated Inconel 600 horizontal LAM. Based on the geometry of the surrounding stress fields, the defects in Figure 200 appear to be densely packed oriented edge dislocations (see Figure 201) [132].

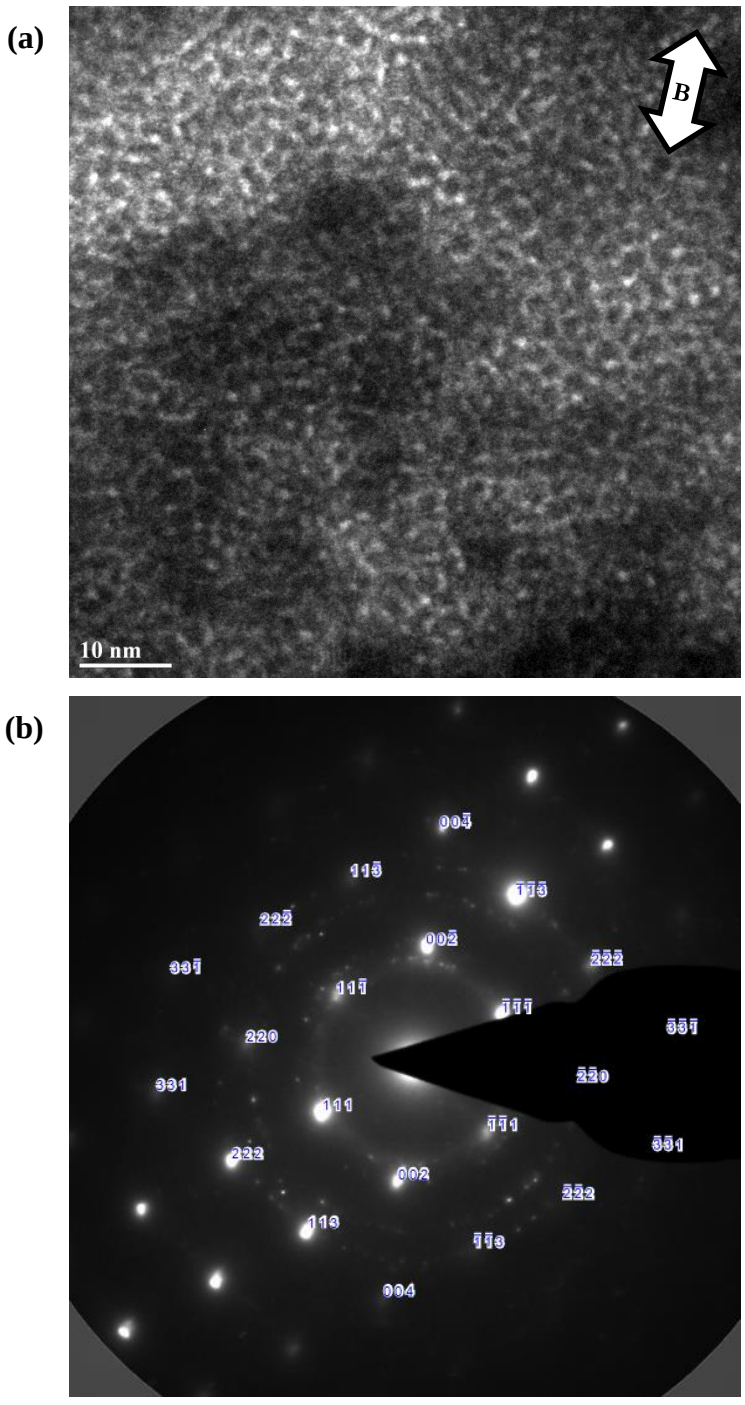

Figure 193: (a) BFTEM Image of Irradiated Inconel 600 Vertical LAM at the Peak Dose Depth, and (b) the Indexed SAPD

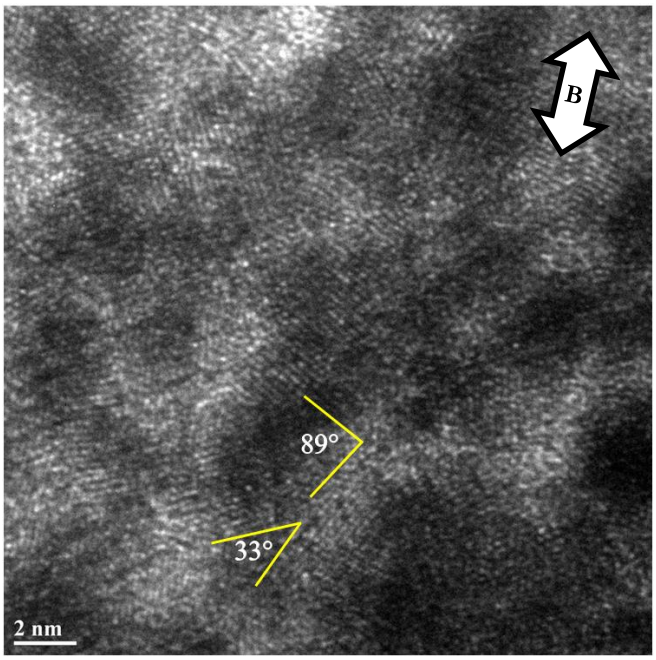

Figure 194: HRTEM Image of Irradiated Inconel 600 Vertical LAM at Peak Dose Depth showing Regions of Misorientation

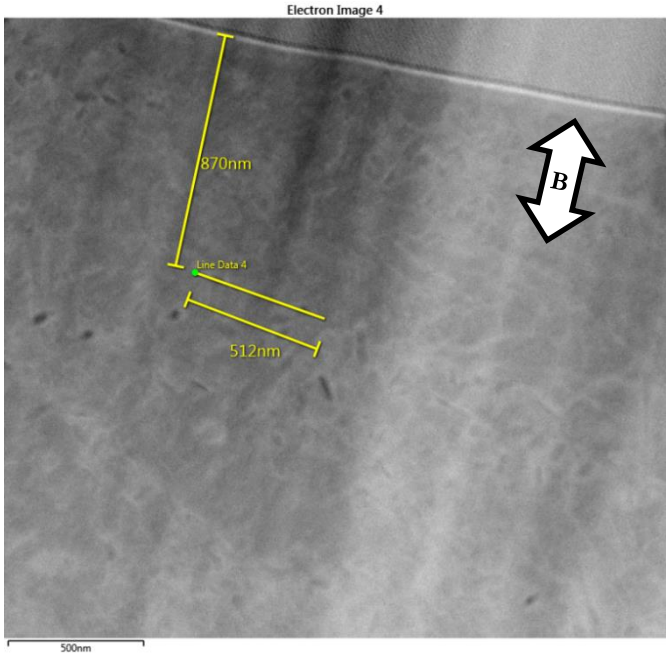

Figure 195: HAADF STEM Image of Dark Features on Irradiated Inconel 600 Vertical LAM near the Peak Dose Depth

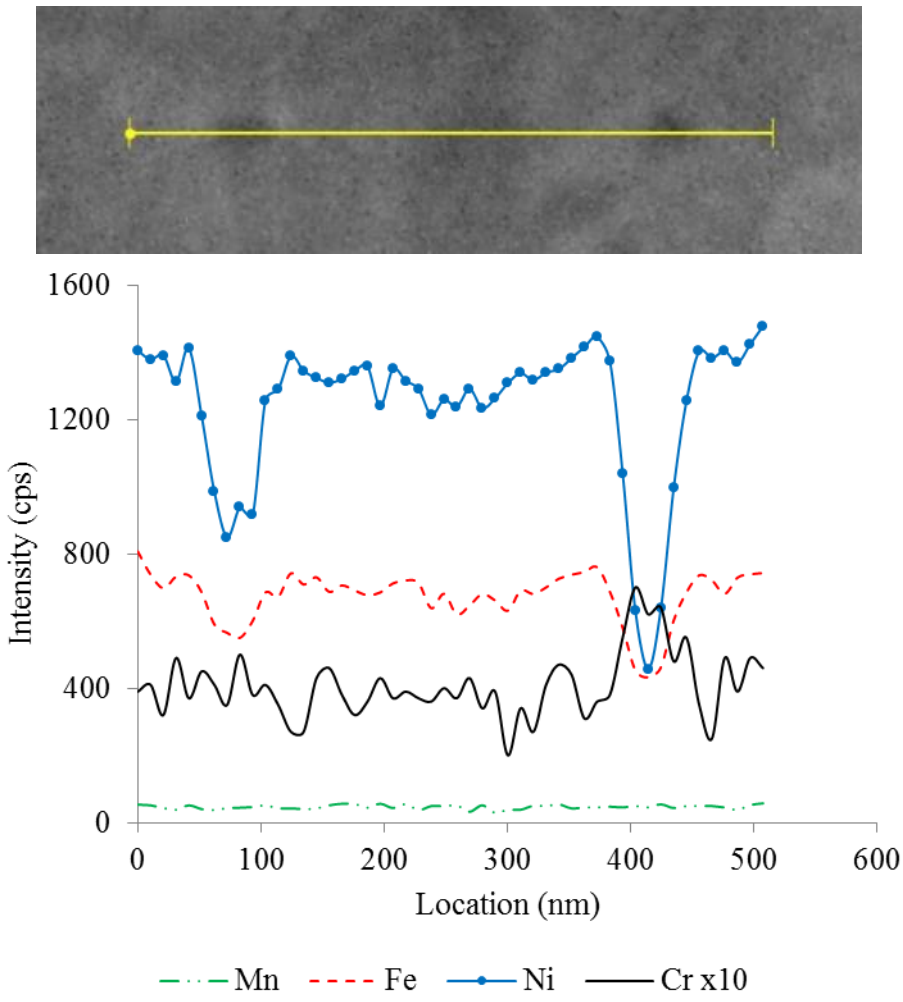

Figure 196: EDS Spectra of HAADF STEM Line Scan over Dark Features on Irradiated Inconel 600 Vertical LAM showing Chromium Precipitates with Drop in Nickel and Iron

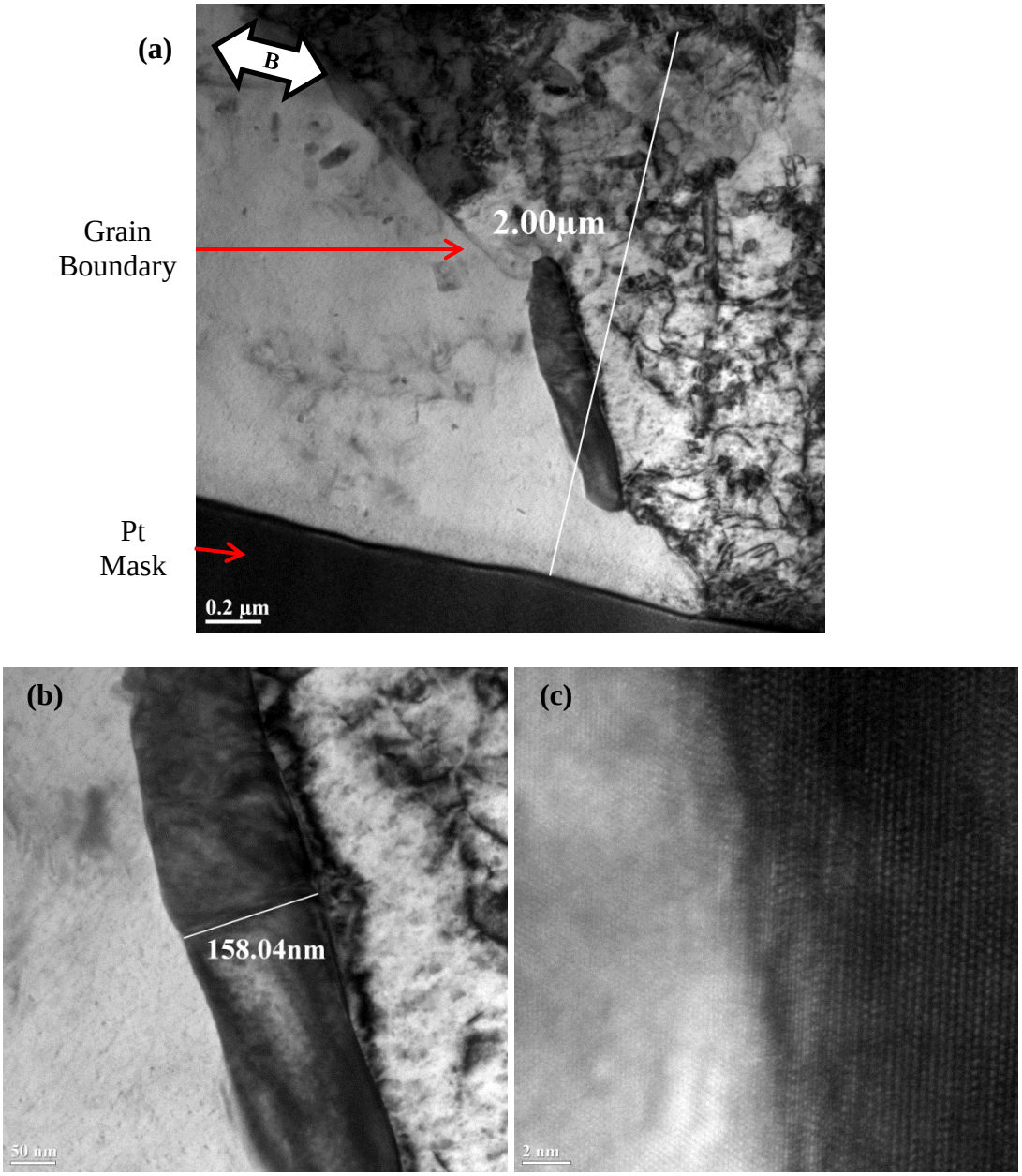

Figure 197: (a) TEM Image of Irradiated Inconel 600 Horizontal LAM, (b) HRTEM of the Dark Feature at the Grain Boundary, and (c) HRTEM Image showing Dark Feature Crystallinity

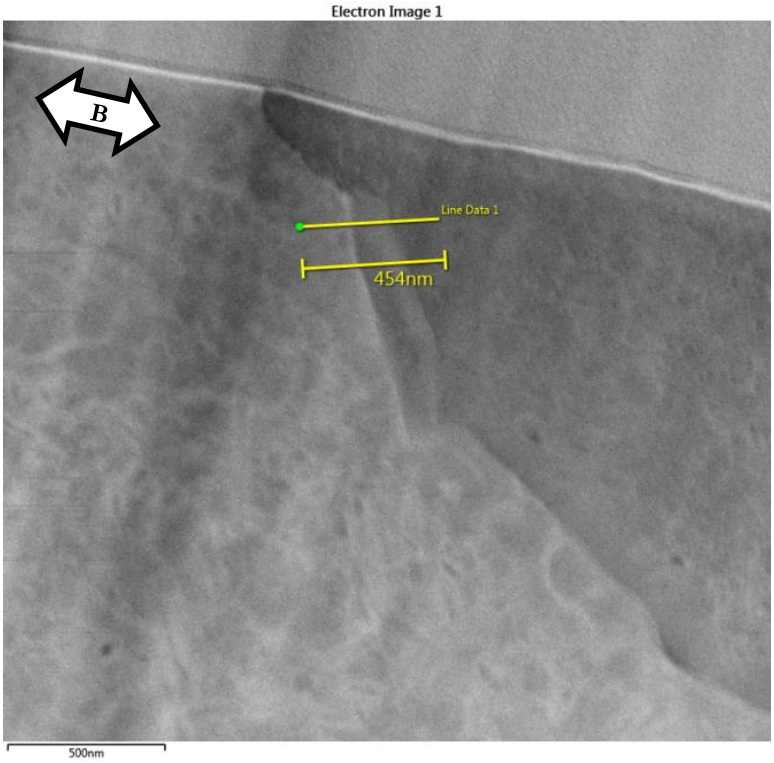

Figure 198: HAADF STEM Image of Peak Dose Feature at the Grain Boundary of Irradiated Inconel 600 Horizontal LAM

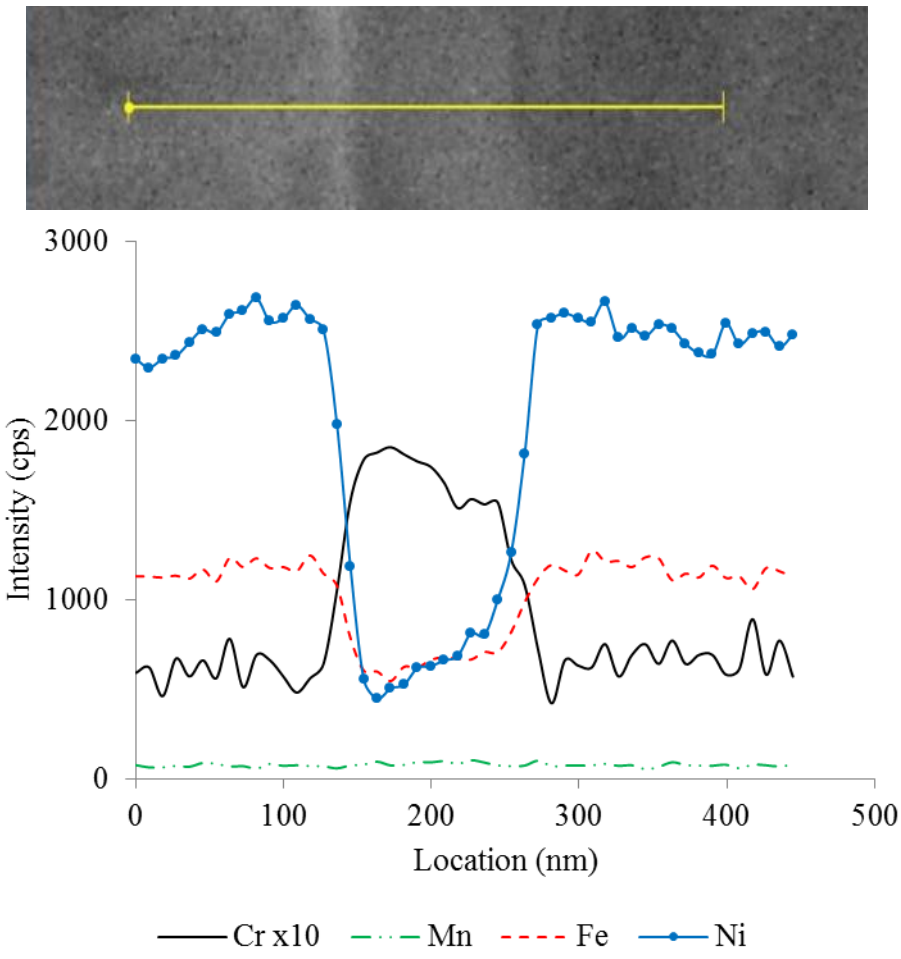

Figure 199: EDS Spectra of HAADF STEM Line Scan showing Chromium Precipitate due to Radiation-induced Chromium Migration to a Grain Boundary in Irradiated Inconel 600 Vertical LAM

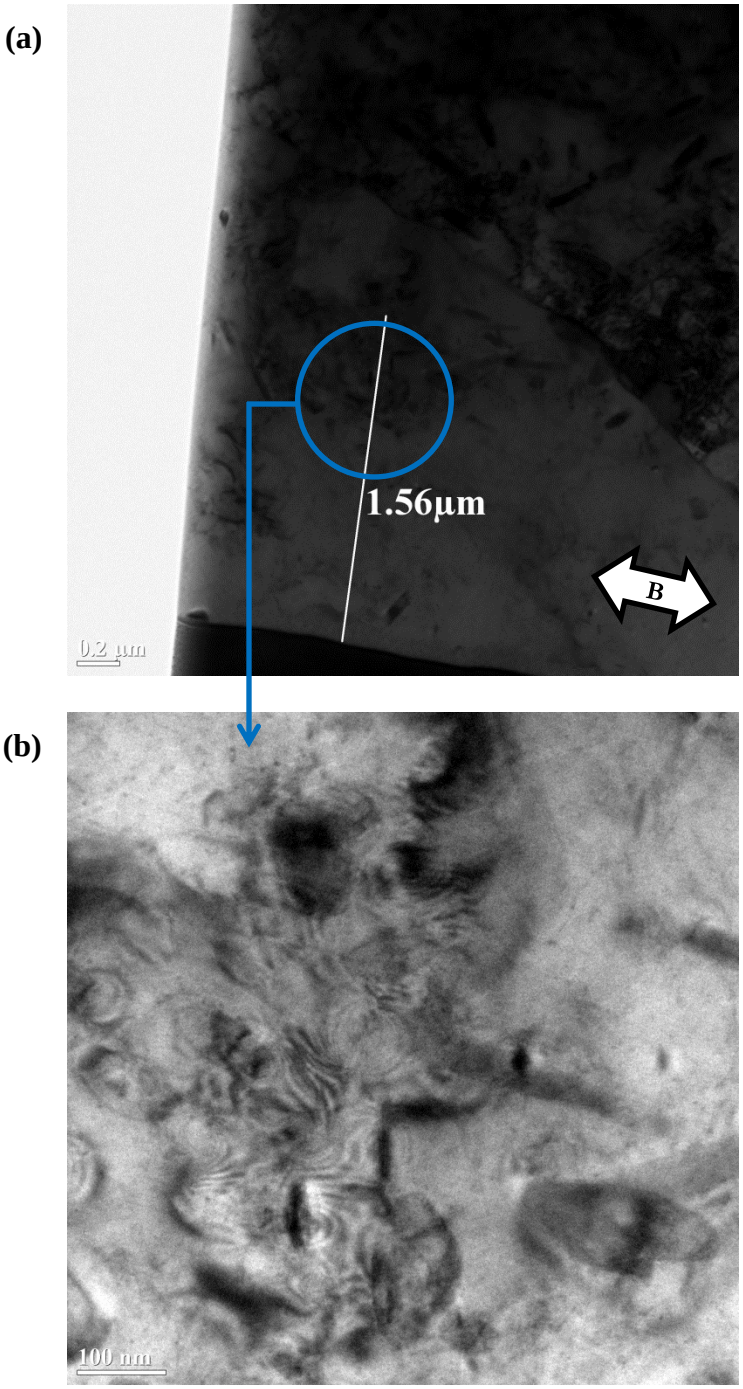

Figure 200: (a) TEM Image of Irradiated Inconel 600 Horizontal LAM, and (b) HRTEM Image Revealing Densely Packed Defects

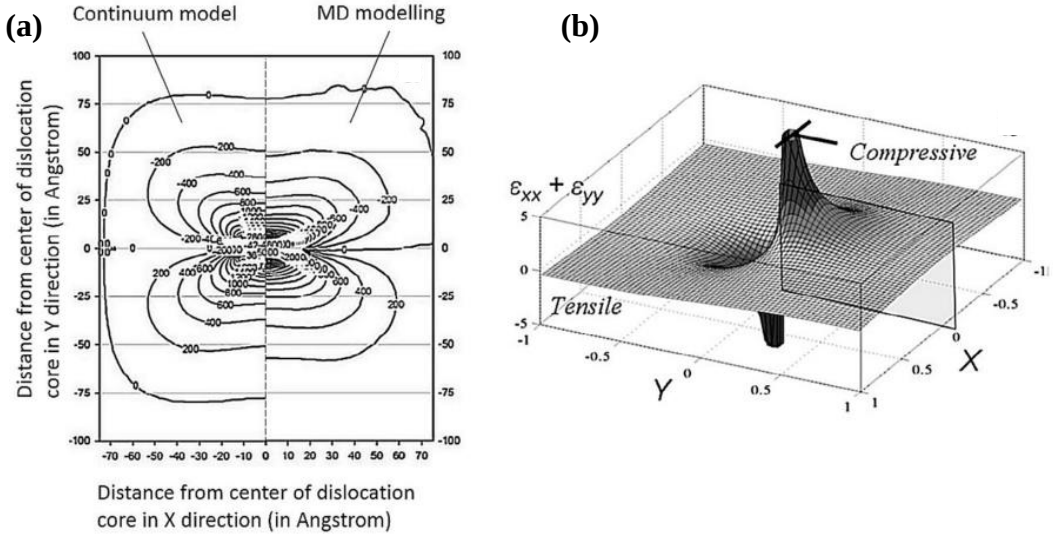

Figure 201: Stress Fields around Interstitial Edge Dislocations, where (a) the Contours Plot Stress Values (in MPa), and (b) the Strain Dipole around the Dislocation

High magnification TEM images of the LAM samples reveal dense regions of elongated oriented dislocation networks, as shown in Figure 202. Though significant residual strain existed before irradiation, the defect structures appear much less elongated in the unirradiated subsurface (see Figure 203).

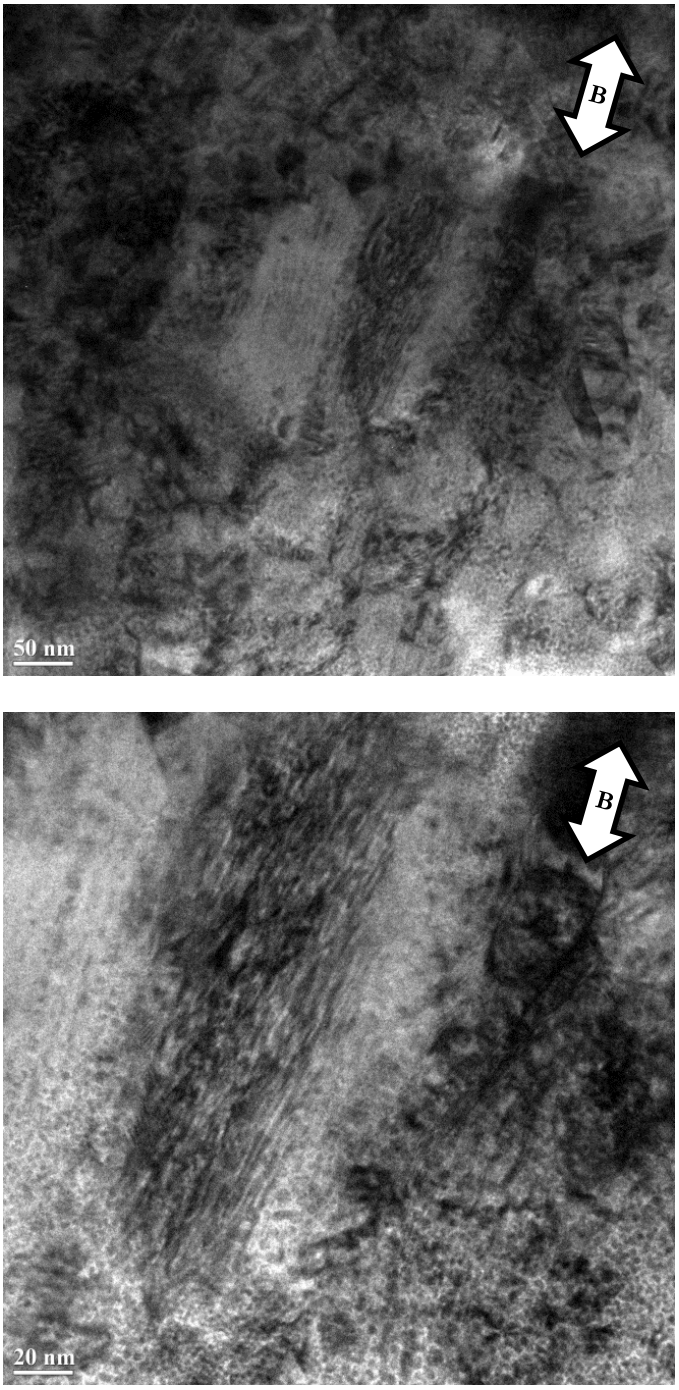

Figure 202: High Magnification TEM Images of Elongated Oriented Dislocation Networks near the Peak Dose Depth of Irradiated LAM Inconel 600

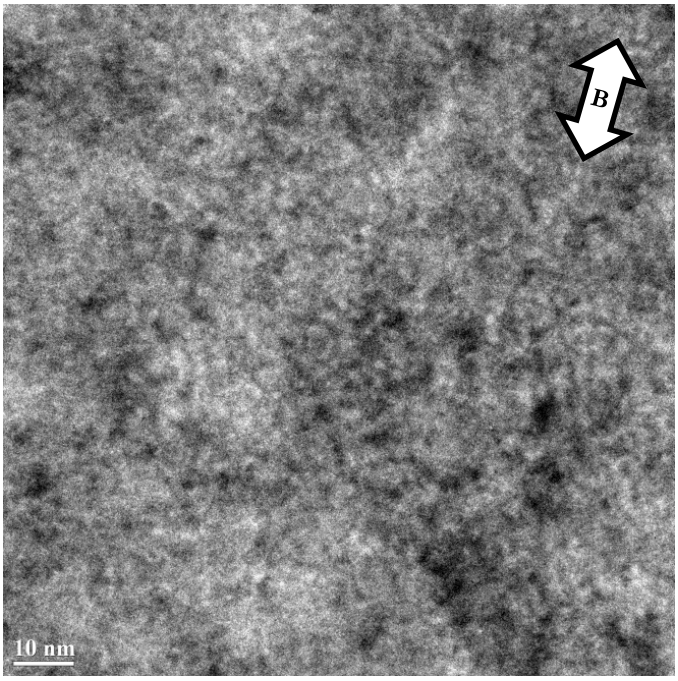

Figure 203: TEM Image of Unirradiated Subsurface in LAM Inconel 600 showing Less Defect Elongation

TEM images of the irradiated 316L stainless steel samples were collected in the same manner as with the Inconel 600. The 316L TEM lamellae took about 8-11 hours to prepare, as compared to the Inconel 600 samples which took 3-5 hours, since the steel samples are more resistant to ion beam damage. All as-fabricated additively manufactured samples contained significantly more defects than the conventionally manufactured control, shown in Figure 204 and Figure 205. The streaks in the 45° LAM are due to FIB damage during lamella preparation (Figure 205b). This sample was the first 316L lamella prepared, after having prepared several Inconel samples. The streaks shown were produced since there was no preset 316L FIB protocol, so the FIB settings for the previous material (Inconel 600) was initially used and eventually optimized for the new material.

The boundary between the irradiated surface and unirradiated subsurface of the samples is much clearer in the 316L than the Inconel 600, probably due to the lower irradiation temperature which is associated with less defect thermal diffusion, lower sputtering yield, etc. The dark features shown in the low magnification TEM images of the 316L samples are barely visible in HAADF STEM imaging (Figure 206). EDS spectra in Figure 207 of the HAADF STEM images (Figure 206) suggest that these features are not radiation-induced precipitates. Large regions of the 316L stainless steel LAM samples appear to contain defects which have dissociated due to radiation damage, as shown in Figure 208.

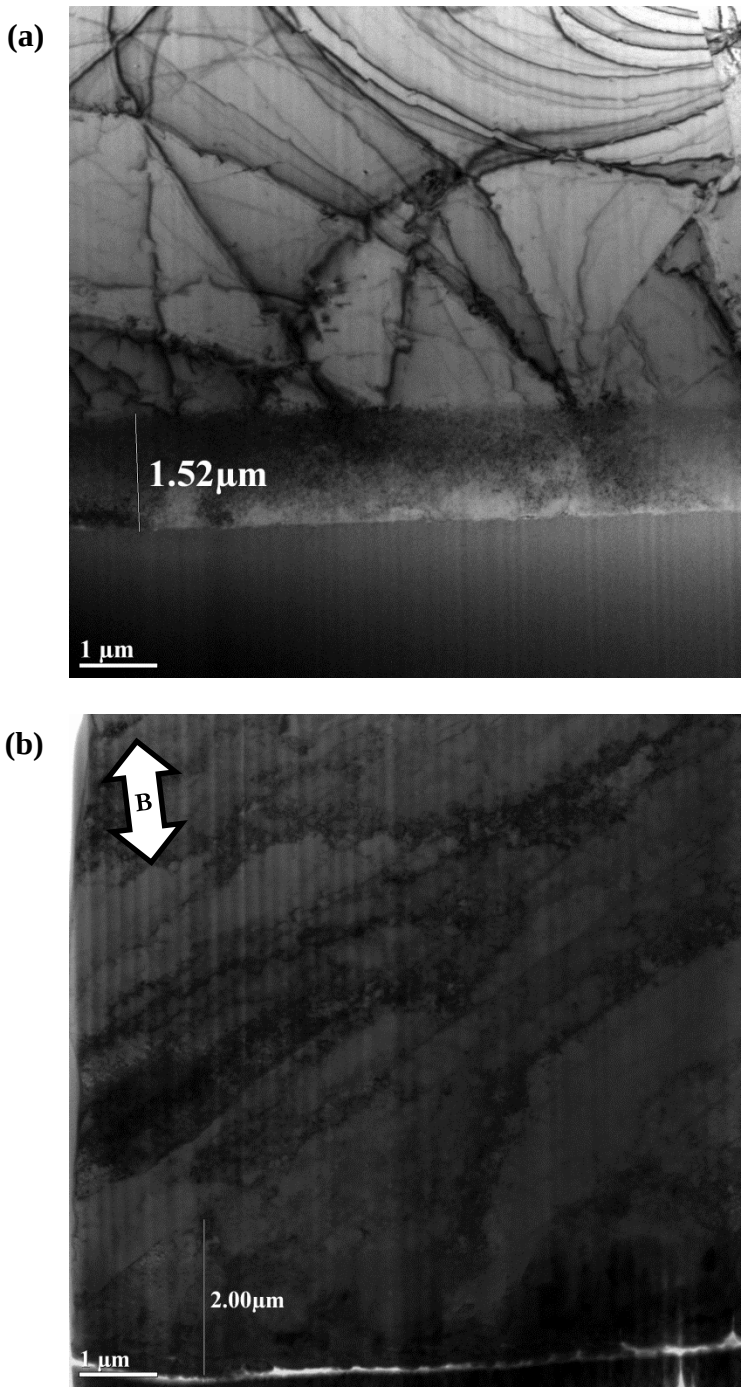

Figure 204: Low Magnification TEM Images of Irradiated 316L Stainless Steel (a) Conventionally Manufactured and (b) Vertical LAM

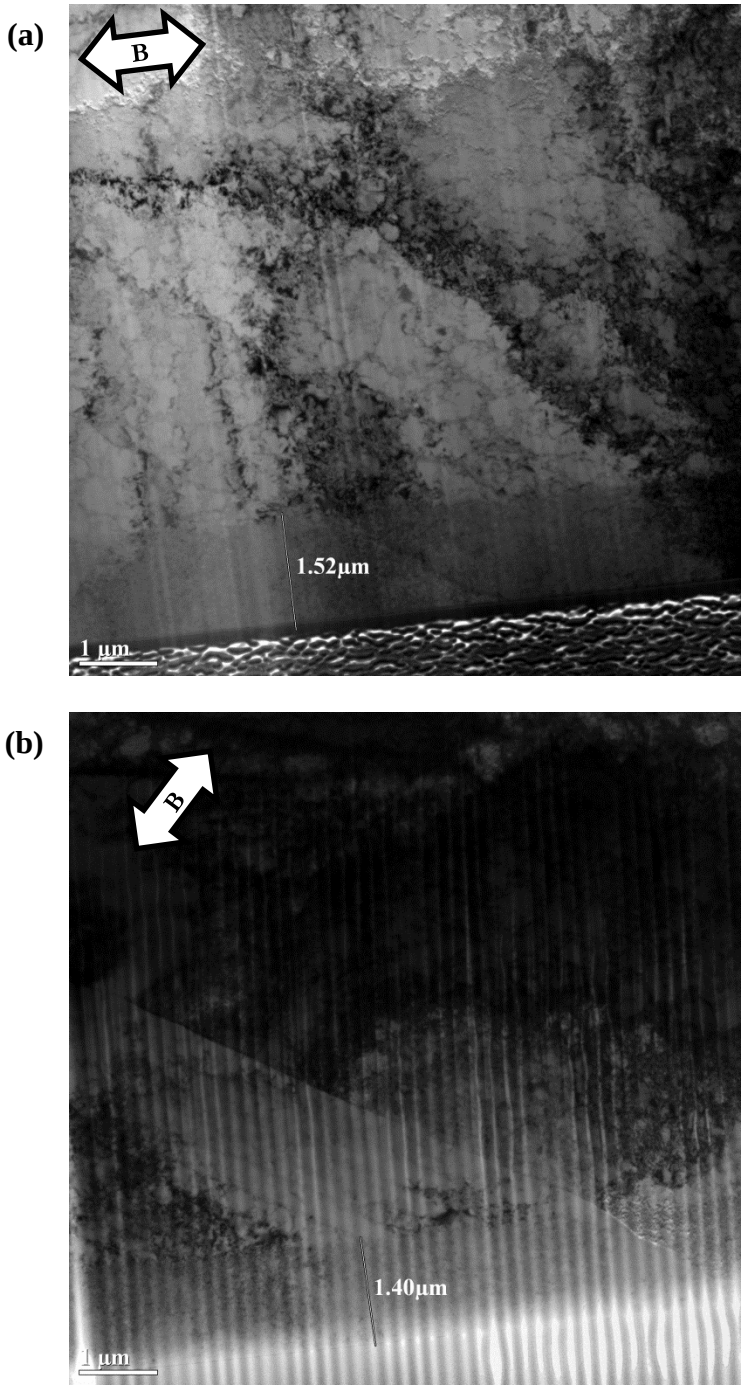

Figure 205: Low Magnification TEM Images of Irradiated 316L Stainless Steel (a) Horizontal LAM and (b) 45° LAM

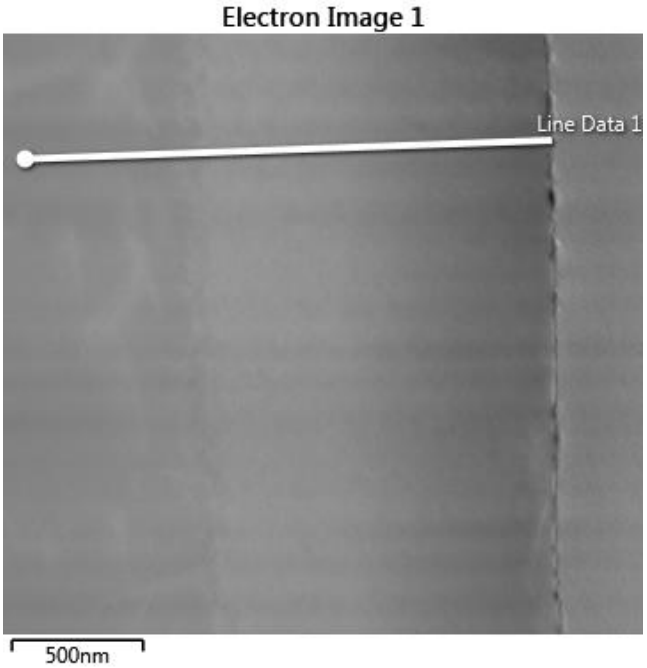

Figure 206: HAADF STEM Image of Irradiated 316L Stainless Steel Conventional Control

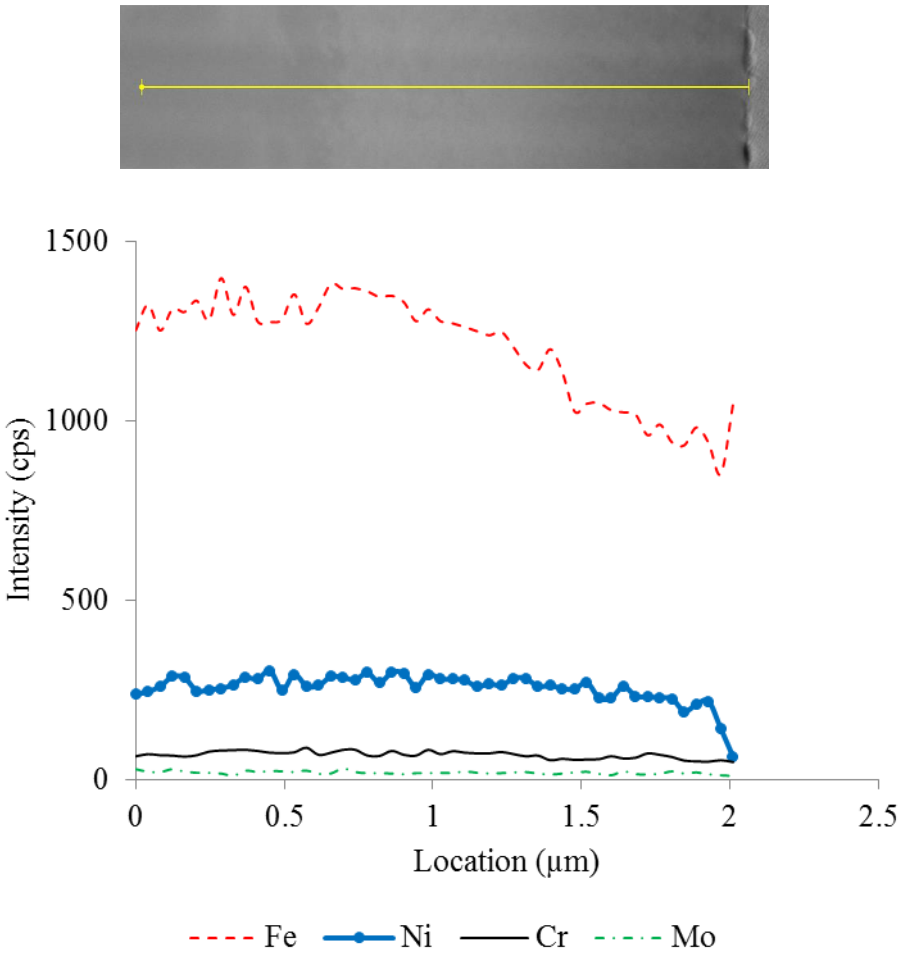

Figure 207: EDS Spectra of Line Scan of Irradiated Surface of Conventionally Manufactured 316L Stainless Steel

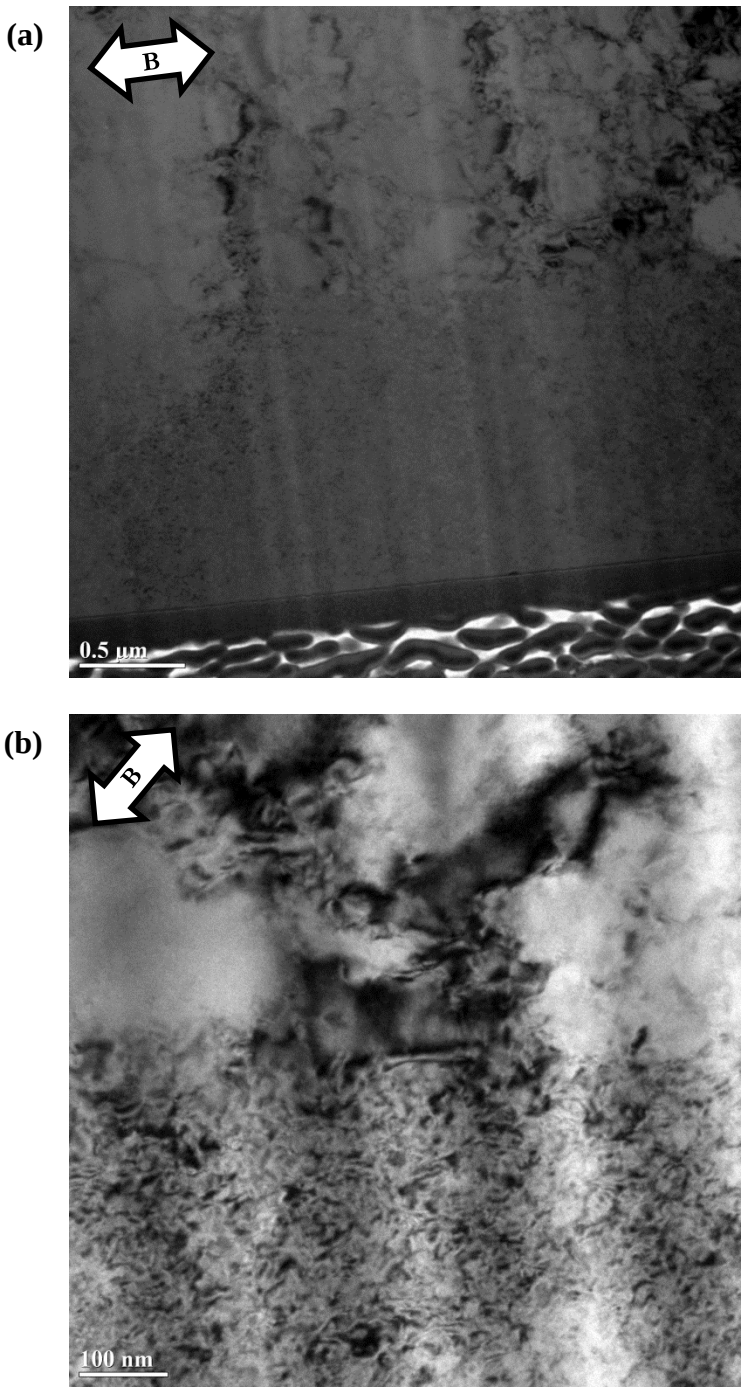

Figure 208: TEM Images showing Radiation-induced Defect Dissociation on the Irradiated Surface of (a) Horizontal LAM 316L and (b) 45° LAM 316L

The unirradiated subsurfaces of the 316L LAM samples contain regions with extremely high defect density. Radiation damage appears to dissociate these dense regions of defects. This can be understood by considering dislocation interactions. As dislocations and other defects are produced due to radiation damage, loops will grow until they encounter network dislocations or each other. When these loops interact, they can coalesce or contribute to the network dislocation density [30]. Assuming a constant dose rate, the radiation-induced dislocation density will eventually saturate. This requires a mechanism to exist which effectively removes dislocations from the matrix. This mechanism is assumed to be the mutual annihilation of pairs of dislocations of opposite sign, implying a reaction rate proportional to the square of the number of dislocations present. As such, the general time-dependent expression of dislocation density $\rho(t)$ during radiation bombardment is given by Eq. 21:

Eq. 21

$$\frac{\partial \rho(t)}{\partial t} = B\rho^{1/2} - A\rho^{3/2}$$

where

$$B \sim b^2\phi\,,\ A \sim v_c\,, \text{ and } v_c = b^2\left[z_i^d D_i C_i - z_v^d D_v C_v + z_c^d D_v C_{v0}^d\right] + v_{th}$$

In Eq. 21, b is the magnitude of the Burger's vector, ϕ is flux, v_c is the dislocation climb velocity, $z_{i,v}$ are the capture efficiencies of interstitials/vacancies of orientation j by dislocations, $D_{i,j}$ are diffusion coefficients of interstitials/vacancies, $C_{i,j}$ are concentrations of interstitials/vacancies, and v_{th} is the thermally-induced climb rate

which determines the rate of recovery in the absence of radiation [133]. Typically, thermally-induced climb is only significant in steels at temperatures above 650 °C [133]. From Eq. 22, the temporal boundary conditions are such that:

- $\rho(t=0)=\rho_0$
- $\rho(t=\infty)=\rho_{sat}=B/A$

where ρ_0 is the initial dislocation density and ρ_{sat} is the saturation dislocation density. Integrating and solving Eq. 21 yields the instantaneous dislocation density in Eq. 22. The dislocation density as a function of ion fluence can be predicted using Eq. 22 where, for example, initial dislocation densities of $5\cdot10^{8}$ cm^{-2} and $7\cdot10^{11}$ cm^{-2} are assumed for regions with low and high as-annealed dislocation densities, respectively, with a saturation density of 10^{11} cm^{-2}. Knowing the 3.5 MeV Fe^{2+} ion beam flux was $3.5\cdot10^{12}$ $ions\cdot cm^{-2}$ for ~13 hours at 475 °C, the dislocation density vs. ion beam fluence can be calculated as shown in Eq. 22.

Eq. 22

$$\rho(t)=\rho_{sat}\cdot\frac{1-e^{-\nu_c t\sqrt{\rho_{sat}}}+\left(1+e^{-\nu_c t\sqrt{\rho_{sat}}}\right)\sqrt{\rho_0/\rho_{sat}}}{1+e^{-\nu_c t\sqrt{\rho_{sat}}}+\left(1-e^{-\nu_c t\sqrt{\rho_{sat}}}\right)\sqrt{\rho_0/\rho_{sat}}}$$

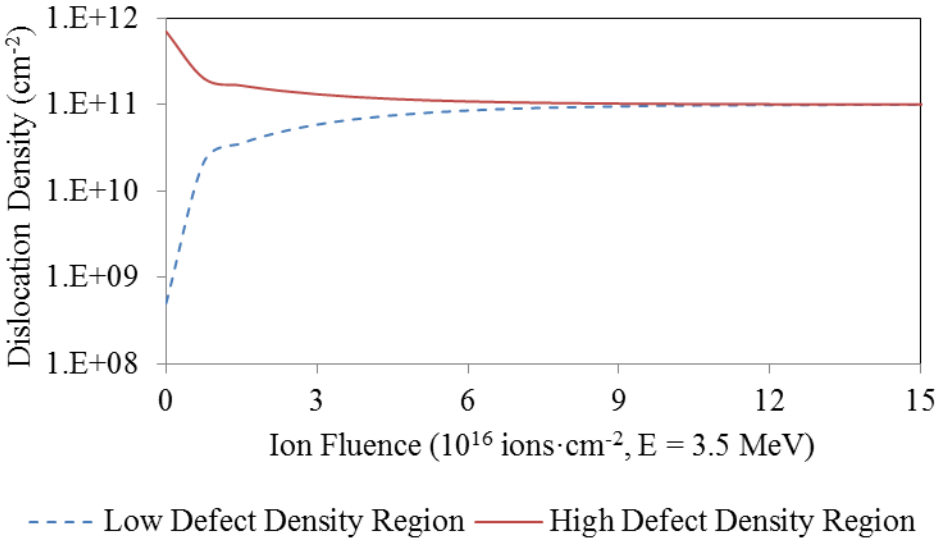

Figure 209: Dislocation Density vs. Ion Fluence for 316L Stainless Steel in Regions with Initially Low and High Defect Density, Calculated from Eq. 22

CHAPTER V

DISCUSSION

Taken altogether, the data from above yielded the following immediate conclusions from this work. The XRD results in Ch. IV.1.1 reveal that the unirradiated as-annealed LAM alloys have significant texture which is strongly dependent on build orientation. In summary, the close-packed atomic planes are predominantly in the build direction, contrary to the least close-packed atomic planes perpendicular to the build direction. The SEM/EDS results in Ch. IV.2 revealed that all Inconel 600 rods, including the conventionally manufactured control, were characterized by the formation of chromium/carbon rich precipitates on the irradiated surface, while no such precipitates were found on the surfaces of any of the irradiated 316L stainless steel samples.

Ch. IV.3 discussed the EBSD characterization of unirradiated and irradiated Inconel 600 and 316L stainless steel rods. Analysis of the grain boundaries showed that the grain sizes of the LAM and conventionally manufactured controls were all within ± 1 μm; however, the grain aspect ratios of the LAM were significantly larger than their conventionally manufactured counterparts. Further, grain slope orientation analysis of the LAM specimens revealed that the elongated grains were strongly oriented parallel to the laser/build direction. This analysis is summarized by the illustration shown in Figure 210.

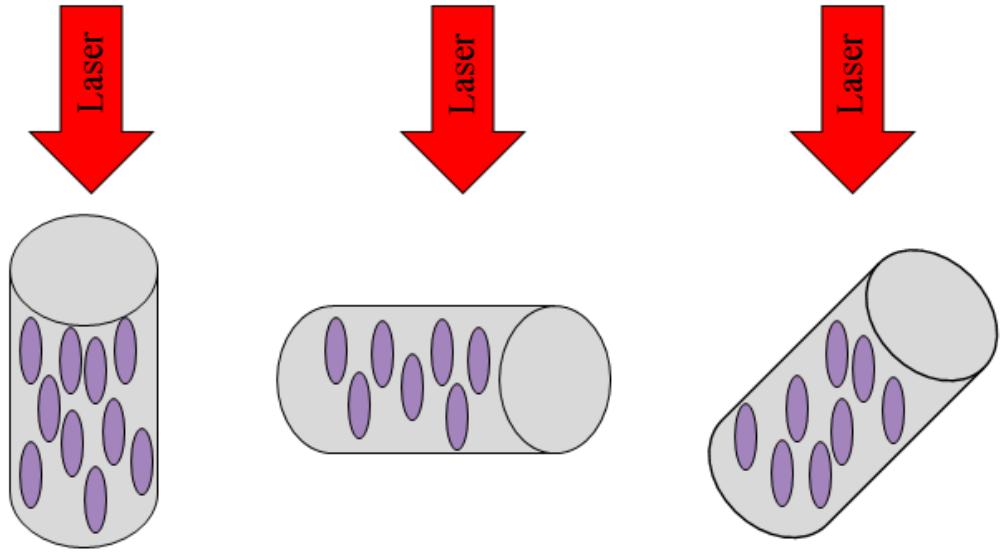

Figure 210: Illustration of the (Left) Vertical LAM, (Middle) Horizontal LAM, and (Right) 45° LAM with Elongated Oriented Grains (Purple Ellipses)

EBSD also revealed that the (elongated) LAM grains also contain significantly more texture than the (equiaxed) conventionally controls' grains. Specifically, inverse pole figures in Ch. IV.3.3 show that the vertical LAM of both Inconel 600 and 316L stainless steel is strongly textured with an accumulation of <110> parallel to the build direction. This analysis is summarized by the illustration shown in Figure 211. The grain boundary character of the LAM rods was much more random in comparison to their conventionally manufactured counterparts. This was described quantitatively in the context of coincidence site lattice theory in Ch. IV.3.4.

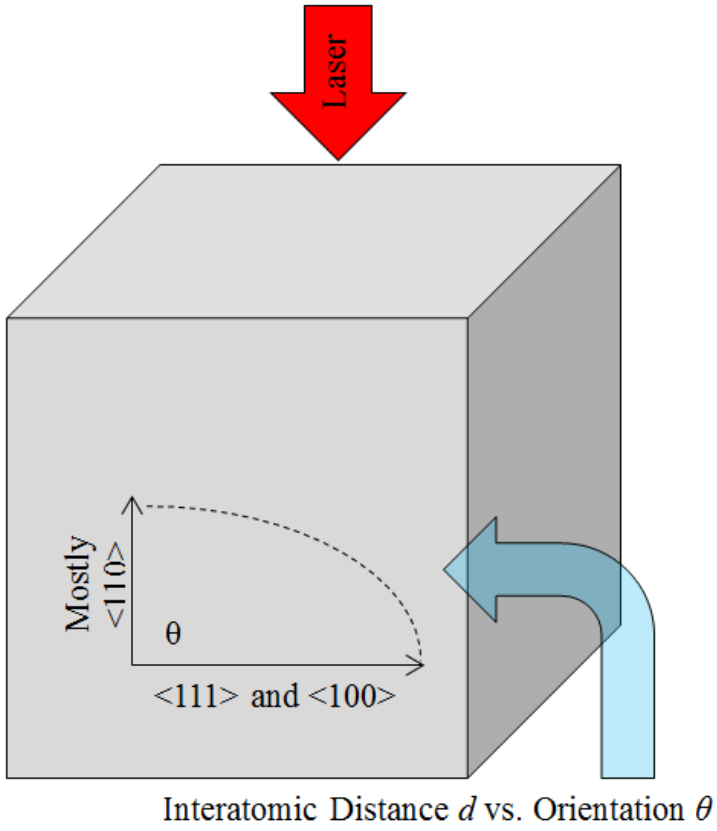

Figure 211: Illustration of Crystallographic Texture and Interatomic Distance vs. Build Orientation in Rods Built by LAM

Nanoindentation of unirradiated and irradiated specimens (see Ch. IV.4) revealed radiation-induced hardening which agrees closely with the tensile testing data collected from a Lockheed Martin unpublished report. In general, the hardening for LAM specimens was larger than for the conventionally manufactured controls. Transmission electron microscopy of irradiated specimens (Ch. IV.5) revealed that a variety of radiation-produced defects, such as precipitates, dislocations, and loops, appear to aggregate into oriented ellipsoidal defects.

There are additional items that require further explanation that are outlined in the following sections. These items arise due to the observed orientation-dependent radiation-induced segregation and hardening, which is strongly influenced by texture, grain orientation, and defect orientation. First, however, bulk material properties of the irradiated LAM rods may be predicted based on the data collected, and will be discussed first in Ch. V.1. The information and calculations developed in the following sections are presented to enable the deeper discussions in Ch. V. The impact of texture and manufacturing orientation on bulk properties is also described. Original derivations for property estimates are presented where necessary.

V.1 Bulk Material Property Relations

V.1.1 Calculation of Yield Strength and Modulus of Resilience

The point at which materials begin to plastically deform, known as the yield strength, σ_y, is related to nanoindentation hardness. Yield strength may be determined in several ways, such as: (1) theoretical derivation, (2) computational simulations, or (3) experimentation involving indentation or tensile testing. The ion beam-irradiated regions within the LAM-produced Inconel 600 and 316L stainless steel alloys are too small to conduct compression/tensile testing (less than 1.5 μm), and computational simulations are beyond the scope of this project. As a result, a brief discussion on a theoretical derivation of the yield strength will be presented which allows the yield strength to be approximated using indentation hardness.

It is important to note that several methods exist to enable the calculation of the yield strength of a material based on its nanoindentation hardness, all of which are empirical and based on a variety of different materials [65, 134, 135]. Clearly, the calculated value for yield strength will vary depending on which method is employed. Busby et. al. derived a relationship between yield strength and hardness using a Vickers indenter (H_V) based on the theoretical approach of Prandtl and von Mises which will be summarized here and is used in this work [134].

With the starting assumption that indentation causes plastic deformation, the subsurface material is considered to respond in a flow pattern similar to the one illustrated below in Figure 212 [65]. Not all of the applied stress is perpendicular to the sample surface during nanoindnetation, but rather stress components parallel to the sample surface (i.e. shear) must also be considered. Plastic deformation initiates when the internal mechanical energy exceeds the limit for yielding, which may be approximated using the von Mises yield criterion shown below in Eq. 23 in standard tensor notation, where T^{VM} is the von Mises stress and t_{ij} are the components of the stress tensor.

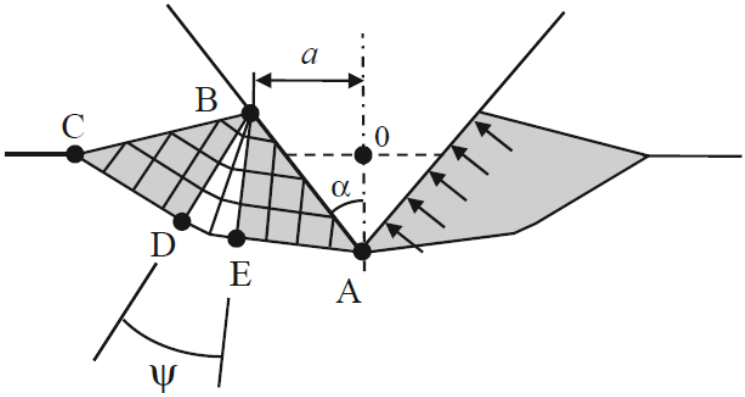

Figure 212: Illustration of Microstructural Flow Pattern in a Ductile Material during Pyramid Probe Nanoindentation (Reprinted from [65])

Eq. 23

$$T^{VM} = \sqrt{-\frac{1}{2}\left(t_{kk}\right)^2 + \frac{3}{2}t_{ij}t_{ij}} = \sqrt{\frac{1}{2}\left[\left(t_{xx}-t_{yy}\right)^2 + \left(t_{yy}-t_{zz}\right)^2 + \left(t_{zz}-t_{xx}\right)^2\right] + 3\left(t_{xy}^2 + t_{yz}^2 + t_{zx}^2\right)}$$

For further background information related to the physics and mathematics of elasticity theory and stress field analysis, the references [136, 137] are recommended. In the standard 2D nanoindentation problem, $t_{zz} = t_{zx} = t_{zy} = 0$, yielding Eq. 24. The von Mises yield criterion occurs at the critical shear stress, $t_{xy} = k$ in Eq. 25, where k is the yield stress of the material in pure shear.

Eq. 24

$$T^{VM} = \sqrt{t_{xx}^2 + t_{yy}^2 - t_{xx}^2 t_{yy}^2 + 3t_{xy}^2}$$

Eq. 25

$$T^{VM} = \sigma_y = \sqrt{3k^2}\ ,\ k = \frac{\sigma_y}{\sqrt{3}}$$

For the case of the Vickers tip, the plastic flow illustrated in Figure 212 is described by the Prandtl solution, yielding a pressure normal to the sample surface (p_n) shown in Eq. 26 [138]. Combining Eq. 25 and Eq. 26 yields Eq. 27 which defines the ratio of indentation load to the indenter/sample contact area. The geometry of the Vickers tip is illustrated in Figure 213 [139]. The projected area (A_{proj}) and contact area (A_{cont}) under the Vickers indenter are also provided, where h is the depth of the indent.

Eq. 26

$$p_n = 2k\left(1+\frac{\pi}{2}\right)$$

Eq. 27

$$p_n = 2\left(\frac{\sigma_y}{\sqrt{3}}\right)\left(1+\frac{\pi}{2}\right) \approx 2.96\sigma_y$$

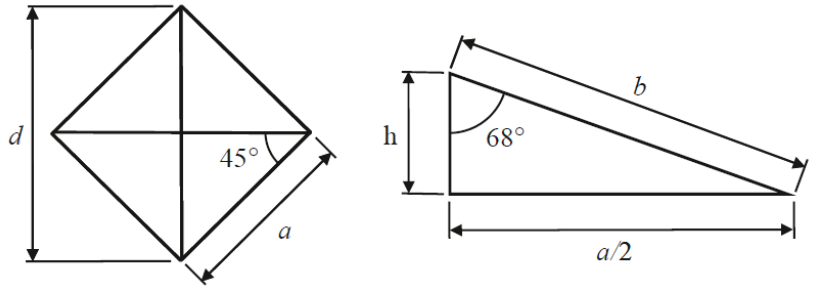

Figure 213: Geometry of the Vickers Indenter Probe (Reprinted from [140])

Projected Area under Vickers Indenter Probe:

$$\sin\left(45°\right) = \frac{d}{\left(2a\right)}$$

$$a = \frac{d}{\sqrt{2}}$$

$$A_{proj} = a^2 = \frac{d^2}{2}$$

$$\tan\left(68°\right) = \frac{a}{\left(2h\right)}$$

$$a = 2h \cdot \tan\left(68°\right)$$

$$A_{proj} = 4h^2 \tan^2\left(68°\right) \approx 24.504h^2$$

Contact Area under Vickers Indenter Probe:

$$A_{cont} = 4\frac{ab}{2}$$

$$\sin\left(68°\right) = \frac{a}{2b}$$

$$b = \frac{a}{2\sin\left(68°\right)}$$

$$A_{cont} = \frac{a^2}{\sin\left(68°\right)} = \frac{4h^2 \tan^2\left(68°\right)}{\sin\left(68°\right)}$$

$$A_{cont} \approx 26.429h^2$$

The hardness measurement from nanoindentation is defined by Eq. 11. The Vickers indentation hardness (H_V) with respect to the normal pressure (p_n) can be determined by combining Eq. 11 and Eq. 28, yielding the important relationship in Eq. 29.

Eq. 28

$$H_V = p_n \cdot \frac{A_{proj}}{A_{cont}}$$

Eq. 29

$$H_V = p_n \cdot \frac{A_{projected}}{A_{contact}} = p_n \cdot \frac{4h^2 \tan^2(68°)}{\left[\frac{4h^2 \tan^2(68°)}{\sin(68°)}\right]} \approx p_n \cdot \frac{24.504 h_c^2}{26.429 h_c^2} = 0.927\, p_n$$

Combining Eq. 27 and Eq. 29 gives Eq. 30 which relates the indentation hardness measured via a Vickers tip to the sample's yield strength, which is the objective of this derivation, where the constant *0.364* is dimensionless. A literature review reveals that finite element analysis of the relationship between indentation hardness and yield strength agrees somewhat with the results from this theoretical approach, though errors in the value of the dimensionless constant exist for different materials [141, 142].

Eq. 30

$$\sigma_y = 0.364 \cdot H_V$$

Experimental data collected from a variety of austenitic and ferritic/martensitic steels show that the constant in Eq. 30 which relates Vickers hardness (H_V) to yield strength (σ_y) varies from *0.217* to *0.372* [142, 143]. Vickers hardness is related to the Berkovich hardness (H_{Berk}) through the suitable scaling parameter in Eq. 31 [144]. By combining Eq. 30 and Eq. 31, the yield strength of the sample can be approximated with the indentation hardness using a Berkovich tip (H_{Berk}) via Eq. 32.

Eq. 31

$$H_V = 0.0926 \cdot H_{Berk}$$

Eq. 32

$$\sigma_y = 0.0337 \cdot H_{Berk}$$

The modulus of resilience, U_r, is defined by the amount of energy per unit surface area a material can absorb elastically before plastic deformation occurs. The modulus of resilience is illustrated by the shaded area under the stress-strain curve in Figure 214, and is a function of yield strength and elastic modulus defined by Eq. 33 [145]. The modulus of resilience can be determined using nanoindentation hardness by combining Eq. 32 and Eq. 33.

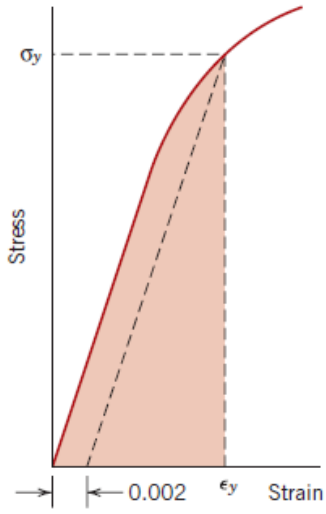

Figure 214: The Modulus of Resilience Represented by the Shaded Area under the Stress-Strain Curve (Reprinted from [145])

Eq. 33

$$U_r = \frac{\sigma_y^2}{2E}$$

Regardless of which method is used to determine yield strength (and therefore modulus of resilience), all relationships which relate Vickers or Berkovich indentation hardness and yield strength are linear. Therefore, it is sufficient to state that higher hardness correlates to higher yield strength, and that the percent change in yield strength ($\Delta\sigma_y$) is identical to the percent change in indentation hardness (ΔH). Based on the data presented in Ch. IV.4, nanoindentation data of unirradiated LAM rods agree closely with the tensile testing data of unirradiated LAM rods; both methods show that the unirradiated yield strength varies with orientation where: horizontal LAM > 45° LAM > vertical LAM. Specifically, the unirradiated yield strength of horizontal LAM is

approximately 0.5% and 2.5% larger than 45° and vertical LAM. The radiation-induced change in yield strength, inferred from nanoindentation data, is also orientation dependent where, from greatest to least: horizontal LAM (56%) > 45° LAM (53%) > vertical LAM (43%) > conventionally manufactured (37%).

V.1.2 Creep, IGSCC, and HIC Resistance

Based on the results of this research, CSL theory suggests that all samples built by LAM are much more susceptible to detrimental phenomena which tend to be worst along grain boundaries. This is evident by the dramatically lower CSL boundary distributions in the LAM specimens in comparison to their conventionally manufactured counterparts, shown in Figure 155 - Figure 162. Microstructural properties, especially those related to grain boundary character, influence the macroscopic properties of the sample (see Ch. II.4.4). The relationship between the CSL boundary distribution and an alloy's susceptibility to detrimental phenomena which tend to be worst along grain boundaries (IGSCC, HIC, etc.) has been discussed previously. Relating to the LAM samples in this research, several salient details can be summarized as follows: (1) ~ $\Sigma 1$ low angle boundaries are extremely resistant to cracking, (2) higher Σ boundaries are generally more susceptible to cracking, and (3) $\Sigma 3$ twin boundaries are extremely resistant to cracking while off-coincidence $\Sigma 3$ boundaries can be sensitive [146].

Inconel 600 susceptibility to intergranular attack and corrosion rate tend to decrease as the CSL boundary low-Σ content increases [54]. This conclusion seems sensible from a thermodynamic perspective since the minimum Gibbs energy of the

system corresponds to a perfect arrangement of atoms in coincidence lattice positions. A relationship exists for Inconel 600 between CSL theory and intergranular stress corrosion cracking (IGSCC) susceptibility. For Inconel 600, ~Σ1 and Σ3 twin boundaries are resistant to IGSCC, while most other boundaries including Σ9 are sensitive to IGSCC [105].

Studies have shown that adjacent grains whose Taylor factor varies dramatically are particularly susceptible to large stress concentrations leading to intergranular cracking [147, 148]. From a micromechanical point of view, these stress concentrations are susceptible to dislocation pileup which increase the probability of intergranular defect nucleation. Based on Figure 166 - Figure 169, Taylor theory suggests that the LAM Inconel 600 and 316L stainless steel in this study are more susceptible to intergranular cracking than their conventionally manufactured counterparts.

The radiation-induced chromium carbide precipitates observed in the Inconel 600 samples via SPM in Figure 170 are much larger in LAM samples than in the conventionally manufactured control. The larger size of these features in the LAM specimens suggests increased chromium mobility under irradiation. This may also be related to the fine grain structure and larger grain aspect ratio associated with the LAM-built samples. It has been observed in Ni-Cr alloys that the overall mobility and effective diffusion coefficient of chromium tends to increase as grain size decreases [104]. Also of possible importance is the unknown carbon content in the LAM samples. However, research conducted by Chen et.al. suggests that the volume and grain boundary diffusion of chromium in Inconel 600 is unaffected by carbon content at high

temperatures [149]. Chromium diffusion is also insensitive to small variations in the Ni-Cr-Fe stoichiometry as well [150]. The presence of these larger precipitates in the LAM specimens may suggest an increased sensitivity to radiation assisted stress corrosion cracking (IASCC) toward which chromium mobility and depletion to the grain boundaries is known to contribute [21, 151]. The results of this study suggest that the increase in chromium mobility in the LAM specimens make them more susceptible to related detrimental phenomena like IASCC, and were likely exacerbated by the manufacturing process.

V.2 Anisotropic Radiation-Induced Segregation

Figure 170 shows that radiation-produced chromium/carbon rich precipitates exist on each of the Inconel 600 sample types. Cr_7C_3 and $Cr_{23}C_6$ may both be present below 760 °C; however, while the cubic crystal structure of $Cr_{23}C_6$ is known to form cuboctahedra similar to that of NaCl, the more abundant Cr_7C_3 phase has a hexagonal crystal structure [152, 153].

Based on the radiation-induced change in RMS surface roughness in Figure 170, simple trigonometric relations exist which relates radiation-induced precipitation to LAM build orientation. The linear curve fit in Eq. 34 is shown in Figure 215, the exponential curve fit in Eq. 35 is shown in Figure 216, and the trigonometric relation in Eq. 36 is shown in Figure 217, where A and B are constants with units of surface roughness (nm). Recall that the mathematical definition of RMS surface roughness is

described by Eq. 14 which is indeed identical to "uncertainty". For this reason, the surface roughness measurements are no associated with uncertainty bars.

Eq. 34

$$\Delta RMS \propto A\theta + B$$

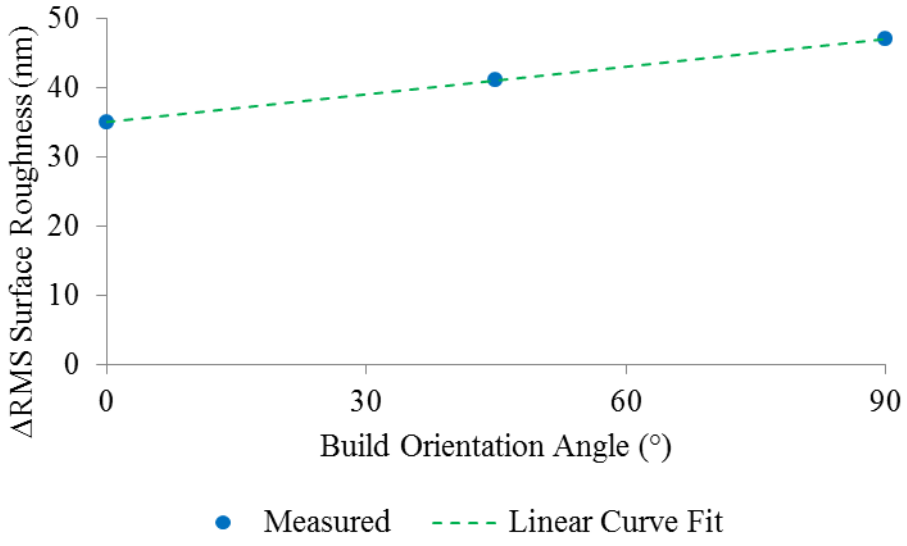

Figure 215: Comparison between Observed Changes in Radiation-Induced RMS Surface Roughness in Inconel 600 and Linear Curve Fit (Eq. 34)

Eq. 35

$$\Delta RMS \propto Ae^{B\theta}$$

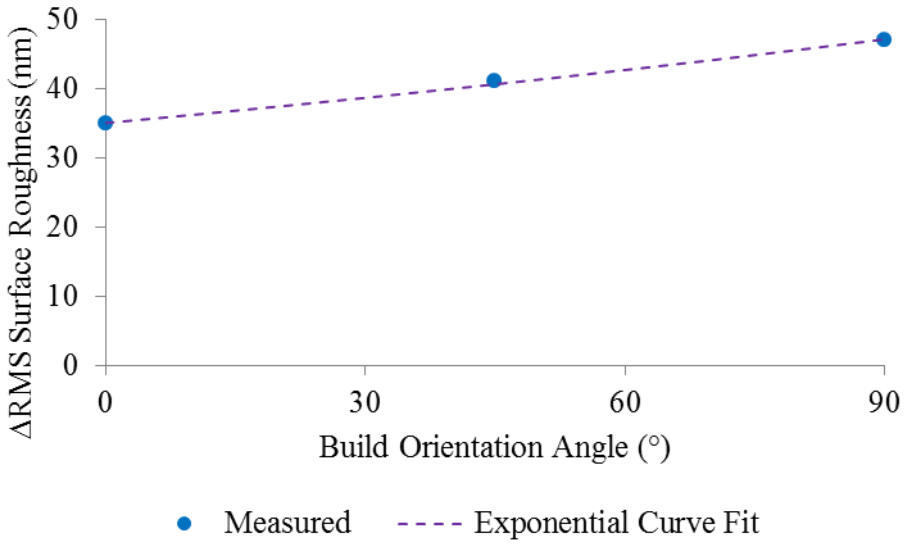

Figure 216: Comparison between Observed Changes in Radiation-Induced RMS Surface Roughness in Inconel 600 and Exponential Curve Fit (Eq. 35)

Eq. 36

$$\Delta RMS \propto A + B\sin(\theta)$$

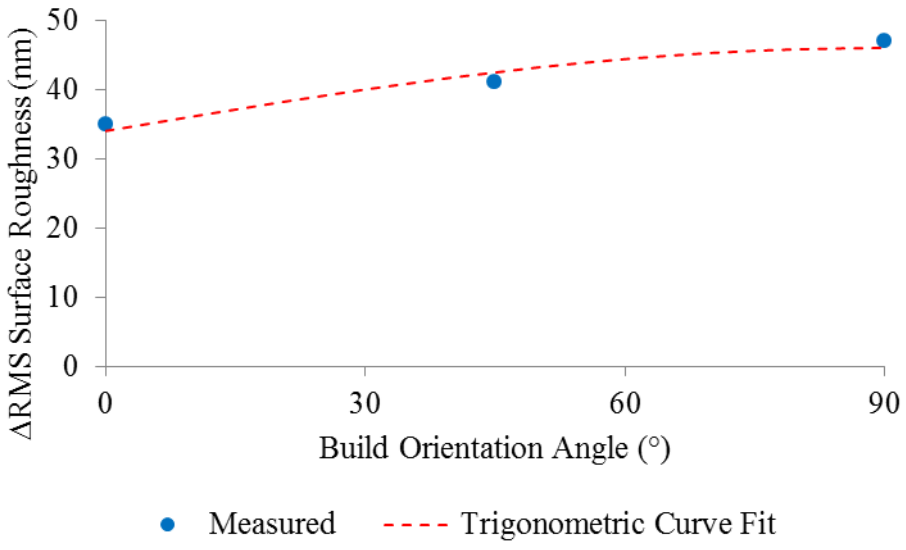

Figure 217: Comparison between Observed Changes in Radiation-Induced RMS Surface Roughness in Inconel 600 and Trigonometric Curve Fit (Eq. 36)

At the outset of data analysis, there was no discernable physical reason to select one data fit (Eq. 34 - Eq. 36) over another. Therefore, a simple method was derived to enable the interpretation of physical meaning from the data, as described below.

- Grain boundary diffusion is significantly faster than diffusion through the crystalline bulk due to the higher disorder associated with the grain boundary; this means that grain boundaries act as atomic transport "highways", particularly for chromium in nickel-based superalloys [149].

- A driving force, such as a temperature or stress field gradient, exists during ion irradiation which is perpendicular to the sample surface, driving thermal diffusion.
- Chromium atoms are initially homogeneously distributed throughout each grain, such that chromium diffusion begins at every point within the grain toward the grain boundary in the direction of the temperature gradient [154].
- Once chromium atoms reach a grain boundary, they agglomerate "immediately" on the irradiated surface of the sample (see Figure 170).
- The average change in surface roughness due to radiation-induced segregation and precipitation is dependent upon orientation-dependent diffusion through each grain, which is a function of:
    - (a) the average distance that diffusing atoms must travel through each elongated grain via thermal diffusion in order to reach a grain boundary, and
    - (b) the crystalline orientation dependence of the diffusion coefficient (assumed to be geometric).
- The grains in the specimens, on average, are ellipsoidal in shape following Eq. 4.

To develop the implications of these assumptions, the LAM alloy grains will first be treated as having isotropic diffusion coefficients (i.e. the diffusion coefficient will be

treated as equal in all crystalline directions). After that condition is established, the solution will be amended to incorporate crystalline diffusion anisotropy.

Assuming the volume of each chromium atom may be considered unchanged as it contributes to the chromium/carbon rich surface features (see Figure 170), the volume of any given surface feature is proportional to the number of atoms inside of it. The volumes of the surface features (V) are approximately proportional to the cube of the feature height. To illustrate that this is the case, the following will be illustrated using the arbitrarily chosen shape of a three sided pyramid, but is valid for a variety of other approximately symmetric shapes (cubes, spheres, etc.). The volume of a pyramid is defined by Eq. 37, where A is the area of the pyramid in contact with the irradiated surface whose sides are length l and height is y.

Eq. 37

$$V = \frac{1}{3} Ay$$

$$A = \frac{\sqrt{3}}{4} l^2$$

Because the volume of each chromium atom may be considered unchanged as it contributes to the chromium/carbon rich surface features, and average change in surface roughness due to radiation-induced segregation and precipitation is dependent upon orientation-dependent diffusion through each grain, the average volume of the pyramids on the irradiated surface is inversely proportional to the average distance that species

must travel through each grain in order to reach a grain boundary ($\bar{d}$). Therefore, the relationship between the average change in surface roughness (Eq. 14) due to radiation-induced segregation/precipitation (*ΔRMS*) and the average distance that species must travel through each grain via thermal diffusion in order to reach a grain boundary can be express mathematically by Eq. 38.

$$\Delta RMS \propto y$$

$$V \propto \text{\# of Atoms in the Pyramids}$$

$$\text{\# of Atoms} \propto \bar{d}^{-1}$$

$$V \propto \bar{d}^{-1}$$

$$V = \frac{\sqrt{3}}{12} l^2 y$$

$$l = y\sqrt{\frac{3}{2}}$$

$$V = \frac{\sqrt{3}}{12}\frac{3}{2} y^3 = \frac{\sqrt{3}}{8} y^3$$

$$V \propto y^3$$

$$\Delta RMS \propto y \propto V^{1/3} \propto \bar{d}^{-1/3}$$

$$\therefore$$

Eq. 38

$$\Delta RMS \propto \bar{d}^{-1/3}$$

Recall that the grain aspect ratio of the grains in the LAM rods is much larger than that of their conventionally manufactured counterparts (see Table 15 and Table 16). Based on EBSD images of the grain structure (Figure 129), the elongated LAM grains are oriented parallel with the build direction such that the grains are oriented with the temperature gradient (ΔT) during ion beam irradiation as shown in Figure 218. The coordinate system in Figure 218 is such that the angle θ between the direction parallel to the temperature gradient (i.e. the direction in which thermal diffusion will occur) and the grain's the major axis (the dotted line) coincides with the build orientation.

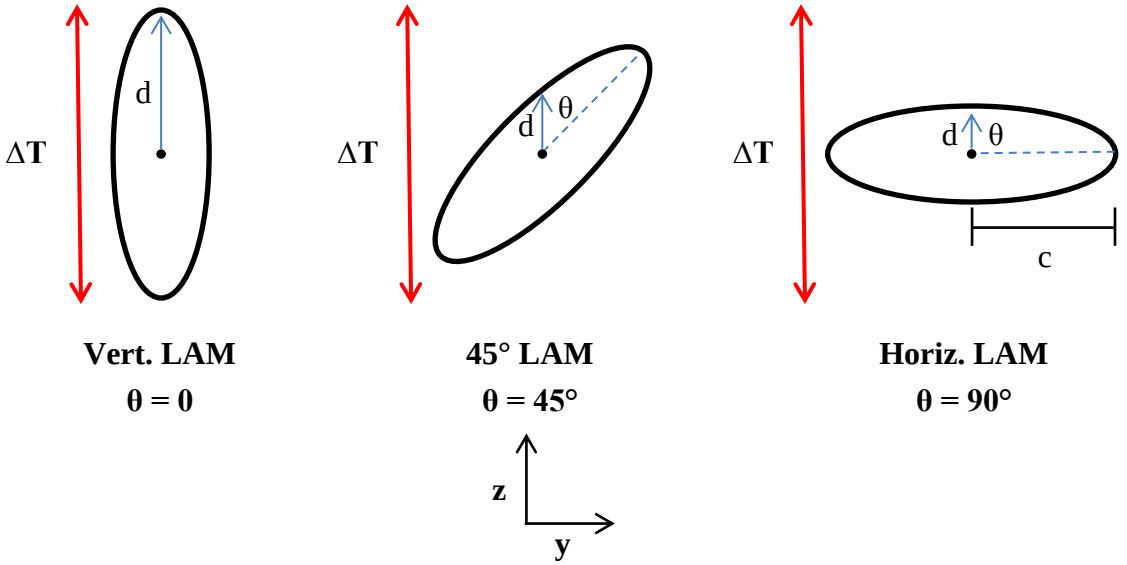

Figure 218: Illustration of LAM Grains Oriented with Temperature Gradient during Ion Beam Irradiation

Since the temperature gradient is in the z-direction (Figure 218), the average motion of atoms in the y-direction (left and right on the page) and x-direction (into and out of the page) is zero. Assume, therefore, that atoms can only reach the grain boundary via thermal diffusion in the z-direction. Instead of rotating the entire grain as shown in Figure 218, however, it is mathematically equivalent to rotate the temperature gradient (and therefore the angle in which diffusion occurs) from 0° to 90°, as illustrated in Figure 219. This convention will be used in order to simplify the derivation to follow since the shape/bounds of the ellipse do not change with angle.

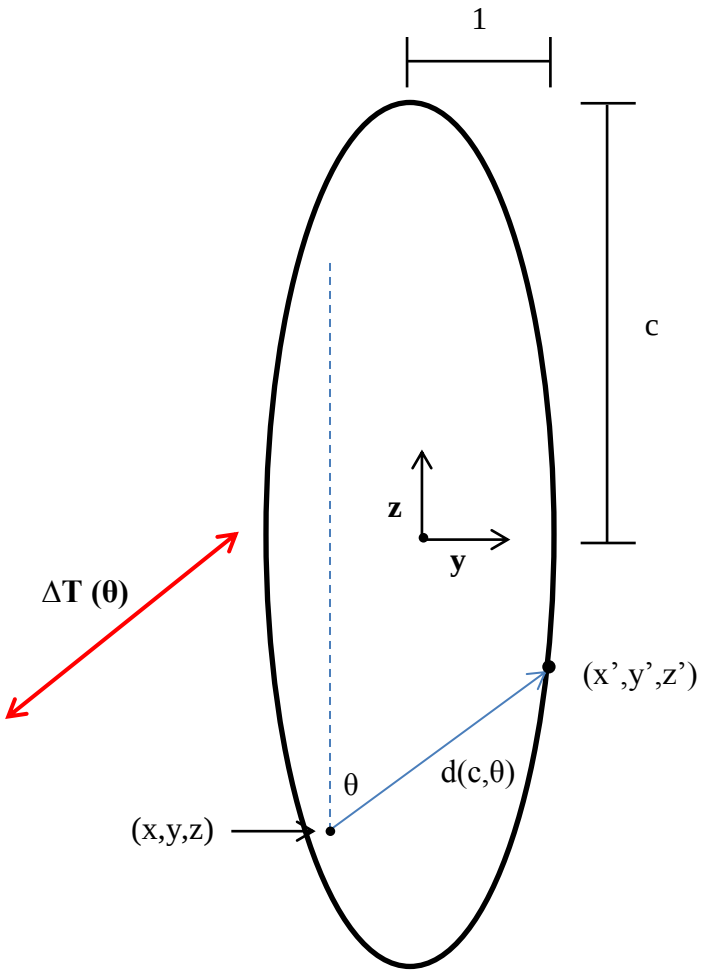

Figure 219: Illustration of Equivalence between Rotating the Grain Orientation (Figure 218) and Rotating the Diffusion Angle

The mathematical definition of an ellipsoid whose boundaries are at coordinates (*x',y',z'*) and is centered at the origin is given by Eq. 39 where it is assumed that *a = b = 1* and the GAR is equal to *c*.

$$\frac{x'^2}{a^2}+\frac{y'^2}{b^2}+\frac{z'^2}{c^2}=1$$

$$a=b=1$$

Eq. 39

$$x'^2+y'^2+\frac{z'^2}{c^2}=1$$

The distance *d* atoms travel via thermal diffusion from a random location within the grain *(x,y,z)* to the grain boundary is given by Eq. 40.

Eq. 40

$$d=\sqrt{\left(x-x'\right)^2+\left(y-y'\right)^2+\left(z-z'\right)^2}$$

$$-c\cdot\sqrt{1-x^2-y^2}\le z\le c\cdot\sqrt{1-x^2-y^2}$$

$$-\sqrt{1-x^2}\le y\le\sqrt{1-x^2}$$

$$-1\le x\le 1$$

$$c\ge 1$$

$$0\le\theta\le\frac{\pi}{2}$$

The average distance atoms must travel via thermal diffusion, $\bar{d}$, is maximum when the temperature gradient is parallel to the major axis of the ellipsoid (the z-axis), i.e. when $\theta = 0$. Let this maximum average thermal diffusion length (which is a function of only c) be defined as $a(c)$. The average distance atoms must travel via thermal diffusion is minimum when the temperature gradient is perpendicular to the major axis of the ellipsoid (the x-y plane), i.e. when $\theta = 90°$. Let this minimum average thermal diffusion distance be defined as $b(c)$. The average distance atoms must travel vs. the orientation of the temperature gradient can be determined by converting Eq. 39 into spherical coordinates and solving for r with the azimuthal angle $\varphi = 0$ (i.e. the temperature gradient is rotated on the y-z plane simplifying the angular dependence to a 2D relationship), as shown in Eq. 47.

The values of $a(c)$ and $b(c)$ are derived using the mathematical definition of the average of a function $f(x,y,z,c)$ whose variables are x, y, and z, given by Eq. 41 where $w(x,y,z)$ is the weight function with respect to its variables. Since this derivation is in Cartesian coordinates, the weight function is unity. When the temperature gradient is parallel to the major axis of the grains (i.e. the z-axis), $\theta = 0$; therefore, Eq. 41 reduces to Eq. 42, and Eq. 40 reduces to Eq. 43. The value of $a(c)$ can then be computed via Eq. 44. Similarly, when the temperature gradient is perpendicular to the major axis of the grains (i.e. the y-axis), $\theta = 90°$; therefore, Eq. 40 reduces to Eq. 45 and the value of $b(c)$ can be computed via Eq. 46.

Eq. 41

$$\overline{f(x,y,z)} = \frac{\iiint f(x,y,z)\cdot w(x,y,z)dxdydz}{\iiint w(x,y,z)dxdydz}$$

$$w(x,y,z) = 1$$

$$\therefore$$

Eq. 42

$$\overline{d(c)} = \frac{\iiint f(x,y,z,c)dxdydz}{\iiint dxdydz}$$

$$x = x'$$

$$y = y'$$

Eq. 43

$$a = d(c, \theta = 0) = \sqrt{(z - z')^2}$$

$$a(c) = \frac{\int_{-1}^{1}\int_{-\sqrt{1-x^2}}^{\sqrt{1-x^2}}\int_{-c\cdot\sqrt{1-x^2-y^2}}^{c\cdot\sqrt{1-x^2-y^2}} \sqrt{(z-z')^2}\,dzdydx}{\int_{-1}^{1}\int_{-\sqrt{1-x^2}}^{\sqrt{1-x^2}}\int_{-c\cdot\sqrt{1-x^2-y^2}}^{c\cdot\sqrt{1-x^2-y^2}} dzdydx}$$

$$z' = c\sqrt{1-x^2-y^2}$$

$$\therefore$$

Eq. 44

$$a(c)=\frac{\int_{-1}^{1}\int_{-\sqrt{1-x^2}}^{\sqrt{1-x^2}}\int_{-c\cdot\sqrt{1-x^2-y^2}}^{c\cdot\sqrt{1-x^2-y^2}}\sqrt{\left(z-c\sqrt{1-x^2-y^2}\right)^2}\,dzdydx}{\int_{-1}^{1}\int_{-\sqrt{1-x^2}}^{\sqrt{1-x^2}}\int_{-c\cdot\sqrt{1-x^2-y^2}}^{c\cdot\sqrt{1-x^2-y^2}}dzdydx}$$

$$a(c)=\frac{3}{4}c$$

Eq. 45

$$b=d\left(c,\theta=90°\right)=\sqrt{\left(y-y'\right)^2}$$

$$b(c)=\frac{\int_{-1}^{1}\int_{-\sqrt{1-x^2}}^{\sqrt{1-x^2}}\int_{-\sqrt{1-x^2-\frac{z^2}{c^2}}}^{\sqrt{1-x^2-\frac{z^2}{c^2}}}\sqrt{\left(y-y'\right)^2}\,dydzdx}{\int_{-1}^{1}\int_{-\sqrt{1-x^2}}^{\sqrt{1-x^2}}\int_{-\sqrt{1-x^2-\frac{z^2}{c^2}}}^{\sqrt{1-x^2-\frac{z^2}{c^2}}}dydzdx}$$

$$y'=\sqrt{1-x^2-\frac{z^2}{c^2}}$$

$\therefore$

Eq. 46

$$b(c)=\frac{\int_{-1}^{1}\int_{-\sqrt{1-x^2}}^{\sqrt{1-x^2}}\int_{-\sqrt{1-x^2-\frac{z^2}{c^2}}}^{\sqrt{1-x^2-\frac{z^2}{c^2}}}\sqrt{\left(y-\sqrt{1-x^2-\frac{z^2}{c^2}}\right)^2}\,dydzdx}{\int_{-1}^{1}\int_{-\sqrt{1-x^2}}^{\sqrt{1-x^2}}\int_{-\sqrt{1-x^2-\frac{z^2}{c^2}}}^{\sqrt{1-x^2-\frac{z^2}{c^2}}}dydzdx}$$

$$b(c)=\frac{3}{8}\left(\frac{3c^2-1}{c^3}\right)$$

The average thermal diffusion length atoms must travel vs. the orientation of the temperature gradient is determined by converting Eq. 39 into spherical coordinates and solving for r with $\varphi = 0$, as shown in Eq. 47. Plugging Eq. 44 and Eq. 46 into Eq. 47 yields the average atomic travel distance through the ellipsoidal grains as function of c and build orientation angle θ, shown in Eq. 48.

$$\left(\frac{x}{a}\right)^2+\left(\frac{y}{b}\right)^2=1$$

$$x=r\cdot\cos(\theta)$$

$$y=r\cdot\sin(\theta)$$

$$\left(\frac{r\cdot\cos(\theta)}{a}\right)^2+\left(\frac{r\cdot\sin(\theta)}{b}\right)^2=1$$

$$r=\frac{ab}{\sqrt{\left(b\cdot\cos(\theta)\right)^2+\left(a\cdot\sin(\theta)\right)^2}}$$

$$\therefore$$

Eq. 47

$$\overline{d}=\frac{a(c)\cdot b(c)}{\sqrt{\left[b(c)\cdot\cos(\theta)\right]^2+\left[a(c)\cdot\sin(\theta)\right]^2}}$$

Eq. 48

$$\overline{d(c,\theta)} = \frac{\left[\frac{\int_{-1}^{1}\int_{-\sqrt{1-x^2}}^{\sqrt{1-x^2}}\int_{-c\cdot\sqrt{1-x^2-y^2}}^{c\cdot\sqrt{1-x^2-y^2}}\sqrt{\left(z-c\sqrt{1-x^2-y^2}\right)^2}\,dzdydx}{\int_{-1}^{1}\int_{-\sqrt{1-x^2}}^{\sqrt{1-x^2}}\int_{-c\cdot\sqrt{1-x^2-y^2}}^{c\cdot\sqrt{1-x^2-y^2}}dzdydx}\right]\cdot\left[\frac{\int_{-1}^{1}\int_{-\sqrt{1-x^2}}^{\sqrt{1-x^2}}\int_{-\sqrt{1-x^2-\frac{z^2}{c^2}}}^{\sqrt{1-x^2-\frac{z^2}{c^2}}}\sqrt{\left(y-\sqrt{1-x^2-\frac{z^2}{c^2}}\right)^2}\,dydzdx}{\int_{-1}^{1}\int_{-\sqrt{1-x^2}}^{\sqrt{1-x^2}}\int_{-\sqrt{1-x^2-\frac{z^2}{c^2}}}^{\sqrt{1-x^2-\frac{z^2}{c^2}}}dydzdx}\right]}{\sqrt{\left[\frac{\int_{-1}^{1}\int_{-\sqrt{1-x^2}}^{\sqrt{1-x^2}}\int_{-\sqrt{1-x^2-\frac{z^2}{c^2}}}^{\sqrt{1-x^2-\frac{z^2}{c^2}}}\sqrt{\left(y-\sqrt{1-x^2-\frac{z^2}{c^2}}\right)^2}\,dydzdx}{\int_{-1}^{1}\int_{-\sqrt{1-x^2}}^{\sqrt{1-x^2}}\int_{-\sqrt{1-x^2-\frac{z^2}{c^2}}}^{\sqrt{1-x^2-\frac{z^2}{c^2}}}dydzdx}\cdot\cos(\theta)\right]^2+\left[\left[\frac{\int_{-1}^{1}\int_{-\sqrt{1-x^2}}^{\sqrt{1-x^2}}\int_{-c\cdot\sqrt{1-x^2-y^2}}^{c\cdot\sqrt{1-x^2-y^2}}\sqrt{\left(z-c\sqrt{1-x^2-y^2}\right)^2}\,dzdydx}{\int_{-1}^{1}\int_{-\sqrt{1-x^2}}^{\sqrt{1-x^2}}\int_{-c\cdot\sqrt{1-x^2-y^2}}^{c\cdot\sqrt{1-x^2-y^2}}dzdydx}\right]\cdot\sin(\theta)\right]^2}}$$

$$\therefore$$

$$\overline{d(c,\theta)} = \frac{\frac{9}{32}\left(3-\frac{1}{c^2}\right)}{\sqrt{\left[\frac{3}{8}\left(\frac{3c^2-1}{c^3}\right)\cdot\cos(\theta)\right]^2+\left[\frac{3}{4}c\cdot\sin(\theta)\right]^2}}$$

The function shown in Eq. 48 is plotted in Figure 220 for several values of *c*. When the grains are equiaxed, *c = 1* and the orientation of the grains (or temperature gradient) does not matter. From Eq. 48, the two components of the denominator are proportional as shown below in Eq. 49. The relationships in Eq. 49 clearly show that as the grains become increasingly elongated (i.e. as *c* increases), the function which describes the average distance species must migrate via thermal diffusion to reach a grain boundary quickly becomes dominated by $\sin^{-1}(\theta)$.

Eq. 49

$$\frac{3}{8}\left(\frac{3c^2-1}{c^3}\right)\cdot\cos(\theta) \propto \frac{\cos(\theta)}{c}$$

$$\frac{3}{4}c\cdot\sin(\theta) \propto c\cdot\sin(\theta)$$

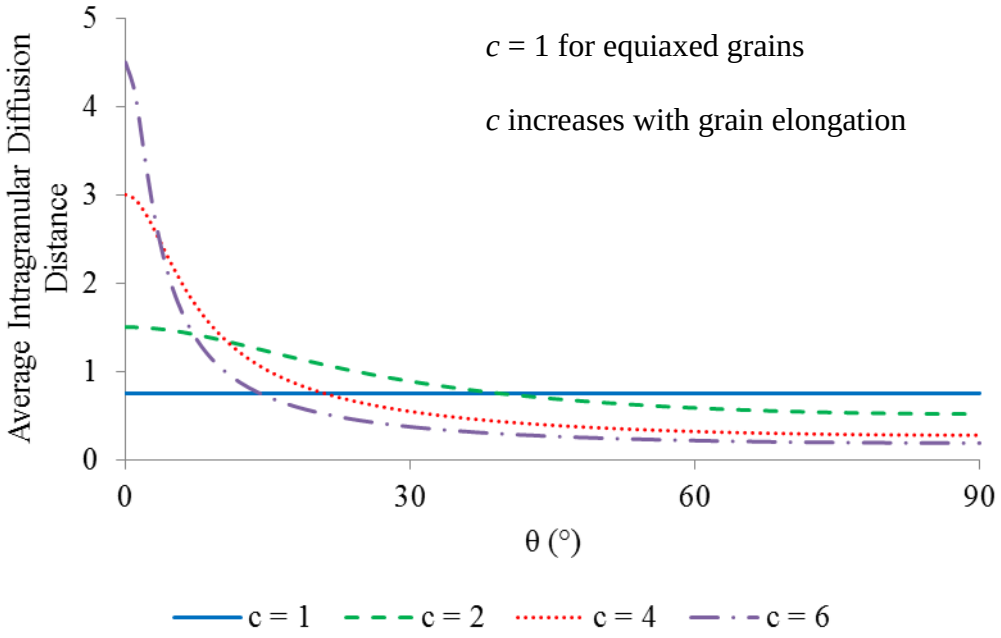

Figure 220: Plot of Eq. 48 for Several Values of *c*

Combining Eq. 48 with Eq. 38 yields Eq. 50 which represents the distance diffusive species must travel through an elongated grain as a function of orientation angle. This is the first stage of the aforementioned two-step problem. In an amorphous solid, Eq. 50 would be the exact solution to this diffusion problem. Inconel 600, however, is fcc in structure. In order to account for anisotropic crystalline diffusion, the orientation dependence of thermal diffusion must be taken into account since the LAM grains are highly textured.

Based on Figure 151 and Figure 152, the LAM process produces grains which are textured such that <101>||**B** (where **B** represents build direction). It is known that the diffusion coefficient of atomic species is greatest along close-packed directions which, for fcc crystals, are the <101> directions [155]. For the case of nickel, the diffusion

coefficient in the <111> directions is approximately half that of the diffusion coefficient in the <101> directions [156-158]. Using the simplifying assumption that, for these LAM alloys with this texture at this temperature, Eq. 51 from literature applies to this system [158], then the RMS surface roughness varies according to Eq. 52.

Eq. 50

$$\Delta RMS \propto \overline{d(c,\theta)}^{-1/3} = \left(\frac{\frac{9}{32}\left(3-\frac{1}{c^2}\right)}{\sqrt{\left[\frac{3}{8}\left(\frac{3c^2-1}{c^3}\right)\cdot\cos(\theta)\right]^2+\left[\frac{3}{4}c\cdot\sin(\theta)\right]^2}} \right)^{-1/3}$$

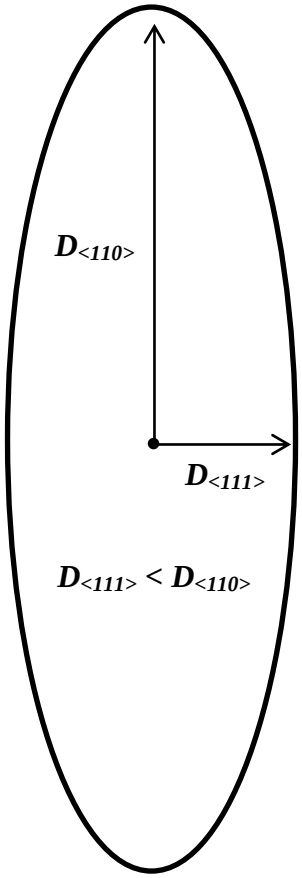

Figure 221: Illustration of Anisotropic Diffusion Coefficients in LAM fcc Crystals

Eq. 51

$$D(\theta) \propto 1.43 - 0.45\sin(\theta)$$

Eq. 52

$$\Delta RMS \propto \left[\overline{d(c,\theta)} \cdot D(\theta)\right]^{-1/3} = \left(\frac{\frac{9}{32}\left(3 - \frac{1}{c^2}\right)\left(1.43 - 0.45\sin(\theta)\right)}{\sqrt{\left[\frac{3}{8}\left(\frac{3c^2 - 1}{c^3}\right) \cdot \cos(\theta)\right]^2 + \left[\frac{3}{4} c \cdot \sin(\theta)\right]^2}} \right)^{-1/3}$$

The new derived expression in Eq. 52 represents the orientation-dependent diffusion paths due to both grain elongation and crystalline texture. Figure 222 shows measured changes in radiation-induced RMS surface roughness in Inconel 600 as a function of build orientation plotted against the trigonometric curve fit (Eq. 36) and derived geometric relationship (Eq. 52) where *GAR = 2.5*. While there is some uncertainty in this predicted value (due to residual stress fields, dislocations, and other defects), this new derived expression agrees closely with observed data (see Table 15). While the empirical curve fits in Eq. 34 - Eq. 36 could be considered adequate for engineering predictions, Eq. 52 represents a phenomena-based derived relationship that fits the data in a remarkable manner, suggesting that the assumptions in the model play a dominant role in the radiation-induced segregation behavior of the LAM alloy.

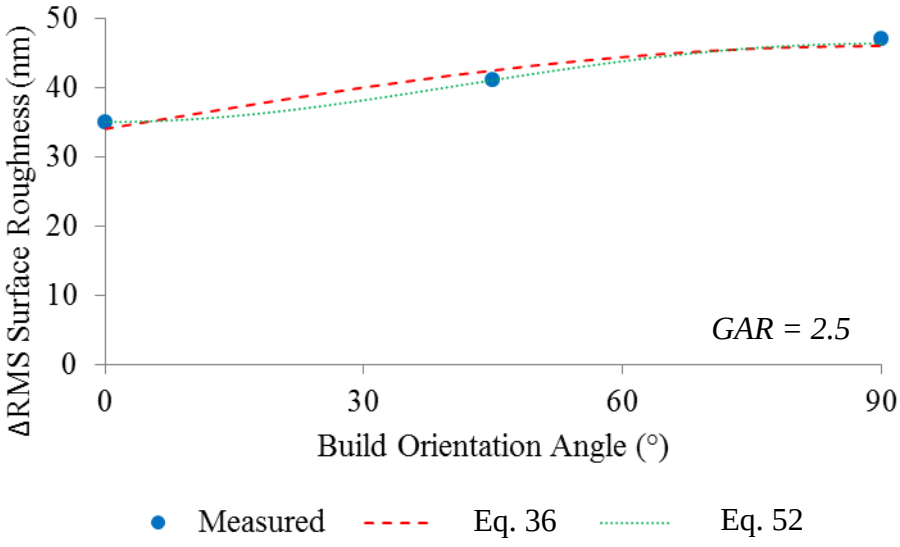

Figure 222: Comparison between Measured Changes in Radiation-Induced RMS Surface Roughness in Inconel 600, Trigonometric Curve Fit (Eq. 36), and Derived Relationship (Eq. 52)

V.3 Anisotropic Radiation-Induced Hardening and Embrittlement

Nanoindentation measurements could not be performed on the nickel superalloy samples since the instrument was irreparably damaged. However, close scrutiny of the data from Figure 189 reveals an observable trend in the orientation dependence of radiation-induced hardening in 316L stainless steel samples, shown in Figure 223 where measured values shown represent the average increase in hardness due to radiation damage at 0° (vertical LAM), 45° LAM, and 90° (horizontal LAM) relative to the load axis at depths shallower than the ion implantation peak (i.e. 200 nm – 800 nm). The dashed line represents an empirical curve fit shown in Eq. 53, where ΔH is the radiation-induced hardening (in percent) with load axis at angle θ relative to the LAM build direction, and A and B are constants. Note the similarity between Eq. 36 and Eq. 53.

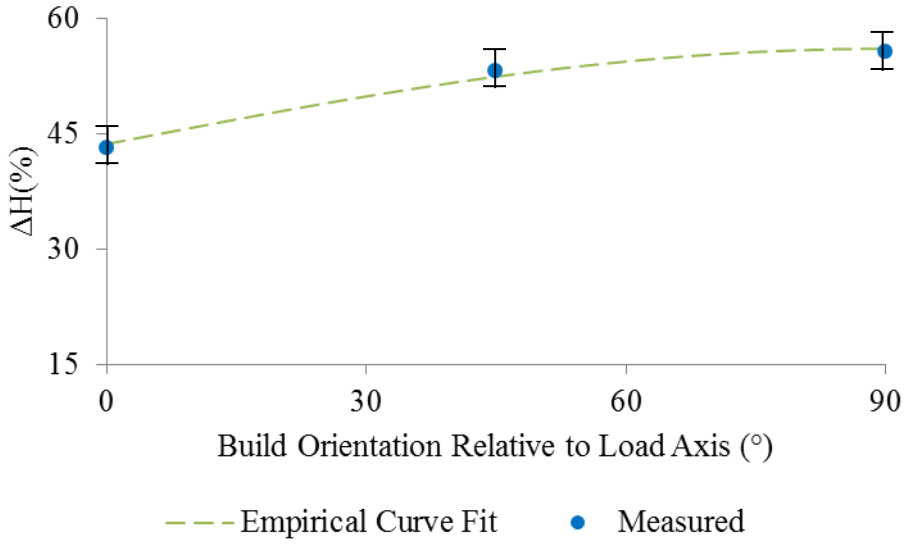

Figure 223: Measured Radiation-induced Hardening in Irradiated 316L Stainless Steel Built by LAM, and Trigonometric Curve Fit from Eq. 53

Eq. 53

$$\Delta H \propto A + B\sin(\theta)$$

As in the Ch. V.2, the simple empirical curve fits of the measured hardness data are useful but do not represent physical meaning. Therefore, the following discussion will consider the orientation dependence of various radiation hardening mechanisms. The objective is to understand the phenomenological meaning of the data variations in Figure 223.

Recall that moving dislocations interact with one another during plastic deformation, thereby causing work hardening [63]. Based on the macroscopic load-extension data in Figure 171, dislocations in the LAM rods clearly interact differently depending on orientation which gives rise to orientation-dependent yield stress, tensile strength, and ductility. Inspection of the TEM image of 316L stainless steel irradiated to 80 dpa shown in Figure 200 reveals that the array of dislocations (called a "multipole") is composed of edge dislocations which are oriented with one another. Consider two parallel edge dislocations whose stress fields interact with the other such that their Burger's vectors are oriented with the x-axis. The forces parallel to the glide direction (F_x) and perpendicular to the glide direction (F_y) are expressed as shown in Eq. 54 where μ is shear modulus, b is Burger's vector, v is Poisson's ratio, r is the distance between the dislocations, and θ is the angle between the two dislocations and the Burger's vector direction. For a detailed derivation of Eq. 54, see *Nonlinear Mechanics of Crystals [159]*.

Eq. 54

$$F_x = \frac{\mu b^2}{2\pi r(1-\nu)}\cos(\theta)\cos(2\theta)$$

$$F_y = \frac{\mu b^2}{2\pi r(1-\nu)}\sin(\theta)\left[2+\cos(2\theta)\right]$$

Edge dislocations can move along the slip plane which contains the dislocation line and its Burger's vector. A plot of Eq. 54 of the pure slip interaction (F_x), pure climb force (F_y), and total force between the two dislocations is shown in Figure 224. Note that if the Burger's vectors of the two dislocations are opposite one another then the interaction between the two will be equal but opposite to that shown in Figure 224.

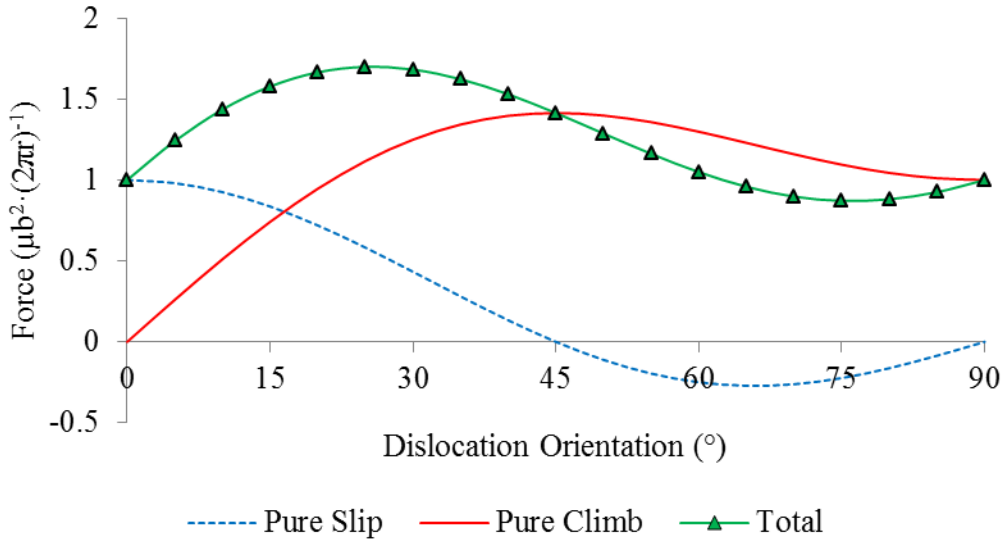

Figure 224: Force vs. Orientation Angle between Two Edge Dislocations with the Same Burger's Vector, from Eq. 54

An illustration of the stress field surrounding an edge dislocation is shown below in Figure 225 [82]. If a barrier (precipitate, grain boundary, etc.) were to restrict the motion of dislocations, dislocation pile-up can occur. In this scenario, the elastic repulsive forces between dislocations can build up, causing a small angle tilt boundary to form (see Figure 226) in which a more stable configuration is achieved since the compressive stress above each dislocation cancels partially with the tensile stress below the neighboring dislocations [82]. In doing so, crystalline misorientation will increase but the energy per dislocation will decrease. Small tilt boundaries appear to contribute significantly to the large misorientation measured by EBSD in the specimens built by LAM (see Figure 163 and Figure 164).

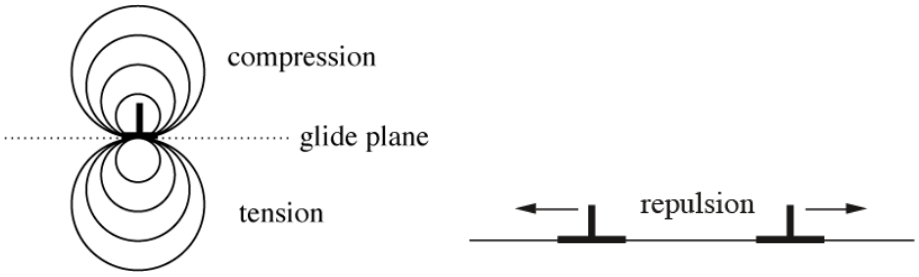

Figure 225: (a) Stress Field Around an Edge Dislocation, and (b) Long Range Repulsive Interaction between Two Edge Dislocations of the Same Sign on the Same Slip Plane (Reprinted from [82])

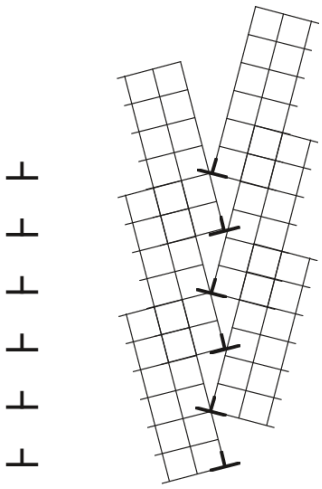

Figure 226: Stable Dislocation Structure Constituting a Small Angle Tilt Boundary
(Reprinted from [82])

Simple trigonometric relationships of the interaction between other types of defects exist as well, such as the orientation-dependent force between two screw dislocations shown in Eq. 55. Similar to edge dislocations, the force between two screw dislocations is equal and opposite if the Burger's vectors are oriented 180° from one another. Regardless of the type of dislocation present, it is apparent from Eq. 54 and Eq. 55 that the radiation-induced hardness is related to the inverse of distance in a similar manner to the orientation-dependent change in RMS surface roughness, thereby recovering the relationship derived in Eq. 36.

Eq. 55

$$F_x = \frac{\mu b^2}{2\pi r}\cos(\theta)$$

$$F_y = \frac{\mu b^2}{2\pi r}\sin(\theta)$$

Several phenomena need to be considered to understand radiation-induced hardening. Understanding these phenomena in terms of crystalline, defect, or load orientation is further complicated by lattice rotations during deformation (*vide infra*). As previously discussed in Ch. II.3, radiation-induced hardening is caused by (a) source hardening, in which the stress required to start a dislocation moving on its glide plane (i.e. pinning) is increased due to radiation-produced defects and stress fields, and (b) friction hardening, in which the already-moving dislocation's motion is impeded by radiation-produced obstacles in or near the slip plane [30].

When a dislocation is in motion, its motion is resisted by obstacles such as precipitates, voids, loops, grain boundaries, and possibly other dislocations. Since radiation damage produces large quantities of dislocations, this is a mechanism of radiation-induced hardening. The alloys produced by LAM clearly have elongated grain structures (Table 15 and Table 16), textured microstructures (Figure 166 - Figure 169), and elongated/oriented radiation-produced defects (Figure 202) whose geometries must be accounted for when characterizing anisotropic radiation-induced hardening.

Consider a set of dislocations approaching a grain boundary. The leading dislocation's motion may be halted by an obstacle, resulting in dislocation pile-up [160, 161]. An illustration of dislocation pile-up near a grain boundary (separating grains "1" and "2) is illustrated in Figure 227 [162]. The leading dislocation feels the repulsive stress fields from the trailing dislocations behind it, resulting in large stress concentrations at the boundary. The more dislocations that participate in pile-up, the

larger the stress concentration at the grain boundary, and therefore the less external stress must be applied to continue dislocation motion into the neighboring grain. The smaller the grain is in the direction of dislocation motion, the less space is available for dislocations in that grain to exist, and therefore fewer dislocations available to participate in pile-up.

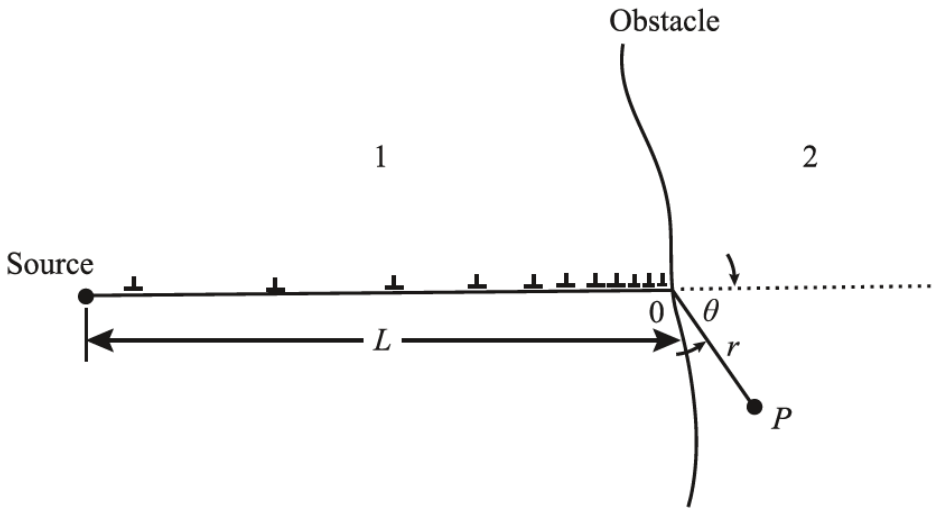

Figure 227: Illustration of Dislocation Pile-up at a Grain Boundary
(Reprinted from [162])

The above process describes an inverse relationship between grain boundary size and grain boundary strengthening, and is expressed by the Hall-Petch formula (Eq. 56 below) where d is the average grain diameter, μ is shear modulus, b is the Burgers vector, κ is unity for screw dislocations and 0.7 for edge dislocations [163], and τ^* is the stress required to initiate dislocation nucleation in the adjacent grain [164-167]. The

influence of grain boundaries, as described in the Hall-Petch formula, assumes an equiaxed grain structure.

Eq. 56

$$\Delta\sigma_{gb} = \frac{k_y}{\sqrt{d}}$$

$$k_y = M \cdot \sqrt{\frac{\mu b \tau^*}{\pi\kappa}}$$

Consider the average ellipsoidal grain constructed to be representative of those found in an additively manufactured polycrystal whose geometry is described by Figure 219 such that the grain's major and minor axis values of *a* and *b*, respectively. Recall that if these values are reduced such that *b* equals unity, then the value of the major axis is equivalent to the GAR. Clearly, due to the geometry of the grain, more dislocations can contribute to pile-up parallel to the major axis than parallel to the minor axis. As such, the average grain diameter in the Hall-Petch relation has orientation dependence for elongated grains, *d(θ)*. Recall also, however, that the stress required to move a dislocation through a crystal is strongly dependent upon crystalline orientation. This is expressed in Eq. 56 as the Taylor factor, *M*. In a polycrystal that lacks texture, *M* is approximately a constant with a value of 3.06 (see Figure 165). EBSD analysis of both LAM Inconel 600 and LAM 316L rods shows that *M* is dependent upon directionality.

For the purposes of this mathematical demonstration, the average Taylor factor values of 3.324, 3.200, and 2.900 will be used for dislocation motion at angles of 0°,

45°, and 90°, respectively. This results in a directionally-dependent Hall-Petch relationship for ellipsoidal grains shown in Eq. 57. The function $M(\theta)$, where the angle is in radians, was generated by an empirical curve fit from the data measured using EBSD. The distance function, $d(\theta)$, can be derived in the same manner as Eq. 47. Assuming shear modulus is constant, the anisotropic Hall-Petch relation for LAM grains (GAR = 2.5) takes the form shown in Figure 228. The reduced grain boundary strengthening parallel to the elongated oriented grain structure shown in Figure 228 is consistent with literature [168]. Considering that the strain field around a single dislocation is a relatively long-range effect, and dislocation pile-up involves several dislocations, dislocation and grain boundary strengthening are long-range phenomena [162].

Eq. 57

$$\Delta\sigma_{gb}(\theta) = k_y(\theta) \cdot d(\theta)^{-1/2}$$

$$k_y(\theta) = M(\theta) \cdot \sqrt{\frac{\mu b \tau^*}{\pi\kappa}}$$

$$M(\theta) = 3.324 - 0.046\theta - 0.143\theta^2$$

$$d(\theta) = \frac{ab}{\sqrt{(b\cos\theta)^2 + (a\sin\theta)^2}}$$

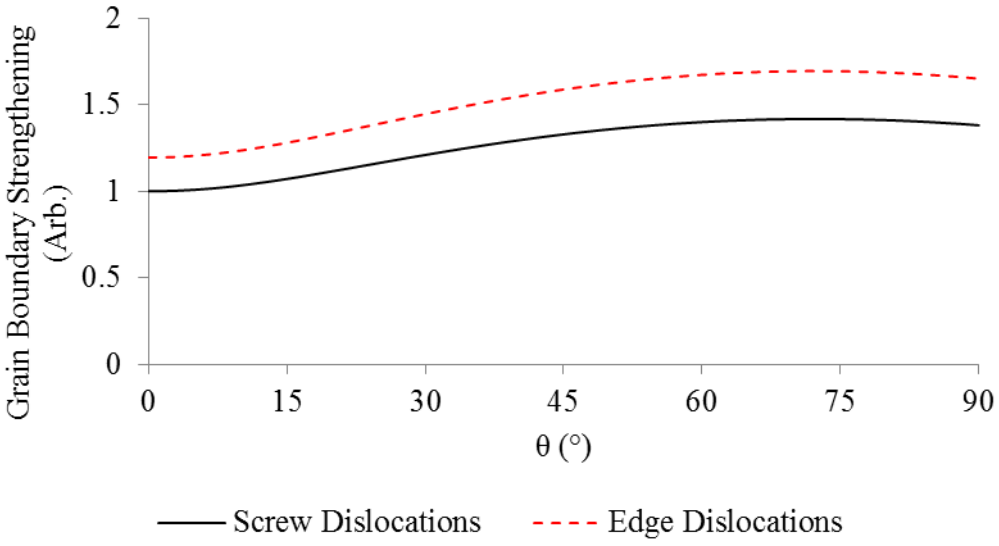

Figure 228: Anisotropic Hall-Petch Grain Boundary Strengthening for LAM Alloys (Eq. 57)

Several other relevant phenomena contribute to radiation-induced hardening, such as:

- dislocation strengthening (σ_D)
- solid solution strengthening (σ_{ss})
- precipitation strengthening (σ_P)

- void strengthening (σ_V)
- and loop strengthening (σ_L).

The hardening due to solid solution strengthening is given by Eq. 58, where k_j are constants relating the strengthening due to elements of type j and c_j are the concentrations of the alloying elements in solution [169-172]. The hardening caused by solid solution strengthening does change due to radiation damage when atoms are removed from solution to form precipitates. This, however, cannot occur anisotropically unless (a) the atoms were distributed anisotropically before irradiation, or (b) atoms return to solution due to radiation damage in an anisotropic manner.

Eq. 58

$$\sigma_{ss} = \sum_{j=1}^{N} k_j \cdot c_j^n$$

The strengthening caused by radiation-produced dislocations is described by Eq. 59 where α is the strength of the obstacle (which will be different depending on the type, size, and composition of obstacle), μ is the shear modulus, b is the Burgers vector, and $\Delta\rho$ is the change in dislocation density [170, 173]. Since the mechanism behind grain boundary strengthening is attributed to dislocation pile-up, dislocation strengthening and grain boundary strengthening are related by $\rho = d^{-1}$ (see Figure 228), which describes the similarity between Eq. 57 and Eq. 59. Accounting for orientation dependence in Eq. 59 yields the relation shown in Eq. 60.

Eq. 59

$$\sigma_D = k_y \sqrt{\Delta\rho}$$

Eq. 60

$$\Delta\sigma_D(\theta) = k_y(\theta) \cdot \sqrt{\rho(\theta)}$$

$$k_y(\theta) = M(\theta) \cdot \sqrt{\frac{\mu b \tau^*}{\pi\kappa}}$$

The strengthening caused by precipitates, voids, and loops are all described by the same general relation in Eq. 61, where σ_{PVL} is the strengthening caused by the obstacle, N is the obstacle density, d_{PVL} is the obstacle size, l is obstacle spacing, and r_c is the radius of the dislocation core which is approaching the obstacle. [30, 170, 174].

Eq. 61

$$\sigma_{PVL} = \alpha M \mu b \sqrt{N d_{PVL}}$$

$$\alpha = \frac{1}{2\pi} \ln\left(\frac{l}{2r_c}\right)$$

Again, however, Eq. 61 does not incorporate directionality or orientation by assuming spherical precipitates, voids, and loops. Diffusion is inherently anisotropic in a single crystal, so polycrystals with significant texture may have anisotropic diffusion coefficients. Furthermore, this process is greatly exacerbated by residual stress fields [175]. Anisotropic strain fields have been observed in this work, and highly anisotropic

residual stress fields are known to be produced in alloys as a result of the LAM fabrication process [11, 176]. Non-spherical defects were frequently observed in this work (ex: Figure 191 or Figure 197), so the resulting anisotropic stress fields will now be considered. For mathematical simplicity, the forthcoming discussion assumes that these radiation-produced obstacles are, on average, ellipsoidal in shape. While the anisotropic stress fields of ellipsoidal obstacles are best described by a full tensoral analysis, this is well beyond the scope of the current study. Instead, the stress increase due to ellipsoidal obstacles will be approximately by applying a purely geometric correction to spherical obstacles (Eq. 61) to quickly obtain exact solutions for illustrating the anisotropic effect of elongated aligned obstacles.

When a moving dislocation approaches a precipitate, void, or dislocation loop, the obstacle retards the continued motion of the dislocation. The short-range behavior of these obstacles can be strong, causing the dislocation to bow around the obstacle, as illustrated in Figure 229. Dislocations can generally cut through voids or bubbles, indicating a relatively small α values when modeled using Eq. 61. For hard obstacles like dislocations, bowing may continue around the obstacle until the adjacent segments touch, causing the dislocation to "pinch off". This results in a dislocation loop surrounding the obstacle in a process similar to that of Frank-Read source multiplication. The dislocation is then able to continue moving, while any future dislocations which approach the obstacle will encounter the resistance of the obstacle as well as the surrounding dislocation loop. This process can repeat itself until the dislocation loops

surrounding the obstacle cause the net obstacles' strengths to be too large for dislocation motion to continue.

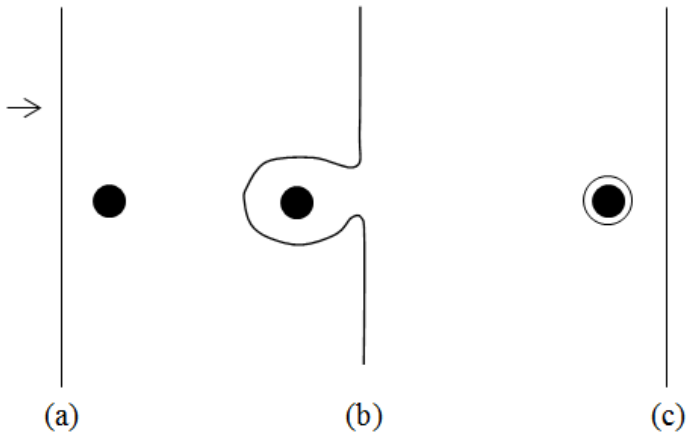

Figure 229: Illustration of (a) a Dislocation Approaching an Obstacle, (b) a Dislocation Bowing around an Obstacle, and (c) a Dislocation Loop around the Precipitate Left by the Passing Dislocation

Based on the above description of obstacle-dislocation interactions, the shape of and orientation of the obstacle relative to the approaching dislocation clearly influence the obstacle's strength. This is illustrated in Figure 230, where the ellipsoidal obstacles have the same volume as each other and the spherical obstacles illustrated in Figure 229.

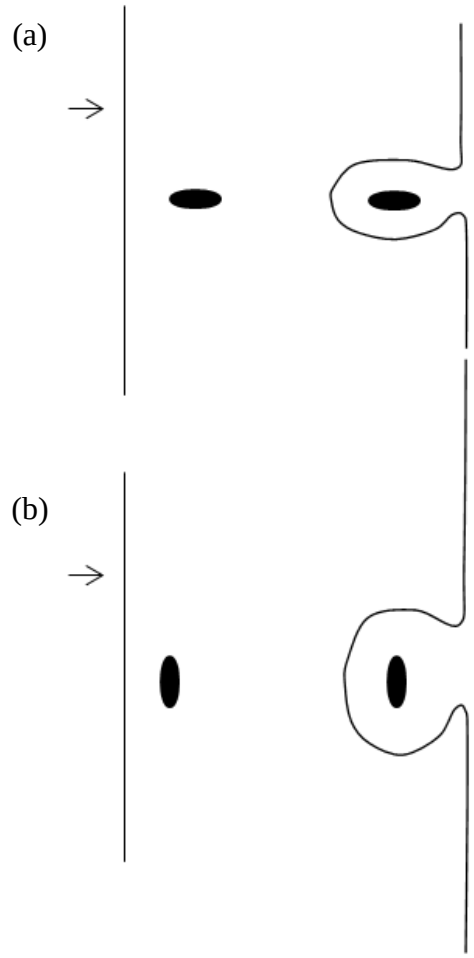

Figure 230: Illustration of Ellipsoidal Obstacle Oriented Relative to an Approaching Dislocation at (a) 0° and (b) 90°

As shown in Figure 230, the approaching dislocation must bow around the ellipsoidal obstacle as if the obstacle diameter were much smaller ($\theta = 0°$) or larger ($\theta = 90°$) than the diameter of the spherical case. This can be mathematically expressed by correcting d_{PVL} in Eq. 61 to account for the orientation dependence of the apparent obstacle diameter, shown in Eq. 62. Assuming shear modulus is constant and radiation-produced obstacles are oriented parallel with the underlying grain structure, the anisotropic hardening caused by precipitates, voids, loops, and "black dots" (clusters of

defects that are too small to resolve in TEM) for LAM samples takes the form illustrated in Figure 231.

Eq. 62

$$\sigma_{PVL} \approx \alpha M(\theta)\mu b\sqrt{N d_{PVL}(\theta)}$$

$$d_{PVL}(\theta) = \frac{ab}{\sqrt{(a\cos\theta)^2 + (b\sin\theta)^2}}$$

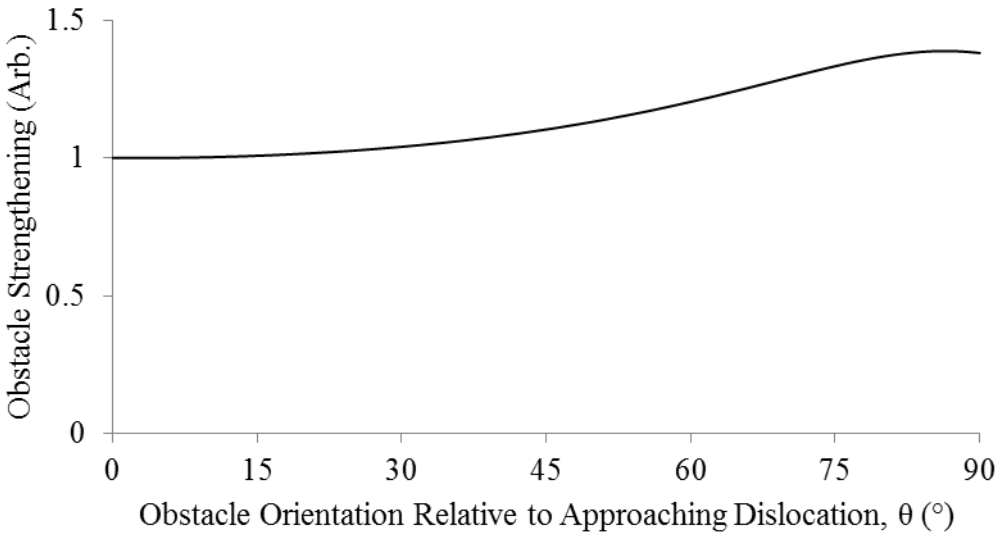

Figure 231: Anisotropic Radiation-Induced Strengthening Caused by Precipitates, Voids, Loops, and "Black Dots" for LAM Alloys

All of the above phenomena contribute to radiation-induced hardening in irradiated alloys; however, the degree of hardening can vary widely depending on alloy type and obstacle properties, such as obstacle type, size, and geometry. The relative strengths of the hardening mechanisms discussed are summarized below in Table 17

[30]. The various radiation-induced hardening mechanisms are plotted vs. orientation in Figure 232. Also included in Figure 232 is the measured radiation-induced hardening (normalized) of LAM rods, and the radiation-induced hardening empirical curve fit (Eq. 53).

Table 17: Relative Strengths of Various Radiation-Induced Hardening Mechanisms

Type of Strengthening	Obstacle Classification	Obstacle Type	Stress Increment	α [30]
Source		Isolated Loops	$\sigma_s = \frac{0.09\mu b}{l}$	
		Loop Network	$\sigma_s \approx \frac{0.06\mu b}{y}$	
Friction	Long-Range	Dislocation Network	$\sigma_D(\theta) = M(\theta)\sqrt{\frac{\mu b \tau^* \rho(\theta)}{\pi\kappa}}$	< 0.2
		Grain Boundary	$\sigma_{gb} = M(\theta)\sqrt{\frac{\mu b \tau^*}{\pi\kappa d(\theta)}}$	
	Short-Range	Precipitates and Voids	$\sigma_{PVL} \approx \alpha M(\theta)\mu b\sqrt{N d_{PVL}(\theta)}$	1.0 (Bowing) 0.3-0.5 (Cutting)
		Dislocation Loops		0.25-0.5
		"Black Dots"		< 0.2

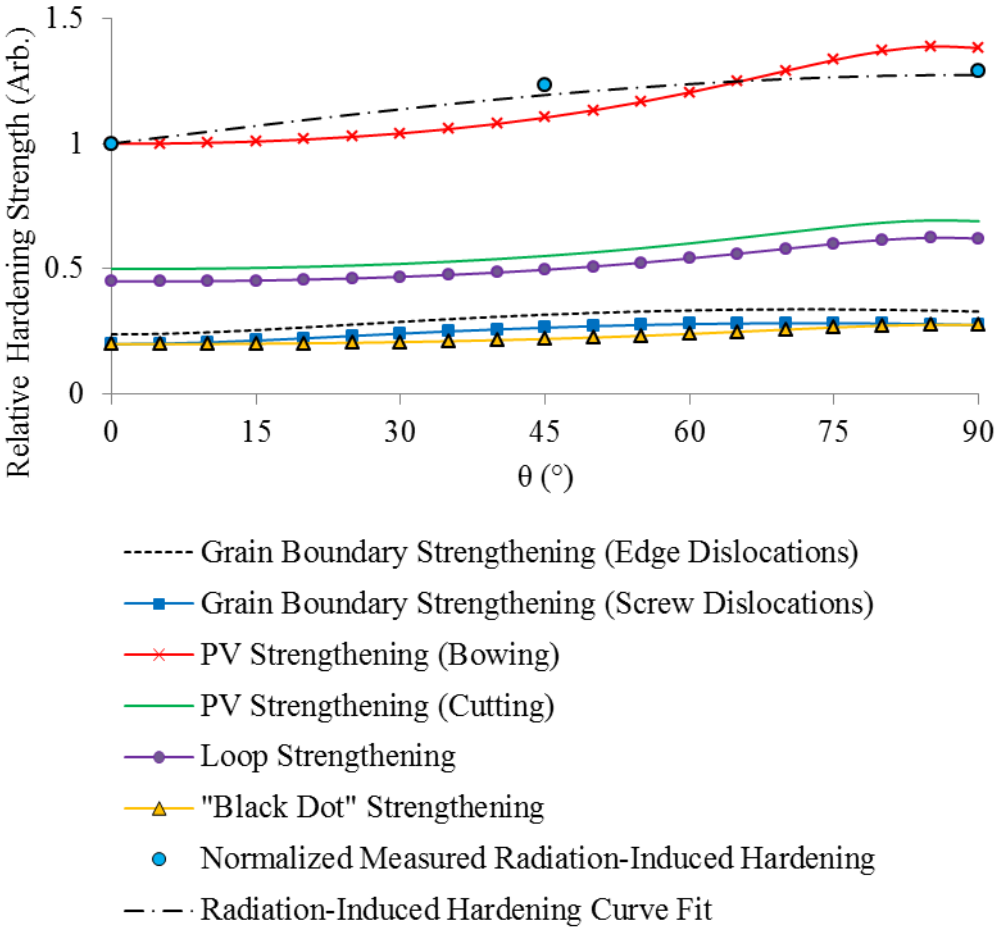

Figure 232: Relative Orientation-Dependent Strengths of Various Radiation-Induced Hardening Mechanisms

The curvature of the various radiation-induced hardening mechanisms vs. the observed hardening in Figure 232 suggests that the influence of grain boundary/dislocation hardening plays a dominant role in the overall radiation-induced hardening of the LAM rods. This is to be expected since (a) grain boundary/dislocation hardening is a long-range phenomenon, and (b) is a function of change of dislocation density, which is large at high radiative doses. To the author's knowledge, is analysis is "first-of-a-kind", and have impact in applications where textured polycrystals with

elongated microstructures (such as alloys built using laser additive manufacturing) are exposed to high dose radiation damage.

V.4 Orientation Dependent Slip Susceptibility and Work Hardening

Based on the load-extension data from Figure 171, the LAM work hardening and ductility under deformation is anisotropic. Slip readily occurs in the lowest energy slip systems in a crystal which are comprised of close-packed atomic planes; for fcc crystals, this occurs on $\{111\}$ planes in $<101>$ directions [61]. Samples experiencing deformation which contain an abundance of texture preferential to the <101>||N axes will more easily allow slip parallel to those axes. Recall that the bulk tensile testing data (Figure 171) as well as the nanoindentation data (Figure 189) collected for the unirradiated specimens show that vertical LAM of both the Inconel 600 and 316L stainless steel have lower yield strength and greater ductility than horizontal LAM. Therefore, it is expected that unirradiated vertical LAM should contain significantly more <101>||N texture than 45° or horizontal LAM. This was indeed observed in IPF_z maps of the LAM specimens (Figure 151 - Figure 154), resulting in the Taylor factor maps/histograms for both unirradiated and irradiated LAM alloys (Figure 166 - Figure 169).

As load increases, the slip systems tend to align parallel to the stress axis in tension and perpendicular to the stress axis in compression. Since the as annealed slip planes in these alloys are parallel to the rod axis for vertical LAM and perpendicular to the rod axis for horizontal LAM rods in the unloaded state (as evidenced by the

accumulation of <101> texture for both I600 and 316L vertical LAM, see Figure 151 and Figure 153), this explains the orientation dependence of the observed LAM work hardening behavior [177]. Furthermore, based on the nanoindentation data from Figure 189, the radiation-induced change of crystal orientation toward the <101>||N axes should be minimal perpendicular to the build direction (i.e. for horizontal LAM) and maximal parallel to the build direction (vertical LAM). This was also observed in Figure 151 - Figure 154.

V.5 LAM Melt Pool Nucleation and Solidification Thermodynamics

For the laser additively manufactured alloys built in this study (in all directions), the measured residual strain was significantly higher than their conventionally manufactured counterparts (see Figure 163 and Figure 164). The residual strain in as-fabricated LAM parts is based on many factors.

To consider possible methodologies to reduce residual strain in parts built by LAM, several observations regarding the nucleation and solidification of the melt pool during LAM must be acknowledged:

- The maximum temperature of the melt increases with increasing laser power [178-180] and increasing linear energy density [181, 182], but decreases marginally with increasing laser scanning speed [179, 180].
- The spatial temperature gradient increases in the melt pool nearly linearly with increased laser power [178, 183], and is larger for materials with lower thermal conductivity.

- The mean melt pool lifetime (from liquidation to solidification) increases with laser power and decreases with laser scanning speed [183].
- The length, width, and depth of the melt pool increase with linear energy density [182] and laser power [180].
- The viscosity of the liquid alloy decreases with increasing linear energy density and temperature [184].
- Liquid-solid diffusion occurs as a result of thermocapillary flow, while the Marangoni effect (i.e. mass transfer along the liquid-solid interface) occurs due to the liquid-solid interfacial energy gradient.
- Surface oxidation reduces the surface interfacial energy [185].

The solid-liquid interface velocity increases with increasing laser scanning speed and increasing powder size [186]; this is due to an increase in melt splashing as laser scan speed is increased [186-188]. Alloy melt pool nucleation is a random-fluctuation process (Arrhenius), but nuclei must be large enough that the solid volume created is large enough to overcome the energy cost of creating the solid-liquid surface. Therefore, the larger the difference between the undercooled volume temperature and the bulk alloy melting temperature, the smaller the nucleus volume needs to be. Nucleation then propagates by diffusion through the liquid.

Optimizing scan parameters such as laser power, scan speed, spot size, etc. may marginally reduce residual strain in LAM parts; however, altering these parameters often effects viscosity and wetting conditions of the alloy melt, which could produce voids and

reduce LAM part density. Furthermore, the significant residual strain in the LAM parts from this research was measured after annealing. Temporal temperature gradients during nucleation and solidification of the LAM melt pool can be in the range of 10^3 – 10^8 $K \cdot s^{-1}$ [183, 189-192]. With temperature gradients this large, the solid-liquid interface between the solid nucleus and surround liquid melt pool could expand at such a high velocity that the randomly oriented atoms in the surrounding liquid melt are unable to form stable crystallographic geometries during solidification. This can cause the alloy microstructure to become "immobilized" in a nonequilibrium state characterized as either crystalline with abundant residual strain or amorphous (i.e. metallic glass) [193-197].

The phenomena related to melt pool and solidification thermodynamics are temporal temperature gradients, spatial temperature gradients, and the resulting residual stress fields that follow. These properties can be explored using classical nucleation theory (CNT) developed primarily by Gibbs, upon which this discussion is based. For further reading related to alloy melt pool solidification thermodynamics, the reference *Alloy Physics* is recommended [198].

Melt pool solidification is an inherently non-equilibrium process; however, an interface exists between the bulk alloy melt and an undercooled melt pool region in which local equilibrium conditions exist. When this occurs, the surface velocity V_u can be described by Eq. 63, where D_S is the surface diffusion coefficient (on the order of $5 \cdot 10^{-10}$ $m^2 \cdot s^{-1}$), and a is the size of the solid structural unit (on the order of $5 \cdot 10^{-10}$ m^{-1}). Note that this case does not apply for the large interfacial velocities (much higher than 1

$m \cdot s^{-1}$), but will lead into the discussion of rapid solidification. The temperature of the alloy interface, T_i, can be computed from the liquidus slope m_L of the alloy phase diagram, shown in Eq. 64, where the subscripts *i*, *m*, and *L* refer to the interface, melt pool, and liquid, respectively.

Eq. 63

$$V_u = \frac{D_S}{a}$$

Eq. 64

$$T_i = T_m + m_L c_i$$

Kinetic undercooling is achieved when this equilibrium condition is perturbed by some amount ΔT_k, defined by Eq. 65, which is the difference between the alloy bulk melting temperature and the interface temperature. In practice, however, defects exist in the nuclei during solidification. Therefore, the velocity v_i and kinetic undercooling for a real-world "faceted" interface can be described by Eq. 66, where K_f is the kinetic coefficient, and $1 < n < 4$ [199]. To the first order approximation, Eq. 66 can be approximated with Eq. 67 where K_r is of the order of 1 [200]. As a result, for conventional metallurgical growth rates (10^{-6} – 10^{-4} $m \cdot s^{-1}$), the kinetic undercooling is negligible.

Eq. 65

$$\Delta T_k = T_m - T_i$$

Eq. 66

$$v_i = K_f \Delta T_k^n$$

Eq. 67

$$v_i = K_r \Delta T_k$$

The spatial and temporal temperature gradients present during the solidification of the LAM alloys are larger than those present during conventional manufacturing. When a region of the liquid alloy melt is cooled below a certain temperature, a driving force exists to initiate solidification (i.e. nucleation), described by Eq. 68 below where ΔG_V is the difference between the free energies of the solid (ΔG^S) and liquid (ΔG^L) phases of the alloy of volume V, solid/liquid interfacial area A^{SL}, and solid/liquid surface energy γ^{SL}. Assuming approximately spherical nuclei, the critical nucleation radius (r^*) is defined by Eq. 69, where ΔS_m is the solidification change in entropy of the melt pool, ΔT is the difference between the undercooled melt pool temperature and the melting temperature of the bulk alloy, and Γ is the Gibbs coefficient (approximately 10^{-7} K·m for metals).

Eq. 68

$$\Delta G = -V_S \left(\Delta G^L - \Delta G^S \right) + A^{SL} \gamma^{SL}$$

Eq. 69

$$r^* = \frac{2\gamma^{SL}}{\Delta S_m \Delta T} = \frac{2\Gamma}{\Delta T}$$

The solid-liquid interface has a capillary undercooling (ΔT_{cap}) effect which depends on the local curvature of the surface, κ, defined by Eq. 70. Based on this curvature, the chemical composition, and the interface velocity, the temperature of the interface can be defined by Eq. 71.

Eq. 70

$$\Delta T_{cap} = \Gamma \kappa$$

Eq. 71

$$T_i = T_m + m_L c_i - \frac{v_i}{K_r} - \Gamma \kappa$$

The composition of the solid nucleus is related to the surrounding liquid alloy composition by a "segregation coefficient" k shown in Eq. 72, where c_s and c_L are the concentration of atoms in the solid and liquid, respectively. The expanding solid-liquid interface then rejects solute in the liquid, yielding a balance of solidified and rejected solute giving a flux toward the liquid, shown in Eq. 73. The flux in Eq. 73 yields a boundary layer in the liquid surrounding the interface whose thickness δ is given by Eq. 74.

Eq. 72

$$k = \frac{c_s}{c_L}$$

Eq. 73

$$-D_L\left(\frac{\partial c}{\partial z}\right)_i = v_i c_i^L\left(1-k\right)$$

Eq. 74

$$\delta = \frac{D_L}{v_i}$$

Using Eq. 64 and Eq. 73, the gradient of the "melting" temperature at the solid-liquid interface (toward the liquid) is given by Eq. 75. Note that if the thermal gradient in the liquid surrounding the interface is lower than this value, the surrounding liquid will solidify onto the nucleus causing it to further expand into the liquid. This is described by Eq. 76.

Eq. 75

$$\left(\frac{dT_m}{dz}\right)_i = \frac{dT_m}{dc}\left(\frac{dc}{dz}\right)_i = -m_L\frac{v_i c_i^L\left(1-k\right)}{D_L}$$

Eq. 76

$$\nabla T_i^L > -m_L\frac{v_i c_i^L\left(1-k\right)}{D_L}$$

Mullins and Sekerka considered the energy cost associated with the increasing interfacial area of an expanding nucleus by studying sinusoidal perturbations at the

interface whose amplitude and period are ε and λ, respectively [201, 202]. These perturbations affect the thermal and chemical field surrounding the interface, yielding the perturbation amplitude variation rate shown in Eq. 77, where Λ and ΔT are the mean values of the liquid and solid regions, respectively, and ξ are (positive) functions of the growth rates.

Eq. 77

$$\frac{1}{\varepsilon}\frac{d\varepsilon}{dt} = m_L \nabla c \xi_c - \Lambda \nabla T \xi_T - \Gamma \frac{4\pi^2}{\lambda^2}$$

Based on Eq. 77, the stability criterion can be derived (Eq. 78 and Eq. 79), where H is enthalpy, by accounting for the mean thermal conductivity, latent heat of transformation, and the capillarity stabilization function *S(A) [203]*. In Eq. 78, when $A = 1$, $S(A) = 0$ and the interface is stable; however, when $A = 0$, $S(A) = 1$ and the stability criterion is identical to Eq. 76.

Eq. 78

$$\left(\frac{\Delta H_m}{2\Lambda_L} + \frac{\nabla T_i^L}{v_i}\right) > -\frac{\left(\Lambda_S + \Lambda_L\right)}{2\Lambda_L} m_L \frac{c_i^L \left(1-k\right)}{D_L} S\left(\mathrm{A}\right)$$

Eq. 79

$$\mathrm{A} = -\frac{\Gamma k v_i}{m_L D_L \left(1-k\right) c_i^L}$$

For the case rapid directional solidification found in LAM, the parameter $A = 1$, which yields Eq. 80 for the absolute stability velocity. Eq. 80 is independent of thermal gradients which are negligible in comparison to the solute gradient at the front of the solid-liquid interface. For sufficiently large growth rates, the resulting solute boundary layer can approach the interface thickness (Eq. 74).

Eq. 80

$$v_a = -\frac{m_L D_L (1-k) c_0}{\Gamma k}$$

If the interface velocity (i.e. the solidification rate) is large enough, the solidification microstructure does not have time to rearrange at the interface into a stable crystallographic arrangement; that is, the liquid solidifies without sufficient segregation, and the solute segregation coefficient approaches unity. The segregation coefficient is therefore a function of interface velocity ($k \rightarrow k_v$), defined by Eq. 81 below [204]. The theoretical maximum interface velocity is equal to the velocity of sound in the alloy liquid (approximately 10^3 m·s^{-1} for most metals).

Eq. 81

$$k_v = \frac{k + \frac{a v_i}{D_s}}{1 + \frac{a v_i}{D_s}}$$

The thermodynamic analysis of LAM alloy melt solidification suggests that even though annealing at higher temperatures for longer periods of time may reduce residual strain in parts built by LAM, it might be more effective to explore LAM methodologies in which parts are fabricated with less residual strain to begin with. The direction of heat flow at any point during solidification is normal to the surface (i.e. downward into the powder bed) [10, 11]. Reducing the temperature gradients between the top and bottom surface of the LAM powder bed melt could reduce the velocity of expanding liquid-to-solid interface of the nuclei during alloy melt solidification.

Since the alloys produced by the EOS M270 in this research are solidifying sufficiently slowly that the rods are crystalline, reduction of the solid-liquid alloy melt interface expansion velocity may be achieved by significantly increasing the temperature of the powder bed during LAM to, say, 2/3 the melting temperature of the alloy being built [205]. Additionally, this may improve the CSL boundary character of parts built by LAM, thereby improving resistance to grain boundary-related phenomena such as IGSCC, HIC, creep, etc. [162, 206-210]. The EOS M270 used in this research is not equipped to heat the powder bed above 80 °C, so this hypothesis has could not been tested.

CHAPTER VI

CONCLUSIONS AND FUTURE WORK

VI.1 Conclusions

Laser additive manufacturing methods were developed by Lockheed Martin Space Systems Company in collaboration with Quad City Manufacturing Laboratory for the manufacturing of Inconel 600 and 316L stainless steel rods. This development was carried out as part of a U.S. Department of Energy program investigating the application of LAM methods for implementation in nuclear energy systems. For this work, sets of these LAM alloys were provided to facilitate the first-of-a-kind evaluation of their irradiation performance. The alloys were irradiated using Ni^{+} and Fe^{+} self-ions up to 80 dpa using the methods outlined in Ch. III. The alloys were characterized using XRD, SEM/EDS, EBSD, nanoindentation, SPM, and FIB/TEM. Orientation-dependent relationships were derived to predictively describe the radiation-induced changes in LAM rod properties.

This study is significant because manufacturing of materials and components for nuclear systems is a large portion of the cost of nuclear systems, and additive manufacturing offers a potentially cheaper method of producing such materials. In order for materials processed through LAM to become qualified for service in a nuclear energy system, the impact of fabrication-specific characteristics of component microstructures and their possible impact on irradiation-exacerbated phenomena must be understood. Microstructure plays a critical role in establishing mechanical properties, and is often

dependent on alloy composition, phase morphology, impurity content, and thermal history.

All Inconel 600 and 316L rods in this study were exposed to neutron damage and, at the time this dissertation was written, remain under exposure to the neutron field in the TAMU TRIGA Reactor to accumulate dose. The 316L and Inconel 600 samples were irradiated using self-ions to simulate high dose neutron damage. Immediate conclusions from post-irradiation examinations are as follows:

- XRD and EBSD revealed that the Inconel 600 and 316L stainless steel rods were additively manufactured with significant texture whose slip planes are parallel to the build direction. Further, the LAM rods have elongated grain microstructures which are oriented parallel to the build direction as well.
- SEM/EDS showed chromium/carbon rich precipitates which formed on the irradiated surface of all Inconel 600 samples (including the conventionally manufactured control).
- SPM data showed that the RMS surface roughness of the radiation-produced precipitates on Inconel 600 is dependent on build orientation where, from greatest to least, horizontal LAM > 45° LAM > vertical LAM > conventionally manufactured.
- Nanoindentation revealed anisotropic radiation-induced hardening where, from greatest to least, horizontal LAM > 45° LAM > vertical LAM > conventionally manufactured. In general, the hardening for LAM specimens was larger than for the conventionally manufactured controls.

- TEM of irradiated specimens revealed that a variety of radiation-produced defects, such as precipitates, dislocations, and loops, appear to aggregate into oriented ellipsoidal defects.

Empirical relationships between radiation-induced increase in surface roughness via chromium/carbide precipitation and LAM build orientation were created. A first-of-a-kind phenomenologically based relationship which describes the orientation dependence of radiation-induced segregation and precipitation in LAM was derived based on geometric and crystalline atomic diffusion principles. The derived relationship agrees closely with the measured data.

Trigonometric relationships between the radiation-induced increase in hardening and LAM build orientation were created. A first-of-a-kind phenomenologically based relationship which describes the orientation dependence of radiation-induced hardening and embrittlement in LAM was derived based on geometric and crystalline radiation hardening principles. Based on the relative strengths of the various hardening mechanisms in comparison to the measured hardening data, the grain shape and crystalline texture strongly influence the orientation dependence of radiation-induced hardening. The derived relationship agrees closely with the measured data.

A method is proposed, based on LAM melt pool solidification thermodynamics, which utilizes a heated powder bed stage to reduce temperature gradients during LAM in order to reduce the solid-liquid interface velocity of the LAM alloy melt during solidification and promote additional annealing/relaxation during manufacturing, thereby reducing residual strain and intergranular disorder of the LAM microstructure.

VI.2 Recommendations and Future Work

The alloys built by LAM in this research have significantly higher residual strain, crystalline misorientation, and grain boundary disorder than their conventionally manufactured counterparts. These properties are likely associated with significant residual stress fields. Stress concentrations are undesirable in nuclear materials since they are susceptible to dislocation pileup, which increase the probability of intergranular defect nucleation and rupture/failure. As such, it is strongly recommended that methodologies be developed for these materials which minimize to residual strain of components built by LAM. One such method has been proposed in this work based on LAM melt pool solidification thermodynamics whereby the LAM powder stage is heated to 2/3 the melting temperature of the alloy during manufacturing.

Build protocol optimization for densified ODS rods manufactured by LAM is desirable. Once this is achieved, irradiation testing and characterization of ODS steels built by LAM should be conducted in order to determine the response of ODS rods to radiation damage which are built by LAM.

LAM alloys should be fabricated at a variety of build orientations (0°, 15°, 30°, 45°, 60°, 75°, and 90°, for example) to more fully understand orientation dependence of mechanical property changes due to radiation damage.

Once meaningful neutron damage has accumulated in the samples inserted in the TAMU TRIGA reactor for this project, these samples should be characterized in order to determine the orientation dependence of LAM specimens to neutron damage.

Finally, the orientation dependence of the thermal conductivity of nuclear materials produced by LAM should be investigated. Since the thermal conductivities of the alloys under investigation in this project are dominated by conduction electron transport, it is possible that the thermal conductivity of these LAM alloys will be relatively insensitive to build orientation. However, ceramic nuclear materials could theoretically be built using LAM. As example of such a material is the accident-tolerant nuclear fuel (ATF) candidate UN/U_3Si_2; it may even be easier to fabricate this ATF using LAM since the powders do not densify until a sintering temperature of at least 1665 °C is reached in order to achieve liquid phase sintering (LPS) of the U_3Si_2 phase [211].

Unlike alloys which have conduction electrons to transport thermal energy, the thermal conductivity of ceramic materials is dominated by phonon transport. The phonon density of states (DOS) is expected to be affected by the elongated oriented grain structure itself due to highly anisotropic phonon scattering with grain boundaries, as well as by the significant texture associated with materials built by LAM due to anisotropic phonon scattering. For example, the thermal conductivity of crystalline pyrolytic carbon differs by as much as 200:1 depending on orientation [212]. This could result in ceramic materials in which the thermal conductivity differs significantly with direction.

REFERENCES

[1] D. L. Bourell, "Perspectives on additive manufacturing", *Annual Review of Materials Research*, vol. 46, pp. 1-18, 2016.

[2] R. Jiang, R. Kleer, F. T. Piller, "Predicting the future of additive manufacturing: A delphi study on economic and societal implications of 3d printing for 2030", *Technological Forecasting and Social Change*, vol. 117, pp. 84-97, 2017.

[3] H. Piili, A. Happonen, T. Vaisto, V. Venkataramanan, J. Partanen, A. Salminen, "Cost estimation of laser additive manufacturing of stainless steel", *15th Nordic Laser Materials Processing Conference, Nolamp 15*, vol. 78, pp. 388-396, 2015.

[4] D. Thomas, "Costs, benefits, and adoption of additive manufacturing: A supply chain perspective", *International Journal of Advanced Manufacturing Technology*, vol. 85, pp. 1857-1876, 2016.

[5] M. Schroder, B. Falk, R. Schmitt, "Evaluation of cost structures of additive manufacturing processes using a new business model", *7th Industrial Product-Service Systems Conference - Ipss, Industry Transformation for Sustainability and Business*, vol. 30, pp. 311-316, 2015.

[6] J. R. Lovering, A. Yip, T. Nordhaus, "Historical construction costs of global nuclear power reactors", *Energy Policy*, vol. 91, pp. 371-382, 2016.

[7] Y. Guerin, G. S. Was, S. J. Zinkle, "Materials challenges for advanced nuclear energy systems", *Mrs Bulletin*, vol. 34, pp. 10-14, 2009.

[8] M. Griffiths, G. A. Bickel, S. R. Douglas, "Irradiation-induced embrittlement of inconel 600 flux detectors in candu (r) reactors", *Proceedings of the 18th International Conference on Nuclear Engineering 2010*, vol. 5, pp. 293-298, 2011.

[9] T. R. Allen, J. T. Busby, R. L. Klueh, S. A. Maloy, M. B. Toloczko, "Cladding and duct materials for advanced nuclear recycle reactors", *The Journal of the Minerals*, vol. 60, pp. 15-23, 2008.

[10] H. L. Wei, J. Mazumder, T. Debroy, "Evolution of solidification texture during additive manufacturing", *Scientific Reports*, vol. 5, pp. 1-7, 2015.

[11] T. Mukherjee, J. S. Zuback, A. De, T. Debroy, "Printability of alloys for additive manufacturing", *Scientific Reports*, vol. 6, pp. 1-7, 2016.

[12] W. J. Sames, F. A. List, S. Pannala, R. R. Dehoff, S. S. Babu, "The metallurgy and processing science of metal additive manufacturing", *International Materials Reviews*, vol. 61, pp. 315-360, 2016.

[13] S. Gorsse, C. Hutchinson, M. Goune, R. Banerjee, "Additive manufacturing of metals: A brief review of the characteristic microstructures and properties of steels, ti-6al-4v and high-entropy alloys", *Science and Technology of Advanced Materials*, vol. 18, pp. 584-610, 2017.

[14] J. J. Lewandowski, M. Seifi, "Metal additive manufacturing: A review of mechanical properties", *Annual Review of Materials Research*, vol. 46, pp. 151-186, 2016.

[15] W. E. Frazier, "Metal additive manufacturing: A review", *Journal of Materials Engineering and Performance*, vol. 23, pp. 1917-1928, 2014.

[16] I. Gibson, D. W. Rosen, B. Stucker, "Additive manufacturing technologies: Rapid prototyping to direct digital manufacturing", Springer, London ; New York, 2010.

[17] J. P. Kruth, L. Froyen, J. Van Vaerenbergh, P. Mercelis, M. Rombouts, B. Lauwers, "Selective laser melting of iron-based powder", *Journal of Materials Processing Technology*, vol. 149, pp. 616-622, 2004.

[18] S. A. David, S. S. Babu, J. M. Vitek, "Welding: Solidification and microstructure", *Jom-Journal of the Minerals Metals & Materials Society*, vol. 55, pp. 14-20, 2003.

[19] M. H. Farshidianfar, A. Khajepour, A. P. Gerlich, "Effect of real-time cooling rate on microstructure in laser additive manufacturing", *Journal of Materials Processing Technology*, vol. 231, pp. 468-478, 2016.

[20] Y. Ustinovshikov, "Phase transformations in alloys of the ni-cr system", *Journal of Alloys and Compounds*, vol. 543, pp. 227-232, 2012.

[21] J. J. Kai, R. D. Lee, "Effects of irradiation on the microstructure of inconel 600-alloy", *Journal of Nuclear Materials*, vol. 191, pp. 717-721, 1992.

[22] M. Griffiths, "The effect of irradiation on ni-containing components in candu reactor cores: A review", *AECL Nuclear Review, Atomic Energy of Canada*, vol. 2, pp. 1-16, 2013.

[23] L. N. Carter, C. Martin, P. J. Withers, M. M. Attallah, "The influence of the laser scan strategy on grain structure and cracking behaviour in slm powder-bed fabricated nickel superalloy", *Journal of Alloys and Compounds*, vol. 615, pp. 338-347, 2014.

[24] X. M. Bai, A. F. Voter, R. G. Hoagland, M. Nastasi, B. P. Uberuaga, "Efficient annealing of radiation damage near grain boundaries via interstitial emission", *Science*, vol. 327, pp. 1631-1634, 2010.

[25] A. Vattre, T. Jourdan, H. Ding, M. C. Marinica, M. J. Demkowicz, "Non-random walk diffusion enhances the sink strength of semicoherent interfaces", *Nature Communications*, vol. 7, pp. 1-10, 2016.

[26] I. J. Beyerlein, A. Caro, M. J. Demkowicz, N. A. Mara, A. Misra, B. P. Uberuaga, "Radiation damage tolerant nanomaterials", *Materials Today*, vol. 16, pp. 443-449, 2013.

[27] N. E. Agency, "Janis nuclear data information system", in: O.f.E.C.-o.a. Development (Ed.) Secondary "Janis nuclear data information system", http://www.oecd-nea.org/janis/, 2014.

[28] "Tables of physical & chemical constants (16th edition 1995). 4.7.1 nuclear fission.". Kaye & Laby Online. Version 1.0 (2005). <http://www.kayelaby.npl.co.uk/atomic_and_nuclear_physics/4_7/4_7_1.html>).

[29] W. R. Leo, "Techniques for nuclear and particle physics experiments : A how-to approach", 2nd rev. ed., Springer, Berlin ; New York, 1994.

[30] G. S. Was, "Fundamentals of radiation materials science: Metals and alloys", Springer, Berlin ; New York, 2007.

[31] G. R. Choppin, G. R. Choppin, J.-O. Liljenzin, J. Rydberg, "Radiochemistry and nuclear chemistry", 3rd ed., Butterworth-Heinemann, Woburn, MA, 2002.

[32] D. Terentyev, A. Bakaev, "Radiation-induced strengthening and absorption of dislocation loops in ferritic fe-cr alloys: The role of cr segregation", *Journal of Physics: Condensed Matter*, vol. 25, pp. 265702, 2013.

[33] G. S. Was, T. R. Allen, J. T. Busby, J. Gan, D. Damcott, D. Carter, M. Atzmon, E. A. Kenik, "Microchemistry and microstructure of proton-irradiated austenitic alloys: Toward an understanding of irradiation effects in lwr core components", *Journal of Nuclear Materials*, vol. 270, pp. 96-114, 1999.

[34] S. M. Bruemmer, E. P. Simonen, P. M. Scott, P. L. Andresen, G. S. Was, J. L. Nelson, "Radiation-induced material changes and susceptibility to intergranular failure of light-water-reactor core internals", *Journal of Nuclear Materials*, vol. 274, pp. 299-314, 1999.

[35] G. Gupta, Z. Jiao, A. N. Ham, J. T. Busby, G. S. Was, "Microstructural evolution of proton irradiated t91", *Journal of Nuclear Materials*, vol. 351, pp. 162-173, 2006.

[36] F. Garner, "Irradiation performance of cladding and structural steels in liquid metal reactors", Materials science and technology, Wiley-VCH Verlag GmbH & Co. KGaA2006.

[37] H. E. K. J.L. Brimhall, "Void formation in irradiated copper, nickel, and copper-nickel alloys", *Radiation Effects*, vol. 15, pp. 259-272, 1972.

[38] J. P. Foster, K. Bunde, M. L. Grossbeck, E. R. Gilbert, "Temperature dependence of the 20% cold worked 316 stainless steel steady state irradiation creep rate", *Journal of Nuclear Materials*, vol. 270, pp. 357-367, 1999.

[39] W. Zhou, Z. L. Wang, "Scanning microscopy for nanotechnology: Techniques and applications", Springer, New York, 2007.

[40] P. P. Ewald, "Fifty years of x-ray diffraction. Dedicated to the international union of crystallography on the occasion of the commemoration meeting in munich", Published for the International Union of Crystallography by A. Oosthoek's Uitgeversmij, Utrecht, 1962.

[41] A. J. Schwartz, M. Kumar, B. L. Adams, "Electron backscatter diffraction in materials science", Kluwer Academic, New York, 2000.

[42] A. J. Schwartz, "Electron backscatter diffraction in materials science", 2nd ed., Springer, New York, 2009.

[43] E. A. Wood, "Crystal orientation manual", Columbia University Press, New York,, 1963.

[44] T. B. Britton, J. Jiang, Y. Guo, A. Vilalta-Clemente, D. Wallis, L. N. Hansen, A. Winkelmann, A. J. Wilkinson, "Tutorial: Crystal orientations and ebsd - or which way is up?", *Materials Characterization*, vol. 117, pp. 113-126, 2016.

[45] "Channel 5 processing software manual", *Oxford Instruments*, vol. 1, pp. 1-506, 2014.

[46] "Standard practice for determining average grain size using electron backscatter diffraction (ebsd) in fully recrystallized polycrystalline materials characterization", ASTM E2627-13, pp. 1-5, 2013.

[47] D. G. Brandon, "Structure of high-angle grain boundaries", *Acta Metallurgica*, vol. 14, pp. 1479-1484, 1966.

[48] L. S. Shvindlerman, B. B. Straumal, "Regions of existence of special and non-special grain-boundaries", *Acta Metallurgica*, vol. 33, pp. 1735-1749, 1985.

[49] G. S. Was, V. Thaveeprungsriporn, D. C. Crawford, "Grain boundary misorientation effects on creep and cracking in ni-based alloys", *Journal of the Minerals, Metals & Materials Society*, vol. 50, pp. 44-49, 1998.

[50] H. Kokawa, T. Watanabe, S. Karashima, "Sliding behavior and dislocation-structures in aluminum grain-boundaries", *Philosophical Magazine a-Physics of Condensed Matter Structure Defects and Mechanical Properties*, vol. 44, pp. 1239-1254, 1981.

[51] J. Don, S. Majumdar, "Creep cavitation and grain-boundary structure in type-304 stainless-steel", *Acta Metallurgica*, vol. 34, pp. 961-967, 1986.

[52] T. Watanabe, "Grain-boundary design for desirable mechanical-properties", *Journal De Physique*, vol. 49, pp. 507-519, 1988.

[53] D. C. Crawford, G. S. Was, "The role of grain-boundary misorientation in intergranular cracking of ni-16cr-9fe in 360-degrees-c argon and high-purity water", *Metallurgical Transactions a-Physical Metallurgy and Materials Science*, vol. 23, pp. 1195-1206, 1992.

[54] K. T. Aust, U. Erb, G. Palumbo, "Interface control for resistance to intergranular cracking", *Materials Science and Engineering a-Structural Materials Properties Microstructure and Processing*, vol. 176, pp. 329-334, 1994.

[55] E. M. Lehockey, G. Palumbo, "On the creep behaviour of grain boundary engineered nickel", *Materials Science and Engineering a-Structural Materials Properties Microstructure and Processing*, vol. 237, pp. 168-172, 1997.

[56] E. M. Lehockey, G. Palumbo, P. Lin, A. M. Brennenstuhl, "On the relationship between grain boundary character distribution and intergranular corrosion", *Scripta Materialia*, vol. 36, pp. 1211-1218, 1997.

[57] E. M. Lehockey, G. Palumbo, A. Brennenstuhl, P. Lin, "Grain boundary engineered lead alloys", *Interfacial Engineering for Optimized Properties*, vol. 458, pp. 243-248, 1997.

[58] G. Palumbo, E. M. Lehockey, P. Lin, U. Erb, K. T. Aust, "A grain boundary engineering approach to materials reliability", *Interfacial Engineering for Optimized Properties*, vol. 458, pp. 273-282, 1997.

[59] E. M. Lehockey, G. Palumbo, K. T. Aust, U. Erb, P. Lin, "On the role of intercrystalline defects in polycrystal plasticity", *Scripta Materialia*, vol. 39, pp. 341-346, 1998.

[60] V. Randle, A. Day, "Use of rodrigues-frank space for representation of microtexture and grain-boundary parameters", *Materials Science and Technology*, vol. 9, pp. 1069-1078, 1993.

[61] D. Hull, D. J. Bacon, "Introduction to dislocations", 4th ed., Butterworth-Heinemann, Oxford Oxfordshire ; Boston, 2001.

[62] E. Schmid, Boas, Walter, "Kristallplastizität", Springer, Ann Arbor, Michigan, 1935.

[63] G. I. Taylor, "Plastic strain in metals", *Journal of the Institute of Metals*, vol. 62, pp. 307-324, 1938.

[64] M. Kulka, N. Makuch, P. Dziarski, A. Piasecki, "A study of nanoindentation for mechanical characterization of chromium and nickel borides' mixtures formed by laser boriding", *Ceramics International*, vol. 40, pp. 6083-6094, 2014.

[65] A. C. Fischer-Cripps, "Nanoindentation", 3rd ed., Springer, New York, 2011.

[66] A. Gouldstone, N. Chollacoop, M. Dao, J. Li, A. M. Minor, Y. L. Shen, "Indentation across size scales and disciplines: Recent developments in experimentation and modeling", *Acta Materialia*, vol. 55, pp. 4015-4039, 2007.

[67] Y. Yang, S. H. Kang, C. H. Zhang, J. Jang, "Nanoindentation on an oxide dispersion strengthened steel and a ferritic/martensitic steel implanted with he ions", *Journal of Nuclear Materials*, vol. 455, pp. 325-329, 2014.

[68] Y. V. Milman, A. A. Golubenko, S. N. Dub, "Indentation size effect in nanohardness", *Acta Materialia*, vol. 59, pp. 7480-7487, 2011.

[69] S. Qu, Y. Huang, G. M. Pharr, K. C. Hwang, "The indentation size effect in the spherical indentation of iridium: A study via the conventional theory of mechanism-based strain gradient plasticity", *International Journal of Plasticity*, vol. 22, pp. 1265-1286, 2006.

[70] J. G. Swadener, E. P. George, G. M. Pharr, "The correlation of the indentation size effect measured with indenters of various shapes", *Journal of the Mechanics and Physics of Solids*, vol. 50, pp. 681-694, 2002.

[71] J. G. Swadener, E. P. George, G. M. Pharr, "The correlation of indentation size effect experiments with pyramidal and spherical indenters", *Thin Films: Stresses and Mechanical Properties Ix*, vol. 695, pp. 451-456, 2002.

[72] W. D. Nix, H. J. Gao, "Indentation size effects in crystalline materials: A law for strain gradient plasticity", *Journal of the Mechanics and Physics of Solids*, vol. 46, pp. 411-425, 1998.

[73] G. M. Pharr, E. G. Herbert, Y. F. Gao, "The indentation size effect: A critical examination of experimental observations and mechanistic interpretations", *Annual Review of Materials Research*, vol. 40, pp. 271-292, 2010.

[74] S. V. Kalinin, A. Gruverman, "Scanning probe microscopy: Electrical and electromechanical phenomena at the nanoscale", Springer, New York, 2007.

[75] D. B. Williams, C. B. Carter, "Transmission electron microscopy: A textbook for materials science", 2nd ed., Springer, New York, 2008.

[76] C. Sun, S. Zheng, C. C. Wei, Y. Wu, L. Shao, Y. Yang, K. T. Hartwig, S. A. Maloy, S. J. Zinkle, T. R. Allen, H. Wang, X. Zhang, "Superior radiation-resistant nanoengineered austenitic 304l stainless steel for applications in extreme radiation environments", *Scientific Reports*, vol. 5, pp. 1-7, 2015.

[77] C. Sun, K. Y. Yu, J. H. Lee, Y. Liu, H. Wang, L. Shao, S. A. Maloy, K. T. Hartwig, X. Zhang, "Enhanced radiation tolerance of ultrafine grained fe-cr-ni alloy", *Journal of Nuclear Materials*, vol. 420, pp. 235-240, 2012.

[78] S. Ukai, M. Fujiwara, "Perspective of ods alloys application in nuclear environments", *Journal of Nuclear Materials*, vol. 307, pp. 749-757, 2002.

[79] T. Y. Chen, E. Aydogan, J. G. Gigax, D. Chen, J. Wang, X. M. Wang, S. Ukai, F. A. Garner, L. Shao, "Microstructural changes and void swelling of a 12cr ods ferritic-martensitic alloy after high-dpa self-ion irradiation", *Journal of Nuclear Materials*, vol. 467, pp. 42-49, 2015.

[80] C. Kittel, "Introduction to solid state physics", 8th ed., Wiley, Hoboken, NJ, 2005.

[81] W. Setyawan, S. Curtarolo, "High-throughput electronic band structure calculations: Challenges and tools", *Computational Materials Science*, vol. 49, pp. 299-312, 2010.

[82] B. Fultz, J. M. Howe, "Transmission electron microscopy and diffractometry of materials", 3rd ed., Springer, Berlin ; New York, 2008.

[83] R. Choudhary, H. Kumar, R. K. Garg, "Analysis and evaluation of heat affected zones in electric discharge machining of en-31 die steel", *Indian Journal of Engineering and Materials Sciences*, vol. 17, pp. 91-98, 2010.

[84] P. T. Eubank, M. R. Patel, M. A. Barrufet, B. Bozkurt, "Theoretical-models of the electrical-discharge machining process .3. The variable mass, cylindrical plasma model", *Journal of Applied Physics*, vol. 73, pp. 7900-7909, 1993.

[85] P. Rupajati, B. O. P. Soepangkat, B. Pramujati, H. C. K. Agustin, "Optimization of recast layer thickness and surface roughness in the wire edm process of aisi h13 tool steel using taguchi and fuzzy logic", *Advances in Applied Mechanics and Materials*, vol. 493, pp. 529-534, 2014.

[86] H. Sidhom, F. Ghanem, T. Amadou, G. Gonzalez, C. Braham, "Effect of electro discharge machining (edm) on the aisi316l ss white layer microstructure and corrosion

resistance", *International Journal of Advanced Manufacturing Technology*, vol. 65, pp. 141-153, 2013.

[87] R. a. W. Matthew M. Nowell, Brian W. True, "Ebsd sample preparation: Techniques, tips, and tricks", *Microscopy and Microanalysis*, vol. 11, pp. 504-505, 2005.

[88] J. P. B. J.F. Ziegler, "Srim", Secondary "Srim", http://www.srim.org/, 2013.

[89] "Astm e521-83, standard practice for neutron radiation damage simulation by charged-particle irradiation", ASTM E521-83, pp. 1-8, 2009.

[90] M. I. Bratchenko, V. V. Bryk, S. V. Dyuldya, A. S. Kalchenko, N. P. Lazarev, V. N. Voyevodin, "Comments on dpa calculation methods for ion beam driven simulation irradiations", *Voprosy Atomnoj Nauki i Tekhniki Fizika Radiatsionnykh Povrezhdenij i Radiatsionnoe Materialovedenie*, vol. 43, pp. 11-16, 2013.

[91] R. E. Stoller, M. B. Toloczko, G. S. Was, A. G. Certain, S. Dwaraknath, F. A. Garner, "On the use of srim for computing radiation damage exposure", *Nuclear Instruments & Methods in Physics Research Section B-Beam Interactions with Materials and Atoms*, vol. 310, pp. 75-80, 2013.

[92] "Effects of radiation on substructure and mechanical properties of metals and alloys", ASTM STP529-EB, pp. 1-530, 1973.

[93] J. G. Gigax, E. Aydogan, T. Chen, D. Chen, L. Shao, Y. Wu, W. Y. Lo, Y. Yang, F. A. Garner, "The influence of ion beam rastering on the swelling of self-ion irradiated pure iron at 450 degrees c", *Journal of Nuclear Materials*, vol. 465, pp. 343-348, 2015.

[94] Z. G. Wang, Z. Y. Zhu, G. M. Jin, "Materials for advanced energy systems and fission & fusion engineering: Proceedings of the seventh china-japan symposium", World Scientific, River Edge, NJ London, 2003.

[95] X. L. Wu, X. Pan, J. F. Stubbins, "Analysis of notch strengthening of 316l stainless steel with and without irradiation-induced hardening using ebsd and fem", *Journal of Nuclear Materials*, vol. 361, pp. 228-238, 2007.

[96] A. Medevielle, I. Hugon, O. Dugne, "Electron backscatter diffraction: Applications for nuclear materials", *Journal of Microscopy-Oxford*, vol. 195, pp. 233-238, 1999.

[97] S. I. Wright, M. M. Nowell, S. P. Lindeman, P. P. Camus, M. De Graef, M. A. Jackson, "Introduction and comparison of new ebsd post-processing methodologies", *Ultramicroscopy*, vol. 159, pp. 81-94, 2015.

[98] T. Karthikeyan, M. K. Dash, S. Saroja, M. Vijayalakshmi, "Evaluation of misindexing of ebsd patterns in a ferritic steel", *Journal of Microscopy*, vol. 249, pp. 26-35, 2013.

[99] S. Raju, K. Sivasubramanian, R. Divakar, G. Panneerselvam, A. Banerjee, E. Mohandas, M. P. Antony, "Thermal expansion studies on inconel-600((r)) by high temperature x-ray diffraction", *Journal of Nuclear Materials*, vol. 325, pp. 18-25, 2004.

[100] C. E. Pinedo, A. P. Tschiptschin, "Low temperature plasma carburizing of aisi 316l austenitic stainless steel and aisi f51 duplex stainless steel", *Rem-Revista Escola De Minas*, vol. 66, pp. 209-214, 2013.

[101] B. E. Warren, "X-ray studies of deformed metals", *Progress in Metal Physics*, vol. 8, pp. 147-202, 1959.

[102] G. P. Airey, "Effect of processing variables on the caustic stress-corrosion resistance of inconel alloy 600", *Corrosion*, vol. 36, pp. 9-17, 1980.

[103] N. Pessall, M. Baron, J. Schreurs, "The influence of ion-implantation on the corrosion-resistance of inconel alloy 600", *Journal of Metals*, vol. 32, pp. 20-20, 1980.

[104] Q. W. Yan Li Wang, Hui Jun Liu, Chao Liu Zeng, "Effect of grain refinement on the corrosion of ni-cr alloys in molten (li,na,k)f", *Corrosion Science*, vol. 109, pp. 43-49, 2016.

[105] V. Y. Gertsman, S. M. Bruemmer, "Study of grain boundary character along intergranular stress corrosion crack paths in austenitic alloys", *Acta Materialia*, vol. 49, pp. 1589-1598, 2001.

[106] B. Alexandreanu, B. Capell, G. S. Was, "Combined effect of special grain boundaries and grain boundary carbides on igscc of ni-16cr-9fe-xc alloys", *Materials Science and Engineering a-Structural Materials Properties Microstructure and Processing*, vol. 300, pp. 94-104, 2001.

[107] L. Tan, K. Sridharan, T. R. Allen, R. K. Nanstad, D. A. Mcclintock, "Microstructure tailoring for property improvements by grain boundary engineering", *Journal of Nuclear Materials*, vol. 374, pp. 270-280, 2008.

[108] D. S. Lee, H. S. Ryoo, S. K. Hwang, "A grain boundary engineering approach to promote special boundaries in pb-base alloy", *Materials Science and Engineering a-Structural Materials Properties Microstructure and Processing*, vol. 354, pp. 106-111, 2003.

[109] M. Shimada, H. Kokawa, Z. J. Wang, Y. S. Sato, I. Karibe, "Optimization of grain boundary character distribution for intergranular corrosion resistant 304 stainless steel by twin-induced grain boundary engineering", *Acta Materialia*, vol. 50, pp. 2331-2341, 2002.

[110] Y. Pan, B. L. Adams, T. Olson, N. Panayotou, "Grain-boundary structure effects on intergranular stress corrosion cracking of alloy x-750", *Acta Materialia*, vol. 44, pp. 4685-4695, 1996.

[111] M. A. Mohtadi-Bonab, M. Eskandari, J. A. Szpunar, "Texture, local misorientation, grain boundary and recrystallization fraction in pipeline steels related to hydrogen induced cracking", *Materials Science and Engineering a-Structural Materials Properties Microstructure and Processing*, vol. 620, pp. 97-106, 2015.

[112] N. Sakaguchi, Y. Ohguchi, T. Shibayama, S. Watanabe, H. Kinoshita, "Surface cracking on sigma 3, sigma 9 csl and random grain boundaries in helium implanted 316l austenitic stainless steel", *Journal of Nuclear Materials*, vol. 432, pp. 23-27, 2013.

[113] N. Sakaguchi, M. Endo, S. Watanabe, H. Kinoshita, S. Yamashita, H. Kokawa, "Radiation-induced segregation and corrosion behavior on sigma 3 coincidence site lattice and random grain boundaries in proton-irradiated type-316l austenitic stainless steel", *Journal of Nuclear Materials*, vol. 434, pp. 65-71, 2013.

[114] C. M. Barr, G. A. Vetterick, K. A. Unocic, K. Hattar, X. M. Bai, M. L. Taheri, "Anisotropic radiation-induced segregation in 316l austenitic stainless steel with grain boundary character", *Acta Materialia*, vol. 67, pp. 145-155, 2014.

[115] A. J. Wilkinson, T. B. Britton, J. Jiang, P. S. Karamched, "A review of advances and challenges in ebsd strain mapping", *Emas 2013 Workshop: 13th European Workshop on Modern Developments and Applications in Microbeam Analysis*, vol. 55, pp. 1-9, 2014.

[116] M. Kamaya, A. J. Wilkinson, J. M. Titchmarsh, "Measurement of plastic strain of polycrystalline material by electron backscatter diffraction", *Nuclear Engineering and Design*, vol. 235, pp. 713-725, 2005.

[117] S. I. Wright, M. M. Nowell, D. P. Field, "A review of strain analysis using electron backscatter diffraction", *Microscopy and Microanalysis*, vol. 17, pp. 316-329, 2011.

[118] D. J. Oliver, J. E. Bradby, S. Ruffell, J. S. Williams, P. Munroe, "Nanoindentation-induced phase transformation in relaxed and unrelaxed ion-implanted amorphous germanium", *Journal of Applied Physics*, vol. 106, pp. 1-6, 2009.

[119] K. Xiong, J. F. Gu, "Understanding pop-in phenomena in feni3 nanoindentation", *Intermetallics*, vol. 67, pp. 111-120, 2015.

[120] A. Barnoush, M. T. Welsch, H. Vehoff, "Correlation between dislocation density and pop-in phenomena in aluminum studied by nanoindentation and electron channeling contrast imaging", *Scripta Materialia*, vol. 63, pp. 465-468, 2010.

[121] S. Bhagavat, I. Kao, "Nanoindentation of lithium niobate: Hardness anisotropy and pop-in phenomenon", *Materials Science and Engineering a-Structural Materials Properties Microstructure and Processing*, vol. 393, pp. 327-331, 2005.

[122] D. Lorenz, A. Zeckzer, U. Hilpert, P. Grau, H. Johansen, H. S. Leipner, "Pop-in effect as homogeneous nucleation of dislocations during nanoindentation", *Physical Review B*, vol. 67, pp. 1-4, 2003.

[123] Y. G. Wang, L. J. Qiao, K. W. Gao, Y. J. Su, W. Y. Chu, Z. L. Wang, "Measurement of the fracture toughness and critical stress for cracking in sno2 nanobelts using nanoindentation", *Acta Metallurgica Sinica*, vol. 40, pp. 594-598, 2004.

[124] G. M. Pharr, D. S. Harding, W. C. Oliver, "Measurement of fracture-toughness in thin-films and small volumes using nanoindentation methods", *Mechanical Properties and Deformation Behavior of Materials Having Ultra-Fine Microstructures*, vol. 233, pp. 449-461, 1993.

[125] T. M. Angeliu, J. T. Ward, J. K. Witter, "Assessing the effects of radiation damage on ni-base alloys for the prometheus space reactor system", *Journal of Nuclear Materials*, vol. 366, pp. 223-237, 2007.

[126] N. Hashimoto, J. D. Hunn, T. S. Byun, L. K. Mansur, "Microstructural analysis of ion-irradiation-induced hardening in inconel 718", *Journal of Nuclear Materials*, vol. 318, pp. 300-306, 2003.

[127] T. S. Byun, K. Farrell, "Tensile properties of inconel 718 after low temperature neutron irradiation", *Journal of Nuclear Materials*, vol. 318, pp. 292-299, 2003.

[128] J. D. Hunn, E. H. Lee, T. S. Byun, L. K. Mansur, "Ion-irradiation-induced hardening in inconel 718", *Journal of Nuclear Materials*, vol. 296, pp. 203-209, 2001.

[129] C. Y. Lu, K. Jin, L. K. Beland, F. F. Zhang, T. N. Yang, L. Qiao, Y. W. Zhang, H. B. Bei, H. M. Christen, R. E. Stoller, L. M. Wang, "Direct observation of defect range

and evolution in ion-irradiated single crystalline ni and ni binary alloys", *Scientific Reports*, vol. 6, pp. 1-10, 2016.

[130] R. Hellborg, H. J. Whitlow, Y. Zhang, "Ion beams in nanoscience and technology", Springer-Verlag, Heidelberg ; New York, 2009.

[131] L. A. Giannuzzi, F. A. Stevie, "Introduction to focused ion beams: Instrumentation, theory, techniques, and practice", Springer, New York, 2005.

[132] P. Rudolph, "Fundamentals and engineering of defects", *Progress in Crystal Growth and Characterization of Materials*, vol. 62, pp. 89-110, 2016.

[133] "A model for the evolution of network dislocation density in irradiated metals", ASTM STP782-EB, pp. 1077-1087, 1982.

[134] J. T. Busby, M. C. Hash, G. S. Was, "The relationship between hardness and yield stress in irradiated austenitic and ferritic steels", *Journal of Nuclear Materials*, vol. 336, pp. 267-278, 2005.

[135] A. Lupinacci, K. Chen, Y. Li, M. Kunz, Z. Jiao, G. S. Was, M. D. Abad, A. M. Minor, P. Hosemann, "Characterization of ion beam irradiated 304 stainless steel utilizing nanoindentation and laue microdiffraction", *Journal of Nuclear Materials*, vol. 458, pp. 70-76, 2015.

[136] A. N. Cleland, "Foundations of nanomechanics : From solid-state theory to device applications", Springer, Berlin ; New York, 2003.

[137] M. H. Sadd, "Elasticity - theory, applications, and numerics", 3rd Edition ed., Elsevier, New York, 2014.

[138] B. Tabarrok, J. S. Xu, R. G. Fenton, "A finite-element procedure for plane-strain metal flow within specified plastic boundaries", *Computer Methods in Applied Mechanics and Engineering*, vol. 63, pp. 1-14, 1987.

[139] A. C. Fischer-Cripps, "Nanoindentation", 3 ed., Springer, New York, 2011.

[140] A. C. Fischer-Cripps, "Nanoindentation third edition", *Nanoindentation, Third Edition*, vol. pp. 235-276, 2011.

[141] P. L. Larsson, "Investigation of sharp contact at rigid-plastic conditions", *International Journal of Mechanical Sciences*, vol. 43, pp. 895-920, 2001.

[142] I. D. G. a. S. I Nyoman Budiarsaa, I Wayan Widiadaa, Ngakan P.G Suardana, "Characterization of material parameters by reverse finite element modelling based on dual indenters vickers and spherical indentation", in: S.C.o. MIMEC2015 (Ed.) Secondary "Characterization of material parameters by reverse finite element modelling based on dual indenters vickers and spherical indentation", Elsevier, University of Udayana.Bali. Indonesia, 2015.

[143] D. Tabor, "The physical meaning of indentation and scratch hardness", *British Journal of Applied Physics*, vol. 7, pp. 159-166, 1956.

[144] "Metallic materials -- instrumented indentation test for hardness and materials parameters -- part 1: Test method", International Organization for Standardization 14577-1, pp. 1-46, 2015.

[145] W. D. Callister, "Materials science and engineering: An introduction", 7 ed., John Wiley & Sons, New York, 2007.

[146] A. F. Gourgues, "Electron backscatter diffraction and cracking", *Materials Science and Technology*, vol. 18, pp. 119-133, 2002.

[147] M. Masoumi, S. S. M. Tavares, J. M. Pardal, T. R. B. Martins, M. J. G. Da Silva, H. F. G. De Abreu, "The role of microstructure and grain orientations on intergranular cracking susceptibility of uns 17400 martensitic stainless steel", *Engineering Failure Analysis*, vol. 79, pp. 198-207, 2017.

[148] E. M. Lehockey, A. M. Brennenstuhl, I. Thompson, "On the relationship between grain boundary connectivity, coincident site lattice boundaries, and intergranular stress corrosion cracking", *Corrosion Science*, vol. 46, pp. 2383-2404, 2004.

[149] T. F. Chen, G. P. Tiwari, Y. Iijima, K. Yamauchi, "Volume and grain boundary diffusion of chromium in ni-base ni-cr-fe alloys", *Materials Transactions*, vol. 44, pp. 40-46, 2003.

[150] J. Cermak, "Diffusion of cr-51 along high-diffusivity paths in ni-fe alloys", *Physica Status Solidi a-Applied Research*, vol. 119, pp. 443-453, 1990.

[151] E. L. Hall, C. L. Briant, "The microstructural response of mill-annealed and solution-annealed inconel 600 to heat-treatment", *Metallurgical Transactions a-Physical Metallurgy and Materials Science*, vol. 16, pp. 1225-1236, 1985.

[152] R. G. Coltters, G. R. Belton, "High-temperature thermodynamic properties of the chromium carbides cr7c3 and cr3c2 determined using a galvanic cell technique", *Metallurgical Transactions B-Process Metallurgy*, vol. 15, pp. 517-521, 1984.

[153] G. S. Was, R. M. Kruger, "A thermodynamic and kinetic basis for understanding chromium depletion in ni-cr-fe alloys", *Acta Metallurgica*, vol. 33, pp. 841-854, 1985.

[154] J. A. Brinkman, "The effect of temperature gradients on diffusion in crystals", *Physical Review*, vol. 93, pp. 345-345, 1954.

[155] R. F. Wood, "Macroscopic theory of pulsed-laser annealing .3. Non-equilibrium segregation effects", *Physical Review B*, vol. 25, pp. 2786-2811, 1982.

[156] J. M. Blakely, H. Mykura, "The effect of impurity adsorption on the surface energy and surface self diffusion in nickel", *Acta Metallurgica*, vol. 9, pp. 595-599, 1961.

[157] E. Koch, F. Stangler, "Determination of activation energies of self diffusion on clean crystal surfaces of fcc nickel and bcc silicon-iron by means of field microscope", *Monatshefte Fur Chemie*, vol. 101, pp. 1606-&, 1970.

[158] P. S. Maiya, J. M. Blakely, "Surface self-diffusion and surface energy of nickel", *Journal of Applied Physics*, vol. 38, pp. 698-704, 1967.

[159] J. D. Clayton, "Nonlinear mechanics of crystals", 1 ed., Springer, Netherlands, 2011.

[160] Z. Shen, R. H. Wagoner, W. a. T. Clark, "Dislocation pile up and grain-boundary interactions in 304 stainless-steel", *Scripta Metallurgica*, vol. 20, pp. 921-926, 1986.

[161] Z. Shen, R. H. Wagoner, W. a. T. Clark, "Dislocation and grain-boundary interactions in metals", *Acta Metallurgica*, vol. 36, pp. 3231-3242, 1988.

[162] D. L. Engelberg, F. J. Humphreys, T. J. Marrow, "The influence of low-strain thermo-mechanical processing on grain boundary network characteristics in type 304 austenitic stainless steel", *Journal of Microscopy*, vol. 230, pp. 435-444, 2008.

[163] H. Lim, M. G. Lee, J. H. Kim, B. L. Adams, R. H. Wagoner, "Simulation of polycrystal deformation with grain and grain boundary effects", *International Journal of Plasticity*, vol. 27, pp. 1328-1354, 2011.

[164] E. O. Hall, "The deformation and ageing of mild steel .3. Discussion of results", *Proceedings of the Physical Society of London Section B*, vol. 64, pp. 747-753, 1951.

[165] N. J. Petch, "The cleavage strength of polycrystals", *Journal of the Iron and Steel Institute*, vol. 174, pp. 25-28, 1953.

[166] C. F. Tipper, W. Barr, M. W. Thring, B. B. Hundy, A. Cracknell, N. J. Petch, B. Watkins, N. H. Polakowski, "Effect of direction of rolling, direction of straining, and ageing on the mechanical properties of a mild steel plate - discussion", *Journal of the Iron and Steel Institute*, vol. 173, pp. 280-284, 1953.

[167] Z. C. Cordero, B. E. Knight, C. A. Schuh, "Six decades of the hall-petch effect - a survey of grain-size strengthening studies on pure metals", *International Materials Reviews*, vol. 61, pp. 495-512, 2016.

[168] K. Wang, D. Wang, F. S. Han, "Effect of crystalline grain structures on the mechanical properties of twinning-induced plasticity steel", *Acta Mechanica Sinica*, vol. 32, pp. 181-187, 2016.

[169] W. C. Leslie, "Iron and its dilute substitutional solid-solutions", *Metallurgical Transactions*, vol. 3, pp. 5-26, 1972.

[170] S. C. Wang, Z. Zhu, M. J. Starink, "Estimation of dislocation densities in cold rolled al-mg-cu-mn alloys by combination of yield strength data, ebsd and strength models", *Journal of Microscopy-Oxford*, vol. 217, pp. 174-178, 2005.

[171] H. A. Roth, C. L. Davis, R. C. Thomson, "Modeling solid solution strengthening in nickel alloys", *Metallurgical and Materials Transactions a-Physical Metallurgy and Materials Science*, vol. 28, pp. 1329-1335, 1997.

[172] Y. Nakada, A. S. Keh, "Solid-solution strengthening in ni-c alloys", *Metallurgical Transactions*, vol. 2, pp. 441-447, 1971.

[173] F. F. Lavrentev, "The type of dislocation interaction as the factor determining work-hardening", *Materials Science and Engineering*, vol. 46, pp. 191-208, 1980.

[174] K. R. Anderson, J. R. Groza, "Microstructural size effects in high-strength high-conductivity cu-cr-nb alloys", *Metallurgical and Materials Transactions a-Physical Metallurgy and Materials Science*, vol. 32, pp. 1211-1224, 2001.

[175] J. S. Koehler, "Diffusion of lattice defects in a stress field", *Physical Review*, vol. 181, pp. 1015-1019, 1969.

[176] T. Mukherjee, W. Zhang, T. Debroy, "An improved prediction of residual stresses and distortion in additive manufacturing", *Computational Materials Science*, vol. 126, pp. 360-372, 2017.

[177] F. R. N. Nabarro, M. S. Duesbery, "Dislocations in solids", North-Holland Pub. Co., Amsterdam ; New York, 1979.

[178] Y. L. Li, D. D. Gu, "Parametric analysis of thermal behavior during selective laser melting additive manufacturing of aluminum alloy powder", *Materials & Design*, vol. 63, pp. 856-867, 2014.

[179] I. Yadroitsev, P. Krakhmalev, I. Yadroitsava, "Selective laser melting of ti6al4v alloy for biomedical applications: Temperature monitoring and microstructural evolution", *Journal of Alloys and Compounds*, vol. 583, pp. 404-409, 2014.

[180] R. D. Li, Y. S. Shi, J. H. Liu, H. S. Yao, W. X. Zhang, "Effects of processing parameters on the temperature field of selective laser melting metal powder", *Powder Metallurgy and Metal Ceramics*, vol. 48, pp. 186-195, 2009.

[181] D. D. Gu, Y. C. Hagedorn, W. Meiners, G. B. Meng, R. J. S. Batista, K. Wissenbach, R. Poprawe, "Densification behavior, microstructure evolution, and wear performance of selective laser melting processed commercially pure titanium", *Acta Materialia*, vol. 60, pp. 3849-3860, 2012.

[182] D. H. Dai, D. D. Gu, "Thermal behavior and densification mechanism during selective laser melting of copper matrix composites: Simulation and experiments", *Materials & Design*, vol. 55, pp. 482-491, 2014.

[183] P. P. Yuan, D. D. Gu, "Molten pool behaviour and its physical mechanism during selective laser melting of tic/alsi10mg nanocomposites: Simulation and experiments", *Journal of Physics D-Applied Physics*, vol. 48, pp. 1-16, 2015.

[184] I. Yadroitsev, A. Gusarov, I. Yadroitsava, I. Smurov, "Single track formation in selective laser melting of metal powders", *Journal of Materials Processing Technology*, vol. 210, pp. 1624-1631, 2010.

[185] X. Zhou, X. H. Liu, D. D. Zhang, Z. J. Shen, W. Liu, "Balling phenomena in selective laser melted tungsten", *Journal of Materials Processing Technology*, vol. 222, pp. 33-42, 2015.

[186] C. L. Qiu, C. Panwisawas, M. Ward, H. C. Basoalto, J. W. Brooks, M. M. Attallah, "On the role of melt flow into the surface structure and porosity development during selective laser melting", *Acta Materialia*, vol. 96, pp. 72-79, 2015.

[187] D. D. Gu, Y. F. Shen, "Balling phenomena in direct laser sintering of stainless steel powder: Metallurgical mechanisms and control methods", *Materials & Design*, vol. 30, pp. 2903-2910, 2009.

[188] D. D. Gu, Y. F. Shen, "Balling phenomena during direct laser sintering of multi-component cu-based metal powder", *Journal of Alloys and Compounds*, vol. 432, pp. 163-166, 2007.

[189] M. Das, V. K. Balla, D. Basu, S. Bose, A. Bandyopadhyay, "Laser processing of sic-particle-reinforced coating on titanium", *Scripta Materialia*, vol. 63, pp. 438-441, 2010.

[190] D. Buchbinder, H. Schleifenbaum, S. Heidrich, W. Meiners, J. Bultmann, "High power selective laser melting (hp slm) of aluminum parts", *Lasers in Manufacturing 2011: Proceedings of the Sixth International Wlt Conference on Lasers in Manufacturing, Vol 12, Pt A*, vol. 12, pp. 271-278, 2011.

[191] N. J. Harrison, I. Todd, K. Mumtaz, "Reduction of micro-cracking in nickel superalloys processed by selective laser melting: A fundamental alloy design approach", *Acta Materialia*, vol. 94, pp. 59-68, 2015.

[192] L. E. Loh, C. K. Chua, W. Y. Yeong, J. Song, M. Mapar, S. L. Sing, Z. H. Liu, D. Q. Zhang, "Numerical investigation and an effective modelling on the selective laser

melting (slm) process with aluminium alloy 6061", *International Journal of Heat and Mass Transfer*, vol. 80, pp. 288-300, 2015.

[193] H. Y. Jung, S. J. Choi, K. G. Prashanth, M. Stoica, S. Scudino, S. Yi, U. Kuhn, D. H. Kim, K. B. Kim, J. Eckert, "Fabrication of fe-based bulk metallic glass by selective laser melting: A parameter study", *Materials & Design*, vol. 86, pp. 703-708, 2015.

[194] X. P. Li, C. W. Kang, H. Huang, L. C. Zhang, T. B. Sercombe, "Selective laser melting of an al86ni6y4.5co2la1.5 metallic glass: Processing, microstructure evolution and mechanical properties", *Materials Science and Engineering a-Structural Materials Properties Microstructure and Processing*, vol. 606, pp. 370-379, 2014.

[195] S. Pauly, L. Lober, R. Petters, M. Stoica, S. Scudino, U. Kuhn, J. Eckert, "Processing metallic glasses by selective laser melting", *Materials Today*, vol. 16, pp. 37-41, 2013.

[196] X. P. Li, C. W. Kang, H. Huang, T. B. Sercombe, "The role of a low-energy-density re-scan in fabricating crack-free al85ni5y6co2fe2 bulk metallic glass composites via selective laser melting", *Materials & Design*, vol. 63, pp. 407-411, 2014.

[197] X. P. Li, M. Roberts, Y. J. Liu, C. W. Kang, H. Huang, T. B. Sercombe, "Effect of substrate temperature on the interface bond between support and substrate during selective laser melting of al-ni-y-co-la metallic glass", *Materials & Design*, vol. 65, pp. 1-6, 2015.

[198] W. Pfeiler, "Alloy physics: A comprehensive reference", Wiley-VCH, Weinheim, 2007.

[199] W. K. Burton, N. Cabrera, F. C. Frank, "The growth of crystals and the equilibrium structure of their surfaces", *Philosophical Transactions of the Royal Society of London Series a-Mathematical and Physical Sciences*, vol. 243, pp. 299-358, 1951.

[200] W. Kurz, D. J. Fisher, "Fundamentals of solidification", 4 ed., Trans Tech Publications, Zuerich, 1998.

[201] W. W. Mullins, R. F. Sekerka, "Stability of planar interface during solidification of dilute binary alloy", *Journal of Applied Physics*, vol. 35, pp. 444-451, 1964.

[202] W. A. Tiller, R. F. Sekerka, "Redistribution of solute during phase transformations", *Journal of Applied Physics*, vol. 35, pp. 2726-2729, 1964.

[203] R. F. Sekerka, "A stability function for explicit evaluation of mullins-sekerka interface stability criterion", *Journal of Applied Physics*, vol. 36, pp. 264-267, 1965.

[204] M. J. Aziz, "Model for solute redistribution during rapid solidification", *Journal of Applied Physics*, vol. 53, pp. 1158-1168, 1982.

[205] R. F. Wood, G. E. Giles, "Control of melt-front velocity during pulsed laser annealing", *Applied Physics Letters*, vol. 38, pp. 422-423, 1981.

[206] T. Watanabe, "An approach to grain-boundary design for strong and ductile polycrystals", *Res Mechanica*, vol. 11, pp. 47-84, 1984.

[207] L. Tan, K. Sridharan, T. R. Allen, "The effect of grain boundary engineering on the oxidation behavior of incoloy alloy 800h in supercritical water", *Journal of Nuclear Materials*, vol. 348, pp. 263-271, 2006.

[208] V. Venegas, F. Caleyo, T. Baudin, J. H. Espina-Hernandez, J. M. Hallen, "On the role of crystallographic texture in mitigating hydrogen-induced cracking in pipeline steels", *Corrosion Science*, vol. 53, pp. 4204-4212, 2011.

[209] H. L. Ming, Z. M. Zhang, P. Y. Xiu, J. Q. Wang, E. H. Han, W. Ke, M. X. Su, "Microstructure, residual strain and stress behavior in 316l heat-affected zone", *Acta Metallurgica Sinica-English Letters*, vol. 29, pp. 848-858, 2016.

[210] H. Grimmer, W. Bollmann, D. H. Warrington, "Coincidence-site lattices and complete pattern-shift lattices in cubic-crystals", *Acta Crystallographica a-Foundation and Advances*, vol. A 30, pp. 197-207, 1974.

[211] L. H. Ortega, B. J. Blamer, J. A. Evans, S. M. Mcdeavitt, "Development of an accident-tolerant fuel composite from uranium mononitride (un) and uranium sesquisilicide (u-3 si-2) with increased uranium loading", *Journal of Nuclear Materials*, vol. 471, pp. 116-121, 2016.

[212] N. E. Todreas, M. S. Kazimi, "Nuclear systems", Hemisphere Pub. Corp., New York, 1990.

[213] R. L. Klueh, D. J. Alexander, M. Rieth, "The effect of tantalum on the mechanical properties of a 9cr-2w-0.25v-0.07ta-0.1c steel", *Journal of Nuclear Materials*, vol. 273, pp. 146-154, 1999.

[214] A. J. Mueller, R. Bianco, R. W. Buckman, "Evaluation of oxide dispersion strengthened (ods) molybdenum and molybdenum-rhenium alloys", *International Journal of Refractory Metals & Hard Materials*, vol. 18, pp. 205-211, 2000.

[215] B. V. Cockeram, R. W. Smith, L. L. Snead, "Tensile properties and fracture mode of a wrought ods molybdenum sheet following fast neutron irradiation at temperatures ranging from 300 degrees c to 1000 degrees c", *Journal of Nuclear Materials*, vol. 346, pp. 165-184, 2005.

[216] S. Yamashita, Y. Yano, S. Ohtsuka, T. Yoshitake, T. Kaito, S. Koyama, K. Tanaka, "Irradiation behavior evaluation of oxide dispersion strengthened ferritic steel cladding tubes irradiated in joyo", *Journal of Nuclear Materials*, vol. 442, pp. 417-424, 2013.

[217] P. Dubuisson, Y. De Carlan, V. Garat, M. Blat, "Ods ferritic/martensitic alloys for sodium fast reactor fuel pin cladding", *Journal of Nuclear Materials*, vol. 428, pp. 6-12, 2012.

[218] J. S. Cheon, C. B. Lee, B. O. Lee, J. P. Raison, T. Mizuno, F. Delage, J. Carmack, "Sodium fast reactor evaluation: Core materials", *Journal of Nuclear Materials*, vol. 392, pp. 324-330, 2009.

[219] G. R. Odette, M. J. Alinger, B. D. Wirth, "Recent developments in irradiation-resistant steels", *Annual Review of Materials Research*, vol. 38, pp. 471-503, 2008.

[220] P. Oiler, J. Malaplate, M. H. Mathon, D. Nunes, D. Hamon, L. Toualbi, Y. De Carlan, L. Chaffron, "Chemical and microstructural evolution on ods fe-14crwti steel during manufacturing stages", *Journal of Nuclear Materials*, vol. 428, pp. 40-46, 2012.

[221] D. Catalini, D. Kaoumi, A. P. Reynolds, G. J. Grant, "Dispersoid distribution and microstructure in fe-cr-al ferritic oxide dispersion-strengthened alloy prepared by

friction consolidation", *Metallurgical and Materials Transactions a-Physical Metallurgy and Materials Science*, vol. 46A, pp. 4730-4739, 2015.

APPENDICES

A.1 Oxide Dispersion Strengthened Steel

Due to the relative abundance of high energy neutrons, alloys in fast spectrum nuclear reactors must maintain their mechanical properties under much higher damage rates than alloys in thermal spectrum nuclear reactors. A comparison between the neutron energy spectra of thermal vs. fast reactors is illustrated in Figure 233 [30]. In comparison to austenitic stainless steels, irradiation studies suggest that ferritic/martensitic (F/M) steels are more resistant to swelling at high dpa [30, 79]. F/M steels can suffer from radiation-induced creep, radiation-induced embrittlement, and large ductile to brittle transition temperature (DBTT) shift [30]. The DBTT shift is a radiation-induced effect in which the temperature-dependent ductile to brittle facture mode transitions at a higher temperature (sometimes higher than room temperature), illustrated in Figure 234 [213].

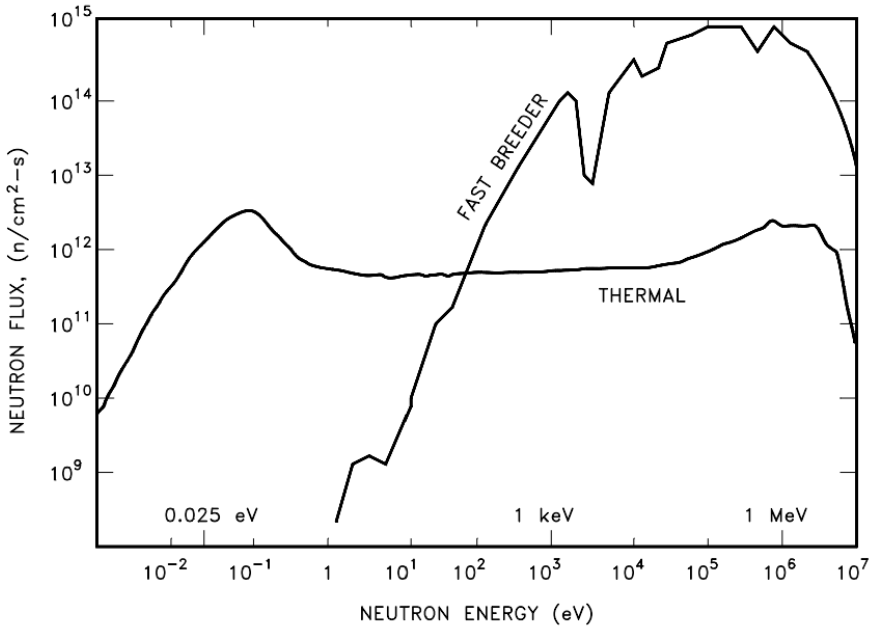

Figure 233: Neutron Energy Spectrum of a Thermal Reactor vs. a Fast Reactor
(Reprinted from [30])

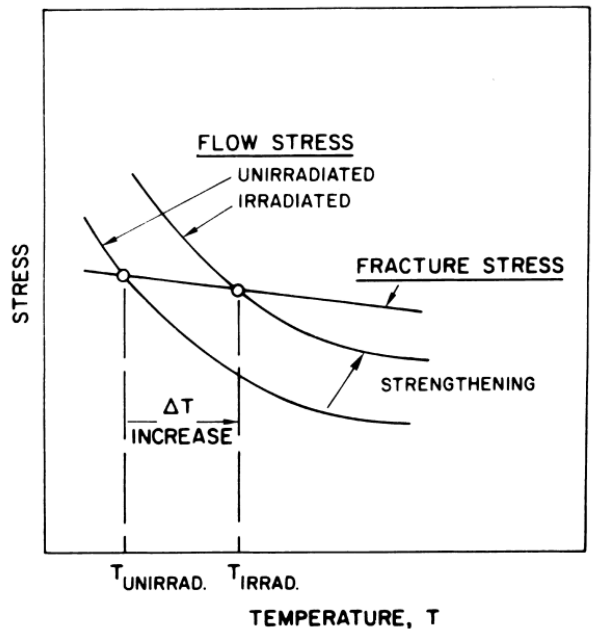

Figure 234: Illustration of the Effect of Fast Neutron Irradiation on DBTT
(Reprinted from [213])

Recent experimental studies suggest that the finer the F/M steel grain structure, the smaller (i.e. more favorable) the DBTT shift [214, 215]. Recent research efforts have been focused on improving the thermophysical properties of advanced steel claddings through nanomaterial enhancement. One such example of nanomaterial enhanced cladding is realized through oxide dispersion strengthening, in which the DBTT has successfully been reduced to below room temperature (see Figure 235) [214]. In general, a homogeneous distribution of oxide nanomaterials produces a dense matrix of thermodynamically stable obstacles to dislocation motion [216].

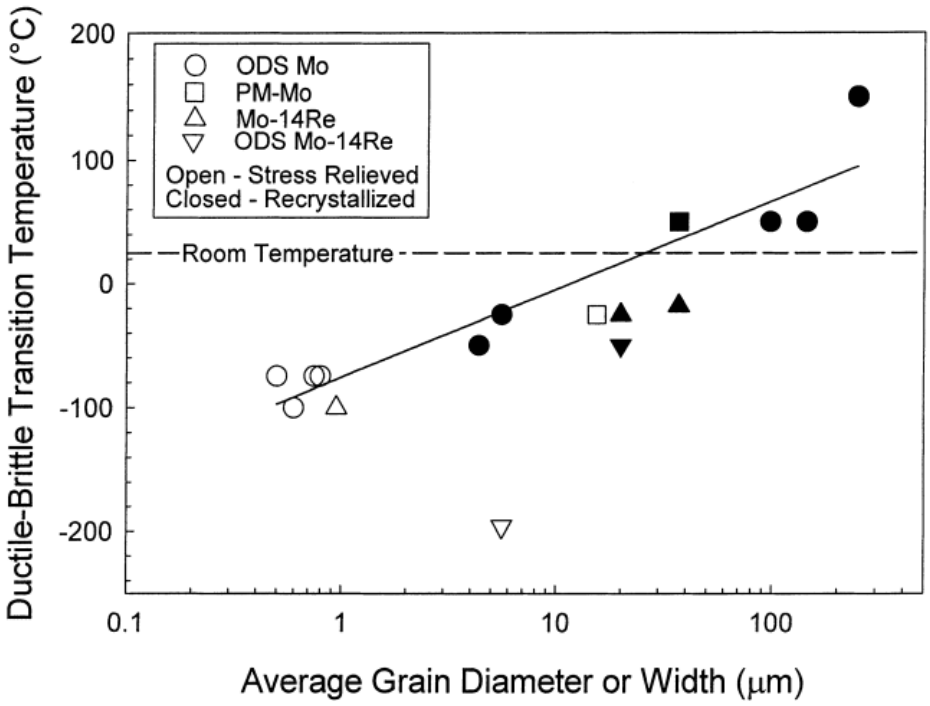

Figure 235: Effect of Oxide Dispersoids and Grain Size on DBTT in Molybdenum ODS Alloys (Reprinted from [214])

There are two primary ODS groups of interest: (a) Fe-9Cr martensitic alloys, and (b) Fe-14/18Cr ferritic alloys. The martensitic ODS alloys are generally more isotropic and are easier to manufacture, but undergo a phase transformation above 800 °C, while the ferritic ODS alloys generally have better corrosion resistance but are more susceptible to radiation-induced embrittlement [217]. Incorporating additional elements into the ODS alloy influence corrosion properties as well as the size distribution of the oxide nanoparticles during mechanical alloying (MA). For example, experimental studies show that adding titanium to ferritic 12Cr powder during MA reduces the Y_2O_3 nanoparticle size distribution (Ø) down to $3 \leq Ø \leq 20$ nm, which is associated with a significant improvement in rupture strength up to very high doses [78]. Irradiation tests in the Fast Flux Test Facility (FFTF) and Phénix sodium cooled fast nuclear reactors (SFRs) suggest that F/M ODS steels exhibit low dimensional changes, even at doses as high as 150 dpa (see Figure 236) [217].

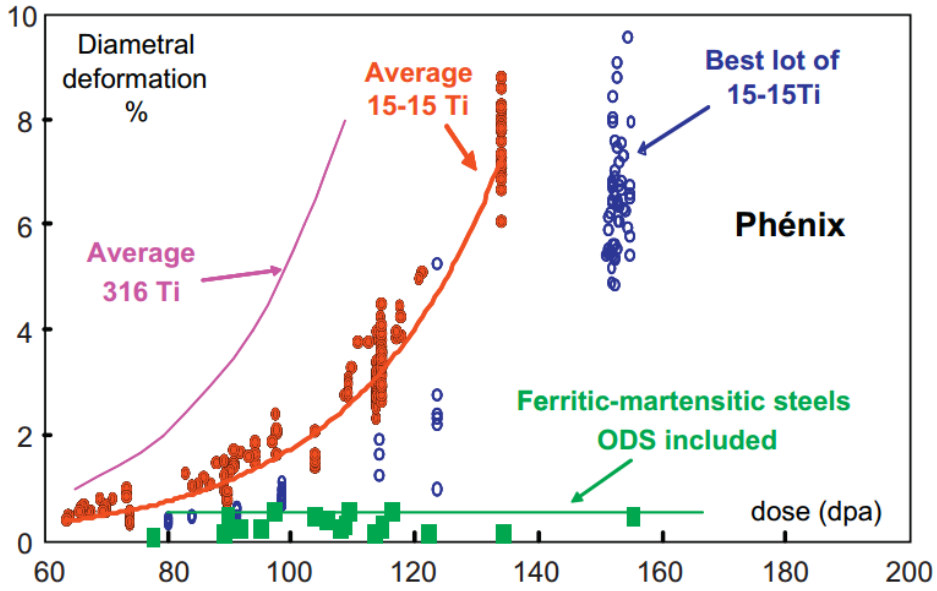

Figure 236: Deformation of Various Candidate SFR Fuel Claddings Irradiated in Phénix vs. Dose (Reprinted with permission from [217])

F/M ODS steel performance in fast reactors is highly dependent on manufacturing process parameters, such as mixing and size distribution of oxide nano-powders. Two early ODS assemblies irradiated in the Phénix were fabricated via a cold-rolling process with an inhomogeneous distribution of oxide powder, resulting in oxide-free strips parallel to the grain boundaries [218]. This lead to rapid strain localization, embrittlement, and rupture of the samples [217].

Regardless of their crystal structure, ODS steels are promising structural material candidates in advanced nuclear reactor systems because of their excellent resistance to radiation damage and high temperature creep [203, 219]. The oxide dispersoids have been shown to mitigate the effects of radiation damage by pinning dislocations and creating traps for radiation-induced defects. ODS steel powders are typically prepared

by mechanically milling yttrium oxide particles with a ferritic alloy powder to give a fine dispersion of Y_2O_3 nanoparticles within the steel, shown in Figure 237 [220].

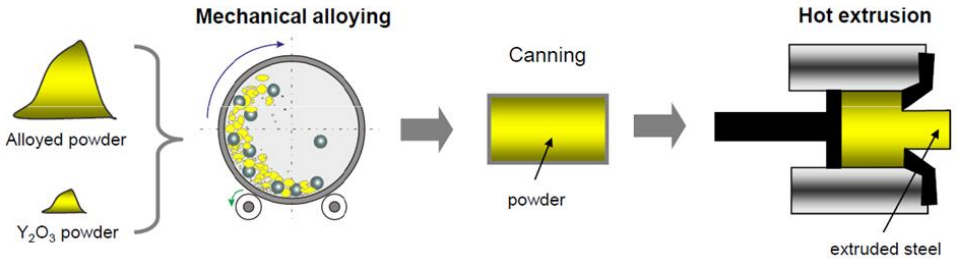

Figure 237: Powder Metallurgy Process for Manufacturing ODS Steel (Reprinted from [220])

Powder from which ODS steel can be fabricated is not commercially available. Therefore, the ODS powder was produced from their individual constituents which were available at the time (44-105 µm 316L stainless steel (fcc), and 40 nm Y_2O_3) and ball milled in a 0.5" diameter cylindrical alumina crucible to yield a dispersion powder shown in Figure 238 (courtesy Lockheed Martin from an unpublished report). The powder was milled for 24 hours, then screened (2 mm, then again at 125 µm) to remove large agglomerates. Due to time constraints, the DED parameters were not fully optimized to minimize porosity in the built parts. Three trials were performed at the QCML to fabricate ODS samples using the LENS system with the parameters shown in Table 18 (courtesy Lockheed Martin from an unpublished report).

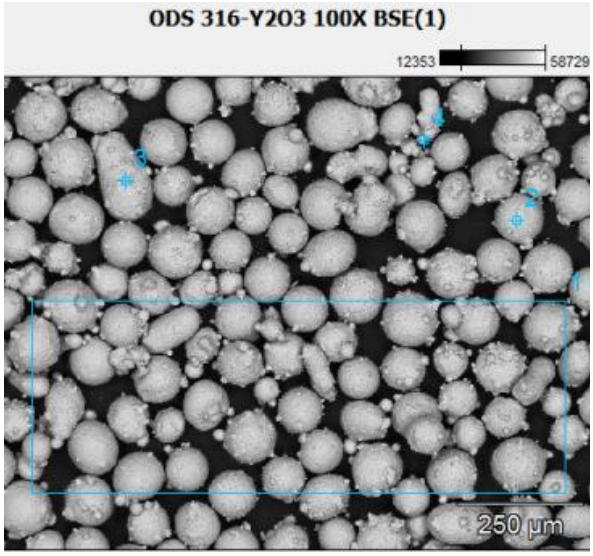

Figure 238: SEM Images of 316L Stainless Steel-based ODS Powder

Table 18: LENS System Trial Parameters to Fabricated ODS Steel Rods Using LENS System

Process Parameter	Trial 1	Trial 2	Trial 3
Speed ($mm \cdot s^{-1}$)	15.0	12.7	15.0
Slicer Vertical Distance (mm)	0.25	0.43	0.43
Slicer Horizontal Distance (mm)	0.90	1.07	1.07
Power (W)	870	780	780
Powder ($g \cdot min^{-1}$)	Pending	Pending	Pending

A.2 Matlab Code for fcc Taylor Factor Calculation

```
% Taylor factor for fcc polycrystal with no texture under uniaxial load
% Jordan A. Evans, April 2016


%                plane    slip vector
slip_system = [ 1  1  1    1 -1  0
                1  1  1    1  0 -1
                1  1  1    0  1 -1
                1  1 -1    1 -1  0
                1  1 -1    1  0  1
                1  1 -1    0  1  1
                1 -1  1    1  1  0
                1 -1  1    1  0 -1
                1 -1  1    0 -1 -1
               -1  1  1   -1 -1  0
               -1  1  1   -1  0 -1
               -1  1  1    0  1 -1 ];
N_slip_system = length(slip_system(:,1));

theta = [0:0.01:1] 12*(pi/4);
phi = [0:0.01:1]*(pi/4);
dtheta = theta(2)-theta(1);
dphi = phi(2)-phi(1);
Ntrial = 3;
dTfactor = 1e-4;
X = zeros(length(theta), length(phi));
Y = X; x = X; y = X; z = X;
activeS = zeros(length(theta), length(phi), N_slip_system);
dissip = zeros(length(theta), length(phi)); weight = dissip;
Taxis = zeros(length(theta), length(phi), 3); netrot = Taxis; dTaxis = Taxis;
Taxisnew = Taxis; Xnew = X; Ynew = Y; dX = X; dY = Y;
```

```
strain = zeros(N_slip_system,6);
rotation = zeros(N_slip_system,3);
for i = 1:length(slip_system(:,1)),
    n = slip_system(i,1:3); n = n/norm(n);
    b = slip_system(i,4:6); b = b/norm(b);
    tmp = (n'*b + b'*n)/2;
    strain(i,:) = [tmp(1,1) tmp(2,2) tmp(3,3) tmp(2,3) tmp(3,1) tmp(1,2)];
    rotation(i,:) = cross(n,b)/2;
end

% compute activation ratio of each slip system
for ai = 1:length(theta),
    if mod(ai,10)==0
        disp(sprintf('ai = %d / %d ', ai, length(theta)));
    end
    for bi = 1:length(phi),

        factor = atan(sin(theta(ai)))/(pi/4);

        x(ai,bi) = sin(theta(ai))*cos(phi(bi)*factor);
        y(ai,bi) = sin(phi(bi)*factor);
        z(ai,bi) = cos(theta(ai))*cos(phi(bi)*factor);
        X(ai,bi) = 2*x(ai,bi)/(1+z(ai,bi));
        Y(ai,bi) = 2*y(ai,bi)/(1+z(ai,bi));
        T = [x(ai,bi) y(ai,bi) z(ai,bi)];
        Taxis(ai,bi,:) = T;
        tmp = (T'*T - (T*T'/3)*eye(3))*(3/2);
        tensile_strain = [tmp(1,1) tmp(2,2) tmp(3,3) tmp(2,3) tmp(3,1) tmp(1,2)];
        %options = optimset('Display','iter','TolFun',1e-8);
        options = optimset('Display','off','TolFun',1e-8);
        % double number of slip systems so that coefficient is non-negative
        Aeq = [strain', -strain'];
        beq = [tensile_strain'];
```

```
        lb = zeros(length(slip_system(:,1))*2,1);
        f= ones(length(slip_system(:,1))*2,1);
        coeff = linprog(f, [], [], Aeq, beq, lb, [], [], options);
        % half # of coeff to store as positive and negative values
        compact_coeff = coeff(1:end/2)-coeff(end/2+1:end);
        activeS(ai,bi,:) = compact_coeff;
        dissip(ai,bi) = sum(abs(compact_coeff));
        netrot(ai,bi,:) = rotation'*compact_coeff;
    end
end

% compute change of T-axis
for ai = 1:length(theta),
    for bi = 1:length(phi),
        dTaxis(ai,bi,:) = cross(netrot(ai,bi,:),Taxis(ai,bi,:));
        Taxisnew(ai,bi,:) = Taxis(ai,bi,:) + dTaxis(ai,bi,:)*dTfactor;
        Xnew(ai,bi) = 2*Taxisnew(ai,bi,1)/(1+Taxisnew(ai,bi,3));
        Ynew(ai,bi) = 2*Taxisnew(ai,bi,2)/(1+Taxisnew(ai,bi,3));
    end
end
dX = Xnew - X; dY = Ynew - Y;

% compute area of mesh
area = zeros(size(weight));
for ai = 1:length(theta)-1,
    for bi = 1:length(phi)-1,
        dr1 = [x(ai+1,bi) y(ai+1,bi) z(ai+1,bi)] - [x(ai,bi) y(ai,bi) z(ai,bi)];
        dr2 = [x(ai,bi+1) y(ai,bi+1) z(ai,bi+1)] - [x(ai,bi) y(ai,bi) z(ai,bi)];
        dr3 = [x(ai+1,bi) y(ai+1,bi) z(ai+1,bi)] ...
            - [x(ai+1,bi+1) y(ai+1,bi+1) z(ai+1,bi+1)];
        dr4 = [x(ai,bi+1) y(ai,bi+1) z(ai,bi+1)] ...
            - [x(ai+1,bi+1) y(ai+1,bi+1) z(ai+1,bi+1)];
        area(ai,bi) = (norm(cross(dr1,dr2))+norm(cross(dr3,dr4)))/2;
    end
```

```
end

% compute integration (quadrature) weight
for ai = 1:length(theta),
    for bi = 1:length(phi),
        weight(ai,bi) = area(ai,bi)/4;
        if ai > 1
            weight(ai,bi) = weight(ai,bi) + area(ai-1,bi)/4;
        end
        if bi > 1
            weight(ai,bi) = weight(ai,bi) + area(ai,bi-1)/4;
        end
        if ai > 1 && bi > 1
            weight(ai,bi) = weight(ai,bi) + area(ai-1,bi-1)/4;
        end
    end
end
mean_dissip = sum(sum(dissip.*weight))/(4*pi/48);

% plot results
fs = 17;
figure(1);
contourf(X,Y,dissip,50);
colorbar
set(gca,'FontSize',fs);
xlabel('x'); ylabel('y');
axis equal
title(sprintf('Mean = %.4f (Taylor Factor)',mean_dissip));
t001 = text( 0.01,0.02,'001');
t101 = text( 0.79,0.02,'101');
t111 = text( 0.70,0.70,'111');

figure(2);
mesh(X,Y,dissip);
```

```
set(gca,'FontSize',fs);
xlabel('x'); ylabel('y');
axis equal
view([30 80]);
title(sprintf('Mean = %.4f (Taylor Factor)',mean_dissip));


figure(3);
skip = 10;
contour(X,Y,dissip,50); hold on
quiver(X(1:skip:end,1:skip:end), Y(1:skip:end,1:skip:end), ...
    dX(1:skip:end,1:skip:end),dY(1:skip:end,1:skip:end));
hold off
set(gca,'FontSize',fs);
xlabel('x'); ylabel('y');
axis equal
title('Rotation of Tensile Axis');
t001 = text( 0.01,0.02,'001');
t101 = text( 0.79,0.02,'101');
t111 = text( 0.70,0.70,'111');
```

A.3 Neutron Irradiation in the 1 MW TAMU TRIGA Reactor

A.3.1 Calculation of Neutron Damage

The method described by Was was used to estimate neutron damage, and is briefly described here [30]. The TRIGA Reactor at the TAMU NSC has a thermal neutron spectrum with a flux of about $2 \cdot 10^{13}$ n·cm^{-2}·s^{-1}. The neutron damage can be approximated using Eq. 82 below, where R is the displacement rate density (i.e. total number of displacements per unit volume per unit time), N is the atomic density of the material, $\phi(E_i)$ is the energy-depended neutron flux, $\sigma_D(E_i)$ is the energy-dependent displacement cross-section, $\sigma(E_i,T)$ is the probability that a particle of energy E_i will impart a recoil energy T to a struck lattice atom, and $\nu(T)$ is the number of displaced atoms resulting from that collision. The quantity R/N is the damage rate in dpa·s^{-1}.

$$R\left[\frac{displacements}{cm^3 \cdot s}\right] = N\int_{\check{E}}^{\hat{E}} \phi(E_i)\sigma_D(E_i)\,dE_i$$

$$\sigma_D(E_i) = \int_{\check{T}}^{\hat{T}} \sigma(E_i,T)\nu(T)\,dT$$

$$\therefore$$

Eq. 82

$$\frac{R}{N}\left[\frac{dpa}{s}\right] = \int_{\check{E}}^{\hat{E}} \phi(E_i)\sigma_D(E_i)\,dE_i$$

The displacement cross-section is a complicated function with contributions from the elastic scattering cross section $\sigma_s\left(E_i,\Omega\right)$ where Ω is the solid angle into which the incoming neutron is scattered, the inelastic scattering cross section $\sigma_{sj}\left(E_i,Q_j,T\right)$ where Q_j is the inelastic neutron-nucleus reaction energy for the *j*th nuclear resonance of the target nucleus, and a variety of absorption-emission nuclear reactions such as $\left(n,2n\right)$, $\left(n,p\right)$, $\left(n,\gamma\right)$, etc. Crystallinity also influences the primary knock-on atom (PKA) damage cascade via phenomena such as channeling (when the ion travels parallel to a major crystal direction, increasing the likelihood of small-angle scattering), illustrated below in Figure 239 [30].

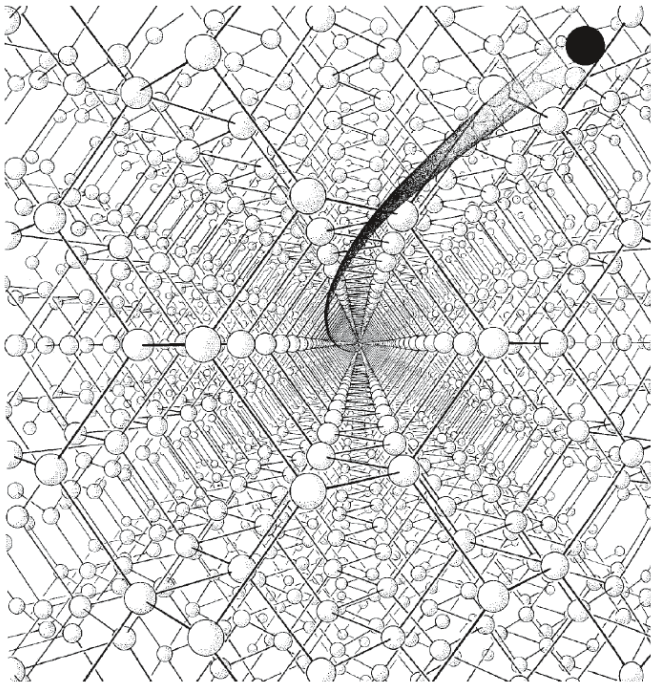

Figure 239: Illustration of a PKA Channeling Through a Crystalline Lattice
(Reprinted from [30])

Since neutrons carry no net electric charge, neutron-nucleus interactions can be approximated as binary colliding "hard spheres". The probability that a neutron elastically scatters off of an atomic nucleus is defined by the double-differential scattering cross section shown in Eq. 83, where E_i and E_f are initial and final neutron energies. Since the scattering probability can be expressed as a function of E_i and the scattering angle only, this can be reduced to the single differential scattering cross section in Eq. 84.

Eq. 83

$$\sigma_s\left(E_i,\Omega\right)=\int\sigma_s\left(E_i,E_f,\Omega\right)dE_f$$

Eq. 84

$$\sigma_s\left(E_i\right)=\int\sigma_s\left(E_i,\Omega\right)d\Omega$$

In order to determine the relationship between the neutron's incident kinetic energy, its scattering angle off an atomic nucleus, and the energy transferred to that nucleus, the conservation of momentum can be applied to the binary hard sphere collision approximation in the center-of-mass system via Eq. 85 where lower case letters refer to the neutron, upper case letters refer to the target nucleus, and the subscript "c" refers to the center-of-mass frame. Conservation of energy requires that Eq. 86 be upheld. Therefore, Eq. 85 and Eq. 86 can be combined to arrive at the relationship shown in Eq. 87.

Eq. 85

$$v_c m - V_c M = 0$$

$$v_c' m - V_c' M = 0$$

Eq. 86

$$\frac{1}{2} m v_c^{\,2} + \frac{1}{2} M V_c^{\,2} = \frac{1}{2} m v_c'^{\,2} + \frac{1}{2} M V_c'^{\,2}$$

$$\left[\frac{1}{2} m \left(\frac{M}{m} \right)^2 + \frac{1}{2} M \right] V_c^{\,2} = \left[\frac{1}{2} m \left(\frac{M}{m} \right)^2 + \frac{1}{2} M \right] V_c'^{\,2}$$

$$\therefore$$

Eq. 87

$$V_c = V_c', \quad v_c = v_c'$$

Rewriting Eq. 87 in the lab frame and combining with Eq. 85 yields Eq. 88, where the lab frame is designated by subscript "l". Note that since the target nucleus is at rest in the lab reference frame, the center-of-mass system itself is moving relative to the lab system with the same as V_c. The velocity of the center-of-mass system relative to the lab frame can therefore be defined as V_{CM}, where $|V_{CM}| = |V_c|$ but are in opposite direction.

Eq. 88

$$v_c = v_l - V_{CM} = v_l - V_c, \quad V_{CM} = \left(\frac{m}{M+m} \right) v_l$$

The target nucleus velocity after collision in the lab system, V_l', can be related to ϕ in Figure 240 by using the law of cosines, shown in Eq. 89 [30]. Rewriting these velocities in terms of kinetic energy yields Eq. 90, which can be combined with Eq. 89 to yield Eq. 91.

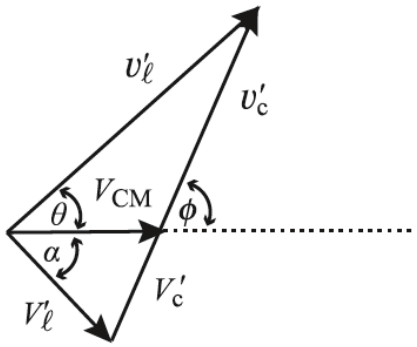

Figure 240: Illustration of Vector Velocities of Center-of-Mass and Lab Reference Frames (Reprinted from [30])

Eq. 89

$$V_l'^2 = V_{CM}^2 + V_c'^2 - 2V_{CM}V_c'\cos(\phi)$$

Eq. 90

$$V_l'^2 = \frac{2T}{M}, \quad V_{CM}^2 = \frac{2E_i}{m}\left(\frac{m}{m+M}\right)^2, \quad V_c'^2 = \frac{2m}{M^2}E_m'$$

$$T = \frac{mM}{(m+M)^2}E_i + \frac{m}{M}E_m' - 2\left(\frac{m}{m+M}\right)\sqrt{E_i E_m'}\cdot\cos(\phi)$$

$\therefore$

Eq. 91

$$T = \eta_1 \eta_2 E_i + \frac{\eta_1}{\eta_2} E_m' - 2\eta_1 \sqrt{E_i E_m'} \cdot \cos(\phi)$$

$$\eta_1 = \frac{m}{m+M}, \quad \eta_2 = \frac{M}{m+M}$$

From Eq. 88, Eq. 92 (velocity) and Eq. 93 (velocities rewritten as energies) can are:

Eq. 92

$$v_c' = v_l - v_l \left(\frac{m}{m+M} \right) = v_l \left(\frac{M}{m+M} \right)$$

Eq. 93

$$E_m' = E_i \left(\frac{M}{m+M} \right)^2 = \eta_2^2 E_i$$

Combining Eq. 92 and Eq. 93 yields Eq. 94 where *T* is the energy transferred to the target nucleus.

Eq. 94

$$T = \frac{\gamma}{2} E_i (1 - \cos\phi)$$

$$\gamma = \frac{4mM}{(m+M)^2} = \frac{4A}{(1+A)^2}, \quad m = 1 \text{ and } M = A$$

Eq. 94 shows that the transferred energy between an incident neutron and a target nucleus of mass number A is dependent upon only the scattering angle ϕ. From Eq. 94, the maximum energy transfer occurs at $\phi = \pi$ (i.e. a "head-on collision"), and is minimum when the scatter angle is zero (a glancing scatter). The scattering cross section can be written in terms of center-of-mass variables since differential probabilities written in transformed variables are equivalent, shown in Eq. 95. From Figure 241 below, $d\Omega$ relates to $d\phi$ via Eq. 96 [30].

Eq. 95

$$\sigma_s\left(E_i, T\right)dT = \sigma_s\left(E_i, \phi\right)d\Omega$$

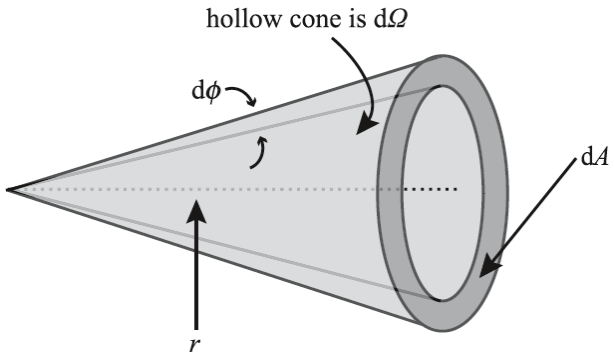

Figure 241: Neutron Scattering into a Solid Angle (Reprinted from [30])

Eq. 96

$$d\Omega = \frac{dA}{r^2} = \frac{rd\phi\left(2\pi r\sin\phi\right)}{r^2} = 2\pi\sin\phi d\phi$$

Substituting Eq. 95 and Eq. 96 yields Eq. 97.

Eq. 97

$$\sigma_s\left(E_i,T\right)dT=\sigma_s\left(E_i,\phi\right)d\Omega=2\pi\sigma_s\left(E_i,\phi\right)\sin\phi d\phi$$

Differentiating Eq. 94 with respect to energy yields Eq. 98. Combining Eq. 97 and Eq. 98 yields Eq. 99.

Eq. 98

$$dT=\frac{\gamma}{2}E_i\sin\phi d\phi$$

Eq. 99

$$\sigma_s\left(E_i,T\right)=\frac{4\pi}{\gamma E_i}\sigma_s\left(E_i,\phi\right)$$

Combining Eq. 84 and Eq. 95 yields the total elastic scattering cross section in Eq. 100.

Eq. 100

$$\sigma_s\left(E_i\right)=\int\sigma_s\left(E_i,\phi\right)d\Omega=2\pi\int\sigma_s\left(E_i,\phi\right)\sin\phi d\phi$$

Assuming elastic scattering in the center-of-mass frame is isotropic (an assumption that is accurate below 1 MeV), then Eq. 101 holds. Eq. 101 is independent of *T*, i.e. the probability that a neutron of energy E_i elastically scattering off of an atom

of mass M will impart a recoil energy of T to the struck atom does not depend on the recoil energy. Using the definition of averaging weighted functions in probability theory yields the average recoil energy in Eq. 102.

Eq. 101

$$\sigma_s\left(E_i\right)=\int\sigma_s\left(E_i,\phi\right)d\Omega=2\pi\sigma_s\left(E_i,\phi\right)\int\sin\phi d\phi=4\pi\sigma_s\left(E_i,\phi\right)$$

$$\sigma_s\left(E_i,T\right)=\frac{\sigma_s\left(E_i\right)}{\gamma E_i}$$

Eq. 102

$$\bar{T}=\frac{\int_{\check{T}}^{\hat{T}}T\sigma_s\left(E_i,T\right)dT}{\int_{\check{T}}^{\hat{T}}\sigma_s\left(E_i,T\right)dT}=\frac{\check{T}+\hat{T}}{2}\approx\frac{\hat{T}}{2}=\frac{\gamma E_i}{2}$$

In order to simplify the mathematics of evaluating Eq. 82, neutron-nucleus absorption contributions to the displacement cross section can be neglected, such as $(n,2n)$, (n,p), (n,γ), since these cross sections are orders of magnitude smaller than the scattering cross sections (particularly for non-actinides). Additionally, inelastic scattering is a threshold reaction (greater than about 1 MeV); since the TRIGA reactor has a thermal neutron spectrum, inelastic scattering can also be neglected without introducing noticeable error. The displacement reaction in a thermal spectrum nuclear reactor is dominated by elastic scattering. The displacement cross section can then be

defined by Eq. 103, where $\nu(T) = T/2E_d$ via the Kinchin-Pease model, and E_d is the atomic displacement energy.

Eq. 103

$$\sigma_D(E_i) = \frac{\sigma_s(E_i)}{\gamma E_i} \int_{E_d}^{\gamma E_i} \frac{T}{2E_d} dT$$

If $\gamma E_i > E_c$ where E_c is the cut-off energy for focusing, then the displacement cross section becomes Eq. 104.

$$\sigma_D(E_i) = \frac{\sigma_s(E_i)}{\gamma E_i} \left[\int_{E_d}^{2E_d} dT + \int_{2E_d}^{E_c} \frac{T}{2E_d} dT + \int_{E_c}^{\gamma E_i} \frac{E_c}{2E_d} dT \right]$$

$\therefore$

Eq. 104

$$\sigma_D(E_i) = \frac{\sigma_s(E_i)}{2\gamma E_i E_d} \left[E_d + \frac{(\gamma E_i)^2}{2} - \frac{E_d^2}{2} + \gamma E_i E_c - E_c^2 \right]$$

Since $\gamma E_i \sim E_c$ and the terms E_d and E_d^2 are negligible, the displacement cross section is approximately described by Eq. 105.

Eq. 105

$$\sigma_D(E_i) \approx \left(\frac{\gamma E_i}{4E_d} \right) \sigma_s(E_i)$$

Plugging Eq. 105 into Eq. 82 yields the approximate displacement rate per unit volume in a thermal neutron spectrum nuclear reactor in Eq. 106. Here, $\bar{E}_i$ is the average neutron energy , and Φ is the total neutron flux above energy E_d/γ [30]. Physically, the term in parenthesis is the number of displacements produced per neutron. Knowing that $\gamma = 0.068$ for Inconel 600, $E_d = 40\,\text{eV}$, and $\Phi \approx 2 \cdot 10^{13}$ $\text{n} \cdot \text{cm}^{-2} \cdot \text{s}^{-1}$ in the TAMU TRIGA reactor, Eq. 106 yields a neutron damage rate of about 0.02 dpa per 400 hours of full power reactor operation. The neutron damage rate in 316L stainless steel is approximately the same as in Inconel 600. Note that the TAMU TRIGA Reactor typically only operates during normal business hours.

$$R = \frac{N\gamma}{4E_d} \int_{E_d/\gamma}^{\gamma} \sigma_s\left(E_i\right) E_i \phi\left(E_i\right) dE_i$$

Eq. 106

$$R\left[\frac{displacements}{cm^3 \cdot s}\right] = N\sigma_s\left(\frac{\gamma \bar{E}_i}{4E_d}\right)\Phi$$

or

$$\frac{R}{N}\left[\frac{dpa}{s}\right] = \sigma_s\left(\frac{\gamma \bar{E}_i}{4E_d}\right)\Phi$$

A.3.2 Neutron Activation Analysis

Notes:

- * Means isotope is calculated by approximate method
- ? Means convergence not reached for nuclide
- & Means gamma spectrum is approximately calculated
- # Means nuclide is stable
- > Means nuclide was present before irradiation
- All values reported in Table 19 and Table 20 are in units of *per gram*.

Table 19: Inconel 600 NAA after 12 Months of Neutron Irradiation in the TAMU TRIGA Reactor and 28 Days of Decay

Nuclide	Atoms	Mass (g)	Activity (Bq)	β-Energy (kW)	α-Energy (kW)	γ-Energy (kW)	Dose Rate ($Sv \cdot hr^{-1}$)	Half Life (Sec)
H 1 #	3.51E+16	5.83E-08	0.00E+00	0.00E+00	0.00E+00	0.00E+00	0.00E+00	Stable
H 2 #	4.01E+12	1.33E-11	0.00E+00	0.00E+00	0.00E+00	0.00E+00	0.00E+00	Stable
H 3	7.02E+09	3.52E-14	1.25E+01	1.14E-17	0.00E+00	0.00E+00	0.00E+00	3.89E+08
He 3 #	1.57E+09	7.84E-15	0.00E+00	0.00E+00	0.00E+00	0.00E+00	0.00E+00	Stable
He 4 #	2.74E+15	1.82E-08	0.00E+00	0.00E+00	0.00E+00	0.00E+00	0.00E+00	Stable
Li 6 #	7.31E+05	7.28E-18	0.00E+00	0.00E+00	0.00E+00	0.00E+00	0.00E+00	Stable
Li 7 #	7.72E+01	8.97E-22	0.00E+00	0.00E+00	0.00E+00	0.00E+00	0.00E+00	Stable
Be 9 #	6.97E+11	1.04E-11	0.00E+00	0.00E+00	0.00E+00	0.00E+00	0.00E+00	Stable
Be 10	6.00E+08	9.97E-15	8.23E-06	3.33E-22	0.00E+00	0.00E+00	0.00E+00	5.05E+13
B 10 #	6.30E+01	1.05E-21	0.00E+00	0.00E+00	0.00E+00	0.00E+00	0.00E+00	Stable
B 11 #	4.96E+08	9.05E-15	0.00E+00	0.00E+00	0.00E+00	0.00E+00	0.00E+00	Stable
C 12 #>	9.87E+18	1.97E-04	0.00E+00	0.00E+00	0.00E+00	0.00E+00	0.00E+00	Stable
C 13 #>	1.11E+17	2.39E-06	0.00E+00	0.00E+00	0.00E+00	0.00E+00	0.00E+00	Stable
C 14	1.31E+10	3.05E-13	5.05E-02	4.00E-19	0.00E+00	0.00E+00	0.00E+00	1.80E+11
N 14 #	4.19E+05	9.74E-18	0.00E+00	0.00E+00	0.00E+00	0.00E+00	0.00E+00	Stable
O 18 #	1.16E+01	3.46E-22	0.00E+00	0.00E+00	0.00E+00	0.00E+00	0.00E+00	Stable
Ne 20 #	9.45E+02	3.14E-20	0.00E+00	0.00E+00	0.00E+00	0.00E+00	0.00E+00	Stable
Ne 21 #	4.06E+05	1.42E-17	0.00E+00	0.00E+00	0.00E+00	0.00E+00	0.00E+00	Stable
Ne 22 #	1.11E+06	4.05E-17	0.00E+00	0.00E+00	0.00E+00	0.00E+00	0.00E+00	Stable
Na 23 #	7.49E+09	2.86E-13	0.00E+00	0.00E+00	0.00E+00	0.00E+00	0.00E+00	Stable
Mg 24 #	2.00E+12	7.97E-11	0.00E+00	0.00E+00	0.00E+00	0.00E+00	0.00E+00	Stable

Table 19 Continued

Nuclide	Atoms	Mass (g)	Activity (Bq)	β-Energy (kW)	α-Energy (kW)	γ-Energy (kW)	Dose Rate ($Sv \cdot hr^{-1}$)	Half Life (Sec)
Mg 25 #	4.43E+12	1.84E-10	0.00E+00	0.00E+00	0.00E+00	0.00E+00	0.00E+00	Stable
Mg 26 #	6.83E+11	2.95E-11	0.00E+00	0.00E+00	0.00E+00	0.00E+00	0.00E+00	Stable
Al 26	8.81E+09	3.80E-13	2.70E-04	1.73E-20	0.00E+00	1.16E-19	8.65E-17	2.26E+13
Al 27 #>	4.89E+19	2.19E-03	0.00E+00	0.00E+00	0.00E+00	0.00E+00	0.00E+00	Stable
Si 28 #>	3.15E+19	1.46E-03	0.00E+00	0.00E+00	0.00E+00	0.00E+00	0.00E+00	Stable
Si 29 #>	1.60E+18	7.70E-05	0.00E+00	0.00E+00	0.00E+00	0.00E+00	0.00E+00	Stable
Si 30 #>	1.05E+18	5.25E-05	0.00E+00	0.00E+00	0.00E+00	0.00E+00	0.00E+00	Stable
Si 32	2.74E+07	1.45E-15	4.56E-03	4.72E-20	0.00E+00	0.00E+00	0.00E+00	4.17E+09
P 31 #>	1.55E+18	7.97E-05	0.00E+00	0.00E+00	0.00E+00	0.00E+00	0.00E+00	Stable
P 32 &	3.37E+11	1.79E-11	1.89E+05	2.10E-11	0.00E+00	5.19E-14	7.46E-11	1.23E+06
P 33	4.28E+08	2.34E-14	1.35E+02	1.66E-15	0.00E+00	0.00E+00	0.00E+00	2.19E+06
S 32 #>	1.78E+17	9.44E-06	0.00E+00	0.00E+00	0.00E+00	0.00E+00	0.00E+00	Stable
S 33 #>	1.41E+15	7.72E-08	0.00E+00	0.00E+00	0.00E+00	0.00E+00	0.00E+00	Stable
S 34 #>	7.87E+15	4.44E-07	0.00E+00	0.00E+00	0.00E+00	0.00E+00	0.00E+00	Stable
S 35	6.30E+10	3.66E-12	5.79E+03	4.52E-14	0.00E+00	0.00E+00	0.00E+00	7.54E+06
S 36 #>	3.74E+13	2.23E-09	0.00E+00	0.00E+00	0.00E+00	0.00E+00	0.00E+00	Stable
Cl 35 #	6.97E+10	4.05E-12	0.00E+00	0.00E+00	0.00E+00	0.00E+00	0.00E+00	Stable
Cl 36	3.95E+07	2.36E-15	2.88E-06	1.26E-22	0.00E+00	8.47E-27	1.81E-23	9.50E+12
Cl 37 #	4.50E+08	2.77E-14	0.00E+00	0.00E+00	0.00E+00	0.00E+00	0.00E+00	Stable
Ar 38 #	7.38E+03	4.65E-19	0.00E+00	0.00E+00	0.00E+00	0.00E+00	0.00E+00	Stable
Ar 39	1.09E+04	7.07E-19	8.92E-07	3.13E-23	0.00E+00	0.00E+00	0.00E+00	8.49E+09
Ar 40 #	1.07E+04	7.12E-19	0.00E+00	0.00E+00	0.00E+00	0.00E+00	0.00E+00	Stable

Table 19 Continued

Nuclide	Atoms	Mass (g)	Activity (Bq)	β-Energy (kW)	α-Energy (kW)	γ-Energy (kW)	Dose Rate ($Sv \cdot hr^{-1}$)	Half Life (Sec)
Ar 42	8.84E+01	6.16E-21	5.88E-08	2.20E-24	0.00E+00	0.00E+00	0.00E+00	1.04E+09
K 41 #	1.41E+02	9.61E-21	0.00E+00	0.00E+00	0.00E+00	0.00E+00	0.00E+00	Stable
Ca 42 #	1.77E+08	1.23E-14	0.00E+00	0.00E+00	0.00E+00	0.00E+00	0.00E+00	Stable
Ca 43 #	1.18E+11	8.46E-12	0.00E+00	0.00E+00	0.00E+00	0.00E+00	0.00E+00	Stable
Ca 44 #	1.64E+11	1.20E-11	0.00E+00	0.00E+00	0.00E+00	0.00E+00	0.00E+00	Stable
Ca 45	8.14E+10	6.07E-12	4.01E+03	4.95E-14	0.00E+00	6.12E-21	6.16E-17	1.41E+07
Ca 46 #	5.91E+09	4.51E-13	0.00E+00	0.00E+00	0.00E+00	0.00E+00	0.00E+00	Stable
Ca 47	1.31E+04	1.02E-18	2.32E-02	1.28E-18	0.00E+00	3.94E-18	2.99E-15	3.92E+05
Ca 48 &	7.43E+04	5.92E-18	3.08E-23	1.08E-38	0.00E+00	2.32E-40	2.05E-37	1.67E+27
Sc 45 #	4.73E+10	3.54E-12	0.00E+00	0.00E+00	0.00E+00	0.00E+00	0.00E+00	Stable
Sc 46	7.86E+11	6.00E-11	7.52E+04	1.35E-12	0.00E+00	2.42E-11	1.93E-08	7.24E+06
Sc 47	1.51E+06	1.18E-16	3.62E+00	9.43E-17	0.00E+00	6.29E-17	4.43E-14	2.90E+05
Sc 48	6.81E+00	5.42E-22	3.00E-05	1.06E-21	0.00E+00	1.61E-20	1.26E-17	1.57E+05
Ti 46 #>	2.69E+18	2.05E-04	0.00E+00	0.00E+00	0.00E+00	0.00E+00	0.00E+00	Stable
Ti 47 #>	2.42E+18	1.89E-04	0.00E+00	0.00E+00	0.00E+00	0.00E+00	0.00E+00	Stable
Ti 48 #>	2.40E+19	1.91E-03	0.00E+00	0.00E+00	0.00E+00	0.00E+00	0.00E+00	Stable
Ti 49 #>	1.77E+18	1.44E-04	0.00E+00	0.00E+00	0.00E+00	0.00E+00	0.00E+00	Stable
Ti 50 #>	1.69E+18	1.40E-04	0.00E+00	0.00E+00	0.00E+00	0.00E+00	0.00E+00	Stable
V 48	2.95E+05	2.35E-17	1.48E-01	3.54E-18	0.00E+00	6.92E-17	5.47E-14	1.38E+06
V 49	1.83E+11	1.49E-11	4.46E+03	2.56E-15	0.00E+00	6.76E-16	5.58E-12	2.85E+07
V 50	2.65E+14	2.20E-08	4.16E-11	1.05E-28	0.00E+00	9.48E-27	7.02E-24	4.42E+24
V 51 #	8.77E+16	7.43E-06	0.00E+00	0.00E+00	0.00E+00	0.00E+00	0.00E+00	Stable

Table 19 Continued

Nuclide	Atoms	Mass (g)	Activity (Bq)	β-Energy (kW)	α-Energy (kW)	γ-Energy (kW)	Dose Rate ($Sv \cdot hr^{-1}$)	Half Life (Sec)
Cr 50 >	8.14E+19	6.76E-03	9.94E-06	1.86E-21	0.00E+00	0.00E+00	0.00E+00	5.68E+24
Cr 51	1.04E+16	8.83E-07	3.02E+09	1.78E-09	0.00E+00	1.58E-08	1.74E-05	2.39E+06
Cr 52 #>	1.57E+21	1.36E-01	0.00E+00	0.00E+00	0.00E+00	0.00E+00	0.00E+00	Stable
Cr 53 #>	1.78E+20	1.57E-02	0.00E+00	0.00E+00	0.00E+00	0.00E+00	0.00E+00	Stable
Cr 54 #>	4.46E+19	4.00E-03	0.00E+00	0.00E+00	0.00E+00	0.00E+00	0.00E+00	Stable
Mn 52	3.48E+02	3.00E-20	4.99E-04	5.73E-21	0.00E+00	2.77E-19	2.19E-16	4.83E+05
Mn 53	2.55E+11	2.24E-11	1.52E-03	9.75E-22	0.00E+00	3.46E-22	2.92E-18	1.16E+14
Mn 54	2.13E+14	1.91E-08	5.47E+06	3.53E-12	0.00E+00	7.33E-10	6.05E-07	2.70E+07
Mn 55 #>	2.29E+19	2.09E-03	0.00E+00	0.00E+00	0.00E+00	0.00E+00	0.00E+00	Stable
Fe 54 #>	5.83E+19	5.23E-03	0.00E+00	0.00E+00	0.00E+00	0.00E+00	0.00E+00	Stable
Fe 55	1.08E+16	9.84E-07	8.66E+07	5.55E-11	0.00E+00	2.30E-11	2.02E-07	8.63E+07
Fe 56 #>	9.15E+20	8.51E-02	0.00E+00	0.00E+00	0.00E+00	0.00E+00	0.00E+00	Stable
Fe 57 #>	2.13E+19	2.02E-03	0.00E+00	0.00E+00	0.00E+00	0.00E+00	0.00E+00	Stable
Fe 58 #>	2.84E+18	2.73E-04	0.00E+00	0.00E+00	0.00E+00	0.00E+00	0.00E+00	Stable
Fe 59	6.36E+13	6.22E-09	1.15E+07	2.17E-10	0.00E+00	2.18E-09	1.68E-06	3.84E+06
Fe 60	9.29E+10	9.24E-12	1.36E-03	1.91E-20	0.00E+00	0.00E+00	0.00E+00	4.73E+13
Co 56	8.97E+08	8.33E-14	9.31E+01	1.82E-15	0.00E+00	5.36E-14	3.88E-11	6.68E+06
Co 57	4.20E+13	3.97E-09	1.24E+06	3.63E-12	0.00E+00	2.49E-11	3.15E-08	2.35E+07
Co 58	1.15E+16	1.10E-06	1.30E+09	7.14E-09	0.00E+00	2.03E-07	1.69E-04	6.12E+06
Co 59 #>	9.12E+18	8.94E-04	0.00E+00	0.00E+00	0.00E+00	0.00E+00	0.00E+00	Stable
Co 60	2.86E+16	2.85E-06	1.19E+08	1.85E-09	0.00E+00	4.78E-08	3.67E-05	1.66E+08
Co 60m*	1.23E+00	1.23E-22	1.36E-03	1.21E-20	0.00E+00	1.48E-21	4.86E-18	6.28E+02

Table 19 Continued

Nuclide	Atoms	Mass (g)	Activity (Bq)	β-Energy (kW)	α-Energy (kW)	γ-Energy (kW)	Dose Rate ($Sv \cdot hr^{-1}$)	Half Life (Sec)
Ni 58 >	5.05E+21	4.86E-01	1.58E-07	4.89E-23	0.00E+00	0.00E+00	0.00E+00	2.21E+28
Ni 59	1.76E+18	1.72E-04	5.08E+05	3.76E-13	0.00E+00	2.07E-13	1.69E-09	2.40E+12
Ni 60 #>	1.94E+21	1.94E-01	0.00E+00	0.00E+00	0.00E+00	0.00E+00	0.00E+00	Stable
Ni 61 #>	8.49E+19	8.60E-03	0.00E+00	0.00E+00	0.00E+00	0.00E+00	0.00E+00	Stable
Ni 62 #>	2.69E+20	2.77E-02	0.00E+00	0.00E+00	0.00E+00	0.00E+00	0.00E+00	Stable
Ni 63	2.88E+17	3.01E-05	6.30E+07	1.76E-10	0.00E+00	0.00E+00	0.00E+00	3.18E+09
Ni 64 #>	6.87E+19	7.30E-03	0.00E+00	0.00E+00	0.00E+00	0.00E+00	0.00E+00	Stable
Cu 63 #>	9.78E+18	1.02E-03	0.00E+00	0.00E+00	0.00E+00	0.00E+00	0.00E+00	Stable
Cu 65 #>	4.37E+18	4.71E-04	0.00E+00	0.00E+00	0.00E+00	0.00E+00	0.00E+00	Stable
Zn 64	1.38E+15	1.47E-07	1.32E-11	2.32E-27	0.00E+00	0.00E+00	0.00E+00	7.26E+25
Zn 65	3.57E+10	3.85E-12	1.17E+03	1.26E-15	0.00E+00	1.09E-13	9.04E-11	2.11E+07
Zn 66 #	7.48E+14	8.20E-08	0.00E+00	0.00E+00	0.00E+00	0.00E+00	0.00E+00	Stable
Zn 67 #	2.60E+10	2.90E-12	0.00E+00	0.00E+00	0.00E+00	0.00E+00	0.00E+00	Stable
Zn 68 #	5.79E+06	6.54E-16	0.00E+00	0.00E+00	0.00E+00	0.00E+00	0.00E+00	Stable
Ga 69 #	1.31E+02	1.50E-20	0.00E+00	0.00E+00	0.00E+00	0.00E+00	0.00E+00	Stable
Sr 87 #	2.30E+01	3.32E-21	0.00E+00	0.00E+00	0.00E+00	0.00E+00	0.00E+00	Stable
Sr 89	5.22E+03	7.70E-19	8.27E-04	7.75E-20	0.00E+00	1.15E-23	9.40E-21	4.37E+06
Sr 90	1.64E+02	2.45E-20	1.25E-07	3.49E-24	0.00E+00	0.00E+00	0.00E+00	9.09E+08
Y 88	2.21E+00	3.23E-22	1.67E-07	1.69E-25	0.00E+00	7.20E-23	6.01E-20	9.21E+06
Y 89 #	1.55E+09	2.30E-13	0.00E+00	0.00E+00	0.00E+00	0.00E+00	0.00E+00	Stable
Y 90	1.68E+03	2.50E-19	5.04E-03	7.53E-19	0.00E+00	9.98E-25	3.05E-20	2.31E+05
Y 91	9.00E+06	1.36E-15	1.23E+00	1.20E-16	0.00E+00	6.20E-19	4.85E-16	5.06E+06

Table 19 Continued

Nuclide	Atoms	Mass (g)	Activity (Bq)	β-Energy (kW)	α-Energy (kW)	γ-Energy (kW)	Dose Rate ($Sv \cdot hr^{-1}$)	Half Life (Sec)
Zr 90 #	7.02E+10	1.05E-11	0.00E+00	0.00E+00	0.00E+00	0.00E+00	0.00E+00	Stable
Zr 91 #	6.46E+07	9.76E-15	0.00E+00	0.00E+00	0.00E+00	0.00E+00	0.00E+00	Stable
Zr 92 #	2.78E+11	4.24E-11	0.00E+00	0.00E+00	0.00E+00	0.00E+00	0.00E+00	Stable
Zr 93	2.67E+11	4.13E-11	3.84E-03	1.18E-20	0.00E+00	0.00E+00	0.00E+00	4.83E+13
Zr 94	6.42E+07	1.00E-14	2.35E-16	4.30E-32	0.00E+00	0.00E+00	0.00E+00	1.89E+23
Zr 95	5.39E+02	8.49E-20	6.75E-05	1.30E-21	0.00E+00	7.92E-21	6.60E-18	5.53E+06
Nb 91	3.68E+08	5.56E-14	1.19E-02	1.12E-20	0.00E+00	2.40E-20	6.16E-16	2.15E+10
Nb 91m	1.16E+07	1.75E-15	1.52E+00	2.28E-17	0.00E+00	9.28E-18	7.07E-14	5.26E+06
Nb 92	6.43E+11	9.81E-11	4.03E-04	5.13E-22	0.00E+00	9.72E-20	1.00E-16	1.11E+15
Nb 92m	1.06E+09	1.62E-13	8.41E+02	8.69E-16	0.00E+00	1.31E-13	1.48E-10	8.77E+05
Nb 93 #>	1.16E+19	1.79E-03	0.00E+00	0.00E+00	0.00E+00	0.00E+00	0.00E+00	Stable
Nb 93m	1.34E+14	2.07E-08	1.82E+05	8.46E-13	0.00E+00	5.71E-14	1.73E-09	5.09E+08
Nb 94	1.81E+15	2.82E-07	1.99E+03	5.36E-14	0.00E+00	5.01E-13	4.11E-10	6.31E+11
Nb 95	3.29E+11	5.19E-11	7.55E+04	5.39E-13	0.00E+00	9.25E-12	7.67E-09	3.02E+06
Nb 95m	1.59E+05	2.51E-17	3.53E-01	1.01E-17	0.00E+00	4.00E-18	1.55E-14	3.12E+05
Mo 93	4.20E+04	6.48E-18	2.31E-07	1.88E-25	0.00E+00	3.97E-25	1.24E-20	1.26E+11
Mo 94 #	6.29E+12	9.81E-10	0.00E+00	0.00E+00	0.00E+00	0.00E+00	0.00E+00	Stable
Mo 95 #	1.26E+12	1.98E-10	0.00E+00	0.00E+00	0.00E+00	0.00E+00	0.00E+00	Stable
Mo 96 #	1.11E+09	1.76E-13	0.00E+00	0.00E+00	0.00E+00	0.00E+00	0.00E+00	Stable
Mo 97 #	7.87E+04	1.27E-17	0.00E+00	0.00E+00	0.00E+00	0.00E+00	0.00E+00	Stable
Mo 98	1.00E+00	1.63E-22	2.21E-22	3.96E-39	0.00E+00	0.00E+00	0.00E+00	3.16E+21
Lu176	3.69E+01	1.08E-20	2.03E-17	9.68E-34	0.00E+00	1.56E-33	1.31E-30	1.26E+18

Table 19 Continued

Nuclide	Atoms	Mass (g)	Activity (Bq)	β-Energy (kW)	α-Energy (kW)	γ-Energy (kW)	Dose Rate ($Sv \cdot hr^{-1}$)	Half Life (Sec)
Lu177	4.61E+01	1.35E-20	5.56E-05	1.31E-21	0.00E+00	2.98E-22	2.47E-19	5.74E+05
Lu177m	1.88E+03	5.52E-19	9.41E-05	1.24E-21	0.00E+00	2.53E-21	2.14E-18	1.39E+07
Hf176 #	2.53E+01	7.41E-21	0.00E+00	0.00E+00	0.00E+00	0.00E+00	0.00E+00	Stable
Hf177 #	7.91E+04	2.33E-17	0.00E+00	0.00E+00	0.00E+00	0.00E+00	0.00E+00	Stable
Hf178 #	9.66E+06	2.86E-15	0.00E+00	0.00E+00	0.00E+00	0.00E+00	0.00E+00	Stable
Hf178n	1.05E+00	3.12E-22	7.47E-10	8.82E-27	0.00E+00	1.47E-25	1.24E-22	9.78E+08
Hf179 #	5.88E+06	1.75E-15	0.00E+00	0.00E+00	0.00E+00	0.00E+00	0.00E+00	Stable
Hf179n	6.18E+01	1.84E-20	1.98E-05	5.90E-22	0.00E+00	2.91E-21	2.46E-18	2.17E+06
Hf180 #	5.65E+09	1.69E-12	0.00E+00	0.00E+00	0.00E+00	0.00E+00	0.00E+00	Stable
Hf181	1.67E+06	5.01E-16	3.16E-01	1.03E-17	0.00E+00	2.69E-17	2.26E-14	3.66E+06
Hf182	3.59E+04	1.08E-17	8.76E-11	4.51E-28	0.00E+00	3.36E-27	2.65E-24	2.84E+14
Ta179	2.37E+07	7.06E-15	3.24E-01	3.84E-19	0.00E+00	1.52E-18	2.00E-15	5.08E+07
Ta180m >	3.78E+12	1.13E-09	4.62E-11	9.31E-28	0.00E+00	4.16E-27	3.56E-24	5.68E+22
Ta181 #>	3.29E+16	9.89E-06	0.00E+00	0.00E+00	0.00E+00	0.00E+00	0.00E+00	Stable
Ta182	7.19E+13	2.17E-08	5.03E+06	1.74E-10	0.00E+00	1.03E-09	8.11E-07	9.91E+06
Ta183	4.98E+09	1.51E-12	7.84E+03	4.39E-13	0.00E+00	3.60E-13	3.38E-10	4.40E+05
W 180 #	1.25E+09	3.73E-13	0.00E+00	0.00E+00	0.00E+00	0.00E+00	0.00E+00	Stable
W 181	3.09E+06	9.29E-16	2.05E-01	4.17E-19	0.00E+00	1.35E-18	1.67E-15	1.05E+07
W 182 #	5.97E+13	1.80E-08	0.00E+00	0.00E+00	0.00E+00	0.00E+00	0.00E+00	Stable
W 183	7.33E+13	2.23E-08	1.46E-11	0.00E+00	2.78E-27	0.00E+00	0.00E+00	3.47E+24
W 183m*	2.02E+03	6.14E-19	2.67E+02	7.86E-15	0.00E+00	5.36E-15	6.71E-12	5.25E+00

Table 19 Continued

Nuclide	Atoms	Mass (g)	Activity (Bq)	β-Energy (kW)	α-Energy (kW)	γ-Energy (kW)	Dose Rate ($Sv \cdot hr^{-1}$)	Half Life (Sec)
W 184	9.71E+10	2.97E-11	5.33E-15	0.00E+00	1.41E-30	0.00E+00	0.00E+00	1.26E+25
W 185	4.81E+06	1.48E-15	5.14E-01	1.04E-17	0.00E+00	4.13E-21	3.98E-18	6.49E+06
W 186	4.57E+03	1.41E-18	1.70E-22	6.68E-39	1.53E-38	0.00E+00	0.00E+00	1.86E+25
Re185 #	4.81E+06	1.48E-15	0.00E+00	0.00E+00	0.00E+00	0.00E+00	0.00E+00	Stable
Re186m	1.48E+01	4.56E-21	1.62E-12	1.77E-29	0.00E+00	1.56E-29	4.94E-26	6.30E+12
Re187	3.88E+00	1.21E-21	1.96E-18	2.07E-37	0.00E+00	0.00E+00	0.00E+00	1.37E+18
Os186	5.82E+03	1.80E-18	6.40E-20	0.00E+00	2.89E-35	0.00E+00	0.00E+00	6.31E+22
Os187 #	2.55E+00	7.93E-22	0.00E+00	0.00E+00	0.00E+00	0.00E+00	0.00E+00	Stable

Table 20: 316L Stainless Steel NAA after 12 Months of Neutron Irradiation in the TAMU TRIGA Reactor and 28 Days of Decay

Nuclide	Atoms	Mass (g)	Activity (Bq)	β-Energy (kW)	α-Energy (kW)	γ-Energy (kW)	Dose Rate ($Sv \cdot hr^{-1}$)	Half Life (Sec)
H 1 #	4.32E+16	7.17E-08	0.00E+00	0.00E+00	0.00E+00	0.00E+00	0.00E+00	Stable
H 2 #	1.13E+13	3.75E-11	0.00E+00	0.00E+00	0.00E+00	0.00E+00	0.00E+00	Stable
H 3	1.30E+13	6.52E-11	2.32E+04	2.12E-14	0.00E+00	0.00E+00	0.00E+00	3.89E+08
He 3 #	1.84E+11	9.18E-13	0.00E+00	0.00E+00	0.00E+00	0.00E+00	0.00E+00	Stable
He 4 #	2.17E+15	1.44E-08	0.00E+00	0.00E+00	0.00E+00	0.00E+00	0.00E+00	Stable
Li 6 #	5.10E+05	5.08E-18	0.00E+00	0.00E+00	0.00E+00	0.00E+00	0.00E+00	Stable
Li 7 #	1.06E+11	1.24E-12	0.00E+00	0.00E+00	0.00E+00	0.00E+00	0.00E+00	Stable
Be 9 #	4.85E+11	7.25E-12	0.00E+00	0.00E+00	0.00E+00	0.00E+00	0.00E+00	Stable
Be 10	6.27E+08	1.04E-14	8.60E-06	3.48E-22	0.00E+00	0.00E+00	0.00E+00	5.05E+13
B 10 #	1.13E+10	1.87E-13	0.00E+00	0.00E+00	0.00E+00	0.00E+00	0.00E+00	Stable
B 11 #	1.25E+15	2.28E-08	0.00E+00	0.00E+00	0.00E+00	0.00E+00	0.00E+00	Stable
C 12 #>	6.87E+18	1.37E-04	0.00E+00	0.00E+00	0.00E+00	0.00E+00	0.00E+00	Stable
C 13 #>	7.72E+16	1.67E-06	0.00E+00	0.00E+00	0.00E+00	0.00E+00	0.00E+00	Stable
C 14	3.60E+16	8.36E-07	1.39E+05	1.10E-12	0.00E+00	0.00E+00	0.00E+00	1.80E+11
N 14 #>	2.56E+20	5.94E-03	0.00E+00	0.00E+00	0.00E+00	0.00E+00	0.00E+00	Stable
N 15 #>	9.41E+17	2.34E-05	0.00E+00	0.00E+00	0.00E+00	0.00E+00	0.00E+00	Stable
O 16 #	3.13E+09	8.31E-14	0.00E+00	0.00E+00	0.00E+00	0.00E+00	0.00E+00	Stable
O 17 #	3.29E+01	9.29E-22	0.00E+00	0.00E+00	0.00E+00	0.00E+00	0.00E+00	Stable
Ne 21 #	4.94E+04	1.72E-18	0.00E+00	0.00E+00	0.00E+00	0.00E+00	0.00E+00	Stable
Ne 22 #	2.11E+06	7.71E-17	0.00E+00	0.00E+00	0.00E+00	0.00E+00	0.00E+00	Stable
Na 23 #	2.02E+03	7.73E-20	0.00E+00	0.00E+00	0.00E+00	0.00E+00	0.00E+00	Stable

Table 20 Continued

Nuclide	Atoms	Mass (g)	Activity (Bq)	β-Energy (kW)	α-Energy (kW)	γ-Energy (kW)	Dose Rate ($Sv \cdot hr^{-1}$)	Half Life (Sec)
Mg 24 #	1.51E+10	6.04E-13	0.00E+00	0.00E+00	0.00E+00	0.00E+00	0.00E+00	Stable
Mg 25 #	8.42E+12	3.50E-10	0.00E+00	0.00E+00	0.00E+00	0.00E+00	0.00E+00	Stable
Mg 26 #	1.01E+12	4.37E-11	0.00E+00	0.00E+00	0.00E+00	0.00E+00	0.00E+00	Stable
Al 26	1.50E+06	6.46E-17	4.59E-08	2.93E-24	0.00E+00	1.97E-23	1.55E-20	2.26E+13
Al 27 #	8.11E+10	3.63E-12	0.00E+00	0.00E+00	0.00E+00	0.00E+00	0.00E+00	Stable
Si 28 #>	5.99E+19	2.78E-03	0.00E+00	0.00E+00	0.00E+00	0.00E+00	0.00E+00	Stable
Si 29 #>	3.04E+18	1.46E-04	0.00E+00	0.00E+00	0.00E+00	0.00E+00	0.00E+00	Stable
Si 30 #>	2.00E+18	9.98E-05	0.00E+00	0.00E+00	0.00E+00	0.00E+00	0.00E+00	Stable
Si 32	8.37E+07	4.44E-15	1.39E-02	1.44E-19	0.00E+00	0.00E+00	0.00E+00	4.17E+09
P 31 #>	4.86E+18	2.50E-04	0.00E+00	0.00E+00	0.00E+00	0.00E+00	0.00E+00	Stable
P 32 &	1.03E+12	5.48E-11	5.80E+05	6.44E-11	0.00E+00	1.59E-13	2.41E-10	1.23E+06
P 33	4.24E+08	2.32E-14	1.34E+02	1.64E-15	0.00E+00	0.00E+00	0.00E+00	2.19E+06
S 32 #>	1.68E+17	8.95E-06	0.00E+00	0.00E+00	0.00E+00	0.00E+00	0.00E+00	Stable
S 33 #>	1.33E+15	7.32E-08	0.00E+00	0.00E+00	0.00E+00	0.00E+00	0.00E+00	Stable
S 34 #>	7.46E+15	4.21E-07	0.00E+00	0.00E+00	0.00E+00	0.00E+00	0.00E+00	Stable
S 35	5.97E+10	3.47E-12	5.49E+03	4.28E-14	0.00E+00	0.00E+00	0.00E+00	7.54E+06
S 36 #>	3.54E+13	2.12E-09	0.00E+00	0.00E+00	0.00E+00	0.00E+00	0.00E+00	Stable
Cl 35 #	6.61E+10	3.84E-12	0.00E+00	0.00E+00	0.00E+00	0.00E+00	0.00E+00	Stable
Cl 36	3.75E+07	2.24E-15	2.73E-06	1.20E-22	0.00E+00	8.03E-27	1.81E-23	9.50E+12
Cl 37 #	4.27E+08	2.62E-14	0.00E+00	0.00E+00	0.00E+00	0.00E+00	0.00E+00	Stable
Ar 38 #	6.99E+03	4.41E-19	0.00E+00	0.00E+00	0.00E+00	0.00E+00	0.00E+00	Stable
Ca 43 #	4.74E+01	3.39E-21	0.00E+00	0.00E+00	0.00E+00	0.00E+00	0.00E+00	Stable

Table 20 Continued

Nuclide	Atoms	Mass (g)	Activity (Bq)	β-Energy (kW)	α-Energy (kW)	γ-Energy (kW)	Dose Rate ($Sv \cdot hr^{-1}$)	Half Life (Sec)
Ca 44 #	6.26E+04	4.58E-18	0.00E+00	0.00E+00	0.00E+00	0.00E+00	0.00E+00	Stable
Ca 45	2.89E+04	2.16E-18	1.42E-03	1.76E-20	0.00E+00	2.17E-27	2.31E-23	1.41E+07
Ca 46 #	8.23E+03	6.29E-19	0.00E+00	0.00E+00	0.00E+00	0.00E+00	0.00E+00	Stable
Sc 45 #	1.12E+04	8.38E-19	0.00E+00	0.00E+00	0.00E+00	0.00E+00	0.00E+00	Stable
Sc 46	6.36E+05	4.85E-17	6.09E-02	1.09E-18	0.00E+00	1.96E-17	1.65E-14	7.24E+06
Sc 47	2.22E+00	1.73E-22	5.32E-06	1.39E-22	0.00E+00	9.24E-23	6.87E-20	2.90E+05
Ti 46 #	1.33E+09	1.02E-13	0.00E+00	0.00E+00	0.00E+00	0.00E+00	0.00E+00	Stable
Ti 47 #	1.85E+12	1.45E-10	0.00E+00	0.00E+00	0.00E+00	0.00E+00	0.00E+00	Stable
Ti 48 #	2.07E+13	1.65E-09	0.00E+00	0.00E+00	0.00E+00	0.00E+00	0.00E+00	Stable
Ti 49 #	5.02E+12	4.08E-10	0.00E+00	0.00E+00	0.00E+00	0.00E+00	0.00E+00	Stable
Ti 50 #	6.33E+12	5.26E-10	0.00E+00	0.00E+00	0.00E+00	0.00E+00	0.00E+00	Stable
V 48	2.94E+05	2.34E-17	1.47E-01	3.53E-18	0.00E+00	6.89E-17	5.74E-14	1.38E+06
V 49	1.82E+11	1.48E-11	4.43E+03	2.55E-15	0.00E+00	6.73E-16	5.86E-12	2.85E+07
V 50	2.64E+14	2.19E-08	4.14E-11	1.04E-28	0.00E+00	9.44E-27	7.37E-24	4.42E+24
V 51 #	8.73E+16	7.39E-06	0.00E+00	0.00E+00	0.00E+00	0.00E+00	0.00E+00	Stable
Cr 50 >	8.10E+19	6.73E-03	9.89E-06	1.85E-21	0.00E+00	0.00E+00	0.00E+00	5.68E+24
Cr 51	1.04E+16	8.79E-07	3.01E+09	1.77E-09	0.00E+00	1.58E-08	1.82E-05	2.39E+06
Cr 52 #>	1.56E+21	1.35E-01	0.00E+00	0.00E+00	0.00E+00	0.00E+00	0.00E+00	Stable
Cr 53 #>	1.77E+20	1.56E-02	0.00E+00	0.00E+00	0.00E+00	0.00E+00	0.00E+00	Stable
Cr 54 #>	4.44E+19	3.98E-03	0.00E+00	0.00E+00	0.00E+00	0.00E+00	0.00E+00	Stable
Mn 52	2.42E+03	2.09E-19	3.47E-03	3.98E-20	0.00E+00	1.93E-18	1.61E-15	4.83E+05
Mn 53	1.77E+12	1.56E-10	1.06E-02	6.78E-21	0.00E+00	2.41E-21	2.14E-17	1.16E+14

Table 20 Continued

Nuclide	Atoms	Mass (g)	Activity (Bq)	β-Energy (kW)	α-Energy (kW)	γ-Energy (kW)	Dose Rate ($Sv \cdot hr^{-1}$)	Half Life (Sec)
Mn 54	1.48E+15	1.32E-07	3.80E+07	2.45E-11	0.00E+00	5.09E-09	4.44E-06	2.70E+07
Mn 55 #>	1.29E+20	1.17E-02	0.00E+00	0.00E+00	0.00E+00	0.00E+00	0.00E+00	Stable
Fe 54 #>	4.05E+20	3.64E-02	0.00E+00	0.00E+00	0.00E+00	0.00E+00	0.00E+00	Stable
Fe 55	6.48E+16	5.91E-06	5.20E+08	3.34E-10	0.00E+00	1.39E-10	1.28E-06	8.63E+07
Fe 56 #>	6.36E+21	5.92E-01	0.00E+00	0.00E+00	0.00E+00	0.00E+00	0.00E+00	Stable
Fe 57 #>	1.48E+20	1.40E-02	0.00E+00	0.00E+00	0.00E+00	0.00E+00	0.00E+00	Stable
Fe 58 #>	1.96E+19	1.89E-03	0.00E+00	0.00E+00	0.00E+00	0.00E+00	0.00E+00	Stable
Fe 59	4.38E+14	4.29E-08	7.91E+07	1.50E-09	0.00E+00	1.51E-08	1.22E-05	3.84E+06
Fe 60	6.19E+11	6.16E-11	9.06E-03	1.27E-19	0.00E+00	0.00E+00	0.00E+00	4.73E+13
Co 56	1.18E+08	1.10E-14	1.23E+01	2.40E-16	0.00E+00	7.05E-15	5.38E-12	6.68E+06
Co 57	5.53E+12	5.23E-10	1.63E+05	4.78E-13	0.00E+00	3.27E-12	4.37E-09	2.35E+07
Co 58	1.51E+15	1.45E-07	1.71E+08	9.40E-10	0.00E+00	2.68E-08	2.34E-05	6.12E+06
Co 59 #	1.54E+15	1.51E-07	0.00E+00	0.00E+00	0.00E+00	0.00E+00	0.00E+00	Stable
Co 60	3.21E+13	3.20E-09	1.34E+05	2.08E-12	0.00E+00	5.37E-11	4.35E-08	1.66E+08
Co 60m*	8.21E+00	8.18E-22	9.06E-03	8.09E-20	0.00E+00	9.86E-21	3.42E-17	6.28E+02
Ni 58 >	6.64E+20	6.40E-02	2.09E-08	6.43E-24	0.00E+00	0.00E+00	0.00E+00	2.21E+28
Ni 59	2.31E+17	2.27E-05	6.69E+04	4.95E-14	0.00E+00	2.73E-14	2.35E-10	2.40E+12
Ni 60 #>	2.56E+20	2.55E-02	0.00E+00	0.00E+00	0.00E+00	0.00E+00	0.00E+00	Stable
Ni 61 #>	1.12E+19	1.13E-03	0.00E+00	0.00E+00	0.00E+00	0.00E+00	0.00E+00	Stable
Ni 62 #>	3.54E+19	3.65E-03	0.00E+00	0.00E+00	0.00E+00	0.00E+00	0.00E+00	Stable
Ni 63	3.80E+16	3.97E-06	8.30E+06	2.32E-11	0.00E+00	0.00E+00	0.00E+00	3.18E+09
Ni 64 #>	9.04E+18	9.61E-04	0.00E+00	0.00E+00	0.00E+00	0.00E+00	0.00E+00	Stable

Table 20 Continued

Nuclide	Atoms	Mass (g)	Activity (Bq)	β-Energy (kW)	α-Energy (kW)	γ-Energy (kW)	Dose Rate ($Sv \cdot hr^{-1}$)	Half Life (Sec)
Cu 63 #>	2.17E+19	2.27E-03	0.00E+00	0.00E+00	0.00E+00	0.00E+00	0.00E+00	Stable
Cu 65 #>	9.68E+18	1.05E-03	0.00E+00	0.00E+00	0.00E+00	0.00E+00	0.00E+00	Stable
Zn 64	3.07E+15	3.26E-07	2.93E-11	5.14E-27	0.00E+00	0.00E+00	0.00E+00	7.26E+25
Zn 65	7.93E+10	8.55E-12	2.60E+03	2.79E-15	0.00E+00	2.43E-13	2.12E-10	2.11E+07
Zn 66 #	1.66E+15	1.82E-07	0.00E+00	0.00E+00	0.00E+00	0.00E+00	0.00E+00	Stable
Zn 67 #	5.78E+10	6.43E-12	0.00E+00	0.00E+00	0.00E+00	0.00E+00	0.00E+00	Stable
Zn 68 #	1.29E+07	1.45E-15	0.00E+00	0.00E+00	0.00E+00	0.00E+00	0.00E+00	Stable
Ga 69 #	2.93E+02	3.36E-20	0.00E+00	0.00E+00	0.00E+00	0.00E+00	0.00E+00	Stable
Sr 86 #	2.52E+01	3.60E-21	0.00E+00	0.00E+00	0.00E+00	0.00E+00	0.00E+00	Stable
Sr 88 #	1.42E+07	2.08E-15	0.00E+00	0.00E+00	0.00E+00	0.00E+00	0.00E+00	Stable
Sr 89	3.54E+03	5.22E-19	5.61E-04	5.25E-20	0.00E+00	7.81E-24	6.72E-21	4.37E+06
Sr 90	1.28E+01	1.91E-21	9.76E-09	2.72E-25	0.00E+00	0.00E+00	0.00E+00	9.09E+08
Y 88	3.24E+07	4.73E-15	2.44E+00	2.48E-18	0.00E+00	1.05E-15	9.29E-13	9.21E+06
Y 89 #	6.51E+10	9.63E-12	0.00E+00	0.00E+00	0.00E+00	0.00E+00	0.00E+00	Stable
Y 89m*	1.44E+00	2.13E-22	6.39E-02	7.42E-20	0.00E+00	9.23E-18	7.94E-15	1.57E+01
Y 91	5.37E+03	8.11E-19	7.36E-04	7.15E-20	0.00E+00	3.70E-22	3.05E-19	5.06E+06
Zr 88	3.70E+07	5.40E-15	3.57E+00	8.03E-18	0.00E+00	2.24E-16	3.73E-13	7.17E+06
Zr 89	2.60E+04	3.85E-18	6.40E-02	9.51E-19	0.00E+00	2.60E-18	4.72E-15	2.82E+05
Zr 90 #	7.24E+09	1.08E-12	0.00E+00	0.00E+00	0.00E+00	0.00E+00	0.00E+00	Stable
Zr 91 #	1.14E+11	1.72E-11	0.00E+00	0.00E+00	0.00E+00	0.00E+00	0.00E+00	Stable
Zr 92 #	9.44E+12	1.44E-09	0.00E+00	0.00E+00	0.00E+00	0.00E+00	0.00E+00	Stable
Zr 93	3.95E+10	6.09E-12	5.67E-04	1.75E-21	0.00E+00	0.00E+00	0.00E+00	4.83E+13

Table 20 Continued

Nuclide	Atoms	Mass (g)	Activity (Bq)	β-Energy (kW)	α-Energy (kW)	γ-Energy (kW)	Dose Rate ($Sv \cdot hr^{-1}$)	Half Life (Sec)
Zr 94	1.54E+10	2.41E-12	5.65E-14	1.04E-29	0.00E+00	0.00E+00	0.00E+00	1.89E+23
Zr 95	4.05E+09	6.39E-13	5.08E+02	9.77E-15	0.00E+00	5.97E-14	5.24E-11	5.53E+06
Zr 96	4.63E+07	7.37E-15	2.61E-20	1.40E-35	0.00E+00	0.00E+00	0.00E+00	1.23E+27
Nb 91	4.79E+11	7.23E-11	1.55E+01	1.46E-17	0.00E+00	3.12E-17	8.46E-13	2.15E+10
Nb 91m	2.83E+10	4.27E-12	3.73E+03	5.58E-14	0.00E+00	2.27E-14	1.82E-10	5.26E+06
Nb 92	1.81E+12	2.76E-10	1.14E-03	1.44E-21	0.00E+00	2.73E-19	2.97E-16	1.11E+15
Nb 92m	3.68E+10	5.61E-12	2.91E+04	3.00E-14	0.00E+00	4.52E-12	5.41E-09	8.77E+05
Nb 93 #	7.12E+09	1.10E-12	0.00E+00	0.00E+00	0.00E+00	0.00E+00	0.00E+00	Stable
Nb 93m	2.50E+10	3.86E-12	3.40E+01	1.58E-16	0.00E+00	1.07E-17	3.40E-13	5.09E+08
Nb 94	1.95E+11	3.04E-11	2.14E-01	5.77E-18	0.00E+00	5.39E-17	4.67E-14	6.31E+11
Nb 95	4.30E+10	6.77E-12	9.85E+03	7.03E-14	0.00E+00	1.21E-12	1.06E-09	3.02E+06
Nb 95m	2.70E+06	4.26E-16	6.00E+00	1.72E-16	0.00E+00	6.80E-17	2.77E-13	3.12E+05
Mo 92 >	1.77E+19	2.70E-03	2.04E-09	5.40E-25	0.00E+00	0.00E+00	0.00E+00	6.00E+27
Mo 93	5.75E+14	8.87E-08	3.16E+03	2.57E-15	0.00E+00	5.43E-15	1.80E-10	1.26E+11
Mo 94 #>	1.10E+19	1.72E-03	0.00E+00	0.00E+00	0.00E+00	0.00E+00	0.00E+00	Stable
Mo 95 #>	1.89E+19	2.98E-03	0.00E+00	0.00E+00	0.00E+00	0.00E+00	0.00E+00	Stable
Mo 96 #>	1.99E+19	3.17E-03	0.00E+00	0.00E+00	0.00E+00	0.00E+00	0.00E+00	Stable
Mo 97 #>	1.14E+19	1.83E-03	0.00E+00	0.00E+00	0.00E+00	0.00E+00	0.00E+00	Stable
Mo 98 >	2.87E+19	4.67E-03	6.31E-03	1.13E-19	0.00E+00	0.00E+00	0.00E+00	3.16E+21
Mo 99	6.29E+07	1.03E-14	1.84E+02	1.16E-14	0.00E+00	4.37E-15	4.33E-12	2.37E+05

Table 20 Continued

Nuclide	Atoms	Mass (g)	Activity (Bq)	β-Energy (kW)	α-Energy (kW)	γ-Energy (kW)	Dose Rate ($Sv \cdot hr^{-1}$)	Half Life (Sec)
Mo100 >	1.15E+19	1.90E-03	2.54E-08	1.24E-23	0.00E+00	0.00E+00	0.00E+00	3.12E+26
Tc 97	5.02E+04	8.07E-18	4.24E-10	3.84E-28	0.00E+00	7.93E-28	2.61E-23	8.21E+13
Tc 97m	2.35E+03	3.78E-19	2.09E-04	2.91E-21	0.00E+00	3.18E-22	8.45E-18	7.79E+06
Tc 98	4.21E+07	6.84E-15	2.20E-07	4.16E-24	0.00E+00	4.98E-23	4.36E-20	1.33E+14
Tc 99	1.74E+15	2.86E-07	1.79E+02	2.45E-15	0.00E+00	2.02E-20	1.10E-16	6.75E+12
Tc 99m*	5.49E+06	9.02E-16	1.76E+02	4.37E-16	0.00E+00	3.57E-15	3.70E-12	2.16E+04
Ru 98 #	7.80E+04	1.27E-17	0.00E+00	0.00E+00	0.00E+00	0.00E+00	0.00E+00	Stable
Ru 99 #	5.83E+10	9.58E-12	0.00E+00	0.00E+00	0.00E+00	0.00E+00	0.00E+00	Stable
Ru100 #	2.72E+12	4.52E-10	0.00E+00	0.00E+00	0.00E+00	0.00E+00	0.00E+00	Stable
Ru101 #	4.98E+14	8.35E-08	0.00E+00	0.00E+00	0.00E+00	0.00E+00	0.00E+00	Stable
Ru102 #	2.47E+11	4.18E-11	0.00E+00	0.00E+00	0.00E+00	0.00E+00	0.00E+00	Stable
Ru103	2.69E+06	4.60E-16	5.51E-01	5.87E-18	0.00E+00	4.38E-17	3.89E-14	3.39E+06
Ru104 #	5.06E+03	8.74E-19	0.00E+00	0.00E+00	0.00E+00	0.00E+00	0.00E+00	Stable
Rh103 #	7.41E+06	1.27E-15	0.00E+00	0.00E+00	0.00E+00	0.00E+00	0.00E+00	Stable
Rh103m*	2.64E+03	4.52E-19	5.45E-01	3.12E-18	0.00E+00	1.47E-19	5.64E-16	3.37E+03
Pd104 #	9.99E+03	1.73E-18	0.00E+00	0.00E+00	0.00E+00	0.00E+00	0.00E+00	Stable

A.4 Cubic Rodrigues-Frank Maps and Pole Figures

Cubic Rodrigues-Frank maps for unirradiated and irradiated Inconel 600 and 316L stainless steel are provided in Figure 243 - Figure 246. The RF map legend is shown in Figure 242. Neither the conventionally manufactured Inconel 600 nor 316L stainless steel contains significant texture before or after irradiation, as to be expected from the previous Euler maps. For both alloy types, the LAM grains tend to align themselves with similar orientations parallel to the build direction. After irradiation, slight rotations about the build direction axis are observed. Gradual rotations (i.e. changes in color) within grains indicate regions of residual strain. Note that these regions exist in all LAM specimens, but none of the conventional controls.

Euler Angle	Axis/ Angle	Color	Comments
0,0,0	0° <000>	Black	Cubic Orientation is Black
0,45,0	45° <100>	Red	Rot. Of 45° about x-axis
90,45,90	45° <010>	Green	Rot. Of 45° about y-axis
45,0,0	45° <001>	Blue	Rot. Of 45° about z-axis

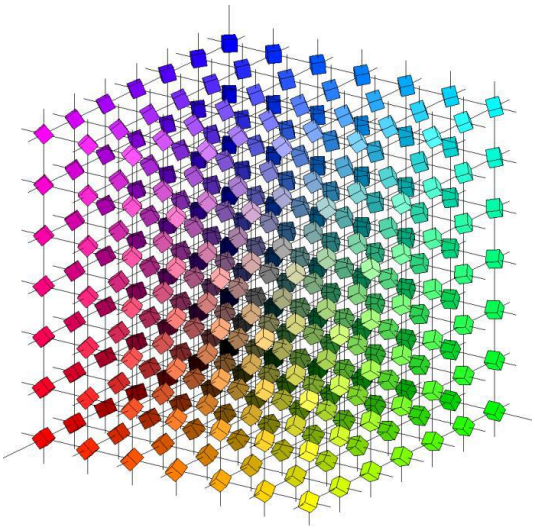

Figure 242: (Left) Cubic RF Orientation Component Legend Table, and (Right)

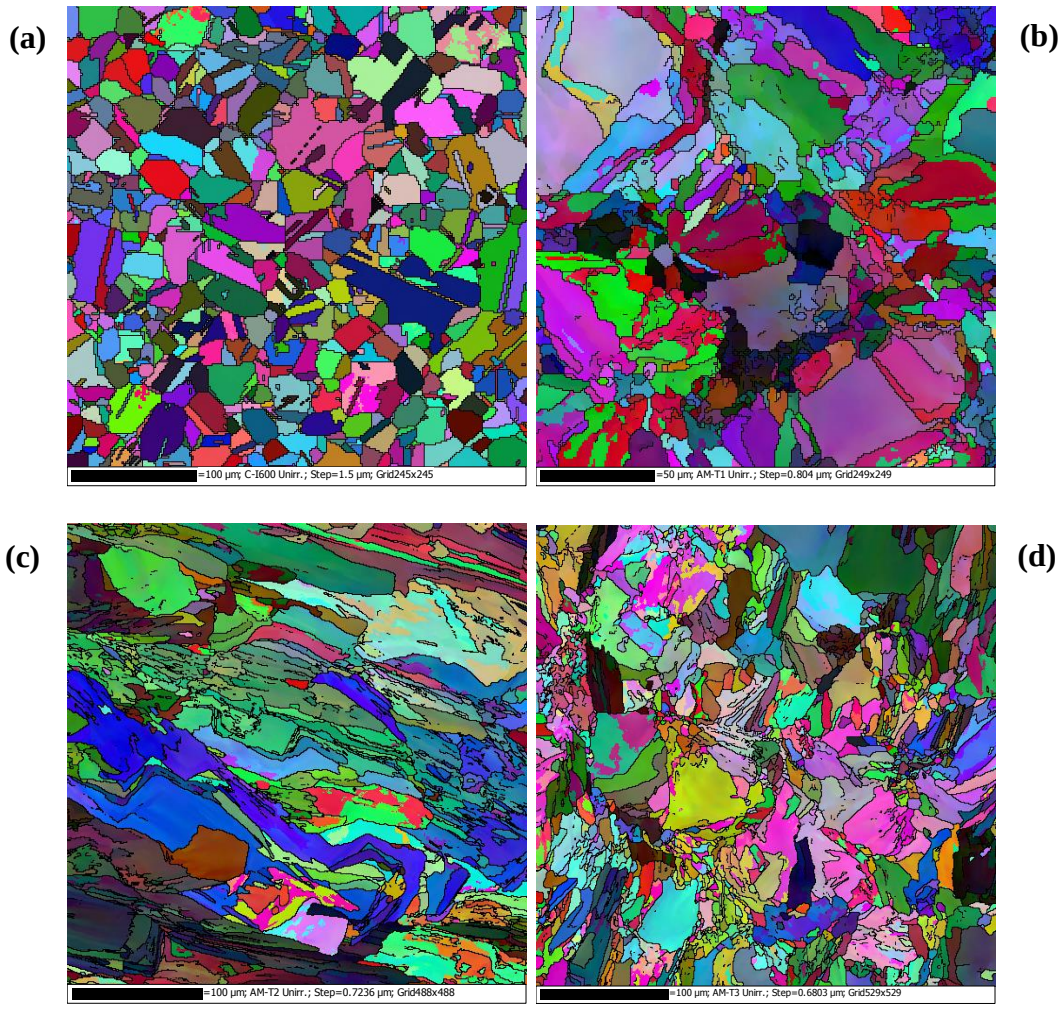

Figure 243: EBSD Cubic Rodrigues-Frank Maps with Respect to (0°, 0°, 0°) for Unirradiated Inconel 600 (a) Conventionally Manufactured, (b) Vertical LAM, (c) Horizontal LAM, and (d) 45° LAM

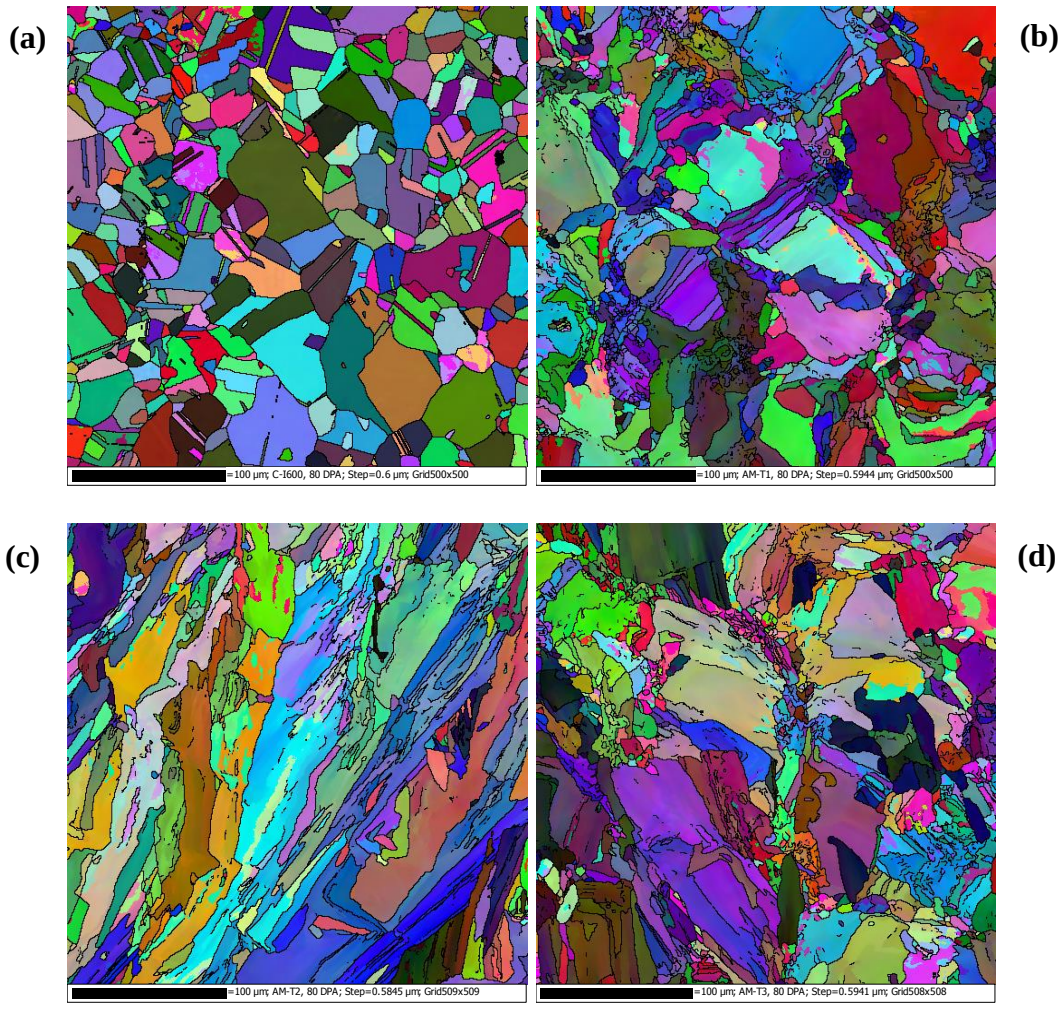

Figure 244: EBSD Cubic Rodrigues-Frank Maps with Respect to (0°, 0°, 0°) for Inconel 600 (a) Conventionally Manufactured, (b) Vertical LAM, (c) Horizontal LAM, and (d) 45° LAM Irradiated to 80 dpa

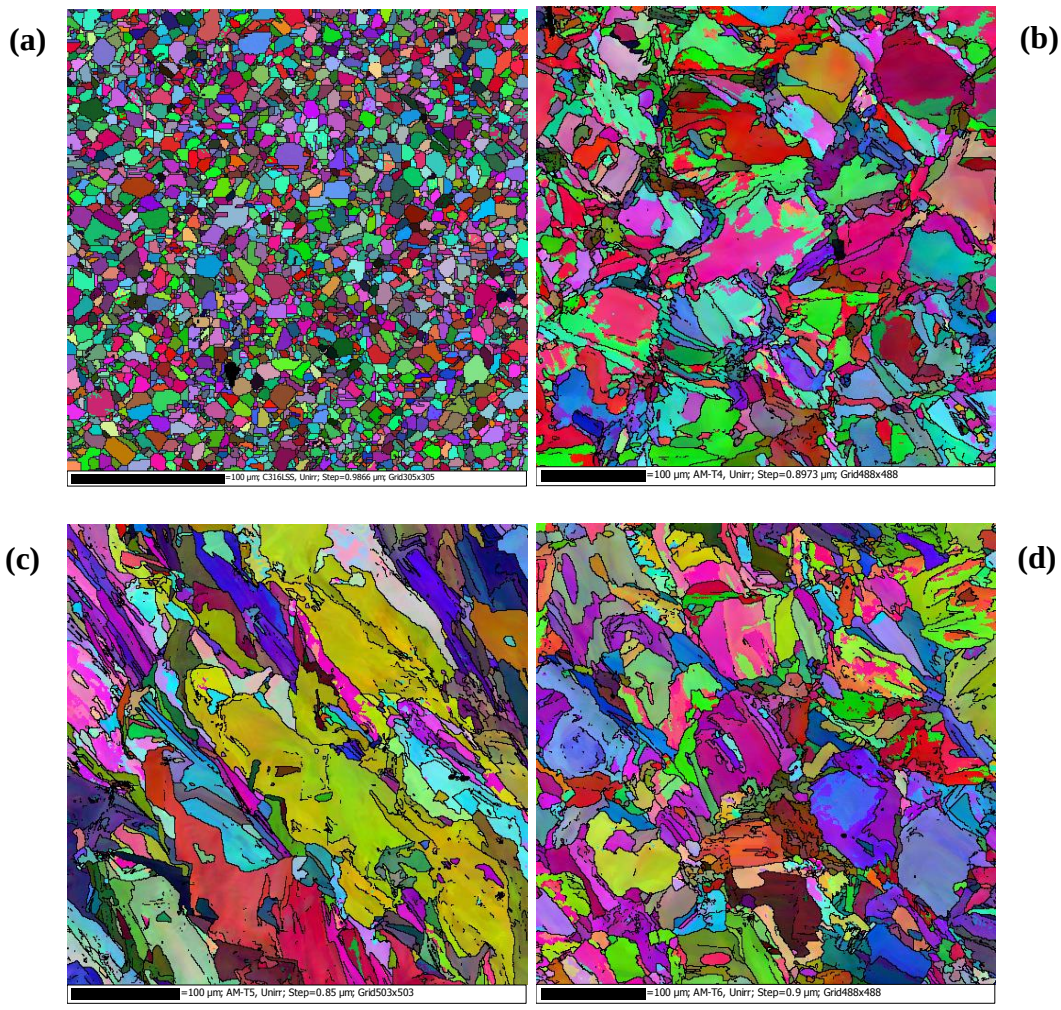

Figure 245: EBSD Cubic Rodrigues-Frank Maps with Respect to (0°, 0°, 0°) for Unirradiated 316L Stainless Steel (a) Conventionally Manufactured, (b) Vertical LAM, (c) Horizontal LAM, and (d) 45° LAM

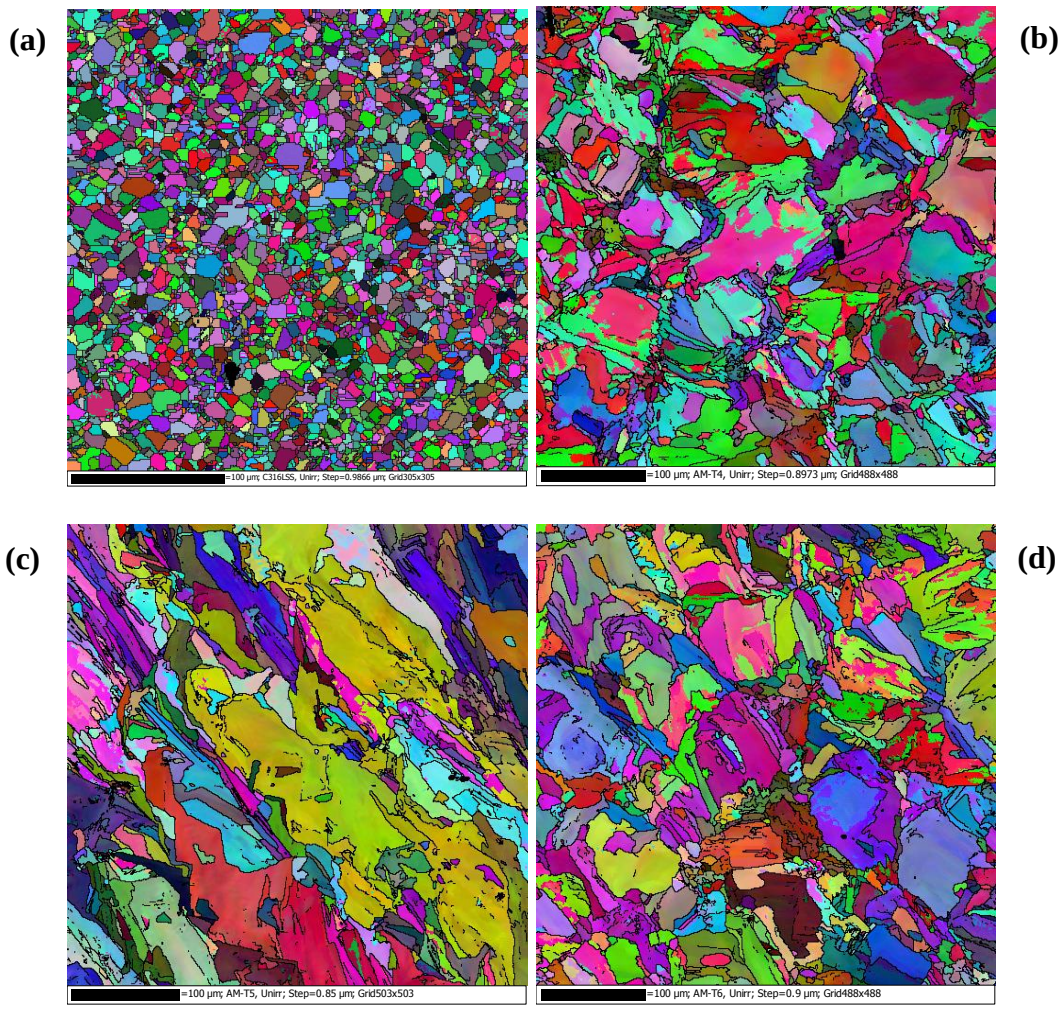

Figure 246: EBSD Cubic Rodrigues-Frank Maps with Respect to (0°, 0°, 0°) for 316L Stainless Steel (a) Conventionally Manufactured, (b) Vertical LAM, (c) Horizontal LAM, and (d) 45° LAM Irradiated to 80 dpa

The figures below show the pole figures for unirradiated and irradiated Inconel 600 (Figure 247 and Figure 248) and unirradiated and irradiated 316L stainless steel (Figure 249 and Figure 250). The statistical intensity of crystalline orientations is given by the multiple of uniform density (MUD) value. A MUD value of unity corresponds to a material with no crystalline orientation, while a MUD value of greater than unity corresponds to a material with crystalline texture.

The conventional controls for both alloys appear to have little texture before or after irradiation. In contrast, the LAM specimens clearly show texture before and after irradiation, as to be expected from the previous XRD results. Specifically, both vertical LAM I600 and 316L show an accumulation of grains with <101>||ND orientation before and after irradiation, while both horizontal LAM I600 and 316L are almost entirely lacking grains with <101>||ND orientation. This suggests that crystallographic texture is inherent to the laser additive manufacturing process of fcc alloys such that <101>||**B**, where **B** is the build direction.

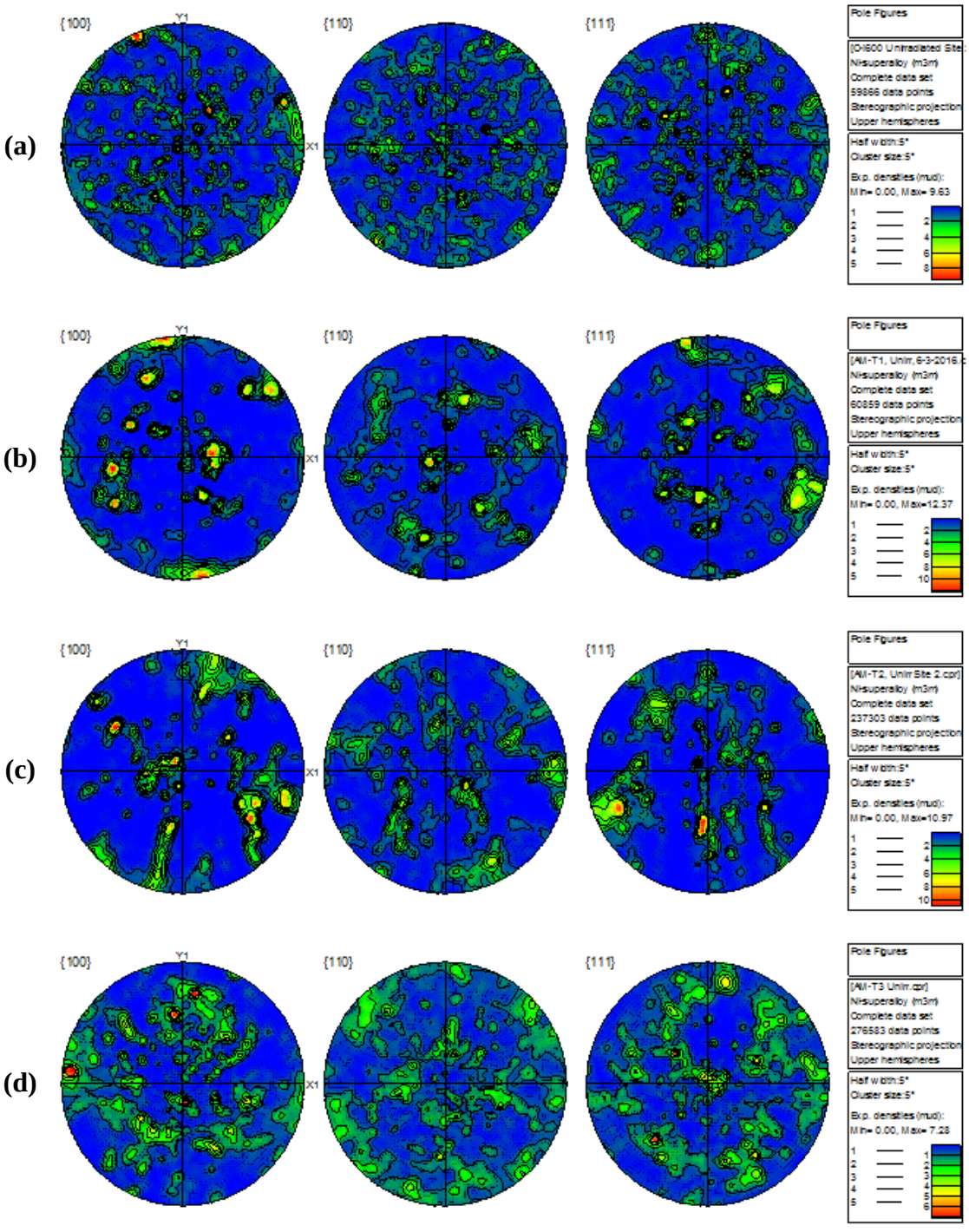

Figure 247: EBSD Stereographic Projection Pole Figures of Unirradiated Inconel 600 (a) Conventionally Manufactured, (b) Vertical LAM, (c) Horizontal LAM, and (d) 45° LAM

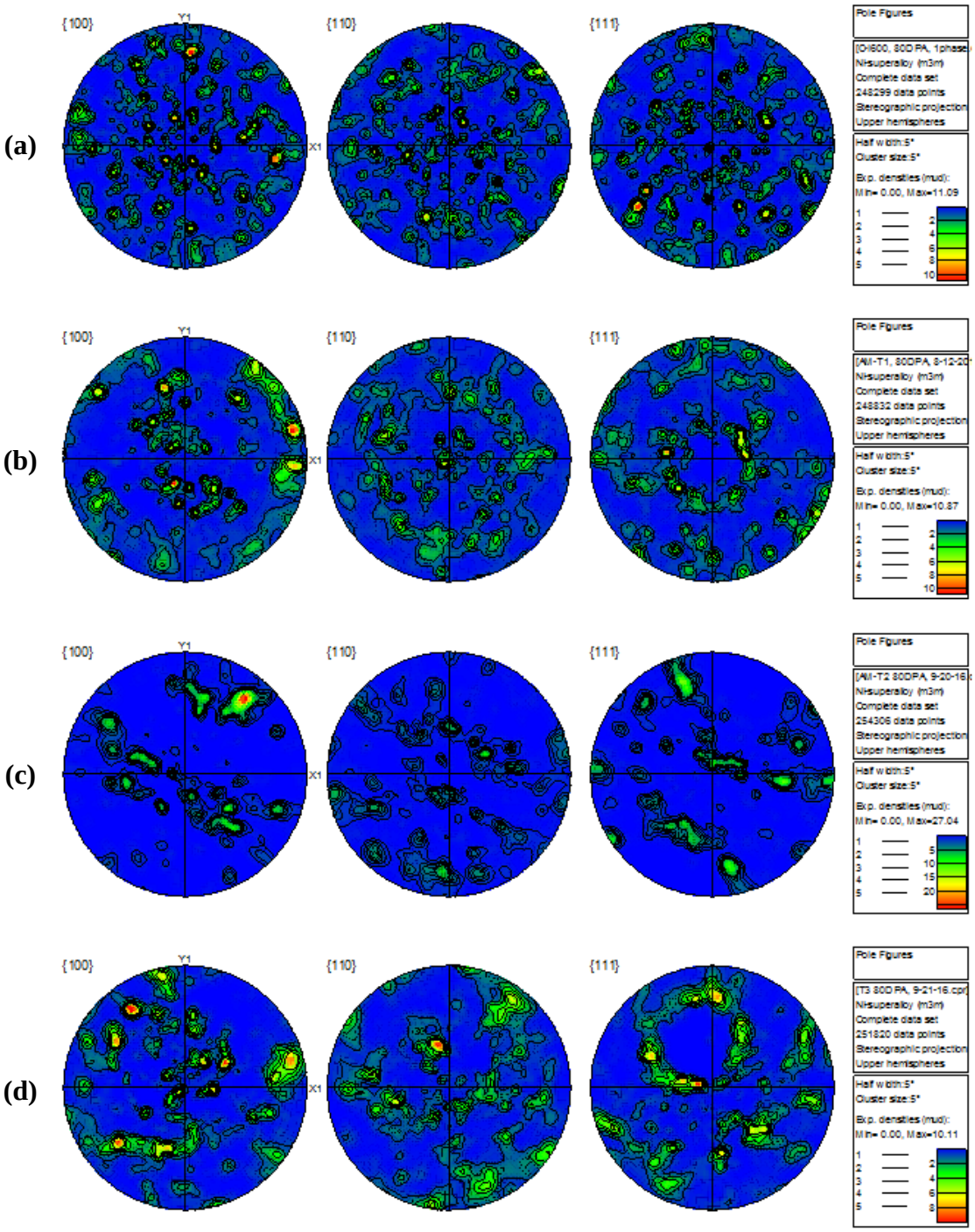

Figure 248: EBSD Stereographic Projection Pole Figures of Inconel 600 (a) Conventionally Manufactured, (b) Vertical LAM, (c) Horizontal LAM, and (d) 45° LAM Irradiated to 80 dpa

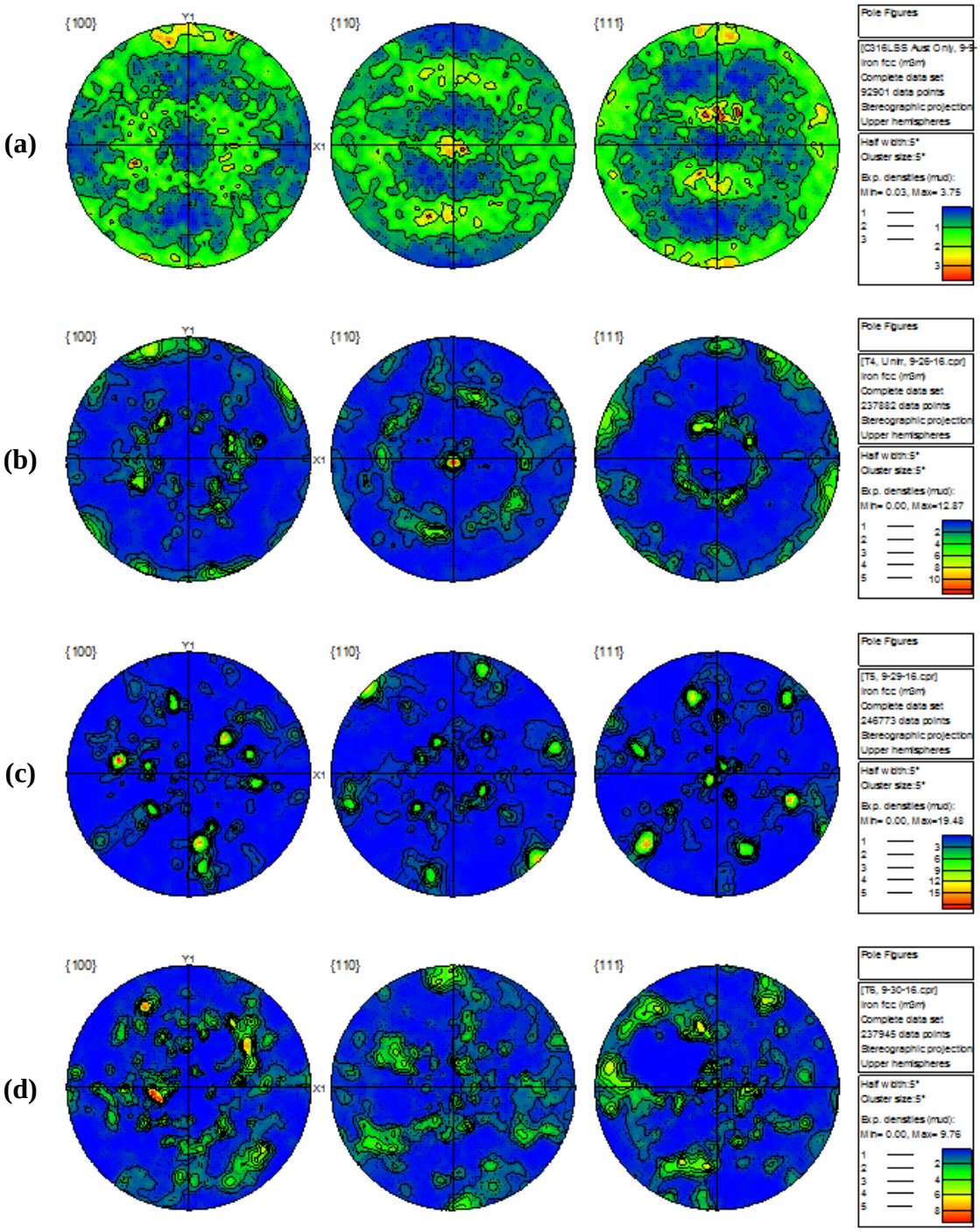

Figure 249: EBSD Stereographic Projection Pole Figures of Unirradiated 316L Stainless Steel (a) Conventionally Manufactured, (b) Vertical LAM, (c) Horizontal LAM, and (d) 45° LAM

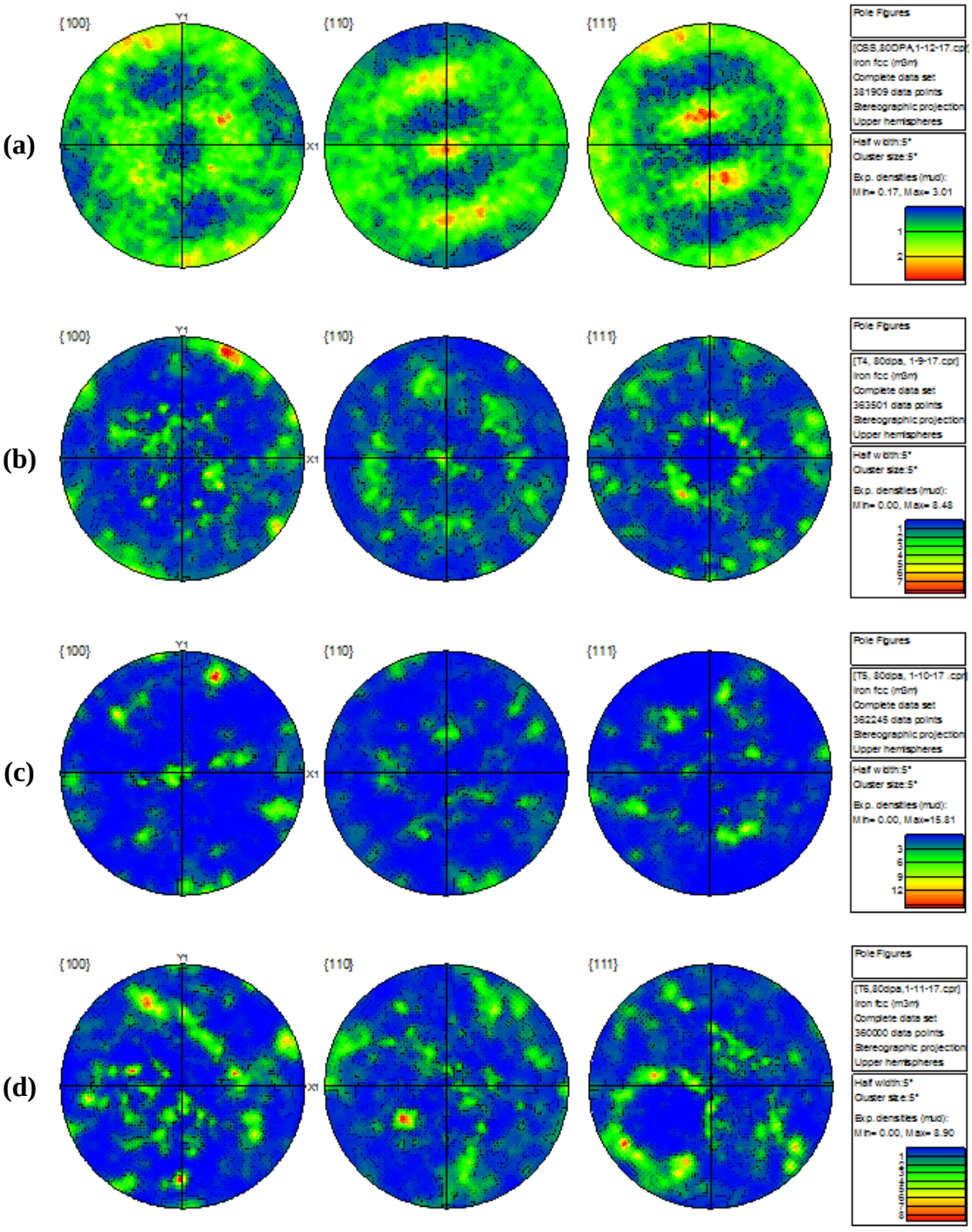

Figure 250: EBSD Stereographic Projection Pole Figures of 316L Stainless Steel (a) Conventionally Manufactured, (b) Vertical LAM, (c) Horizontal LAM, and (d) 45° LAM Irradiated to 80 dpa

A.5 Electron Backscatter Diffraction of Unirradiated ODS Steel

For completeness, EBSD was performed in the ODS samples as well. The grain boundary and grain aspect ratio images and associated histograms are shown in Figure 251 - Figure 253. The grain slope orientation maps of the austenite phase of the additively manufactured ODS samples are shown in Figure 254. The EBSD analysis of the ODS steel samples incorporated indexing of both austenitic and yttria phases. On the scale measured, individual yttria dispersoids were far too small to see individually; however, their diffraction pattern was easily distinguishable. This provides a unique method of viewing the dispersoid distribution on a large scale. As a result, large concentrations of dispersoids appear as spots on the images. This makes determining certain crystallographic features impossible, such as number of neighboring grains, since the software considers dispersoids to be grains within the austenite matrix. Any data provided (such as grain size, grain aspect ratio, etc.) applies only to the austenite matrix unless otherwise specified, though this assumption may also contain significant error if dispersoids have preferentially migrated to austenite grain boundaries. Many EBSD maps of the ODS steel samples appear to have discolored features resulting from the yttria features which were excluded from post-processing. This analysis suggests that standard EBSD methods for determining grain size and other microstructural characteristics of alloys may be insufficient for characterization of ODS alloys produced by LAM.

The unirradiated grain sizes and GARs of the austenitic phase (i.e. excluding yttria agglomerates) of the LAM ODS steel are provided in Table 21. The number of

neighboring grains is not provided for the ODS steel samples in Table 21 since yttria agglomerates were erroneously indexed as individual small grains. Previous research with Fe-Cr-Al ferritic ODS prepared by mechanical alloying and hot extrusion suggest that the size distribution of dispersoid precipitates is directly proportional to grain size, and higher process energy input correlates to higher relative amount of dispersoid precipitates [221]. Furthermore, and perhaps most importantly, these images show that the dispersoid density varies from grain to grain. Since the beneficial properties of ODS steels are strongly dependent upon the homogeneity of the distribution of the dispersoids, these images suggest that the LAM ODS manufacturing process parameters need further optimization in order to obtain a more homogeneous dispersoid distribution.

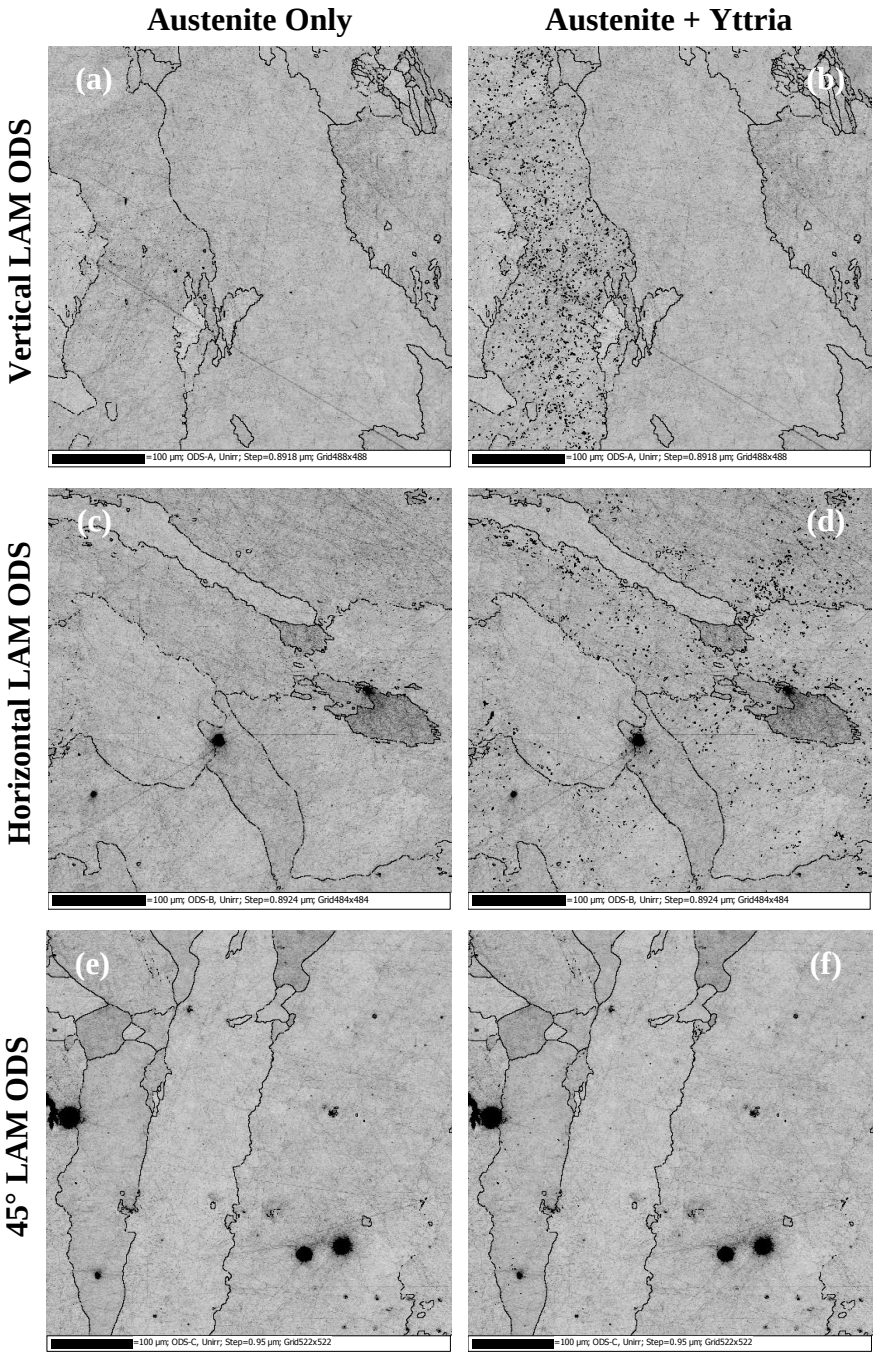

Figure 251: EBSD Grain Boundary Maps with Band Contrast of Unirradiated (a) Vertical LAM ODS with Austenite Only, (b) Vertical LAM ODS with Austenite and Yttria, (c) Horizontal LAM ODS with Austenite Only, (d) Horizontal LAM ODS with Austenite and Yttria, (e) 45° LAM ODS with Austenite Only, and (f) 45° LAM ODS with Austenite and Yttria

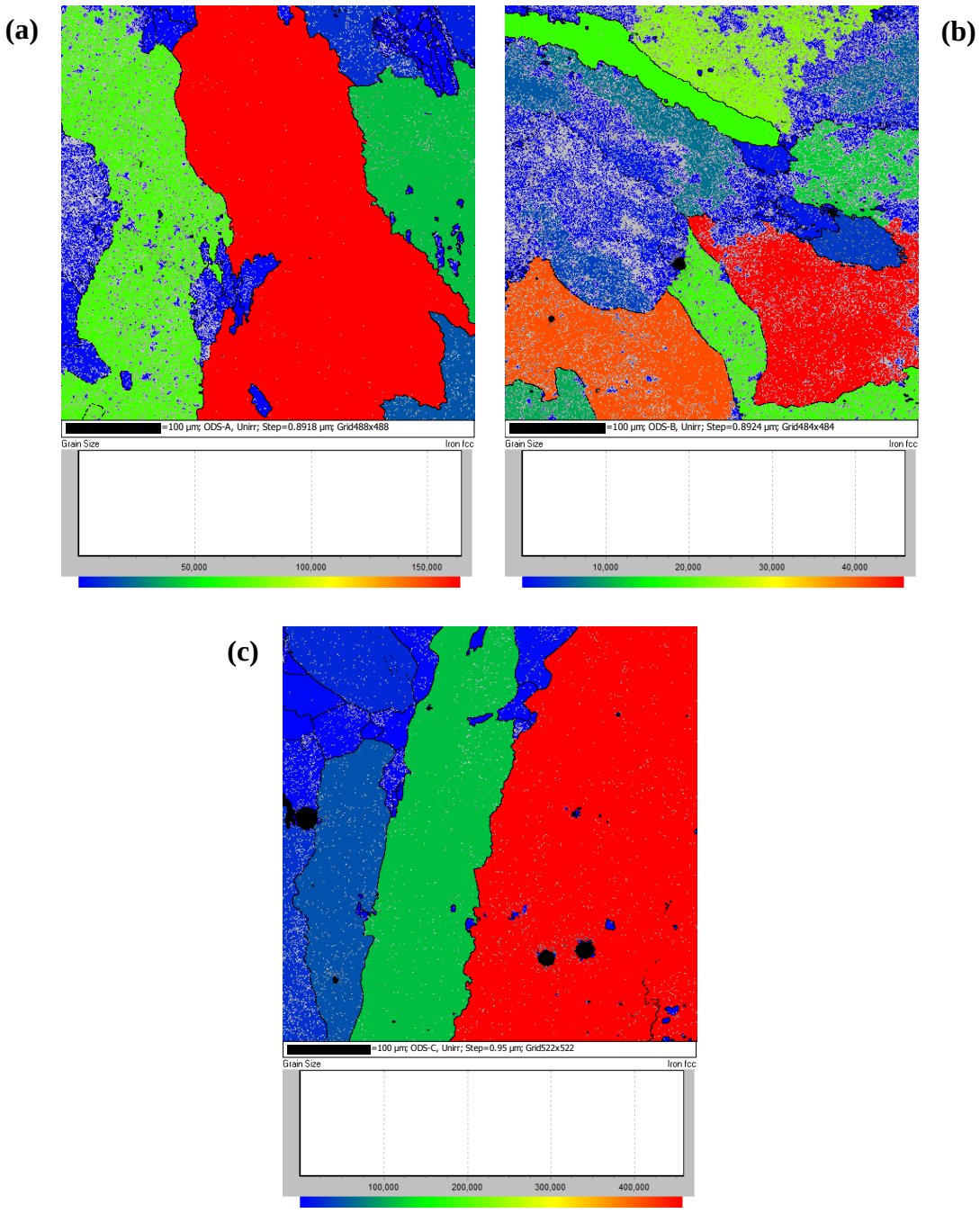

Figure 252: EBSD Grain Size Maps of Unirradiated ODS (a) Vertical LAM, (b) Horizontal LAM, and (c) 45° LAM (Austenite Phase Only)

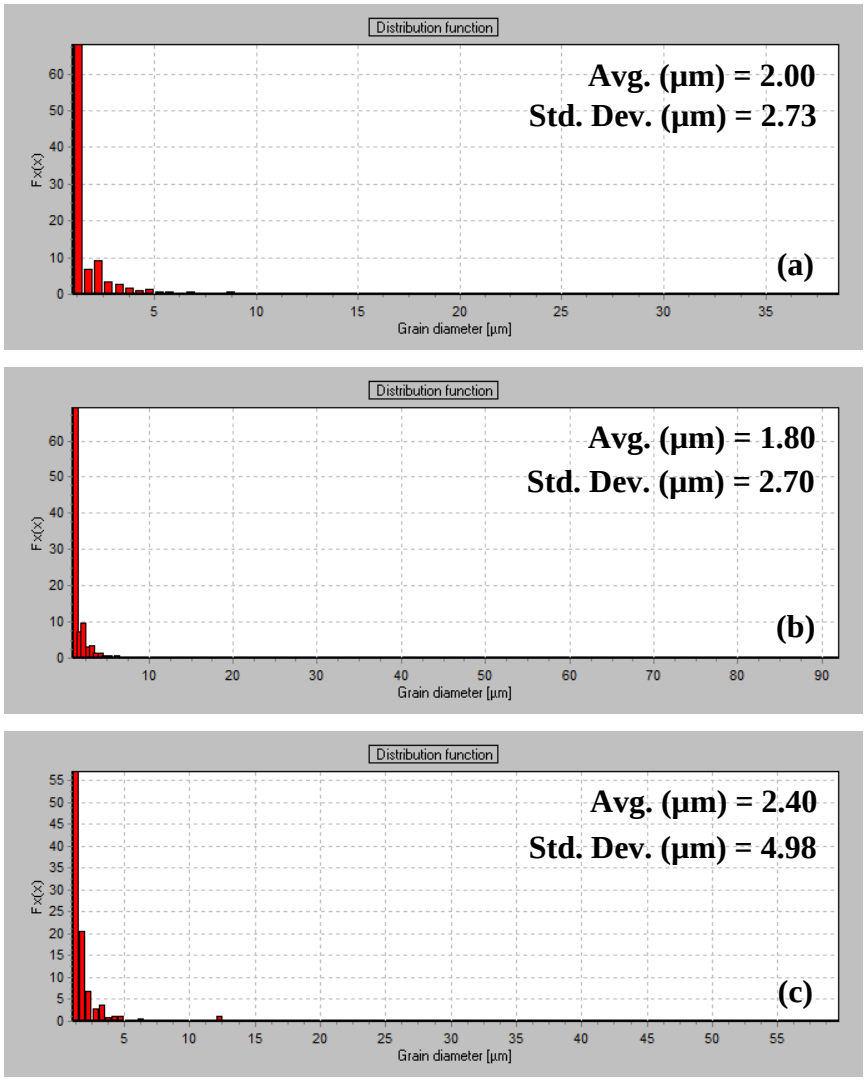

Figure 253: Grain Size Distribution Histograms of Unirradiated ODS Steel (a) Vertical LAM, (b) Horizontal LAM, and (c) 45° LAM

Table 21: Summary of Grain Sizes and Aspect Ratios of ODS Steel Vertical LAM, Horizontal LAM, and 45° LAM

Parameter	Vertical LAM	Horizontal LAM	45° LAM
Grain Size (μm)	2.01	1.80	2.40
GAR	1.8	1.8	1.8

Euler maps of unirradiated LAM ODS are shown in Figure 255 - Figure 257. As expected, images are grainy and unclear due to incorrect indexing associated with the yttria phase. Cubic RF maps for LAM ODS samples are shown in Figure 258. CSL boundary maps could not be generated due to the uncertainty of grain boundary identification due to the yttria dispersoid phase. Stereographic projection pole figures, inverse pole figures, residual strain maps, and Taylor factor histograms/maps are shown in Figure 259 - Figure 263.

The texture in the Inconel 600 and 316L LAM is not observed in the LAM ODS specimens, possibly due to (a) LAM build protocol which had not been optimized to the same standard as for the Inconel 600 or 316L, (b) insufficient statistics due to a small scan area, (c) a variation in texture due to the presence of the dispersoids, or (d) incorrect indexing due to the yttria phase.

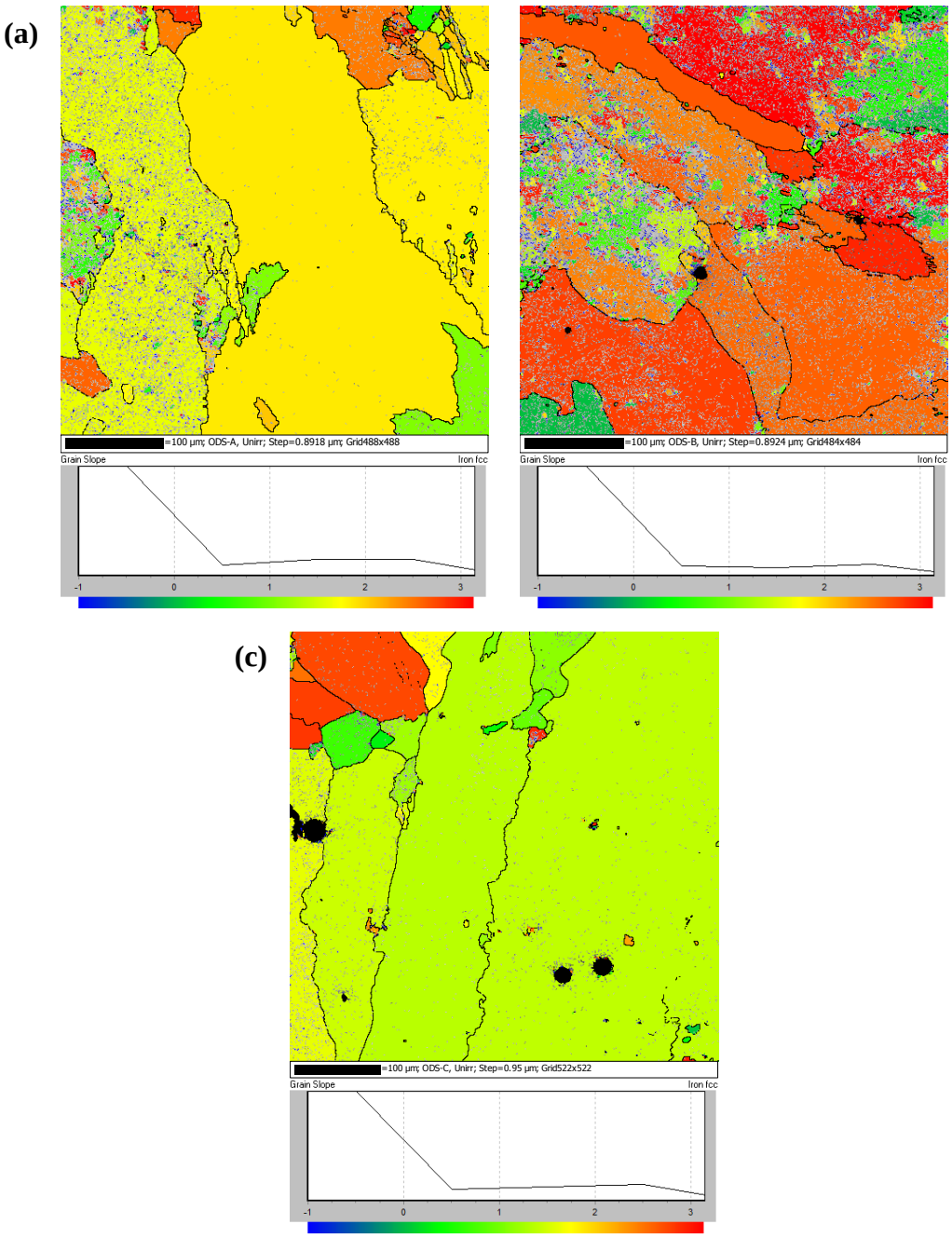

Figure 254: EBSD Grain Slope Orientation for Austenite Phase of Unirradiated (a) Vertical LAM ODS, (b) Horizontal LAM ODS, and (c) 45° LAM ODS

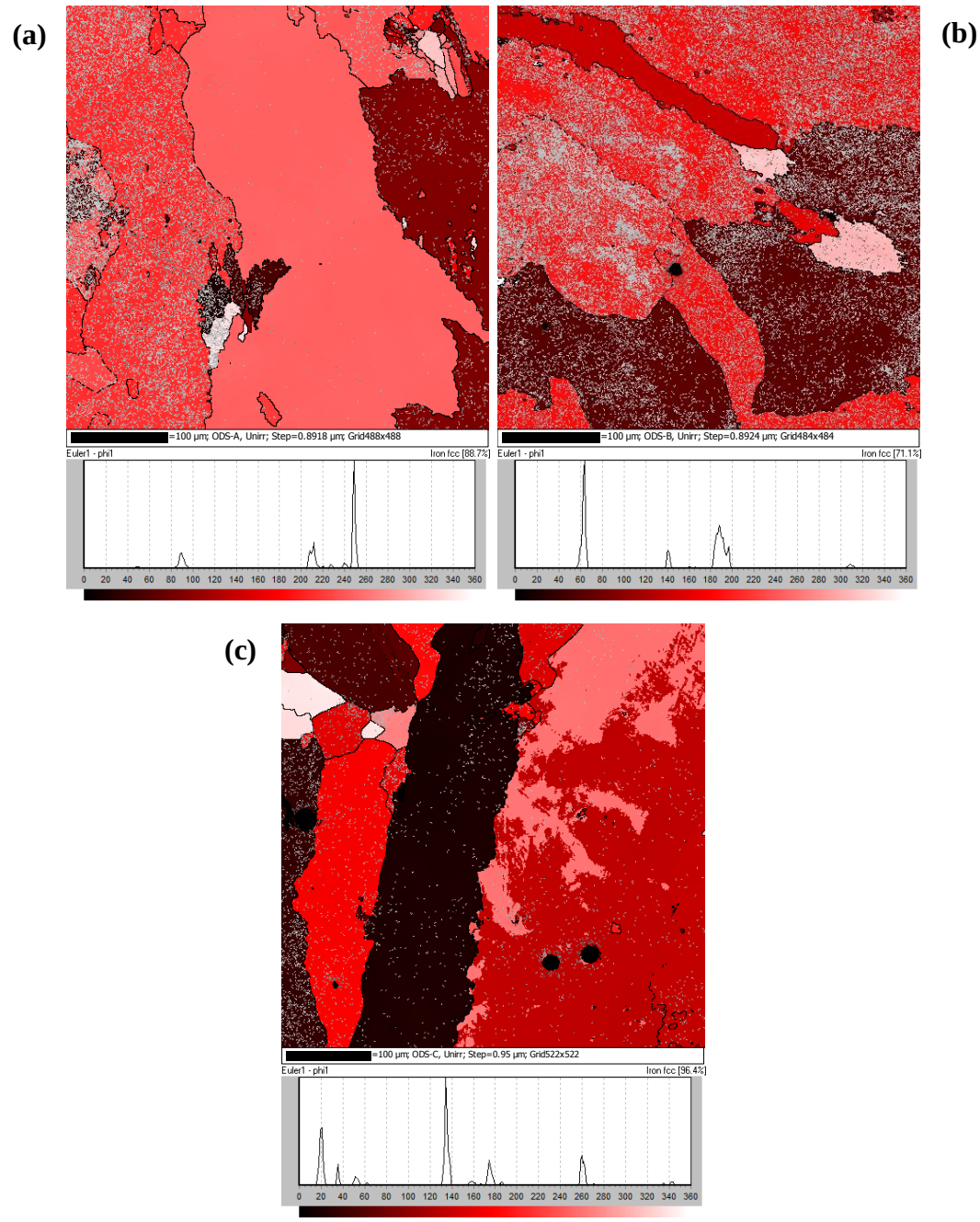

Figure 255: EBSD Euler Maps of φ_1 for Unirradiated ODS Steel (a) Vertical LAM, (b) Horizontal LAM, and (c) 45° LAM (Austenite Only)

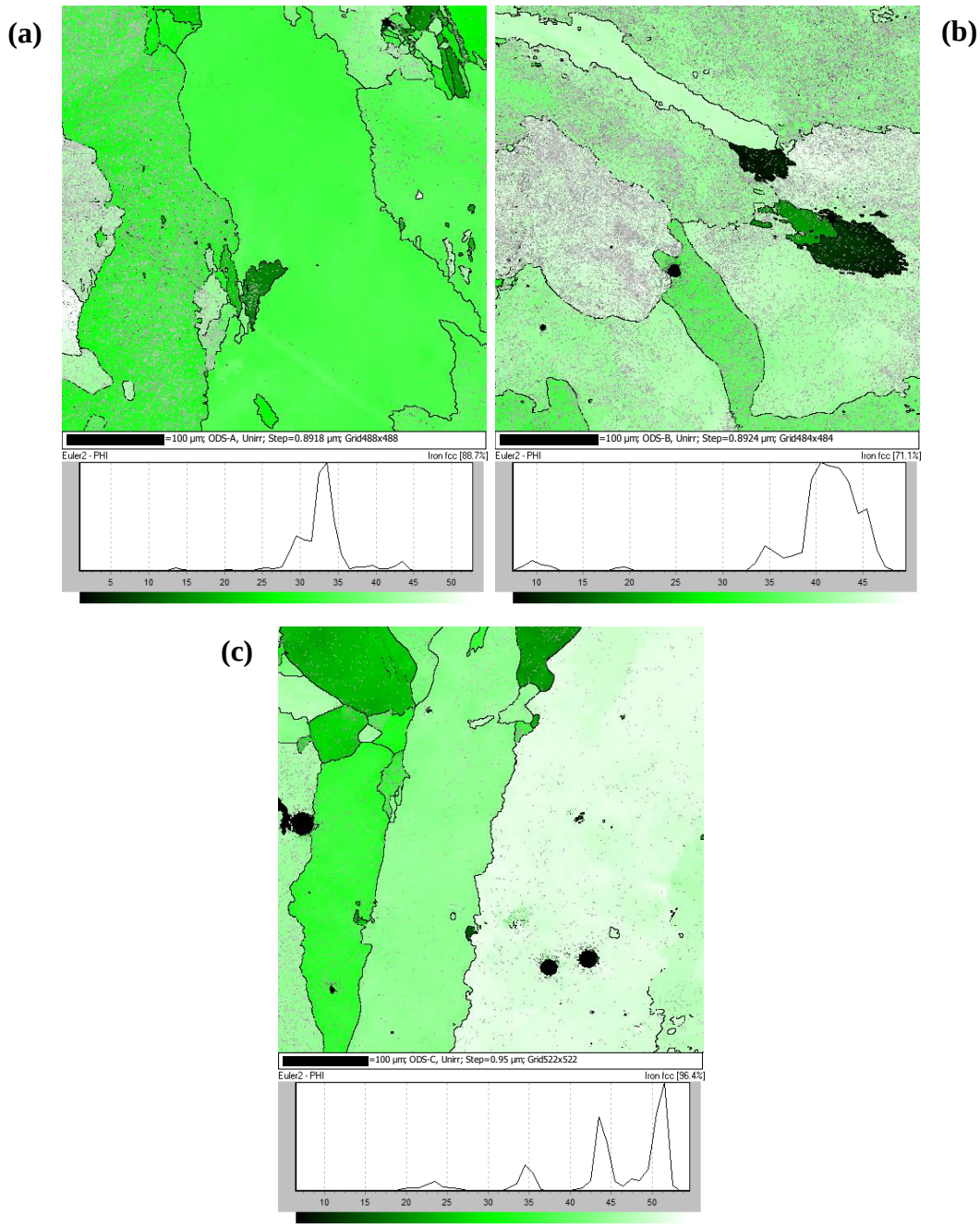

Figure 256: EBSD Euler Maps of Φ for Unirradiated ODS Steel (a) Vertical LAM, (b) Horizontal LAM, and (c) 45° LAM (Austenite Only)

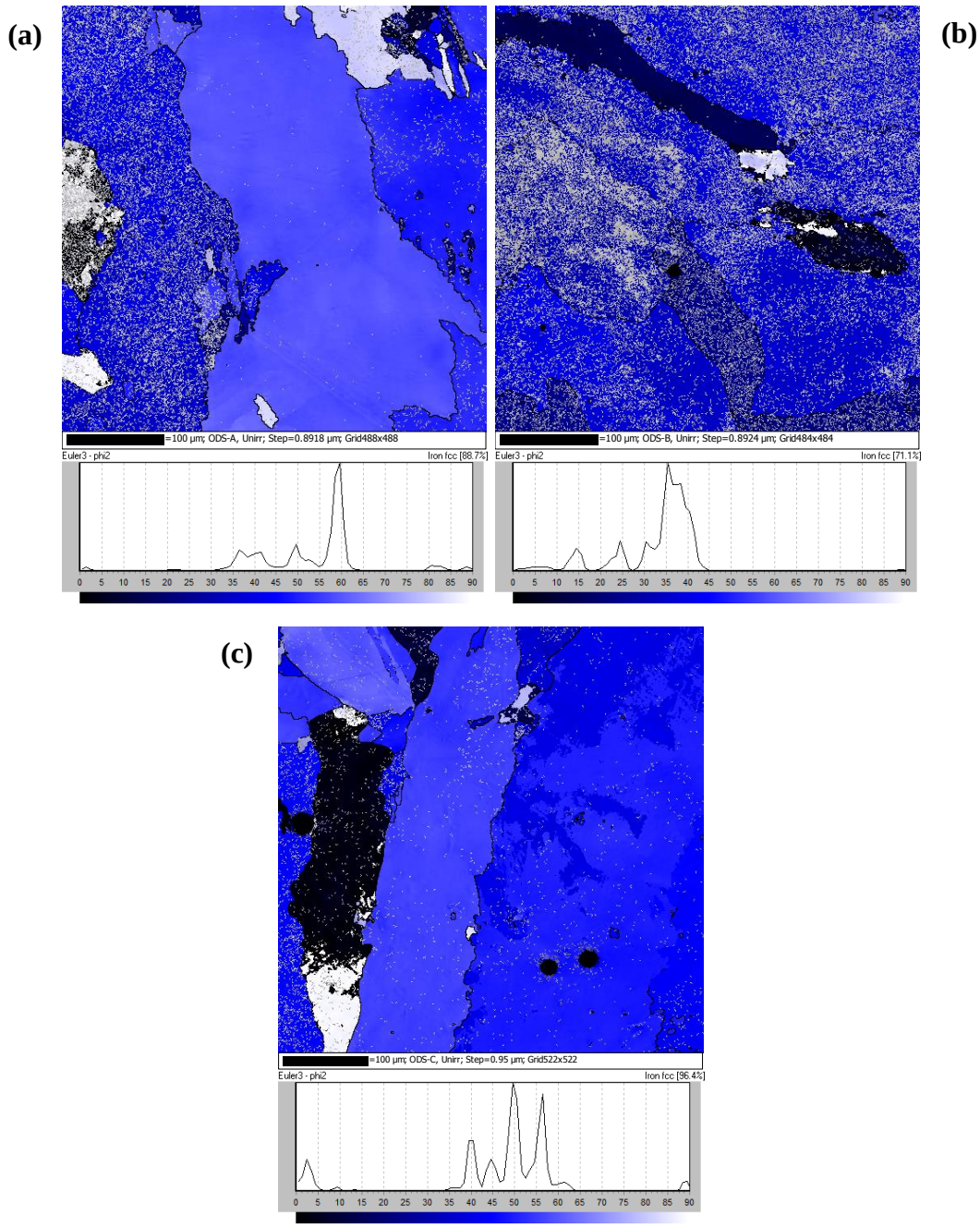

Figure 257: EBSD Euler Maps of φ_2 for Unirradiated ODS Steel (a) Vertical LAM, (b) Horizontal LAM, and (c) 45° LAM (Austenite Only)

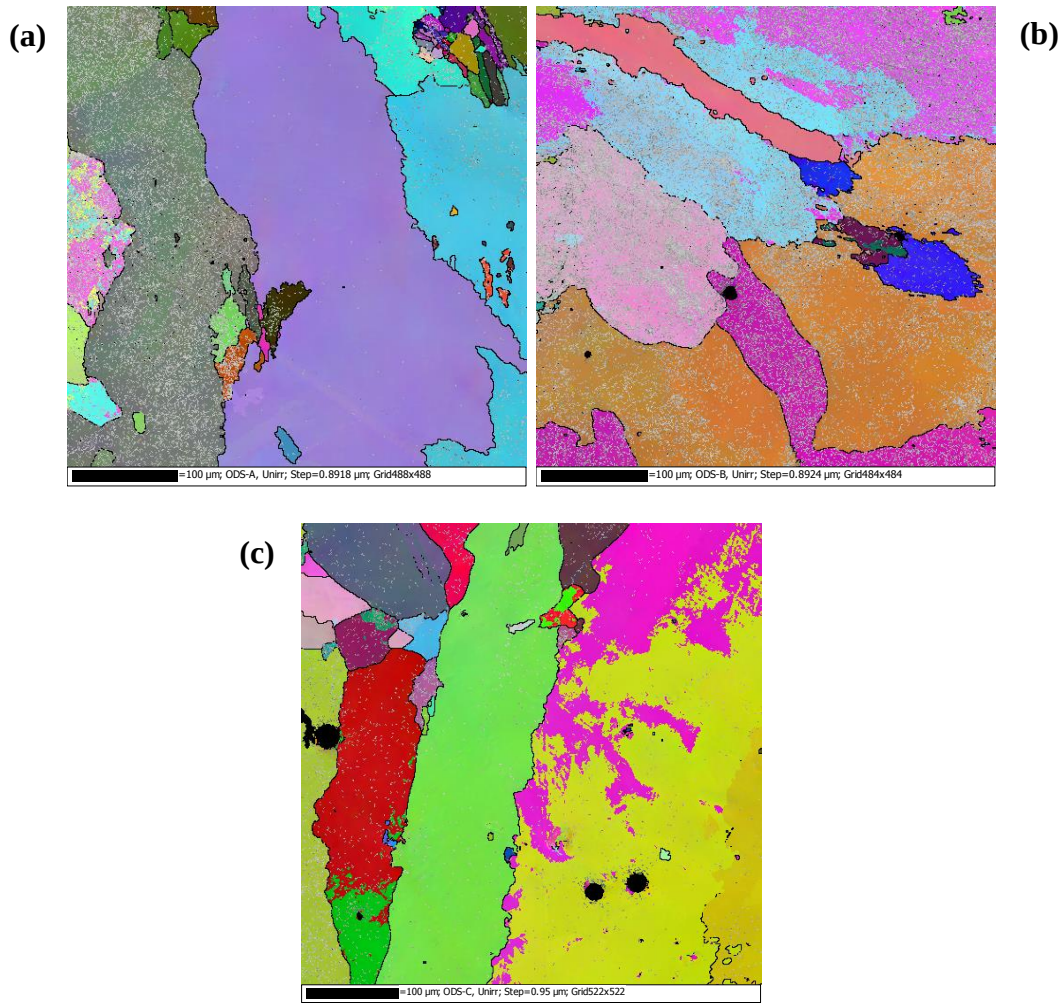

Figure 258: EBSD Cubic Rodrigues-Frank Maps with Respect to (0°, 0°, 0°) for Unirradiated ODS Steel (a) Vertical LAM, (b) Horizontal LAM, and (c) 45° LAM

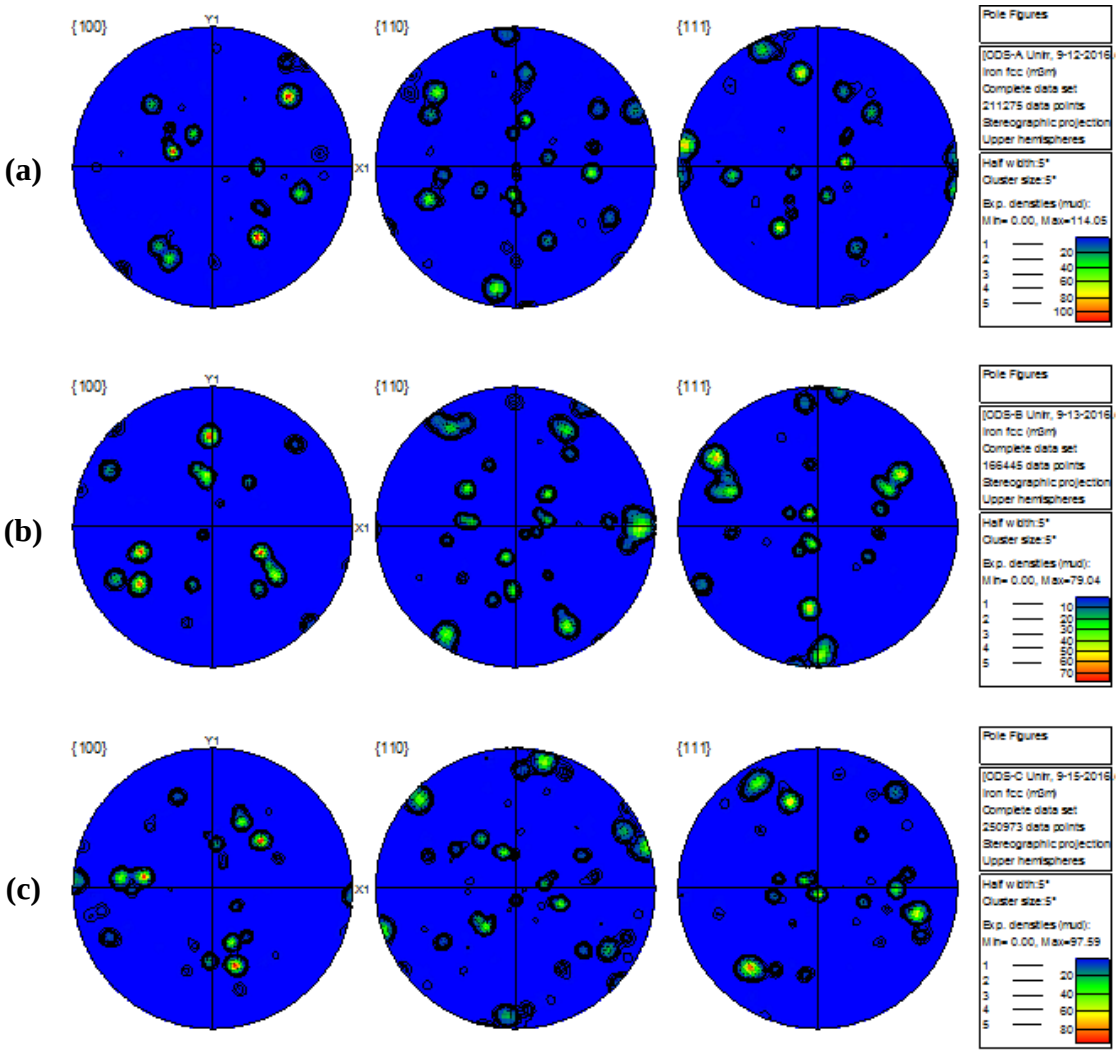

Figure 259: EBSD Stereographic Projection Pole Figures of Unirradiated ODS Steel (a) Vertical LAM, (b) Horizontal LAM, and (c) 45° LAM

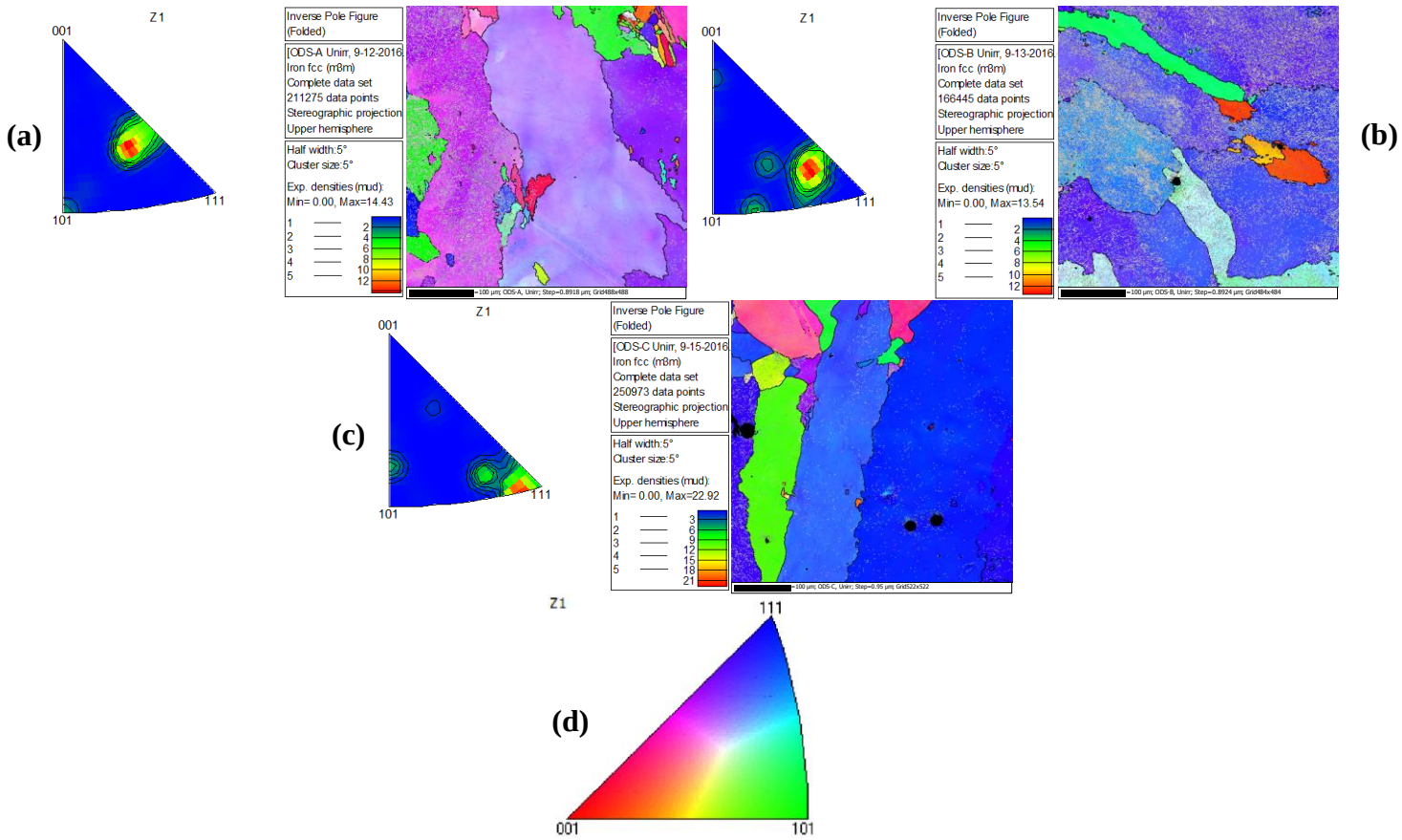

Figure 260: EBSD Stereographic Projection IPFs and IPF Maps for Unirradiated ODS Steel (a) Vertical LAM, (b) Horizontal LAM, (c) 45° LAM, and (d) IPF Map Legend

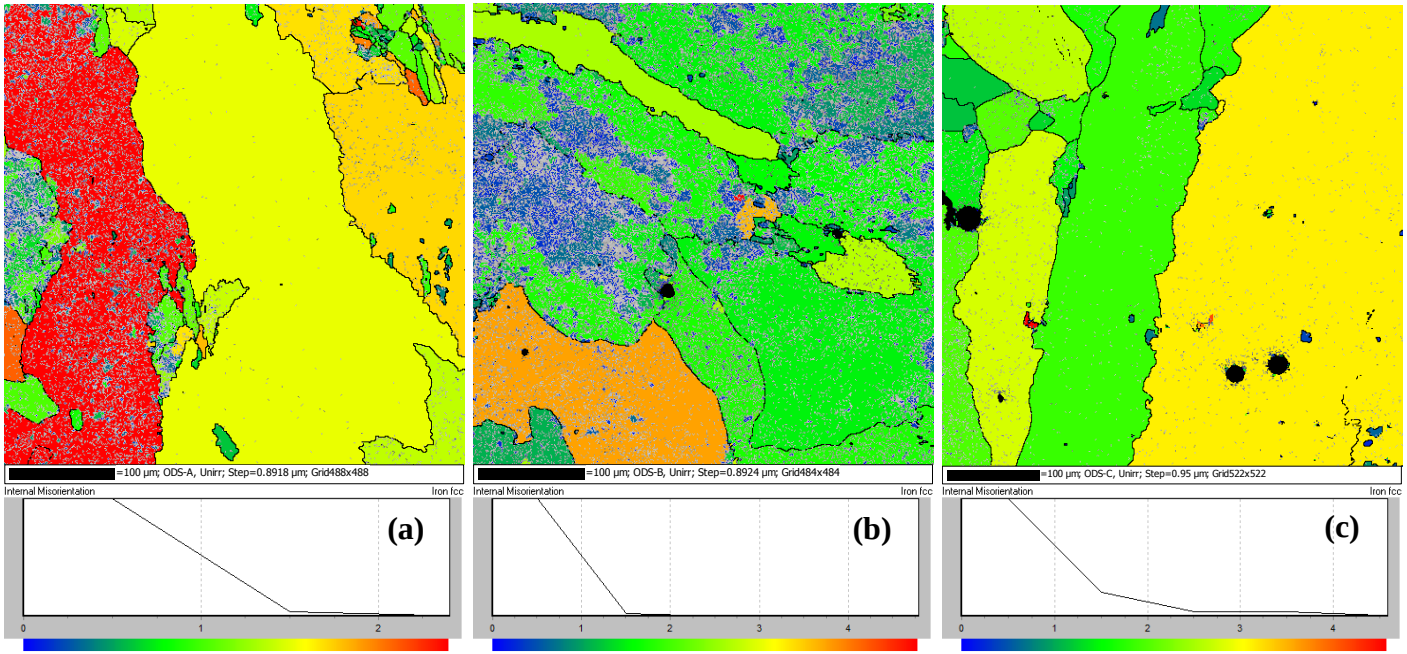

Figure 261: EBSD Misorientation Maps of Unirradiated ODS Steel (a) Vertical LAM, (b) Horizontal LAM, and (c) 45° LAM

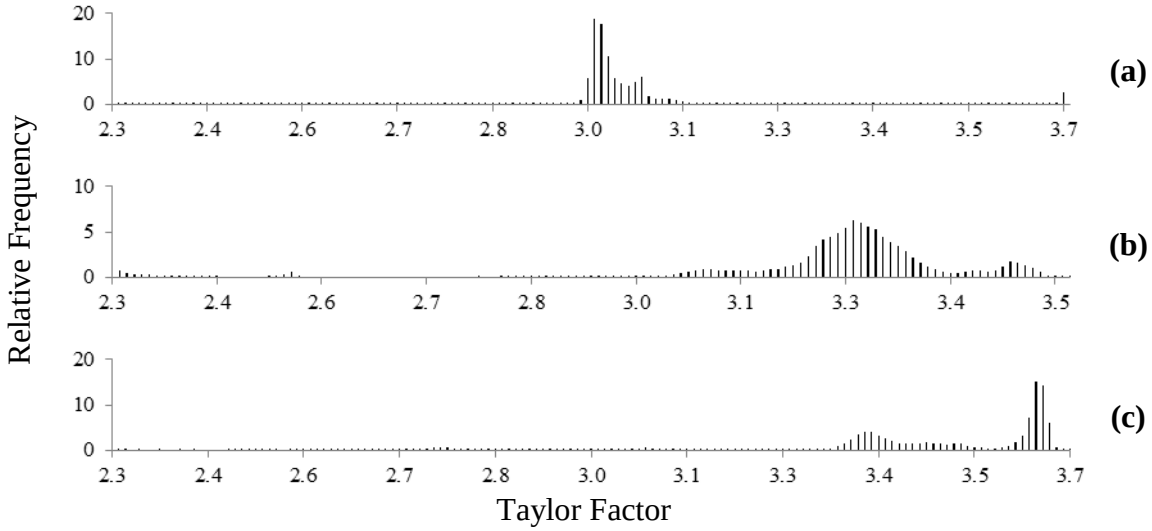

Figure 262: Taylor Factor Histograms of Unirradiated ODS Steel (a) Vertical LAM, (b) Horizontal LAM, and (c) 45° LAM (Austenite Only)

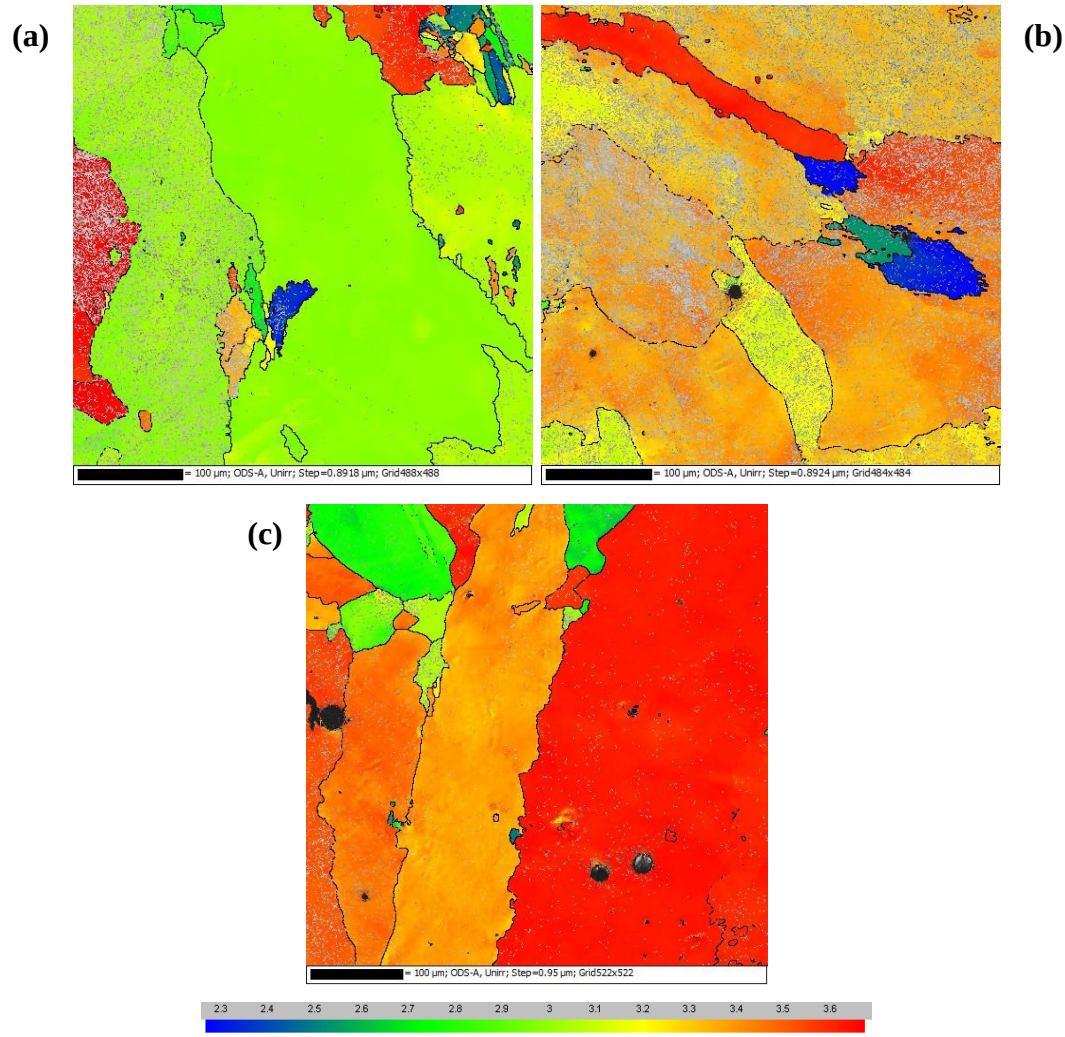

Figure 263: Taylor Factor Maps of Unirradiated ODS Steel (a) Vertical LAM, (b) Horizontal LAM, and (c) 45° LAM

A.6 Metallurgical Test Reports of Conventionally Manufactured Controls

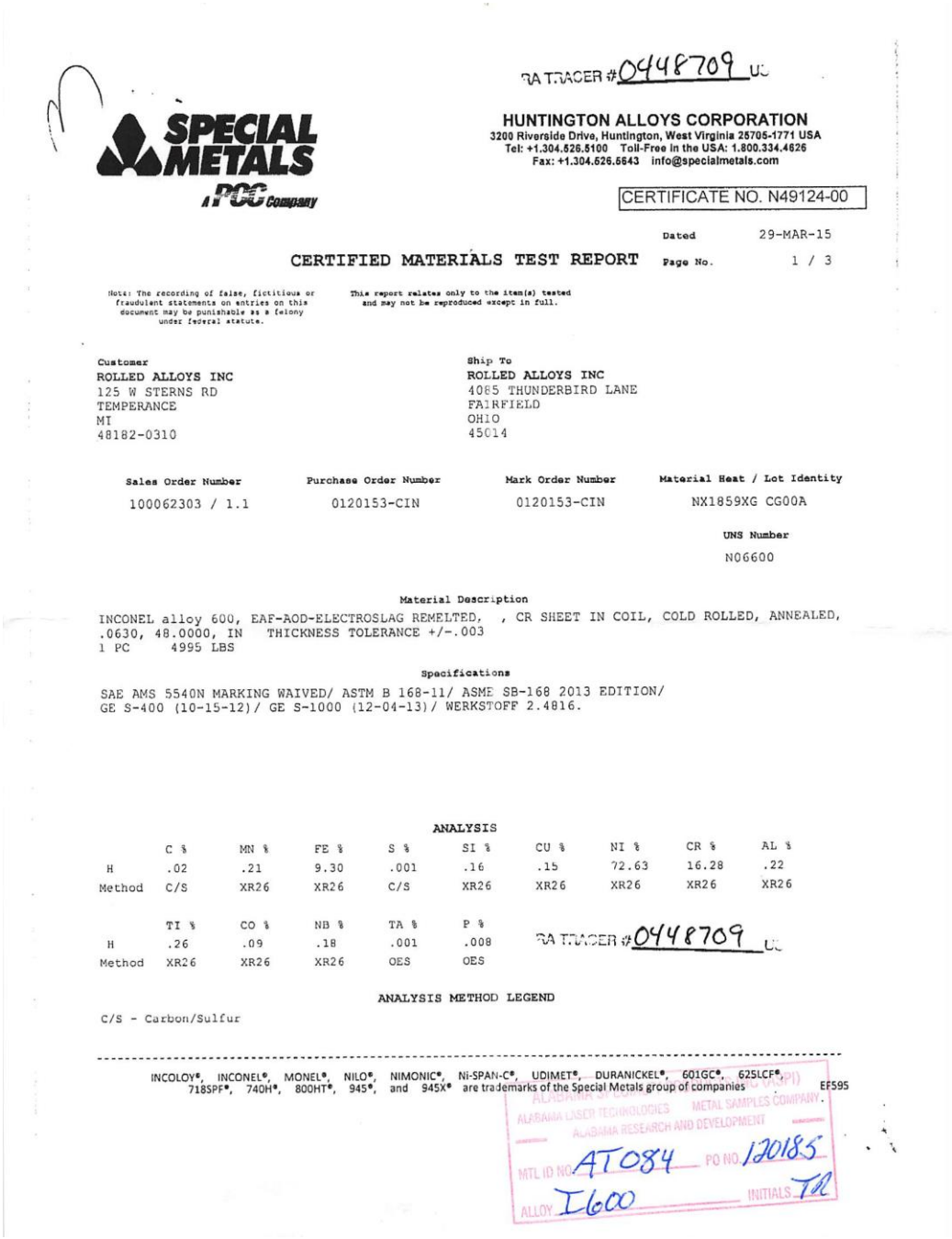

RA TRACER #0448709 UC

SPECIAL METALS
PCC Company

HUNTINGTON ALLOYS CORPORATION
3200 Riverside Drive, Huntington, West Virginia 25705-1771 USA
Tel: +1.304.526.5100 Toll-Free in the USA: 1.800.334.4626
Fax: +1.304.526.5643 info@specialmetals.com

CERTIFICATE NO. N49124-00

Dated 29-MAR-15

CERTIFIED MATERIALS TEST REPORT Page No. 1 / 3

Note: The recording of false, fictitious or fraudulent statements on entries on this document may be punishable as a felony under federal statute.

This report relates only to the item(s) tested and may not be reproduced except in full.

Customer
ROLLED ALLOYS INC
125 W STERNS RD
TEMPERANCE
MI
48182-0310

Ship To
ROLLED ALLOYS INC
4085 THUNDERBIRD LANE
FAIRFIELD
OHIO
45014

Sales Order Number	Purchase Order Number	Mark Order Number	Material Heat / Lot Identity
100062303 / 1.1	0120153-CIN	0120153-CIN	NX1859XG CG00A

UNS Number
N06600

Material Description
INCONEL alloy 600, EAF-AOD-ELECTROSLAG REMELTED, , CR SHEET IN COIL, COLD ROLLED, ANNEALED, .0630, 48.0000, IN THICKNESS TOLERANCE +/-.003
1 PC 4995 LBS

Specifications
SAE AMS 5540N MARKING WAIVED/ ASTM B 168-11/ ASME SB-168 2013 EDITION/ GE S-400 (10-15-12)/ GE S-1000 (12-04-13)/ WERKSTOFF 2.4816.

ANALYSIS

	C %	MN %	FE %	S %	SI %	CU %	NI %	CR %	AL %
H	.02	.21	9.30	.001	.16	.15	72.63	16.28	.22
Method	C/S	XR26	XR26	C/S	XR26	XR26	XR26	XR26	XR26

	TI %	CO %	NB %	TA %	P %
H	.26	.09	.18	.001	.008
Method	XR26	XR26	XR26	OES	OES

RA TRACER #0448709 UC

ANALYSIS METHOD LEGEND
C/S - Carbon/Sulfur

INCOLOY®, INCONEL®, MONEL®, NILO®, NIMONIC®, Ni-SPAN-C®, UDIMET®, DURANICKEL®, 601GC®, 625LCF®, 718SPF®, 740H®, 800HT®, 945®, and 945X® are trademarks of the Special Metals group of companies. EF595

ALABAMA LASER TECHNOLOGIES METAL SAMPLES COMPANY
ALABAMA RESEARCH AND DEVELOPMENT
MTL ID NO. AT084 PO NO. 120185
ALLOY I600 INITIALS TR

Figure 264: Metallurgical Test Report for Conventionally Manufactured Inconel 600, Page 1

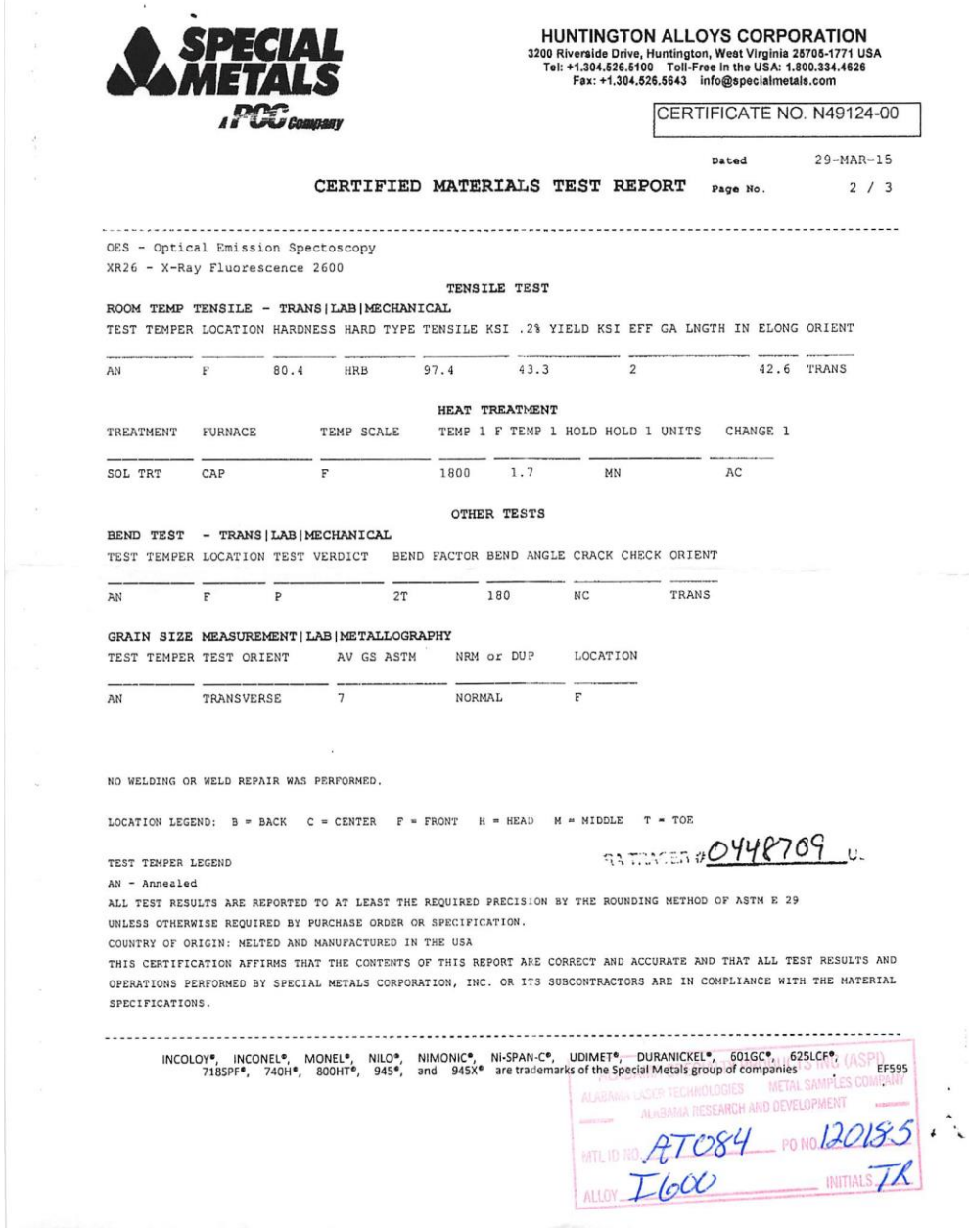

HUNTINGTON ALLOYS CORPORATION
3200 Riverside Drive, Huntington, West Virginia 25705-1771 USA
Tel: +1.304.526.5100 Toll-Free in the USA: 1.800.334.4626
Fax: +1.304.526.5643 info@specialmetals.com

CERTIFICATE NO. N49124-00

Dated 29-MAR-15

CERTIFIED MATERIALS TEST REPORT Page No. 2 / 3

OES - Optical Emission Spectoscopy
XR26 - X-Ray Fluorescence 2600

TENSILE TEST

ROOM TEMP TENSILE - TRANS|LAB|MECHANICAL

TEST TEMPER	LOCATION	HARDNESS	HARD TYPE	TENSILE KSI	.2% YIELD KSI	EFF GA LNGTH IN	ELONG	ORIENT
AN	F	80.4	HRB	97.4	43.3	2	42.6	TRANS

HEAT TREATMENT

TREATMENT	FURNACE	TEMP SCALE	TEMP 1 F	TEMP 1 HOLD	HOLD 1 UNITS	CHANGE 1
SOL TRT	CAP	F	1800	1.7	MN	AC

OTHER TESTS

BEND TEST - TRANS|LAB|MECHANICAL

TEST TEMPER	LOCATION	TEST VERDICT	BEND FACTOR	BEND ANGLE	CRACK CHECK	ORIENT
AN	F	P	2T	180	NC	TRANS

GRAIN SIZE MEASUREMENT|LAB|METALLOGRAPHY

TEST TEMPER	TEST ORIENT	AV GS ASTM	NRM or DUP	LOCATION
AN	TRANSVERSE	7	NORMAL	F

NO WELDING OR WELD REPAIR WAS PERFORMED.

LOCATION LEGEND: B = BACK C = CENTER F = FRONT H = HEAD M = MIDDLE T = TOE

TEST TEMPER LEGEND
AN - Annealed
ALL TEST RESULTS ARE REPORTED TO AT LEAST THE REQUIRED PRECISION BY THE ROUNDING METHOD OF ASTM E 29
UNLESS OTHERWISE REQUIRED BY PURCHASE ORDER OR SPECIFICATION.
COUNTRY OF ORIGIN: MELTED AND MANUFACTURED IN THE USA
THIS CERTIFICATION AFFIRMS THAT THE CONTENTS OF THIS REPORT ARE CORRECT AND ACCURATE AND THAT ALL TEST RESULTS AND OPERATIONS PERFORMED BY SPECIAL METALS CORPORATION, INC. OR ITS SUBCONTRACTORS ARE IN COMPLIANCE WITH THE MATERIAL SPECIFICATIONS.

INCOLOY®, INCONEL®, MONEL®, NILO®, NIMONIC®, Ni-SPAN-C®, UDIMET®, DURANICKEL®, 601GC®, 625LCF®, 718SPF®, 740H®, 800HT®, 945®, and 945X® are trademarks of the Special Metals group of companies EF595

Figure 265: Metallurgical Test Report for Conventionally Manufactured Inconel 600, Page 2

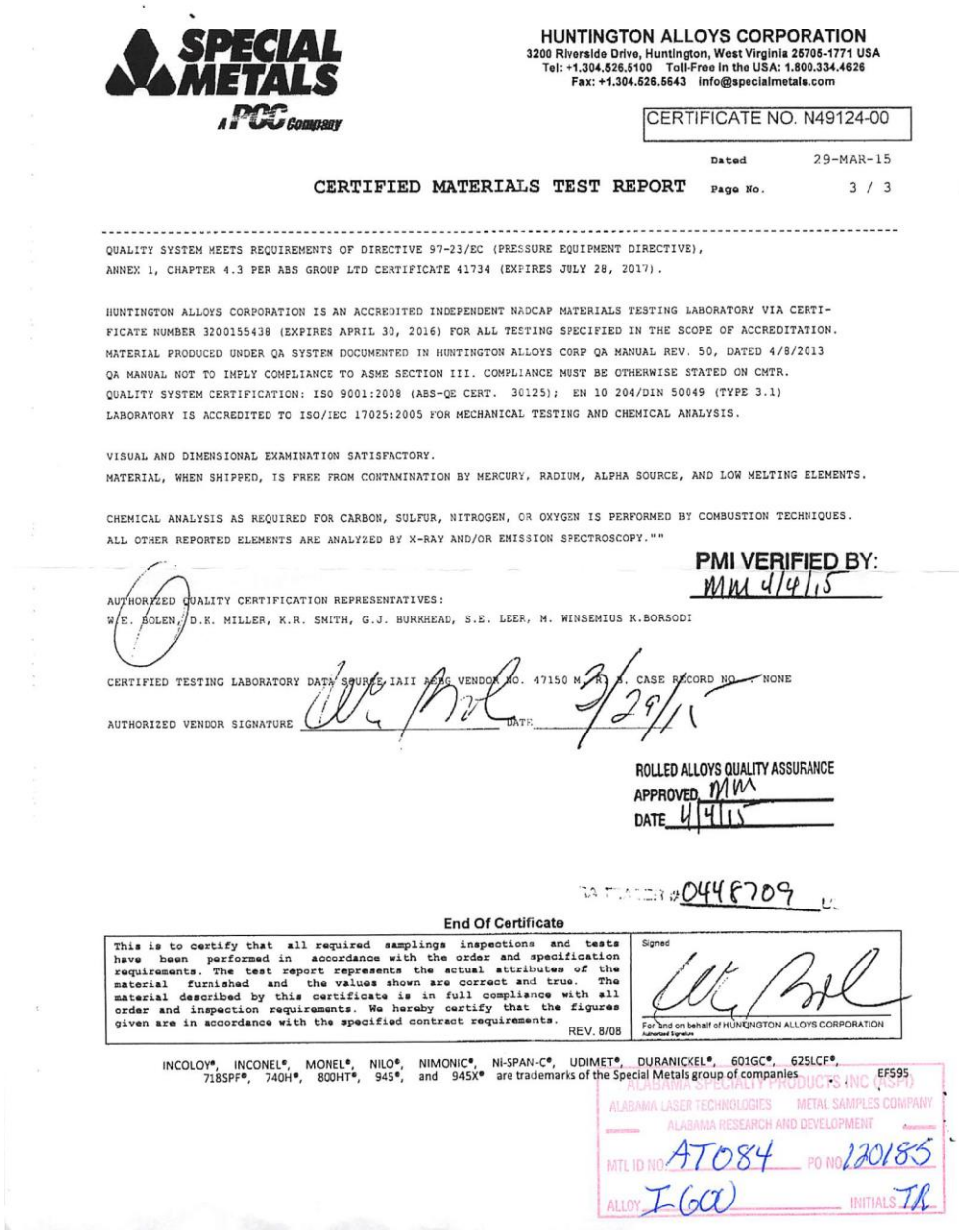

SPECIAL METALS
A PCC Company

HUNTINGTON ALLOYS CORPORATION
3200 Riverside Drive, Huntington, West Virginia 25705-1771 USA
Tel: +1.304.526.5100 Toll-Free in the USA: 1.800.334.4626
Fax: +1.304.526.5643 info@specialmetals.com

CERTIFICATE NO. N49124-00

Dated 29-MAR-15

CERTIFIED MATERIALS TEST REPORT Page No. 3 / 3

QUALITY SYSTEM MEETS REQUIREMENTS OF DIRECTIVE 97-23/EC (PRESSURE EQUIPMENT DIRECTIVE), ANNEX 1, CHAPTER 4.3 PER ABS GROUP LTD CERTIFICATE 41734 (EXPIRES JULY 28, 2017).

HUNTINGTON ALLOYS CORPORATION IS AN ACCREDITED INDEPENDENT NADCAP MATERIALS TESTING LABORATORY VIA CERTIFICATE NUMBER 3200155438 (EXPIRES APRIL 30, 2016) FOR ALL TESTING SPECIFIED IN THE SCOPE OF ACCREDITATION. MATERIAL PRODUCED UNDER QA SYSTEM DOCUMENTED IN HUNTINGTON ALLOYS CORP QA MANUAL REV. 50, DATED 4/8/2013 QA MANUAL NOT TO IMPLY COMPLIANCE TO ASME SECTION III. COMPLIANCE MUST BE OTHERWISE STATED ON CMTR. QUALITY SYSTEM CERTIFICATION: ISO 9001:2008 (ABS-QE CERT. 30125); EN 10 204/DIN 50049 (TYPE 3.1) LABORATORY IS ACCREDITED TO ISO/IEC 17025:2005 FOR MECHANICAL TESTING AND CHEMICAL ANALYSIS.

VISUAL AND DIMENSIONAL EXAMINATION SATISFACTORY.
MATERIAL, WHEN SHIPPED, IS FREE FROM CONTAMINATION BY MERCURY, RADIUM, ALPHA SOURCE, AND LOW MELTING ELEMENTS.

CHEMICAL ANALYSIS AS REQUIRED FOR CARBON, SULFUR, NITROGEN, OR OXYGEN IS PERFORMED BY COMBUSTION TECHNIQUES. ALL OTHER REPORTED ELEMENTS ARE ANALYZED BY X-RAY AND/OR EMISSION SPECTROSCOPY.""

PMI VERIFIED BY: MM 4/4/15

AUTHORIZED QUALITY CERTIFICATION REPRESENTATIVES:
W.E. BOLEN, D.K. MILLER, K.R. SMITH, G.J. BURKHEAD, S.E. LEER, M. WINSEMIUS K.BORSODI

CERTIFIED TESTING LABORATORY DATA SOURCE IAII AERG VENDOR NO. 47150 M, R, N. CASE RECORD NO. : NONE

AUTHORIZED VENDOR SIGNATURE _____ DATE 3/29/15

ROLLED ALLOYS QUALITY ASSURANCE
APPROVED MM
DATE 4/4/15

DATA PACKET # 0448709

End Of Certificate

This is to certify that all required samplings inspections and tests have been performed in accordance with the order and specification requirements. The test report represents the actual attributes of the material furnished and the values shown are correct and true. The material described by this certificate is in full compliance with all order and inspection requirements. We hereby certify that the figures given are in accordance with the specified contract requirements.
REV. 8/08

Signed
For and on behalf of HUNTINGTON ALLOYS CORPORATION
Authorized Signature

INCOLOY®, INCONEL®, MONEL®, NILO®, NIMONIC®, Ni-SPAN-C®, UDIMET®, DURANICKEL®, 601GC®, 625LCF®, 718SPF®, 740H®, 800HT®, 945®, and 945X® are trademarks of the Special Metals group of companies. EF595

ALABAMA SPECIALTY PRODUCTS, INC (ASPI)
ALABAMA LASER TECHNOLOGIES METAL SAMPLES COMPANY
ALABAMA RESEARCH AND DEVELOPMENT
MTL ID NO AT084 PO NO 120185
ALLOY I-600 INITIALS TR

Figure 266: Metallurgical Test Report for Conventionally Manufactured Inconel 600, Page 3

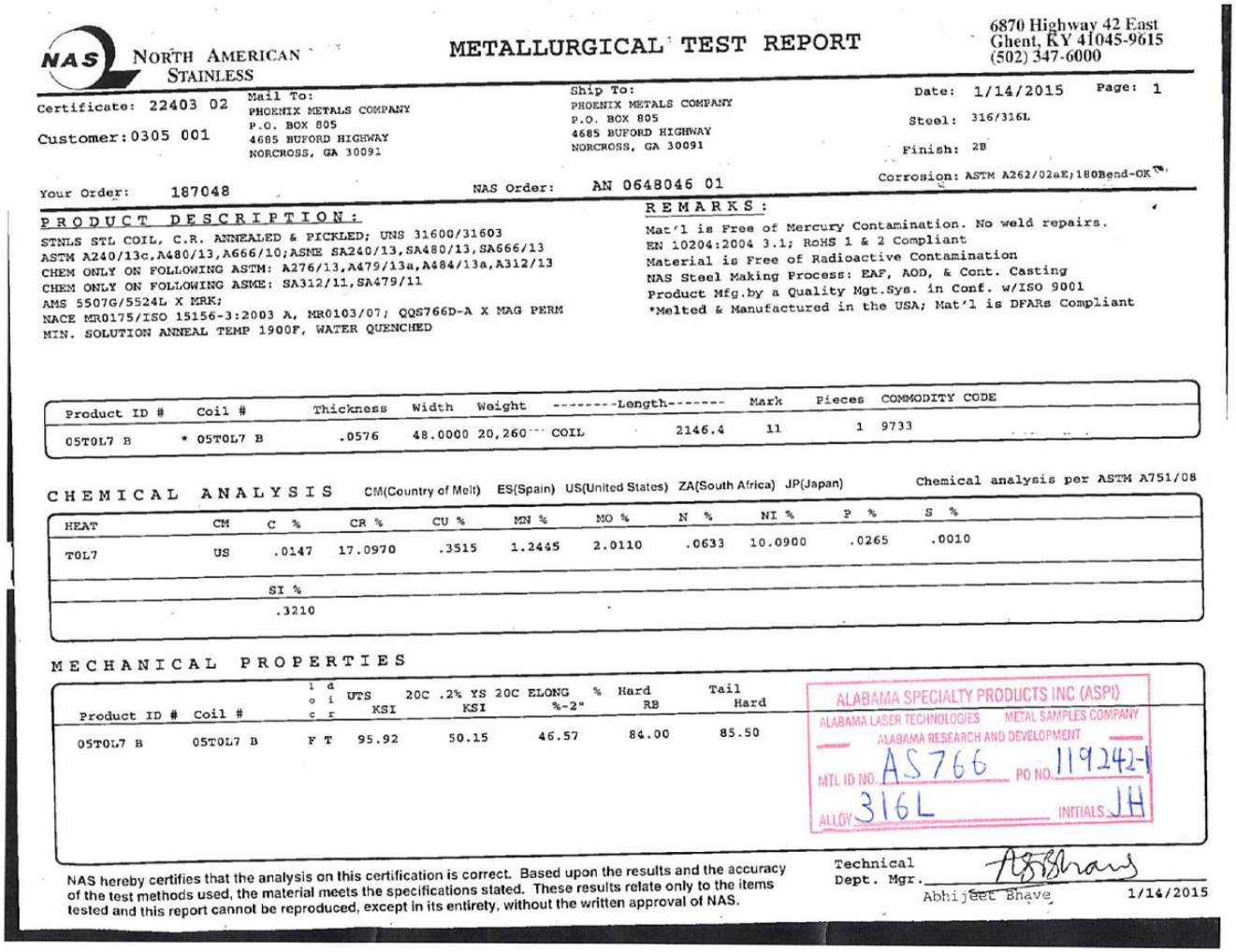

NAS NORTH AMERICAN STAINLESS

METALLURGICAL TEST REPORT

6870 Highway 42 East
Ghent, KY 41045-9615
(502) 347-6000

Certificate: 22403 02
Customer: 0305 001

Mail To:
PHOENIX METALS COMPANY
P.O. BOX 805
4685 BUFORD HIGHWAY
NORCROSS, GA 30091

Ship To:
PHOENIX METALS COMPANY
P.O. BOX 805
4685 BUFORD HIGHWAY
NORCROSS, GA 30091

Date: 1/14/2015 Page: 1
Steel: 316/316L
Finish: 2B
Corrosion: ASTM A262/02aE;180Bend-OK

Your Order: 187048 NAS Order: AN 0648046 01

PRODUCT DESCRIPTION:

STNLS STL COIL, C.R. ANNEALED & PICKLED; UNS 31600/31603
ASTM A240/13c,A480/13,A666/10;ASME SA240/13,SA480/13,SA666/13
CHEM ONLY ON FOLLOWING ASTM: A276/13,A479/13a,A484/13a,A312/13
CHEM ONLY ON FOLLOWING ASME: SA312/11,SA479/11
AMS 5507G/5524L X MRK;
NACE MR0175/ISO 15156-3:2003 A, MR0103/07; QQS766D-A X MAG PERM
MIN. SOLUTION ANNEAL TEMP 1900F, WATER QUENCHED

REMARKS:

Mat'l is Free of Mercury Contamination. No weld repairs.
EN 10204:2004 3.1; RoHS 1 & 2 Compliant
Material is Free of Radioactive Contamination
NAS Steel Making Process: EAF, AOD, & Cont. Casting
Product Mfg.by a Quality Mgt.Sys. in Conf. w/ISO 9001
*Melted & Manufactured in the USA; Mat'l is DFARs Compliant

Product ID #	Coil #	Thickness	Width	Weight	--------Length-------		Mark	Pieces	COMMODITY CODE
05T0L7 B	* 05T0L7 B	.0576	48.0000	20,260	COIL	2146.4	11	1	9733

CHEMICAL ANALYSIS CM(Country of Melt) ES(Spain) US(United States) ZA(South Africa) JP(Japan) Chemical analysis per ASTM A751/08

HEAT	CM	C %	CR %	CU %	MN %	MO %	N %	NI %	P %	S %
T0L7	US	.0147	17.0970	.3515	1.2445	2.0110	.0633	10.0900	.0265	.0010

SI %
.3210

MECHANICAL PROPERTIES

Product ID #	Coil #	Ind Loc	Dir	UTS KSI	20C .2% YS KSI	20C ELONG %-2"	% Hard RB	Tail Hard
05T0L7 B	05T0L7 B	F	T	95.92	50.15	46.57	84.00	85.50

ALABAMA SPECIALTY PRODUCTS INC (ASPI)
ALABAMA LASER TECHNOLOGIES METAL SAMPLES COMPANY
ALABAMA RESEARCH AND DEVELOPMENT
MTL ID NO. AS766 PO NO. 119242-1
ALLOY 316L INITIALS JH

NAS hereby certifies that the analysis on this certification is correct. Based upon the results and the accuracy of the test methods used, the material meets the specifications stated. These results relate only to the items tested and this report cannot be reproduced, except in its entirety, without the written approval of NAS.

Technical Dept. Mgr. Abhijeet Bhave 1/14/2015

Figure 267: Metallurgical Test Report for Conventionally Manufactured 316L Stainless Steel